University of Sydney

Doctoral thesis

Gravitational lensing models as probes of dark matter scenarios

Student: Joseph Allingham
joseph.allingham@sydney.edu.au

Supervisor: Prof. Céline Bœhm
celine.boehm@sydney.edu.au
Co-supervisor: Prof. Mathilde Jauzac
mathilde.jauzac@durham.ac.uk
Secondary supervisor: Prof. Geraint Lewis
geraint.lewis@sydney.edu.au

THE UNIVERSITY OF SYDNEY

A thesis submitted in fulfilment of the requirements for the degree of Doctor of Philosophy
School of Physics, Faculty of Science, The University of Sydney

19 August 2019 – 23 November 2022

Abstract

Although the nature of dark matter remains elusive, it is estimated to compose $\sim 84\%$ of the mass of the Universe. This begs the question of its distribution. Gravitational lensing is a powerful tool for this inquiry, as it is directly sensitive to all massive matter components in cosmological structures. This opens new pathways to study the interplay between dark and ordinary, baryonic matter in clusters of galaxies. While the latter is made of composite objects such as stars ($\sim 10\%$), its vast majority lies under the form of hot gas ($\sim 90\%$). Gauging the correlation between dark matter and baryons in galaxy clusters is fundamental to uncover their physical properties.

In this thesis, I present the lensing analyses of two galaxy clusters MACS J0242 and MACS J0949, using a combination of imaging data from *HST* and DES, together with spectroscopic data from VLT/MUSE. In order to understand the relationship between dark matter and the intra-cluster medium (ICM), the general ICM thermodynamics are calibrated using *XMM-Newton* X-rays observations for a sample of clusters. With these models, I then use the gravitational potential obtained with strong lensing to infer the ICM properties, in the context of dynamically relaxed clusters. This novel technique allows to derive the electron distribution, opposite to the method commonly used, whereby one uses the ICM observations to infer the dark matter content.

Combining this powerful technique with the strong lensing, I apply it to cluster Abell S1063, using the *Hubble* Frontier Fields data. I perform the joint ICM-strong lensing optimisation, with 25 multiply-imaged systems and *Chandra* X-ray observations. The ICM is assumed to trace the large-scale dark matter halo. This hypothesis yields a good quality lens model, in agreement with the lensing-only and ICM-only optimisations. Moreover, this model matches the results established with weak lensing in the outskirts of the cluster, further confirming the method to be valid on large scales. With this new holistic description of galaxy clusters, we show we can derive the ICM density using multi-scale lensing.

This thesis allows to infer the ICM distribution independently from direct measurements, such as X-rays and SZ effect. Through strong lensing and ICM modelling, we propose a more general canvas to describe the gravitational relationship between baryons and dark matter in galaxy clusters. This sets the path to constrain the interactions between these two main components of the Universe.

Statement of originality

I declare the intellectual content of this thesis to be the product of my own work, and that all the assistance received in preparing this thesis and sources have been acknowledged. The owners of the many data set utilised are cited in the thesis. This thesis has not been submitted for any degree or other purposes.

In particular, specific contributions must be pointed out:

- In Chapter 4, the formula of the polytropic temperature distribution with a varying index and its X-COP fit were established by Dominique Eckert. The associated figures are also his own work. In the same Chapter, Sections 4.1 and 4.2 are largely inspired by the drafted article Section 4.3, as it covers the same physical results.
- In Chapter 5, Benjamin Beauchesne modified `Lenstool` so that a joint X-ray and strong lensing optimisation would be possible. I brought my own contributions in collaboration with him to encode my models, but the global canvas to make these possible is his own work. He also extracted and treated the *Chandra* X-ray data. In the same Chapter, Dominique Eckert performed the *XMM-Newton* data treatment.

Joseph Allingham November 23rd, 2022 Signature:

Attesting publication authorship

Chapters 3 and 4 are both shaped as MNRAS articles.

The former has been submitted to MNRAS, and is readily available on arXiv, in an anterior version. This is the joint work of all coauthors: my supervisors Céline Bœhm, Mathilde Jauzac and Geraint Lewis, strong lensing experts David Lagattuta and Guillaume Mahler, X-ray astronomy expert Dominique Eckert, VLT/MUSE data owner Alastair Edge and *XMM-Newton* data owner Stefano Ettori.

The second article (Section 4.3) will be submitted shortly after this thesis. It is the joint effort of the same coauthors as the first article, and of Sunyaev-Zel'dovich effect astronomy expert Matt Hilton.

Acknowledgements

I want to address special thanks to my supervisor Céline Bœhm for more than three years of guidance. She introduced me to the most important concepts in dark matter physics, taught me to take a step back to look at the greater picture, permanently encouraged me to think outside of the box, not to mention she kindly re-read many times my papers. Thank you Mathilde Jauzac for supervising my thesis from the UK, teaching me strong lens modelling – notably how to use `Lenstool` – and carefully proof-reading my papers and suggesting pertinent modifications. Thank you Geraint Lewis for acting as secondary supervisor, always available to provide advice on various fields of astronomy. Under their supervision, I was able to connect with scientific collaborators in large range of fields of astrophysics, who I warmly thank as well. I am thinking of David Lagattuta, for educating me to photometric and spectroscopic detections, of Dominique Eckert for providing a large access to treated X-ray data, and introducing me to the intra-cluster medium physics of galaxy clusters, of Guillaume Mahler, for sensible advice on lens modelling and article writing, and of Matt Hilton for teaching me the bases of SZ astronomy.

I also want to warmly thank Benjamin Beauchesne for our fruitful collaboration on joint X-ray and lens modelling, which is, I hope, only starting. I want to acknowledge his collaborators Jean-Paul Kneib, Benjamin Clément, Pascal Hibon, and Éric Jullo without whom this collaboration may not have been possible. I was looking forward meeting all of you at the EAS conference on June 2022, but I was retained in my hotel room by petty covid.

I more broadly want to thank the Sydney Consortium for Particle Physics and Cosmology (Sydney-CPPC), the Sydney Institute for Astronomy (SIfA) and the ARC Centre of Excellence for Dark Matter Particle Physics for the various discussions and seminar they fed me with. Moreover I want to thank the Beyond Ultra-deep Frontier Fields And Legacy Observations (BUFFALO) collaboration for giving me the opportunity to participate in large, lively astronomical discussions. Alberto Krone-Martins, José-Maria Diego, Alastair Edge and David Harvey are also to be credited for insightful discussions and advice.

I have been supported during the whole length of my PhD by the International Postgraduate Research Scholarship in Astroparticle Physics/Cosmology at the University of Sydney, but also by the Postgraduate Research Support Scheme (PRSS) of the University of Sydney, awarded for years 2020, 2021 and 2022, and by the Australian-French Association for Research and Innovation (AFRAN) grant.

My research groups members and other academic siblings Markus Mosbech, Zachary Picker, Ciaran O'Hare, Miro Astore, Alair Yu, Angela Ng, Ben Li, Peter Verwayen, Nataša Lazarević, Florian List, William Oliver, Lawrence Dam, Rasel Hossen, Sonia Ema, Chengyi Wang, Georgio Katisifis, Alon Loeffler, Oliver Bickerton, Matthew Rahme, Shyam Balaji, Nada Salama, Purmortal Wang, Alison Wong made this an academically exciting and a day-to-day enjoyable time by their kindness and quirkiness.

My friends in Sydney out of academia also played a key role in my growth and fulfilment in Australia. Vladimir, Chloé, Alix, Matt, Lindy, Sophie, Charlotte, Arthur, Bridget, Chris, Chiara, Michelle, Samantha, Ruben and Tiama made me feel here at home, and Carl, Benedetto, Antonella, Ginevra, David, Donia, Sélim, Alex, Florian, and Cecilie took me out and had me properly visit Australia's coasts and forests, nights and cinemas. Thank you also to my friends in France and disseminated around the world Aymeric, Roxane, Matthieu, Léa, Aurore, Ariane, Lucas, Martin, and Thomas, they are not only inexhaustible sources of laughs and intelligence, but also have

always been present when needed.

Words are failing me to thank properly Julie, and so I let it to the ineffable. At last, I want to deeply thank my family to have supported me through my countless academic endeavours. This thesis is dedicated to them.

Contents

1 An introduction to cosmology **1**
1.1 A relativistic cosmological model . . . 1
1.1.1 Context . . . 1
1.1.2 Elements of General Relativity . . . 3
1.1.3 Friedmann-Lemaître-Robertson-Walker metric . . . 3
1.1.4 Cosmological redshift . . . 4
1.1.5 Hubble's law . . . 4
1.1.6 Friedmann equations . . . 5
1.1.7 Remarks on dark energy and curvature . . . 7
1.1.8 Distances in cosmology . . . 9
1.1.9 Power spectrum . . . 11
1.2 Dark matter . . . 14
1.2.1 Astronomical motivations for dark matter . . . 15
1.2.2 Summary of dark matter models . . . 17
1.2.3 Self-Interacting Dark Matter constraints . . . 24
1.3 The physics of galaxy clusters . . . 26
1.3.1 The formation of galaxy clusters . . . 26
1.3.2 Relaxed galaxy clusters . . . 27
1.3.3 Density profiles of galaxy clusters . . . 28
1.3.4 Thermodynamics of galaxy clusters . . . 33

2 An introduction to gravitational lensing **43**
2.1 Theory of gravitational lensing . . . 43
2.1.1 A short history of gravitational lensing . . . 43
2.1.2 Existing lensing surveys and forthcoming . . . 46
2.1.3 Formalism of gravitational lensing . . . 49
2.1.4 Strong lensing configurations . . . 57
2.1.5 Lensing in the context of cosmology . . . 59
2.2 Quantitative strong lensing measurements . . . 60
2.2.1 Lens optimisation techniques . . . 60
2.2.2 A few lensing observables profiles . . . 62
2.2.3 Lensing software . . . 63
2.2.4 Lens modelling with Lenstool . . . 67
2.2.5 Clusters as thin lenses . . . 70

3 Constraining the mass distribution with strong gravitational lensing **71**

3.1 Introduction . . . 71
3.2 Spectroscopy . . . 72
3.2.1 Overview . . . 72
3.2.2 Spectroscopy and gravitational lensing . . . 74
3.2.3 More applications of spectroscopy . . . 75
3.3 Photometry . . . 75
3.3.1 Overview . . . 75
3.3.2 Imaging data and extraction . . . 76
3.3.3 Photometric selection . . . 77
3.3.4 Stellar mass . . . 77
3.4 Article: Joint *HST*, VLT/MUSE and *XMM-Newton* observations to constrain the mass distribution of the two strong lensing galaxy clusters: MACS J0242.5-2132 & MACS J0949.8+1708 . . . 80

4 Intra-cluster medium reconstruction using strong gravitational lensing 101
4.1 Introduction . . . 101
4.1.1 Motivations . . . 101
4.1.2 Observations . . . 103
4.2 General models for ICM reconstruction . . . 103
4.2.1 Self-similar polytropic temperature models with varying index . . . 103
4.2.2 Gas fraction Arctan model . . . 104
4.2.3 Analytical ICM density models . . . 107
4.2.4 Optimisation of the lensing parameters with the ICM . . . 110
4.3 Article: A full reconstruction of two galaxy clusters intra-cluster medium with strong gravitational lensing . . . 111

5 Joint Strong Lensing - X-ray galaxy cluster reconstruction 143
5.1 Abell S1063: data . . . 144
5.1.1 Photometry . . . 144
5.1.2 Spectroscopy . . . 144
5.1.3 Preexisting gravitational lensing models . . . 144
5.1.4 X-ray and SZ effect data . . . 146
5.2 Simple SL model . . . 147
5.3 X-ray `idPIE` optimisation . . . 148
5.4 Cluster joint reconstruction . . . 149
5.5 Discussion . . . 156

6 Conclusion 159

References 161

A Remarks on `Lenstool` I

B Ellipse and ellipsoid V

C Cluster member catalogues VII
C.1 MACS J0242 . . . VII
C.2 MACS J0949 . . . IX

C.3 Abell S1063 XIV

List of Figures

1.1 Content of the Universe according to *Planck* . . . 7
1.2 Scale factor a in various cosmologies . . . 8
1.3 Compared distances in cosmology . . . 10
1.4 Evolution of the Universe . . . 12
1.5 Mollweide projection of the CMB observed by *Planck* . . . 13
1.6 Temperature power spectrum . . . 14
1.7 Bullet Cluster convergence and X-ray contours . . . 16
1.8 MACHO constraints . . . 19
1.9 Dark matter mass range . . . 20
1.10 Dark matter freeze-out . . . 21
1.11 WIMP constraints . . . 23
1.12 Dark matter *freeze-in* comoving densities for different $\langle \sigma v \rangle$ . . . 24
1.13 Axion constraints . . . 25
1.14 Perseus cluster *Chandra X-ray* observation . . . 38
1.15 Compared spectral intensities of the CMB, tSZ and kSZ effects . . . 42

2.1 Examples of gravitational lensing observations . . . 45
2.2 Sketch of gravitational lensing of a quasar source . . . 46
2.3 Various gravitational lensing configurations . . . 47
2.4 Gravitational lensing formalism . . . 50
2.5 Convergence and shear . . . 57
2.6 Examples of strong lensing configurations . . . 58

3.1 Example of spectroscopic emission and absorption . . . 72
3.2 Example of a quasar spectrum . . . 73
3.3 Ly-α detection in MACS J0949 . . . 74
3.4 *HST*/ACS and WFC3 throughput curves used in HFF . . . 76
3.5 Example of a colour-magnitude diagram . . . 78

4.1 Full workflow diagram of the thesis research work . . . 102
4.2 Examples of gas fraction measurements in X-COP . . . 105

5.1 ICM optimisation cornerplot of Abell S1063 'DMH only' model . . . 151
5.2 ICM optimisation cornerplot of Abell S1063 'DMH & BCG' model . . . 152
5.3 X-ray surface brightness S_X with `idPIE` model for cluster Abell S1063 . . . 153
5.4 *HST* image of cluster Abell S1063 . . . 155
5.5 *Chandra* Abell S1063 count maps (observed, simulated, residuals) . . . 156
5.6 Density of joint optimisation of Abell S1063 . . . 157

A.1 MACS J0242 `Lenstool` optimisation II
A.2 MACS J0949 `Lenstool` optimisation III
A.3 Abell S1063 `Lenstool` joint optimisation IV

List of Tables

1.1 Cosmological parameters measurements 7

2.1 Summary of the different types of lensing 46

4.1 Varying polytropic temperature model 104

5.1 Spectroscopic detections of 25 multiply-lensed systems in Abell S1063 145
5.2 Best fit parameters models for Abell S1063 compared 150
5.3 Comparison of $M_{500,c}$ and $R_{500,c}$ for different models of cluster Abell S1063 150

C.1 Cluster members in the cluster MACS J0242 VII
C.2 Cluster members in the MACS J0949 IX
C.3 Cluster members in the Abell S1063 XIV

Notations

Conventions

- The bold notations $\boldsymbol{r}$ describe vectors;
- The arrow $\vec{r}$ describes a three-dimensional vector (which can be understood as one or two-dimensional);
- The tilde $\tilde{r}$ describes a four-dimensional vector;
- The hat on a boldsymbol $\hat{\boldsymbol{r}}$ describes a unitary vector;
- The hat on a function $\hat{f}$ describes a Fourier transform;
- Conjugated Latin indices (e.g. i in $u^i u_i$) denote a summation for three spatial dimensions; conjugated Greek indices denote a summation over four space-time dimensions.

Mathematics

- $\partial_x = \partial/\partial x$;
- $\vec{\nabla} = \partial_x \hat{\boldsymbol{x}} + \partial_y \hat{\boldsymbol{y}} + \partial_z \hat{\boldsymbol{z}} = (\partial_x; \partial_y; \partial_z)$;
- We choose for the Fourier transform the convention:

$$\hat{f}(\boldsymbol{k}) = \int_{\mathbb{R}^n} \mathrm{d}^n \boldsymbol{x} f(\boldsymbol{x}) \exp(i\boldsymbol{x} \cdot \boldsymbol{k}).$$

Constants

- $c = 299,792,458\,\mathrm{m.s^{-1}}$ is the celerity of light;
- $G = 6.67430 \times 10^{-11}\,\mathrm{m^3.kg^{-1}.s^{-2}}$ is the constant of gravitation;
- $k_B = 1.380649 \times 10^{-23}\,\mathrm{m^2.kg.s^{-2}.K^{-1}}$ is the Boltzmann constant;
- $m_a = m\left({}^{12}C\right)/12 = 1.660539 \times 10^{-27}\,\mathrm{kg}$ is a Dalton, or unified atomic mass unit;
- $\sigma_T = 6.6525 \times 10^{-29}\,\mathrm{m^2}$ is Thomson cross-section of the electron;
- $M_\odot = 1.989 \times 10^{30}\,\mathrm{kg}$ is the mass of the Sun;
- $L_\odot = 3.828 \times 10^{26}\,\mathrm{W}$ is the nominal luminosity of the Sun[1];
- $Z_\odot = 0.0122$ is the metallicity of the Sun.

Cosmology

- We choose a metric signature $(-;+;+;+)$;
- $\mathrm{d}s$ is the space-time element;
- $k \in \{-1; 0; 1\}$ is the curvature of space;
- η is the conformal time;
- χ is the comoving distance;

[1] https://www.iau.org/static/resolutions/IAU2015_English.pdf

- $\mathcal{D}$ is the transverse comoving distance;
- $\mathrm{d}\Omega = \sqrt{\mathrm{d}\theta^2 + \sin^2\theta \mathrm{d}\phi^2}$ is solid angle element;
- t_0 is the current age of the Universe;
- z is the cosmological redshift;
- $a(t) = (1+z)^{-1}$ is the scale factor;
- $H(t) = \dot{a}/a$ is the Hubble parameter; $H_0 = H(t_0)$ is the Hubble constant;
- Λ is the cosmological constant;
- Indices $\{r; m; k; \Lambda; b; \nu\}$ respectively denote radiation, matter (dark matter included), curvature, dark energy, baryons and neutrinos.

Acronyms

Acronym	Meaning
ALP	Axion-like Particles
AGN	Active Galaxy Nucleus
BAO	Baryon Acoustic Oscillations
BBN	Big Bang Nucleosynthesis
BCG	Brightest Cluster Galaxy
BSM	Beyond Standard Model (of particle physics)
CDM	Cold Dark Matter
CMB	Cosmic Microwave Background
DM	Dark Matter
DMH	Dark Matter Halo
FDM	Fuzzy Dark Matter
FIMP	Feebly Interacting Massive Particle
FLRW metric	Friedmann-Lemaître-Robertson-Walker metric
GGL	Galaxy-Galaxy Lensing
GR	General Relativity
ICM	Intra-Cluster Medium
IDM	Interacting Dark Matter
HDM	Hot Dark Matter
ΛCDM	Cosmological model with cold dark matter and a cosmological constant
LSS	Large-Scale Structures
MACHO	MAssive Compact Halo Object
MG	Modified Gravity
MOND	Modified Newtonian Dynamics
PBH	Primordial Black Hole
PSF	Point-Spread Function
QSO	Quasi-Stellar Object (quasar)
SED	Spectral Energy Distribution
SIDM	Self-Interacting Dark Matter
SL	Strong Lensing
SM	Standard Model (of particle physics)
TeVeS	Tensor-Vector-Scalar
WDM	Warm Dark Matter
WIMP	Weakly Interacting Massive Particle
WL	Weak Lensing

Acronym	Meaning	Purpose
ACT	Atacama Cosmology Telescope	CMB observations
BUFFALO	Beyond the Ultra-deep Frontier Fields And Legacy Observation	Lensing
Chandra X-ray	*Chandra X-ray Observatory* (*CXO*)	X-ray astronomy
CLASH	Cluster Lensing And Supernovae survey with *Hubble*	Strong lensing
COBE	Cosmic Background Explorer	Measure the CMB
COSMOGRAIL	COSmological MOnitoring of GRAvItational Lenses	Time delays of lensed quasars
DES	Dark Energy Survey	Optical observations of dark energy
eBOSS	Extended Baryon Oscillation Spectroscopic Survey	Cosmography
EROS	Expérience pour la Recherche d'Objets Sombres	Microlensing
Euclid		Optical observations for cosmology
Gaia		Astrometry
GLASS	Grism Lens Amplified Survey from Space	Strong lensing
GRaL	*Gaia* gravitational lenses	Gravitational lensing
HFF	*Hubble* Frontier Fields	Strong lensing
H0LiCOW	H_0 Lenses in COSMOGRAIL's Wellspring	Lensing time delay cosmography
HST	*Hubble Space Telescope*	Optical imaging
JWST	*James Webb Space Telescope*	Infra-red imaging and spectroscopy
KiDS	Kilo-Degree Survey	Optical imaging for cosmology
LIGO	Laser Interferometer Gravitational-Wave Observatory	Gravitational wave interferometry
MACHO	MAssive Compact Halo Object	Microlensing
MUSE	Multi Unit Spectroscopic Explorer	Spectroscopy
NGRST (*WFIRST*)	*Nancy Grace Roman Space Telescope*	Infra-red imaging and spectroscopy
Planck		CMB observations
OGLE	Optical Gravitational Lensing Experiment	Microlensing
Pantheon+		Supernovae Ia & Cepheids for cosmography
RELICS	REionization LensIng Cluster Survey	Strong lensing
RELIKT-1		Measure the CMB
SDSS	Sloan Digital Sky Survey	Optical imaging
SH0ES	Supernova H0 for the Equation of State	Measure H_0
SLACS	Sloan Lens ACS	Strong lensing
SPT	South Pole Telescope	CMB observations
VIMOS	VIsible Multi-Object Spectrograph	Spectroscopy
Virgo		Gravitational wave interferometry
VLT	Very Large Telescope	Imaging, spectroscopy
WMAP	Wilkinson Microwave Anisotropy Probe	Measure the CMB
X-COP	*XMM* Cluster Outskirts Project	Cluster physics
XMM-Newton	X-ray Multi-Mirror Mission	Interstellar X-ray sources

Chapter 1

An introduction to cosmology

In girum imus nocte et consumimur igni

We enter the circle after dark and are consumed by fire

— Unknown

1.1 A relativistic cosmological model

1.1.1 Context

In the 6th century BC, Thales of Miletus described the world as being based on a single material substance (αρχή): water (Aristotle, *Metaphysics*, 1992, 983b6 8–11). Nietzsche comments on this attempt to explain the nature of the world by a material principle, instead of myths and unobservable supernatural forces (in *Philosophy in the Tragic Age of the Greeks*, §3, 1962):

> 'Greek philosophy seems to begin with an absurd notion, with the proposition that water is the primal origin and the womb of all things. Is it really necessary for us to take serious notice of this proposition? It is, and for three reasons. First, because it tells us something about the primal origin of all things; second, because it does so in language devoid of image or fable, and finally, because contained in it, if only embryonically, is the thought, "all things are one". The first reason still leaves Thales in the company of the religious and the superstitious; the second takes him out of such company and shows him as a natural scientist, but the third makes him the first Greek philosopher.'

Thales' hypothesis, soon to be followed by many other, was revolutionary in that it did not only attempt to explain the *nature* of all things, but also their *origin*. It was the first known description of the Universe with observational matter, and thus the first real materialist cosmogony. In that, Thales could be considered to be the first physicist (Kirk et al., 1983). Today, modern physics faces the same timeless challenge to explain the nature of matter and its origin.

In order to address this challenge of describing the world rationally, philosopher, mathematician and physicist René Descartes provided the *Discourse on the Method of Rightly Conducting One's*

Reason and of Seeking Truth in the Sciences (1637), i.e. a scientific method[1], and a rational, a *Cartesian* description of space. After Newton used this method and this classical and *absolute* space to describe motion, a scientific sense of time and space was going to supplant the cosmogonic traditions. The 'beginning of the world' described by most religions and mythologies, from Gaia emerging from Chaos in the Greek mythology to the five creations of the suns according to the Aztecs, was doomed to be superseded by the Newtonian understanding of time and space, infinite and eternal. With philosophers such as Immanuel Kant going as far as to prove time and space to be *a priori* forms of the intuition, before any experience, their eternity was not only held to be the result of observations, but the victory of reason over tradition (Kant, 1998). Classical philosophers progressively transformed a physical theory into an intuition: the Universe was a frame (space and time), and thus could not be considered to be bounded or limited[2]. The dialogue between physics and philosophy progressively modified the perception of the world for the whole humanity. Not only did it overtake cosmogonic myths, but it lead to the contemplation of forms which artists could never have conceived. The quest for a rational explanation of the phenomena[3] did not only lead to a better physical explanation of nature, but also to a philosophical paradigm shift, to technological and artistic revolutions, and to a form of intimate understanding of space, time, and the Universe for many, including physicists.

Special and general relativity (see Section 1.1.2) proved this intuition to be a biased, *a posteriori* understanding of space and time, as they were unified into a continuum, and their comprehension was bounded to that of matter. In spite of this, the dominant assumption that the Universe was eternal remained. After discovering the existence of other galaxies than the Milky Way, Hubble (1929) proposed his law, according to which the recessional velocity of galaxies increases with their distance to the observer[4]. When the priest Georges Lemaître proposed to interpret these observations through his theory of the 'primordial atom' (Lemaître, 1931), stating a constantly expanding Universe yielded an infinite concentration of matter at some point in the past, he was criticised by his pairs. Some feared an attempt to re-introduce the 'beginning of the world', and some of the most eminent physicists of the time – amongst whom Albert Einstein – were reluctant to admit such a possibility at first. Although this *Big Bang* was later confirmed by observations, this comes to outline the biases of even the greatest scientists. The millennial struggle to understand nature, and to free its explanation from tradition, to root it in theory and experience, did not come without a few prejudices of its own. My understanding of the everlasting dialogue between philosophy and physics is rooted in this history: science brings empirical and theoretical innovations, which must be enlightened and justified philosophically *a posteriori*. Conversely, scientists can find in epistemology and philosophy of knowledge a way to take a step back on their field, to consider their own biases. In the past centuries, this dialogue has been one of the most important motors of history. It is the most ethical and the most efficient way to pursue Thales' quest to understand matter and the cosmos.

[1] Descartes was far from being the first scientist as the scientific method was becoming increasingly clear and widely spread from the late Renaissance, with thinkers as Francis Bacon or Galileo Galilei playing a key role. Moreover we can trace paradigms such as empiricism at least as far as the great Aristotle. Descartes' key role must be sought in his association of a philosophical doubt with a systematic method of enquiry, inspired by mathematics.

[2] There was never a unique understanding of the Universe; however the common conception of physical time and space as absolute and infinite, beyond the content of the Universe, dominated the 18^{th} and 19^{th} centuries.

[3] According to Kant, a phenomenon is an event which appears to an observer.

[4] Vesto Slipher previously showed galaxies were moving away from the observer. Georges Lemaître proved the Hubble law two years before Hubble himself, but had a limited impact (Lemaître, 1927).

1.1.2 Elements of General Relativity

Whether it is due to the outstanding progress of instruments, or to the scientific revolution atmosphere in physics, the hypothesis of eternity of the Universe collapsed within 26 years after its absolute, Newtonian, character. Indeed, in 1905 Albert Einstein proposed that space and time would be bounded through the metric element $\mathrm{d}s$, writing the one time dimension $\mathrm{d}t$ and the three spatial ones $(\mathrm{d}x, \mathrm{d}y, \mathrm{d}z)$:

$$\mathrm{d}s^2 = g_{\mu\nu}\mathrm{d}x^\mu \mathrm{d}x^\nu, \tag{1.1}$$

where $g_{\mu\nu}$ is the metric tensor, $(\mu;\nu) \in \{0;1;2;3\}$ representing respectively the time and the three spatial dimensions. When these indices appear in a same expression as covariant and contravariant, they are implicitly summed. In such a *space-time continuum*, a free particle is only submitted to the metric curvature, i.e. to gravitation.

Because of the mass-energy equivalence, first established by Einstein (1905), we can introduce at once all forces in $T_{\mu\nu}$, the energy-momentum tensor:

$$T_{\mu\nu} = \left(\rho + \frac{P}{c^2}\right) u^\mu u^\nu - P g^{\mu\nu}, \tag{1.2}$$

where c is the speed of light, u^μ is the space-time quadrivector of speed, ρ the mass-energy density and P the pressure.

Introducing the Ricci tensor $R_{\mu\nu}$, describing the local space-time curvature, let us write $R = g^{\mu\nu}R_{\mu\nu}$ the scalar curvature. The Einstein tensor $G_{\mu\nu}$ describes the space-time geometry, as it is defined only by the curvature $g_{\mu\nu}$ and its derivatives:

$$G_{\mu\nu} = R_{\mu\nu} - \frac{1}{2} R g_{\mu\nu}. \tag{1.3}$$

The intuition of Einstein (1915) was to relate the space-time curvature to the local matter-energy content. This is the core idea of General Relativity (GR), which writes as the Einstein field equation:

$$G_{\mu\nu} + \Lambda g_{\mu\nu} = \frac{8\pi G}{c^4} T_{\mu\nu}, \tag{1.4}$$

where G is the Newtonian constant of gravitation and Λ the cosmological constant, added added by Einstein (1917) to allow for the Universe to be static. Retrospectively, there was no valuable scientific motivation to add it, as Einstein could not know whether or not the Universe was static. He accepted the possibility of an evolving Universe in 1931, and called the cosmological constant 'the greatest stupidity of his life'. $\kappa = 8\pi G/c^4$ is called the Einstein gravitational constant.

1.1.3 Friedmann-Lemaître-Robertson-Walker metric

Learning from Copernicus, astronomers did not have any reason to assume a particular position or direction to be privileged in the Universe. This was elevated to the rank of *cosmological principle*: on the large scales, the Universe would have to appear homogeneous and isotropic. Applying GR to the entire Universe therefore yields a general form for the metric:

$$\mathrm{d}s^2 = -c^2\mathrm{d}\tau^2 = -c^2\mathrm{d}t^2 + a(t)^2\left(\frac{\mathrm{d}r^2}{1-kr^2} + r^2\mathrm{d}\Omega^2\right), \tag{1.5}$$

in spherical coordinates $(r;\theta;\phi)$ $\mathrm{d}\Omega^2 = \mathrm{d}\theta^2 + \sin^2\theta \mathrm{d}\phi^2$. This is known as the Friedmann-Lemaître-Robertson-Walker metric (FLRW, see Friedmann, 1922; Lemaître, 1927; Robertson, 1929, 1935, 1936a,b; Walker, 1937). We chose the metric signature $(-;+;+;+)$. This convention yields equivalent physics to its opposite, but we need to fix the geometric basis.

We introduced τ the proper time. Defining $R(t)$ the radius of the observable Universe at a given time, and R_0 its present day value, one defines $a(t) = R(t)/R_0$ the scale factor (with $a_0 = 1$). Its existence leads to counter-intuitive results: for instance, the distance between two distant motionless objects may vary. Moreover, if the local velocities are capped in GR to the celerity of light, distant regions may move away faster than light. Their peculiar motions matter little to this result: it is the geometric manifold that is the cosmological space-time which evolves to carry these regions away from one another. At last, k is the curvature factor. Let us notice that $k \in \{-1;0;1\}$ correspond respectively to an open, flat, and closed Universe (i.e. a hyperbolic, Euclidean and spherical geometry respectively). With

$$S_k(\chi) = \begin{cases} \sinh(\chi) & k = -1 \\ \chi & \text{for } k = 0 \\ \sin(\chi) & k = 1, \end{cases} \tag{1.6}$$

we can define the comoving distance χ such that $r = S_k(\chi)$, and use it to rewrite the FLRW metric:

$$\mathrm{d}s^2 = -c^2\mathrm{d}t^2 + a(t)^2\left(\mathrm{d}\chi^2 + S_k^2(\chi)\mathrm{d}\Omega^2\right). \tag{1.7}$$

1.1.4 Cosmological redshift

As a direct consequence of the existence of the stretching of the space-time continuum by the increase of the scale factor with time, the wavelength of a luminous source progressively gets *redshifted*, i.e. the wave front emitted at time t, and at wavelength $\lambda(t)$, extends with physical distances. It is thus observed at $t = t_0$ with a redshift:

$$z = \frac{\lambda_0}{\lambda(t)} - 1 = \frac{a_0}{a(t)} - 1, \tag{1.8}$$

where λ_0 is the observed wavelength. As the position and shape of various spectral lines is a property of chemical elements, detecting a shift in the spectrum of distant cosmological objects directly lets observers measure their cosmological distances.

In practice, as the scale factor continuously increased during the history of the Universe, the cosmological redshift z is used as a measurement of distances or cosmic time from the observer (see e.g. Figure 1.4, and equation 1.23 relating distance and redshift). It is in some situations a more simple observable because the Hubble flow (Universe expansion) makes the space-time continuum non-Minkowskian at large distances.

1.1.5 Hubble's law

One can define the Hubble factor as

$$H(t) = \frac{\dot{a}}{a}. \tag{1.9}$$

H_0, the present-day value of the Hubble constant, was measured by the *Planck* mission (Planck Collaboration, 2020) using the Cosmological Microwave Background (CMB, read Durrer, 2015, for

a review) to be $67.66 \pm 0.42\,\mathrm{km.s^{-1}.Mpc^{-1}}$, by the Supernova H_0 for the Equation of State collaboration (SH0ES, Riess et al., 2022) on Cepheids and supernovae Ia to be $73.04 \pm 1.04\,\mathrm{km.s^{-1}.Mpc^{-1}}$, by the Pantheon+ collaboration (Brout et al., 2022) on a larger set of supernovae Ia to be $73.40^{+0.99}_{-1.22}\,\mathrm{km.s^{-1}.Mpc^{-1}}$, and by the H_0 Lenses in COSMOGRAIL's Wellspring collaboration (H0LiCOW, Wong et al., 2020) on six gravitationally lensed quasars with measured time delays to be $73.3^{+1.7}_{-1.8}\,\mathrm{km.s^{-1}.Mpc^{-1}}$. This large discrepancy between the local Universe and CMB measurements for H_0 value is known in modern cosmology as the H_0 tension, and is the source of many speculations (see for a review Schöneberg et al., 2022).

The value of H_0 allows to predict the recessional velocity v of distant objects, due solely to the Hubble flow – i.e. the expansion of the Universe. Given D the proper distance, the Hubble law writes:

$$v = H_0 D. \tag{1.10}$$

We can also define the Hubble radius $R_H = c/H_0$, and the age of the Universe $1/H_0 \simeq 13.8\,\mathrm{Gyr}$.

1.1.6 Friedmann equations

We can now write the Einstein field equation (1.4) for the FLRW metric. To satisfy the isotropic principle, the universal fluid must be motionless on average. Thus its quadri-velocity only has a temporal component: $u^\alpha = (1, 0, 0, 0)$. The variation of pressure and energy-momentum density can thus only be over time. From the time component only of the Einstein field equations, we derive the first Friedmann equation; from the latter and the trace of equation, we derive the second:

$$\begin{aligned} \left(\frac{\dot{a}}{a}\right)^2 &= \frac{8\pi G}{3}\rho - k\frac{c^2}{a^2} + \frac{\Lambda c^2}{3}, \\ \frac{\ddot{a}}{a} &= -\frac{4\pi G}{3}\left(\rho + \frac{3}{c^2}P\right) + \frac{\Lambda c^2}{3}. \end{aligned} \tag{1.11}$$

One can notice that the cosmological constant is still present in these equations, as contemporary cosmology suggests the existence of a *dark energy* field, acting as a repulsive force, counterbalancing the effects of gravity (see notably Perlmutter et al., 1998; Riess et al., 1998; Perlmutter et al., 1999). The most recent measurements suggest a very small value for $\Lambda = (1.01 \pm 0.02) \times 10^{-35}\,\mathrm{s^{-2}}$ (according to Prat et al., 2022).

Using the mass-energy conservation:

$$\nabla^\mu T_{\alpha\mu} = 0, \tag{1.12}$$

we can include Λ in the equations defining ρ and P:

$$\rho_\Lambda = -\frac{\Lambda c^2}{8\pi G} \quad \text{and} \quad P_\Lambda = \frac{\Lambda c^4}{8\pi G}, \tag{1.13}$$

yielding a reformulation of the two Friedmann equations (1.11):

$$\begin{aligned} H^2 = \left(\frac{\dot{a}}{a}\right)^2 &= \frac{8\pi G}{3}\rho - k\frac{c^2}{a^2}, \\ \dot{H} + H^2 = \frac{\ddot{a}}{a} &= -\frac{4\pi G}{3}\left(\rho + \frac{3}{c^2}P\right), \\ \dot{\rho} &= -3H\left(\rho + \frac{1}{c^2}P\right) = -3H\rho(1+w), \end{aligned} \tag{1.14}$$

where $w = P/\rho c^2$. We can thus define the critical density of the Universe:

$$\rho_c = \frac{3H^2}{8\pi G} \tag{1.15}$$

which evolves with the Hubble factor. This critical density is given in physical units and can thus be written ρ_c^P for clarity. In a flat cosmology ($k = 0$), the first Friedmann equation thus writes $\rho = \rho_c^P$.

For a non-relativistic, matter-dominated Universe, the low velocity of particles allows to neglect the pressure $P_m \simeq 0$, leading to an equation of state $w_m = 0$. In the case of a radiation dominated Universe, the radiative pressure is $P_r = \rho_r c^2/3$, thus leading to $w_r = 1/3$. The dark-energy equation of state writes $w_\Lambda = -1$, according to equation (1.13). At last, we can reformulate the first Friedmann equation (1.14) so that the curvature term would be worth $\rho_k = 3kc^2/8\pi G a^2$. Thus, the second Friedmann equation necessitates to write $P_k = -c^2\rho_k/3$, and therefore $w_k = -1/3$.

One can then define the density parameter:

$$\Omega = \frac{\rho}{\rho_c^P}, \tag{1.16}$$

which is composed of a combination of radiation, matter and dark energy components:

$$\Omega = \Omega_r + \Omega_m + \Omega_\Lambda. \tag{1.17}$$

The curvature density parameter is then defined as:

$$\Omega_k = 1 - (\Omega_r + \Omega_m + \Omega_\Lambda). \tag{1.18}$$

so, if for instance $\Omega_k > 0$, $\Omega < 1$, implying $k = -1$, the Universe is open (hyperbolic geometry). Assuming w to be constant for each substance i of the Universe, we thus can integrate the energy continuity equation:

$$\rho = \sum_i \rho_{0,i} a^{-3(1+w_i)}, \tag{1.19}$$

and thus the first Friedmann equation in the case of a flat Universe may be rewritten:

$$E^2(a) = \left(\frac{H}{H_0}\right)^2 = \Omega_{0,\Lambda} + \Omega_{0,k} a^{-2} + \Omega_{0,m} a^{-3} + \Omega_{0,r} a^{-4}. \tag{1.20}$$

where the $\Omega_{0,i}$ are the density parameters of each substance today. Present-day measurements of the different density parameters suggest the values given in Table 1.1, and represented in Figure 1.1. Let us assume that non-relativistic matter is divided into visible matter (described by the standard model of particle physics), and a more mysterious *dark matter*, whose interaction with other species is assumed to only be gravitational (read Section 1.2.1 for more details). Using a combination of the first Friedmann equation (1.14) and equation (1.19), one can find the time evolution of the scale factor for the domination of the different species – which we call *eras* of the Universe. For example, during the eras of radiation, matter and dark energy, the scale factor evolves respectively as:

$$a(t) \propto \begin{cases} t^{1/2} & w_r = 1/3 \\ t^{2/3} & \text{for } w_m = 0 \\ \exp\sqrt{\Lambda/3}\, t & w_\Lambda = -1. \end{cases} \tag{1.21}$$

By utilising cosmological abundance observations, such as *Planck*'s, we may find the time of equality of density of different species with equation (1.19). The dark energy era is that of the accelerated expansion. The radiation-matter equality occurs at a cosmological redshift $z \sim 3400$, and the dark energy-matter equality at $z \sim 0.3$.

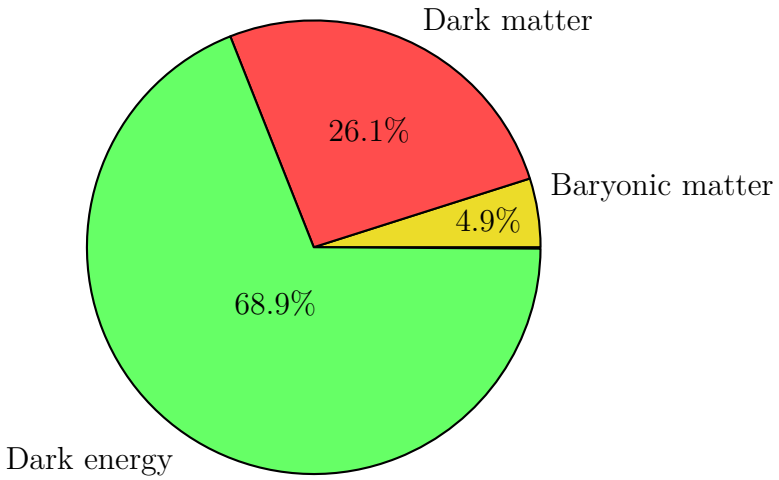

Figure 1.1: Content of the Universe according to the satellite *Planck* (Planck Collaboration, 2020).

Table 1.1: Cosmological parameters measurements. H_0 is given in km.s^{-1}.Mpc^{-1}. $h = H_0/(100\,\text{km.s}^{-1}\text{.Mpc}^{-1})$. Ω_b and Ω_c denote respectively the density parameters of baryons and cold dark matter. *Planck* data are presented in Planck Collaboration (2020).

	Planck mission	This thesis
H_0	67.66 ± 0.42	70
Ω_m	0.3111 ± 0.0056	0.30
$\Omega_b h^2$	0.0224 ± 0.0001	0.0237
$\Omega_c h^2$	0.1193 ± 0.0009	0.1233
Ω_Λ	0.6889 ± 0.0056	0.70
Ω_r	$(9.18 \pm 0.18) \times 10^{-5}$	0

1.1.7 Remarks on dark energy and curvature

Since Copernicus, cosmologists and scientists in general have become wary of coincidences placing observers or the mankind as a whole in a specific region of the Universe, without any better justification than luck. Because the matter-dark energy equality is so close in time to us as observers ($\sim$ 4 Gyr in the past), the dark energy density approximately equals that of matter density today. Even though this does not cause any observational problem, it could be qualified as *suspicious* in Copernican terms[5], suggesting the mankind lives at a 'special moment' of cosmological history. This *coincidence problem* is a philosophy of science argument, but adds to a number of other criticisms which can be addressed to dark energy. Indeed, as previously outlined, the cosmological constant was reintroduced to explain the acceleration of the observed cosmological expansion, but was not motivated by any specific theoretical prediction. This is not to say there is no explanation to what dark energy could be (a simple field of energy of space-time, or fifth essence[6] i.e. quintessence), but simply that the canonical cosmological model with dark energy must be considered cautiously and for what it is – an empirical model.

[5] 'Whenever we find coincidences in a physical theory, we should be highly suspicious about the theory.' – D'Inverno (1992).

[6] The *first* four essences being radiation, baryons, dark matter and curvature.

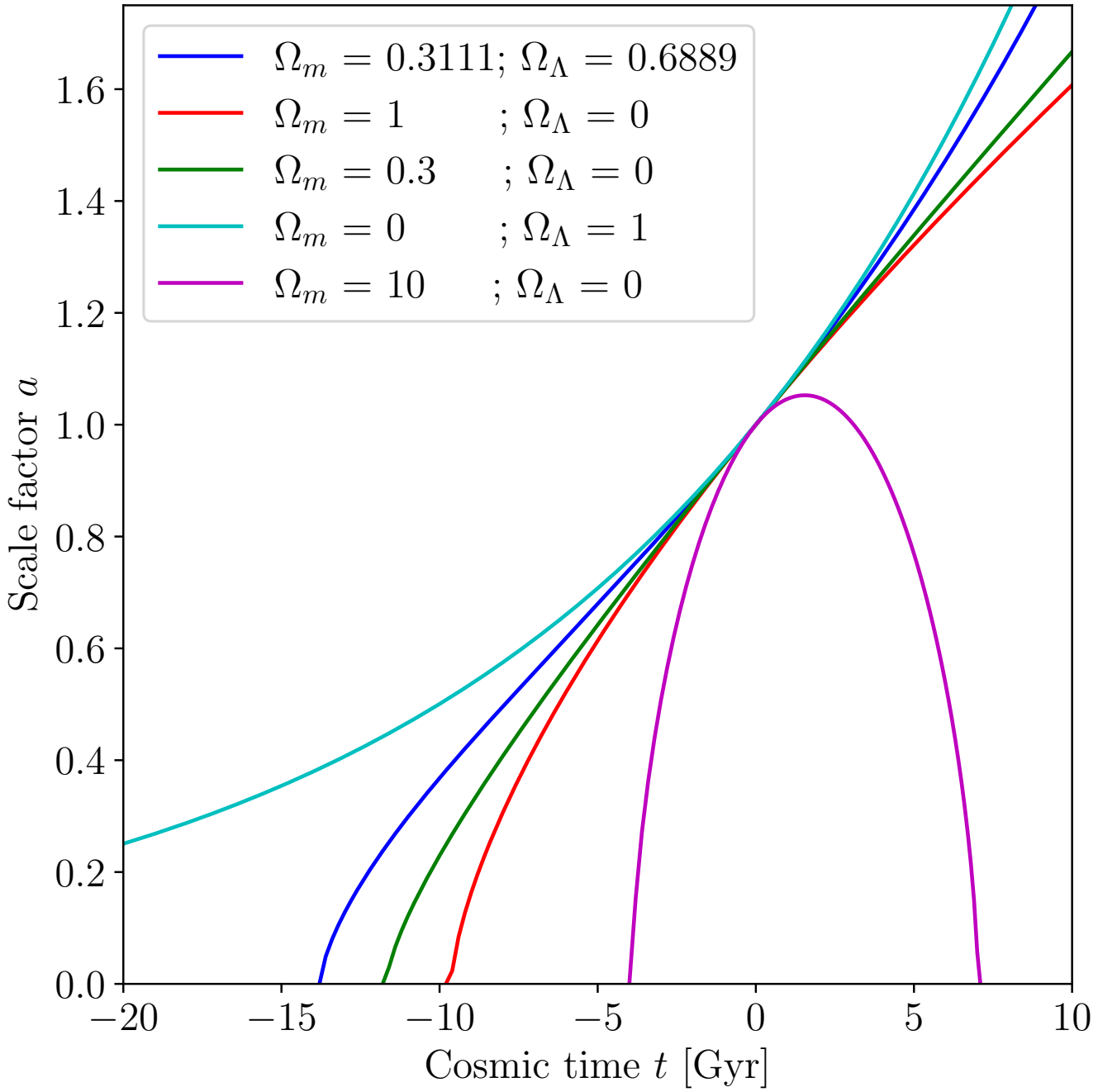

Figure 1.2: Scale factor a in different cosmologies, obtained solving the second Friedmann equation. $h = 0.6766$ in all cases. *Blue*: *Planck* values. *Red*: Einstein-de Sitter cosmology with matter only $\Omega_m = 1$. *Green*: Underdense Universe with matter only. *Cyan*: Einstein-de Sitter cosmology with dark energy only $\Omega_\Lambda = 1$. *Magenta*: Overdense Universe with $\Omega_m = 10$, leading to a Big Crunch (collapse of the Universe).

Moreover, having this field to be of constant energy is the most simple model, but other parametrisations exist. The equation of state of dark energy writes (according to Chevallier and Polarski, 2001; Linder, 2003):

$$w_\Lambda = w_0 + w_a(1 - a). \tag{1.22}$$

Let us notice a number of other dark energy parametrisations are possible (Wetterich, 2004; Bar-

boza and Alcaniz, 2008; Öztaş et al., 2018; Öztaş, 2018).

The optimisation of solely w_0 (with $w_a = 0$) using the *Planck* dataset yields -1.04 ± 0.10. Marginalising over all cosmological data (*Planck* mission; SDSS IV, see Alam et al., 2021, notably Figure 12) an extended cosmological model allowing non-zero curvature and non-constant dark energy, one finds values $k = 0$, $w_0 = -1$ and $w_a = 0$ to be favoured. Similarly to the coincidence problem, the fact that the Universe appears to have no curvature could be a form of fine tuning (Ω_k could be any value but appears to be 0) and is sometimes referred to as the *flatness* problem.

In the previous sections and from now on, we choose a cosmological model FLRW metric with a cosmological constant Λ and cold dark matter (referred to as ΛCDM, or *concordance model*) – cold dark matter (CDM) only interacts gravitationally with baryons[7]. We use the cosmological parameters presented in Table 1.1, which also contains the reference values considered in this thesis. The radiation content of the Universe $\Omega_{0,r} = (9.18 \pm 0.18) \times 10^{-5}$ can be neglected. We assume a flat cosmology $k = 0$, and no deviation from the dark energy equation of state $w_\Lambda = -1$.

1.1.8 Distances in cosmology

1.1.8.1 Comoving distance

Given the definition of the comoving radial distance χ between an observer and an object at a given redshift z in Section 1.1.3, let us write it (e.g. in Lachièze-Rey et al., 1999; Bernardeau and Valageas, 2000)[8]:

$$\chi(z) = \frac{d(t)}{a(t)} = \frac{c}{H_0}\int_0^z \frac{\mathrm{d}\zeta}{E(\zeta)} = \frac{c}{H_0}\int_0^z \frac{\mathrm{d}\zeta}{\sqrt{\Omega_\Lambda + \Omega_k(1+\zeta)^2 + \Omega_m(1+\zeta)^3 + \Omega_r(1+\zeta)^4}}, \tag{1.23}$$

with d the physical distance. We could rewrite Hubble's law (equation 1.10):

$$\frac{\mathrm{d}\chi}{\mathrm{d}t} = 0 \implies \frac{\mathrm{d}d}{\mathrm{d}t} = \frac{\dot{a}}{a}d. \tag{1.24}$$

1.1.8.2 Transverse comoving distance

The comoving distance is unaffected by expansion. We may define a specific distance, also unaffected by curvature, the transverse comoving distance f_K:

$$f_K(z) = \begin{cases} \frac{c}{H_0}(\Omega_k)^{-1/2}\sinh\left(\sqrt{\Omega_k}\frac{H_0}{c}\chi(z)\right) & \Omega_k > 0 \\ \chi(z) & \text{for } \Omega_k = 0 \\ \frac{c}{H_0}(-\Omega_k)^{-1/2}\sin\left(\sqrt{-\Omega_k}\frac{H_0}{c}\chi(z)\right) & \Omega_k < 0. \end{cases} \tag{1.25}$$

An sphere at a constant comoving radius χ would have a constant area $4\pi a^2(\chi) f_K^2(\chi)$. The transverse comoving distance is thus sometimes called the areal comoving radius (Fleury, 2015).

[7] In astronomy, *baryonic matter* does not only designate protons and neutrons, but also electrons and all objects formed by them, even in black holes. Neutrinos, radiation, and critically dark matter are not considered to be baryonic. One can read this on the SAO Encyclopedia of Astronomy.

[8] To check a comoving distance calculus, one can for instance use `iCosmos`.

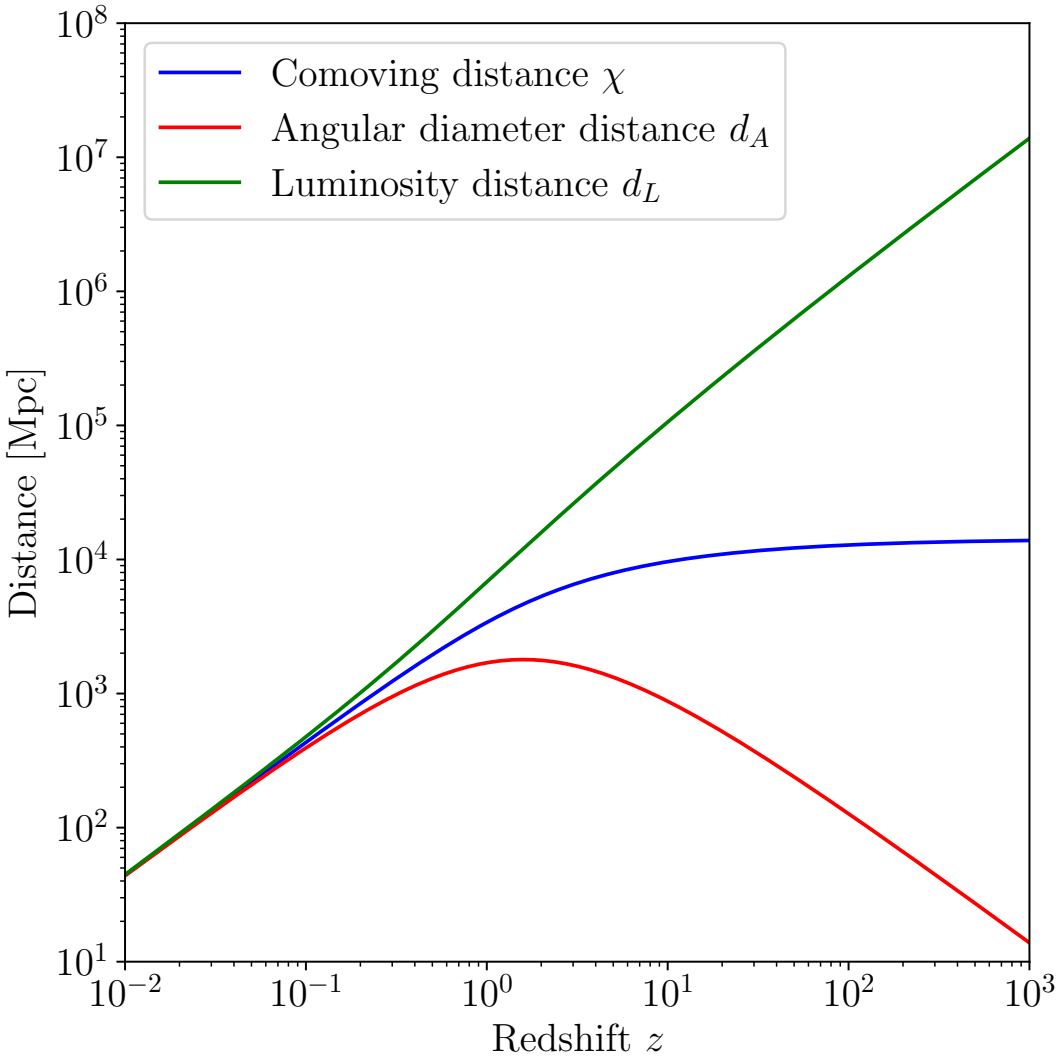

Figure 1.3: Compared distances in cosmology, with the *Planck* values.

1.1.8.3 Luminosity distance

Let us denote the bolometric luminosity (i.e. the integrated luminosity over the whole spectrum) and flux of an astronomical object (e.g. a galaxy) L and F respectively. One can thus define the luminosity distance d_L such that:

$$\begin{aligned} F &= \frac{L}{4\pi d_L^2(z)}, \\ d_L(z) &= (1+z) f_K(z), \end{aligned} \tag{1.26}$$

where the factor $(1+z)$ is due to the redshift of the photon (the spectrum is dilated with time, on top of the three spatial dimensions dilatation embedded in the comoving f_K).

1.1.8.4 Angular diameter distance

If we examine an object of physical size l, then it will appear under an angle α, allowing to define d_A, the angular diameter distance:

$$\begin{aligned} \alpha &= \arcsin \frac{l}{d_A(z)} \approx \frac{l}{d_A(z)}, \\ d_A(z) &= \frac{f_K(z)}{1+z}. \end{aligned} \tag{1.27}$$

The division by $(1+z)$ comes from the fact that the wavefront is a surface, hence only redshifted in two spatial dimensions (where $f_K(z)$ is in three).

1.1.8.5 Comoving volume

The comoving volume element in cosmology thus reads:

$$\mathrm{d}V^C = \frac{c}{H_0} \frac{(1+z)^2 d_A^2(z)}{E(z)} \mathrm{d}z \mathrm{d}\Omega, \tag{1.28}$$

where $E(z)$ is defined in equation (1.20), for a volume element $\mathrm{d}\Omega$. In the case $k = 0$:

$$V^C = \frac{4\pi}{3} f_K^3(z). \tag{1.29}$$

1.1.8.6 Comoving density

We can define comoving observables, such as the volume density:

$$\rho_c^C = \rho_c^P a^3 = \frac{3H_0^2}{8\pi G} a^3 E^2(a). \tag{1.30}$$

The critical density specific to a matter-dominated Universe reads:

$$\rho_{c,m}^C = \frac{3H_0^2}{8\pi G} \Omega_{0,m}, \tag{1.31}$$

and the density contrast (or overdensity):

$$\delta(\vec{x}, t) = \frac{\rho_m^P(\vec{x}, t) - \rho_{c,m}^P(t)}{\rho_{c,m}^P(t)} = \frac{\rho_m^C(\vec{x}, t) - \rho_{c,m}^C(t)}{\rho_{c,m}^C(t)}, \tag{1.32}$$

which is defined only for matter. The division makes the definition relevant for comoving or physical densities. This definition is valid in the specific case of flat geometry ($k = 0$), as it assumes the critical density equals the mean density of the Universe.

1.1.9 Power spectrum

In order to understand the distribution of matter in the Universe, we use the two-point correlation function of $\boldsymbol{r}$ distant points. We denote this two-point correlation function $\zeta_{\Theta\Xi}(\boldsymbol{r}) =$

[9] *Transparent* here means *free-streaming*, as for CMB photons. Interactions are still possible, but extremely rare.

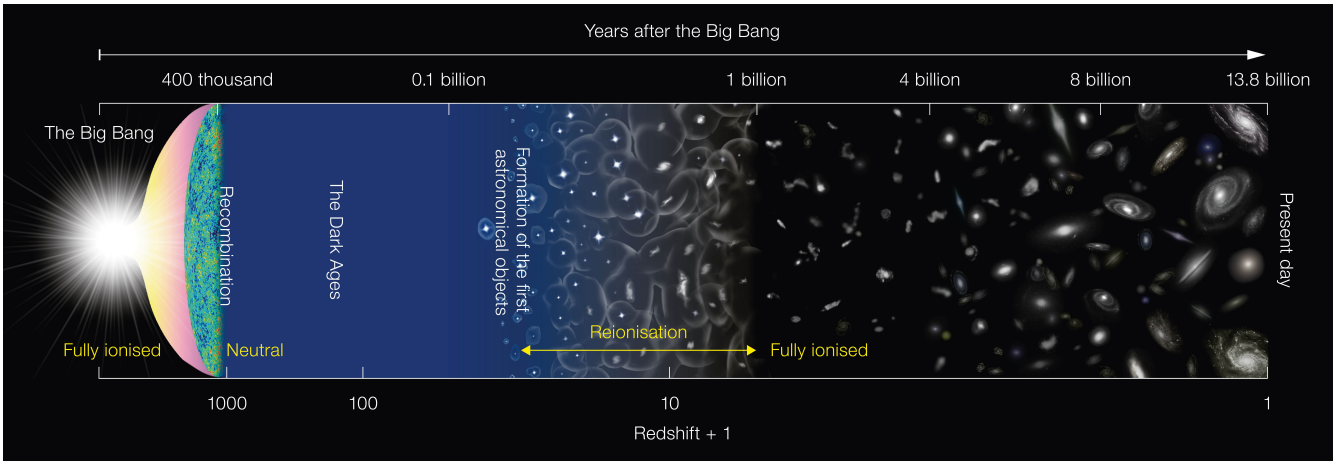

Figure 1.4: Evolution of the Universe. After Big Bang (BB), the four fundamental forces decouple and inflation expands the Universe by a factor $\sim e^{60}$. Afterwards, as the Universe cools down while expanding, it becomes transparent to neutrinos[9], yielding the Cosmic Neutrino Background (CνB). Between $\sim$ 2 and 20 minutes after BB, the Big Bang Nucleosynthesis (BBN) fuses hydrogen nuclei into a variety of light elements, mostly helium. At $z_{\rm rec} \sim 1100$, the temperature reaches $\sim 3000\,$K, allowing for electrons to recombine with nuclei, making the Universe transparent to light. This produces the Cosmic Microwave Background (CMB). The density fluctuations observed at that time (see Figure 1.5) progressively grew by gravitational collapse. The CMB decoupling was followed by the Dark Ages, where the only occasional light production was through hydrogen 21 centimetre line emission. As Large Scale Structures (LSS) formed, the first galaxies and quasars radiated charged particles, resulting into a reionisation of the Universe (at $z_{\rm rei} \in [7; 30]$). Through successive mergers, galaxy clusters then grew in scale to produce the Universe as it is today.
Credits: ESO.

$\langle \Theta^*(\boldsymbol{x})\Xi(\boldsymbol{x}+\boldsymbol{r})\rangle_{\boldsymbol{x}}$, for homogeneous Θ and Ξ fields. Defining the Fourier transform for a function f, in a n dimensional real space as:

$$\hat{f}(\boldsymbol{k}) = \int_{\mathbb{R}^n} \mathrm{d}^n\boldsymbol{x} f(\boldsymbol{x}) \exp(i\boldsymbol{x}\cdot\boldsymbol{k}), \tag{1.33}$$

we define $P_{\Theta\Xi}$ the power spectrum of a wavenumber k in the general case (Harrison, 1970; Zel'dovich, 1972):

$$P_{\Theta\Xi}(k) = \int \frac{\mathrm{d}^3\boldsymbol{r}}{(2\pi)^3} \langle \Theta^*(\boldsymbol{x})\Xi(\boldsymbol{x}+\boldsymbol{r})\rangle_{\boldsymbol{x}} \exp(\mathrm{i}\boldsymbol{k}\cdot\boldsymbol{r}) = \frac{1}{(2\pi)^3}\langle \Theta^*(\boldsymbol{k})\Xi(\boldsymbol{k})\rangle, \tag{1.34}$$

as in general:

$$\langle \Theta^*(\boldsymbol{k})\Xi(\boldsymbol{k'})\rangle = (2\pi)^3\ \delta_D(\boldsymbol{k}-\boldsymbol{k'})\ P_{\Theta\Xi}(k), \tag{1.35}$$

where δ_D represents the Dirac distribution.

This power spectrum allows to analyse the correlation of two different observables at different scales in the Universe. For example, $P_{\delta\delta}$, the overdensity power spectrum describes the density contrast of the Universe as a function of scale.

We may further decompose an observable Θ into spherical harmonics Θ_{lm} in order to study

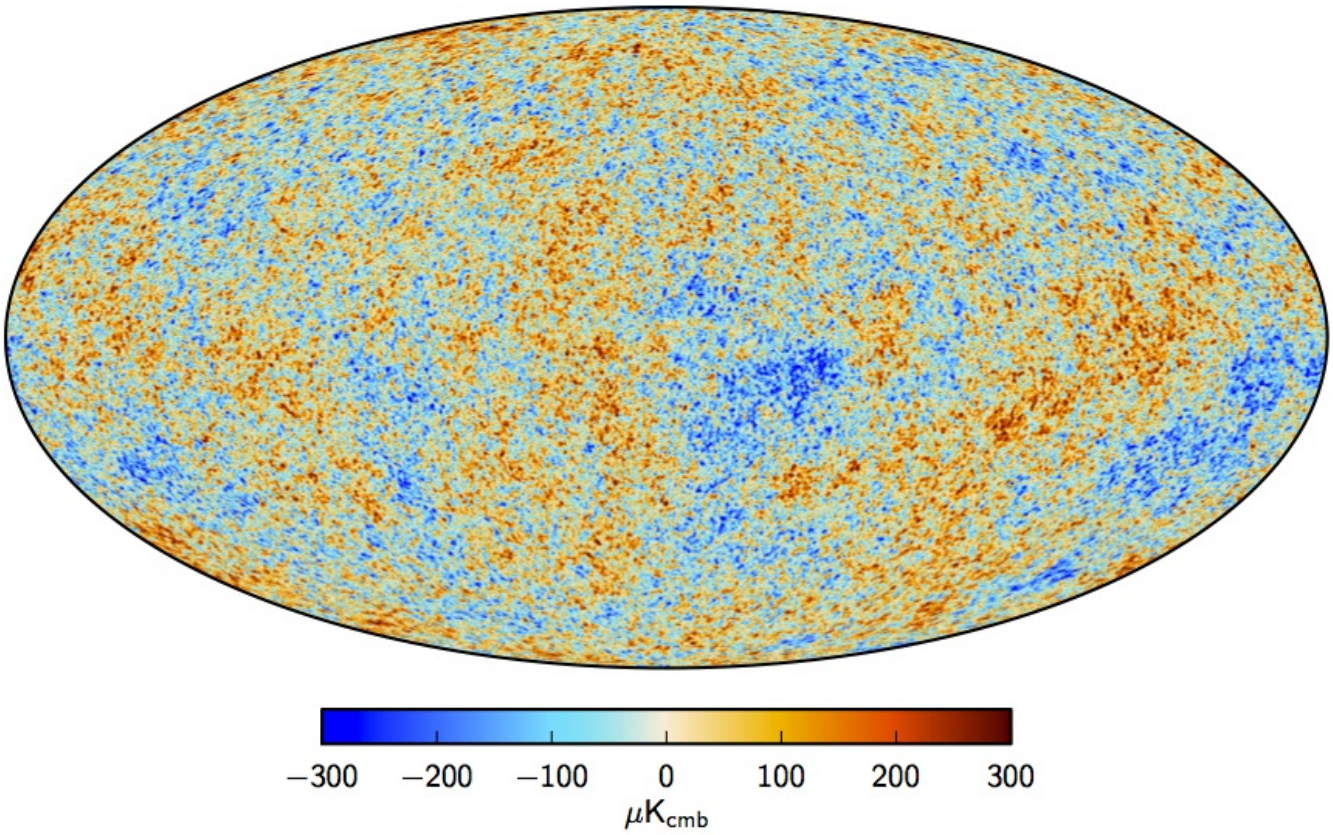

Figure 1.5: Mollweide projection of the CMB, as observed by satellite *Planck*. Credits: Planck Collaboration (2016).

their average value and fluctuation:

$$\Theta_{lm} = \int \mathrm{d}\boldsymbol{n}\ Y^*_{lm}(\boldsymbol{n})\ \Theta(\boldsymbol{n}) = \int \frac{\mathrm{d}\boldsymbol{k}}{(2\pi)^3}\ 4\pi i^l j_l(k\mathcal{D}_\Theta)\ Y^*_{lm}(\boldsymbol{k})\ \Theta(\boldsymbol{k}), \tag{1.36}$$

where $\int \mathrm{d}\boldsymbol{n}$ is the integral over all directions on a sphere, Y_{lm} are the normalised Laplace spherical harmonics[10], j_l are the Bessel spherical functions, only depending on the norm k of $\boldsymbol{k}$ and $\mathcal{D}_\Theta = f_K(z_\Theta)$ the transverse comoving distance of the decomposition sphere. One can derive the spherical correlation coefficient (Hu, 2003)[11]:

$$C_l^{\Theta\Xi} = \langle \Theta^*_{lm}(\boldsymbol{k})\ \Xi_{lm}(\boldsymbol{k'})\rangle = \frac{1}{2\pi^2}\int \mathrm{d}^3\boldsymbol{k}\ j_l(k\mathcal{D}_\Theta) j_l(k\mathcal{D}_\Xi)\ P_{\Theta\Xi}(k), \tag{1.37}$$

In practice, to take a closer look at possible high-order l – small distances – differences, we examine the correlation coefficients through:

$$D_l = \frac{l(l+1)}{2\pi} C_l. \tag{1.38}$$

[10] Where we have the normalisation $|Y_{lm}|^2 = \frac{1}{4\pi}$.

[11] Let us notice we have implicitly used the ergodic hypothesis to write:

$$\left\langle \int \mathrm{d}\boldsymbol{k} \int \mathrm{d}\boldsymbol{k'}\ \Theta^*(\boldsymbol{k})\ \Xi(\boldsymbol{k'}) \right\rangle = \int \mathrm{d}\boldsymbol{k} \int \mathrm{d}\boldsymbol{k'}\ \langle \Theta^*(\boldsymbol{k})\ \Xi(\boldsymbol{k'})\rangle.$$

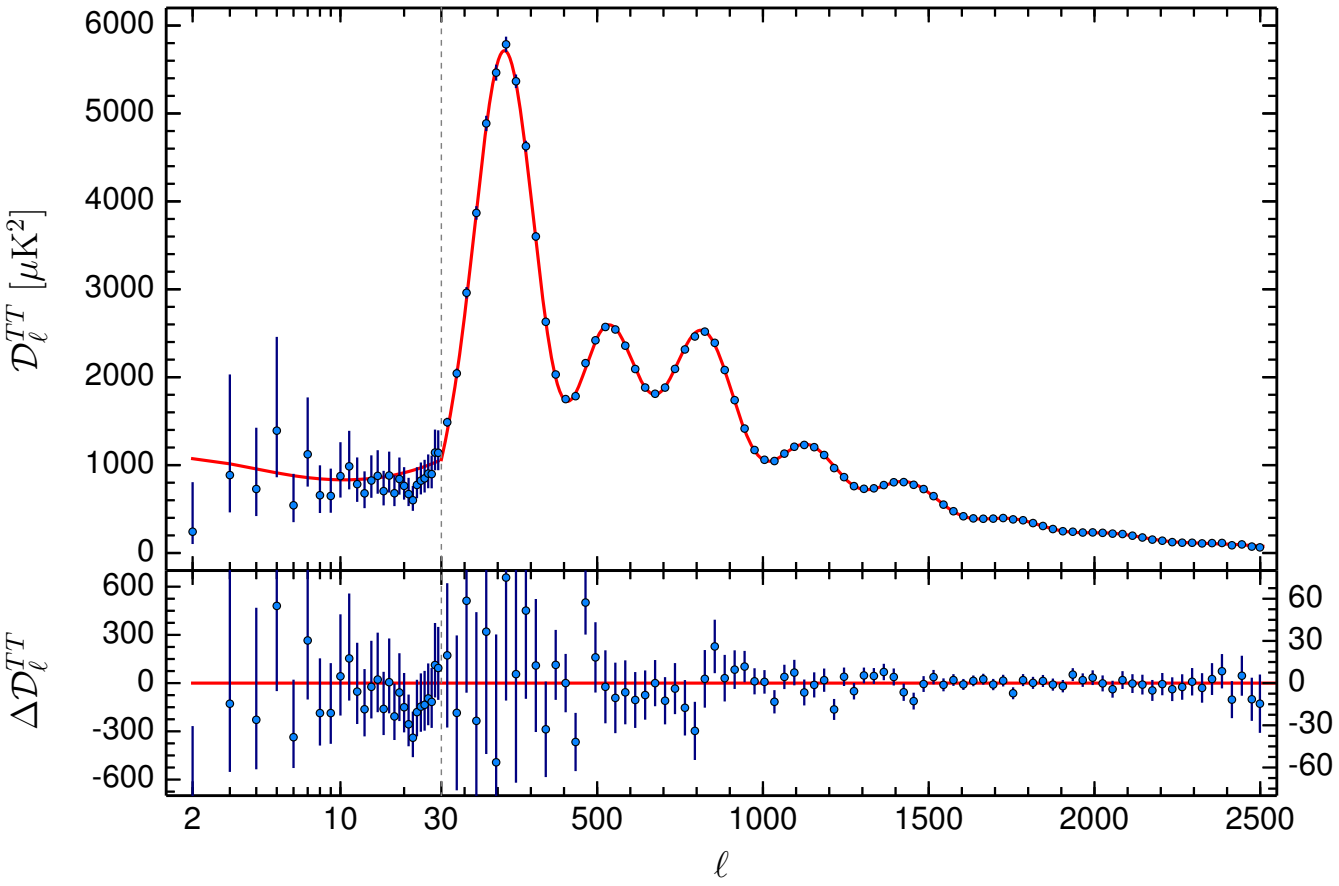

Figure 1.6: Temperature power spectrum (Planck Collaboration, 2016). This shows the remarkable agreement between the standard model of cosmology ΛCDM and the observational *Planck* data. $l = 30$ is displayed with a grey dashed line. For $l \geq 30$, the best fit is provided by `Plik`, and for $l < 30$, with `Commander`.

At large $l \gg 1$, one can use the flat-sky and the Limber approximations ($l \approx k f_K(z)$, see Limber, 1954) to simplify this expression for the temperature contrast:

$$D_l^{TT} \approx \frac{k^3 P_{TT}(k)}{2\pi^2}. \tag{1.39}$$

Planck measured precisely this observable as presented on Figure 1.6, concluding to a remarkable agreement with the ΛCDM cosmological model. More generally, the power spectrum (of temperature, of the overdensity δ, etc.) contains important information on the cosmological model.

1.2 Dark matter

We have already hinted in the previous section at a non-relativistic matter component, not made of baryons: dark matter (DM). We discuss its observational motivations, and review a few models to explain its nature.

1.2.1 Astronomical motivations for dark matter

Excessive velocity dispersions were first discussed, in the case of stars in the Milky Way, by Lord Kelvin, and Henri Poincaré called this idea '*matière obscure*' ('dark matter', Poincaré, 1906). Historically, the first evidence of missing massive matter came from the velocity dispersion of individual galaxies in the Coma and Virgo galaxy clusters. Indeed, Zwicky (1933), Smith (1936), and Zwicky (1937b) noticed the enormous velocity dispersion of galaxies in these clusters. Zwicky applied the virial theorem to determine their mass (see equation 1.46), and found evidence of missing matter he called 'dunkle Materie' ('dark matter'). He was however conscious the intergalactic, baryonic medium could not be taken into account, as its density had not been measured yet. A more complete history record of the origins and first ideas of dark matter can be found in Bertone and Hooper (2018).

The problem was then found to also extend to galaxies themselves. The rotation velocity in the outskirts of the neighbour spiral galaxy Andromeda (M31) was found to be much higher than expected, and the mass-to-light ratio to be very small (Babcock, 1939; Oort, 1940). In Davidsen et al. (1973), the intracluster gas in the Coma cluster was proven to not be sufficient to bound it gravitationally, excluding a possible baryonic explanation. Moreover, Rubin and Ford (1970) and Rubin et al. (1980) used stellar observations to provide evidence the rotation curves of galaxies were approximately flat out of the very core, meaning the rotation speed are constant. This result was consolidated at larger radii by Bosma (1981), who utilised 21 cm astronomy to observe the rotation velocity of neutral hydrogen in spiral galaxies. No explanation with observable matter could be provided, and dark matter started appearing to be a possible beyond-Standard Model of particle physics element. An empirical explanation was then proposed, under the form of the existence of a dark matter halo associated to each galaxy and cluster of galaxies (in Einasto et al., 1974; Ostriker et al., 1974).

In the 1980s, the first strong gravitational lensing observations provided a new probe of total gravitational potential of galaxy clusters. Indeed, as presented in details in Chapter 2, in GR massive astrophysical objects (the *lenses*) may distort the space-time continuum. As a result, the light travelling from a background luminous source close to the lens – observer line-of-sight may be deflected. This creates an image of the source with a different position and geometry than without the foreground lensing object. This *lensing* effect may even produce one background source to be multiply-imaged to the observer. With precise lens modelling, it is possible to infer the gravitational properties of a lensing galaxy cluster, as pioneered in Walsh et al. (1979). As a result, the massive dark matter could be detected with gravitational lensing, as reviewed in Ellis (2010). The agreement between this mass measuring technique and dynamical studies pointed to about 85 % of the mass of clusters missing.

In Clowe et al. (2004, 2006), the merging cluster 1E0657-558, nicknamed the 'Bullet Cluster', was found to present a large offset between the baryonic hot gas ICM observed in the X-rays, and the gravitational potential distribution, reconstructed with gravitational lensing. This allowed to set important constraints on the possible self-interaction rate of dark matter as pioneered in Markevitch et al. (2004): assuming the collision occurs in the plane of the sky, the gas lagging behind the centre of the main subcluster galaxies provides important information on the difference of collision occurring in each component. The gas is submitted to ram pressure (see Section 1.3.4.1) while galaxies and dark matter appear to be collisionless. This scenario was then discovered in other clusters such as MACS J0025.4-1222 in Bradač et al. (2008). As a result, Markevitch et al. (2004) find the DM self-interaction cross-section to mass ratio to be $\sigma_{\chi\chi}/m_\chi < 1\,\mathrm{cm}^2.\mathrm{g}^{-1}$.

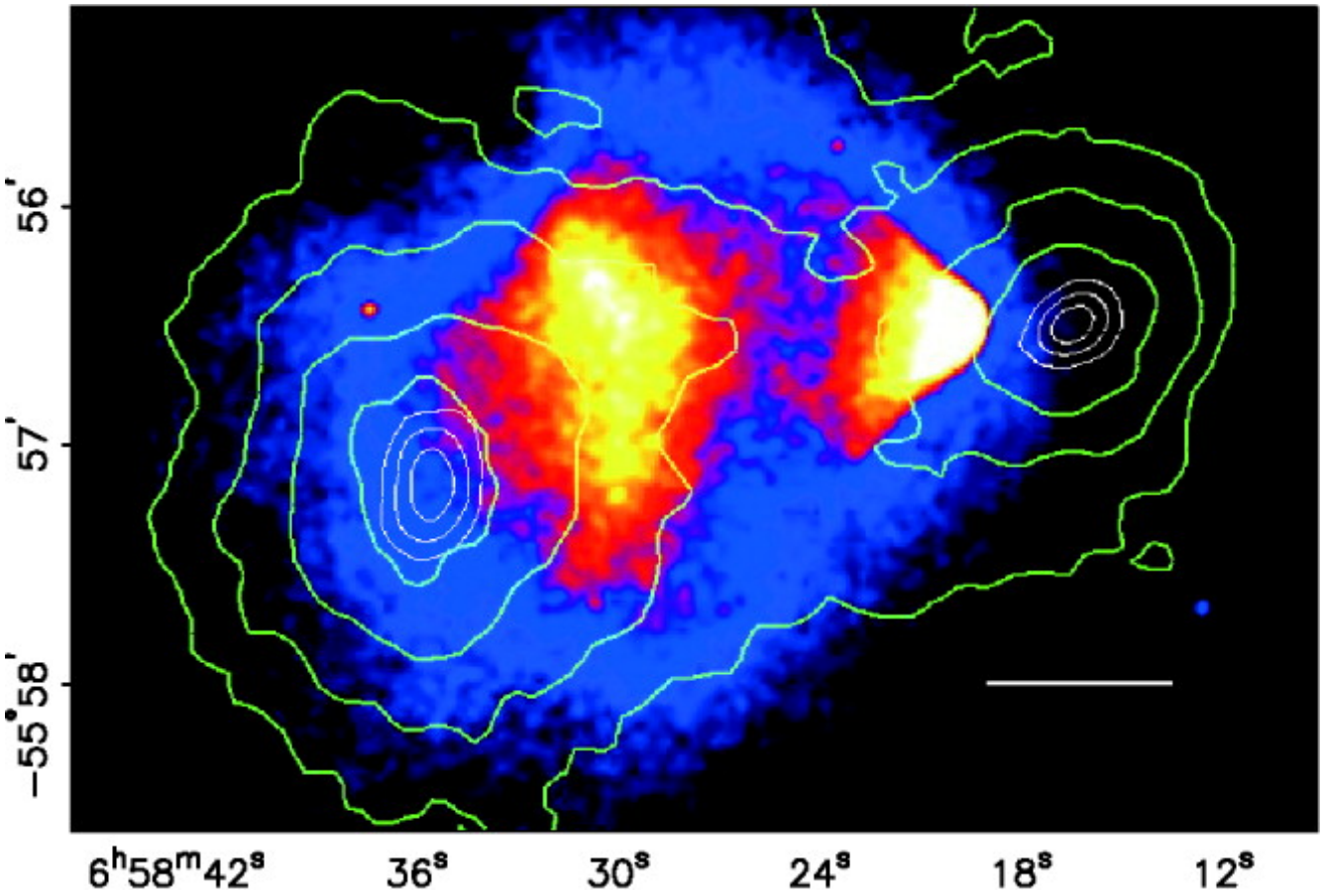

Figure 1.7: Bullet Cluster, as observed in Clowe et al. (2006). The green contours denote the convergence κ, reconstructed with weak lensing. The convergence peaks are presented in white, denoting the highest mass – and thus dark matter – densities. The image presents *Chandra* X-ray data, therefore showing the intra-cluster medium to lag behind the massive components of the cluster, due to the ram stripping pressure.

In the 1980s and 1990s, missions *RELIKT-1* and the *Cosmic Background Explorer* (*COBE*, Smoot et al., 1992) provided the first CMB temperature anisotropy measurement, but it is its successor, the Wilkinson Microwave Anisotropy Probe (WMAP, see Bennett et al., 2003; Hinshaw et al., 2013) which provided proof of the existence of another type of non-relativistic matter.

At last, N-body simulations in the recent years have also risen new problems. We briefly discuss the cusp-core problem in Section 1.3.3.2. Simulations also yield a much larger number of satellite galaxies to the Milky Way than observations (Drlica-Wagner et al., 2015), yielding the Missing Satellite Galaxies problem (Klypin et al., 1999; Moore et al., 1999b). Probing satellite galaxies to the Milky Way is also a way to set constraints on some dark matter models (see Boehm et al., 2014; Nadler et al., 2021). Moreover, the local Universe does not seem to contain as many massive galaxies as it should according to ΛCDM structure formation models predictions. Because halos of $10^{10} M_{\odot}$ should form stars efficiently, they should be observable. This is referred to as the 'too-Big-to-Fail' problem (Boylan-Kolchin et al., 2011). In 2022, the search for dark matter is one of *the most* pressing problems both in astrophysics and particle physics. (for reviews of dark matter in the context of astronomy, see Bullock and Boylan-Kolchin, 2017; Buckley and Peter, 2018).

1.2.2 Summary of dark matter models

In Section 1.2.1, we have alluded to astronomical motivations for dark matter, including the rotation curves of galaxies, galaxy clusters physics, gravitational lensing, the CMB and simulations. In this Section, we present the more general context of dark matter particle candidates research.

1.2.2.1 Dark matter properties

In spite of being the most precise theoretical model ever elaborated, the Standard Model of particle physics (SM) can not be considered to be complete. From an observational astronomy perspective, it notably fails to propose a candidate for dark matter. Indeed, to be a possible DM candidate, a particle needs to be following the following properties.

- Besides gravitationally, the interaction of DM with SM particles is constrained, i.e. the $\sigma_{\chi b}$ cross-section is weaker than the SM electromagnetic or strong interactions. Otherwise, merging clusters such as the Bullet Cluster could present visible ICM-DM interactions[12]. Moreover, this possible interaction should be weak enough not to suppress the matter power spectrum at early cosmic times, as baryonic matter and radiation could prevent DM density perturbation growth.
- Strong DM self-interactions could modify the matter power spectrum, e.g. creating dark matter acoustic oscillations (see Bœhm et al., 2001, 2002, 2003). This could delay the growth of structures. As a consequence, the observed size of DM halos in clusters and galaxies constrains the scattering of DM – with other species including itself.
- Dark matter models are commonly distinguished between *Cold* DM (CDM, see Peebles, 1982), *Warm* DM (WDM, see Bond et al., 1982; Blumenthal et al., 1982, 1984) and *Hot* DM (HDM, see Doroshkevich et al., 1981; Zel'dovich et al., 1982; Bond and Szalay, 1983; White et al., 1983). These terms however do not refer to the temperature of the DM fluid, but to the speed of particles in the epoch of structure formation: the 'hottest' dark matter scenarios correspond to the fastest DM particles (Bertone and Hooper, 2018). As a consequence, HDM presents ultra-relativistic DM velocities, and therefore large free-streaming scales (see Boehm and Schaeffer, 2005), which results into the suppression of small-scale structures. The early formed massive structures would then have fragmented to form the Universe known today. Conversely, CDM presents a much smaller free-streaming scale, allowing the formation of small structures, and thus for a hierarchical model of structure formation. CMB surveys such as *Planck* present an isotropic early Universe, which could not have formed the earliest galaxies observed if the free-streaming scale of DM was too important. As a consequence, HDM is considered to be ruled out as the only explanation for DM. Let us note the particle free-streaming decreases as the DM particle mass is increasing. As this small-scale suppression depends on DM mass (and free-streaming length), an intermediate mass range WDM ($m_\chi \sim$keV, see Schaeffer and Silk, 1988; Bode et al., 2001) may be allowed, as long as it allows to explain the existence of the smallest observed structures requiring DM clustering from e.g. the Lyman-α forest[13] (Yèche et al., 2017; Murgia et al., 2018), stellar streams

[12] This yields $\sigma_{\chi b} \lesssim 10^{-25}$ cm^2, which is still allowed to be larger than the Thomson scattering, i.e. commensurable with an electroweak interaction.

[13] The Lyman-α forest, discovered by Lynds (1971), arises from an electronic transition in neutral hydrogen. This neutral hydrogen emitted light in the early Universe, e.g. in quasars, yielding a Lyman-α emission peak. The 'forest' is composed of absorption lines due to the foreground gas. Its observation allows to constrain the cosmological model (Weinberg et al., 2003). One can visualise the forest with this animation.

(Banik et al., 2021) and strong gravitational lensing (Gilman et al., 2020). WDM may even alleviate the too-Big-to-Fail problem (Lovell et al., 2017). A candidate as WDM could be sterile neutrinos (Boyarsky et al., 2019).

- The Big Bang Nucleosynthesis (BBN) model predicts extraordinarily well the atomic abundances of light elements, constraining the SM critical density Ω_b to be smaller than the total matter density Ω_m: $\Omega_b < \Omega_m$. A possible strong coupling between DM and baryonic matter is allowed before BBN, but the density of DM should be compatible with BBN, and explain the $\Omega_m - \Omega_b$ difference (see e.g. Bœhm et al., 2013).
- Given that the non-baryonic, non-relativistic critical density observed before BBN and at present day are sensibly the same, DM can not decay at a significant rate compared to the lifetime of Universe. This constrain is set by the matter power spectrum (the DM inverse lifetime must be $\lesssim 10^{-2}\,\mathrm{Gyr}^{-1}$, see Poulin et al., 2016).

We shortly summarise here a few different types of candidates to explain dark matter, represented on Figure 1.9. More thorough, useful reviews include Griest and Kamionkowski (1990), Feng (2010), Bauer and Plehn (2017), Bertone and Hooper (2018), and Lin (2019).

1.2.2.2 Modified gravity

Modified gravity is the main alternative to dark matter. Its core idea is to modify the laws of gravity. It was first explored by Milgrom's Modified Newtonian Dynamics (MOND, see Milgrom, 1983a,b,c), which explains the rotation curves of galaxies without dark matter (Sanders, 1996). According to this model, gravity behaves differently than predicted in Newtonian physics in the weak acceleration limit. This may explain the baryonic Tully-Fisher relationship (see McGaugh, 2012, and equation 1.50). Another advantage of modifying gravity could be to explain naturally dark energy, such as in Nojiri and Odintsov (2003). Moreover, Chae et al. (2020) point to a breakdown of the strong equivalence principal, one of the cornerstones of general relativity but not of MOND.

In order to unify modified gravity (MG, see Nojiri et al., 2017, for a review) with the observational successes of GR, Bekenstein proposed a covariant Tensor-Vector-Scalar (TeVeS) modified gravity, matching MOND in the weak field limit and GR in stronger fields (Bekenstein, 2004). The major problem of TeVeS however is that it fails to explain CMB observations, and notably the difference between the baryon density Ω_b and the matter density Ω_m, or the power spectrum of large scale structures (Skordis et al., 2006; McGaugh, 2015). Some models try to address this issue (such as Skordis, 2009; Skordis and Złośnik, 2021).

Nevertheless, the weak lensing KiDS survey appears to be in agreement with MOND as of Brouwer et al. (2021) and weak lensing surveys may in fact allow to discriminate modified gravity models from ΛCDM in the future. However, strong lensing may be more powerful tool to rule out modified gravity models (see Capozziello et al., 2006, for a review). Nieuwenhuizen (2017) argues the measured potential in the centre of clusters, where Newtonian dynamics should apply, requires a dark matter explanation. A number of MG analyses indeed need to add more matter to be justified (Sanders, 2007). Moreover, the joint ICM and lensing analysis of the Bullet Cluster suggests the ICM (composing the majority of the baryonic mass) presents a strong positional offset from the mass distribution centres. This tends to favour a matter component rather than MG.

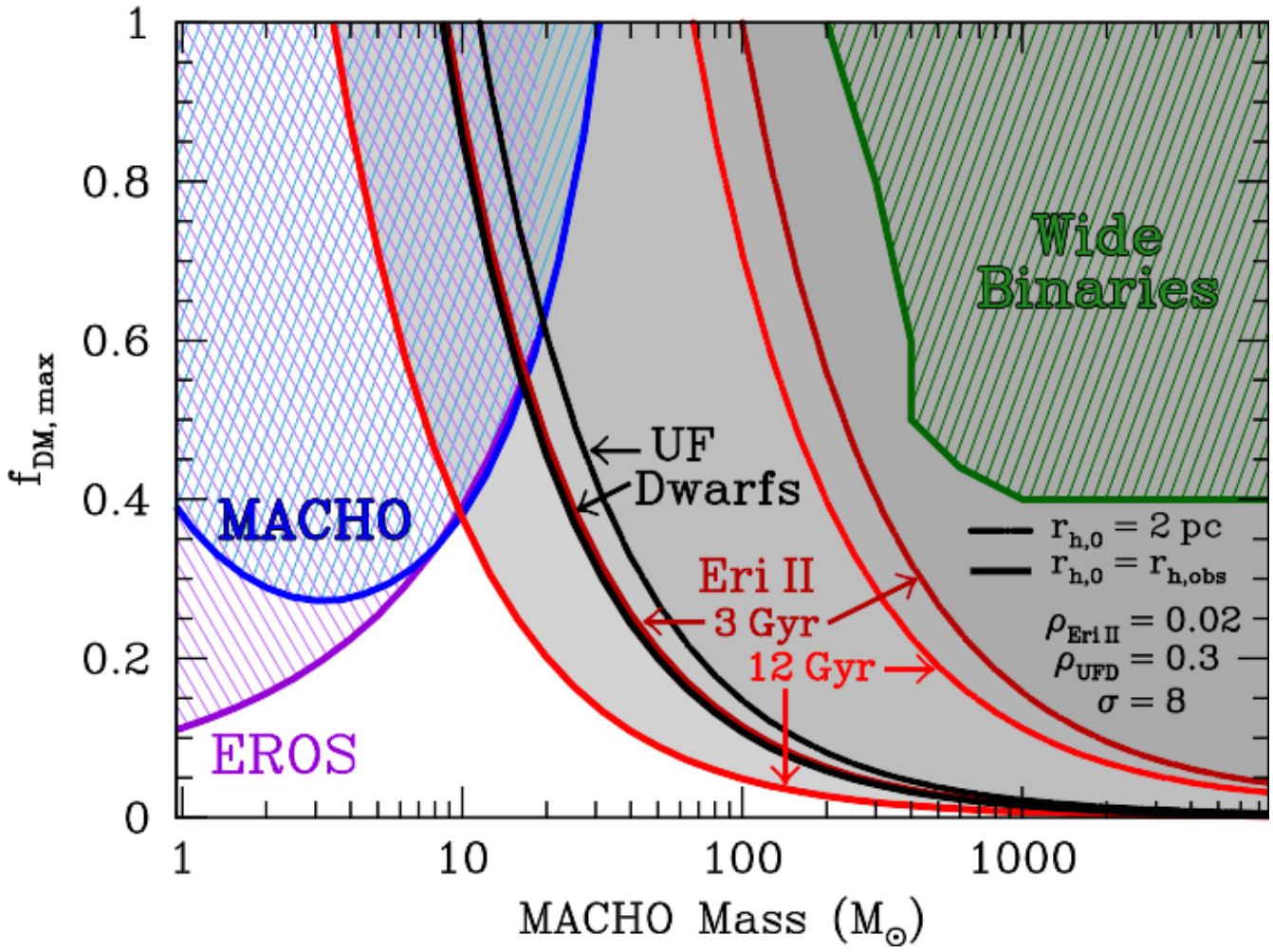

Figure 1.8: MACHO constraints presented in Brandt (2016). $f_{\mathrm{DM,max}}$ represents the maximum fraction of DM which can be MACHO.

1.2.2.3 Massive compact halo objects (MACHO)

Massive compact halo objects (MACHO) are candidates to explain the missing mass in galaxies without requiring a new type of matter, but rather dim baryonic objects. These could be composed of compact objects, brown dwarfs, rogue planets and other faint baryonic objects. These objects generate microlensing events, i.e. lensing by compact objects as described in Chapter 2. The observation of the number of occurrences of such events allows to constrain the fraction of MACHO which may be considered as DM. The present-day surveys suggest such objects are disqualified to represent a sizeable fraction of dark matter (see Freese et al. 2000; Alcock et al. 2001; surveys include the MACHO Project, Alcock et al. 1997, the *Expérience pour la Recherche d'Objets Sombres* – EROS, Tisserand et al. 2007, and the Optical Gravitational Lensing Experiment – OGLE, Udalski et al. 1997). Other considerations such as the observation of compact stellar systems (Brandt, 2016) or metallicity measurement also allow to constrain the 'MACHO as DM' parameter space: the maximum fraction of MACHO possible for DM in the stellar mass range is $f_{\mathrm{DM,max}} \lesssim 0.4$, as represented on Figure 1.8. Research in this field continues, and the possibility of MACHO being a part of the missing mass alongside another component, such as e.g. primordial black holes (Calcino et al., 2018) is still explored.

1.2.2.4 Primordial Black Holes (PBH)

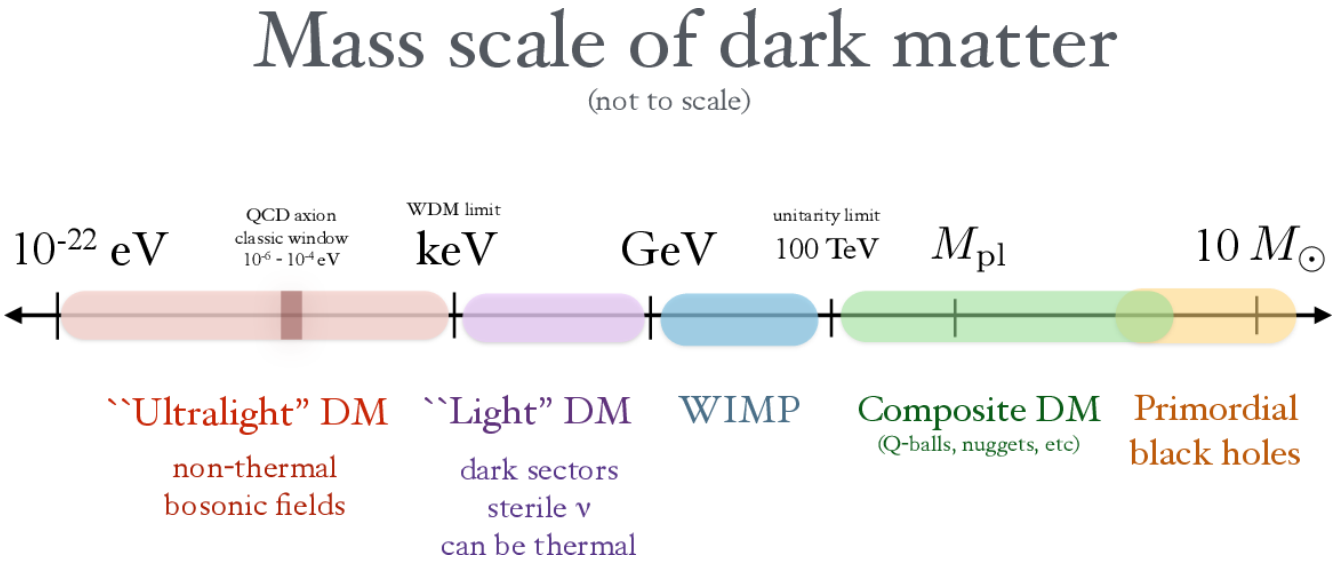

Figure 1.9: A few dark matter candidates allowed mass range, taken from Lin (2019).

Primordial Black Holes (PBH, first presented in Zel'dovich and Novikov, 1967; Hawking, 1971; Carr and Hawking, 1974; Chapline, 1975) are assumed to have formed from the collapse of density perturbations of the early Universe. In this way, they are a type of MACHO, as they do not require beyond standard model (BSM) physics to be explained. If forming before the BBN, PBH could be considered to be non-baryonic, and thus would be similar to CDM and compatible with BBN. For a review on PBH as DM, one may read Carr and Kühnel (2020, 2021). As MACHO, they could be constrained using microlensing events (see Tisserand et al., 2007), but also through their expected Hawking radiation (see Hawking 1975 for Hawking radiation, and Carr et al. 2010 for the constraints on PBH), dynamical effects on stellar systems (Brandt, 2016), extragalactic lensing (Zumalacárregui and Seljak, 2018) and early accretion (Hektor et al., 2018).

Since 2019 and the detection of an intermediate mass range black hole merger with LIGO/Virgo (Abbott et al., 2020a,b), PBH as DM have benefited a renewed interest. Indeed, this mass range of black holes could be explained by PBH (Bird et al., 2016), and not by star formation models. Assuming PBH to constitute a sizeable fraction of DM, Sasaki et al. (2016) and Ali-Haïmoud et al. (2017) claim that their binary production rate should be much higher than observed by gravitational wave interferometry LIGO/Virgo. However it may be possible to evade these constraints in the $30 - 100 M_\odot$ range treating PBH with a Thakurta metric instead of Schwarzschild (Bœhm et al., 2021).

1.2.2.5 Weakly Interacting Massive Particles (WIMP)

Given the few known DM properties (see Section 1.2.2.1), the remaining class of candidates needs to be made of weakly interacting massive particles, referred to as WIMP (see Bertone et al. 2005; Bauer and Plehn 2017 for a theoretical review, and Schumann 2019 for WIMP detection review).

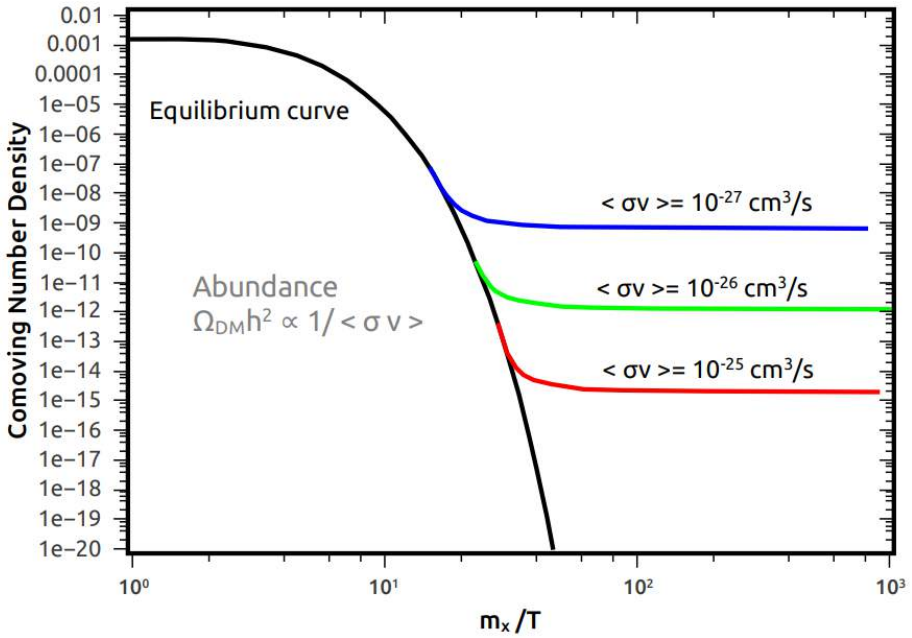

Figure 1.10: Dark matter *freeze-out* comoving densities, given different $\langle \sigma v \rangle$. In the first phase ($m_\chi < T$), the thermal bath of SM particles is in chemical equilibrium with DM annihilation, and thus the comoving densities are constant. Under the effect of expansion, the DM annihilation back reaction stops as the temperature of the Universe drops $T < m_\chi$. As a result, the comoving DM density exponentially decreases. The black curve represents the chemical equilibrium. The chemical decoupling of the SM and DM densities, due to the statistically low probability of DM self-interaction, *freezes-out* the DM comoving density to a constant value, observed in the later Universe. The value of the comoving DM critical density parameter $\Omega_\chi h^2$ is inversely proportional to the annihilation cross-section times velocity $\langle \sigma_{\chi\chi} v \rangle$, as presented for the blue, green and red curves. Credits: Arcadi et al. (2018).

Thermal production

The standard mechanism to produce WIMP particles as DM (χ) is to assume they were in chemical equilibrium with SM particles (f) in the early Universe thermal bath: $\chi\chi \rightleftharpoons ff$, described by the Boltzmann equation (see Hut, 1977; Lee and Weinberg, 1977; Kolb and Turner, 1990):

$$\frac{\mathrm{d}n_\chi}{\mathrm{d}t} + 3Hn_\chi = -\langle \sigma_{\chi\chi} v \rangle \left[n_\chi - (n_\chi^{\mathrm{eq}})^2 \right], \tag{1.40}$$

where $\langle \sigma_{\chi\chi} v \rangle$ is the thermally averaged DM annihilation cross-section times velocity, and n_χ^{eq} the dark matter equilibrium number density. With s the comoving entropy density, one can rewrite equation (1.40) with the relic yield $Y = n_\chi / s$ as a function of $x = m_\chi / T$:

$$\begin{aligned} \frac{\mathrm{d}Y}{\mathrm{d}x} &= -\frac{C\langle \sigma_{\chi\chi} v \rangle}{x^2} \left[Y^2(x) - Y_{\mathrm{eq}}^2(x) \right], \\ C &= \sqrt{\frac{\pi g_\star}{45}} M_{\mathrm{Pl}} m_\chi, \end{aligned} \tag{1.41}$$

where M_{Pl} is the Planck mass, and $g_\star$ the number of relativistic degrees of freedom of the temperature (Steigman et al., 2012). As long as the temperature of the Universe is sufficient, the

comoving density of both species remains constant. As the Universe expanded, it cooled down. As a result, the DM annihilation only remained: $\chi\chi \to ff$, as the thermal bath of SM particles was not energetic enough to yield the reverse reaction ($T < m_\chi$). Consequently, the DM density decreases exponentially, following a distribution $n_\chi \propto (m_\chi T)^{3/2} \exp(-m_\chi/T)$.

When the annihilation rate of DM Γ_χ reaches the Hubble factor:

$$\Gamma_\chi = n_\chi^{\rm eq} \langle \sigma_{\chi\chi} v \rangle = H, \tag{1.42}$$

the self-interaction of DM becomes *statistically impossible*[14], and DM decouples from the SM thermal bath to keep a constant DM comoving density. As a result, the density of DM in the later Universe is the relic of this early time chemical decoupling of SM, and of the subsequent DM *freeze-out* (see Figure 1.10). The class of DM particles produced thermally in the early Universe and frozen-out by expansion is known as the *thermal relics* (Zel'dovich, 1965; Chiu, 1966; Steigman, 1979; Scherrer and Turner, 1986). For a relic abundance generated with a WIMP mass scale ($m_\chi \sim 100\,\mathrm{GeV}$), the comoving critical density parameter reads:

$$\Omega_\chi h^2 \simeq 0.1 \left(\frac{3 \times 10^{-26}\,\mathrm{cm}^3.\mathrm{s}^{-1}}{\langle \sigma_{\chi\chi} v \rangle} \right), \tag{1.43}$$

i.e. the cross-section $\langle \sigma_{\chi\chi} v \rangle \sim 3 \times 10^{-26}\,\mathrm{cm}^3.\mathrm{s}^{-1}$ is compatible with the present-day measurements of the DM abundance. This corresponds to the scale of electroweak interactions. The natural WIMP mass range[15] and annihilation cross-section explaining the thermal relic density required to constitute dark matter belongs to the same range as expected supersymmetric BSM models (Srednicki et al., 1988; Gondolo and Gelmini, 1991; Jungman et al., 1996). This coincidence is known as the 'WIMP miracle'. We present the direct detection WIMP constraints on Figure 1.11.

Non-thermal production

The WIMP mass range can be complemented by another type of candidates: the Feebly Interacting Massive Particles (FIMP, see Hall et al., 2010; Bernal et al., 2017; Agrawal et al., 2021, for a review). In the SM thermal bath of the early Universe, their density would initially have been insignificant. They would have been produced non-thermally by a *freeze-in* mechanism – see Figure 1.12. As FIMP interact very feebly with the SM sector, they were progressively produced at very high temperature $T > m_\chi$ in the early Universe SM thermal bath: $ff \to \chi\chi$. Their comoving density never reached chemical equilibrium with the SM thermal bath (contrarily to the freeze-out mechanism), and was thermally frozen by expansion, as the temperature dropped to $T < m_\chi$. The FIMP production would have stopped because of the cooling down of the SM particle bath. The comoving relic density would then depend on the DM coupling. To recover the present-day DM density, we estimate the self-interaction of DM should be $\langle \sigma_{\chi\chi} v \rangle \sim 10^{-47}\,\mathrm{cm}^3.\mathrm{s}^{-1}$. The FIMP mass range could extend much further the WIMP scale, possibly reaching the ultra-light DM range. Some proposed candidates are also motivated by other SM problems, such as the strong CP problem or the neutrino mass.

[14] This does not mean that it can not happen in some localised structures, but it does not govern the Universe as a whole.

[15] $m_\chi \in [10\,\mathrm{GeV}, 100\,\mathrm{TeV}]$, the higher bound being due to the unitary bound, or overclosure problem (Griest and Kamionkowski, 1990). Lighter thermal DM candidates are however possible (Bœhm and Fayet, 2004).

[16] This is not a hard limit, and is described statistically. Here, it is defined as the cross section σ_d at which a given experiment has a 90% probability to detect a WIMP with a scattering cross section $\sigma > \sigma_d$ at ≥ 3 sigma.

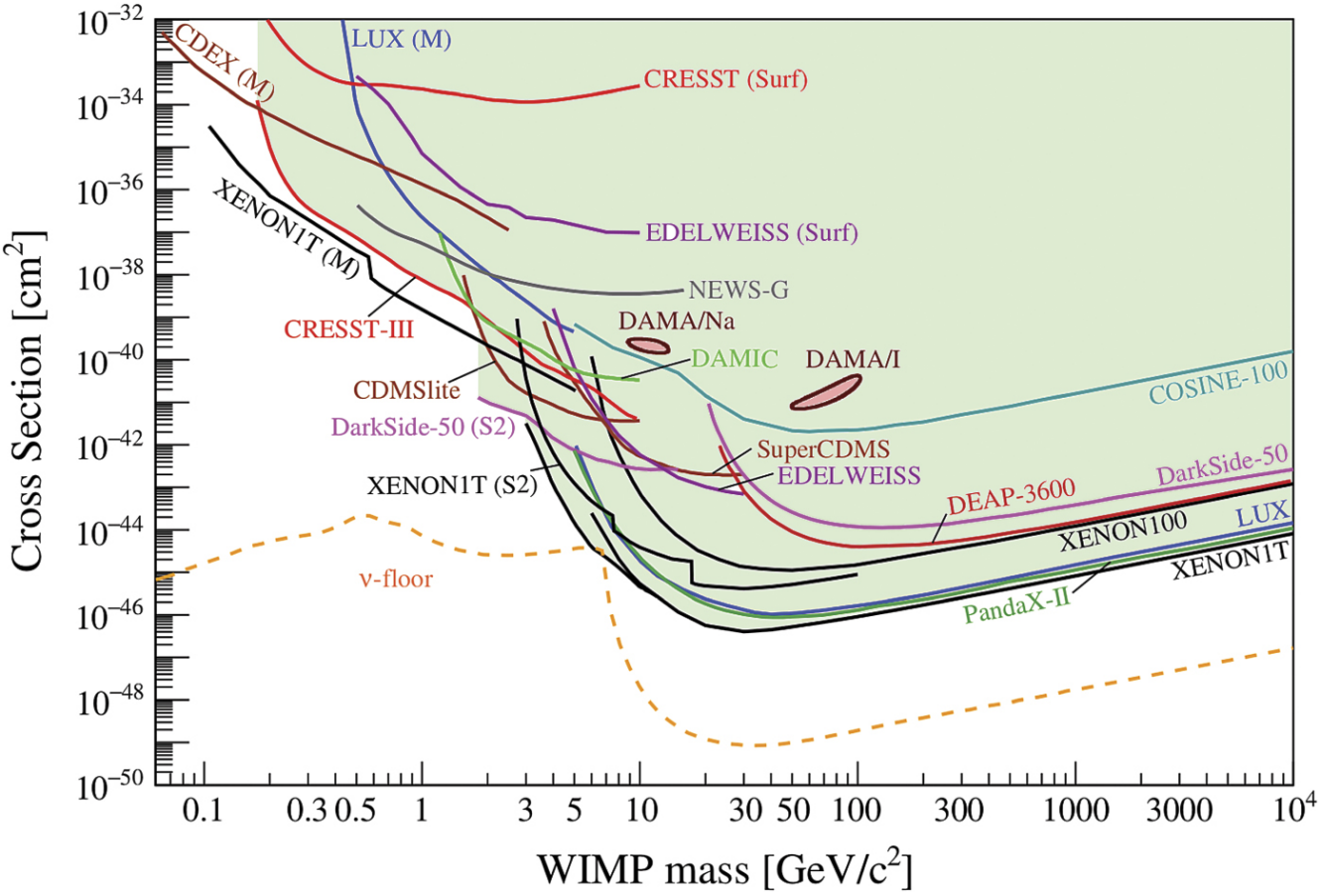

Figure 1.11: Direct detection constraints on a spin-independent elastic WIMP-nucleus scattering. The green background is the excluded (90% probability) parameter space for a WIMP DM. The yellow dashed line is the 'neutrino floor', i.e. the limit under which coherent neutrino scattering is expected to be detected, and not distinguished from WIMP[16]. All coloured plain lines refer to direct detection experiments. This is a reproduction of Figure 3 of Billard et al. (2022).

1.2.2.6 Ultra-light dark matter

Below the eV mass range, we refer to DM candidates as ultra-light dark matter (see Ferreira, 2021, for a review). The statistical behaviour of such light candidates follows that of coherent fields. In the presence of a gravitational potential, it thus presents a Jeans scale (corresponding to the de Broglie wavelength in the case of galaxies, i.e. the most compressed particles may be), below which growth of perturbations is suppressed, resulting into a change of the small scale power spectrum, and more cored DM halos. Dwarf spheroidal galaxies, the Lyman-α forest and superradiance can therefore be used to set a constrain on the largest scales which can not be washed out by ultralight dark matter: as typically these must be $R_J = \lambda_{\rm dB} \lesssim 1\,{\rm kpc}$, this yields a minimal mass $m_\chi \gtrsim 10^{-22}\,{\rm eV}$. This specific limit case at $m_\chi \sim 10^{-22}\,{\rm eV}$ is called fuzzy cold dark matter (FDM) and was proposed to solve the cusp-core halo problem (Hu et al., 2000; Hui et al., 2017; Davoudiasl and Denton, 2019).

Axions in particular are pseudoscalar light particles, first proposed to explain the absence of CP violation in quantum chromodynamics (QCD, see Peccei and Quinn, 1977; Kim and Carosi, 2010, for axions as solutions to this strong CP problem). More generally, string theory has provided

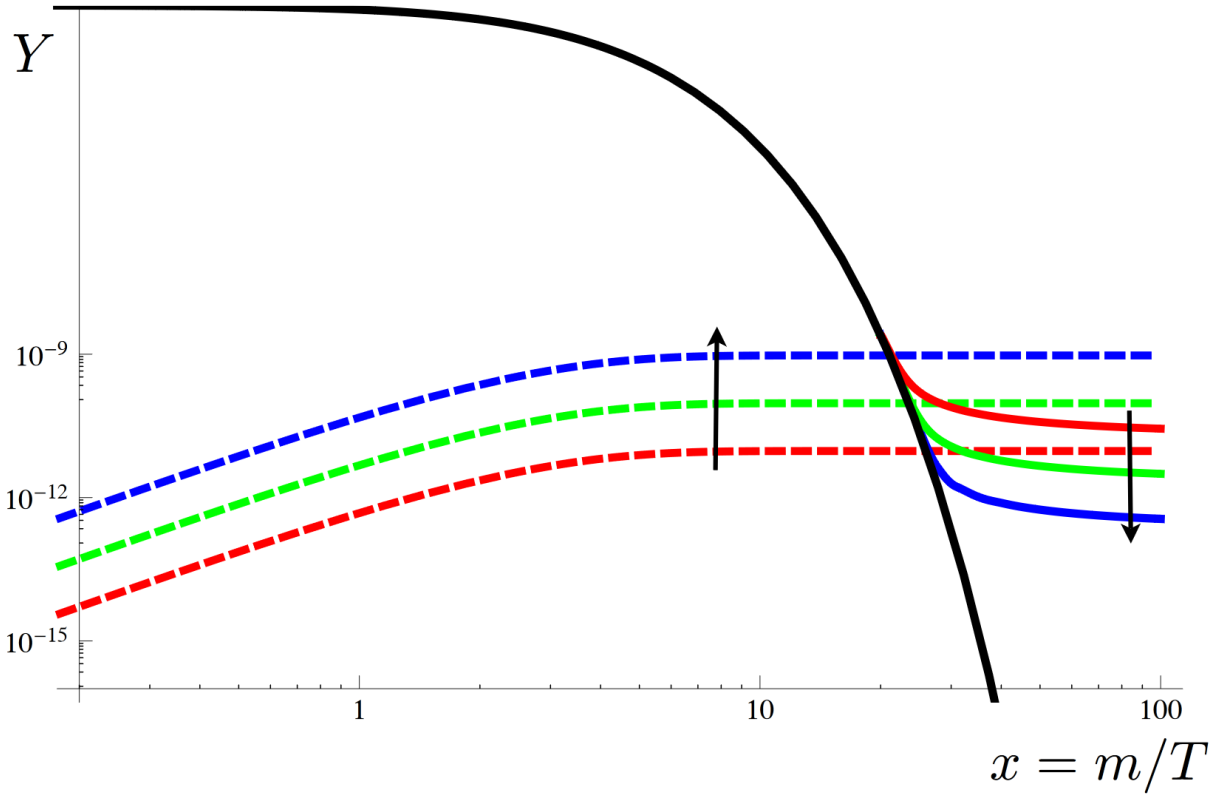

Figure 1.12: Dark matter *freeze-in* comoving densities for different $\langle\sigma v\rangle$. The solid black line represent the relic yield $Y = n_\chi/s$ assuming the SM particles to be in equilibrium with the DM, where s is the entropy density of the plasma. The solid coloured lines represent the freeze-out evolution of the relic yield; and the dashed coloured lines the freeze-in evolution. The arrows indicate the effect of increasing the $\langle\sigma v\rangle$ coupling strength for both processes. This is a reproduction of Figure 1 of Hall et al. (2010).

motivations to look for axion-like particles (ALP) sharing the same type of properties, with different theoretical motivations. To explain the possible generation of axions and ALP, a range of non-thermal mechanisms have been imagined, such as the 'misalignment mechanism'.

1.2.3 Self-Interacting Dark Matter constraints

In this Section, we present different methods used to constrain Self-Interacting Dark Matter (SIDM, see Tulin and Yu, 2018, for a review) scenarios. SIDM can alleviate tensions between the results of DM-only simulations, and observational problems such as the cusp-core problem (Kochanek and White, 2000), the missing satellite galaxies problem or the too-Big-to-Fail problem (Vogelsberger et al., 2016).

Gravitational lensing can be used as a probe of the DM self-interaction through the study of the offset between the luminous galaxies and the dark matter halo (DMH). The strongest constraints to this day are claimed by Meneghetti et al. (2001) at $\sigma_{\chi\chi}/m_\chi \lesssim 0.1$ cm^2.g^{-1}, in the context of giant cluster arcs, for a DM-DM particle relative velocity $v_{\chi\chi} = 1000\,\mathrm{km.s^{-1}}$.

In CDM scenarios without DM interactions, merging clusters simulations predict the dark

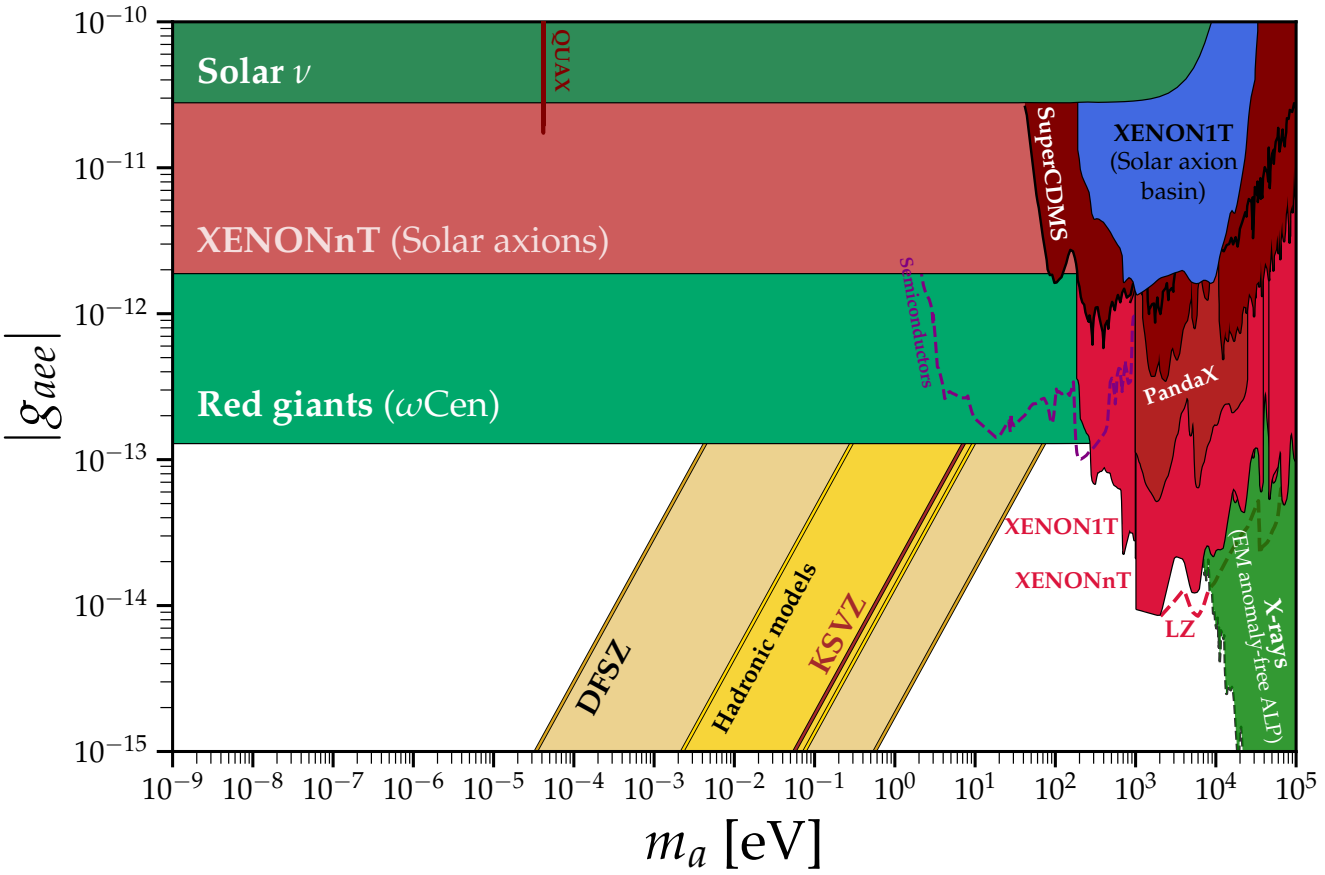

Figure 1.13: Observational and experimental constraints on axions (and ALP), provided by O'Hare (2020).

matter halo centre to be the same as that of luminous matter, whilst conversely SIDM scenarios with a sizeable self-interaction predict the DMH to be slowed down (for SIDM simulations, see Massey et al., 2011; Harvey et al., 2015; Robertson et al., 2017a,b)[17]. As a result, comparing the respective positions of luminous and dark matter allows to set constraints on the self-interaction.

Moreover, including baryons in hydrostatic equilibrium in simulations, CDM scenarios as well as SIDM appear to be possible, as baryons seem to alleviate a number of CDM-only simulational problems. For instance, Despali et al. (2022) present simulations including baryons at hydrostatic equilibrium, compatible with both CDM and with a self-interaction $\sigma_{\chi\chi}/m_\chi = 1\,\mathrm{cm}^2.\mathrm{g}^{-1}$, while Robertson et al. (2019) claim to be in slight tension with strong lensing for the same $\sigma_{\chi\chi}/m_\chi$ value. Using the X-COP cluster sample and self-interacting DM hydrodynamical simulations of cluster formation (`BAHAMAS-SIDM`), Eckert et al. (2022a) find $\sigma_{\chi\chi}/m_\chi < 0.19\,\mathrm{cm}^2.\mathrm{g}^{-1}$. This outlines the importance of baryons in understanding the DM distribution, and therefore its physical nature.

Another type of possible observational effect of SIDM is the modification of structure formation. Using SIDM scattering rates through cosmic times of galaxy clusters, Robertson et al. (2015, 2017a) present an analytical calculation of the rate of DM-DM scattering events $\Gamma_{\chi\chi}$, for particle physics models with velocity-independent (viSIDM) or velocity-dependent (vdSIDM) cross-sections. The former case is found to mostly affect massive structures ($\gtrsim 10^{12} M_\odot$) at late times ($z \lesssim 1$), while the

[17]Let us note SIDM simulations may probe different models, e.g. elastic or inelastic scattering, or velocity-dependent cross section.

latter may peak at much earlier time, on smaller structures. While the former does not significantly modify the power spectrum, the latter may wash out some small structures, producing effects similar to that of WDM.

The study of the density power-spectrum, especially on the small physical scales, thus allows to set constraints on the nature of DM. The local understanding of the distribution of DM and of the overall physics of galaxy clusters is one of the most promising pathway to understand dark matter.

1.3 The physics of galaxy clusters

1.3.1 The formation of galaxy clusters

When the expansion of the Universe cooled down the cosmological fluid to $\sim 3000\,\mathrm{K}$, the electrons combined to the atomic nuclei and the Universe became transparent to photons (see Figure 1.4). This *recombination* occurred about 380,000 years after Big Bang (i.e. $z_{\mathrm{CMB}} \sim 1100$) and produced the Cosmic Microwave Background (CMB) observed for instance by satellite *Planck*. The Universe was then isotropic at large scales, but presented small local overdensities (temperature fluctuations of scale $\delta T/T \simeq 10^{-5}$, possibly caused by quantum fluctuations during inflation). According the hierarchical scenario of structure formation, primordial density fluctuations progressively formed overdense regions through their gravitational collapse. The structures thus formed would then progressively merge together to assemble into more and more massive objects. This model is progressively detailed in Press and Schechter (1974), White and Rees (1978), Lacey and Cole (1993), and Percival (2005). In particular, any self-gravitating structure of average density $\bar{\rho}$, whose pressure is insufficient to counter-act the gravitational forces is a Jeans instability. They are characterised by a limit Jeans mass M_J. A structure of mass $M > M_J$ is unstable and collapses, where:

$$\begin{aligned} M_J &= \frac{4\pi}{3}\bar{\rho}R_J^3, \\ R_J &= \frac{2\pi}{k_J} = c_S\sqrt{\frac{\pi}{G\bar{\rho}}}, \end{aligned} \tag{1.44}$$

with c_S is the local speed of sound, R_J Jeans' length and k_J Jeans' wavenumber. With γ the ratio of specific heats of the gas (e.g. $\gamma = 5/3$ for a mono-atomic gas), $m_a = 1$ Dalton[18] the atomic mass constant ($m_a \simeq m_H$ the mass of an atom of hydrogen), and μ_g the mean molecular weight of gas (see equation 1.77), the speed of sound writes:

$$c_S = \sqrt{\frac{5k_BT_g}{2\pi^2(\gamma-1)\mu_g m_a}}, \tag{1.45}$$

with $k_B = 1.3806 \times 10^{-23}\,\mathrm{m^2.kg.s^{-2}.K^{-1}}$ the Boltzmann constant and T_g the gas temperature.

In an idealised spherical collapse, the structure growth follows four steps: (i) a linear evolution, (ii) a non-linear collapse, (iii) a transition phase including oscillations of the size of the structure, evolving towards equilibrium (this phase is sometimes called *virialisation*), and (iv) a relaxed phase, at virial equilibrium. In the early Universe, the strong photon pressure in the structure exerted an opposite force to that of the gravitational collapse. The opposite forces created acoustic waves,

[18] The Dalton, or *unified atomic mass unit*, is defined as $1\,\mathrm{Da} = m(^{12}C)/12 \simeq 1.6605 \times 10^{-27}\,\mathrm{kg}$.

whose effects are bounded to the size of perturbations at a given redshift, i.e. the maximum distance travelled by a sound wave. This effect, called *baryon acoustic oscillations* (BAO), is observed in the (baryonic) large-scale structures (LSS), and as peaks in the density power-spectrum (Peebles and Yu, 1970; Harrison, 1970; Zel'dovich, 1972; Seljak and Zaldarriaga, 1996; Eisenstein et al., 2005). Their present day size is $\simeq 150\,\mathrm{Mpc} \simeq 100h^{-1}\,\mathrm{Mpc}$[19].

Upon reaching a critical density, baryons clustered into stars, which then formed galaxies, which themselves evolved into groups and clusters of galaxies (observed as early as in Messier, 1781). The latter two of these structures are bounded gravitationally by a mass much higher than that of baryons. Assuming General Relativity to be valid at long range, we thus assume dark matter (DM) to play a fundamental role in the formation of large cosmological structures (as first suggested by Zwicky, 1933). Relaxed clusters are therefore assumed to be mostly constituted of three components: the easily observable stars in galaxies ($\sim 5\%$), the hot ionised baryonic gas known as the intra-cluster medium (ICM, $\sim 15\%$), and a large-scale dark matter halo (see Flores and Primack, 1994, DM amounting to $\sim 80\%$ of the clusters' mass). The hierarchical model of structure formation is more complex than a simple spherical collapse as it implies the existence of a number of subhalos in the larger scale halos. These subhalos generally are a mixture of baryons and dark matter, and their disruption, both through gravity and interactions with the ICM, is an interesting avenue to probe the formation of structures, the ICM and dark matter itself (on subhalos of galaxies or clusters, see e.g. Moore et al., 1999b; Gao et al., 2004; Carlberg, 2009; Boylan-Kolchin et al., 2011; Boehm et al., 2014; Iocco et al., 2015; Dai et al., 2018).

Today galaxy clusters are the largest, most massive gravitationally-bound structures observable. Their observation has repeatedly proven to be a fantastic laboratory to explore the physics of the Universe, from the dark matter distribution and the hierarchical model of structure formation to hot plasma physics (see e.g. Allen et al., 2011; Kravtsov and Borgani, 2012; Eckert et al., 2022a). Their typical mass varies between orders of 10^{13} to $10^{15} M_\odot$. There is no clear objective distinction between clusters and groups of galaxies, but a rule of thumb can be to define groups of at least tens of galaxies as a cluster. For a review on clusters, see Voit (2005).

1.3.2 Relaxed galaxy clusters

1.3.2.1 Virial theorem

A self-gravitating structure can be considered *relaxed* if the changes in the velocities of its particles, due to encounters or interaction with its gravitational potential, are comparable to their original velocities Binney and Tremaine (1987, Chapter 4). In other words, a system is relaxed if it has largely forgotten its initial conditions. Once a structure achieves this sort of stability, it is well described by it the virial theorem:

$$2K + U = 0, \tag{1.46}$$

where K and U are the kinetic and gravitational potential energy of the structure respectively. Their expressions change depending on the distribution of matter and energy within the structure, but making a number of assumptions allows to evaluate the mass of galaxies and galaxy clusters, as was first suggested by Zwicky (1937b). For a spherical body of uniform density, these values

[19] We remind we took $h = 0.7$ in this thesis.

write:

$$K = \frac{1}{2}Mv^2 = \frac{3}{2}M\sigma^2,$$
$$U = -\frac{3}{5}\frac{GM^2}{R}, \tag{1.47}$$

where M is the mass of the structure, R the radius of the structure, v the average velocity of the particles and σ the unidimensional average velocity dispersion. There, we assume that the relationship between velocity and velocity dispersion to be Gaussian, such as in e.g. Yahil and Vidal (1977), therefore leading to a mass:

$$M = \frac{5R\sigma^2}{G}. \tag{1.48}$$

1.3.2.2 Overdensity mass and radius

More generally, the exact velocity dispersion and size of the structure are quite difficult to measure for bound structures of numerous particles. For galaxy clusters, for an overdensity Δ (given as a number, e.g. $\Delta = 200$), we define a given overdensity mass $M_{\Delta,c}$ and radius $R_{\Delta,c}$ (see e.g. Nelson et al., 2014):

$$R_{\Delta,c} = \left\{ R \;\middle|\; \frac{M(<R)}{\frac{4}{3}\pi R^3} = \Delta \cdot \rho_c^P(z) \right\},$$
$$M_{\Delta,c} = \frac{4\pi}{3} R_{\Delta,c}^3 \Delta \rho_c^P(z), \tag{1.49}$$

where ρ_c^P is the physical critical density at the cluster redshift z, and $M(<R)$ the total mass enclosed within a given radius, R. Let us notice $M_{\Delta,m}$ and radius $R_{\Delta,m}$ also exist, and use the same formula (1.49), but substituting ρ_c^P by $\rho_{c,m}^P$ (see equation 1.31).

1.3.2.3 Empirical luminosity of galaxies

A number of galaxy typologies exist, although the most well-known ones are described in de Vaucouleurs (1959) and Sérsic (1963). In the interest of establishing empirical laws between galaxies' luminosity L and velocity of its members v, we consider spiral and elliptical galaxies. The former obey the Tully-Fisher relationship described in Tully and Fisher (1977) and McGaugh et al. (2000):

$$L \propto W^\alpha, \tag{1.50}$$

where $W(v)$ is the asymptotic rotation curve of spiral galaxies, and α an exponent, found to range within 3.5 to 4. In the case of elliptical galaxies, the relationship is given by the Faber-Jackson empirical relationship (Faber and Jackson, 1976):

$$L \propto \sigma^\gamma, \tag{1.51}$$

where σ is the velocity dispersion in the fundamental plane of elliptical galaxies (see equation 3.1), and $\gamma \simeq 4$ found experimentally.

1.3.3 Density profiles of galaxy clusters

1.3.3.1 Abel projection and deprojection

Galaxy clusters are observed at all possible wavelengths, but we only merely observe a two-dimensional sky plane. The density profiles of galaxy clusters are obtained notably by de-projecting

their observed density. In order to relate the densities found within a plane, for instance using strong gravitational lensing, and in three dimensions, we hereafter describe the Abel transform. In Cartesian coordinates (x, y, z), writing the three dimensional radius r, and the bidimensional, projected radius R:

$$\begin{aligned} R =& \sqrt{x^2 + y^2}, \\ r =& \sqrt{R^2 + z^2}, \end{aligned} \tag{1.52}$$

the surface and volume densities Σ and ρ are connected by the Abel transform:

$$\Sigma(R) = 2 \int_R^\infty \frac{\rho(r) r}{\sqrt{r^2 - R^2}} \mathrm{d}r, \tag{1.53}$$

and, if $\forall r,\ \exists \{\alpha < -1, A \in \mathbb{R}^{+*}\} |\ \rho(r) < A r^\alpha$, then the Abel deprojection writes:

$$\rho(r) = -\frac{1}{\pi} \int_r^\infty \frac{\mathrm{d}\Sigma}{\mathrm{d}R}(R) \frac{\mathrm{d}R}{\sqrt{R^2 - r^2}}. \tag{1.54}$$

1.3.3.2 Navarro–Frenk–White (NFW) profile

From now on, we will write ρ the total matter density, i.e. the sum of baryons and dark matter. The determination of a general density function of galaxy clusters ranging from the inner galaxies to the host dark matter halo (DMH) is important to understand their formation history, but also the dynamics of the ICM, the formation and interaction of galaxies, the distribution of DM and its interplay with baryonic matter. For decades, this density was simply modelled by a power-law:

$$\rho(r) \propto r^{-\beta}, \tag{1.55}$$

with a flat core, using simple number counts of galaxies (for instance in Gunn and Gott, 1972; Yahil, 1974).

In the era of large N-body simulations, collisionless dark matter particles may form substructures without spherical symmetry assumptions. Cosmological evolution (expansion) could also be taken into account. Although there is no 'perfect' function to fit all observations, the most popular is the Navarro-Frenk-White (NFW) profile for clusters in equilibrium:

$$\rho(r) = \frac{\rho_S}{\frac{r}{r_S}\left(1 + \frac{r}{r_S}\right)^2}, \tag{1.56}$$

where ρ_S the density normalisation, and r_S the scale radius, are different parameters for each halo. A number of analyses (such as Duffy et al., 2008) study the correlation between these two parameters, both in simulations, and observations (X-rays, lensing). It was introduced in order to fit dark matter simulations in Navarro et al. (1995, 1996). It was later confirmed to be a strong candidate in other N-body simulations (e.g. Jing, 2000) and more significantly at large radii with weak lensing data in Okabe et al. (2013). However, this density profile is *cuspy* in the core of clusters. This means it has a minimal radius limit of application, as observations suggest that the content of dark matter at the centre of galaxies present a flat density profile (Collett et al., 2017). This so-called *cusp-core problem*, i.e. the disagreement between cold dark matter simulations and observations, is summarised in de Blok (2010) and Del Popolo and Le Delliou (2022). A possible solution would be to introduce interactions between DM and baryons (as in Bœhm et al., 2001,

2002), or a self-interaction for DM (for instance Li and Chen, 2009; Robertson et al., 2015), or a fuzzy dark matter.

Let us derive the associated mass contained within a radius:

$$M_{\rm NFW}(r) = 4\pi\rho_0 r_S^3 \left[\ln\left(1+\frac{r}{r_S}\right) - \frac{r}{r+r_S}\right]. \tag{1.57}$$

The total mass is therefore the mass contained within the virial radius. As mentioned in equation (1.49), we use an overdensity Δ to characterise arbitrarily the mass. This allows to define the concentration parameter:

$$c_\Delta = \frac{r_S}{R_\Delta}, \tag{1.58}$$

where R_Δ is defined in equation (1.49).

The gravitational potential $\Psi = -\Phi$ of this profile writes:

$$\Psi(r) = 4\pi G\rho_S \frac{r_S^3}{r} \ln\left(1+\frac{r}{r_S}\right). \tag{1.59}$$

Here is the analytical formula of the 2D density of a NFW profile (Bartelmann, 1996):

$$\begin{aligned}\Sigma(R) &= 2\int_R^{+\infty} {\rm d}r \frac{r\rho(r)}{\sqrt{r^2-R^2}} \\ &= \begin{cases} \frac{2\rho_S r_S^3}{(r_S^2-R^2)^{2/3}}\left[r_S\,\mathrm{arccosh}\left(\frac{r_S}{R}\right) - \sqrt{r_S^2-R^2}\right] & \text{if } R<r_S, \\ \frac{2\rho_S r_S}{3} & \text{if } R=r_S, \\ \frac{2\rho_S r_S^3}{(R^2-r_S^2)^{2/3}}\left[\sqrt{R^2-r_S^2} - r_S\arccos\left(\frac{r_S}{R}\right)\right] & \text{if } R>r_S, \end{cases}\end{aligned} \tag{1.60}$$

which diverges for $R \to 0$.

This yields a cylindrical mass:

$$M_{\rm NFW,2D} = 4\pi r_S^3 \rho_S \left[\ln\frac{r}{2r_S} + K(R)\right], \tag{1.61}$$

where

$$K(R) = \begin{cases} \frac{r_S}{\sqrt{r_S^2-R^2}}\mathrm{arccosh}\left(\frac{r_S}{R}\right) & \text{if } R<r_S, \\ 1 & \text{if } R=r_S, \\ \frac{r_S}{\sqrt{R^2-r_S^2}}\arccos\left(\frac{r_S}{R}\right) & \text{if } R>r_S. \end{cases} \tag{1.62}$$

1.3.3.3 Generalised NFW and Moore profiles

A number of other density models have been proposed (see Keeton, 2001, for a review in clusters). In order to allow for the inner slope of the NFW profile to increase, as suggested in Moore et al. (1998, 1999a), the generalised NFW profile (gNFW) was introduced. The number of free parameters can vary from one to three, depending on those being fixed to their NFW value. It was outlined in Zhao (1996), Kravtsov et al. (1998), and Jing and Suto (2000), although it was proposed as early as in Hernquist (1990):

$$\rho(r) = \frac{\rho_0}{\left(\frac{r}{r_S}\right)^\gamma \left[1+\left(\frac{r}{r_S}\right)^\alpha\right]^{(\beta-\gamma)/\alpha}}. \tag{1.63}$$

In particular, the Moore profile is the case $(\alpha;\beta;\gamma) = (1;3;3/2)$. The standard NFW is $(\alpha;\beta;\gamma) = (1;3;1)$. The goal of this collection of profiles was simply to attempt to describe the density distribution of DM as precisely as possible. For instance, Wyithe et al. (2001) uses a gNFW profile to describe the density in the case of self-interacting DM.

1.3.3.4 Hernquist profile

This profile was introduced in (Hernquist, 1990), and is the specific gNFW case $(\alpha;\beta;\gamma) = (1;4;1)$:

$$\rho(r) = \frac{\rho_0}{\left(\frac{r}{r_S}\right)\left(1+\frac{r}{r_S}\right)^3}. \tag{1.64}$$

It was proposed in order to describe the density of elliptical galaxies and bulges for a de Vaucouleurs (1959) luminosity profile.

1.3.3.5 King profile

King (1962, 1966) provide with the King density profile:

$$\rho(r) = \rho_0 \left[1 + \left(\frac{r}{r_c}\right)^2\right]^{-3/2}, \tag{1.65}$$

where r_c is the core radius. This profile was first proposed to explain the density distribution in globular clusters, and is not used much anymore to describe the total density distribution, but it has inspired an electron density profile which is still commonly used (see equation 1.79).

1.3.3.6 Einasto profile

Einasto (1965) introduced his eponymous profile to describe the stellar density in the Milky Way:

$$\rho(r) = \rho_{-2} \exp\left\{\frac{-2}{\alpha}\left[\left(\frac{r}{r_{-2}}\right)^\alpha - 1\right]\right\}, \tag{1.66}$$

however it continues to be an appropriate profile for galaxy clusters (for instance in Gao et al., 2008; Eckert et al., 2022b). It depends on three parameters: a density normalisation ρ_{-2}, a transition radius r_{-2}, and an index α representing the density slope at large radii. Comparing its spatial and lensing properties to NFW by analytical means, Retana-Montenegro et al. (2012) support a better fit by an Einasto profile.

1.3.3.7 Dual pseudo-isothermal mass distribution (dPIE) profile

The dual pseudo-isothermal mass distribution (dPIE) profile was defined in Kassiola and Kovner (1993) and detailed in Elíasdóttir et al. (2007):

$$\rho(r) = \rho_0 \left\{\left[1 + \left(\frac{r}{r_{\rm core}}\right)^2\right]\left[1 + \left(\frac{r}{r_{\rm cut}}\right)^2\right]\right\}^{-1}, \tag{1.67}$$

where ρ_0 is the density normalisation, $a \equiv r_{\rm core}$ the core radius, describing the pivot between the inner, flat density and the $\propto r^{-2}$ isotherm-like region, and $s \equiv r_{\rm cut} > a$ the pivot between this latter region and a very peaky $\propto r^{-4}$ region. For the dark matter halo of a cluster, the typical

values are $r_{\rm core} \sim 50$ kpc, and $r_{\rm cut} \sim 1$ Mpc. It is inspired by the singular isothermal sphere (SIS) model, which describes the flat rotation curves of spiral galaxies, but differs as a flatter (non-divergent) core region was added, and a large-scale 'cut radius', characterising a rapid cut-off of the density at a chosen scale, making it quite adaptable for both galaxies and clusters (Natarajan and Kneib, 1996; Elíasdóttir et al., 2007, see respectively). Keeton (2001) refers to this same profile as pseudo-Jaffe, as it presents two inflections as the Jaffe profile (Jaffe, 1983), but is more parametrisable. It is also referred to as the Chameleon profile (Maller et al., 2000; Schuldt et al., 2019).

We summarise the main properties of this profile:

$$M_{\rm 3D}(r) = 4\pi \int_0^r \rho(x) x^2 {\rm d}x = 4\pi\rho_0 \frac{a^2 s^2}{s^2 - a^2} \left[s \arctan\left(\frac{r}{s}\right) - a \arctan\left(\frac{r}{a}\right) \right]. \tag{1.68}$$

The gravitational potential $\Psi = -\Phi$ therefore writes:

$$\begin{aligned} \Psi(r) &= G \int_r^\infty \frac{M_{\rm 3D}(x)}{x^2} {\rm d}x \\ &= 4\pi G \rho_0 \frac{a^2 s^2}{s^2 - a^2} \left[\frac{s}{r} \arctan\left(\frac{r}{s}\right) - \frac{a}{r} \arctan\left(\frac{r}{a}\right) + \frac{1}{2} \ln\left(\frac{r^2 + s^2}{r^2 + a^2}\right) \right], \end{aligned} \tag{1.69}$$

and the cylindrical (projected) mass:

$$\Sigma(r) = \Sigma_0 \frac{as}{s - a} \left[\left(R^2 + a^2\right)^{-1/2} - \left(R^2 + s^2\right)^{-1/2} \right], \tag{1.70}$$

where

$$\Sigma_0 = \pi \frac{as}{a + s} \rho_0. \tag{1.71}$$

We can thus also provide the 2D mass distribution:

$$M_{\rm 2D}(R) = 2\pi\Sigma_0 \frac{as}{s - a} \left[\sqrt{R^2 + a^2} - a - \sqrt{R^2 + s^2} + s \right]. \tag{1.72}$$

The dPIE profile has a finite mass for $r \to \infty$:

$$M_{\rm TOT} = 2\pi^2 \rho_0 \frac{a^2 s^2}{a + s}, \tag{1.73}$$

but it is rarely used, as $M_{200,c}$, for instance, is commonly used for all density profiles.

We can also directly read the velocity dispersion σ_0 at the centre of the cluster (see Limousin et al., 2005; Bergamini et al., 2019):

$$\rho_0 = \frac{\sigma_0^2}{2\pi G} \frac{a + s}{a^2 s}, \tag{1.74}$$

where, for a DMH, $\sigma_0 \sim 10^3\,{\rm km.s^{-1}}$ typically and thus for $a = 50\,{\rm kpc}$ and $s = 1000\,{\rm kpc}$, we get $\rho_0 \approx 10^{-21}\,{\rm kg.m^{-3}}$.

1.3.4 Thermodynamics of galaxy clusters

1.3.4.1 The intra-cluster medium (ICM)

As summarised in Vikhlinin et al. (2006) and Bahcall and Kulier (2014), galaxy clusters are composed of 1% of stars directly observable with optical telescopes, roughly 11% of hot plasma (temperatures ranging typically around $10^7 - 10^8$ K), distributed on large scales of the cluster and observable in the X-rays, and of about 88% dark matter, whose influence can be observed through its gravitational effect on the baryonic matter (distribution of stars in galaxies, of galaxies in clusters, gravitational lensing).

As presented in Gunn and Gott (1972), Hester (2006), Vulcani et al. (2022), and Durret et al. (2022), when galaxies fall into their seed cluster, most of their interstellar plasma falls into the main cluster DM clump (which becomes the DM halo). This *ram pressure stripping* leaves galaxies without the necessary gas to form new stars, and the galaxies' evolution stops. This was observed for instance in the Coma and Virgo clusters (in Bravo-Alfaro et al., 2000; Vollmer et al., 2005). As a consequence, in a relaxed cluster, galaxies are expected to present similar stellar populations (metallicity, age, colour). This allows for a *photometric* study of galaxy clusters, indeed relaxed clusters galaxy members are expected to present main sequences of colour (and most importantly a red colour sequence, see Gladders and Yee, 2000; Hao et al., 2009). This is by all means an imperfect categorisation, but allows to identify galaxies in the same field as cluster members or not, using several pass-band observations. This colour sequence is due, on the one hand, to a same cosmological redshift of all cluster members, and, on the other hand, to a common metallicity, due to the cluster mass influencing the supernova feedback in heavy elements (heavier clusters retain these elements more easily, see Arimoto and Yoshii, 1987; Stott et al., 2009).

This is a simplistic model however, as different galaxies are captured at different times in the cluster, and therefore their stellar formation rate (SFR) can increase for a limited time, under the ram pressure compression. This can also yield spectacular tails of stripped plasma, sometimes of kpc length, and often containing blue knots revealing intense star formation (studied e.g. in Owen et al., 2006). These galaxies were names 'jellyfish' in Bekki (2009) Figure 2, because of the stripping of their halo leaving these tails as 'tentacles', and studied systematically in Ebeling et al. (2014) and Poggianti et al. (2016).

1.3.4.2 Metallicities

Whichever the case, older, more massive clusters present higher metallicities. The metallicity, denoted Z, is commonly defined as the abundance in metal. In astronomy, all elements other than hydrogen and helium are defined as a metal.

$$Z = 1 - X - Y = \sum_{i \notin \{H,He\}} \frac{m_i}{M}, \tag{1.75}$$

where X and Y are the hydrogen and helium abundance, m_i the total mass of a species i, and M the total mass of the structure. The dependencies of the metallicity to the cluster mass, merger state or redshift have been studied in Ellison et al. (2009), McDonald et al. (2016), and Lovisari and Reiprich (2019). The core metallicity of dynamically relaxed clusters appears to only mildly depend on the temperature. Disturbed objects tend to present lower core metallicities. The metallicity cores in the centre of clusters, but more steeply in the relaxed ones. This paints the picture of cluster mergers scattering heavier elements on large scales.

1.3.4.3 Baryonic number density and mean molecular weight μ

The number density of a species i, n_i is defined as:

$$n_i(r) = \mathcal{F}_I(r)\frac{\rho_g(r)}{\mu_i m_a}, \tag{1.76}$$

where ρ_g is the gas volume density, $\mathcal{F}_I$ is the local ionisation fraction which is taken to be 1 in this thesis, and μ_i is the mean molecular weight of species i. Let us define respectively the mean molecular weight of electron μ_e, ion μ_I, and gas μ_g:

$$\begin{aligned}
\mu_e &= \left(\sum_i \frac{x_i Z_i f_i}{A_i}\right)^{-1}, \\
\mu_I &= \left(\sum_i \frac{x_i}{A_i}\right)^{-1}, \\
\mu_g &= \left(\mu_e^{-1} + \mu_I^{-1}\right)^{-1},
\end{aligned} \tag{1.77}$$

where i are the atomic element's number, x_i the fraction of a species, A_i the atomic weight of a species, and Z_i the atomic number. In practice $\mu_g \approx 0.60$, $\mu_e \approx 1.15$, $\mu_I \approx 1.25$ and $\mu_H \approx 1.35$. We can define:

$$n_g = n_I + n_e = \frac{\rho_g \mathcal{N}_A}{\mu_g}, \tag{1.78}$$

where $\mathcal{N}_A$ is the Avogadro constant.

Let us review a number of density models (see Birkinshaw, 1999). Because these were built with X-rays, which directly probe the X-rays number density, we use this observable to describe them.

The β model

With the Cavaliere and Fusco-Femiano (1976) model of the surface brightness of galaxy clusters, using the King profile (King, 1962, 1966) for total density (see section 1.3.3.5), the electron density reads:

$$n_e(r) = n_{e,0}\left[1 + \left(\frac{r}{r_c}\right)^2\right]^{-3\beta/2}, \tag{1.79}$$

where $n_{e,0}$ is a normalisation, r_c core inflexion radius, and β an exponent. This originally assumed the temperature of the ICM to be constant, with a constant one-dimensional velocity dispersion (for more on the history of these assumptions, read e.g. Felten et al., 1966), yielding:

$$\frac{\mathrm{d}\ln\rho_g}{\mathrm{d}r} = -\frac{\mu_g m_a}{k_B T_g}\frac{\mathrm{d}\Phi}{\mathrm{d}r} = \beta_{th}\frac{\mathrm{d}\ln\rho_t}{\mathrm{d}r}, \tag{1.80}$$

through the Poisson equation (Sarazin, 1988; Voit, 2005), where ρ_t outlines the total matter density (including DM), described by a King profile. Thus, in theory, the adimensional β exponent reads:

$$\beta_{th} = \frac{\mu_g m_a \sigma_{1\mathrm{D}}^2}{k_B T_g}, \tag{1.81}$$

where $\sigma_{1\mathrm{D}}$ is the one-dimensional velocity dispersion. However, as mentioned in Sarazin (1988), it is common knowledge this exponent is not giving the observed density (in practice, $\beta_{\mathrm{fit}} \simeq 0.65$,

ranging between 0.5 and 1). This β problem partly arises from the isotropic hypothesis, as shown in Hallman et al. (2007), but also because the total matter density is not perfectly described by the King profile. This profile remains however very helpful and popular, mostly with X-rays observations and analyses, in spite of slightly underestimating the central density and slightly overestimating the outskirts density ($r \gg r_c$, see Mohr et al., 1999).

A large range of different cluster density models are possible, as for instance the double beta model (Shitanishi et al., 2018), the Vikhlinin model (Vikhlinin et al., 2006; Ansarifard et al., 2020), the alpha-beta parameterisation (Böhringer et al., 2016), and the alpha-beta-eta model (Ghirardini et al., 2017). These models can all be defined with or without a density cut.

Vikhlinin model

In order to allow more degrees of freedom, and notably to take into account the difference between the inner and outer regions of a cluster, a number of models were developed. The most general of these is the Vikhlinin model summarised in Vikhlinin et al. (2006), but some anterior inspirations are mentioned in other articles such as Pointecouteau et al. (2004). It was forged to take into account a number of observational effects, thus complexifying the β model. The total model electron density reads:

$$n_e(r) = \left\{ n_{0,1}^2 \left(\frac{r}{r_{c,1}}\right)^{-\alpha} \left[1 + \left(\frac{r}{r_{c,1}}\right)^2\right]^{-3\beta_1+\alpha/2} \left[1 + \left(\frac{r}{r_s}\right)^\gamma\right]^{-\epsilon/\gamma} + n_{0,2}^2 \left[1 + \left(\frac{r}{r_{c,2}}\right)^2\right]^{-3\beta_2} \right\}^{1/2}, \tag{1.82}$$

where α was added to represent essential features of the observed X-ray surface brightness profiles. Gas density in the centres of relaxed clusters, usually presents a power-law cusp instead of a flat core. The ϵ power and r_s typical radius were added to take into account the X-ray brightness profile steepening at large radii, compared to the β power law extrapolated from smaller radii. The γ parameter controls the width of that transition region. A second β model was added, yielding two β_i powers, core radii $r_{c,i}$ and central densities $n_{0,i}$, with the second component ($i = 2$) of smaller core radius to increase the modelling freedom near the cluster centre.

This is a whopping ten free parameters. This type of profile presenting too many parameters, it is therefore barely used with all ten free parameters, but reduced versions are. In practice, all clusters appear to be fit with $\gamma = 3$, and $\epsilon < 5$ to exclude unphysical sharp density breaks (Vikhlinin et al., 2006). We present simpler models hereafter, all reduced, as simpler fits allow to explain the surface brightness.

Double-β model

A popular reduced model of the Vikhlinin one is the double-β model (see e.g. Shitanishi et al., 2018):

$$n_e(r) = \left\{ n_{0,1}^2 \left[1 + \left(\frac{r}{r_c}\right)^2\right]^{-3\beta} + n_{0,2}^2 \left[1 + \left(\frac{r}{r_s}\right)^2\right]^{-3\beta} \right\}^{1/2}, \tag{1.83}$$

where $(n_{0,i})_{i\in\mathbb{N}_2}$ are the electronic central densities for each component and r_c and r_s the core and the scale radii respectively. This model is quite popular, and often found to be a good fit of the underlying physics, notably outlining the separation between the core and the larger radii (Mohr et al., 1999).

β - γ - ϵ model

Ansarifard et al. (2020) proposed the reduced model:

$$n_e(r) = n_0 \left[1 + \left(\frac{r}{r_c}\right)^2\right]^{-3\beta/2} \left[1 + \left(\frac{r}{r_s}\right)^\gamma\right]^{-\epsilon/\gamma}, \tag{1.84}$$

in order to precisely describe the electron distribution in galaxy clusters, observed with X-rays. The α power law and the second β power law are avoided in order to focus on the regions of clusters outside the centre. In practice, fixing $\gamma = 3$ further reduces this model to the β - ϵ model.

α - β model

Böhringer et al. (2016) use the reduced model:

$$n_e(r) = n_0 \left(\frac{r}{r_c}\right)^\alpha \left[1 + \left(\frac{r}{r_c}\right)^2\right]^{-3\beta/2+\alpha/2}, \tag{1.85}$$

which is found to be sufficient, in the framework of this study, to fit the electron density (using the data sets presented in Böhringer et al., 2007). The parameters are adjusted to $\alpha = 0.41$ and $\beta = 0.64$ for the REXCESS sample of clusters.

In Chapter 4, we derive more electron density models.

1.3.4.4 Hydrostatic equilibrium in galaxy clusters

For relaxed galaxy clusters, one can assume the ICM to be in hydrostatic equilibrium. One can then write its pressure gradient (see e.g. Eckert et al., 2019):

$$\frac{\mathrm{d}P_g}{\mathrm{d}r} = -\rho_g(r)\frac{GM(<r)}{r^2}, \tag{1.86}$$

where index g denotes the gas in the ICM. From the ideal gas law,

$$P_g = k_B n_g T_g = \frac{k_B T_g \rho_g}{\mu_g m_a}, \tag{1.87}$$

we get the hydrostatic mass enclosed in r:

$$M(<r) = -r\frac{k_B T_g(r)}{G}\left(\frac{\mathrm{d}\ln\rho_g(r)}{\mathrm{d}r} + \frac{\mathrm{d}\ln T_g(r)}{\mathrm{d}r}\right). \tag{1.88}$$

1.3.4.5 Pressure and temperature models

As the pressure in galaxy clusters is of the order of 10^{10} Pa, one can safely assume the plasma to be thermalised, and therefore the temperature of the gas to be the same as that of the electrons. At low pressure values, a distinction should be established however.

Beyond the most simple model assuming the plasma distribution to be isotropic, it is common practice to describe the plasma as polytropic, i.e. the pressure to follow a power-law of the density,

with an index γ[20]. One can write the polytropic pressure P_e and temperature T_e following Capelo et al. (2012):

$$\begin{aligned} P_e(r) &= P_0 \left(\frac{n_e(r)}{n_{e,0}} \right)^{\gamma}, \\ T_e(r) &= T_0 \left(\frac{n_e(r)}{n_{e,0}} \right)^{\gamma-1}, \end{aligned} \tag{1.89}$$

where P_0 and T_0 are the central pressure and temperature (respectively). Ghirardini et al. (2017) provides a range of $\gamma \in [0.85; 1.5]$, and an evolution with redshift. Using the X-COP cluster sample, Ghirardini et al. (2019a, Table 3, Figure 4) show one can almost universally take $\gamma = 1.2$ by analysing the fitted polytropic index at various radii of 12 clusters. This agrees to numerical simulations (Capelo et al., 2012).

In Chapter 4, we derive an additional polytropic temperature model, fitting the Ghirardini et al. (2019a) polytropic index analysis at smaller radii for a finer description of the most central regions.

1.3.4.6 X-ray brightness

The hot ICM radiates in the X-rays through *bremsstrahlung*, and through the emission lines of the various elements in the plasma (mostly hydrogen and helium, but heavier elements also play a role). It contains valuable information on the ICM density, its temperature, metallicity, but also can reveal the dynamics with the possible presence of shocks. For an overview of cosmology using galaxy cluster X-rays observations, one can read Clerc and Finoguenov (2022).

For any type of luminous source, with L the luminosity, F the total bolometric flux (in J.m^{-2}.s^{-1}), d the transverse comoving distance to the object, D the total width of the object, α the total angle under which the object is perceived, and S the total surface bolometric brightness of the object (in J.m^{-2}.s^{-1}.sr^{-1}), one could write in a Newtonian Universe:

$$\begin{aligned} F &= \frac{L}{4\pi d^2}, \\ S &= \frac{F}{\alpha^2} = \frac{L/4\pi d^2}{D^2/d^2} = \frac{L}{4\pi D^2} \end{aligned} \tag{1.90}$$

but in the expanding Universe (see 1.1.8), we obtain:

$$S = \frac{L/4\pi d_L^2}{D^2/d_A^2} = \frac{L}{4\pi D^2 (1+z)^4}. \tag{1.91}$$

In practice, for a local flux in redshift F_{loc}:

$$\begin{aligned} F_{loc} &= \frac{1}{4\pi} \int n_e(\boldsymbol{r}) n_H(\boldsymbol{r}) \Lambda_N(E, T_e, Z) \mathrm{d}l, \\ S(\theta) &= \frac{F_{loc}}{(1+z)^4}, \end{aligned} \tag{1.92}$$

with n_H the hydrogen density, Λ_N the normalised cooling function (in J.m^3.s^{-1}) at a given energy of photons E, electron temperature T_e and metallicity Z. The dl element denotes a line-of-sight

[20] This γ is not related to the indices denoted with the same letter previously introduced.

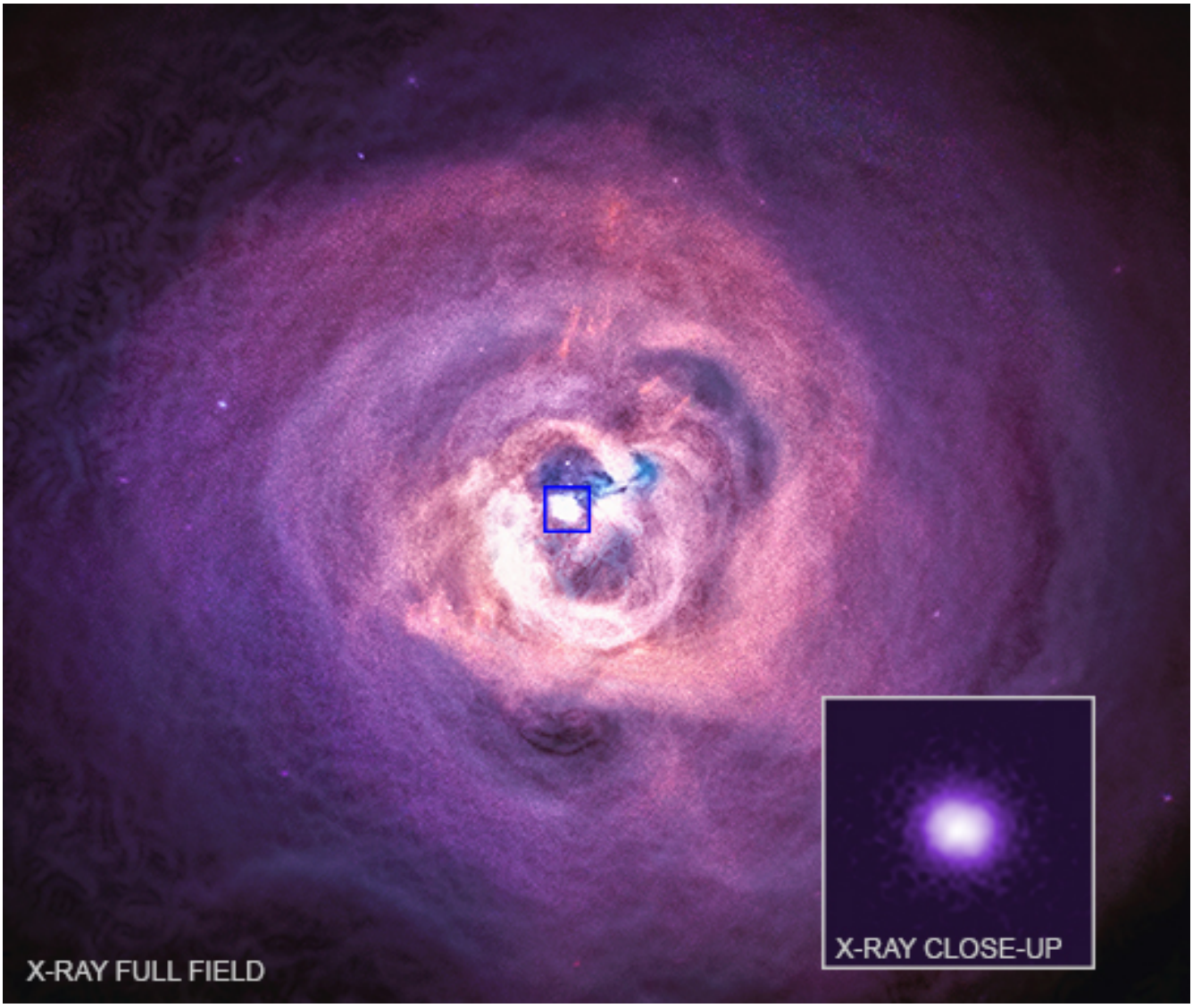

Figure 1.14: *Chandra X-ray* observations of the Perseus cluster. Credits: NASA/*Chandra X-ray*.

integration. For more information about the cooling function, the difference between net and normalised, one can read Sutherland and Dopita (1993) and Wang et al. (2014). Hereafter let us write $\Lambda \equiv \Lambda_N$.

If a X-rays telescope has an observational energy band ΔE, the frequency at emission ν_e should be taken into account, and not at reception ν_o:

$$\nu_e = (1+z)\nu_o, \tag{1.93}$$

This relationship is known as the 'K-correction' (see Wirtz, 1918; Hogg et al., 2002).

Therefore the X-ray surface brightness within a band writes (see Birkinshaw, 1999; Arnaud et al., 2002; Arnaud, 2005; Böhringer and Werner, 2010):

$$S_X(\Delta E^o) = \frac{1}{4\pi(1+z)^4}\frac{\mu_e}{\mu_H}\int n_e^2(\boldsymbol{r})\Lambda(\Delta E^e, T_e, Z)\mathrm{d}l, \tag{1.94}$$

where $\Lambda(\Delta E, T_e, Z)$ is the X-ray *cooling curve*. This function does not necessarily vary a lot within a galaxy cluster, as it is almost constant at high temperatures and low metallicities. It is therefore sometimes taken out of the integral, such as in Bonamigo et al. (2017).

A number of equivalent observables can also be used to characterise X-ray observations. For instance, Sarazin (1986) and Ettori (2000) use X-ray spectral emissivity, which they define as $\epsilon_X = \Lambda n_P^2$, with n_P the proton number density. More precisely, with the emission measure along the line-of-sight, defined as (Arnaud et al., 2002):

$$EM(r) = \int n_e n_H \mathrm{d}l, \tag{1.95}$$

and approximating the cooling function to be constant across all radii in the observed object, the surface brightness is:

$$S_X(r, \Delta E^o) = \frac{1}{4\pi(1+z)^4} \epsilon(T_e, z, \Delta E^o) EM(r), \tag{1.96}$$

where ϵ is the emissivity in a band ΔE^o:

$$\epsilon(T_e, z, \Delta E^o) = \int_{\Delta E^o} \mathrm{d}E \mathcal{A}(E) e^{-\sigma(E) N_H} f_T((1+z)E)(1+z)^2, \tag{1.97}$$

where $\mathcal{A}(E)$ is the effective area of the detector at energy E, $\sigma(E)$ is the absorption cross-section, N_H is the galactic hydrogen column density, causing the absorption at $z = 0$, and f_T the emissivity in photons.cm^3.s^{-1}.keV^{-1} (Arnaud et al., 2002). For more details on the cooling function and emissivity, one can read Peterson and Fabian (2006).

1.3.4.7 Sunyaev-Zel'dovich effect

The CMB photons are permanently bathing the Universe. As a result, they can occasionally interact with physical objects at an observable scale. The thermal, non-relativistic, hot electrons of the ICM create the condition for an inverse Compton scattering: in a spectral band-width of CMB photons, one can observe the broadening of the band due to the Doppler effect. With ν_i the incoming frequency of photons, ν_f the outcoming, and $\Delta\nu = \nu_f - \nu_i$, h the Planck constant and θ the scattering angle:

$$\frac{\Delta\nu}{\nu_i \nu_f} = -\frac{h}{m_e c}(1 - \cos\theta). \tag{1.98}$$

Because of the frequency shift, we can observe small perturbations in the relic radiation, i.e. 'holes' in the CMB at some frequencies, and more flux in some others (typically the flux is magnified for $\nu_r > 218$ GHz, see Carlstrom et al. 2002). Because the CMB is isotropic and the scattering by the ICM is also assumed to be, we do not particularly detect a privileged scattering direction. This effect was first described in Sunyaev and Zel'dovich (1970a,b), and is therefore named after them. Before the discovery of the Sunyaev-Zel'dovich effect (SZ), Felten and Morrison (1966) had already investigated the inverse Compton scattering within clusters. One can read Sunyaev and Zel'dovich (1980, 1981), Rephaeli (1995), Birkinshaw (1999), Carlstrom et al. (2002), and Mroczkowski et al. (2019) for a review on the SZ effect.

Let us now consider the case of soft CMB photons. This implies the Compton scattering can be taken in its Thomson limit (as $h\nu \ll m_e c^2$). Given a CMB temperature $T_r \simeq 2.726\,\mathrm{K}$ today, the reduced frequency is defined as:

$$x = \frac{h\nu}{k_B T_r}, \tag{1.99}$$

and its associated x_e, the reduced frequency at the electron temperature T_e, which, given $T_e > 10^7$ K $\gg T_r$, implies $x_e \ll 1$.

Thermal SZ effect

Let us write N the photon occupation number for a radiation. Its evolution due to the Thomson scattering by a non-relativistic, isotropic and Maxwellian electron gas is an approximation of the Fokker-Planck equation, summarised in the Kompaneets (1957) equation:

$$\frac{\partial N}{\partial t} = \frac{k_B T}{m_e c^2} \frac{n_e \sigma_T c}{x_e^2} \frac{\partial}{\partial x_e} \left[x_e^4 \left(\frac{T_e}{T} \frac{\partial N}{\partial x_e} + N + N^2 \right) \right], \tag{1.100}$$

where n_e and T_e are the electron density and temperature, and assumed to be constant, $\sigma_T = 6.65 \times 10^{-25}\,\mathrm{cm}^2$ the Thomson cross-section, and T the radiation temperature.

As long as the scattering is weak, the photon occupation number obeys the Bose-Einstein statistics on the temporary condensate:

$$N(x_e) = \left(e^{x_e} - 1\right)^{-1}. \tag{1.101}$$

Introducing the Compton parameter:

$$y = \int \frac{k_B T_e}{m_e c^2} n_e \sigma_T c \mathrm{d}t = \frac{k_B \sigma_T}{m_e c^2} \int T_e(r) n_e(r) \mathrm{d}l, \tag{1.102}$$

and the optical depth:

$$\tau_e = \int \sigma_T n_e \mathrm{d}l, \tag{1.103}$$

and using the Bose-Einstein statistics to compare the three terms in the frequency derivative in equation (1.100) yields the reduced equation (as $e^{x_e} \simeq 1$):

$$\frac{\partial N}{\partial y} \simeq \frac{1}{x_e^2} \frac{\partial}{\partial x_e} \left[x_e^4 \frac{\partial N}{\partial x_e} \right]. \tag{1.104}$$

Given the homogeneity of this equation, we can replace x_e by x. This equation can be resolved in the limit of low optical depth and electron temperature, meaning:

$$\frac{\partial N}{\partial y} \sim \frac{\Delta N}{y} \quad \Longrightarrow \quad \Delta N \simeq xy \frac{e^x}{\left(e^x - 1\right)^2} \left[x \coth\left(\frac{x}{2}\right) - 4 \right]. \tag{1.105}$$

Given the spectral intensity of the CMB:

$$I_0 = \frac{2}{c^2} \frac{k_B^3 T_R^3}{h^2}, \tag{1.106}$$

and the Planck black-body radiation:

$$I(x) = I_0 \frac{x^3}{e^x - 1}, \tag{1.107}$$

the spectral intensity SZ change writes:

$$\Delta I = I_0 x^3 \Delta N. \tag{1.108}$$

Deriving the black-body spectral intensity in temperature yields the thermal SZ (tSZ) temperature contrast:

$$\Theta_r = \frac{\Delta T}{T_r} = \frac{(e^x-1)^2}{x^4 e^x}\frac{\Delta I}{I_0} = \frac{(e^x-1)^2}{x e^x}\frac{\Delta N}{N} = \left[x\coth\left(\frac{x}{2}\right) - 4\right] y. \tag{1.109}$$

Let us notice this final expression does not take relativistic corrections into account. For more on corrections, but also on the polarised SZ effect, one can read Emritte et al. (2016). In the regime of small frequencies (let us say $\nu < 10$ GHz), this expression can be reduced to:

$$\Theta_r \simeq -2y. \tag{1.110}$$

In practice, at a given pass-band, one can simply provide the Compton parameter in order to infer the electron density and temperature profiles. Telescopes such as the Atacama Cosmology Telescope (ACT, see Naess et al., 2020; Hilton et al., 2021) or the South Pole Telescope (SPT, see Bocquet et al., 2019), not to mention the *Planck* mission (Aghanim et al., 2019), are extensively using this SZ effect to detect galaxy clusters.

Kinematic SZ effect

If the galaxy cluster exhibits a peculiar velocity projected along the line-of-sight v_z, then the occupation number of the photon condensate changes, and equation (1.101) rewrites:

$$N(x_e) = \left[\exp\left(x_s \gamma_z (1-\beta_z)\right) - 1\right]^{-1}, \tag{1.111}$$

where $\beta_z = v_z \cos\theta / c$ is the ratio of peculiar velocities along the line-of-sight, with θ the angle between the incoming photon direction and that of the cluster velocity, γ_z the associated Lorentz factor, and x_s the shifted reduced frequency. Indeed, because of its peculiar velocity, the reduced frequency sees its frequency and temperature components evolve, as the CMB temperature changes with redshift, and the frequency is submitted to the Doppler effect.

This yields a kinematic SZ effect (kSZ):

$$\Theta_r = \frac{\Delta T_r}{T_r} \simeq -\tau_e \frac{v_z}{c}, \tag{1.112}$$

added to the tSZ effect. This kinematic effect is usually much fainter than the thermal one. While this expression does not present any frequency dependence, it is not the case of the measured signal, the spectral intensity:

$$\frac{\Delta I}{I_0} = -\frac{x^4 e^x}{\left(e^x-1\right)^2}\tau_e \frac{v_z}{c}. \tag{1.113}$$

according to equation (1.109).

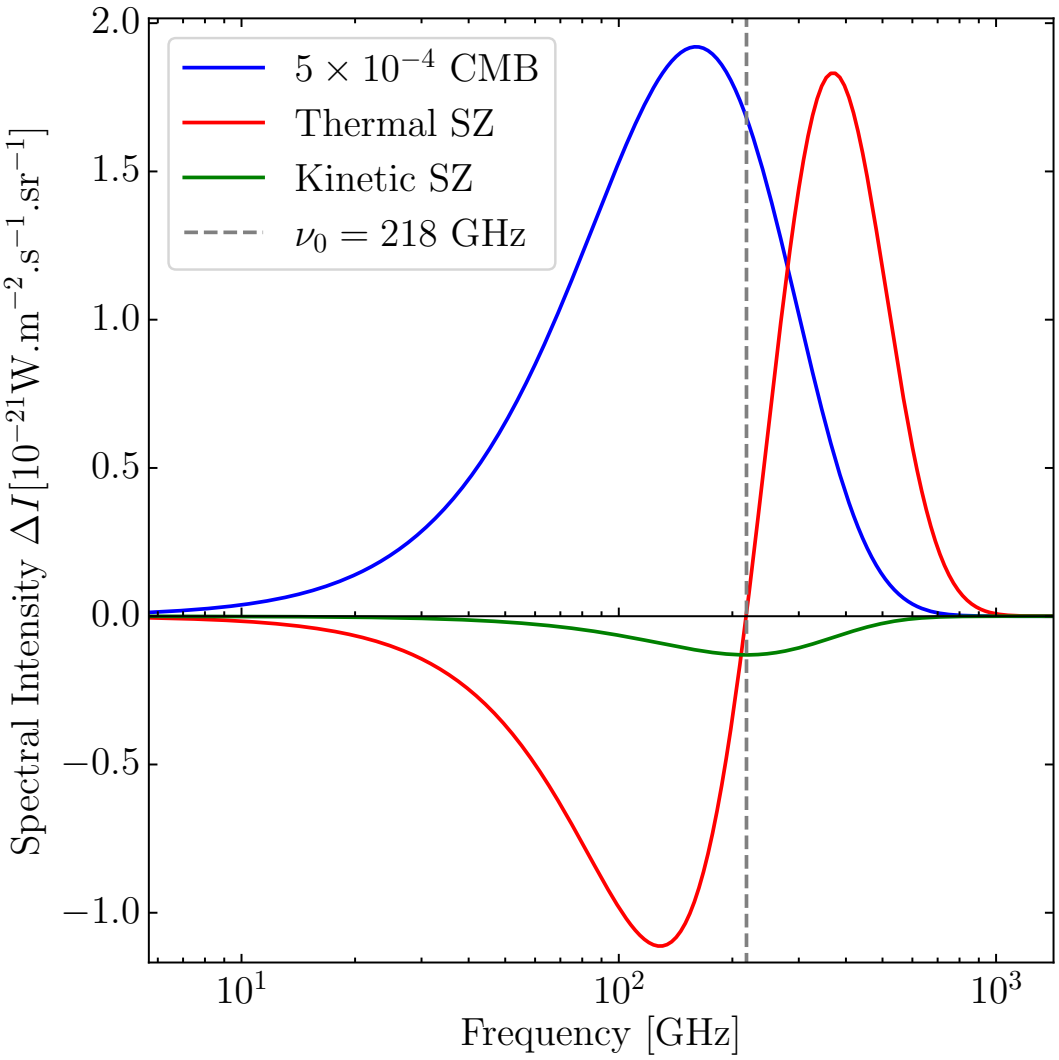

Figure 1.15: Spectral intensity as a function of frequency. *Blue:* Black-body of the CMB, according to equation (1.107). It was scaled here, to be sizeable with the SZ effect. *Red:* Thermal SZ effect for a Compton parameter $y = 10^{-4}$, which is rather typical. The grey line at 218 GHz is the point at which the thermal SZ effect becomes positive and the CMB smaller energy photons are accelerated to higher energies. *Green:* Kinematic SZ effect for a cluster of isotropic temperature 10^8 K and a line-of-sight velocity $v_z = 500\,\mathrm{km.s^{-1}}$.

Chapter 2

An introduction to gravitational lensing

Lens-like action of a star by the deviation of light in the gravitational field.

Some time ago, R. W. Mandl paid me a visit and asked me to publish the results of a little calculation, which I had made at his request. This note complies with his wish.

— Albert Einstein, *Science* 84 (1936)

2.1 Theory of gravitational lensing

2.1.1 A short history of gravitational lensing

When Einstein published his theory of General Relativity (GR, in Einstein, 1915, see equation 1.4), it appeared complicated to test. Einstein's theory was solving the problem of the anomalous perihelion advance of Mercury, but for such a scientific revolution to be firmly accepted, the theory needed to make a number of testable predictions[1]. In Newtonian physics, massive objects were predicted to deflect light rays, as already noted by Newton in his *Opticks* (1704). Johann G. von Soldner made these calculations in *Ueber die Ablenkung eines Lichtstrals von seiner geradlinigen Bewegung* (Berliner Astronomisches Jahrbuch, 1804, republished in 1921), at a time the nature of light was still polemical:

> 'Hopefully no one finds it problematic, that I treat a light ray almost as a ponderable body.'

As it turns out however, the Einstein's GR predictions for the lensing deflection angle α were twice those of Soldner's, yielding a testable observation. During a total solar eclipse in 1919, Arthur Eddington was mandated by the Royal Society to measure the deflection of a group of stars, the Hyades, in the near background of the Sun during the total eclipse of the 29th of May.

[1] We here adopt the definition of a paradigm shift in science as defined in *The Structure of Scientific Revolutions*, Kuhn (1962). According to this definition, a new paradigm appears to solve a number of problems, whilst also explaining pre-existing results. To be validated completely, i.e. for the the paradigm shift, the scientific revolution to be complete, a paradigm must make testable predictions, which must be successfully verified.

Their findings, published in Dyson et al. (1920), were rather unambiguous in validating General Relativity. However, this was later debated to be caused by a confirmation bias, and the results of their expedition in Príncipe, a small island in western Africa, were in tension with those of another expedition sent to Sobral (Brazil), more compatible with Soldner's deflection angle value. This tension however appeared to have surfaced from the relatively poor instrumental analysis made available to the Sobral team, and more recent re-analyses (Kennefick, 2007; Gilmore and Tausch-Pebody, 2020) of these results seem to alleviate the tension in favour of GR. Rather ironically, Eddington declared in verse to the Royal Astronomical Society:

> 'Oh leave the Wise our measures to collate
> One thing at least is certain, light has weight
> One thing is certain and the rest debate
> Light rays, when near the Sun, do not go straight.'

Observational gravitational lensing was born.

It was only formalised later in Einstein (1936). Then, Zwicky (1937a) suggested galaxies and the 'missing mass' in clusters could act as gravitational lenses. The first strong lensing observations however would have to wait for a significant improvement in instrumentation. In Walsh et al. (1979, see the left panel of Figure 2.1), the first double image of a background quasar – appropriately baptised the Twin Quasar, lensed by a giant elliptical cD-type galaxy and its surrounding cluster was discovered. The corresponding lens was later discovered in Young et al. (1980). It was quickly followed by the discovery of the first Einstein cross in Huchra et al. (1985, see the right panel of Figure 2.1), i.e. four multiple images of a same background quasar arranged in a cross around the lens. This phenomenon occurs when the lens and the source are approximately aligned (see Figures 2.2 and 2.3). Soucail et al. (1987) were the first to detail the discovery of a giant luminous arc, i.e. highly magnified images of a background source, in the cluster Abell 370, although the available data could not quite conclude about its nature. We display this cluster on the bottom panel of Figure 2.1. Paczyński (1987) was the first to suggest these arcs were an impressive case of strong gravitational lensing, and Hammer (1987) and Kovner (1987) independently offered the first lens models. Soucail et al. (1988), Miller and Goodrich (1988), and Lynds and Petrosian (1988) re-examined the observed candidate lensing arc and found it to be indeed at much higher redshift than its lens galaxy cluster. Lynds and Petrosian (1989) later drew the attention to a number of observations which could be interpreted to be giant lensing arcs, which they had mentioned in a note (Lynds and Petrosian, 1986). Hewitt et al. (1988) reported the first partial Einstein ring[2] detection with the Very Large Telescope (VLT). This apparent lensing configuration may only be observed when the source and lens are almost perfectly aligned. It is important to note that the difference between an Einstein cross and ring stems from the lens configuration. Spherical lenses yield Einstein rings, and more elongated lenses yield Einstein crosses. The first full Einstein ring observation was reported in King et al. (1998). We display the most common lensing configurations on Figure 2.3.

The size of galaxies is small compared to that of clusters, whose lensing cross-section was first outlined by Webster (1985). Thanks to the richness of clusters, acting both as sources and lenses, the observational Universe appears to be filled with gravitational lensing phenomena. It is thus at the end of the 1980s that astronomers started to give more attention to lensing observations. As outlined in Tyson et al. (1990), strong gravitational lensing spectacular observations would allow to directly probe the dark matter distribution. Indeed, as dark matter interacts gravitationally

[2] Also called 'Einstein-Chwolson ring'.

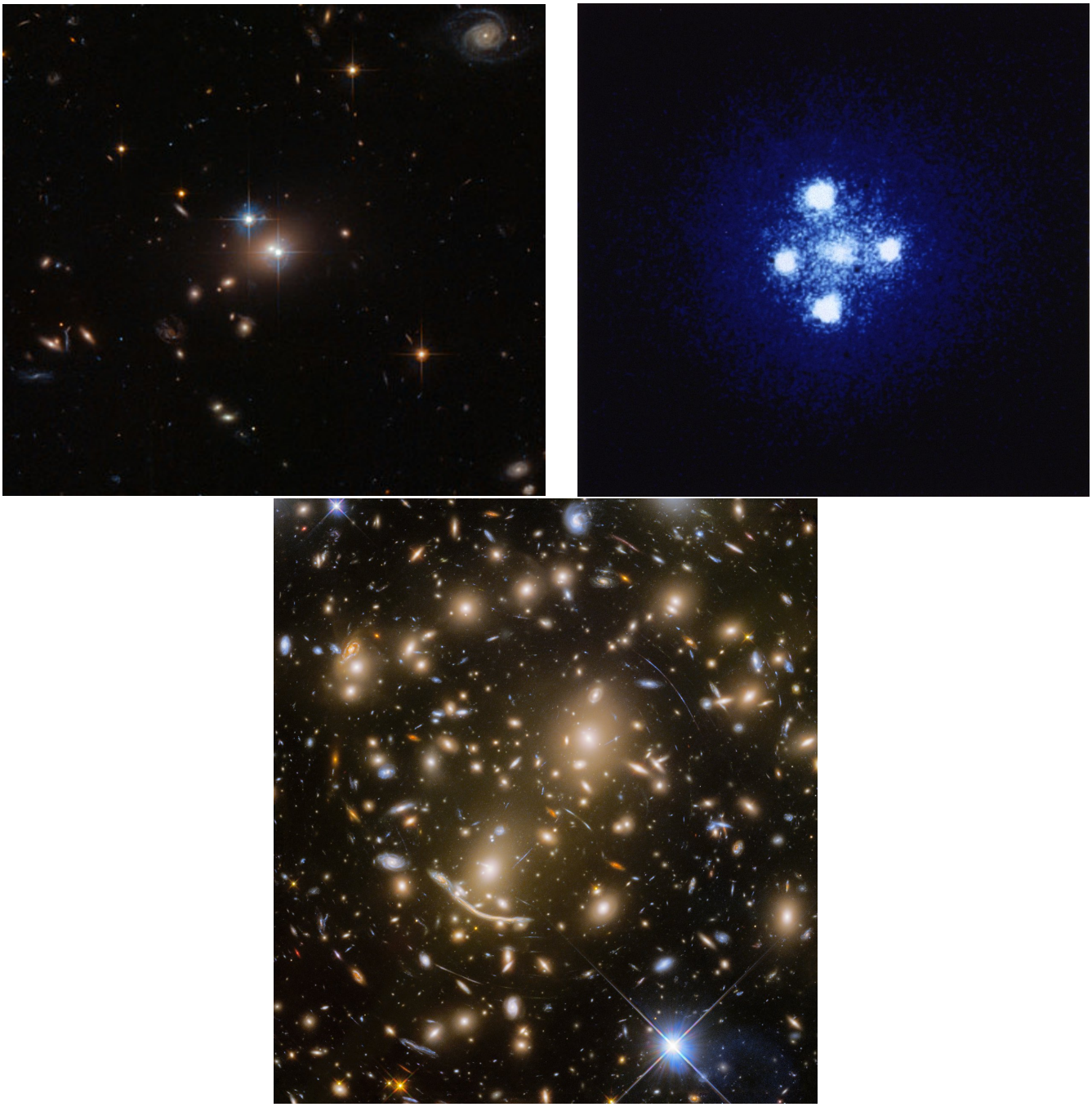

Figure 2.1: *Left:* QSO 0957+561 A/B, i.e. the Twin Quasar, discovered in Walsh et al. (1979), are displayed in the centre of the image. They are lensed by the giant elliptical galaxy YGKOW G1 visible between them. Credits: ESA/*Hubble* & NASA. *Right*: Lensed quasar QSO 2237+0305 by the centre of galaxy Huchra's lens, forming an Einstein cross. Credits: NASA, ESA, STScI. *Bottom*: Cluster Abell 370, as observed by *HST* for the *Hubble* Frontier Fields programme. The giant lensing arc is clearly distinguishable in the south. Credits: NASA, ESA/*Hubble*, HST Frontier Fields.

but not with ordinary matter in a significant way, detecting its gravitational influence would be the only way to astronomically characterise it. This was already done for the rotation curves of galaxies (by construction), but gravitational lensing should allow to map the dark matter density

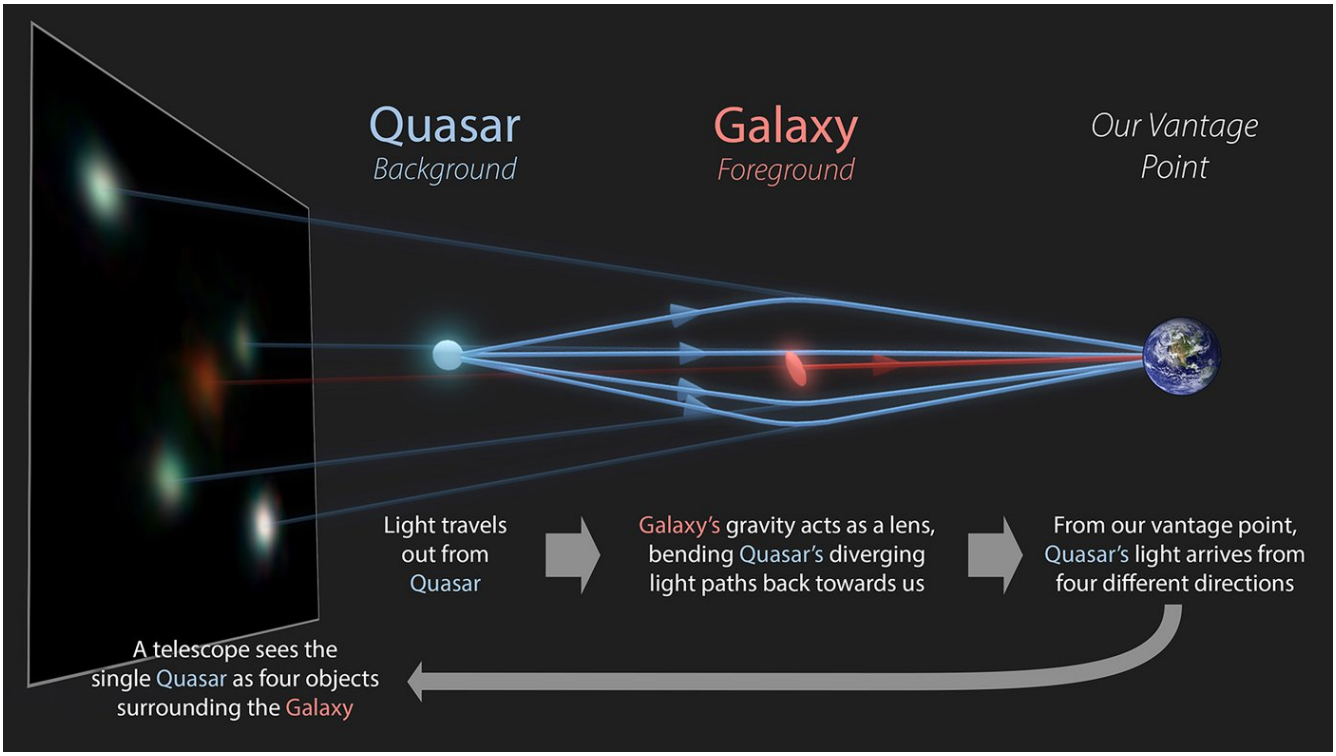

Figure 2.2: Gravitational lensing of a quasar source by a galaxy cluster lens. The observed image is an Einstein cross. Credits: R. Hurt (IPAC/Caltech)/The GraL Collaboration.

and therefore to set constraints on its physical nature eventually. Kassiola et al. (1992), Mellier et al. (1993), and Kneib et al. (1993) successfully modelled galaxy clusters as lenses producing multiple arcs, matching observations.

2.1.2 Existing lensing surveys and forthcoming

Table 2.1: Inexhaustive summary of the different types of lensing.

Type	Observable	Lens	Missions	Physical interest
Microlensing	Time-evolving magnification	Compact object, star	OGLE, EROS	Primordial black holes, exoplanets
Strong lensing	Giant arcs, multiple images	Galaxies, clusters	CLASH, HFF, GLASS	Clusters mass, DM constraints, cosmology
Weak lensing	Distortions, magnification	Galaxies, clusters	DES, LSST, *Euclid*	Clusters, halos, cosmology
CMB lensing	CMB temperature distortions	Large-scale structures	*Planck*	Cosmology

Since the 1990s, a number of gravitational lensing observations campaigns were launched, amongst which we can quote the Sloan Lens ACS program (SLACS, Bolton et al., 2006), the Cluster Lensing And Supernovae survey with Hubble (CLASH, Postman et al., 2012), the Hubble Frontier Fields (HFF, Lotz et al., 2017), the REionization LensIng Cluster Survey (RELICS, Coe et al., 2019), the SDSS Giant Arcs Survey (SGAS, Sharon et al., 2020), the Gaia gravitational

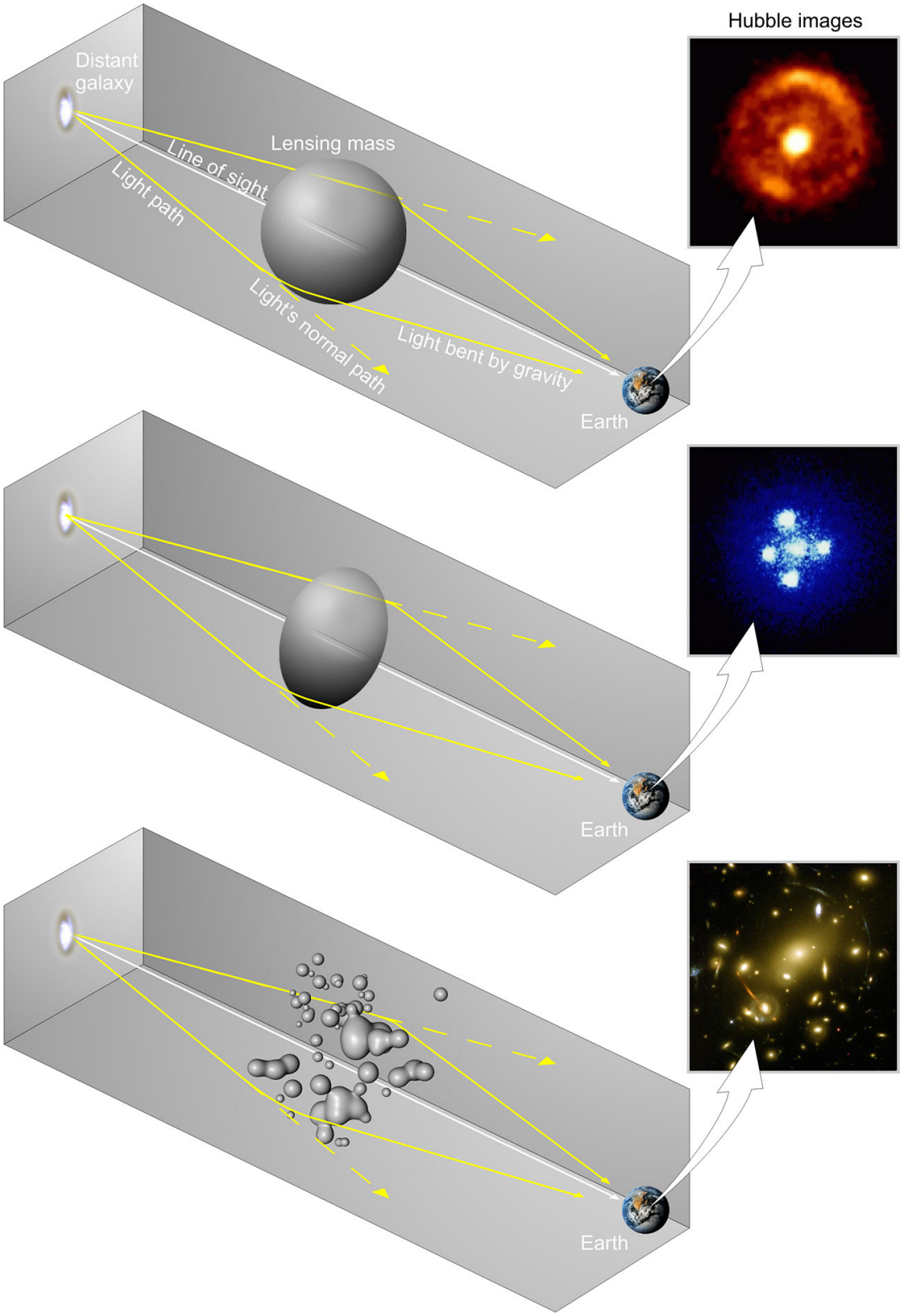

Figure 2.3: Gravitational lenses produce different shaped images depending on the shape of the lensing body. *Top:* A spherical lens produces an Einstein ring. *Middle:* An elongated lens produces an Einstein cross. *Bottom:* More complex lens geometries, such as that of a galaxy cluster yield arcs, arclets, and/or a number of multiple images. Credits: ESA.

lenses (Gaia GraL, Krone-Martins et al., 2018; Stern et al., 2021), the Beyond the Ultra-deep Frontier Fields And Legacy Observation programme (BUFFALO, Steinhardt et al., 2020), and the new GLASS-JWST Early Release Science (GLASS-JWST-ERS, Treu et al., 2022) for strong gravitational lenses.

Galaxy clusters act as magnifying lenses in the sky, and therefore as telescopes, allowing us to see further in the Universe with equal instruments. More generally, strong gravitational lensing (SL) plays a key role in various fields of modern day cosmology, amongst which the determination of the mass distribution within the lens, i.e. galaxy clusters and galaxies, with a remarkable amount of details (see for instance Richard et al., 2014; Jauzac et al., 2015, 2016b; Diego et al., 2015a,b, 2016, 2018, 2020; Grillo et al., 2015; Caminha et al., 2017; Williams et al., 2018), cosmography without using the distance ladder or the CMB (see Refsdal, 1964; Suyu et al., 2017; Wong et al., 2020, the two latter presenting the ideas and results of the H0LiCOW collaboration), including the dark energy equation (Sim et al., 2013), and, last but not least, to constrain dark matter (see e.g. Oguri and Keeton, 2004; Gilman et al., 2020), as we already mentioned with the Bullet Cluster example in Section 1.2.1 (see Markevitch et al., 2004; Clowe et al., 2004, 2006; Bradač et al., 2008, let us notice this was actually performed with weak lensing). In particular, the offset between the position of the centre of dark matter, luminous galaxies and X-ray emission in merging galaxy clusters allows to constrain the cross-section of self-interacting dark matter (SIDM, as introduced in Section 1.2.3, see Tulin and Yu, 2018, for an overview). This is due to the self-interaction to create damping in the dark matter dynamics upon collision, and therefore SIDM simulations show this to lag behind the luminous galaxies (see e.g. Massey et al., 2011; Robertson et al., 2017a,b), which is not the case in a collisionless model (CDM). Merten et al. (2011), Harvey et al. (2015), Massey et al. (2015, 2018), and Jauzac et al. (2016b, 2018) use that type of constraints.

In the weak lensing regime, i.e. far enough from the Einstein radius (i.e. the characteristic radius at which lensed multiple images appear, defined in equation 2.33), lensing does not produce multiple images of a same source, but still distorts and magnifies the image. This regime is called *weak lensing* (WL). With first detections in Bacon et al. (2000), Wittman et al. (2000), and Rhodes et al. (2001), surveys now include the Sloan Lens ACS program (SLACS, see Gavazzi et al., 2007), the Kilo-Degree Survey (KiDS, see Giblin et al., 2021), the Dark Energy Survey (DES, see Becker et al., 2016; Zürcher et al., 2022), the Hyper Suprime-Cam survey (HSC, see Aihara et al., 2018) and the Extended Baryon Oscillation Spectroscopic Survey (eBOSS, as part of SDSS IV, see Alam et al., 2021). The Large Synoptic Survey Telescope at the Vera C. Rubin Observatory (LSST, see LSST Dark Energy Science Collaboration, 2012) and the *Euclid* spacecraft (Euclid Collaboration, 2022) should be serviceable by the end of 2023. To complete this inexhaustive list, the *Nancy Grace Roman Space Telescope* (*NGRST*, previously known as WFIRST, see Hemmati et al., 2019) should also be probing weak lensing.

Because of its weaker effect, WL is inherently useful on a large number of objects, where statistics can be performed. Its use include probing large-scale structures, and thus the power-spectrum of different observables (see Section 1.1.9), allowing to probe cosmology (setting constraints on for instance H_0, σ_8 or dark energy equation of state), investigating the formation of structures, and probing the outskirts density distribution of individual galaxies or clusters. One can read Kilbinger (2015), Dodelson (2017), Bartelmann and Maturi (2017), and Mandelbaum (2018) for a review.

Other types of lensing include microlensing and CMB lensing, but are not the topic of this thesis. Microlensing occurs when an intra-galactic object (a planet, a star, a compact object) acts as a lens. Due to the size and proximity of such phenomena, their evolution can usually be observed over a reasonable human timescale – this subdomain being called *time-domain astronomy*.

Microlensing is notably being used to constrain some dark matter candidates: the massive compact halo objects (MACHO, see Alcock et al., 1998, 2000; EROS Collaboration, 2002; Tisserand et al., 2007, for the MACHO project and EROS surveys) and primordial black holes (PBH, see Niikura et al., 2019b,a, with Subaru/HSC and OGLE); but also to detect exoplanets (see Bond et al., 2004, for the first exoplanet detection), and compact objects (Sahu et al., 2022; Lam et al., 2022).

As for CMB lensing, it is the integrated effect of the weak lensing of structures from CMB to a present-day observer, modifying the temperature and polarisation anisotropies. One can read Lewis and Challinor (2006) and Hanson et al. (2010) for a review, and Planck Collaboration et al. (2020) for the *Planck* quantitative results.

Table 2.1 summarises a few properties of the various forms of lensing.

2.1.3 Formalism of gravitational lensing

Lens equations

In order to introduce the quantitative formalism of gravitational lensing, we refer the reader to reviews, e.g. Bartelmann and Schneider (2001), Keeton (2001), Treu (2010), Bartelmann (2010), Wagner (2019), and Meneghetti (2021). Let us consider a system composed of an observer (O), a source (S) at an angular diameter distance D_S of the observer (see Section 1.1.8 for distances definition), and a lens (L) at an angular diameter distance D_L from the observer. This is represented in Figure 2.4. We assume here a FLRW metric in a ΛCDM Universe, and thus transverse comoving distances are equal to comoving distances. Let us notice that in cosmology, the angular diameter distance between the source and the lens D_{LS} is not the difference of angular diameter distances $D_{LS} \neq D_S - D_L$. We can also define angular distances: β is the angular distance between the source and the lens (OL), and θ the angular distance between the image and the lens. $\alpha = \theta - \beta$ is the deflection angle in the observer plane (or reduced deflection angle), and $\hat{\alpha}$ the deflection angle in the lens plane. A bit of trigonometry yields:

$$\tan \hat{\boldsymbol{\alpha}} = \frac{D_S}{D_{LS}} \left(\tan \boldsymbol{\theta} - \tan \boldsymbol{\beta} \right), \tag{2.1}$$

where, in the vast majority of cases, the angles are small enough to consider $\tan \theta \approx \theta$, as the lens and source angular size would never be larger than a few arcminutes:

$$\hat{\boldsymbol{\alpha}} \approx \frac{D_S}{D_{LS}} \left(\boldsymbol{\theta} - \boldsymbol{\beta} \right). \tag{2.2}$$

Therefore, the reduced deflection angle may be rewritten:

$$\boldsymbol{\alpha} \approx \frac{D_{LS}}{D_S} \hat{\boldsymbol{\alpha}}. \tag{2.3}$$

The path of free particles in GR follows the geodesic equation:

$$\frac{\mathrm{d}^2 x^\alpha}{\mathrm{d}\lambda^2} = -\Gamma^\alpha_{\beta\gamma} \frac{\mathrm{d}x^\beta}{\mathrm{d}\lambda} \frac{\mathrm{d}x^\gamma}{\mathrm{d}\lambda}, \tag{2.4}$$

where λ is the path parametrisation, x^μ the position quadrivector of the particle and $\Gamma^\alpha_{\beta\gamma}$ the Christoffel symbol of the metric.

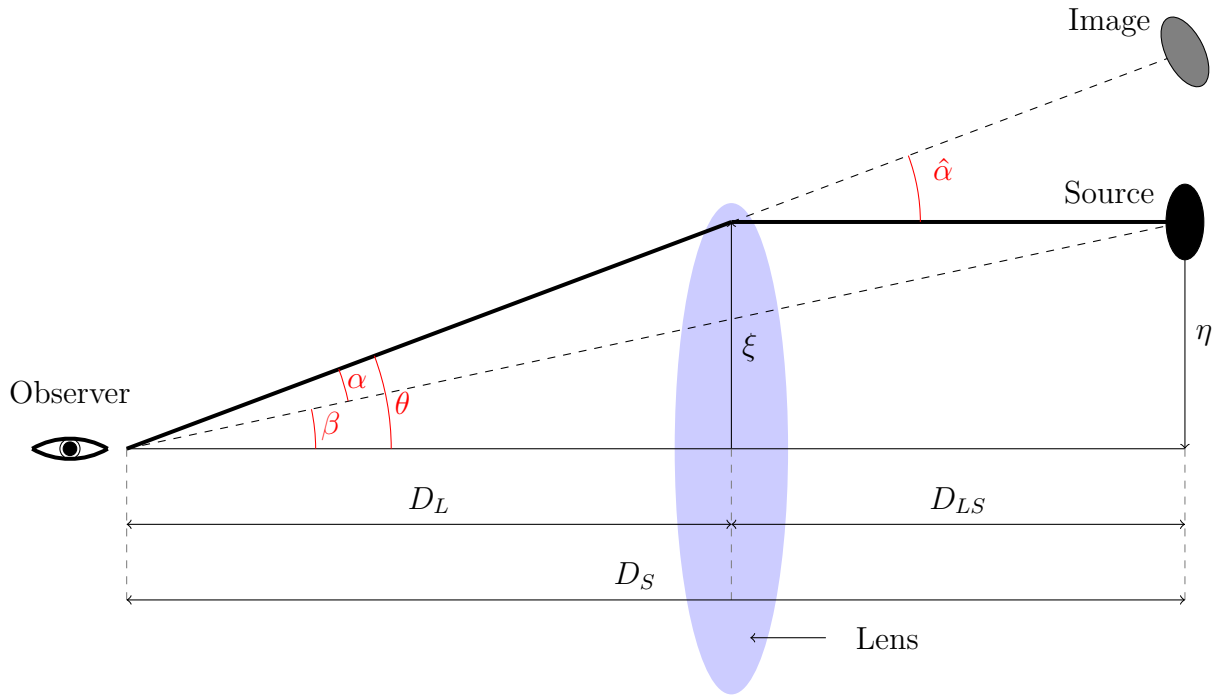

Figure 2.4: Gravitational lensing formalism. α is the deflection angle in the observer plane, while $\hat{\alpha}$ is the deflection angle in the lens plane. $\xi \approx \theta D_L$ is the impact parameter in the lens, here represented in 1D.

In order to determine the path of photons from the source to the observer, one can apply Fermat's principle (see Kovner, 1990; Pérez and Françon, 1996; Born and Wolf, 1999): given γ a null curve connecting the source to the observer, then γ is a null geodesic if, and only if, its proper time of arrival at the observer τ_O extremises the arrival times τ of all null curves connecting S to O. In other words, 'light always takes the shortest path':

$$\tau_O = \int_0^{\tau_O} \mathrm{d}t = c^{-1} \int_\gamma n \mathrm{d}\lambda, \tag{2.5}$$

where n is the refraction index of the fluid in which light travelled, including the pseudo-index of the gravitational field:

$$n = \frac{c}{c'} = c \frac{\mathrm{d}t}{|\mathrm{d}\boldsymbol{x}|}, \tag{2.6}$$

where c' is the celerity of light within the gravitational potential.

Let us define the conformal time η:

$$\eta = \int_0^t \frac{\mathrm{d}t'}{a(t')}. \tag{2.7}$$

Around an object of mass M, let us assume the metric $g_{\mu\nu}$ to be described with the Bardeen potentials (describing the metric perturbations, see Lewis and Challinor, 2006, for more details), in the conformal Newtonian gauge:

$$\mathrm{d}s^2 = g_{\mu\nu}\mathrm{d}x^\mu \mathrm{d}x^\nu = -a^2(\eta)\left[\left(1 + \frac{2\Phi_N}{c^2}\right)c^2\mathrm{d}\eta^2 - \left(1 + \frac{2\Psi_N}{c^2}\right)\mathrm{d}\boldsymbol{\chi}^2\right], \tag{2.8}$$

where $\Phi_N = -GM/r$ is the local Newtonian gravitational potential and Ψ_N the Newtonian curvature perturbation.

Defining the Weyl potential $\Psi_W \equiv \frac{1}{2}(\Psi_N - \Phi_N)$, let us rewrite the metric with $\Phi = -\Psi_W$. Given that one shall use this metric only on null geodesics, i.e. $\mathrm{d}s^2 = 0$, one can rescale the metric by any factor, e.g. $(1 - 2\Phi/c^2)$. In the limit of weak potential, $2\Phi/c^2 \ll 1$, the metric rewrites:

$$\mathrm{d}s^2 \approx -\left(1 + \frac{4\Phi}{c^2}\right) c^2 \mathrm{d}t^2 + \mathrm{d}\boldsymbol{x}^2. \tag{2.9}$$

Let us notice this weak field hypothesis is verified in almost all cases, as e.g. in galaxy clusters $|\Phi/c^2| < 10^{-4}$. Using the null geodesic equation $\mathrm{d}s^2 = 0$ provides the pseudo-refraction index defined equation (2.6):

$$n = \sqrt{\frac{c^2 - 2\Phi}{c^2 + 2\Phi}} \approx 1 - \frac{2\Phi}{c^2}, \tag{2.10}$$

in the weak field regime approximation.

Alongside the light path $\boldsymbol{x}$ parameterised by a (normalised) curve parameter λ, we can define the unitary tangent vector to the light path $\boldsymbol{e} = \frac{\mathrm{d}\boldsymbol{x}}{\mathrm{d}\lambda}$. $\boldsymbol{x}$ and $\boldsymbol{e}$ point towards the observer. The light path may be described with the Euler-Lagrange equations alongside a null geodesic (Meneghetti, 2021) as:

$$\frac{\mathrm{d}}{\mathrm{d}\lambda}(n\boldsymbol{e}) - \boldsymbol{\nabla} n = 0. \tag{2.11}$$

which we may rewrite:

$$\frac{\mathrm{d}\boldsymbol{e}}{\mathrm{d}\lambda} = \boldsymbol{\nabla}_\perp \ln n, \tag{2.12}$$

where $\boldsymbol{\nabla}_\perp$ is the gradient in the sky plane, pointing away from the line-of-sight. With equation (2.10), we may further simplify it into:

$$\frac{\mathrm{d}\boldsymbol{e}}{\mathrm{d}\lambda} \approx -\frac{2}{c^2}\boldsymbol{\nabla}_\perp \Phi. \tag{2.13}$$

We can define the total deflection angle $\hat{\boldsymbol{\alpha}}$ as the total deflection variation between the source and the observer:

$$\hat{\boldsymbol{\alpha}} = \boldsymbol{e}_S - \boldsymbol{e}_O = -\int_S^O \mathrm{d}\lambda \frac{\mathrm{d}\boldsymbol{e}}{\mathrm{d}\lambda}. \tag{2.14}$$

Integrating equation (2.13), we get the general equation for the total deflection angle:

$$\hat{\boldsymbol{\alpha}} \approx -\frac{2}{c^2}\int_0^S \mathrm{d}\lambda \boldsymbol{\nabla}_\perp \Phi. \tag{2.15}$$

Let us now define the 3D orthonormal, physical coordinates centred on the observer (O, ξ_1, ξ_2, ξ_3). Let us notice that $\xi_3 = a\chi$ represents the depth[3], and χ the comoving distance. We take $\boldsymbol{\xi} = (\xi_1, \xi_2)$ to be the vector towards the light ray in the sky plane. According to the Born approximation, we assume the potential alongside the deflected light path to be well approximated by the potential alongside the unperturbed path. This allows to simplify the parameter λ into a line-of-sight integration:

$$\hat{\boldsymbol{\alpha}}(\boldsymbol{\xi}) \approx \frac{2}{c^2}\int_0^S \mathrm{d}\xi_3 \boldsymbol{\nabla}_\perp^P \Phi(\boldsymbol{\xi}; \xi_3), \tag{2.16}$$

[3]The depth is measured from the observer. This means that $(\boldsymbol{\nabla}_\perp; \xi_3)$ is indirectly oriented.

where $\boldsymbol{\nabla}_\perp^P$ is the gradient on the sky plane, in physical (proper) coordinates. Using $\mathrm{d}\xi_3\boldsymbol{\nabla}_\perp^P = \mathrm{d}\chi\boldsymbol{\nabla}_\perp^C$, where $\boldsymbol{\nabla}_\perp^C$ is the gradient on the sky plane in comoving coordinates, we remap the deflection angle with comoving coordinates:

$$\hat{\boldsymbol{\alpha}}(\boldsymbol{\theta}) \approx \frac{2}{c^2}\int_0^{\chi_S} \mathrm{d}\chi \boldsymbol{\nabla}_\perp^C \Phi(\boldsymbol{\theta} D_A(\chi);\chi), \tag{2.17}$$

where $\boldsymbol{\theta}$ is the angular position vector. In the flat-sky approximation, the relationship between the different Laplacian derivatives, with ξ_i the comoving impact parameter in the lens plane according to coordinate i (for $i \in \mathbb{N}_2$; and simply the comoving depth coordinate $a\chi$ for $i = 3$), is:

$$\Delta_{\boldsymbol{\theta}} = \frac{\partial^2}{\partial\theta_1^2} + \frac{\partial^2}{\partial\theta_2^2} \approx D_A^2\left(\frac{\partial^2}{\partial\xi_1^2} + \frac{\partial^2}{\partial\xi_2^2}\right) = D_A^2\left(\Delta_{\mathrm{3D}}^P - \frac{\partial^2}{\partial\xi_3^2}\right) = D_A^2\Delta_\perp^P, \tag{2.18}$$

where $\Delta_\perp^P$ is the physical Laplacian on the sky plane (assumed Euclidean by flat-sky approximation), and Δ_{3D}^P the physical 3D distance Laplacian. Let us notice this relationship is also valuable for gradients: $\boldsymbol{\nabla}_{\boldsymbol{\theta}} \approx D_A\boldsymbol{\nabla}_\perp^P$. We can use the relationship $\boldsymbol{\nabla}_\perp^C = f_K^{-1}(\chi)\boldsymbol{\nabla}_{\boldsymbol{\theta}}$ to rewrite $\hat{\boldsymbol{\alpha}}$:

$$\hat{\boldsymbol{\alpha}} \approx \frac{2}{c^2}\int_0^{\chi_S} \frac{\mathrm{d}\chi}{f_K(\chi)}\boldsymbol{\nabla}_{\boldsymbol{\theta}}\Phi(\boldsymbol{\theta} D_A(\chi);\chi). \tag{2.19}$$

Differenciating relationship (2.3), we get the reduced deflection angle:

$$\begin{aligned}
\boldsymbol{\alpha}(\boldsymbol{\theta}) &\approx \frac{2}{c^2}\int_0^{\chi_S} \mathrm{d}\chi \frac{D_A(\chi_S-\chi)}{D_A(\chi_S)}\boldsymbol{\nabla}_\perp^C\Phi(\boldsymbol{\theta} D_A(\chi);\chi) \\
&= \frac{2}{c^2}\int_0^{\chi_S} \mathrm{d}\chi \frac{f_K(\chi_S-\chi)}{f_K(\chi_S)}\boldsymbol{\nabla}_\perp^C\Phi(\boldsymbol{\theta} D_A(\chi);\chi) \\
&\approx \frac{2}{c^2}\int_0^{\chi_S} \frac{\mathrm{d}\chi}{f_K(\chi)}\frac{f_K(\chi_S-\chi)}{f_K(\chi_S)}\boldsymbol{\nabla}_{\boldsymbol{\theta}}\Phi(\boldsymbol{\theta} D_A(\chi);\chi),
\end{aligned} \tag{2.20}$$

where $D_A(\chi_S-\chi)/D_A(\chi_S) = f_K(\chi_S-\chi)/f_K(\chi_S)$. We can then introduce the relationship between the effective lensing potential Ψ[4], and the Newtonian, three-dimensional potential Φ, with the effective lensing potential:

$$\Psi(\boldsymbol{\theta}) = \frac{2}{c^2}\int_0^{\chi_S} \mathrm{d}\chi \frac{f_K(\chi_S-\chi)}{f_K(\chi)f_K(\chi_S)}\Phi(\boldsymbol{\theta} D_A(\chi);\chi) = \frac{2}{c^2}\int_0^S \mathrm{d}\xi_3 \frac{D_A(\xi_{3,S}-\xi_3)}{D_A(\xi_3)D_A(\xi_{3,S})}\Phi(\boldsymbol{\xi};\xi_3), \tag{2.21}$$

which is related to the reduced deflection angle:

$$\boldsymbol{\alpha} = \boldsymbol{\nabla}_{\boldsymbol{\theta}}\Psi. \tag{2.22}$$

We can thus rewrite the lens equation (2.1) with the lensing potential (Schneider et al., 1992; Kneib and Natarajan, 2011):

$$\boldsymbol{\beta} = \boldsymbol{\theta} - \boldsymbol{\nabla}_{\boldsymbol{\theta}}\Psi(\boldsymbol{\theta}). \tag{2.23}$$

If we assume the lens to be *thin*, as done in the strong lensing regime, the lens is assumed to be localised at a redshift χ_L:

$$\begin{aligned}
\hat{\boldsymbol{\alpha}}(\boldsymbol{\theta}) = \frac{D_S}{D_{LS}}\boldsymbol{\alpha}(\boldsymbol{\theta}) &\approx \frac{2}{c^2}\int_0^S \mathrm{d}\xi_3 \boldsymbol{\nabla}_\perp^P\Phi(\boldsymbol{\xi};\xi_3), \\
\Psi(\boldsymbol{\theta}) &= \frac{2}{c^2}\frac{D_{LS}}{D_L D_S}\int_0^S \mathrm{d}\xi_3\Phi(\boldsymbol{\xi};\xi_3).
\end{aligned} \tag{2.24}$$

[4]This Ψ is neither the Bardeen nor the Weyl one.

With the local volume density as given by the Poisson equation:

$$\Delta^P_{3\mathrm{D}}\Phi = 4\pi G\rho^P_m, \tag{2.25}$$

We can then define the surface mass density $\Sigma \equiv \Sigma^P$ at a lens redshift z_L:

$$\Sigma(\boldsymbol{\xi}) = \int_0^S \mathrm{d}\xi_3 \rho^P_m(\boldsymbol{\xi}, \xi_3) = \frac{1}{4\pi G}\int_0^S \mathrm{d}\xi_3 \Delta^P_{3\mathrm{D}}\Phi(\boldsymbol{\xi}, \xi_3). \tag{2.26}$$

With the observation angle $\boldsymbol{\theta}$, integrated over an angle $\boldsymbol{\theta'}$ describing the whole lens plane, and reminding the relationship to the impact parameter: $\boldsymbol{\xi} \approx \boldsymbol{\theta} D_L$, the Laplacian thus can be rewritten using the Poisson equation associated Green's function:

$$\Phi(\boldsymbol{\xi}) = -\int \mathrm{d}\xi_3 \int \mathrm{d}^2\boldsymbol{\xi'} \frac{G\rho^P_m}{|\boldsymbol{\xi'} - \boldsymbol{\xi}|}, \tag{2.27}$$

where ξ_3 is the angular diameter distance alongside the line-of-sight, centred on the lens. Thus the gradient in the sky plane is:

$$\boldsymbol{\nabla}_\perp \Phi(\boldsymbol{\xi}) \approx 2G \int \mathrm{d}\boldsymbol{\xi'} \Sigma(\boldsymbol{\xi'}) \frac{\boldsymbol{\xi} - \boldsymbol{\xi'}}{|\boldsymbol{\xi} - \boldsymbol{\xi'}|^2}, \tag{2.28}$$

where the factor 2 stems from transforming the integration over ξ_3 from $]-\infty;+\infty[$ into the interval $[0;+\infty[$. Finally, equation (2.24) can be rewritten using equation (2.26) as:

$$\begin{aligned} \hat{\boldsymbol{\alpha}}(\boldsymbol{\theta}) &\approx \frac{4G}{c^2}\int \mathrm{d}^2\boldsymbol{\xi'} \Sigma(\boldsymbol{\xi'}) \frac{\boldsymbol{\xi} - \boldsymbol{\xi'}}{|\boldsymbol{\xi} - \boldsymbol{\xi'}|^2} \\ &\approx \frac{4GD_L}{c^2}\int \mathrm{d}^2\boldsymbol{\theta'} \Sigma(\boldsymbol{\theta'}) \frac{\boldsymbol{\theta} - \boldsymbol{\theta'}}{|\boldsymbol{\theta} - \boldsymbol{\theta'}|^2}, \end{aligned} \tag{2.29}$$

which corresponds to summing the contributions of all the mass elements $\Sigma(\xi)\mathrm{d}^2\boldsymbol{\xi}$. We define the cylindrical mass contained within an angular radius (Narayan and Bartelmann, 1996):

$$M(<\theta) = 2\pi \int_0^\xi \Sigma(\xi')\xi' \mathrm{d}\xi' = 2\pi D_L^2 \int_0^\theta \Sigma(\theta')\theta' \mathrm{d}\theta', \tag{2.30}$$

and the critical surface density:

$$\Sigma_{\mathrm{cr}} = \frac{c^2}{4\pi G}\frac{D_S}{D_{LS}D_L}. \tag{2.31}$$

In the case of a circularly symmetric lens, equation (2.29) reduces to:

$$\hat{\alpha}(\boldsymbol{\theta}) = \frac{4GM(<\xi)}{c^2\xi} = \frac{4GM(<\theta)}{c^2 D_L \theta}. \tag{2.32}$$

The Einstein angle (related to the Einstein radius $R_E = D_L\theta_E$) is defined as the solution to equation (2.2) in the case $\beta = 0$ (source along the line-of-sight), for a circular source:

$$\theta_E = \sqrt{\frac{4GM(<\theta_E)}{c^2}\frac{D_{LS}}{D_L D_S}}, \tag{2.33}$$

where we note $M(<\theta_E)$, the mass enclosed within the Einstein radius, with $M(<\theta_E) = \pi D_L^2 \theta_E^2 \Sigma_{\mathrm{cr}}$. The Einstein angle is the size of the Einstein ring, and the typical distance between the lensed images and the centre of the lens. Roughly speaking, the Einstein angle and the critical surface density define the outer limit of the strong lensing regime. Out of this angle, the comoving surface density is too small ($\Sigma \ll \Sigma_{\mathrm{cr}}$) to allow multiple images or arcs configuration.

Short summary of lensing approximations

1. Small angles $\implies \tan\theta \approx \theta$, i.e. plane-parallel approximation; which is equivalent to the flat-sky approximation.
2. Weak field $|2\Phi/c^2| \ll 1$.
3. Born approximation, i.e. the deflected potential is approximated by the undeflected one.
4. Thin lens approximation. This is not strictly necessary, but is assumed from Section 2.1.4.

In particular, assumptions 2-4 are by far the strongest, and one can not claim to derive exact strong lensing results with them.

In terms of strong gravitational lensing, we refer the reader to Schneider et al. (1992) and Kochanek (2006) for a full review, and as for weak lensing, we refer to the Sachs formalism (defined in Sachs, 1961), and to Bartelmann and Schneider (2001) and Schneider (2005) for reviews. A discussion about the separation between the strong and weak lensing formalism, with solutions to use a more precise formalism for weak lensing and to take line-of-sight integrated effects into account was proposed by Fleury et al. (2017, 2021).

In cosmology, it is fundamental to avoid some or all of these assumptions. A way to avoid using them is to deviate from the lensing formalism, and to follow light rays from emission to observation theoretically (see e.g. Bernardeau et al., 2010, for a full-sky theoretical derivation of a lensing observable) or numerically (see e.g. Rasera et al., 2022, for a full ray-tracing simulation suite, from which lensing observables can be derived).

Observables

We can easily define the *convergence* as a reduced surface density with equations (2.26) and (2.31):

$$\kappa = \frac{\Sigma(\boldsymbol{\theta})}{\Sigma_{\rm cr}}. \tag{2.34}$$

With equation (2.29), the reduced deflection angle can be rewritten:

$$\boldsymbol{\alpha}(\boldsymbol{\theta}) = \frac{1}{\pi}\int \mathrm{d}^2\theta' \kappa(\boldsymbol{\theta'}) \frac{\boldsymbol{\theta}-\boldsymbol{\theta'}}{|\boldsymbol{\theta}-\boldsymbol{\theta'}|^2}. \tag{2.35}$$

With equations (2.18) and (2.26), we can rewrite the convergence (without the thin lens approximation):

$$\begin{aligned}\kappa &= \frac{1}{c^2}\int_0^S \mathrm{d}\xi_3 \frac{D_A(\xi_{3,S}-\xi_3)}{\xi_{3,S} D_A(\xi)} \Delta^P_{\rm 3D}\Phi(\boldsymbol{\xi},\xi_3) \\ &= c^{-2}\int_0^{\chi_S} \mathrm{d}\chi \frac{f_K(\chi) f_K(\chi_S-\chi)}{f_K(\chi_S)} \Delta^C_{\rm 3D}\Phi(\boldsymbol{\theta} D_A(\chi);\chi),\end{aligned} \tag{2.36}$$

as $\Delta^C_{\rm 3D} = a^2 \Delta^P_{\rm 3D}$.

There is another manner to define the lensing convergence:

$$\begin{aligned}\kappa_{\rm eff} = \boldsymbol{\nabla}_{\boldsymbol{\theta}}\cdot\boldsymbol{\alpha} = \Delta_{\boldsymbol{\theta}}\Psi &\approx \frac{2}{c^2}\int_0^{\chi_S} \mathrm{d}\chi \frac{f_K(\chi) f_K(\chi_S-\chi)}{f_K(\chi_S)} \Delta^C_{\perp}\Phi(\boldsymbol{\theta} D_A(\chi);\chi) \\ &\approx \frac{2}{c^2}\int_0^{\chi_S} \mathrm{d}\chi \frac{f_K(\chi) f_K(\chi_S-\chi)}{f_K(\chi_S)} \left(\Delta^C_{\rm 3D} - \partial^2_\chi\right)\Phi(\boldsymbol{\theta} D_A(\chi);\chi) \\ &= \kappa_\perp + \kappa_\parallel,\end{aligned} \tag{2.37}$$

where $\kappa_\perp$ is the convergence on the sky, similar to formula (2.36), and $\kappa_\parallel$ the part due to the comoving distance:

$$\begin{aligned}\kappa_\perp &= c^{-2}\int_0^{\chi_S} \mathrm{d}z \frac{f_K(\chi_S-\chi)f_K(\chi)}{f_K(\chi_S)}\Delta_{3\mathrm{D}}\Phi(\boldsymbol{\theta}D_A(\chi);\chi),\\ \kappa_\parallel &= -c^{-2}\int_0^{\chi_S} \mathrm{d}\chi \frac{f_K(\chi_S-\chi)f_K(\chi)}{f_K(\chi_S)}\partial^2_\chi\Phi(\boldsymbol{\theta}D_A(\chi);\chi),\end{aligned} \tag{2.38}$$

where $\Delta^C_{3\mathrm{D}}$. The non-trivial expression of $\kappa_\parallel$ is commonly neglected. Indeed, when applying the Born approximation (assuming the lens to be a gravitationally bounded structure), the expression simplifies to $\kappa_\parallel \propto \partial_\chi\Phi$, which is null at the boundaries of the thin lens. For a perfect calculation of the convergence, notably when probing the large-scale structures, this term should however be calculated. As noted in Fleury (2015), this partial derivative ∂^2_χ takes into account the formation of structures (similarly to the integrated Sachs-Wolfe effect) and can thus not be trivially integrated by parts. However, neglecting this time evolution:

$$\frac{\mathrm{d}\Phi}{\mathrm{d}\chi} = \partial_\chi\Phi - \frac{\mathrm{d}\eta}{\mathrm{d}\chi}\partial_\eta\Phi = \partial_\chi\Phi - c^{-1}\partial_\eta\Phi \approx \partial_\chi\Phi, \tag{2.39}$$

as it is much slower than the spatial evolution of structures yields:

$$\kappa_\parallel \approx c^{-2}\left[-\Phi_S - \Phi_0 + 2\int_0^{\chi_S}\frac{\mathrm{d}\chi}{\chi_S}f'_K(\chi_S-2\chi)\Phi(\boldsymbol{\theta}D_A(\chi);\chi)\right], \tag{2.40}$$

where $f'_K(\chi)$ is the comoving derivative to the transverse comoving distance defined equation (1.25):

$$f'_K(\chi) = \begin{cases}\cosh(\chi/d_k) & \\ 1 & \text{for}\\ \cos(\chi/d_k) & \end{cases}\begin{matrix}\Omega_k>0\\ \Omega_k=0\\ \Omega_k<0.\end{matrix} \tag{2.41}$$

with $d_k = |\Omega_k|^{-1/2}\,c/H_0$.

Let us disregard the $\kappa_\parallel$ effect from now on: $\kappa_{\mathrm{eff}} \approx \kappa_\perp = \kappa$. Under the Born approximation, with $W(z) = f_K(\chi_S-\chi)f_K(\chi)/f_K(\chi_S)$ the lensing kernel, defining the lensing efficiency, the convergence thus writes:

$$\kappa \approx c^{-2}\int \mathrm{d}\chi W(\chi)\Delta_{3\mathrm{D}}\Phi \approx c^{-2}\frac{D_L D_{LS}}{D_S}\Delta_{3\mathrm{D}}\int\mathrm{d}\chi\Phi = \frac{1}{2}\Delta_{3\mathrm{D}}\Psi, \tag{2.42}$$

Computing the lensing kernel numerically shows that the most optimal lensing configuration therefore is $D_L = D_{LS} = D_S/2$.

With equation (2.35), we write the reduced deflection potential in terms of convergence:

$$\Psi(\boldsymbol{\theta}) = \frac{1}{\pi}\int \mathrm{d}^2\theta'\kappa(\boldsymbol{\theta'})\ln|\boldsymbol{\theta}-\boldsymbol{\theta'}|. \tag{2.43}$$

The convergence κ is a measurement of the magnification of an image caused by lensing: a positive convergence signals an increase of apparent size (while conserving the same surface brightness), while a negative convergence (which can be found in under-dense regions of the Universe, between the large-scale structures) is synonymous with an apparent size decrease.

We shall define the amplification matrix $\mathcal{A}(\boldsymbol{\theta})$ as the Jacobian of the unlensed position $\boldsymbol{\beta}$ and the lensed position $\boldsymbol{\theta}$ (see Bartelmann and Schneider, 2001):

$$\begin{aligned}\mathcal{A}(\boldsymbol{\theta}) = \frac{\partial \boldsymbol{\beta}}{\partial \boldsymbol{\theta}} &= \left(\delta_{ij} - \frac{\partial \alpha_i}{\partial \theta_j}\right)_{(i,j)\in\mathbb{N}_2^2} = \left(\delta_{ij} - \frac{\partial^2 \Psi}{\partial \theta_i \partial \theta_j}\right)_{(i,j)\in\mathbb{N}_2^2} \\ &= \begin{pmatrix} 1-\kappa-\gamma_1 & -\gamma_2+\omega \\ -\gamma_2-\omega & 1-\kappa+\gamma_1 \end{pmatrix},\end{aligned} \tag{2.44}$$

where ω is the antisymmetric rotation angle, which will from now on considered to be $\omega = 0$ (as we can simply rotate the sky plane referential), and with Ψ the deflection potential defined equations (2.21) and (2.43). Additional terms of higher-order (such as the *flexion*) can be taken into account for higher precision measurements, and to use statistical analysis. Such terms are described in e.g. Bernardeau et al. (2010) and Birrer (2021).

In equation (2.44), the shear component γ is composed of:

$$\gamma_1 = \frac{1}{2}(\Psi_{,11} - \Psi_{,22}) \quad ; \quad \gamma_2 = \Psi_{,12}, \tag{2.45}$$

where the total shear is:

$$\gamma = \gamma_1 + i\gamma_2 = |\gamma| e^{2i\varphi}. \tag{2.46}$$

Identifying this complex notation with $\mathbb{C} \equiv \mathbb{R}^2$, i.e. the lens plane, γ_1 is responsible of the shear deformation alongside the Cartesian axes, while γ_2 performs the same effect at 45 deg. φ is the angle of shear deformation, when only considering the modulus $|\gamma|$. Let us notice that the convergence can be measured as the trace of the amplification matrix:

$$\kappa = \frac{1}{2}\Delta_{\boldsymbol{\theta}}\Psi = 1 - \frac{1}{2}\,\mathrm{Tr}(\mathcal{A}). \tag{2.47}$$

A circular source of radius R would thus appear as an ellipse of semi-major and semi-minor axes a and b:

$$\begin{aligned} a &= \frac{R}{1-\kappa-|\gamma|}, \\ b &= \frac{R}{1-\kappa+|\gamma|}. \end{aligned} \tag{2.48}$$

Let us now introduce the reduced shear g:

$$g = \frac{\gamma}{1-\kappa}, \tag{2.49}$$

which is invariant with the scaling of the Amplification matrix $\mathcal{A}$. Let us note that in weak lensing $\kappa \ll 1$ and $|\gamma| \ll 1$, implying $g \approx \gamma$. The reduced shear is sometimes referred to, in weak lensing, as the lensing *ellipticity*. This effect is only an image distortion, and has nothing to do with the genuine ellipticity of the source (read Meneghetti, 2021, for more). However, it has the merit to be a directly measurable observable.

We can also introduce the flux magnification of an image μ:

$$\mu = [\det(\mathcal{A})]^{-1} = \frac{1}{(1-\kappa)^2 - |\gamma|^2} = \frac{1}{(1-\kappa)^2(1-g)^2}. \tag{2.50}$$

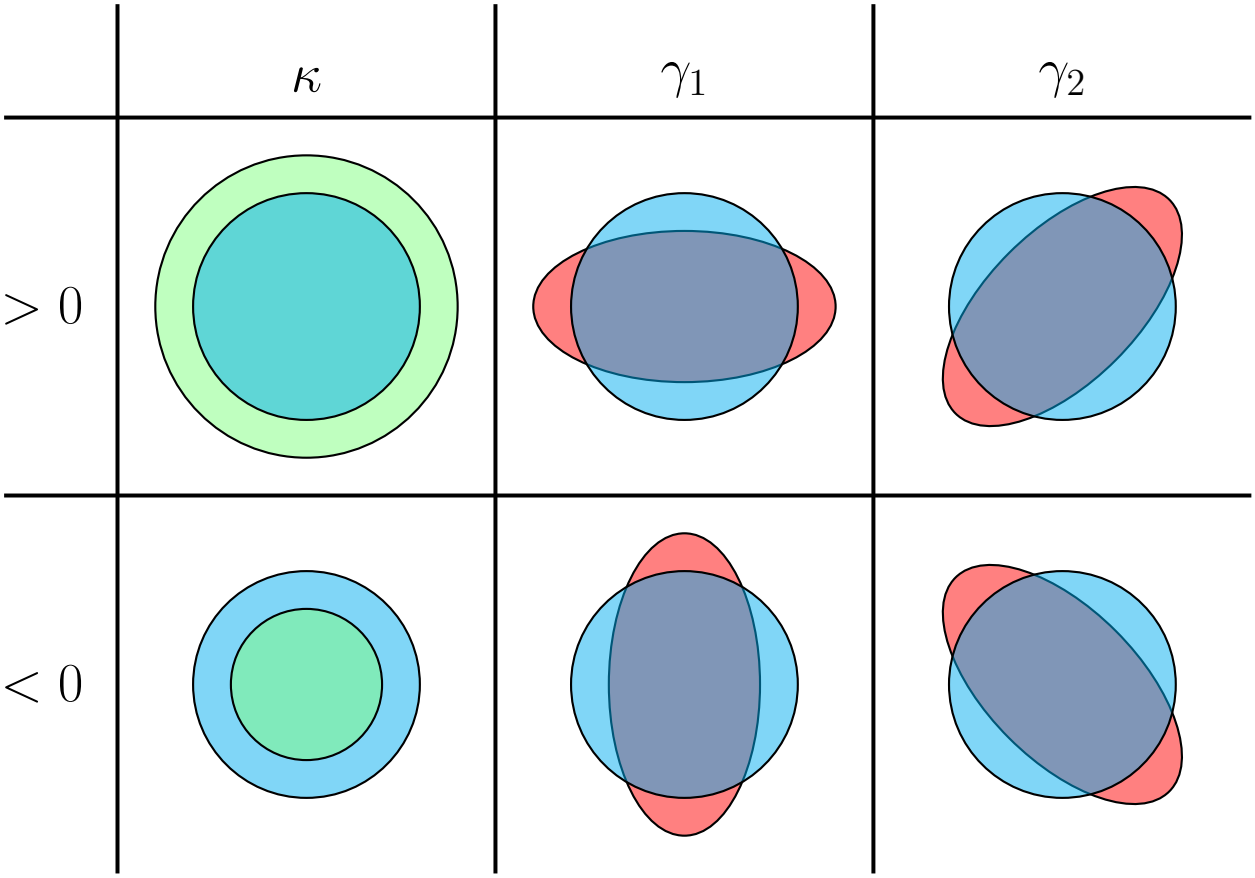

Figure 2.5: Effects of convergence and shear: the cyan circle represents the size of a circular source. The green circle shows the effects of the convergence κ, while the red ellipses showcase the role of shear γ.

In the strong lensing regime, the reduced shear can reach values of $g = \pm 1$. This defines two never crossing lines in the lens plane where the magnification is infinite: the *critical lines*. Their equation writes:

$$\det \mathcal{A}_{\rm crit} = (1 - \kappa_{\rm crit})^2 - |\gamma_{\rm crit}|^2 = 0. \tag{2.51}$$

The associated projected lines in the source plane are called the *caustic lines*, and as critical lines, they are closed, but can intersect. These pairs are usually composed of an internal line, where deformations are radial, and an external one, where deformations are tangential (see Kneib and Natarajan, 2011). In empirical strong lensing analyses, these lines are extremely useful to identify the distribution of multiply-imaged systems.

2.1.4 Strong lensing configurations

The number of multiple images from a same source must be odd, according to the odd number theorem (proven in McKenzie, 1985)[5]. In multiply-lensed images configurations, the number is 3 or 5. That number is given by the number of solutions to equation (2.1), where $\boldsymbol{\beta}$ is constant for a given source, and $\boldsymbol{\theta}$ a variable. If we consider a source far from the line-of-sight and thus only

[5]Gottlieb (1994) argues they rigorously need not to be. His argument is that the odd number theorem was proven in a Euclidean space, while the sensibility of strong lensing images requires to take into account the Lorentzian nature of space.

weakly lensed, and move it progressively toward the line-of-sight, each crossing of a caustic would add 2 multiple images on each side of the associated critical line. These new images would appear to 'mirror' each other. Let us notice that in practice, multiple images can 'merge', as best shown in the Einstein ring configuration. Some multiple images can also be strongly demagnified (Schneider et al., 1992). As a result, an even number of observed images is often observed, as exampled with the Einstein cross (see Figure 2.6, left panel).

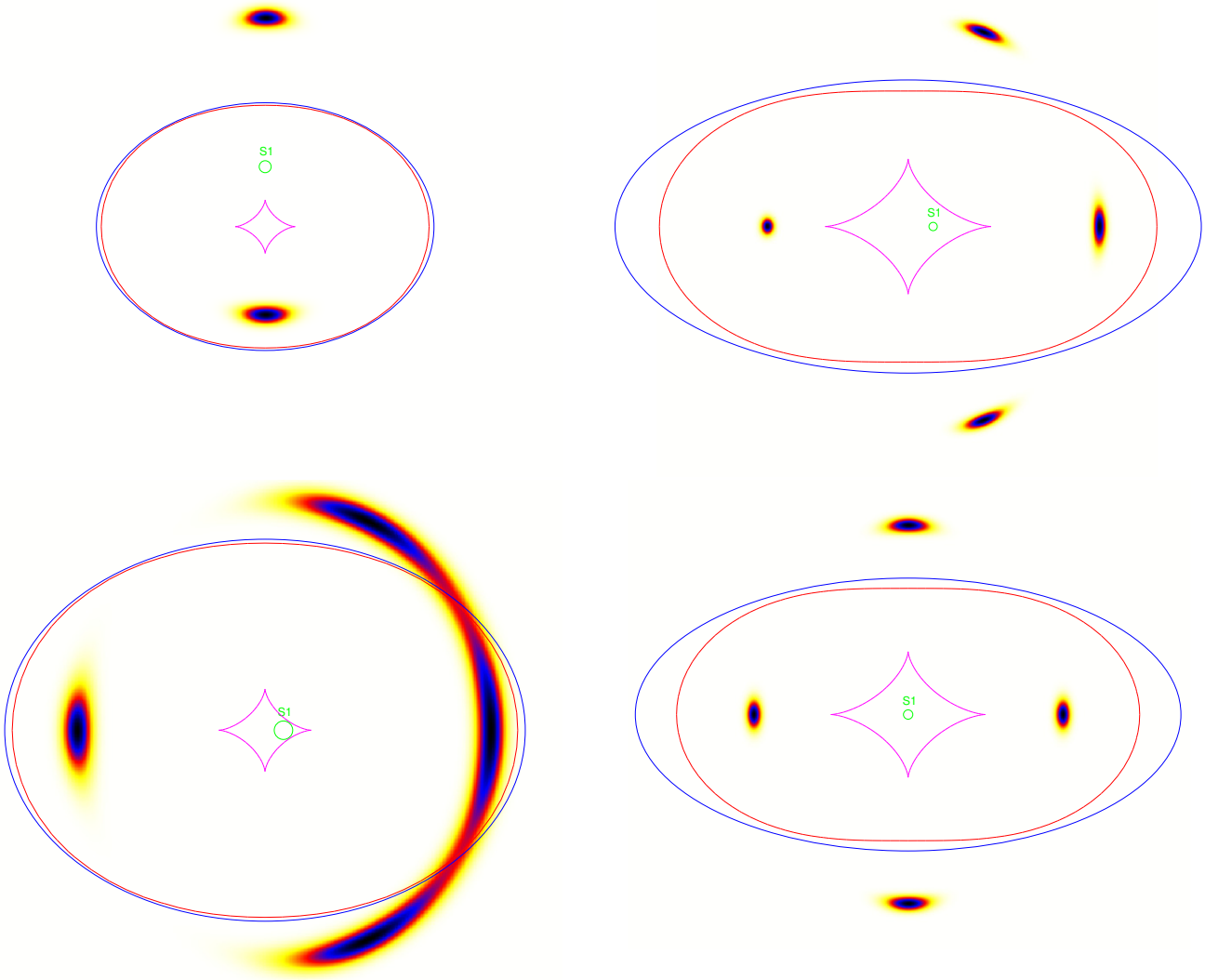

Figure 2.6: Examples of strong lensing configurations (for more examples, see Kneib and Natarajan, 2011, Fig. 11). *Top left:* Double multiply-imaged system of one source, also called radial arc. *Top right:* Quadruple multiply-imaged system of a source. *Bottom left:* Cusp arc, where the source S1 is almost lined with potential. *Bottom right:* Einstein cross: a specific case of quadruply-lensed source, where the source is aligned with the lens. The background surface heat map represents the brightness of the lensed image. The blue curve represents the same singular isothermal sphere (SIS) potential. It has the same geometry for the both left panels (ellipticity 0.3), and for both right panels (ellipticity 0.6). The green circle represents the source. The magenta and red curves are respectively the caustic and critical line (the SIS profile configuration only yielding one of each).

We here present the most common strong lensing images configurations, following Kneib and

Natarajan (2011). We present some examples on Figure 2.6. Other configurations are possible, due to perturbed lens geometries (see Orban de Xivry and Marshall, 2009; Meena and Bagla, 2021, for a review of more 'exotic' configurations).

Doubles

Doubly-lensed images were historically the first type of strong lensing configuration to be discovered, with the Twin Quasars (as mentioned in Section 2.1.1 and Figure 2.1 top left panel). These configurations tend to occur when the source is situated out of the tangential (inner) caustic line (the yellow, astroid-shaped one on Figure 2.3 top left panel).

Quadruple

The first quadruply-imagining lens discovered was the lensing galaxy known as Huchra's lens (QSO 2237+0305 G, see Huchra et al., 1985, see the right panel of Figure 2.1). The resulting Einstein cross is typical of quadruply-imaged configurations, which commonly require the source to be aligned with the lens, and the lens to be oblong. More generally, quadruply-lensed images require the source to be within the tangential caustic lines, and the lens to be elliptical. Let us notice that, as for the doubly-lensed images, there is the same number of images out of the critical lines as within. A fifth image may appear close to the centre of the lens. It is however often too dim to be observed, as it is the case for the lensed quasar images of QSO 2237+0305 G.

Arclets and giant arcs

All lensed images are distorted, but when the source is close to the tangential caustic line, this can cause the images to be distributed following a cusp arc, as presented on the bottom panel of Figure 2.1 and on the bottom left panel of Figure 2.3. In practice, one or several of the multiple images is simply extremely distorted, sometimes even appearing connected to the other multiple images. The most extreme case this can reach is that of the Einstein-Chwolson ring, appearing as a ring-like structure around the lens.

2.1.5 Lensing in the context of cosmology

In the analysis of large-scale structure, or other large portions of the Universe with weak lensing, it can be useful to consider lensing indicators in a field, to conduct some posterior statistical analysis.

With equations (1.30) and (1.32), a the scale factor, δ the overdensity, $\rho^P_{c,m}$ the critical density of matter in physical density units, $\rho^P_m = \rho^P_{c,m}(1+\delta)$ the physical matter density, ρ^C_m the comoving matter density, $\rho^C_{c,m}$ the critical comoving matter density, and using $\rho = \rho^C_m = \rho^P_m a^3$ the local volume density as given by the Poisson equation, we complete equation (2.25):

$$\Delta^C_{3\mathrm{D}}\Phi = a^2\Delta^P_{3\mathrm{D}}\Phi = 4\pi G\rho^P_m a^2 = 4\pi G\rho^P_{c,m}(1+\delta)a^2 = 4\pi G\rho^C_{c,m}(1+\delta)a^{-1}, \tag{2.52}$$

where we can let alone the constant part of the Lagrangian $4\pi G\rho^C_{c,m}a^{-1}$.

Using the comoving critical matter density parameter defined equation (1.31), the convergence κ (equation 2.42) rewrites:

$$\kappa(\boldsymbol{\theta}) \approx \frac{3H_0^2\Omega_{0,m}}{2c^2}\int_0^{\chi_S} \mathrm{d}\chi(1+z)W(\chi)\delta(\chi\boldsymbol{\theta},\chi). \tag{2.53}$$

In order to connect the observed shear to the convergence, and thus get a full description of the weak lensing effect, one can use the Kaiser-Squires theorem (Kaiser and Squires, 1993), allowing to derive the lensing potential from the shear[6].

2.2 Quantitative strong lensing measurements

2.2.1 Lens optimisation techniques

Let us consider the specific case of strong lensing observations with multiply-imaged systems (for a review, see Kneib and Natarajan, 2011). If the lens is a massive galaxy cluster at intermediate redshift ($0.2 \leq z \leq 0.5$), we can consider in most cases the lens to be thin, i.e. to respect the Born approximation. This is due to the rarity of finding two massive clusters extremely well aligned along the line-of-sight, as clusters are rare objects. Lensing by foreground or background (relative to the lens) objects is always possible however, and should then be modelled independently. This is for instance the case if two clusters appear aligned along the line-of-sight, but are distributed at very different redshifts. Therefore, observations of different multiple images allow to constrain the Newtonian potential Φ of the lens, i.e. the volume density ρ. However, only the projected density Σ can be directly probed through lensing without making assumptions about the shape of the potential (e.g. ellipsoidal symmetry), as an observer may only observe lensed images projected on the lens plane.

Position of the multiple images

In order to use all the constraints provided by the different lensing configurations (see Section 2.1.4) to describe the lens' properties, one can incrementally modify the lens model. Using such a lens model, one may compute the lensing potential Ψ (with equation 2.23). With the multiply-imaged systems already detected, one may optimise the position of the sources of these systems. Re-projecting the reconstructed sources into the image plane yields predicted multiple images. The offset between these and the observations provides an idea of the quality of the model. Moreover, the predicted multiple images which do not have an observational counterpart may be investigated. For instance, on Figure 2.3 top right panel, if three out of the four multiple images are observed, and the lens effectively modelled, the fourth image should be predicted. If further observations discover the predicted counterpart, this confirms the predictive quality of the model. Otherwise, it shows its limitations.

In this optimisation, one can choose whether or not to invert the lens equation (2.23), i.e. to respectively characterise the model error in the *lens* or in the *source* plane (see Kochanek, 2006).

- *Source plane optimisation:* It can be computationally expensive to invert this equation, and in the case of a model with good priors, it is possible to project the images onto the source plane and then minimise the difference between the projected source positions. For a single source, this is:

$$\chi^2_{\rm source} = \sum_{i=1}^{N_{\rm images}} \left(\frac{\boldsymbol{\beta}_i^{\rm pred} - \boldsymbol{\beta}^{\rm mod}}{\sigma_{s,i}} \right)^2 , \tag{2.54}$$

[6]Fleury et al. (2017) have however presented the limits of such a technique, which is bounded to the assumption of infinitesimal beams. This does not take into account properly the lensing effect of point lenses within the light beam, which statistically matters.

where $\boldsymbol{\beta}_i^{\rm pred}$ are the positions of the sources predicted using the lens equation for a given lens model, $\boldsymbol{\beta}^{\rm mod}$ is the position of the source in a model, treated as a parameter, and $\sigma_{s,i}$ are the measurement error on the position of the images, projected on the source plane. This method allows to compute the error faster, and thus to run a faster optimisation. It also avoids divergences in the inverse amplification matrix. Nevertheless, it comes with an important built-in drawback: the error on the images in the source plane $\sigma_{s,i}$ is not known. The measured errors on the images $\sigma_{l,i}$ are tied to the lens plane, and therefore using them in the source plane directly makes little physical sense. If the priors on the lens model are satisfactory however, a way to take the magnification of the error effect into account is to use the corrected source error:

$$\chi^2_{\rm source,corr} \approx \sum_{i=1}^{N_{\rm images}} \frac{\left(\boldsymbol{\beta}_i^{\rm pred} - \boldsymbol{\beta}^{\rm mod}\right) \times \mathcal{M}_i^2 \times \left(\boldsymbol{\beta}_i^{\rm pred} - \boldsymbol{\beta}^{\rm mod}\right)}{\sigma_{l,i}^2}, \tag{2.55}$$

where $\mathcal{M}_i = \mathcal{A}_i^{-1}$ is the magnification matrix at the position of image i. This approximation is only valid if $\left|\boldsymbol{\beta}_i^{\rm pred} - \boldsymbol{\beta}^{\rm mod}\right| \to 0$.

- *Lens plane optimisation:* Alternatively, one can invert the lens equation, find the position of the source image on the lens plane, and thus more generally constrain the model of the lens without requiring strong priors. In this case, the positional error may be used directly:

$$\chi^2_{\rm images} = \sum_{i=1}^{N_{\rm images}} \left(\frac{\boldsymbol{\theta}_i^{\rm pred} - \boldsymbol{\theta}_i^{\rm obs}}{\sigma_{l,i}}\right)^2, \tag{2.56}$$

where $\boldsymbol{\theta}_i^{\rm pred}$ are the predicted image positions and $\boldsymbol{\theta}_i^{\rm obs}$ the observed image positions. This is the exact solution, but is more numerically heavy.

For instance, Remolina González et al. (2018) provide examples of the source and lens plane scatter assessments, allowing to compare both methods.

Multiple images' geometry and symmetries

Multiple images exhibit different individual shapes (as presented on Figure 2.3), which allow to detect the direction and magnitude of the potential. The separation between multiple images of a same source obeys certain symmetry rules which differ depending on the type of lens. The rule of thumb is to consider multiple images of a system as symmetric of one another around a critical line. Therefore, local properties of the lens around a critical point (i.e. a point of infinite amplification) can be found by the appropriate analysis of the individual images geometry with respect to each other (i.e. a Taylor expansion of the Fermat potential of order four around each critical point, as detailed in Wagner, 2019). The investigation of these symmetries utilises geometric constraints on the multiple images, and as a result, it yields results which may be redundant with the amplification matrix inversion. It can be used as a complement, putting together the image shapes and their overall geometric distribution.

Redshift measurement

In addition to these purely geometric information, multiple-band astronomy contains more information about the redshift of a source. In fact, the comparison between different filters allows to compare the colour variation of different images. If this colour variation is the same for several

multiply-imaged system candidates, this hints towards a unique source, as lensing does not modify the colour. This can also lead to the determination of a photometric redshift, or of a much more precise spectroscopic redshift. Although these two techniques are detailed in the next Chapter 3, we shortly present them here:

- *Photometry* is the measurement of the magnitude of an astronomical object in multiple pass-band filters. Because of the Hubble flow due to cosmological expansion, objects situated at a cosmological distance from an observer appear redder (see Section 1.1.4). As a result, assuming the spectral distribution of an object given its type (galaxy, quasar, etc.), the typical spectral energy distribution of more distant objects appears redshifted. We can use this to determine the cosmological distance of the object.
- *Spectroscopy* is the measurement of the spectrum (or a segment of the spectrum) of an astronomical object, notably to detect spectral lines, i.e. an excess or a default in the spectrum due to the abundance of a chemical element. The wavelength of the spectral lines being bounded to an element, the wavelength of the lines is known at emission. The comparison with the wavelength of the same lines at reception yields the cosmological redshift. This allows for a finer measurement of the redshift, as spectral lines are very narrow in wavelength.

Given the distance between pass-band filters is much larger than the spectral resolution, photometric redshifts have much larger random errors. Spectroscopy also does not require to make strong predictions on the object spectral distribution, thus presenting smaller systematic errors. However, photometric redshift measurements retain a major advantage, as they can be performed using a few pass-bands, which is much less observational time consuming than spectroscopic surveys. With large sky surveys such as *HST*, detecting a large number of faint, distant objects, both types of redshift measurements have a role to play: photometry as a statistically significant but less precise measurement, and spectroscopy as more precise albeit time consuming. As a result, precise, spectroscopic information about the multiply-lensed images allows to set the most stringent constrains on the lens model.

Fluxes

The lensing magnification also yields different magnitude fluxes for different images of a same system (see e.g. Figure 2.3). Because they depend on the geometry (position of the source and the lens), the use of various fluxes to optimise the reconstruction must be conducted in conjunction with the multiple image geometry analysis. In the mass modelling, the former characterise the magnitude of the amplification matrix $\mathcal{A}$ to be inverted, whilst the latter characterise its geometry. It may also be difficult to estimate precisely the diffuse source flux and to decorrelate it from the lens'. As a result, this is mostly used for sources whose luminosity can be efficiently determined, such as quasars or supernovae (and in particular of the type Ia, as they act as standard candles).

2.2.2 A few lensing observables profiles

Using the definitions of the convergence and shear (respectively equations 2.34 and 2.46), we can calculate these observables for dark matter or total matter density profiles.

Navarro-Frenk-White (NFW)

We use here the definition of the surface density in a NFW distribution (see equation 1.56), and define $x \equiv R/r_S$:

$$\begin{aligned} \kappa(R) &= \frac{\rho_S r_S}{\Sigma_{\rm cr}} A(x), \\ \gamma(R) &= \frac{\rho_S r_S}{\Sigma_{\rm cr}} B(x), \end{aligned} \tag{2.57}$$

where A and B and defined by parts, for $x > 0$:

$$A(x) = \begin{cases} \frac{2}{x^2-1}\left[1 - \frac{2}{\sqrt{1-x^2}} \arctan\sqrt{\frac{1-x}{1+x}}\right], \\ \frac{2}{3}, \\ \frac{2}{x^2-1}\left[1 - \frac{2}{\sqrt{x^2-1}} \arctan\sqrt{\frac{x-1}{1+x}}\right], \end{cases} \quad ; \quad B(x) = \begin{cases} b(x) & \text{if } x < 1, \\ \frac{10}{3} - 4\ln 2 & \text{if } x = 1, \\ b(x) & \text{if } x > 1, \end{cases} \tag{2.58}$$

$$b(x) = 4\left(\frac{2}{x^2} + \frac{1}{x^2-1}\right)|1-x^2|^{-1/2} \arctan\sqrt{\frac{|1-x|}{1+x}} + \frac{4}{x^2}\ln\left(\frac{x}{2}\right) - \frac{2}{x^2-1}.$$

These expressions were derived in e.g. Golse and Kneib (2002).

Dual Pseudo-Isothermal Elliptical Matter Distribution (dPIE)

We use here the definition of the surface density in a dPIE distribution (see equation 1.70):

$$\begin{aligned} \kappa(R) &= \frac{\Sigma_0}{\Sigma_{\rm cr}}\left[\left(R^2+a^2\right)^{-1/2} - \left(R^2+s^2\right)^{-1/2}\right], \\ \gamma(R) &= \frac{\Sigma_0}{\Sigma_{\rm cr}}\frac{as}{s-a}\times \\ &\quad \left\{2\left[\left(a+\sqrt{R^2+a^2}\right)^{-1} - \left(s+\sqrt{R^2+s^2}\right)^{-1}\right] + \left[\left(R^2+a^2\right)^{-1/2} - \left(R^2+s^2\right)^{-1/2}\right]\right\}. \end{aligned} \tag{2.59}$$

2.2.3 Lensing software

In order to model the potential of the lens, two families of strong lensing software have been created:

1. *Free-form* models, in which the potential is tessellated on a grid, allowing for the local density in a grid bin to vary[7];
2. *Parametric* models, which assume a certain type of density distribution in the lens (NFW, dPIE, etc.), and optimise a given number of parameters.

Meneghetti et al. (2017) provide with a thorough comparison between various software in the context of the *Hubble* Frontier Fields observation campaign. They submit them to the challenge of reconstructing the lens model of two simulated clusters *Ares* and *Hera* (mimicking the observational properties of the HFF clusters) using cluster simulated images only. Looking at the performance of the ten groups who took part to this collaboration, Meneghetti et al. (2017) notably conclude that:

[7]They can also be called 'non-parametric', but this is not strictly true as the size of the grid, its resolution, etc. are parameters. Coe et al. (2010) call them 'non-light-traces-mass' (non-LTM), as they need not to make hypotheses over the mass distribution *a priori* using the lens luminous counterpart.

- Free-form and parametric methods perform equally well at measuring the convergence and mass profiles.
- Parametric methods generally capture better the two-dimensional properties of the lens cores (shape, local values of the convergence and of the magnification).
- The determination of the mass enclosed within the Einstein radius (or any other radius characteristic of the strong lensing constrains) was extremely robust for all methods.
- The largest uncertainties in the lens models are found near substructures (here cluster galaxies) and around the cluster critical lines. Some parametric models allow to constrain the substructure mass with $\sim 10\%$ error.
- Parametric models appear to generally better model *Ares*, the purely parametric simulated cluster. For the more realistic *Hera* simulation, the gap in quality between parametric and free-form models models is reduced.
- Several groups use similar software, and yet, despite using the same data, they obtain different reconstructions. This outlines the modeller's intervention and the importance of the priors used in different models, even with a same software.

Let us moreover note that, in both simulated clusters, the cluster galaxies were good tracers of the mass distributions, which may hide possible weaknesses in the parametric methods. Indeed, in the case of a disturbed distribution where galaxies would not be at the centre of their dark matter halo, we would expect parametric models, which require priors, to be at a disadvantage.

Free-form software

The main advantage of free-form models is to avoid assuming a mass profile *a priori*. They are notably used to constrain mass distribution with weak lensing constraints, but can be adapted to strong lensing if enough constraints are available (see e.g. Diego et al., 2018). Indeed, this type of models divides the field into a mesh, where the lensing observables are mapped, and which is then transformed into a pixelated mass distribution. As a result, because it does not set strong priors on the density distribution, a weak number of constraints could easily lead to over-fitting, where too many degrees of freedom allow for a non-physical distribution. The other possible downside to these models is 'dissection' of the lens information in the grid. Localised constraints may constrain extremely well the potential in the corresponding regions of the observed field, but not in others, irrespective of the distance to the centre for instance. Regardless, *a posteriori* regularisations are possible. Here is a short, non-exhaustive summary of these techniques:

- PixeLens, presented in Saha and Williams (1997) and Williams and Saha (2004), describes the mass density directly. Priors may be imposed on the convergence map (non-negative, smooth), on the symmetry of the lens, on the lens ellipticity, on the radial density profile slope, and on the external shear.
- SWUnited (Bartelmann et al., 1996) was for weak lensing only, and extended in Bradač et al. (2004, 2009) to include SL (using multiply-imaged systems). It uses an adaptive grid, optimised and refined at each iteration. It does not require any potential assumption (such as light-traces-mass , i.e. a massive component is to be associated to a luminous counterpart), and performs an optimisation in the source plane, i.e. searches for the best source positions to produce a system of multiple images, but also over the WL ellipticities.

- WSLAP+ (Diego et al., 2005, 2007; Sendra et al., 2014) describes the mass density directly, or alternatively indirectly using the lensing potential. This means that each bin of a large-scale grid corresponds to a given mass. Two mass components intervene: that of the red-sequence galaxies, whose mass is determined using the mass-to-light ratio, $\Upsilon = M/L$, modulated with a correction factor; and a diffuse component modelled through a Gaussian superposition on the grid. The optimisation then occurs in the source plane, i.e. each iteration tries a source position to describe a multiply-imaged system. It is not an entirely free-form model, as it assumes some light tracing mass through the galaxy distribution, and is sometimes referred to as *hybrid*.
- Grale, described and showcased in Liesenborgs et al. (2006, 2007), Mohammed et al. (2016), Liesenborgs et al. (2020), and Ghosh et al. (2021), does not make the LTM assumption, nor does it require to assume a lens plane mass distribution *a priori*. Instead, it lets the mass distribution free to be optimised on a grid with a number of basis functions. The type, number and position of these basis functions are fixed as model parameters, and the optimisation occurs on the weight of the functions. Liesenborgs et al. (2020) for instance use projected Plummer density models as basis functions. As Grale uses an adaptive grid, i.e. the binning evolves with the precision required, the densest regions are more precisely refined. The inversion of the amplification matrix $\mathcal{A}$ is performed following a genetic algorithm (for a description of such algorithms, see e.g. Eiben and Smith, 2013), allowing to let the parameter space evolve following multiple objectives (e.g. to invert the amplification matrix, predicting the position of a source from the lens model which would both reproduce the observed multiple images, and not produce more than observed).
- LensPerfect (Coe et al., 2008, 2010) is a non-LTM method, which uses inversion to model the images by exploring curl-free interpolations (i.e. a method to interpolate scattered data points, see Fuselier, 2008) of the deflection field, and the Kaiser and Squires (1993) weak lensing inversion method to constrain the distortion of images.
- SaWLens (Cacciato et al., 2006; Merten et al., 2009) primarily estimates the lensing potential using weak lensing. It optimises lens models in order to optimise the shear. Moreover, it improves the constraints with strong lensing multiple images where possible, approximating the location of the critical curves.
- `Lenstool` was first developed as a SL, parametric software, but this was combined with a free-form approach in Jullo and Kneib (2009), and later made compatible with weak lensing in Jauzac et al. (2012). It is only recently that Niemiec et al. (2020) made the joint strong and weak lensing optimisation possible in `hybrid-Lenstool`, combining both parametric and free-form methods. This allows for an optimal multi-scale approach. Whichever the method utilised, cluster galaxies are always described by parametric mass models, whereas the smoother, large-scale mass distribution can be either modelled non-parametrically or with specific profiles.

Parametric software

Parametric lens software assume a potential distribution to start with. They can optimise these distributions' parameters, and not only the 'density' ones, but also the geometry (position, ellipticity) of the mass distribution under certain circumstances. We shortly, inexhaustively present them:

- `LTM`, for *Light-Traces-Mass* was presented in Zitrin et al. (2012, 2013). It allows to quickly get a cluster lens model, as it assumes mass (including DM) to be located where a luminous counterpart appears. This highly predictive software uses a minimal number of free parameters: an exponent to the mass-to-light ratio power-law for the whole cluster galaxy catalogue, a Gaussian kernel degree to smooth with splines the galaxy component in order to describe the DM distribution on large scales, a ratio between the galaxy and DM halo masses, and a global lens model normalisation to a redshift or multiply-images system. Some additional parameters can be added, e.g. the BCG light-to-mass ratio scaling, ellipticity, core radius or external shear. The optimisation uses a χ^2 criterion with a Metropolis-Hastings MCMC (Markhov Chain Monte-Carlo) algorithm, comparing multiply-imaged systems to their predictions in the image plane. Its downside is a lower precision than other software because of less flexibility, due to fewer free parameters.
- `PIEMDeNFW` (Zitrin et al., 2015) is an extension of `LTM`, albeit fully parametric. It allows for more flexibility, lacking in `LTM`, and improved fits through a semi-independent method, modelling the DM halo independently from the light component. As it lends itself to a comparison with `LTM`, Meneghetti et al. (2017) find that the flexibility comes at a cost, `PIEMDeNFW` yielding a lesser predictive power for multiple images, and physical results less reliable. This is due to the introduction of a large number of free parameters to model subhalos in complex structures, without justification that these are fundamental parameters.
- `Glafic` (Oguri, 2010) assumes each galaxy member to be modelled with a projected pseudo-Jaffe profile, and its velocity dispersion and truncation radius parameters follow the Faber-Jackson relationship for the former, $\sigma \propto L^{1/4}$, and a power-law for the latter, $s \propto L^{\eta}$. The geometric parameters are fixed through photometric data analysis. `Glafic` can either perform the multiple images optimisation in the image or in the source plane, using different optimisation methods such as the downhill simplex one (i.e., for a parameter space of dimension N, the iterative reduction of a $N+1$ dimensional polytrope, which ends up describing the final constraints), or through a MCMC. It can also take flux ratios, time delays, external shear and higher order perturbations into account for lens modelling. It is however limited when multiple lens modelling is required, i.e. to take into account the effect of several lenses on the same line-of-sight at different redshifts.
- `Lenstool` (Kneib et al., 1996; Jullo et al., 2007) can work both as a parametric or free-form software, and can even run in hybrid mode (see previous paragraph). In the parametric mode, similarly to `Glafic`, it uses a galaxy catalogue of detected geometric positions through photometry. Classically, their luminosities are all related to one another using the Faber-Jackson profile, however it is possible to let its indices vary. Moreover, any cluster member can be taken out of this catalogue to be modelled independently, if for instance they are close to a multiple image and the Faber-Jackson optimisation yields limited results. Although a large number of profiles are available, dPIE are the most commonly used. Then, each galaxy is associated to a core assumed to be baryonic and a small dark matter clump, more diffuse. On top of the luminous component, a dark matter halo (or more if motivated) are added and optimised in addition to cluster galaxies. It presents a number of degeneracies (most notably that between the cored and cluster-size components, see Section 2.2.4), relatively well understood (Limousin et al., 2016). Several algorithms using MCMC methods (`BayesSys` introduced in Jullo et al. 2007, which may be used in different manners[8] and the Python

[8] https://projets.lam.fr/projects/lenstool/wiki/RunMode#inverse-int1-float1-float2

`emcee`) allow to perform the multiple images optimisation in the image or the source plane. Errors are propagated using a Bayesian approach.

2.2.4 Lens modelling with Lenstool

All lens models in this thesis were obtained using `Lenstool`[9], in its parametric mode. We systematically used dPIE profiles, because they present a flat core profile and are parametric. Binney and Tremaine (1987) and Elíasdóttir et al. (2007) provide the relationship bounding the velocity dispersion to the galaxy density in general:

$$\sigma^2(r) = \frac{G}{\rho(r)} \int_r^\infty \mathrm{d}x \frac{M_{3\mathrm{D}}(x)\rho(x)}{x^2}. \tag{2.60}$$

One can derive the relationship between the dPIE velocity dispersion σ_0, and the normalised density ρ_0 (Limousin et al., 2005):

$$\rho_0 = \frac{\sigma_0^2}{2\pi G} \frac{a+s}{a^2 s}. \tag{2.61}$$

However, in `Lenstool`, the σ parameter really is the line-of-sight velocity dispersion, and thus writes $\sigma = \sqrt{2/3}\sigma_0$, as detailed in Bergamini et al. (2019, Appendix C).

Galaxy catalogue

Multi-band photometric data, introduced in Section 2.2.1, was used for two main purposes: on the one hand, it allowed to detect multiple images systems ; on the other hand, this yielded the geometric and flux information necessary to establish the cluster member galaxies catalogue. The position parameters (distance to the cluster centre, ellipticity, rotation angle) of all galaxies, unless mentioned otherwise, is then fixed. We always utilised the Faber-Jackson relationship (equation 1.51) to establish the dPIE profile parameters, fixing the reference core radius to an arbitrary small value. Let us notice one can use an extended version, for each individual galaxy (see e.g. Jullo et al., 2007):

$$\begin{aligned} \sigma_0 &= \sigma_0^\star \left(\frac{L}{L^\star}\right)^{1/\sigma_{\mathrm{slope}}}, \\ a_0 &= a_0^\star \left(\frac{L}{L^\star}\right)^{1/2}, \\ s_0 &= s_0^\star \left(\frac{L}{L^\star}\right)^{2/s_{\mathrm{slope}}}, \end{aligned} \tag{2.62}$$

where the starred values $\sigma_0^\star$, $a_0^\star$ and $s_0^\star$ are the pivot Faber-Jackson optimised values, $L^\star$ is the typical luminosity of an elliptical galaxy at the redshift of the cluster. In this thesis, we constantly assume $\sigma_{\mathrm{slope}} = 4$, and $s_{\mathrm{slope}} = 4$, and fix $a_0^\star$ to an arbitrary small value. This way, only two dPIE parameters have to be constrained for the whole catalogue mass to be derived. Leauthaud et al. (2011) for instance offer a different technique, using the stellar-to-halo mass relation to directly extract the stellar mass from that of the halo.

[9] https://projets.lam.fr/projects/lenstool/wiki

Dark matter halo

In addition, cluster models systematically add a dPIE cluster-scale halo – which we refer to as the dark matter halo (DMH), mostly representing the dark matter potential, but also the intra-cluster medium (ICM) to a much lesser extent[10]. The velocity dispersion σ of these DMH typically range around 10^3 km.s^{-1}, and the cut radius s of the DMH fixed to an arbitrary large value, taken to be much higher than the Einstein radius, and thus it has very little influence on the strong lensing (see e.g. Elíasdóttir et al., 2007). In the modelling, gravitation is matter-agnostic, i.e. only probes mass, irrespective of its nature. Therefore, even if one assumes dPIE to model both a baryonic core and a larger dark matter clump, only the total density of matter ρ_m is constrained.

Multiple images catalogue

When available, spectroscopy is a very powerful tool to detect multiply-imaged systems, and to determine precisely their redshifts. The redshift of the lens may also be observed through spectroscopy. To these detections, one may add multiple images detected only through imaging data. If their redshifts are unknown, these may be treated as free parameters. These additional multiple images assist in constraining lens models, but to a lesser extent than spectroscopic detections.

Incremental model construction

In the models established, one can follow an incremental approach. First, the model is composed of the DMH dPIE and the cluster galaxies catalogue. The DMH parameters (geometry, core radius a, velocity dispersion σ) are let free to vary, with an ellipticity constrained to $\mathcal{E} < 0.7$ (to keep to physical values for relaxed clusters, as shown in Despali et al., 2017), a velocity dispersion typically of the order of 10^3 km.s^{-1}, and a cut radius of the DMH fixed to an arbitrary large value $s \gg a$ in general. This value is taken to be much higher than the Einstein radius, and thus has very little influence on the strong lensing. Given this parameter vector, the lens model optimisation is conducted a first time. For precision, all optimisations are inverting the lens equation, i.e. they are performed in the lens plane.

Second, in order to take into account the influence of dominant galaxies, these may be detached from the cluster galaxies catalogue, i.e. their potential is not being tied to the Faber-Jackson relationship anymore. For example, the brightest cluster galaxy (BCG) is so luminous that it dominates at the same time the galaxy catalogue optimisation and the total mass it yields. Moreover, the BCG can present unique features due to its higher mass, but also its position in the centre, meaning it progressively clustered a number of smaller galaxies, which may be older (and thus more metal-rich). This can lead to a mass-to-light ratio different from the other, main red sequence galaxies. However, the BCG geometric parameters are still useful, and in a 'light traces mass' assumption, one can fix these parameters. Sometimes, they may be left free to vary, as the dark matter clump associated to the BCG may have a geometry different from the BCG itself. Let us however notice this BCG optimisation is often degenerated with the DMH one. In other words, for a central BCG, this means the core radius and velocity dispersion of the DMH are in competition in the optimisation with the cut radius and velocity dispersion of the BCG to describe the central density. Several observables may allow to minimise this degeneracy, such as a high number of constraints by multiply-imaged systems at various radii in the cluster. For instance,

[10]Dynamically relaxed clusters are modelled with one DMH, however merging clusters often require more than one DMH to explain the lensing potential (such as e.g. MACS J0416.1-2403, see Jauzac et al., 2015).

Limousin et al. (2008) present a large number of radial arcs in relaxed cluster Abell 1703, coupled to a central lensed ring in the vicinity of the centre of the cluster. These unique features allow the authors to stringently constrain the central density of the cluster, and thus to disentangle the BCG from the DMH parameters. One may also use the emission or the lack of emission in X-rays to constrain the baryonic density (represented *a priori* in a dPIE profile by the core region, e.g. in Limousin et al., 2022). Using the 'light-traces-mass' hypothesis for the DMH may also alleviate some nonphysically large cut radii or velocity dispersions optimisations for the BCG. Newman et al. (2009) combine three probes of the mass distribution in order to lift the degeneracy: stellar velocity-dispersion measures in the BCG, strong and weak lensing, which allows to break the degeneracy. Additionally, other galaxies of high mass or strategic position (close to multiple images) can be optimised individually too. For instance, in MACS J0416.1-2403, a galaxy re-lenses a multiple image yielded by the cluster-size lens, producing more multiple images (Vanzella et al., 2017). At last, if a foreground or background galaxy happens to be in the field, and to be important to lensing, it must be included in the lens model, and optimised independently. In order to avoid the `Lenstool` limitations for multi-plane lensing, one can project the object's lensing potential in the lens plane.

If important deformations of the images appear on the field, one can add an external shear field, accounting for neighbouring lenses and cosmic shear. It is characterised by its normalisation and rotation angle. This may improve the theoretical quality of the model, reducing the error between observations and the predicted images. Although there can be well-motivated physical reasons to justify such a field, in most cases these fields simply reduce the error in the model prediction by encapsulating lensing effects in an nonphysical field, which should instead be described through the complexity of the lens model (Etherington et al., 2023). The use of such fields may therefore degrade the measurement of parameters interpreted as physical, and we avoided them in this thesis.

Analysing a model

The χ^2 value optimised by `Lenstool` for a parameter vector Θ is the sum of the distances between predicted and observed multiple images[11]:

$$\chi^2(\Theta) = \sum_{j=1}^{N_{\text{source}}} \sum_{i=1}^{N_{\text{im}}^j} \left(\frac{\left| \boldsymbol{x}_{i,j}^{\text{pred}}(\Theta) - \boldsymbol{x}_{i,j}^{\text{obs}}(\Theta) \right|}{\Delta x_{i,j}} \right)^2 , \tag{2.63}$$

where $\boldsymbol{x}$ is the position on the sky, i the multiple image index, j the index of the system (i.e. number of source), and $\Delta x_{i,j}$ the positional uncertainty of the image. The final goodness of fit is given in a unit more physically meaningful than the χ^2: we take the root-mean-square angular separation on the sky between the observed multiple images and their predicted counterparts:

$$rms = \left(\frac{1}{N_{\text{im}}^{\text{Tot}}} \sum_{i=1}^{N_{\text{im}}^{\text{Tot}}} \left| \boldsymbol{x}_i^{\text{pred}} - \boldsymbol{x}_i^{\text{obs}} \right|^2 \right)^{1/2} . \tag{2.64}$$

Once the incremental tests of the model have reached the best rms value possible using realistic values for the parameter vector, we retain this best-fit model. Once a satisfactory model is produced, the photometric and spectroscopic data may be re-analysed to attempt to find the brightest multiple images predicted by `Lenstool`. In order to reconstruct the critical and caustic

[11] This is simply a reformulation of equation (2.56).

lines, one can use the MARCHINGSQUARE algorithm of Lenstool, described in Jullo et al. (2007, Appendix A). Comparing the predicted position of these lines to the position and configuration of the multiply-lensed images constitutes an additional verification of the quality of the best-fit model.

2.2.5 Clusters as thin lenses

Gravitational lenses, such as galaxy clusters described in this thesis, are triaxial objects. Therefore, beyond their assumed elliptical shape, one must take into account the depth of the cluster when describing them, i.e. rescaling the 3D radius to the centre:

$$r = \sqrt{\left(\frac{x}{a}\right)^2 + \left(\frac{y}{b}\right)^2 + \left(\frac{z}{c}\right)^2}, \tag{2.65}$$

where a, b and c are the semi-major axis, semi-minor axis and 'semi-depth' respectively. We here leave aside the rotation angle between the sky plane and ellipsoidal description of clusters, i.e. we describe the clusters' projection on the sky plane. However, in strong gravitational lensing and under the Born approximation, the lens is considered to be thin, and thus the lensing observables do not constrain this parameter, as the convergence κ is computed to get the deflection potential and the deflection angle. As these are on-sky observables, no assumption or prediction on c can be made. From now on, for all lensing purposes, we consider the depth and the rotation angle between the plane of the sky and the line-of-sight to be redundant parameters, and a and b are given as the projected semi-major and semi-minor axes observed on the sky.

Chapter 3

Constraining the mass distribution with strong gravitational lensing

Night Thoughts

Stars, you are unfortunate, I pity you,
Beautiful as you are, shining in your glory,
Who guide seafaring men through stress and peril
And have no recompense from gods or mortals,
Love you do not, nor do you know what love is.
Hours that are aeons urgently conducting
Your figures in a dance through the vast heaven,
What journey have you ended in this moment,
Since lingering in the arms of my beloved
I lost all memory of you and midnight.

— Johann Wolfgang von Goethe

3.1 Introduction

The knowledge of the distribution of mass in galaxy clusters allows to probe a number of critical problems of astrophysics, and notably the physical nature of dark matter, as detailed in Section 1.2.1. With strong gravitational lensing (SL), we are able to set stringent constraints on the density distribution of the lens. All the theoretical tools required to understand SL and its modelling with `Lenstool` were introduced in the two previous Chapters. In this Chapter, I showcase how we can get a lens potential reconstruction of good quality combining imaging data and spectroscopy, and adding X-rays for a comparison. Such a combination of *Hubble Space Telescope* (*HST*) and the Multi-Unit Spectroscopic Explorer at the Very Large Telescope data (VLT/MUSE, see Bacon et al., 2014) has already been exhibited in Treu et al. (2016), Lagattuta et al. (2017, 2019), Jauzac et al. (2016a, 2019, 2021), Grillo et al. (2016), Mahler et al. (2018), and Caminha et al. (2019). The same type of analysis was performed by Mahler et al. (2022), Caminha et al. (2022), and Golubchik et al. (2022), using the *James Webb Space Telescope* (*JWST*) public release on galaxy cluster SMACS J0723.3-7327, combined to other imaging (*HST*, from the RELICS survey), spectroscopic (VLT/MUSE), and X-ray (*Chandra*) data.

To perform a similar analysis, I collected data on two galaxy clusters, MACS J0242.5-2132 and MACS J0949.8+1708 (i.e. RXC J0949.8+1707), hereafter MACS J0242 and MACS J0949 respectively, initially discovered by the MAssive Cluster Survey (MACS, PI: Ebeling, Ebeling et al., 2001). The imaging data I exploited are composed of multiple *HST* pass-bands for both clusters, as well as three pass-bands from the Dark Energy Survey (DES) for cluster MACS J0242. These were complemented by VLT/MUSE spectroscopy, for cluster member galaxies and multiply-lensed images redshift identification. At last, the *XMM-Newton* X-ray satellite observations were used to compare the lens model density to that measured using the Intra-Cluster Medium (ICM).

We introduce hereafter the techniques used to extract the cluster member galaxies catalogue and the multiply-lensed images catalogue, using photometric and spectroscopic methods. We moreover discuss how the stellar mass of clusters may be measured. We present the results of our spectroscopic, photometric and lens model analyses in our article submission thereafter Section 3.4.

3.2 Spectroscopy

3.2.1 Overview

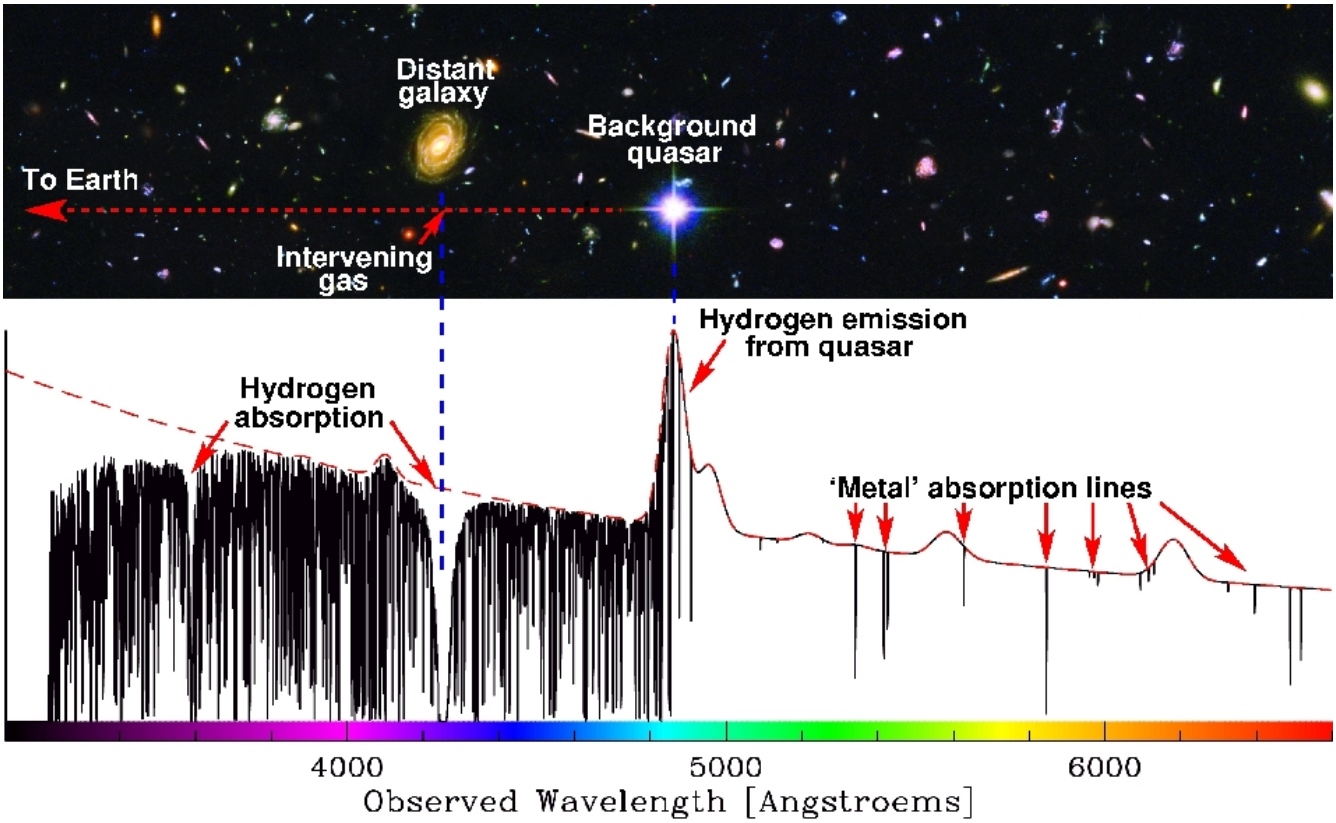

Figure 3.1: As light from distant quasars is absorbed by the neutral hydrogen on the line-of-sight, their light is absorbed, producing characteristic absorption features in the spectra of quasars: the Lyman-α forest. These are located at emission at wavelengths $\lambda < 121.6\,\mathrm{nm}$, but for a redshift $z \sim 3$, the hydrogen emission peak emitted by the quasar is detected at $\sim 490\,\mathrm{nm}$. Credits: Michael Murphy.

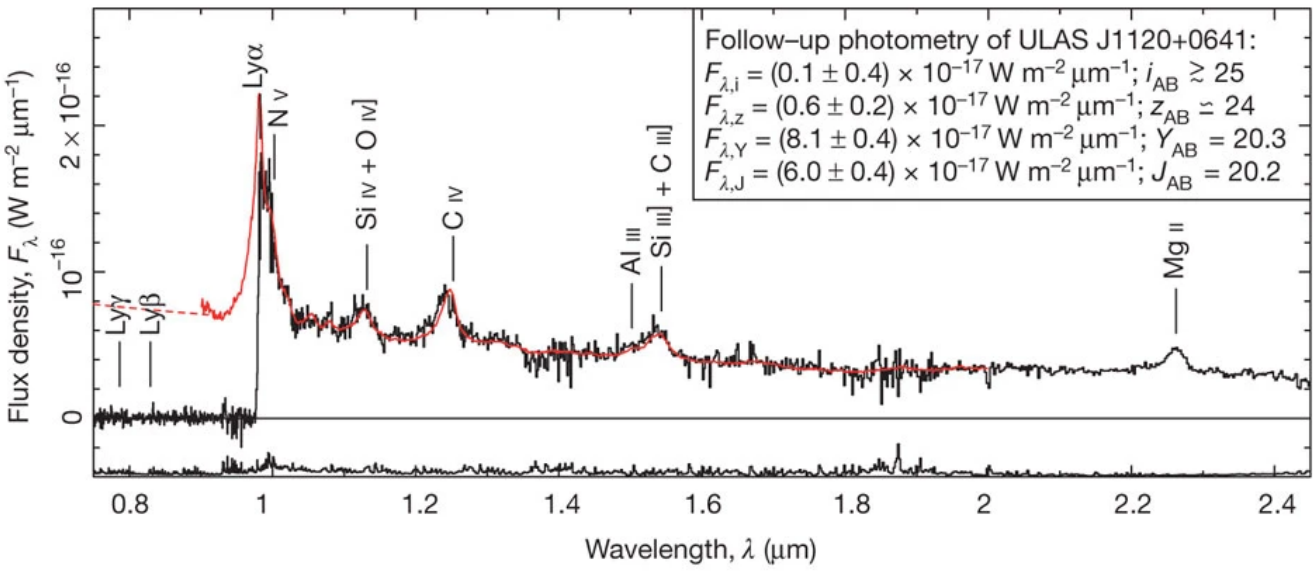

Figure 3.2: As light from distant quasars travels to the observer from a cosmological distance, the Hubble flow redshifts the luminous wave packets. As a consequence, identifying specific emission or absorption features detected from a template allows to measure the *spectroscopic* redshift with great precision. Credits: Mortlock et al. (2011).

The fundamental idea of spectroscopy was shortly introduced in Section 2.2.1: luminous sources such as cluster galaxies or quasars present a typical spectrum shape. These notably present emission lines for some specific metal transitions, such as the double [OII] peak, and the notable Lyman-α break, of characteristic shape (peak and break). It is emitted when an excited electron in a hydrogen atom transitions from orbital $n = 2$ to the ground state $n = 1$. Because hydrogen constitutes most of the baryons, this transition may be very bright – and thus particularly noticeable. We present a sketch of the effect of the hydrogen emission in quasars in Figure 3.1, and an example of quasar spectrum in Figure 3.2, where the red curve is the characteristic quasar spectrum template, and the black curve the observed spectrum of quasar ULAS J1120+0641. The emitted typical spectrum is redshifted as the wave packets of light travel through an expanding Universe. Therefore, fitting the observed spectrum to a redshifted source template spectrum allows to detect precisely the spectroscopic redshift of the source.

Other spectral rays can be measured, such as those of carbon and silicon. However, there is a 'redshift desert' between the strong spectroscopic features of [OII] and the Lyman break, corresponding to redshifts of $1.4 \lesssim z \lesssim 2.5$ with ground-base imaging (see e.g. Steidel et al., 2005; Renzini and Daddi, 2009). This is due to the atmosphere's almost total opacity to infra-red and ultra-violet light. Critically, this prevents from fully observing the 'Cosmic Noon', i.e. the time when star formation rate, active galactic nuclei activity, galaxy growth, mass assembly and morphological differentiation all culminated, at redshift $2 \lesssim z \lesssim 3$. Although this can be lifted with spatial spectroscopic surveys, or using a range of techniques (such as optical photometric selection and highly efficient UV spectroscopy, see Steidel et al., 2005), this still hinders ground-based surveys, which choose the more efficient optical window of wavelengths. MUSE[1] is notably in this case, as $1' \times 1'$ field of view samples the spectral window $465 - 930$ nm, corresponding to

[1] https://www.eso.org/sci/facilities/develop/instruments/muse.html

Lyman-α spectroscopic redshifts $2.9 \lesssim z \lesssim 6.65$.

Let us moreover note that ground-based detectors must take into account the spectral lines of the atmosphere. This can overshade a number of spectral slices, especially in the redder optical colours. Hanuschik (2003) describe this phenomenon in details, and Streicher et al. (2011) provide the values of these lines for VLT/MUSE.

3.2.2 Spectroscopy and gravitational lensing

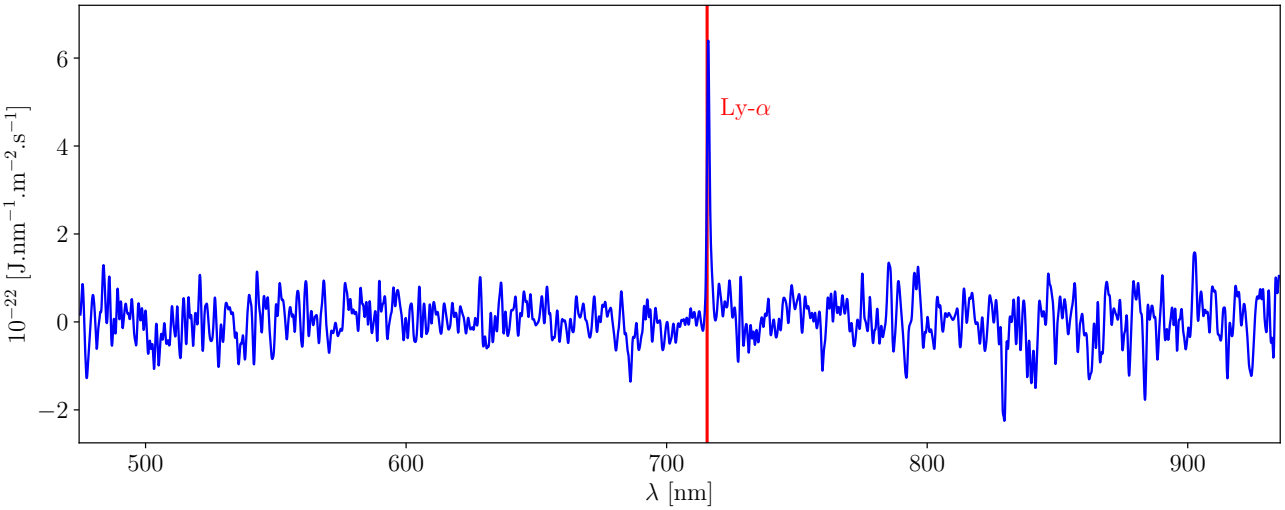

Figure 3.3: VLT/MUSE Lyman-α detection in cluster MACS J0949, of image 1.1 of a multiply-lensed quasar (see Section 3.4, position $(\alpha, \delta) = (147.4683753, 17.11409360)$ deg). The resulting spectroscopic redshift is $z_{1.1} = 4.8888$.

In the context of gravitational lensing, spectroscopic detections are crucial to identify cluster member galaxies, and to unambiguously discriminate galaxies in the field as being members of the lensing cluster – and thus exerting a weight, or a possible line-of-sight effect. Even more importantly, it allows to detect the redshift of multiply-imaged sources, to confirm multiple images share the same emitter, but also to use the source redshift as a powerful constraint of the lensing mass model.

In our analysis of both lensing cluster MACS J0242 and MACS J0949, we have used VLT/MUSE spectroscopic observations, centred on the cluster field of view (more details on the observations can be found Section 3.4). In order to process the data of the 3681 spectral bands of MUSE, we resorted to a suite of computational methods. The bright galaxies in the field were subtracted from the field using the MUSE Line Emission Tracker[2] (`MUSELET`, a package of the Muse Python Data Analysis Framework – `MPDAF`, see Bacon et al., 2016). This allows for an easier detection of dim sources, thus maximising the chances to detect multiply-lensed images (Piqueras et al., 2017).

We then could extract the spectrum out of regions of the MUSE datacube, and fit the emission and absorption lines known for various astronomical objects (stars, galaxies, quasars) to the spectral detections. To automate this spectroscopic image detection, we used `CatalogueBuilder` (see

[2] https://mpdaf.readthedocs.io/en/latest/muselet.html

Richard et al., 2021), a modified version of `MARZ` (see Hinton et al., 2016) adapted to the MUSE detections.

On Figure 3.3, we present the spectrum extracted for a region of cluster MACS J0949 from MUSE observations. We clearly identified the Lyman-α break, thus determining the quasar source spectroscopic redshift at $z = 4.8888$.

3.2.3 More applications of spectroscopy

More generally, spectroscopy notably allows to determine line-of-sight velocity dispersion of galaxies (Lagattuta et al., 2022), which is a much more reliable tool to scale the galaxy catalogue velocity dispersions than the Faber-Jackson relation (Faber and Jackson, 1976, detailed in Sections 1.3.2.3 and 2.2.4), based on luminosities, and which may contain contamination, exhibiting an important intrinsic scatter.

The Faber-Jackson relationship was moreover published at a time cosmologists used luminosity as a cornerstone parameter to describe the physics of clusters, and thus relates the velocity dispersion to the luminosity (Schaeffer et al., 1993). A fundamental plane (FP) relation, relating three observables in elliptical galaxies was later described in Dressler et al. (1987), Djorgovski and Davis (1987), Bender et al. (1992), and Schaeffer et al. (1993). This bidimensional relationship relates R_e the effective radius, i.e. the radius of the isophote containing half of the total luminosity, σ_0 the central stellar velocity dispersion, and $\langle S_e \rangle$ the average surface brightness within R_e:

$$\ln R_e = \alpha \ln \sigma_0 + \beta \langle S_e \rangle + \gamma, \tag{3.1}$$

where α, β, γ are parameters for a cluster of elliptical galaxies. This relationship is calibrated with a combination of photometry and spectroscopy, which offers the advantage of a lower scatter than the Faber-Jackson relationship, while being more general. In practice, the FP relation is simply a deprojection of the Faber-Jackson relationship onto the $\ln R_e$ axis. Granata et al. (2022) apply this technique to the strong lensing modelling of cluster Abell S1063, and find it to yield better results than the more classic Faber-Jackson, as they find that a more accurate estimate of the total mass of the cluster members allows for a reduction in the scatter on the determination of some parameters of the dark matter halo (DMH).

3.3 Photometry

3.3.1 Overview

As mentioned in the previous Section, astronomical objects present typical spectra associated to their physical nature. In the absence of spectroscopic information, i.e. of a decomposition of the spectrum into small wavelength bins ($\sim 0.1\,\mathrm{nm}$ for MUSE), one can use broadband filters (a few hundred nm wide, see Figure 3.4 for *HST* filters). As those capture a larger flux than a spectrograph band, they require a much smaller exposure time to acquire a neat image. The trade-off to this luminous efficiency is the reduction of the spectral precision by a factor ~ 1000. With multiple pass-band filters, one can therefore describe a spectrum at very low resolution: this is the Spectral Energy Distribution (SED, see Bolzonella et al., 2000)[3].

[3]Let us notice the SED is technically not a spectrum, as it is the energy as a function of the wavelength $E(\lambda)$, and not of the spectral density as a function of wavelength $f_\lambda(\lambda)$.

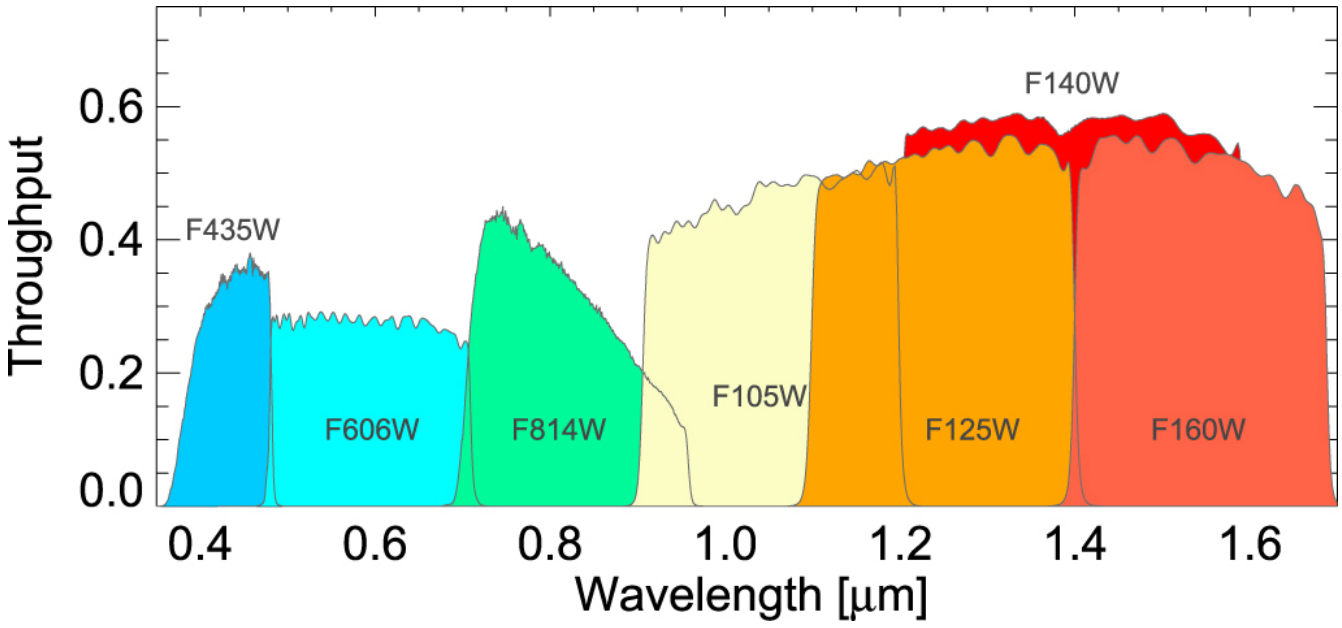

Figure 3.4: Throughput curves of the *HST*/ACS and WFC3 filters used for the HFF observations. Credits: Atek et al. (2015).

Baum (1962) was the first to use this technique, comparing the SED of elliptical galaxies in the Virgo cluster, and in the Abell 0801 cluster. He was able to measure the displacement between the two energy distributions, and, as the redshift of Virgo was known, that of the second cluster. This photometric redshift measurement allowed to set constraints on the distance to a handful of clusters, before spectroscopy overshadowed it with more precise measurements. In the era of large angular surveys however, the photometric measurement of the redshift gained back momentum, as it allowed to appoint a redshift to a vast number of objects not surveyed with spectrographs.

Let us note that the technique of Baum (1962) is not the only way to recover a photometric redshift. For example, using an empirical SED obtained on the Virgo cluster may be substituted by a theoretical model of stellar populations (such as that of Bruzual and Charlot, 2003), allowing to extend the model to spiral galaxies. Moreover, instead of using the SED, one may convert the expected spectra at a given redshift into colours, i.e. differences between magnitudes measured in different pass-bands. A diagram representing a distribution of one colour as a function of another colour can then be graphed (Koo, 1985). This method allows to define a region of the colour-colour plane where a given photometric redshift is permitted by the SED models. In other words, the redshift of photometric detections, when placed in this colour-colour diagram, could be constrained.

3.3.2 Imaging data and extraction

Even if spectroscopy is much more precise than photometry to determine the 3-dimensional position of galaxies, its imaging resolution is limited by the long exposure time required, and by the atmosphere. Moreover its field is also to $1'$ diameter, which represents ~ 300 kpc at the typical redshift of lensing clusters MACS J0242 and MACS J0949 ($z \in [0.3, 0.4]$). Consequently, we paired the spectroscopic MUSE observation to optical and near-IR imaging from *HST*[4] and the Dark

[4] https://hla.stsci.edu/

Energy Survey[5] (DES), whose field on the clusters is wider, and which allows for a more efficient extraction of geometric parameters (position, ellipticity, angle) of the emitters.

To this purpose, we used the `SExtractor` software (see Bertin and Arnouts, 1996) on the imaging data, yielding a catalogue of parameters for each pass-band, such as the position, the ellipiticity, the rotation angle, the Kron-like magnitude, etc. We only retained detections judged to be of sufficient quality, i.e. of sufficient signal-to-noise ratio, identified as a galaxy, and detected on all the bands of a same instrument.

3.3.3 Photometric selection

For a same instrument (e.g. the *HST* Advanced Camera for Surveys – ACS), we compared the colour between two pass-bands to the highest wavelength of the magnitudes constituting this same colour (for instance the colour $(m_{\mathrm{F606W}} - m_{\mathrm{F814W}})$ to the magnitude m_{F814W} as $606 < 814\,\mathrm{nm}$). In rich galaxy clusters[6], this colour-magnitude graph allows to identify clearly a main red colour sequence for galaxy clusters (see e.g. Gladders and Yee, 2000; Hao et al., 2009). This is due to a population of coeval, old, red and elliptical galaxies, formed at high redshifts. As these galaxies do not represent the total population of the cluster, but the most massive members, they are the most critical to characterise the (galaxy) lensing effect and the stellar mass, i.e. they are the galaxies which scale according to the Faber-Jackson relationship. We present an example of such a colour-magnitude diagram for instrument *HST*/ACS in cluster MACS J0949 in Figure 3.5, with the colour composed with bands F606W and F814W, $(m_{\mathrm{F606W}} - m_{\mathrm{F814W}})$, and the magnitude with band F814W, m_{F814W}.

In practice, we adjusted the red colour sequence with the spectroscopic detections. We only retained spectroscopic detections within the cluster redshift boundaries, and linearly fit the remaining spectroscopic detections[7]. This allows to fit the sequence, and define a selection box around it, in which the photometric detections are assumed to be elliptical galaxies, of photometric redshift compatible with that of the cluster.

We thus constitute all possible colour-magnitude diagrams, on all instruments. For an instrument with $N_b \geq 2$ pass-bands, we plot $\binom{N_b}{2}$ colour-magnitude diagrams. If a photometric detection is within the red colour sequence for all these diagrams, we consider it selected for an instrument. If it is selected for at least half the instruments, we consider it part of the final cluster members catalogue[8]. Ultimately, we keep all cluster member spectroscopic detections, and add to these all photometric detections selected after all these tests.

3.3.4 Stellar mass

Although the main focus of this thesis is the ICM and DM content of clusters, a few percents ($\lesssim 2\%$) of the clusters' mass resides in the baryons of galaxies. For short, we refer to it as the *stellar mass* $M_\star$ of clusters, although galaxies are also host to compact objects, dust, etc.

[5] https://www.legacysurvey.org/

[6] i.e. clusters populated by a large number of galaxies.

[7] As detailed in Section 3.4, we only kept the spectroscopic detections corresponding to photometric detections of sufficiently low magnitude. The magnitude cut-off depends on the instrument. This is performed as we are attempting to fit the red colour sequence, and other cluster member detections may be due to other types of galaxies.

[8] For clarity, if there were 3 instruments, we would require the detection to be identified on all colour-magnitude diagrams of at least two instruments.

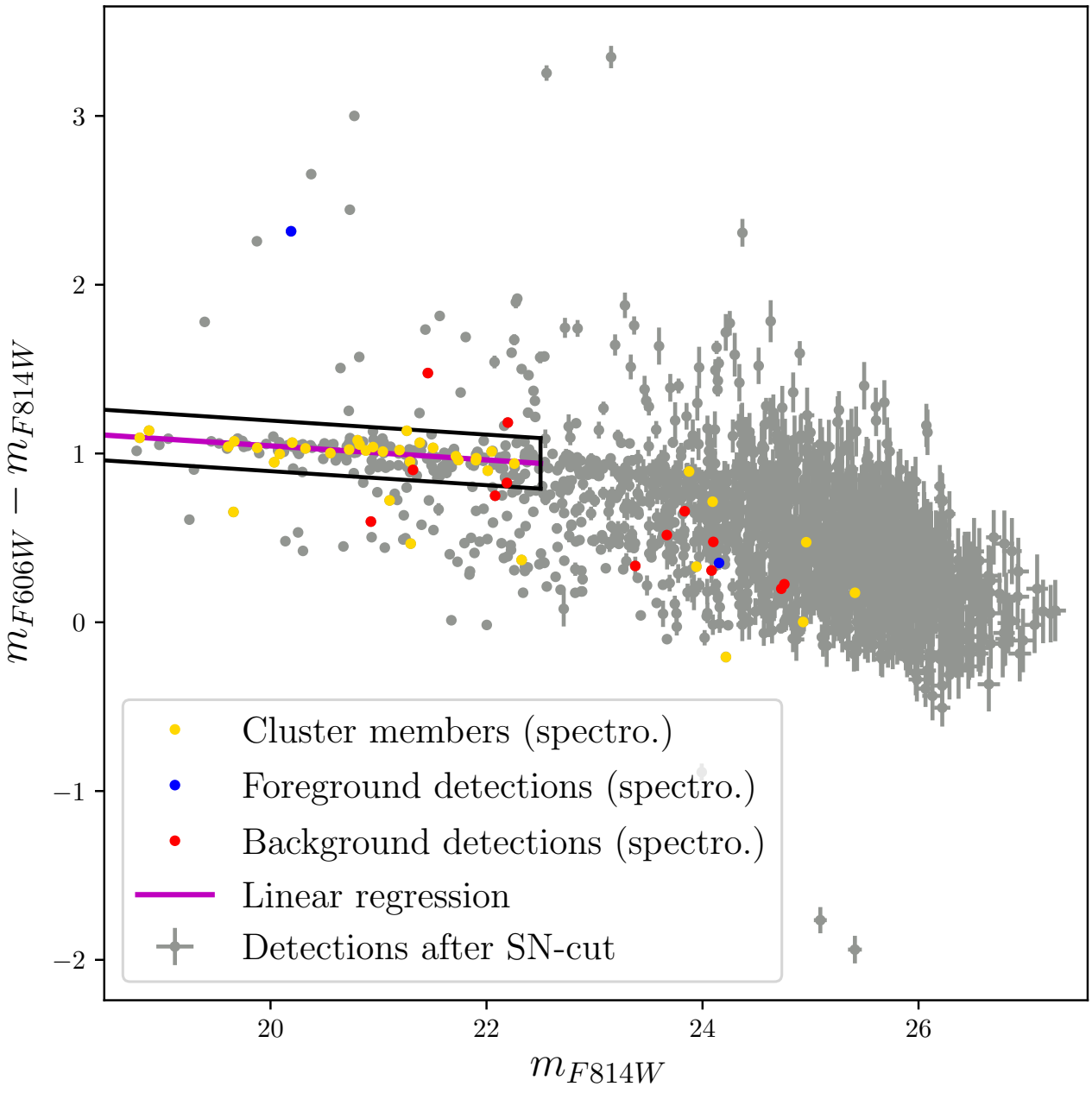

Figure 3.5: Colour-magnitude diagram of ($m_{\mathrm{F606W}} - m_{\mathrm{F814W}}$, colour) versus m_{F814W} (magnitude), for instrument *HST*/Advanced Camera for Surveys (ACS), for cluster MACS J0949. The magnitudes were extracted with `SExtractor`. *Grey:* All `SExtractor` galaxy detections of sufficient signal-to-noise ratio, appearing on both pass-bands F606W and F814W. *Gold:* Cluster member galaxies, identified with MUSE spectroscopy. *Blue:* Foreground detections, identified by MUSE. *Red:* Background detections, identified by MUSE. *Black lines:* Red-sequence cut. *Magenta line:* Red sequence linear fit. The grey and golden dots within the red sequence limits are selected red-sequence galaxies (see Section 3.4 for more details; these galaxies are pre-selected to compose the cluster member galaxies catalogue, alongside spectroscopic detections).

Using the SED

Using a SED modelling of multicolour photometric observations, it is possible to theoretically derive an average mass-to-light ratio $\Upsilon_\star \equiv M_\star/L$ for a given pass-band filter. Indeed, the stellar population's SED being known, assuming an stellar initial mass function and a theoretical stellar population model, the evolution of the cluster can be theoretically modelled. As a consequence, one can model the average star history in the cluster, both in mass and luminosity. Using scaling relationships to convert all magnitudes detected across various pass-bands into luminosities in a given pass-band, a simple multiplication $\Upsilon_\star \times L$ yields the desired stellar masses. This is showcased in Newman et al. (2013a,b), Grillo et al. (2015), and Annunziatella et al. (2017).

Using L_K luminosities

In this thesis however, we focused primarily on strong lensing, and the limited data to our disposal did not allow to perform a SED fit. Instead, we used the cluster member catalogues established though spectroscopy and photometry, using the magnitudes of an arbitrary pass-band filter. These luminosities were converted into K-band luminosities L_K[9]. We scaled the magnitudes to the K-band at the clusters' redshifts using relationships Hogg et al. (2002) and Lin et al. (2006). Then, we used all other available filters for the remaining detections, all calibrated with common detections.

Once this K-band luminosity catalogues created, we used a mass-to-light ratio $\Upsilon_\star \equiv M_\star/L$ relationship. We can find such relationships using photometric information at large scales, for disc galaxies (Schombert et al., 2019, 2022) and for red quiescent galaxies (e.g. López-Sanjuan et al., 2018, in the ALHAMBRA survey). In this thesis, we used the adapted Salpeter stellar initial mass function (see Salpeter, 1955), and the mass-to-light relationship for red quiescent galaxies derived by Arnouts et al. (2007) on the SWIRE-VVDS-CFHTLS surveys, based on the Bruzual and Charlot (2003) stellar population models, as they match better the type of clusters we investigated. With parameters $\{a, b\} = \{-0.18 \pm 0.04, +0.07 \pm 0.04\}$, this relationship writes:

$$\log_{10}\left[\frac{M_\star}{M_\odot}\frac{L_\odot}{L_K}\right] = az + b. \tag{3.2}$$

Our studied clusters MACS J0242.5-2132 and MACS J0949.8+1708 are at respective redshifts $z = 0.3131$ and $z = 0.3830$. The redshift range $0.3 < z < 0.4$, presents large uncertainties in the relationship presented in Arnouts et al. (2007, see Figure 9). However, Ilbert et al. (2010, Appendix D, Figure 28) provide a thorough analysis of a large redshift space including that of our clusters. It concludes that equation (3.2) overestimates the stellar mass by an average 0.2 dex for red sequence galaxies, but it is reasonably well calibrated for $z \in [0.3, 0.4]$. We thus used this relationship.

[9]To perform the conversion, we used the SVO website, to get the KPNO Flamingos Ks filter.

3.4 Article: Joint *HST*, VLT/MUSE and *XMM-Newton* observations to constrain the mass distribution of the two strong lensing galaxy clusters: MACS J0242.5-2132 & MACS J0949.8+1708

In order to constrain the density distribution in galaxy clusters through strong gravitational lensing, including that of dark matter, it is fundamental to understand their luminous content. For this reason, the understanding of spectroscopy (Section 3.2) and photometry (Section 3.3) is key to using multiply-imaged sources to yield a lens model (as described in Chapter 2). We present the combination of these techniques to present galaxy cluster lens models of MACS J0242.5-2132 and MACS J0949.8+1708 in our submitted article:

Joint HST, VLT/MUSE and XMM-Newton observations to constrain the mass distribution of the two strong lensing galaxy clusters: MACS J0242.5-2132 & MACS J0949.8+1708, **Joseph F. V. Allingham**, Mathilde Jauzac, David J. Lagattuta, Guillaume Mahler, Céline Bœhm, Geraint F. Lewis, Dominique Eckert, Alastair Edge, Stefano Ettori, July 2022, arXiv:2207.10520 [astro-ph.CO], submitted to MNRAS[10].

[10]If any difference appears between the version submitted here and that of the arXiv, it is because of changes made to address the referee report given to MNRAS. As of submission of this thesis, the version enclosed here should be the most recent.

Joint *HST*, VLT/MUSE and *XMM-Newton* observations to constrain the mass distribution of the two strong lensing galaxy clusters: MACS J0242.5−2132 & MACS J0949.8+1708

Joseph F. V. Allingham[1]★, Mathilde Jauzac[2,3,4,5], David J. Lagattuta[2,3], Guillaume Mahler[2,3], Céline Bœhm[1], Geraint F. Lewis[1], Dominique Eckert[6], Alastair Edge[2], and Stefano Ettori[7,8]

[1]*School of Physics, A28, The University of Sydney, NSW 2006, Australia;*
[2]*Centre for Extragalactic Astronomy, Department of Physics, Durham University, South Road, Durham DH1 3LE, UK;*
[3]*Institute for Computational Cosmology, Department of Physics, Durham University, South Road, Durham DH1 3LE, UK;*
[4]*Astrophysics Research Centre, University of KwaZulu-Natal, Westville Campus, Durban 4041, South Africa;*
[5]*School of Mathematics, Statistics & Computer Science, University of KwaZulu-Natal, Westville Campus, Durban 4041, South Africa;*
[6]*Department of Astronomy, University of Geneva, ch. d'Écogia 16, CH-1290 Versoix Switzerland;*
[7]*INAF - Osservatorio di Astrofisica e Scienza dello Spazio di Bologna, via Piero Gobetti 93/3, 40129 Bologna;*
[8]*INFN, Sezione di Bologna, viale Berti Pichat 6/2, 40127 Bologna, Italia.*

Submitted to MNRAS

ABSTRACT

We present the strong lensing analysis of two galaxy clusters: MACS J0242.5-2132 (MACS J0242, $z = 0.313$) and MACS J0949.8+1708 (MACS J0949, $z = 0.383$). Their total matter distributions are constrained thanks to the powerful combination of observations with the *Hubble Space Telescope* and the MUSE instrument. Using these observations, we precisely measure the redshift of six multiple image systems in MACS J0242, and two in MACS J0949. We also include four multiple image systems in the latter cluster identified in *HST* imaging without MUSE redshift measurements. For each cluster, our best-fit mass model consists of a single cluster-scale halo, and 57 (170) galaxy-scale halos for MACS J0242 (MACS J0949). Multiple images positions are predicted with a *rms* 0.39″and 0.15″for MACS J0242 and MACS J0949 models respectively. From these mass models, we derive aperture masses of $M(R < 200\,\mathrm{kpc}) = 1.67^{+0.03}_{-0.05} \times 10^{14} M_{\odot}$, and $M(R < 200\,\mathrm{kpc}) = 2.00^{+0.05}_{-0.20} \times 10^{14} M_{\odot}$. Combining our analysis with X-ray observations from the *XMM-Newton Observatory*, we show that MACS J0242 appears to be a relatively relaxed cluster, while conversely, MACS J0949 shows a relaxing post-merger state. At 200 kpc, X-ray observations suggest the hot gas fraction to be respectively $f_g = 0.115^{+0.003}_{-0.004}$ and $0.053^{+0.007}_{-0.006}$ for MACS J0242 and MACS J0949. MACS J0242 being relaxed, its density profile is very well fitted by a NFW distribution, in agreement with X-ray observations. Finally, the strong lensing analysis of MACS J0949 suggests a flat dark matter density distribution in the core, between 10 and 100 kpc. This appears consistent with X-ray observations.

Key words: cosmology: observations, cosmology: dark matter, gravitational lensing: strong, galaxies: clusters: general

1 INTRODUCTION

One of the most promising avenues towards understanding the nature of dark matter is to study its gravitational influence on the Universe's large-scale structure, particularly within the most massive galaxy clusters. These gravitationally bound clusters act as the largest natural laboratories, allowing not only to observe the large-scale baryonic physics, but also to indirectly probe dark matter thanks to the effect of gravitational lensing. Gravitational lensing is the phenomenon of optical distortion of background images, occurring when a massive foreground object – like a cluster, the "lens" – is on its line-of-sight. Gravitational lenses act as magnifying telescopes of objects in the background, creating in some cases multiple images of a same source, and allowing observers to study objects in the distant Universe (for a review, see Kneib & Natarajan 2011).

For all these reasons, since the first discovery of the gravitational giant arc of Abell 370 (Hammer 1987; Soucail et al. 1988) to the modern surveys of galaxy clusters and gravitational lenses such as the Cluster Lensing And Supernovae survey with Hubble (CLASH, Postman et al. 2012), the Hubble Frontier Fields (HFF, PI: Lotz, Lotz et al. 2017), the REionization LensIng Cluster Survey (RELICS, PI: Coe, Coe et al. 2019), the SDSS Giant Arcs Survey (SGAS, PI: Gladders, Sharon et al. 2020) and the Beyond the Ultra-deep Frontier Fields And Legacy Observation programme (BUFFALO, PI: Steinhardt & Jauzac, Steinhardt et al. 2020), gravitational lensing has emerged as a field of cosmology, capable of bringing key information to comprehend the structure formation and the nature of dark matter.

In particular, the study of a system of multiple images originating

★ E-mail: joseph.allingham@sydney.edu.au

from one source through gravitational lensing allows one to constrain the mass distribution within the lens, and to characterise the dark matter density profile within it. The descriptive potential of gravitational lensing has already been showcased at multiple occasions such as in (Richard et al. 2014a; Jauzac et al. 2014, 2016c; Diego et al. 2015a,b, 2016, 2018, 2020; Grillo et al. 2015; Caminha et al. 2017; Williams et al. 2018). Using the combination of high resolution images taken with the *Hubble Space Telescope* (*HST*) and the Dark Energy Survey (DES) for photometric analysis in the one hand, and the Multi-Unit Spectroscopic Explorer (MUSE, see Bacon et al. 2014) for spectroscopy in the other, we were able to securely identify cluster members and multiple images systems. This combination has proven to be particularly successful over the past few years (e.g. Treu et al. 2016; Lagattuta et al. 2017, 2019; Jauzac et al. 2016a, 2019, 2021; Grillo et al. 2016; Mahler et al. 2017; Caminha et al. 2019).

In this paper, we repeat a similar exercise, looking at two galaxy clusters, MACS J0242.5−2132 and MACS J0949.8+1708 (i.e. RXC J0949.8+1707), hereafter MACS J0242 and MACS J0949 respectively, initially discovered by the MAssive Cluster Survey (MACS, PI: Ebeling, Ebeling et al. 2001). We combined multi-band *HST* and ground-based imaging with spectroscopy from VLT/MUSE with the lensing modelling technique presented in detail in Richard et al. (2014b) which makes use of the publicly available Lenstool software (Kneib et al. 1996; Jullo et al. 2007). We then confront our lensing results to the intra-cluster gas distribution observed by the *XMM-Newton X-ray Observatory*.

It is common practice to use the combined baryonic analysis of the X-ray signal and the Sunyaev-Zel'dovich effect (SZ) to understand the thermodynamics of galaxy clusters. One can then reconstruct the total matter density of galaxy clusters by making a number of hypotheses such as hydrostatic equilibrium or polytropic temperature distribution (see Tchernin et al. 2018). Furthermore, as the analysis of multi-wavelengths observations (optical, Sunyaev-Zel'dovich effect, X-rays) characterises the thermodynamics of the intra-cluster medium (ICM; see Sereno et al. 2017), a careful comparison between these and a strong lensing analysis can provide clues on the possible differences between expected and observed baryon and dark matter distributions.

As an example, the study in merging galaxy clusters of the offset between the position of the centre of dark matter, luminous galaxies and X-ray emission can be used to constrain the cross-section of self-interacting dark matter (SIDM, see Tulin & Yu 2018, for an overview). In fact, simulations of colliding clusters suggests the cold dark matter (CDM) distribution to be bounded to the luminous distribution; while in SIDM scenarios dark matter lags behind baryonic matter (Massey et al. 2011; Robertson et al. 2016, 2017). For instance, Robertson et al. (2017) present SIDM simulations with anisotropic scattering, yielding an offset between the galaxies centre and that of DM smaller than 10 kpc for an interaction $\sigma/m = 1$ cm^2.g^{-1}. This was pioneered in Clowe et al. (2004) and Bradač et al. (2008), and has now become more and more popular as shown in, e.g. Merten et al. (2011); Harvey et al. (2015); Massey et al. (2015, 2018); Jauzac et al. (2016b, 2018).

In this article, we focus on the lensing-based mass reconstructions of the two clusters. Utilising the ICM detected in the X-rays to infer the dark matter halo profile, we compare the results of our lensing reconstruction to the *XMM-Newton* X-ray data from CHEX-MATE Collaboration et al. (2021), processed following the X-COP pipeline (Ghirardini et al. 2019) for these two clusters. We present a broader context for such comparisons, i.e. new models of baryonic matter distribution rooted in lensing analysis to constrain the electronic densities of galaxy clusters, in a companion paper (Allingham et al. in prep.).

Our paper is organised as follows. In Section 2, we present the observations used for our analysis. The methods to extract multiple image candidates, and to build cluster galaxy catalogues are presented in Section 3. The lensing reconstruction method is introduced in Section 4, the mass models are described in Section 5, and conclusions are presented in Section 6. Throughout this paper, we assume the ΛCDM cosmological model, with $\Omega_m = 0.3$, $\Omega_\Lambda = 0.7$, and $H_0 = 70$ km/s/Mpc. All magnitudes use the AB convention system (Oke 1974).

2 DATA

To determine the cluster mass distributions as robustly as possible, we include both imaging and spectroscopic information when constructing lens models. This combination is especially powerful, allowing us to identify and confirm individual components of the model (such as multiple-image constraints and cluster members), while simultaneously rejecting interlopers along the line of sight. We complement the observations we have with *HST* and VLT/MUSE with *XMM-Newton X-ray Observatory* observations to cross-check our lensing model results.

2.1 Imaging

2.1.1 Hubble Space Telescope

As part of the MACS survey (Ebeling et al. 2001), both targets in our study have publicly available *HST* data. Snapshot (1200s) imaging of MACS J0242 taken with the Wide Field Planetary Camera 2 (WFPC2, Holtzman et al. 1995) exist for both the F606W and F814W bands (PID:11103, PI: Ebeling), supplemented by an additional 1200s image taken with the Advanced Camera for Surveys (ACS, Ford et al. 1998) in F606W (PID: 12166, PI: Ebeling). Similarly, shallow imaging for MACS J0949 have been taken with the ACS in both F606W (PID:10491, PI: Ebeling) and F814W (PID: 12166, PI: Ebeling). Archival processed versions of these datasets are available from the *Hubble* Legacy Archive[1].

Following the initial MACS data, MACS J0949 was subsequently observed as part of the RELICS survey (Coe et al. 2019) – under the name RXC J0949.8+1707 – and thus there are additional data sets for this cluster. Specifically, ACS imaging in F435W, F606W and F814W provide wider, deeper coverage of the cluster field in optical bands, while coverage in F105W, F125W, F140W and F160W bands using the Wide Field Camera 3 (WFC3, Kalirai et al. 2009) provide information in the near-IR regime. These data are also publicly available[2], and therefore in this work combine all of the imaging (save for the F435W band, which is too low S/N for our purposes) to create our master data set. A summary of all available *HST* imaging can be found in Table 1.

2.1.2 DESI Legacy Survey

Since the available *HST* imaging for MACS J0242 are shallow and colour information is limited to a WFPC2-sized footprint, we complement these data with additional multi-band ground-based imaging from the DESI legacy archive. To enhance the *HST* data as

[1] https://hla.stsci.edu/
[2] https://archive.stsci.edu/prepds/relics/

much as possible, we extract cutout images in three optical bands – g, r and z, see Abbott et al. (2018). The images are centred around the MACS J0242 brightest cluster galaxy (BCG) located at (α = 40.6497 deg, δ = −21.5406 deg), and extend over a full ACS field of view. Combining the space- and ground-based information allow us to improve our galaxy selection function during lens modelling (see section 3). The DESI data are summarised in Table 2.

2.2 Spectroscopy

In addition to imaging, our lensing reconstruction makes use of the Multi Unit Spectroscopic Explorer (MUSE; Bacon et al. 2014) observations at the Very Large Telescope. Such observations are invaluable to obtain redshift information. Both clusters were observed with MUSE as part of the filler large programme "A MUSE Survey of the Most Massive Clusters of Galaxies - the Universe's Kaleidoscopes" (PI: Edge). Data for each cluster consists of a single MUSE pointing, divided in a series of three exposures of 970 seconds. To reduce the effects of bad pixels, cosmic rays, and other systematics, each successive exposure is rotated by 90 degrees, and a small ($\sim 0.05''$) dither pattern is applied. We reduce the raw data following the procedure detailed in Richard et al. (2021). Details of the observations for both clusters are summarised in Table 3.

2.3 X-ray data

We searched the *XMM-Newton* archive for publicly available observations of the two systems of interest. MACS J0242 was observed for a total of 70 ks (OBSID:0673830101), and MACS J0949 for a total of 36 ks (OBSID:0827340901). We analysed the two observations using XMMSAS v17.0, and the most up-to-date calibration files. We used the XMMSAS tools `mos-filter` and `pn-filter` to extract light curves of the observations and filter out periods of enhanced background, induced by soft proton flares. After flare filtering, the available clean exposure time is 61 ks (MOS) and 53 ks (PN) for MACS J0242, and 35 ks (MOS) and 34 ks (PN) for MACS J0949.

3 SPECTROSCOPIC & PHOTOMETRIC ANALYSES

In this section, we present the key steps to obtain cluster galaxy catalogues and (candidate) background multiple image systems for both MACS J0242 and MACS J0949: from the source extraction to the selections of galaxies and identification of cluster galaxies specifically, using both the multi-band imaging in hand for the two clusters as well as the spectroscopy from VLT/MUSE.

3.1 Spectroscopic analysis

We here present the analysis of the spectroscopic observations described in Sect. 2.2. In spite of the field of view of the MUSE cubes, $1' \times 1'$, being smaller than that of *HST* or DES, we can still access the redshift of a large number of foreground, cluster and background galaxies.

In order to detect specifically multiple image systems, we use `MUSELET` (MUSE Line Emission Tracker), a package of `MPDAF` (Muse Python Data Analysis Framework) which removes the constant emission from bright galaxies in the field, and is optimised for the detection of the faintest objects. For more details about the technique, we refer the reader to (Bacon et al. 2016) and (Piqueras et al. 2017). We go through each of the 3681 slices of this subtracted MUSE datacube, and identify the bright detections.

We complete this technique with `CatalogueBuilder` (see Richard et al. 2021) for a thorough and systematic analysis. The latter embeds the `MUSELET` analysis, but also uses a modified version of `MARZ` (see Hinton et al. 2016), which is better tuned to the resolution and spectral profiles specific to MUSE data. `CatalogueBuilder` also uses the position data of the deepest field available (in this case *HST*/ACS). These make it easier to confirm the likely source of the multiple images which we are looking for. Using the spectroscopic information, we adjust with our own custom *redshifting* routine the detected spectra to the known absorption lines, and notably [OII], [OIII] and Ly-α. We then obtain catalogues containing coordinates and redshifts, such as Tables 6 and A1. We also consider multiple detections within a radius of $< 0.5''$ and a redshift separation of $\delta z < 0.05$ to be a unique object. All redshifts are supposed known with a precision estimated to $\delta z = 0.0001$.

We can associate to these detections Signal-to-Noise (S/N) ratios. As we also know the type of pattern the absorption lines should match, we can use the S/N ratio and spectral patterns to define different confidence levels. We only keep in all catalogues, including for example in Sect. A, detections judged to be "good" or "excellent" (identifiers 3 and 4 in `MARZ` and `CatalogueBuilder`). In the case of several detections representing a same object, we merge them keeping the best quality of detection.

The distribution of redshifts in each cluster is shown in Fig. 3 for the full MUSE frame. We measure 36 and 96 good spectroscopic redshifts in MACS J0242 and MACS J0949 respectively. Due to the small statistics, this distribution is not Gaussian but it is sufficient to constrain the redshift of the clusters, which we estimate to be $0.300 \leq z \leq 0.325$ and $0.36 \leq z \leq 0.41$ for MACS J0242 and MACS J0949 respectively. For the current analysis, we define the redshift of each cluster by that of their BCG, i.e. respectively 0.3131 and 0.383 for MACS J0242 and MACS J0949 respectively.

3.2 Photometric analysis

3.2.1 Source extraction

We first align all images from a given instrument (*HST*/ACS, *HST*/WFC3, *HST*/WFPC2 and DESI) to the same *wcs* coordinates, and pixelate them accordingly to allow for direct colour comparison of detected objects. In order to extract all detected objects from the multi-band imaging in hand for each cluster, we run the `SExtractor` software (Bertin & Arnouts 1996) in dual-image mode, for each pass-band of each instrument. For each instrument, we adopt a reference pass-band and a position of reference. The former sets the Kron-like magnitude of each detection, while the latter sets its location. The number of bands per instrument as well as the reference pass-band used are listed in Tables 4 and 5 for MACS J0242 and MACS J0949 respectively.

For each instrument, we then apply several cuts and selection criteria to the output catalogues from SExtractor. That allows us to build a complete multi-band catalogue composed only of galaxies. We summarise the different steps of this process:

(i) All detections without reliable magnitude measurements (i.e. MAG_AUTO=-99) and incomplete (or corrupted) data are removed from all catalogues. This includes isophotal data and memory overflow that occurs during deblending or extraction.

(ii) All objects with a stellarity greater than 0.2 are removed as they are likely to be stars rather than galaxies. We additionally mask all detections very close to bright stars.

(iii) For a given cluster, only objects detected in all pass-bands are kept.

Table 1. Summary of the *HST* observations used in this analysis for MACS J0242 and MACS J0949.

Galaxy cluster	Date of observation	Proposal	Camera/Filter	RA (°, J2000)	Dec (°, J2000)	Exposure time (s)
MACS J0242	29/02/2012	12166	ACS/F606W	40.645985	-21.541129	1200
	30/11/2007	11103	WFPC2/F606W	40.649625	-21.540556	1200
	27/10/2008	11103	WFPC2/F814W	40.649625	-21.540556	1200
MACS J0949	09/10/2015	14096	WFC3/F105W	147.462029	17.120908	706
	09/10/2015	14096	WFC3/F125W	147.462029	17.120908	356
	09/10/2015	14096	WFC3/F140W	147.462029	17.120908	331
	09/10/2015	14096	WFC3/F160W	147.462029	17.120908	906
	20/11/2015	14096	ACS/F606W	147.463077	17.120878	1013
	20/11/2015	14096	ACS/F814W	147.463077	17.120878	1013
	23/04/2011	14096	ACS/F814W	147.463077	17.120878	1440
	25/10/2005	14096	ACS/F606W	147.463077	17.120878	1200

Table 2. Summary of the DESI observations used in this analysis for MACS J0242.

Date of Observation[a]	Proposal	Filter	RA (°, J2000)	Dec (°, J2000)	Exposure time (s)	Seeing (″)[a]
24/09/2016	2012B-0001	DES/g	40.6497	-21.5406	810	0.738
05/11/2016	2012B-0001	DES/r	40.6497	-21.5406	720	0.701
16/11/2016	2012B-0001	DES/z	40.6497	-21.5406	810	0.859

[a] Median values, determined over all observations

Table 3. Summary of MUSE observations for MACS J0242 and MACS J0949. Columns 1 to 3 indicate respectively the name of the cluster, its average redshift, and the ID of the ESO programme. For each pointing, we then give the observation date in column 4, the right ascension, R.A., and declination, Dec., of the centre of the field of view in columns 5 and 6, the total exposure time in column 7, and the FWHM of the seeing during the observations in column 8.

Galaxy cluster	z	Date of observation	ESO proposal	RA (°, J2000)	Dec (°, J2000)	Exposure time (s)	Seeing (″)
MACS J0242	0.3131	26/12/2017	0100.A-0792(A)	40.650167	-21.5401389	2910	0.63
MACS J0949	0.383	20/02/2020	0104.A-0801(A)	147.465792	17.119528	2910	0.71

Table 4. Number of detections (Nod) after each source extraction selections as listed in Sect. 3.2.1 for MACS J0242.

Observable	DES	*HST*/WFPC2	*HST*/ACS
Number of bands	3	2	1
Reference band	z	F814W	F606W
Nod (0)	186	808	559
Nod (i)	185	540	559
Nod (ii)	180	492	456
Nod (iii)	180	429	456
Nod (iv)	142	202	402
Colour-Magnitude	51	45	179
Final		58	

Table 5. Number of detections (Nod) after each source extraction selections as listed in Sect. 3.2.1 for MACS J0949.

Observable	*HST*/WFC3	*HST*/ACS
Number of bands	4	2
Reference band	F160W	F814W
Nod (0)	3114	3055
Nod (i)	2388	2700
Nod (ii)	2172	2639
Nod (iii)	1648	2490
Nod (iv)	773	1708
Colour-Magnitude	42	172
Final	170	

(iv) All objects with a Signal-to-Noise ratio (S/N) smaller than 10 are removed.

Tables 4 and 5 are listing the number of detections remaining once each of these criteria are applied for each instrument, for MACS J0242 and MACS J0949 respectively.

3.2.2 *Spectroscopic redshift identification*

Now that we have a galaxy catalogue for each instrument, we can match our detection with spectroscopic redshift measurements from VLT/MUSE. In order to ensure a MUSE detection corresponds to a photometric one, we compare the positions measured by `Sextractor` in the different filters for all objects, using a Haversine

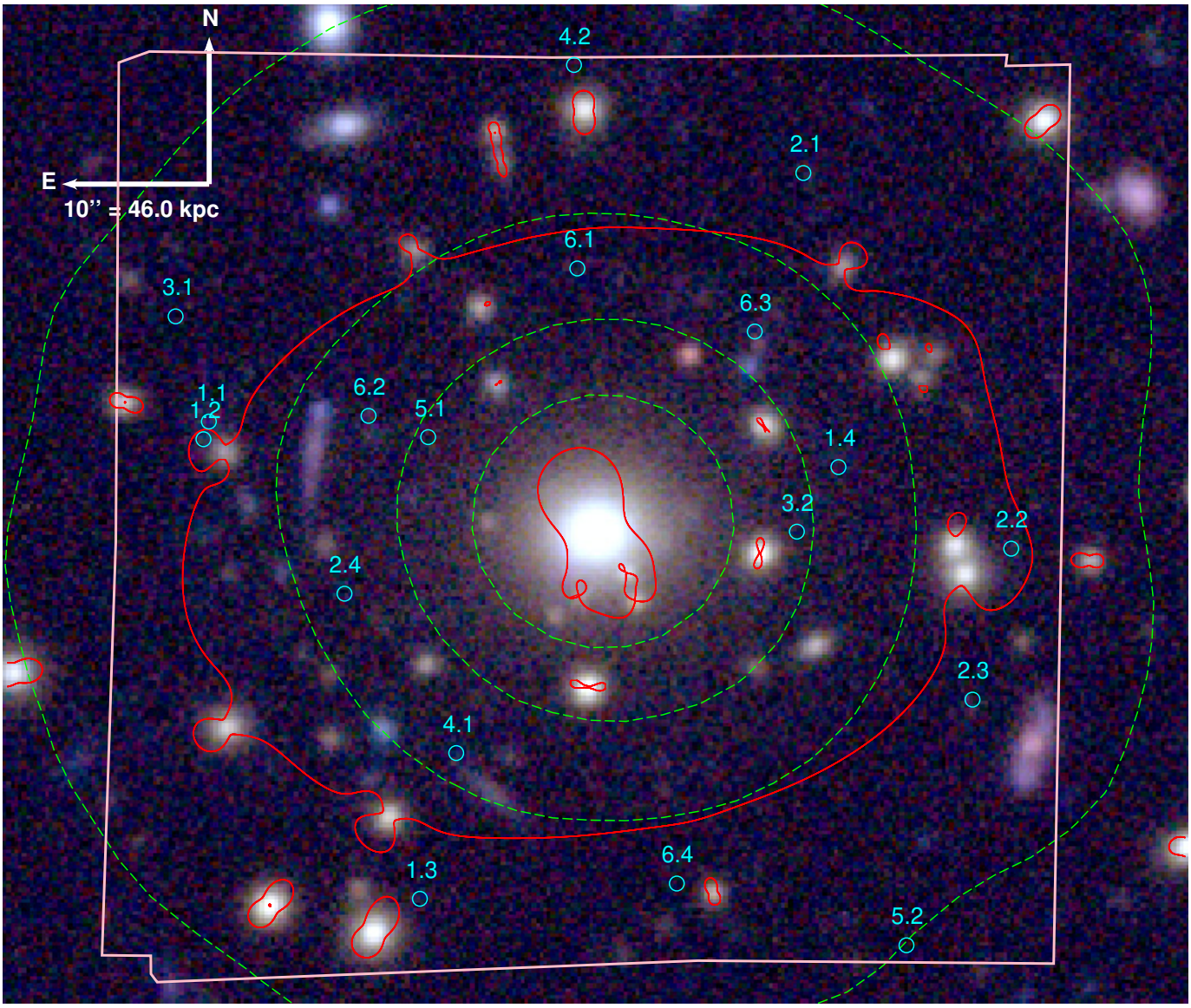

Figure 1. Composite DES colour image of MACS J0242. The gas distribution obtained from *XMM-Newton* observations is shown with dashed green contours. In cyan, we highlight the positions of the multiple images used to constrain the mass model, and which are listed in Table 6. Critical lines for a source at $z = 3.0627$ (redshift of system 1) are shown in red. The MUSE field of view is shown in pink.

function[3]. If the separation angle between objects from the spectroscopic and the photometric catalogues is smaller than $0.5''$, we consider the detection to be of the same objects, and hence associate the spectroscopic redshift to the photometric detection. This error is equal to 2.5 MUSE pixels, and captures the positional uncertainty on spectroscopic detections.

Out of this step, we attribute a spectroscopic redshift to 20, 25, and 25 sources in the DES, *HST*/WFPC2 and *HST*/ACS catalogues for MACS J0242. In the case of MACS J0949, we attribute a spectroscopic redshift to 54, and 49 sources in the *HST*/ACS and *HST*/WFC3 catalogues.

[3] The Haversine angle reads as

$$\mathcal{H} = 2\arcsin\sqrt{\sin^2\left(\frac{\delta_2-\delta_1}{2}\right)+\cos\delta_1\cos\delta_2\sin^2\left(\frac{\alpha_2-\alpha_1}{2}\right)}.$$

3.2.3 *Cluster galaxy selection*

The next step is the identification of cluster galaxies specifically. For that we are using colour-magnitude selections for each clusters.

The first step consists in applying the red sequence technique (e.g. Gladders & Yee 2000). Using the catalogues after source extraction selections and spectroscopic redshift identification, we compute for both clusters a series of colour-magnitude (CM) diagrams. We compute these for each instrument. As each pass-band represents a magnitude, we can respectively compute 3 and 1 CM diagrammes for DES and *HST*/WFPC2 for MACS J0242 (none for *HST*/ACS as only one band is available), and 1 and 6 for *HST*/ACS and *HST*/WFC3 for MACS J0949.

As shown in Fig. 4, cluster members are expected to follow a main sequence (magenta line). To calibrate our selections, we use spectroscopically confirmed cluster members. We then remove all detections with a magnitude exceeding $m_{\rm max}$, which varies depending on

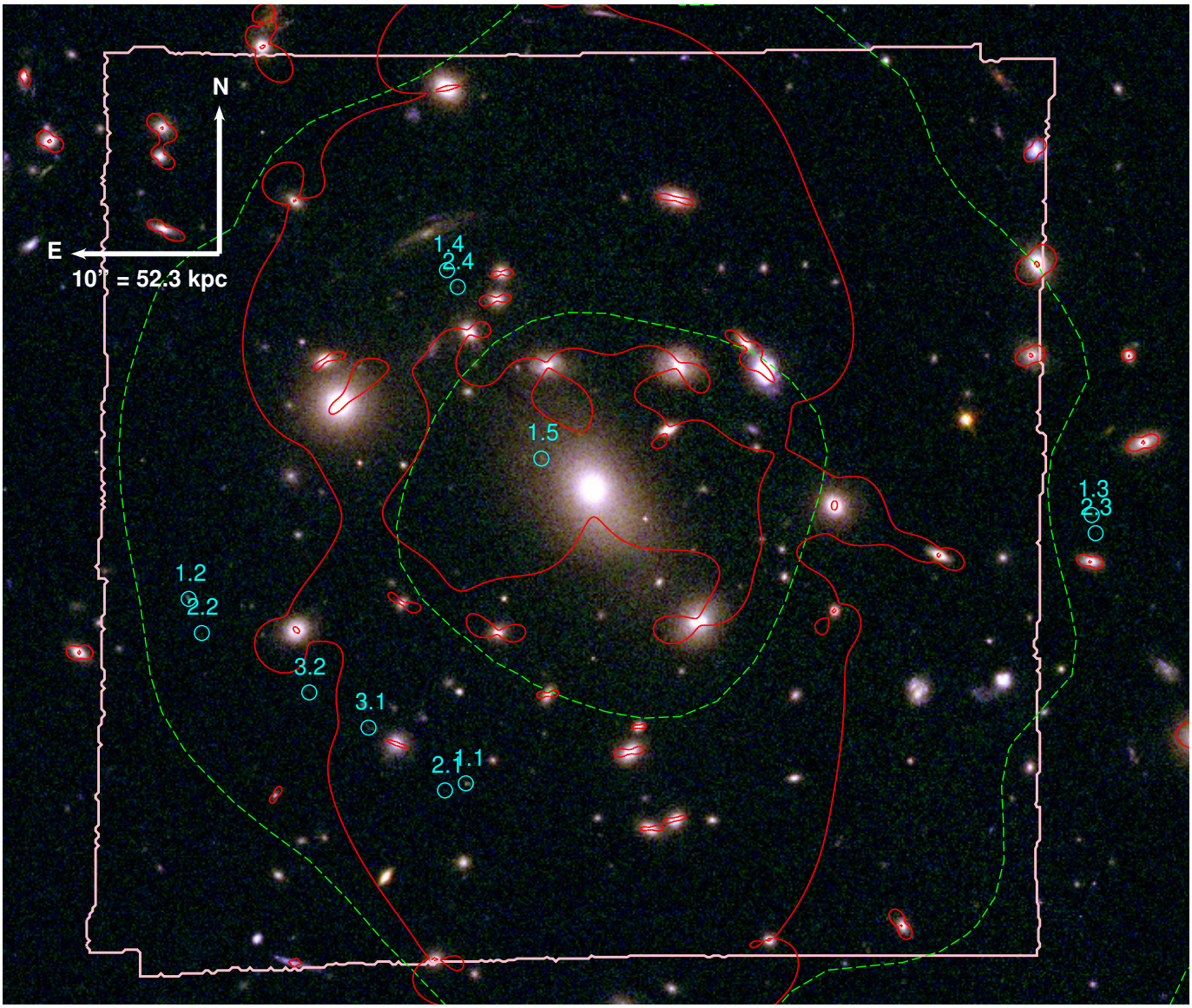

Figure 2. Composite colour *HST* image of MACS J0949. The critical lines of system 1, at redshift 4.8902, are shown in red. The gas distribution obtained thanks to *XMM-Newton* observations are shown with dash green contours. In cyan, we highlight the positions of the multiple images used to constrain the mass model. They are listed in Table 8. In pink, we display the MUSE field of view.

instruments and filters. For MACS J0242, we have $m_{\rm max}$ = 22 for *HST*/WFPC2, 23.5 for DES/z, and 24.5 for DES/r. For MACS J0949, we have $m_{\rm max}$ = 21.5 for *HST*/WFC3 and 22.5 for *HST*/ACS. We then perform a linear regression and obtain the main sequence. We give in Appendix B the fits for all colour-magnitudes used for both clusters.

Galaxies selected as cluster members are galaxies which have a colour within $2\sigma_C$ of the main red sequence for *HST*/ACS and *HST*/WFC3, and within $3\sigma_C$ for *HST*/WFPC2 and DES. σ_C is the weighed colour standard deviation of the spectroscopically confirmed cluster galaxy sample. These limits are highlighted as black rectangles in Fig. 4. For an instrument with more than 2 pass-bands, we can compute more than one CM diagram, and thus only retain cluster member identifications compatible with *all* colour-magnitude diagram selections. We summarise in Tables 4 and 5 for MACS J0242 and MACS J0949 respectively, the number of galaxies identified as cluster members per instrument once these colour-magnitude selections are applied. In some cases, spectroscopically confirmed cluster galaxies fall outside the colour-magnitude selection. These objects are ultimately conserved in our cluster galaxy catalogue. However, we do not include them in the CM cut counts, to show the effect of the photometric selection.

3.2.4 *Instrument catalogue combination*

We now assemble the galaxy catalogues for each instrument before merging these into a final cluster galaxy catalogue for each cluster. We match the coordinates of sources with the already defined 0.5″ separation angle.

MACS J0242 and MACS J0949 were imaged with different instruments, and thus have different coverage. We define the camera of reference as the camera with the highest resolution. In the

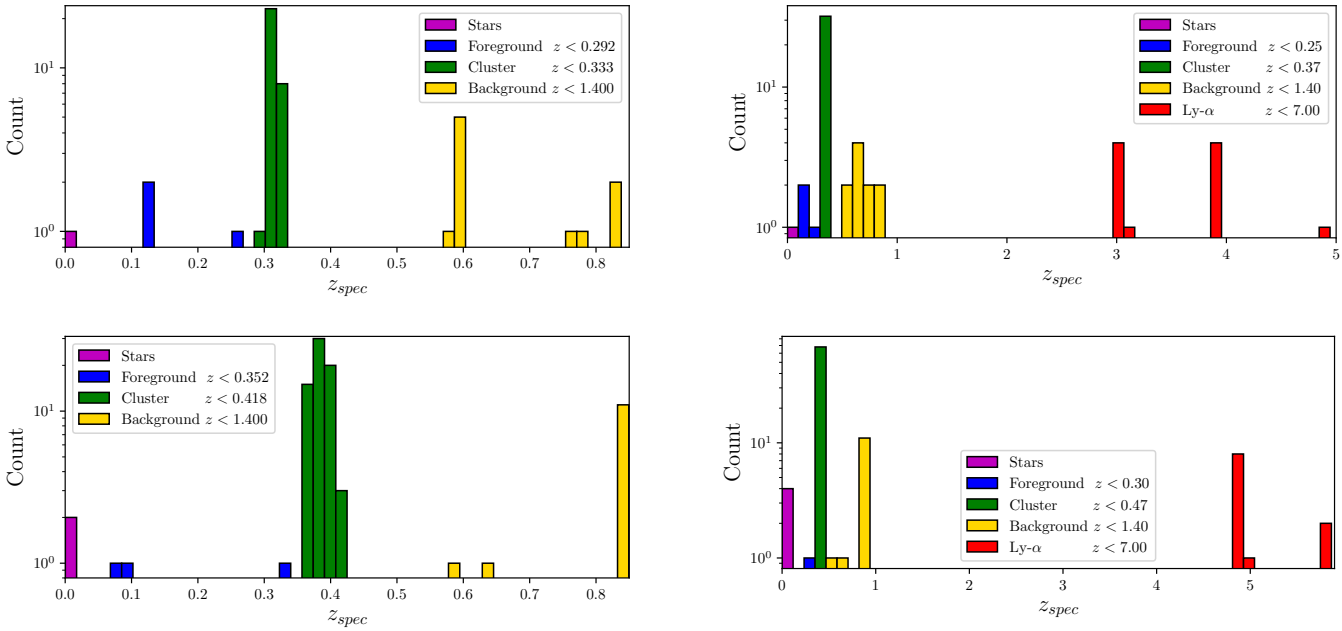

Figure 3. Redshift distribution of all MUSE detected objects. *Top row*: Cluster MACS J0242. Objects identified as being in the cluster are shown in green, while foreground and background objects are shown in blue and yellow respectively. We highlight Lyman-α emitters in red. At last, objects within the Milky Way (stars, etc.) are displayed in purple. *Left panel:* Redshift distribution of objects located at small redshifts $z < 1$. – *Right panel:* Redshift distribution of all objects with a measured redshift. *Bottom row*: Cluster MACS J0949. *Left panel:* Redshift distribution of objects located at small redshifts $z < 1$. – *Right panel:* Redshift distribution of all objects with a measured redshift.

case of the both clusters, it is *HST*/ACS, but the reference band is chosen as F606W for MACS J0242, and F814W for MACS J0949. MACS J0242 was observed with *HST*/ACS in only one band. Moreover, MACS J0242 was observed with *HST*/WFPC2 in 2 pass-bands, but the shape of the camera field of view does not cover the entire ACS field of view. MACS J0242 has DES observations in 3 pass-bands, covering a wide field of view. However the quality of these observations is lower than the ones we have from space. We therefore require for a given cluster member selected galaxy in *HST*/ACS to be at least present in DES or WFPC2 in order to be included into the final cluster member catalogue. MACS J0949 was imaged with *HST*/ACS and WFC3 cameras. *HST*/WFC3 has a smaller field of view than ACS. We detected multiply imaged systems out of the WFC3 field of view. In order to account for the gravitational effect of individual galaxies on these systems, we include all galaxies detections from at least one camera to our galaxies catalogue.

Finally, cluster galaxies located at a distance larger than 40″ from the cluster centre and with a magnitude difference to the BCG of $\Delta m > 4$ are ignored. Due to their small mass, these galaxies would only have a very small impact on the strong lensing configurations observed.

3.3 Final catalogues

3.3.1 Cluster galaxy catalogues

Sect. 3.2 describes all the steps for the identification of cluster members, including colour-magnitude selections as well as spectroscopic identifications. All galaxies identified as cluster members and used for our lensing modelling are listed in Appendix, in Tables A3 and A4 for MACS J0242 and MACS J0949. Our final catalogues include 58 and 170 galaxies for MACS J0242 and MACS J0949 respectively.

In order to probe the robustness of our catalogues, we conducted the following verification analysis. We isolated only the spectroscopic detections, and then reinjected them into our photometric selection. We found respectively 15 out of 16 and 34 out of 34 galaxies retained within the photometric selection for MACS J0242 and MACS J0949. As these spectroscopic detections were used to define these selections, they are expected to be selected. Thus, in order to estimate the contamination by galaxies out of the cluster redshift boundaries, we examined the number of selected spectroscopic detections out of the cluster. We find a maximum 2 (2) out of 54 (97) galaxies of our sample contaminants, i.e. 4% (2%) contamination of our sample in cluster MACS J0242 (MACS J0949). Thus we are confident in our galaxy selection. Nevertheless, for accuracy, we removed these known out-of-cluster galaxies from the final catalogue.

3.3.2 Multiple image systems

In Sect. 3.1, we described the preliminary steps leading to the multiple image system catalogue. At this point, this is simply a catalogue of reliable detections with redshift $z > 0.6$. The second step in the identification of multiple image systems is to look for similarities between these detections, starting with their spectra. We then look at their positions and see if they are compatible with a lensing geometry. The MUSE field of view being narrower than the *HST* one, one can also look at the colour and morphology of possible multiple images. If a given set of multiple images presents at the same time compatible positions, colours, morphologies and, if available, redshift, we consider them as a multiple image system.

In Fig. 5, we show a colour composite *HST* image of four MUSE detections, 4 multiple images of the same galaxy located at redshift $z = 4.89$. In the case of MACS J0949, we force extract emission from the MUSE cube corresponding to the location of multiple images previously identified by the RELICS collaboration (obtained through

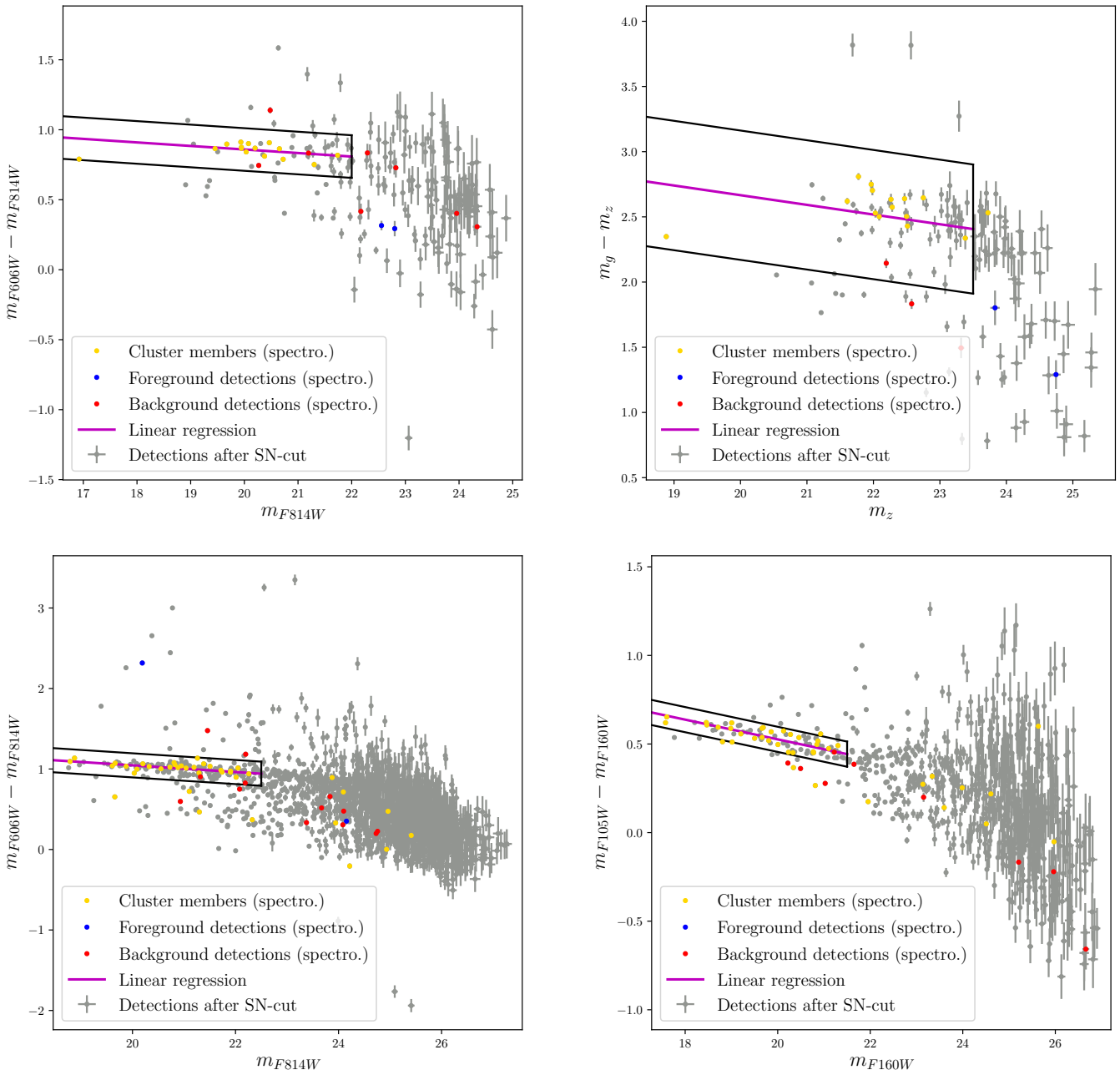

Figure 4. Colour-magnitude diagrams. *Top row:* Cluster MACS J0242. *Left panel:* Instrument *HST*/WFPC2 – m_{F814W} vs ($m_{\mathrm{F606W}} - _{\mathrm{F814W}}$). *Right panel:* Instrument DES – m_z vs ($m_g - m_z$). Grey filled circles (with their error bars) have successfully passed all selections described in Section 3.2.1. The magenta line represents the main sequence regression. Blue, gold and red dots represent spectroscopic detections of foreground, cluster and background objects respectively. *Bottom row:* Cluster MACS J0949. *Left panel:* Instrument *HST*/ACS – m_{F814W} vs ($m_{\mathrm{F606W}} - m_{\mathrm{F814W}}$). *Right panel:* Instrument *HST*/WFC3 – m_{F160W} vs ($m_{\mathrm{F105W}} - m_{\mathrm{F160W}}$).

private communication); we only reveal marginal identification as explained in Sec. 5.1.2. The final list of system used in this analysis is presented in Table 8.

4 STRONG LENSING MASS MODELLING

The mass distribution of each cluster is reconstructed using the `Lenstool` software[4] (Kneib et al. 1996; Jullo et al. 2007), in its parametric mode. The optimisation is performed in the image plane with a Markhov Chain Monte-Carlo algorithm (MCMC) assuring the sampling of parameter space. It optimises the predicted positions of multiple images while fitting an underlying mass distribution com-

[4] https://projets.lam.fr/projects/lenstool/wiki

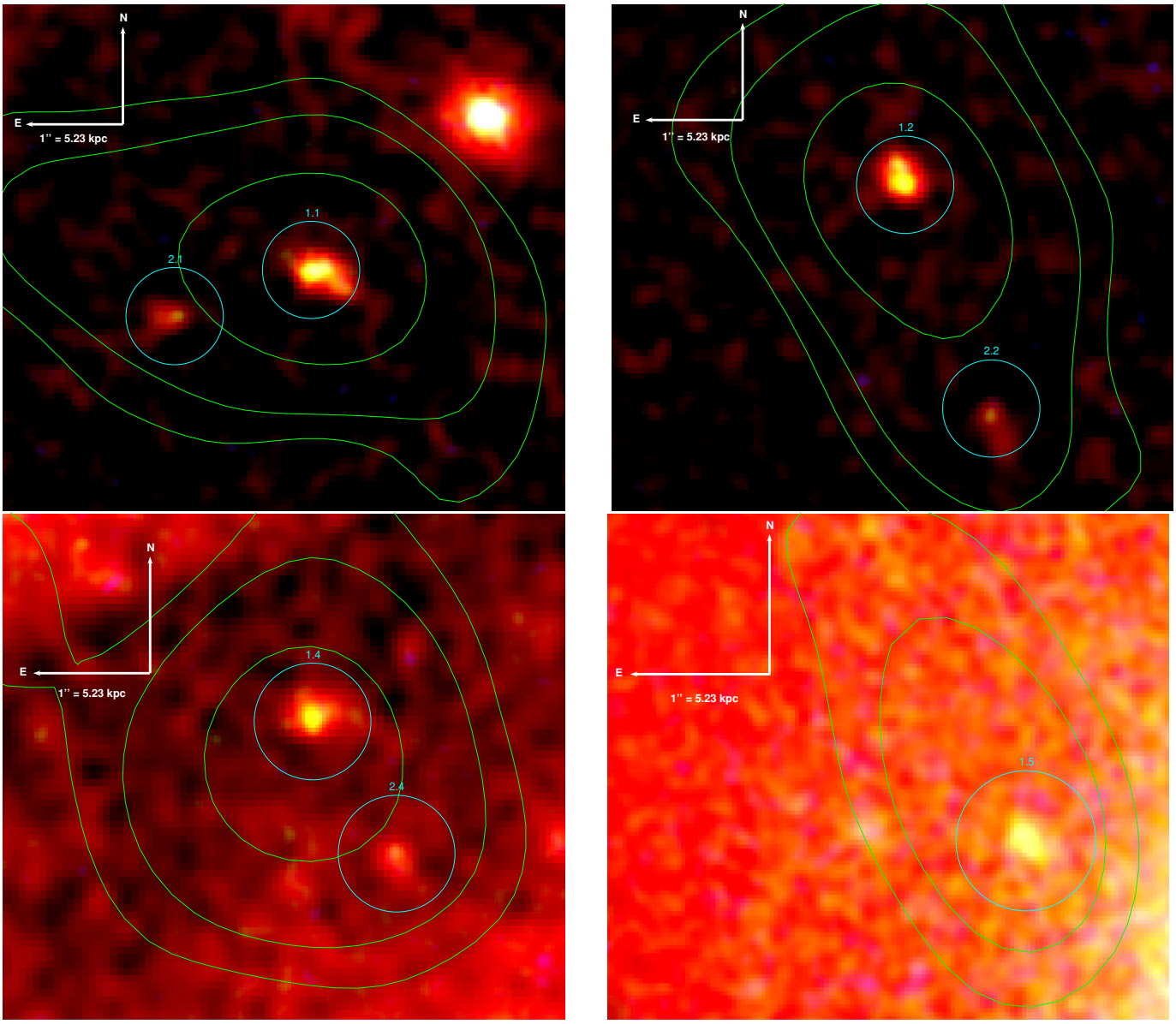

Figure 5. *HST* composite colour image of the four multiple images of System 1 detected in MACS J0949 with VLT/MUSE observations. Colours were enhanced to outline the multiple images. Labelled cyan circles show the positions of the multiple images and correspond to the peak of the Lyman-α emission. The green contours show flux density levels at 1.500, 2.125 and 4.000 $\times$ 10^{-20} erg s^{-1} cm^{-2} Å^{-1}. This narrow-band image is shown in Fig. 9.

posed of large-scale halo(s) to describe the overall cluster potential, and small-scale halos to account for local perturbers such as cluster galaxies.

For both clusters, we describe any potential using a dual Pseudo-Isothermal Elliptical matter distribution (dPIE, see Kassiola & Kovner 1993) which, as described in Elíasdóttir et al. (2007), has two different pivot scales: a *core radius*, which describes the potential evolution due to the baryonic matter content, and a *cut radius* that describes the dark matter potential. A dPIE potential is described by seven parameters (excluding the redshift): the central coordinates, the ellipticity e, the position angle θ, the core and cut radii, $r_{\rm core}$ and $r_{\rm cut}$ respectively, and a fiducial central velocity dispersion σ. The fiducial central velocity dispersion in `Lenstool` σ relates to the true three dimensional central velocity dispersion with $\sigma_0 = \sqrt{3/2}\sigma$, as detailed in Bergamini et al. (2019), Appendix C.

For each cluster, we assume one single large-scale dark matter halo to describe the overall cluster potential. It is described by a large velocity dispersion ($\sim 10^3$ km.s^{-1}), a large core radius ($\sim 10^2$ kpc) and large cut radius. We optimise all the parameters of the potential, excluding the cut radius which we fixed to values $\geq$1 Mpc as it is located far from the strong lensing region and thus cannot be constrained by multiple images only. The position of each cluster halo is allowed to vary within 10″ of the cluster centre, i.e. the position of the BCG. The ellipticity of the halo is limited to values < 0.8. The cut radius is fixed to 1.5 Mpc for both MACS J0242 and MACS J0949, as our investigation to model the ICM through lensing shows that this value provides a better fit to the X-ray observations (see our companion paper Allingham et al. in prep.). This value is in agreement with Chang et al. (2018), taking in consideration the higher mass range of the clusters we are exploring here.

The BCG of each cluster is also modelled independently, using a dPIE potential. The BCG has a strong gravitational influence in the cluster core, and will thus impact the geometry of multiple images quite strongly (Newman et al. 2013a). We fix their $r_{\rm core}$ to a

small value of 0.30 kpc for cluster MACS J0242 and 0.25 kpc for MACS J0949. For their positions, position angle, and ellipticity, we fix their values to the shape parameters in outputs of `SExtractor`. Finally, we only optimise its their velocity dispersion and cut radius.

Each individual cluster member is modelled by its own dPIE potential. Their positions, ellipticities and position angles are obtained with the photometric extraction.

We again assume a small but non-null value for $r_{\rm core}$. Their cut radii and velocity dispersions are optimised using their magnitude and assuming the Faber-Jackson scaling relation (Faber & Jackson 1976). All cluster members cut radii and velocity dispersions are rescaled with regard to a unique set of parameters ($r_{\rm cut,0}$, σ_0). This allows us to optimise each cluster galaxy potential using a remarkably small number of parameters. $r_{\rm cut}$ and σ are allowed to vary between 1 and 50 kpc, and 100 and 300 km.s^{-1} respectively. As mentioned earlier, the Faber-Jackson relation being scaled to a reference magnitude mag_0, we use the reference pass-band of the main camera for each cluster, ACS/F606W (mag_0 = 20.0205) and ACS/F814W (mag_0 = 19.5085) for MACS J0242 and MACS J0949 respectively.

As the centre of the cluster-scale halo and the BCG are aligned, the $r_{\rm core}$, $r_{\rm cut}$ and σ parameters of both potentials are degenerate. Due to the limited number of lensing constraints, we proceed incrementally to model the potential, to narrow the parameters space. First, we include the BCG in the scaling relation of the cluster galaxies and optimise the cluster-scale halo and the scaling relation parameters as described above. Second, we run a model with the BCG optimised independently, only optimising $r_{\rm cut}$ and σ as explained above. However in this case, the cluster-scale halo parameters are allowed to vary within a restricted range, defined gaussianly around the best fit values obtained from the first model. This way, we can limit the degeneracy between the cluster-scale and BCG halos, and obtain physical values to describe the BCG potential.

Finally, we added a completely free dPIE potential south to the main cluster halo of MACS J0949. This structure has already been included in the public RELICS models and correspond to the location of three candidate multiply-imaged systems 4, 5 and 6 as shown in Fig. 7. We optimised their redshifts as well as the potential and to prevent nonphysically high value we imposed gaussian priors on $r_{\rm core}$, $r_{\rm cut}$ and velocity dispersion.

5 RESULTS

5.1 Strong lensing mass models

5.1.1 MACS J0242 model

In MACS J0242, we detected six systems of multiple images with MUSE. Their positions and redshifts are given in Table 6. We provide the best fit parameters of our model in Table 7. The fixed values are highlighted by an asterisk. Our best-fit model yields predicted multiple images with a *rms* of 0.39″of the observed positions. The inclusion of an external shear component does not provide a significant improvement to the mass model, i.e. a *rms* of 0.38″compared to our best-fit mass model of 0.39″. This error is smaller than the positional error associated to spectroscopic detections. However, the error on the position of the multiply-lensed images is associated to their photometric detections, with much smaller positional error.

The geometry of the cluster is typical of a relaxed cool-core cluster. The density profiles peak in the centre, and the transition between the BCG and the DM halo appears to be very smooth as illustrated in Fig. 6. No other significant structure are identified. Figure 6 shows the surface density profile, Σ, and includes a 68% confidence interval around the best contours, as a function of the distance to the cluster centre. The inner part of the profile, $R \lesssim 50$ kpc, is dominated by the BCG potential, while at larger radii, the dark matter halo takes over. This pivot scale of about 50 kpc corresponds to the core radius of the DM halo, and the separation between the two different regimes of the dPIE potential. However, disentangling the potential influence of the BCG and the DM of the halo would require a much finer study of the stellar mass distribution of the BCG with a spectral energy distribution (SED) fit, which is beyond the scope of this article.

Table 6. List of multiple images detected with VLT/MUSE in MACS J0242. We here list their ID, coordinates, R.A. and Decl., given in degrees (J2000), and their measured spectroscopic redshift z.

Id.	R.A.	Decl.	z
1.1	40.6574070	-21.5383801	3.0627
1.2	40.6575168	-21.5387136	3.0627
1.3	40.6531265	-21.5473860	3.0627
1.4	40.6446350	-21.5392391	3.0627
2.1	40.6453464	-21.5336906	3.8681
2.2	40.6411296	-21.5407791	3.8681
2.3	40.6419142	-21.5436276	3.8681
2.4	40.6546554	-21.5416287	3.8681
3.1	40.6580815	-21.5363952	3.8682
3.2	40.6454775	-21.5404581	3.8682
4.1	40.6523889	-21.5446358	3.0615
4.2	40.6499994	-21.5316520	3.0615
5.1	40.6529585	-21.5386743	4.9492
5.2	40.6432539	-21.5482627	4.9492
6.1	40.6499320	-21.5354918	1.3010
6.2	40.6541677	-21.5382729	1.3010
6.3	40.6463323	-21.5366811	1.3010
6.4	40.6479134	-21.5470977	1.3010

We find the total density profile (baryonic and dark matter) of MACS J0242 to be well fitted by a Navarro-Frenk-White profile (NFW, see Navarro et al. 1996) in the region between 20 and 1000 kpc. We limit the reconstruction to radii $r \geq 20$ kpc as the Kron-like magnitude radius of the BCG is about 10 kpc, and we attempt to limit the influence of stellar physics within the fit. In order to compare it to the NFW fit of cluster MACS J0949, we arbitrarily take 20 kpc to be a good compromise of strong lensing potential reconstruction without stellar physics contamination. For regions $r > 200$ kpc, the cluster-scale DM halo should dominate the whole matter distribution. As the DM halo dPIE parameters ρ_0 and $r_{\rm core}$ are well constrained through strong lensing, this region beyond multiple images constraints and below the cut-off radius $r_{\rm cut}$ is expected to be well represented by a NFW profile. With NFW parameters $\rho_S = 3.42 \times 10^{-22}$ kg.m^{-3} and $r_S = 209.9$ kpc, we find a reduced $\chi^2 = 1.11$.

In order to compare our results to the X-ray data, we extrapolate the masses $M_{\Delta,c}$ comprised within an overdensity Δ using

$$R_\Delta = \left\{ R \;\middle|\; \frac{M(<R)}{\frac{4}{3}\pi R^3} = \Delta \cdot \rho_c(z) \right\}, \quad (1)$$

where ρ_c is the critical density at the cluster redshift, and $M(<R)$ the total mass enclosed within a given radius, R. At large radii ($R >$ 200 kpc), the strong lensing mass reconstruction only provides an estimate of the true mass distribution as there is no strong lensing constraints to precisely and accurately estimate the mass distribution in the outskirts. It therefore only provides a pure extrapolation of the inner core mass distribution, and only a weak-lensing analysis

Table 7. Best fit parameters of the strong lensing mass models for MACS J0242 and MACS J0949. We here list the central coordinates, Δ_α and Δ_δ in arcsec, relative to the centre, the ellipticity, e, the position angle in degrees, θ, the core radius in kpc, $r_{\rm core}$, the cut radius in kpc, $r_{\rm cut}$, and the velocity dispersion in km.s^{-1}, σ, for each component of the model. The centres are taken to be respectively $(\alpha_c, \delta_c) = (40.649555, -21.540485)$ deg and $(\alpha_c, \delta_c) = (147.4659012, 17.1195939)$ deg for MACS J0242 and MACS J0949. The asterisks highlight parameters which are fixed during the optimisation.

	Δ_α	Δ_δ	e	θ	$r_{\rm core}$	$r_{\rm cut}$	σ
				MACS J0242			
DM halo	$-0.138^{+0.085}_{-0.143}$	$0.136^{+0.111}_{-0.179}$	$0.287^{+0.037}_{-0.027}$	$17.884^{+0.762}_{-1.830}$	$57.194^{+6.044}_{-8.414}$	1500*	$918.479^{+28.984}_{-36.074}$
BCG	0.044*	−0.090*	0.226*	$155.758^{+10.766}_{-9.604}$	0.300*	$177.575^{+32.245}_{-57.950}$	$524.516^{+58.810}_{-43.956}$
Galaxy catalogue					0.030*	$5.625^{+7.845}_{-1.808}$	$199.242^{+30.721}_{-53.257}$
				MACS J0949			
DM halo	$-1.936^{+0.215}_{-2.843}$	$-0.671^{+0.565}_{-0.666}$	$0.249^{+0.398}_{-0.045}$	$92.434^{+0.570}_{-1.289}$	$116.246^{+24.108}_{-51.661}$	1500*	$1236.094^{+59.307}_{-310.553}$
Southern halo	$4.800^{+0.748}_{-0.464}$	$-60.133^{+2.391}_{-1.417}$	$0.097^{+0.294}_{-0.061}$	$128.629^{+41.438}_{-27.521}$	$20.548^{+31.596}_{-8.771}$	$232.502^{+180.124}_{-119.902}$	$323.220^{+120.202}_{-54.851}$
BCG	0*	0*	0.475*	120.130*	0.250*	$98.044^{+153.739}_{-34.342}$	$253.749^{+196.474}_{-18.473}$
Galaxy catalogue					0.150*	$23.135^{+111.473}_{-2.053}$	$139.314^{+25.804}_{-18.547}$

would provide a precise mass estimate in this region of the cluster, however this is beyond the scope of this analysis. We also compute $M_{2D}(R < 200\,\mathrm{kpc})$, the integrated mass within a radius of 200 kpc. This mass is a direct output of the lensing mass reconstruction. These values are all listed in Table 9.

5.1.2 *MACS J0949 model*

In MACS J0949, we identified several objects located behind the cluster with the MUSE observations. However most of them appear to be singly lensed. Through the techniques exposed in Sect. 3, we detected a multiple image system in the MUSE field at redshift $z = 4.8902$. This system 1 is composed of five multiple images, including four in the field, and one counterpart 1.3 located outside the MUSE field of view, and detected in the *HST* imaging. We also detect a fifth image, image 1.5, located close the BCG of the cluster. Images 1.4 and 1.5 (see Fig. 2), straddling the central critical curve of the cluster, allow to set stringent constraints on the inner slope of the mass density profile (as exhibited in Schneider et al. 1992; Newman et al. 2013b; Caminha et al. 2017).

Careful consideration of the *HST* images allowed us to detect secondary, fainter emission knots for four multiple images in system 1 – all except the central one which is hidden by the emission of the BCG. This is shown in Fig. 5. The MUSE spectroscopic analysis of these three images which compose system 2 shows a faint Ly-α peak for all of them, allowing us to measure a redshift of 4.8844, very close to that of system 1. We interpret system 2 either as part of the same galaxy, or a companion galaxy of system 1's source. The Ly-α halo of system 1 extends, and the potential secondary peak emission coincides with system 2 emission knots. We include 4 multiple images of system 2 as additional constraints to our mass model, the fifth image being demagnified we restrain ourselves from including it in our mass model. The coordinates and redshifts of the multiply imaged systems are given in Table 8. We give a list of the singly imaged objects in Appendix A.

The inspection of *HST* images also led to the discovery of system 3, composed of two multiple images. These faint detections in the South of the cluster were equally present in the MUSE field. A faint and *a priori* inconclusive detection of Ly-α – see Fig. 8 – is consistent with the redshift optimisation of this system using only system 1, or 1 and 2 as constraints. We therefore conclude that this system's redshift is 5.8658. However the stack of the spectra presents a S/N ratio < 2, and the MUSE data are sensible to sky perturbations in the speculated Ly-α bandwidth. We therefore decide not to use this as a redshift constraint, but to let the redshift free during the model optimisation.

At last, we detect three candidate multiply lensed images in the South of the *HST* field of view, in a region not covered by the MUSE observations. We included these three candidate systems 4, 5 and 6 in our mass model, letting their redshifts as free parameters. Their detection supposes the presence of a Southern halo as described in Sect. 4. For systems 3, 4, 5 and 6, our best fit mass model gives the respective redshifts: $4.85^{+1.52}_{-0.70}$, $3.76^{+1.57}_{-0.80}$, $3.63^{+1.67}_{-0.74}$ and $3.57^{+0.35}_{-1.08}$.

Similarly to MACS J0242, we model the mass distribution of the cluster scale halo and the BCG galaxy separately. The best-fit mass model parameters are listed in Table 7, and gives a *rms* of 0.15″. The addition of an external shear component does not improve the mass model, and gives a *rms* of 0.16″. In a similar fashion to MACS J0242, although the degeneracy between the cluster scale halo and the BCG is still present, the BCG optimisation converges. The *rms* is particularly small which may be explained by the lack of constraints in our model. Indeed, as shown in e.g. Johnson & Sharon (2016), a larger number of constraints may increase the value of the *rms* but could also improve the accuracy of the model. Similarly to MACS J0242, we compute integrated and 3D masses for MACS J0949. These are listed in Table 9 and discussed further in Sect. 6.

We compare our model of MACS J0949 to the two publicly available models from the RELICS collaboration[5]. Comparing the surface density profiles, we find a 1σ agreement between the model presented in this article and the `Lenstool` RELICS model as can be seen in Fig. 6. As for the RELICS model obtained using the `Glafic` lensing algorithm (presented in Oguri 2010), its density profile is in agreement with our model, although the most stringent constraints (in the $R \in [40, 100]$ kpc region) yield a slightly smaller surface density. The overall profile from the `Lenstool` RELICS public release model presents a flatter density profile and an excess in mass after 80 kpc (coincidental with the Einstein radius of system 1). This could be partially explained by the more massive structure

[5] https://archive.stsci.edu/prepds/relics/

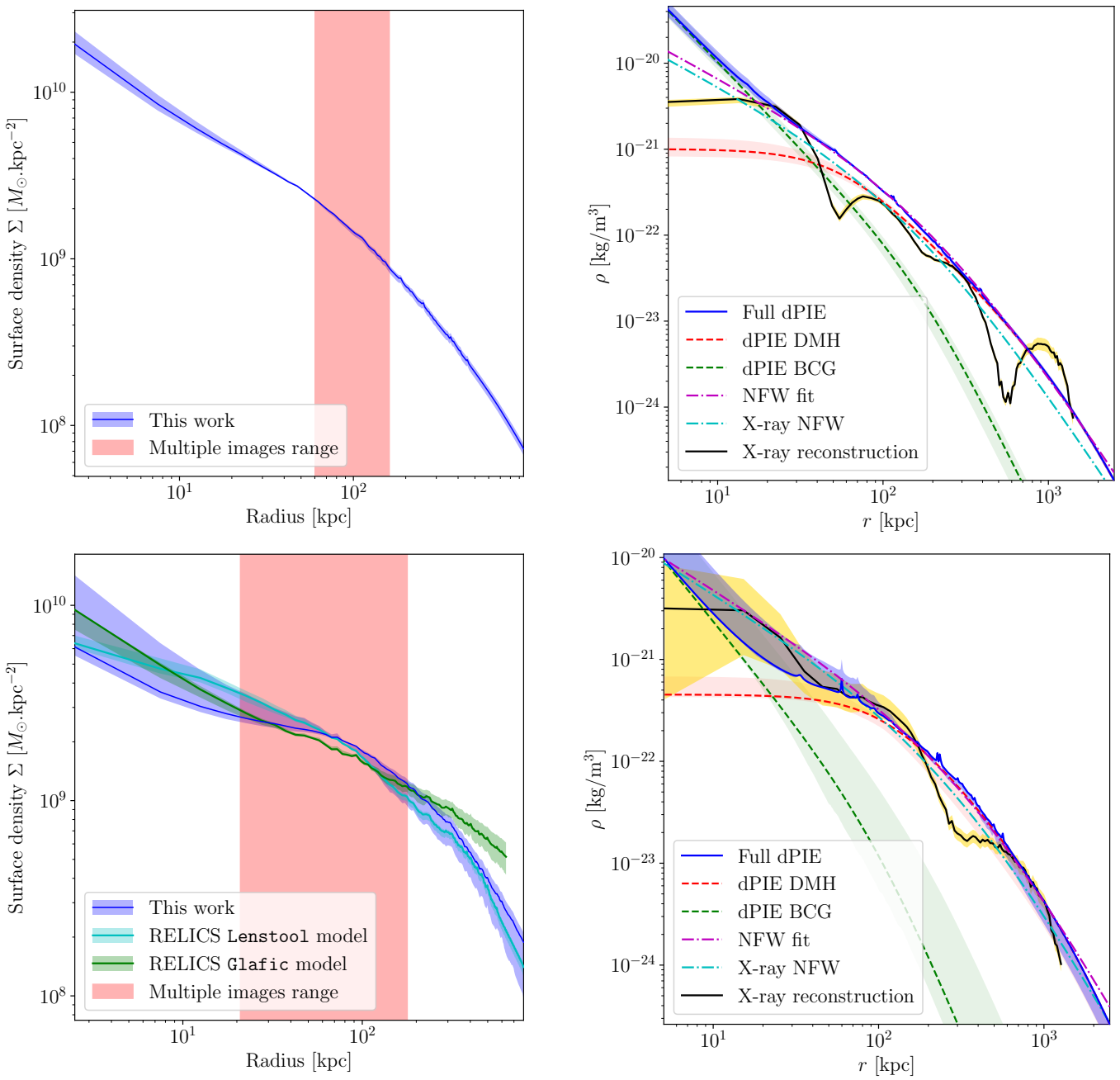

Figure 6. *Top row*: Cluster MACS J0242. *Left panel:* Surface mass density profile derived from the best-fit mass model. Shaded regions show the 68% confidence interval. We display in red the range of the multiple images, and thus the regions in which the constraints are the most stringent. – *Right panel:* Volume mass density. The reconstruction of the *XMM-Newton* observations are shown in black, given with 1σ error bars in yellow. The green and red curves – with error bars – represent respectively the BCG and DM halo reconstructions, and the full cluster is shown in blue. The magenta dashed line represents the NFW fit of the total density from `Lenstool` reconstruction – all galaxies and DM halo. The cyan line shows the fit to the X-ray data. *Bottom row*: Cluster MACS J0949. *Blue:* Our model, with 68% confidence interval. *Cyan:* `Lenstool` model from RELICS. We note that error bars were obtained on a different sample (2,000 realisations for our model, 100 for RELICS). *Green:* `Glafic` RELICS model, realised under the same conditions. *Red:* region of the multiple images constraints.

– *Right panel:* Volume mass density. The reconstruction of the *XMM-Newton* data is shown in black, given with 1σ error bars in yellow. The green and red curves represent respectively the BCG and DM halo reconstruction, and the full cluster is shown in blue. The magenta dashed line represents the NFW fit to the `Lenstool` reconstruction. The cyan line shows the fit to the X-ray data.

in the South of the cluster, which is slightly offset from the South bright galaxy surrounded by systems 4, 5, and 6 as mentioned before ($M_{2D}(< 100\,\mathrm{kpc}) = 13.02 \times 10^{12} M_\odot$ compared to $M_{2D}(< 100\,\mathrm{kpc}) = 7.65 \times 10^{12} M_\odot$ for our model). We report a very good agreement between the measured spectroscopic redshift obtained from MUSE observations with the photo-z used by the RELICS team (obtained through private communication with K. Sharon). Our model presents a significantly lower *rms* of $0.15''$, in comparison to $0.58''$.

The reconstructed mass distribution appears to be more elliptical than the X-ray surface brightness obtained with *XMM-Newton* as shown in Fig. 2. The 3D density profile is presented in Fig. 6. It confirms the inflexion point in the density profile at $r \simeq 100\,\mathrm{kpc}$,

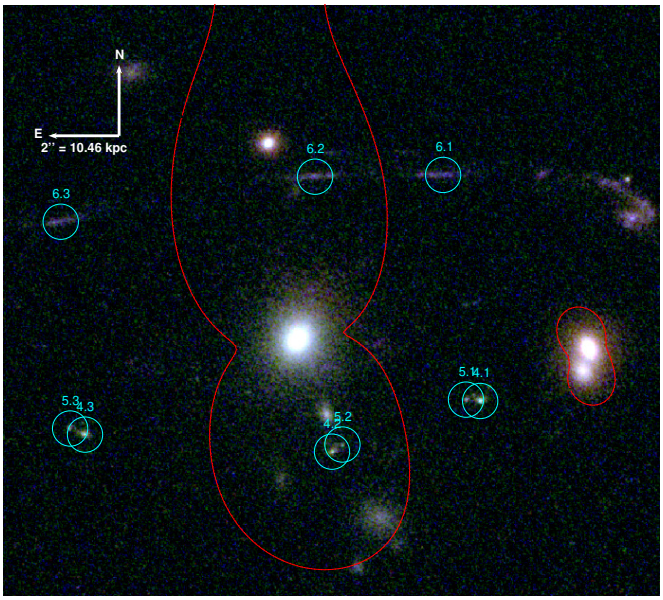

Figure 7. Composite colour *HST* image of the Southern clump in MACS J0949. In cyan, we highlight the positions of the multiple images identified with *HST*, and listed in Table 8. The external/tangential critical lines for a source at redshift $z = 3.65$ are represented in red – this redshift being compatible with sources 4, 5 and 6, according to the best fit optimisation.

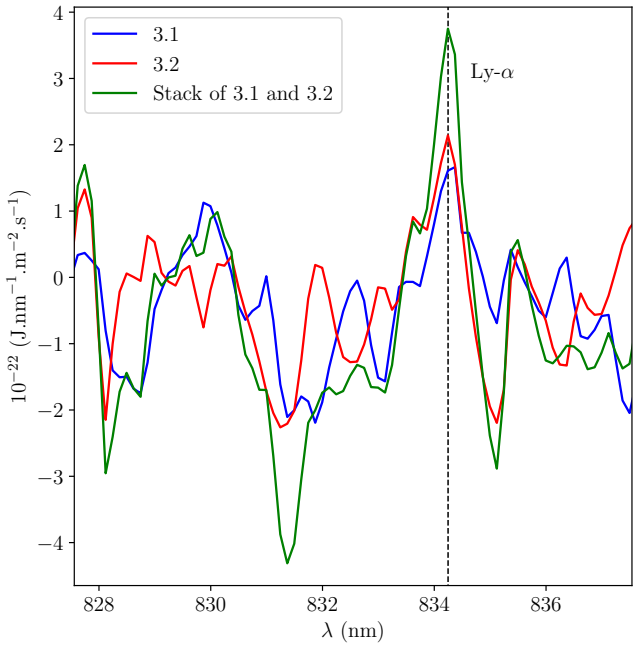

Figure 8. Spectra of images 3.1 and 3.2 of cluster MACS J0949 obtained by VLT/MUSE. We can observe a faint signal, possibly Ly-α. *Blue*: spectrum of 3.1; *Red*: spectrum of 3.2; *Green*: summed spectra. The redshift measured would be of 5.8658. However, the confidence level of our measurements is low due to high sky noise at this wavelength.

Table 8. List of the multiple images detected with VLT/MUSE in MACS J0949. We here list their ID, coordinates, R.A. and Decl. given in degrees (J2000), and their measured spectroscopic redshift z. Values within brackets were obtained after `Lenstool` redshift optimisation.

Id.	R.A.	Dec.	z
1.1	147.4683753	17.11409360	4.8902
1.2	147.4738000	17.11754490	4.8902
1.3	147.4561230	17.11911410	4.8902
1.4	147.4687438	17.12369520	4.8902
1.5	147.4668972	17.12016960	4.8902
2.1	147.4687829	17.11396160	4.8844
2.2	147.4735428	17.11690610	4.8844
2.3	147.4560463	17.11877380	4.8844
2.4	147.4685346	17.12338060	4.8844
3.1	147.4702800	17.11513600	$[4.85^{+1.52}_{-0.70}]$
3.2	147.4714400	17.11579400	$[4.85^{+1.52}_{-0.70}]$
4.1	147.4630587	17.10291430	$[3.76^{+1.57}_{-0.80}]$
4.2	147.4642781	17.10251570	$[3.76^{+1.57}_{-0.80}]$
4.3	147.4663104	17.10264970	$[3.76^{+1.57}_{-0.80}]$
5.1	147.4631754	17.10292500	$[3.63^{+1.67}_{-0.74}]$
5.2	147.4641921	17.10257190	$[3.63^{+1.67}_{-0.74}]$
5.3	147.4664329	17.10269780	$[3.63^{+1.67}_{-0.74}]$
6.1	147.4633639	17.10469208	$[3.57^{+0.35}_{-1.08}]$
6.2	147.4644174	17.10467818	$[3.57^{+0.35}_{-1.08}]$
6.3	147.4665100	17.10432399	$[3.57^{+0.35}_{-1.08}]$

and therefore suggests that the cluster is still undergoing a relaxing phase. The NFW profile fit in the $r \in [20, 1000]$ kpc region yields NFW parameters $\rho_S = 1.23 \times 10^{-22}$ kg.m^{-3}, $r_S = 405.5$ kpc, for a reduced $\chi^2 = 1.90$. The quality of this fit is thus not comparable to that of cluster MACS J0242, mostly due to the flatter density profile in the $R \in [40, 100]$ kpc region.

Looking at the galaxy distribution within the cluster, we observe four bright and massive galaxies, of comparable magnitude to the BCG[6]. We could extrapolate all of these bright galaxies to have been the BCG of former galaxy clusters, which would have merged with MACS J0949 in the past. However, the X-ray observations show a diffuse emission centred on the BCG and thus do not provide any evidence of recent merger events. Therefore, our analysis strongly suggests a unique dominant cluster scale dark matter component. Nonetheless, we stress that the magnitude gap between the BCG and the second-brightest cluster galaxy in MACS J0242 is much larger than in MACS J0949. According to Trevisan & Mamon (2017), this is an additional argument to claim that the former cluster is more relaxed, and that MACS J0949 went through a recent merging event.

Our interpretation of the dynamical state of MACS J0949 and its lensing power could be further constrained with additional spectroscopic or imaging observations. The clear identification of the spectroscopic redshift of system 3, and of additional systems would particularly assist constraining the dark matter halo ellipticity, core radius and velocity dispersion.

[6] The maximum magnitude separation between these five galaxies being 0.29 on the reference band ACS/F814W.

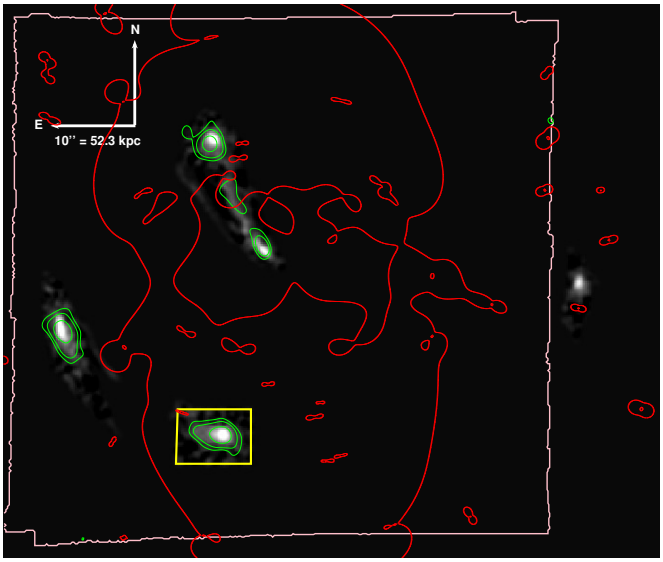

Figure 9. MACS J0949 reconstruction of the full image plane of system 1 from the unique extended emission images 1.1 and 2.1. Their region, highlighted with the yellow box is cut out and deprojected into the source plane, and casted back in the image plan to produce the full system. We clearly observe a continuous emission between the North-East image 1.4 and the central one 1.5. We display in green the contours of the Ly-α extended emission from the VLT/MUSE narrow-band image centred at 715.869 nm and 1.625 nm wide, showing the four detected multiple images of system 1, and three of system 2 (see Fig. 2 for more details). The last images 1.3 and 2.3 of these systems are located outside of the VLT/MUSE field of view. The critical lines are displayed in red, for redshift $z = 4.8902$ of system 1. The pink overlay represents the MUSE narrow-band contours.

5.1.3 Relensing in MACS J0949

On Fig. 9, we display the extracted emission of images 1.1 and 2.1 detected in MACS J0949 from the MUSE narrow-band centred on $\lambda = 715.869$ nm within a yellow box. In order to verify the robustness of the lensing model of MACS J0949, we then infer the emission in the source plane ($z = 4.8902$), before projecting it back to the image plane with our lens model, to obtain a re-lensed prediction.

The other multiple images on the MUSE field, 1.2, 1.4, 1.5, 2.2 and 2.4 are correctly predicted. Their Lyman-α detections are also listed in Table 8. Images 1.4 and 1.5 emission appear to be connected. This is simply due to the extended source emission of system 1 and 2, as a number of faint multiple images of system 2 are predicted between 1.4 and 1.5, in agreement to the MUSE observations on the narrow-band.

5.2 Stellar mass estimate

The strong lensing analyses are giving us an estimate of the total mass enclosed in each clusters.

We further compare our strong lensing mass with an estimate stellar mass. We use the reference cluster members catalogue magnitudes described in Sect. 3, converted into K-band luminosity L_K[7], and use it as a proxy for stellar mass. For the scaling relations we refer the reader to Hogg et al. (2002); Lin et al. (2006). These catalogues were established over the entire observable clusters, although the faintest galaxies were cut out beyond distances of 40″ from the centre.

[7] We take the K-band reference here to be the KPNO Flamingos Ks filter.

Once the L_K catalogue established, we adapt the Salpeter initial mass function, and use the mass-to-light relationship for red quiescent galaxies derived by Arnouts, S. et al. (2007) on the SWIRE-VVDS-CFHTLS surveys, based on the Bruzual & Charlot (2003) stellar population models:

$$\log_{10}\left[\frac{M_\star}{M_\odot}\frac{L_\odot}{L_K}\right] = az + b, \tag{2}$$

given the parameters $\{a, b\} = \{-0.18 \pm 0.04, +0.07 \pm 0.04\}$. While we acknowledge our studied clusters are within a redshift range presenting large uncertainties in the relationship presented in Arnouts, S. et al. (2007, see Fig. 9), we refer the reader to the detailed comparison made in Appendix D, Fig. 28 of Ilbert et al. (2010). Although the former appears to overestimate the stellar mass by an average 0.2 dex for red sequence galaxies, it also appears to be reasonably well calibrated for $z \in [0.3, 0.4]$. We present the inferred stellar masses for both clusters in Table 9.

In order to have a theoretical reference, we compare our estimates with the stellar mass predicted using the formula derived by Giodini et al. (2009). This relationship, established for poor clusters, with redshifts $0.1 \leq z \leq 1$, relates the total mass of the cluster to its stellar fraction ($M_\star/M_{500}$ here) using the relation:

$$f^\star_{500} = 0.05^{+0.001}_{-0.001}\left(\frac{M_{500}}{5\times10^{13}M_\odot}\right)^{-0.37\pm0.04}. \tag{3}$$

Let us notice the high ($\sim 50\%$) logarithmic scatter in the data fitting this relationship. As this relationship was established using X-ray measurements of M_{500}, and that strong lensing is not a direct probe of this value, we use the NFW reconstruction obtained through X-ray for the M_{500} values (see Fig. 6).

For MACS J0242, the field of view considered is quite large (DES: 182″), as we consider all galaxy in *HST*/WFPC2 or DES, and thus our cluster member catalogue is assumed to be relatively complete. We measure a stellar mass $M_\star = (6.484 \pm 0.615) \times 10^{12} M_\odot$ for MACS J0242. Let us notice these error bars are only associated to the error on the measured magnitude and the parameters a and b eq. (2). We obtain a difference between our measured value and the predicted value of $M_{\star,\mathrm{Giodini}} = (8.332 \pm 1.128) \times 10^{12} M_\odot$. We may explain this discrepancy by the variable conditions for selecting a galaxy within the galaxy catalogue. Indeed, the field of view being different between WFPC2, ACS and DES, as well as the poorer imaging quality of the latter instrument, we expect our error bars to be far larger than those computed given the error on the measured magnitude.

For MACS J0949, we require that a galaxy is detected in either *HST*/ACS or *HST*/WFC3 to include it in the final catalogue. Because the field of view of WFC3 is smaller than that of ACS, a large number of selected cluster member galaxies are weakly constrained, as ACS only contains two bands here. This method is adapted to our lensing analysis, the main goal of this paper, as galaxies far from the cluster centre are particularly important to constrain the southern halo. However, when considering the stellar content of the cluster, we might be selecting too many galaxies. Our analysis yields $M_\star = (1.392 \pm 0.137) \times 10^{13} M_\odot$. Similarly to MACS J0242, we compare our measurement with the predicted value following the Giodini et al. (2009) formula. We obtain a stellar mass $M_{\star,\mathrm{Giodini}} = (1.369 \pm 0.302) \times 10^{13} M_\odot$. This difference, however small, can give us an estimate of the overestimation of our cluster member catalogue. We summarise the estimated stellar fractions for both clusters, $f^\star_{500} = M_\star/M_{500}$, as well as the predicted values with the Giodini et al. (2009) formula in Table 10.

Table 9. Mass and radius measurements for MACS J0242 and MACS J0949. All error bars show a 68% confidence interval. We here list $M_\star$, the stellar mass, $M_{2D}(R < 200\,\mathrm{kpc})$, the mass distribution obtained in projection on the plane of the cluster, within a radius of 200 kpc, and M_Δ and R_Δ, defined in eq. (1). Masses are given in $10^{14} M_\odot$ and distances in kpc. The X-ray masses are following the NFW fit.

	MACS J0242		MACS J0949	
Mass ($10^{14} M_\odot$)	Lensing	X-ray	Lensing	X-ray
$M_\star$	0.065 ± 0.006		0.139 ± 0.014	
$M_{2D}(R < 200\mathrm{kpc})$	$1.667^{+0.032}_{-0.052}$	$1.163^{+0.036}_{-0.039}$	$1.996^{+0.051}_{-0.199}$	$1.635^{+0.065}_{-0.072}$
M_{2500}	$3.113^{+0.160}_{-0.200}$	$1.875^{+0.070}_{-0.069}$	$5.621^{+0.122}_{-0.942}$	$3.439^{+0.281}_{-0.266}$
M_{1000}	$4.628^{+0.289}_{-0.342}$	$2.695^{+0.122}_{-0.121}$	$8.848^{+0.000}_{-2.215}$	$5.547^{+0.778}_{-0.693}$
M_{500}	$5.954^{+0.400}_{-0.455}$	$3.379^{+0.168}_{-0.168}$	$11.483^{+0.000}_{-3.417}$	$7.429^{+1.310}_{-1.137}$
M_{200}	$7.748^{+0.538}_{-0.598}$	$4.343^{+0.238}_{-0.237}$	$14.790^{+0.000}_{-4.824}$	$10.165^{+2.234}_{-1.799}$
	MACS J0242		MACS J0949	
Radius (kpc)	Lensing	X-ray	Lensing	X-ray
R_{2500}	$541.2^{+9.1}_{-11.9}$	466^{+5}_{-6}	$641.7^{+4.6}_{-38.1}$	555^{+15}_{-15}
R_{1000}	$838.3^{+17.1}_{-21.2}$	713^{+11}_{-11}	$1013.2^{+0.0}_{-92.8}$	884^{+39}_{-39}
R_{500}	$1148.7^{+25.2}_{-30.1}$	969^{+16}_{-16}	$1392.4^{+0.0}_{-154.6}$	1227^{+68}_{-66}
R_{200}	$1702.0^{+38.5}_{-45.0}$	1430^{+26}_{-27}	$2056.1^{+0.0}_{-253.5}$	1849^{+126}_{-116}

Table 10. Comparison between the star fractions $f^\star_{500} = M_\star / M_{500}$ measured with this work, and the predictions from the Giodini et al. (2009) formula. M_{500} is taken to be the NFW X-ray extrapolated value. All results are in percentage.

$f^\star_{500}$ (%)	MACS J0242	MACS J0949
This work	1.919 ± 0.205	1.873 ± 0.360
Prediction	2.466 ± 0.334	1.842 ± 0.407

5.3 X-ray analysis

5.3.1 Analysis procedure

We used the X-COP analysis pipeline (Ghirardini et al. 2019) to analyse the data and compute the hydrostatic mass profiles of the two systems. We extracted X-ray photon images in the [0.7-1.2] keV band, which maximises the signal-to-background ratio. To estimate the non X-ray background, we used the unexposed corners of the MOS detectors to estimate the cosmic-ray-induced flux at the time of the observations. The difference between the scaled high-energy count rates inside and outside the field of view were then used to estimate the residual soft proton contribution, which was next modelled following the method described in Ghirardini et al. (2018). To determine the spectroscopic temperature profile of the two systems, we extracted spectra in logarithmically spaced concentric annuli centred on the surface brightness peak. The sky background emission was measured in regions located well outside of the cluster's virial radius and described by a three-component model including the cosmic X-ray background, the local hot bubble, and the galactic halo. The sky background spectrum was then rescaled appropriately to the source regions and added as an additional model component. Finally, the source spectrum was modelled by a single-temperature APEC model (Smith et al. 2001) absorbed by the Galactic N_H, which was fixed to the HI4PI value (HI4PI Collaboration et al. 2016).

5.3.2 Hydrostatic mass reconstruction

We used the publicly available Python package `hydromass`[8] (Eckert et al. 2022) to deproject the X-ray data and recover the mass under the hypothesis of hydrostatic equilibrium. The X-ray surface brightness and spectroscopic temperature profiles are fitted jointly using a NFW profile to recover the X-ray mass profile. The technique employed here is similar to the method described in Ettori et al. (2019), in which the gas density profile and the parametric mass profile are used to integrate the hydrostatic equilibrium equation and predict the 3D pressure and temperature profiles. The 3D temperature profile is then projected along the line of sight using spectroscopic-like weights (Mazzotta et al. 2004) and adjusted onto the observed spectroscopic temperature profile. The model temperature and gas density profiles are convolved with the *XMM-Newton* PSF to correct for the smearing introduced by the telescope's spatial resolution, in particular in the cluster's central regions.

5.3.3 MACS J0242

MACS J0242 exhibits all the features of a relaxed, cool-core cluster. Its X-ray morphology is regular and it shows a pronounced surface brightness peak, a central temperature drop, and a metal abundance peak in its core. The dynamical state of the cluster is best gauged from the X-ray emission, but the optical emission lines of the BCG is an additional, relatively faithful tracer of the presence of a cool core. The NFW mass reconstruction returns a mass

[8] https://github.com/domeckert/hydromass

$M_{500} = (3.4 \pm 0.2) \times 10^{14}\,M_\odot$. In order to compare it directly to the lensing mass where multiply imaged systems yield important constraints, we project the NFW density in 2D, and compute $M_{2D}(< 200\,\mathrm{kpc}) = 1.163^{+0.036}_{-0.039} \times 10^{14} M_\odot$. For an average temperature of 4.5 keV, this is in agreement with the expectations of mass-temperature relations (e.g. Lovisari et al. 2020). The cluster appears to be highly concentrated, with a fitted NFW concentration $c_{200} = 8.2 \pm 0.5$. At 200 kpc, X-ray observations suggest the gas fraction to be $f_{g,200\,\mathrm{kpc}} = 0.115^{+0.003}_{-0.004}$. The ellipticity of the cluster obtained with our lensing mass model is not recovered by the X-ray analysis, as it presents a spherical surface brightness. The ICM has its own dynamics and thus is not expected to present a similar ellipticity to the total density of matter. The discrepancy between the ICM and DM halo ellipticity is documented in e.g. (Lee & Suto 2003; Debattista et al. 2008; Lau et al. 2012; Umetsu et al. 2018; Stapelberg et al. 2022). It stems from the collisional character of baryons, allowing the ICM to geometrically relax faster than the cold dark matter halo counterpart, non-collisional.

5.3.4 *MACS J0949*

MACS J0949 exhibits a regular X-ray morphology with no obvious large substructure. However, its brightness distribution is relatively flat, it shows a high central entropy and central cooling time, and no temperature drop in its core. Therefore, MACS J0949 is not a relaxed cool-core cluster, but its regular morphology indicates that it is not strongly disturbed either. Such properties are typical of post-merger clusters in the process of relaxation after a merging event. The hydrostatic mass profile is well described by an NFW model with $c_{200} = 5.3^{+1.3}_{-1.0}$ and $M_{500} = 7.4^{+1.4}_{-1.2} \times 10^{14} M_\odot$. The NFW projected mass yields $M_{2D}(< 200\mathrm{kpc}) = 1.635^{+0.065}_{-0.072} \times 10^{14} M_\odot$. Its hydrostatic gas fraction $f_{g,500} = 0.155^{+0.016}_{-0.014}$ is consistent with the Universal baryon fraction (Ade et al. 2016). At 200 kpc, the same gas fraction is measured at $f_{g,200\,\mathrm{kpc}} = 0.053^{+0.007}_{-0.006}$. Similarly to MACS J0242, the X-ray signal does not present any ellipticity.

6 DISCUSSION & CONCLUSION

In order to reconstruct the mass distribution of strong lensing galaxy clusters MACS J0242 and MACS J0949, we have used the combination of imaging (*HST*, DES) and spectroscopic (VLT/MUSE) surveys to detect respectively 6 and 2 spectroscopically confirmed multiple image systems. Adding to that, in MACS J0949, we identified four multiply imaged systems, without a confirmed spectroscopic redshift – the spectroscopic emission line not fitting spectral templates convincingly enough, or the images being out of the VLT/MUSE field of view. The imaging data, calibrated with the spectroscopic detections of cluster members, allowed to establish conservative cluster galaxy catalogues, of respectively 58 and 170 galaxies for MACS J0242 and MACS J0949. We then established the strong lensing mass models of both galaxy clusters. We modelled each individual galaxy with a dPIE profile, and included for each cluster a dPIE cluster-scale halo. We present our main results as follows:

(i) The *rms* on the multiple image positions for the best-fit models are respectively of 0.39″ and 0.15″, which is considered as a good quality indicator of the reconstruction. We found that adding a shear-field does not improve the quality of the reconstruction. We note that degeneracies between the BCG and the dark matter halo could hinder the lens model optimisations, and could thus affect our conclusion regarding the morphology of the dark matter distribution in these clusters (see e.g. Limousin et al. 2016).

(ii) Using *XMM-Newton* X-ray observations from CHEX-MATE Collaboration et al. (2021), processed with the X-COP pipeline Ghirardini et al. (2019), we compare the ICM to the reconstructed dark matter density. The combination of the lensing mass reconstructions with the X-ray analyses of the ICM and the VLT/MUSE spectroscopy shows that MACS J0242 is in a cool-core, relaxed dynamical state, compatible with a NFW profile, while MACS J0949 has a flat distribution between radii of 50 to 100 kpc because it is still undergoing the relaxing process, being in a post-merger dynamical state. In particular, the hot gas fractions at 200 kpc of MACS J0242 and MACS J0949 are $f_{g,200\,\mathrm{kpc}} = 0.115^{+0.003}_{-0.004}$ and $0.053^{+0.007}_{-0.006}$ respectively. We can for instance compare these results to those of Bonamigo et al. (2018). In Fig. 6, the authors present the cumulative hot gas fraction of each of the three clusters analysed. MACS J0416 is presented as a merging cluster, while MACS J1206 and Abell S1063 (RXC J2248) show a cool-core. These clusters have $f_{g,200\,\mathrm{kpc}} \simeq 0.09$, 0.11 and 0.13 respectively, thus exhibiting the trend of more relaxed clusters displaying higher hot gas fraction values at 200 kpc. This is an additional indication of the relaxed dynamical state of MACS J0242, and the post-merger state of MACS J0949.

(iii) Converting the cluster member catalogue magnitudes into K-band luminosities, we used the Arnouts, S. et al. (2007) mass-to-light ratio relationship to extrapolate the stellar mass detected in both clusters. SED fitting should be performed to obtain a more precise measurement, but this is beyond the scope of this paper. We compare the obtained stellar masses of $M_\star = (6.48 \pm 0.62) \times 10^{12} M_\odot$ and $(1.39 \pm 0.14) \times 10^{13} M_\odot$ for MACS J0242 and MACS J0949 respectively to the predictions of Giodini et al. (2009), yielding respectively $(8.33 \pm 1.13) \times 10^{12} M_\odot$ and $(1.37 \pm 0.30) \times 10^{13} M_\odot$. Although not identical in the case of MACS J0242, this means our stellar mass estimates appear to be reasonable.

(iv) We fit the *XMM-Newton* observations to a NFW profile. Projecting this reconstruction, we can measure $M_{2D}(< 200\,\mathrm{kpc})$, allowing for a direct comparison with the strong lensing model mass estimates. For MACS J0242, we measure $M_{2D}(< 200\,\mathrm{kpc}) = (1.16 \pm 0.04) \times 10^{14} M_\odot$ from the X-rays, to be compared to $1.67^{+0.03}_{-0.05} \times 10^{14} M_\odot$ obtained from our strong lensing analysis. We obtain a sizeable 12.75σ difference between these two values. Discrepancies between the X-ray hydrostatic and lensing masses are common, and may be explained by the hydrostatic hypothesis bias, or by the presence of asymmetric structures along the line-of-sight. In the former case, the gas is not perfectly relaxed, and the thermal pressure only accounts for a fraction of the gravitational pressure. Thus, the hydrostatic mass would underestimate the true mass. Moreover, if there is a distribution of substructures or an elongation of the dark matter component along the line-of-sight, the projected lensing mass may overestimate the 3D mass. For instance, Umetsu et al. (2015) display a combination of both these scenarios.

(v) As for MACS J0949, we measure $M_{2D}(< 200\,\mathrm{kpc}) = (1.64 \pm 0.07) \times 10^{14} M_\odot$ with the X-rays, to be compared with $2.00^{+0.05}_{-0.20} \times 10^{14} M_\odot$ obtained with the strong lensing analysis. These values differ by 3.85σ. The `Lenstool` and `Glafic` RELICS strong lensing models provide $M(R < 200\,\mathrm{kpc}) = 1.84^{+0.03}_{-0.03} \times 10^{14} M_\odot$ and $M(R < 200\,\mathrm{kpc}) = 1.85^{+0.08}_{-0.07} \times 10^{14} M_\odot$ respectively, in good agreement with our model. At last, we compare this latter value to the one obtained with the *Planck* SZ data of $M_{2D}(< 200\,\mathrm{kpc}) = 1.59^{+0.38}_{-0.00} \times 10^{14} M_\odot$ (see Fox et al. 2022), assuming a NFW profile. This 1.49σ difference with the strong lensing value outlines a good agreement with our model.

In order to compare cylindrical masses, we define $R_{10\%} = 0.1R_{200,c}$. For MACS J0242, with $R_{10\%} = 170.2^{+0.39}_{-0.45}$ kpc, we obtain $M_{2D}(< R_{10\%}) = (1.41 \pm 0.03) \times 10^{14} M_\odot$ with our strong lensing analysis (for which M_{200} is extrapolated). With $R_{10\%} = 143.0^{+2.7}_{-2.6}$ kpc, we get $M_{2D}(< R_{10\%}) = (8.06 \pm 0.21) \times 10^{13} M_\odot$ with the X-rays NFW inferred profile, yielding ratios of $M_{2D}(< R_{10\%})/M_{200,c} = 0.181 \pm 0.014$ and 0.186 ± 0.012 respectively. This allows us to characterise the ratios of masses measured in the centre and in the outskirts as quite close for X-ray and lensing, in spite of the remarkable difference between the mass measurements. As the strong lensing inferred M_{200} mass obtained here is an extrapolation at larger radii of a profile based on gravitational lensing occurring at $R < 200$ kpc, we cannot claim the strong lensing ratios to be firmly established. Nonetheless, the extrapolated lensing distribution appears to follow a profile similar to that of the X-rays, at different masses. We can compare this result to the ratios found by Bonamigo et al. (2018) for three clusters exhibiting varied dynamical states (Abell S1063, MACS J0416 and MACS J1206), all around 0.13. Let us notice this study uses three to four potentials across all clusters, and thus our models should be expected to yield larger ratios of core-to-outskirts densities. Moreover, as this comparison uses M_{200} values from weak-lensing shear-and-magnification analyses (see Umetsu et al. 2014), we can only cautiously compare it to our X-rays and extrapolated strong lensing measurements. As the ratio is much higher for MACS J0242, this comparison is one more indication that the concentration of mass in the centre of MACS J0242 is particularly high relative to its total mass. This is in good agreement with our conclusion of the cluster being in a cool-core, relaxed dynamical state.

In the case of MACS J0949, the cylindrical mass at $R_{10\%} = 205.6^{+0.00}_{-25.4}$ is $M_{2D}(< R_{10\%}) = (2.07 \pm 0.14) \times 10^{14} M_\odot$ using our strong lensing measurements, and with $R_{10\%} = 184.9^{+12.6}_{-11.6}$, $M_{2D}(< R_{10\%}) = (1.48 \pm 0.05) \times 10^{14} M_\odot$ with the X-rays NFW inferred profile. The respective ratios are 0.140 ± 0.025 and 0.146 ± 0.029. For this cluster again, we notice these ratios to be quite close to one another, supporting the quality of the strong lensing M_Δ extrapolation in spite of the large difference between the X-rays and strong lensing measured masses. Interestingly, the comparison with the 0.13 ratio from Bonamigo et al. (2018) hints towards a relative concentration of mass slightly more important in MACS J0949.

As we have established through strong lensing models the total matter density distribution in two galaxy clusters, we laid the foundations of our companion paper (Allingham et al. in prep.). In this forthcoming paper, we describe a new method using analytical models of galaxy cluster potentials to predict the ICM distribution, and in the foreseeable future to put constraints on interacting dark matter.

ACKNOWLEDGEMENTS

JA would like to thank Markus Mosbech for comments and discussions. JA is supported by the International Postgraduate Research Scholarship in Astroparticle Physics/Cosmology at the University of Sydney. MJ and DJL are supported by the United Kingdom Research and Innovation (UKRI) Future Leaders Fellowship 'Using Cosmic Beasts to Uncover the Nature of Dark Matter' (grant number MR/S017216/1). DJL is partially supported by ST/T000244/1 and ST/W002612/1. The authors acknowledge the Sydney Informatics Hub and the use of the University of Sydney high performance computing cluster, Artemis. This work is based on observations taken by the RELICS Treasury Program (GO 14096) with the NASA/ESA HST, which is operated by the Association of Universities for Research in Astronomy, Inc., under NASA contract NAS5-26555. GM acknowledges funding from the European Union's Horizon 2020 research and innovation programme under the Marie Skłodowska-Curie grant agreement No MARACHAS - DLV-896778. ACE acknowledges support from STFC grant ST/P00541/1.

DATA AVAILABILITY

The galaxy and spectroscopic detections catalogues and the lens models are available upon reasonable request to the corresponding author.

References

Abbott T. M. C., et al., 2018, The Astrophysical Journal Supplement Series, 239, 18
Ade P. A. R., et al., 2016, Astronomy & Astrophysics, 594, A13
Arnouts, S. et al., 2007, A&A, 476, 137
Bacon R., et al., 2014, The Messenger, 157, 13
Bacon R., Piqueras L., Conseil S., Richard J., Shepherd M., 2016, MPDAF: MUSE Python Data Analysis Framework (ascl:1611.003)
Bergamini P., et al., 2019, A&A, 631, A130
Bertin E., Arnouts S., 1996, A&AS, 117, 393
Bonamigo M., et al., 2018, ApJ, 864, 98
Bradač M., Allen S. W., Treu T., Ebeling H., Massey R., Morris R. G., von der Linden A., Applegate D., 2008, ApJ, 687, 959
Bruzual G., Charlot S., 2003, MNRAS, 344, 1000
CHEX-MATE Collaboration et al., 2021, A&A, 650, A104
Caminha G. B., et al., 2017, A&A, 607, A93
Caminha G. B., et al., 2019, A&A, 632, A36
Chang C., et al., 2018, ApJ, 864, 83
Clowe D., Gonzalez A., Markevitch M., 2004, ApJ, 604, 596
Coe D., et al., 2019, ApJ, 884, 85
Debattista V. P., Moore B., Quinn T., Kazantzidis S., Maas R., Mayer L., Read J., Stadel J., 2008, ApJ, 681, 1076
Diego J. M., Broadhurst T., Molnar S. M., Lam D., Lim J., 2015a, MNRAS, 447, 3130
Diego J. M., Broadhurst T., Zitrin A., Lam D., Lim J., Ford H. C., Zheng W., 2015b, MNRAS, 451, 3920
Diego J. M., Broadhurst T., Wong J., Silk J., Lim J., Zheng W., Lam D., Ford H., 2016, MNRAS, 459, 3447
Diego J. M., et al., 2018, MNRAS, 473, 4279
Diego J. M., et al., 2020, ApJ, 904, 106
Ebeling H., Edge A. C., Henry J. P., 2001, ApJ, 553, 668
Eckert D., Ettori S., Pointecouteau E., van der Burg R. F. J., Loubser S. I., 2022, A&A, 662, A123
Elíasdóttir Á., et al., 2007, arXiv e-prints, p. arXiv:0710.5636
Ettori S., et al., 2019, A&A, 621, A39
Faber S. M., Jackson R. E., 1976, ApJ, 204, 668
Ford H. C., et al., 1998, in Bely P. Y., Breckinridge J. B., eds, Society of Photo-Optical Instrumentation Engineers (SPIE) Conference Series Vol. 3356, Space Telescopes and Instruments V. pp 234–248, doi:10.1117/12.324464
Fox C., Mahler G., Sharon K., Remolina González J. D., 2022, ApJ, 928, 87
Ghirardini V., Ettori S., Eckert D., Molendi S., Gastaldello F., Pointecouteau E., Hurier G., Bourdin H., 2018, A&A, 614, A7
Ghirardini V., et al., 2019, A&A, 621, A41
Giodini S., et al., 2009, The Astrophysical Journal, 703, 982
Gladders M. D., Yee H. K. C., 2000, The Astronomical Journal, 120, 2148–2162
Grillo C., et al., 2015, ApJ, 800, 38
Grillo C., et al., 2016, The Astrophysical Journal, 822, 78
HI4PI Collaboration et al., 2016, A&A, 594, A116

Hammer F., 1987, in Bergeron J., Kunth D., Rocca-Volmerange B., Tran Thanh Van J., eds, High Redshift and Primeval Galaxies. pp 467–473
Harvey D., Massey R., Kitching T., Taylor A., Tittley E., 2015, Science, 347, 1462–1465
Hinton S., Davis T. M., Lidman C., Glazebrook K., Lewis G., 2016, Astronomy and Computing, 15, 61–71
Hogg D. W., Baldry I. K., Blanton M. R., Eisenstein D. J., 2002, arXiv e-prints, pp astro–ph/0210394
Holtzman J. A., Burrows C. J., Casertano S., Hester J. J., Trauger J. T., Watson A. M., Worthey G., 1995, PASP, 107, 1065
Ilbert O., et al., 2010, ApJ, 709, 644
Jauzac M., et al., 2014, Monthly Notices of the Royal Astronomical Society, 446, 4132–4147
Jauzac M., et al., 2016a, MNRAS, 457, 2029
Jauzac M., et al., 2016b, MNRAS, 463, 3876
Jauzac M., et al., 2016c, Monthly Notices of the Royal Astronomical Society, 463, 3876–3893
Jauzac M., Harvey D., Massey R., 2018, MNRAS, 477, 4046
Jauzac M., et al., 2019, MNRAS, 483, 3082
Jauzac M., Klein B., Kneib J.-P., Richard J., Rexroth M., Schäfer C., Verdier A., 2021, MNRAS, 508, 1206
Johnson T. L., Sharon K., 2016, The Astrophysical Journal, 832, 82
Jullo E., Kneib J. P., Limousin M., Elíasdóttir Á., Marshall P. J., Verdugo T., 2007, New Journal of Physics, 9, 447
Kalirai J., MacKenty J., Bohlin R., Baggett S., Deustua S., Kimble R., Riess A., Sabbi E., 2009, Space Telescope WFC Instrument Science Report
Kassiola A., Kovner I., 1993, ApJ, 417, 450
Kneib J.-P., Natarajan P., 2011, The Astronomy and Astrophysics Review, 19
Kneib J. P., Ellis R. S., Smail I., Couch W. J., Sharples R. M., 1996, ApJ, 471, 643
Lagattuta D. J., et al., 2017, Monthly Notices of the Royal Astronomical Society, 469, 3946
Lagattuta D. J., et al., 2019, Monthly Notices of the Royal Astronomical Society, 485, 3738
Lau E. T., Nagai D., Kravtsov A. V., Vikhlinin A., Zentner A. R., 2012, ApJ, 755, 116
Lee J., Suto Y., 2003, ApJ, 585, 151
Limousin M., et al., 2016, A&A, 588, A99
Lin Y.-T., Mohr J. J., Gonzalez A. H., Stanford S. A., 2006, ApJ, 650, L99
Lotz J. M., et al., 2017, The Astrophysical Journal, 837, 97
Lovisari L., et al., 2020, ApJ, 892, 102
Mahler G., et al., 2017, Monthly Notices of the Royal Astronomical Society, 473, 663–692
Massey R., Kitching T., Nagai D., 2011, Monthly Notices of the Royal Astronomical Society, 413, 1709
Massey R., et al., 2015, MNRAS, 449, 3393
Massey R., et al., 2018, MNRAS, 477, 669
Mazzotta P., Rasia E., Moscardini L., Tormen G., 2004, MNRAS, 354, 10
Merten J., et al., 2011, MNRAS, 417, 333
Navarro J. F., Frenk C. S., White S. D. M., 1996, ApJ, 462, 563
Newman A. B., Treu T., Ellis R. S., Sand D. J., Nipoti C., Richard J., Jullo E., 2013a, The Astrophysical Journal, 765, 24
Newman A. B., Treu T., Ellis R. S., Sand D. J., 2013b, ApJ, 765, 25
Oguri M., 2010, glafic: Software Package for Analyzing Gravitational Lensing, Astrophysics Source Code Library, record ascl:1010.012 (ascl:1010.012)
Oke J. B., 1974, ApJS, 27, 21
Piqueras L., Conseil S., Shepherd M., Bacon R., Leclercq F., Richard J., 2017, MPDAF - A Python package for the analysis of VLT/MUSE data (arXiv:1710.03554)
Postman M., et al., 2012, The Astrophysical Journal Supplement Series, 199, 25
Richard J., et al., 2014a, MNRAS, 444, 268
Richard J., et al., 2014b, Monthly Notices of the Royal Astronomical Society, 444, 268–289
Richard J., et al., 2021, Astronomy & Astrophysics, 646, A83
Robertson A., Massey R., Eke V., 2016, Monthly Notices of the Royal Astronomical Society, 465, 569

Table A1. Spectroscopic detections of singly imaged objects in MACS J0242. Coordinates are in degrees (J2000). The reference for right ascension and declination are taken to be the centre of the cluster.

Id.	R.A.	Dec.	z
10	40.6559072	-21.5412424	0.5756
11	40.6536287	-21.5327925	0.5928
12	40.6546722	-21.5328188	0.5937
13	40.6466813	-21.5480705	0.5942
14	40.6517158	-21.5453613	0.5943
15	40.6566147	-21.5399484	0.5943
16	40.6552620	-21.5388619	0.7707
17	40.6551537	-21.5382257	0.7713
18	40.6407123	-21.5444971	0.8363
19	40.6508138	-21.5463873	0.8380
20	40.6457745	-21.5366071	3.1120

Table A2. Spectroscopic detections of singly imaged objects images in MACS J0949. Coordinates are in degrees (J2000). The reference for R.A. and declination are taken to be the centre of the cluster.

Id.	R.A.	Dec.	z
10	147.46989360	17.11231290	0.5841
11	147.46892360	17.12212680	0.6395
12	147.45946988	17.11584094	0.8472
13	147.46832980	17.11256280	0.8473
14	147.46913850	17.12435220	0.8488

Robertson A., Massey R., Eke V., 2017, Monthly Notices of the Royal Astronomical Society, 467, 4719
Schneider P., Ehlers J., Falco E. E., 1992, in Gravitational Lenses. Springer Berlin, Heidelberg, doi:10.1007/978-3-662-03758-4
Sereno M., Ettori S., Meneghetti M., Sayers J., Umetsu K., Merten J., Chiu I.-N., Zitrin A., 2017, Monthly Notices of the Royal Astronomical Society, 467, 3801–3826
Sharon K., et al., 2020, The Astrophysical Journal Supplement Series, 247, 12
Smith R. K., Brickhouse N. S., Liedahl D. A., Raymond J. C., 2001, ApJ, 556, L91
Soucail G., Mellier Y., Fort B., Mathez G., Cailloux M., 1988, A&A, 191, L19
Stapelberg S., Tchernin C., Hug D., Lau E. T., Bartelmann M., 2022, A&A, 663, A17
Steinhardt C. L., et al., 2020, The Astrophysical Journal Supplement Series, 247, 64
Tchernin C., et al., 2018, Astronomy & Astrophysics, 614, A38
Treu T., et al., 2016, ApJ, 817, 60
Trevisan M., Mamon G. A., 2017, MNRAS, 471, 2022
Tulin S., Yu H.-B., 2018, Physics Reports, 730, 1
Umetsu K., et al., 2014, ApJ, 795, 163
Umetsu K., et al., 2015, ApJ, 806, 207
Umetsu K., et al., 2018, ApJ, 860, 104
Williams L. L. R., Sebesta K., Liesenborgs J., 2018, MNRAS, 480, 3140

APPENDIX A: SPECTROSCOPIC DETECTIONS OF INTEREST

We present additional spectroscopic good detections in the background of both clusters MACS J0242 and MACS J0949, respectively in Tables A1 and A2. We present in Tables A3 and A4 (respectively for clusters MACS J0242 and MACS J0949) a few cluster members

Table A3. The brightest cluster members in the cluster MACS J0242. Coordinates are in degrees (J2000). We remind that the reference coordinates are (40.649555; −21.540485) deg. Magnitudes are given on the reference band ACS/F606W. All spectroscopic redshift detections are also provided.

Id.	Δ_α	Δ_δ	a	b	θ	Mag.	z
1	0.04387	−0.08964	1.886	1.499	1.83	17.765	0.3130
2	−31.28771	72.89640	1.027	0.396	2.34	19.898	_
3	59.25290	79.37028	0.595	0.593	−14.20	20.055	_
4	82.31906	−5.37408	0.829	0.501	23.90	20.081	_
5	−47.40417	−5.82480	0.731	0.410	−4.47	20.214	_

Table A4. Brightest cluster members in the MACS J0949. Coordinates are in degrees (J2000). We remind that the reference coordinates are (α_c, δ_c) = (147.4659012, 17.1195939). Magnitudes are given on the reference band ACS/F814W.

Id.	Δ_α	Δ_δ	a	b	θ	Mag.	z
1	−51.61743	−32.11128	1.344	0.709	45.31	18.761	_
2	0.05608	−0.15120	1.344	0.740	−57.20	18.789	0.3829
3	−17.02960	5.76108	0.704	0.657	60.72	18.875	0.3817
4	51.33490	121.06692	0.742	0.529	50.52	18.970	_
5	15.93092	−74.92248	0.812	0.526	−24.40	19.054	_

Table B1. Equations of the main colour sequences and standard deviations on colours for all colour-magnitude diagrammes of MACS J0242. m_1 represents the magnitude in abscissa. Associated graphs are Fig. 4 and B1.

Filter 1	Filter 2	σ_C	Main colour sequence equation
		HST/WFPC2	
F814W	F606W	0.0508	$-0.0307m_1 + 1.6176$
		DES	
z	r	0.0466	$-0.0382m_1 + 2.078$
z	g	0.1651	$-0.0744m_1 + 4.651$
r	g	0.1319	$-0.0415m_1 + 2.779$

in their final catalogue format: their positions and all geometrical components (semi-major and minor axes a and b, rotation angle θ) as well as their magnitudes are coming from the photometric analysis, while the redshifts are detected through spectroscopy.

APPENDIX B: ADDITIONAL INFORMATION ON COLOUR-MAGNITUDE DIAGRAMMES SELECTIONS

We here provide the equation of each main red colour sequence for both galaxy cluster MACS J0242 and MACS J0949, according to process described in Section 3.2.3. We also provide all the additional colour-magnitude diagrammes we can plot. Tables B1 and B2 provide respectively the equations of the main colour sequences of clusters MACS J0242 and MACS J0949, and the weighed colour standard deviation of the spectroscopically confirmed cluster galaxy sample σ_C. The height of the selection box is $2\sigma_C$ away from the main red sequence for *HST*/ACS and *HST*/WFC3, and $3\sigma_C$ for *HST*/WFPC2 and DES.

This paper has been typeset from a TEX/LATEX file prepared by the author.

Table B2. Equations of the main colour sequences and standard deviations on colours for all colour-magnitude diagrammes of MACS J0949. m_1 represents the magnitude in abscissa. Associated graphs are Fig. 4 and B2.

Filter 1	Filter 2	σ_C	Main colour sequence equation
		HST/ACS	
F814W	F606W	0.1956	$-0.0317m_1 + 2.0530$
		HST/WFC3	
F160W	F140W	0.0230	$-0.0121m_1 + 0.4217$
F160W	F125W	0.0365	$-0.0253m_1 + 0.8511$
F160W	F105W	0.0684	$-0.0483m_1 + 1.6344$
F140W	F125W	0.0220	$-0.0158m_1 + 0.5043$
F140W	F105W	0.0523	$-0.0361m_1 + 1.2308$
F125W	F105W	0.0371	$-0.0209m_1 + 0.7565$

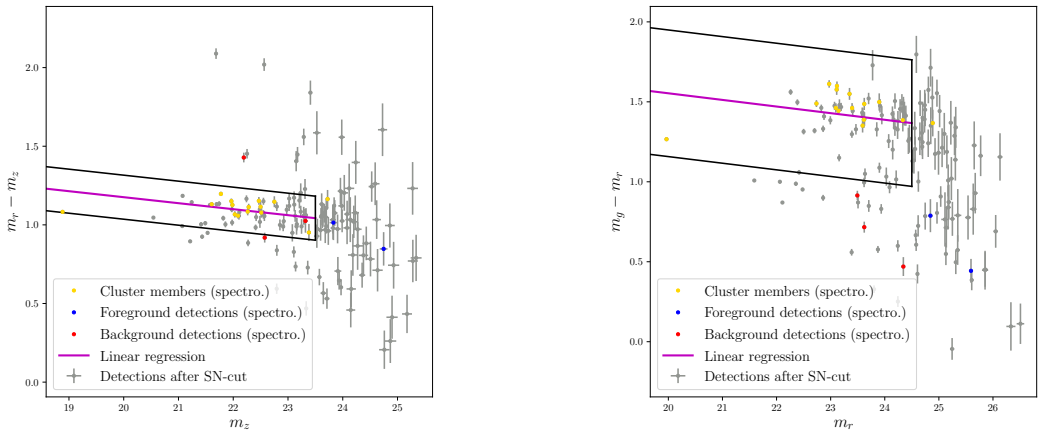

Figure B1. Colour-magnitude diagramme for MACS J0242, instrument DES. *Top row: Left:* The colour is ($m_r - m_z$), and the magnitude m_z. *Right:* m_z vs ($m_g - m_r$). Grey filled circles (with their error bars) have successfully passed all selections described in Section 3.2.1. The magenta line represents the main sequence regression. Blue, gold and red dots represent spectroscopic detections of foreground, cluster and background objects respectively.

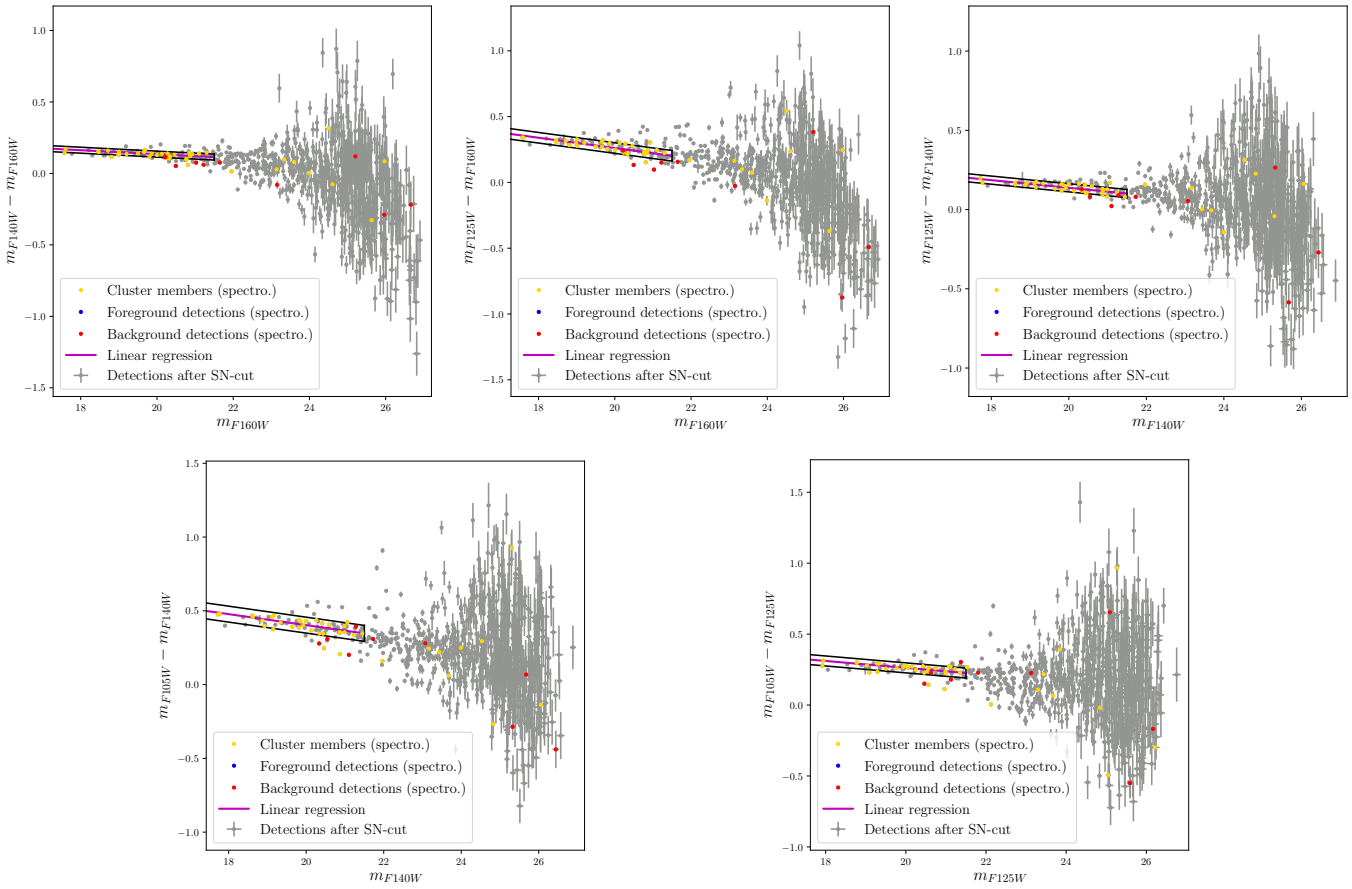

Figure B2. Colour-magnitude diagrammes for cluster MACS J0949, instrument *HST*/WFC3. *Top row: Left:* The colour is ($m_{\rm F140W} - m_{\rm F160W}$), and the magnitude $m_{\rm F160W}$. *Middle:* $m_{\rm F160W}$ vs ($m_{\rm F125W} - m_{\rm F160W}$). *Right:* $m_{\rm F140W}$ vs ($m_{\rm F105W} - m_{\rm F140W}$). *Bottom row: Left:* $m_{\rm F140W}$ vs ($m_{\rm F105W} - m_{\rm F140W}$). *Right:* $m_{\rm F125W}$ vs ($m_{\rm F105W} - m_{\rm F125W}$). Grey filled circles (with their error bars) have successfully passed all selections described in Section 3.2.1. The magenta line represents the main sequence regression. Blue, gold and red dots represent spectroscopic detections of foreground, cluster and background objects respectively.

Chapter 4

Intra-cluster medium reconstruction using strong gravitational lensing

X-rays will prove to be a hoax.

— Lord Kelvin

4.1 Introduction

4.1.1 Motivations

In order to understand the physics of galaxy clusters, parallel observations and descriptions of their different components is not enough: a general model, relating the history, the dynamics, the gravitational influence of the multiple components is necessary to a unified understanding. For example, simulations including the baryonic content of galaxy clusters are quite different from dark matter (DM) only simulations (Robertson et al., 2019, 2021). The density profiles of the dark matter component, and of the baryonic content of clusters, mostly in the intra-cluster medium (ICM), are commonly separated into different, unrelated descriptions (see Sections 1.3.3 and 1.3.4.3). In spite of a number of baryonic effects (summarised in e.g. Tozzi and Norman, 2001; Ghirardini et al., 2019b, such as the Active Galaxy Nuclei and supernovae feedback, and the cooling of the plasma), which generate a lot of turbulence in the ICM, a more holistic path to study galaxy clusters may be to describe the DM and ICM contents in a unified model.

After describing the basic physics of galaxy clusters in Section 1.3 and presenting the strong lensing reconstruction of the total density (DM and baryons) of clusters MACS J0242.5-2132 and MACS J0949.8+1708 in Chapter 3, we describe in this Chapter the reconstruction of the ICM observables (electron density n_e, electron temperature T_e, but also X-ray surface brightness S_X or thermal Sunyaev-Zel'dovich effect – tSZ – temperature contrast Θ_r) using the strong lensing models, assuming the clusters to be dynamically relaxed. We present new models for the temperature and the gas fraction f_g. At last, we revert the perspective, optimising the SL parameters with ICM data, in order to verify the robustness of our method. I present the results of this analysis in Section 4.3, under the form of an article[1]. This general workflow, alongside the idea of the whole thesis, is summarised on Figure 4.1.

[1]This article has not yet been submitted.

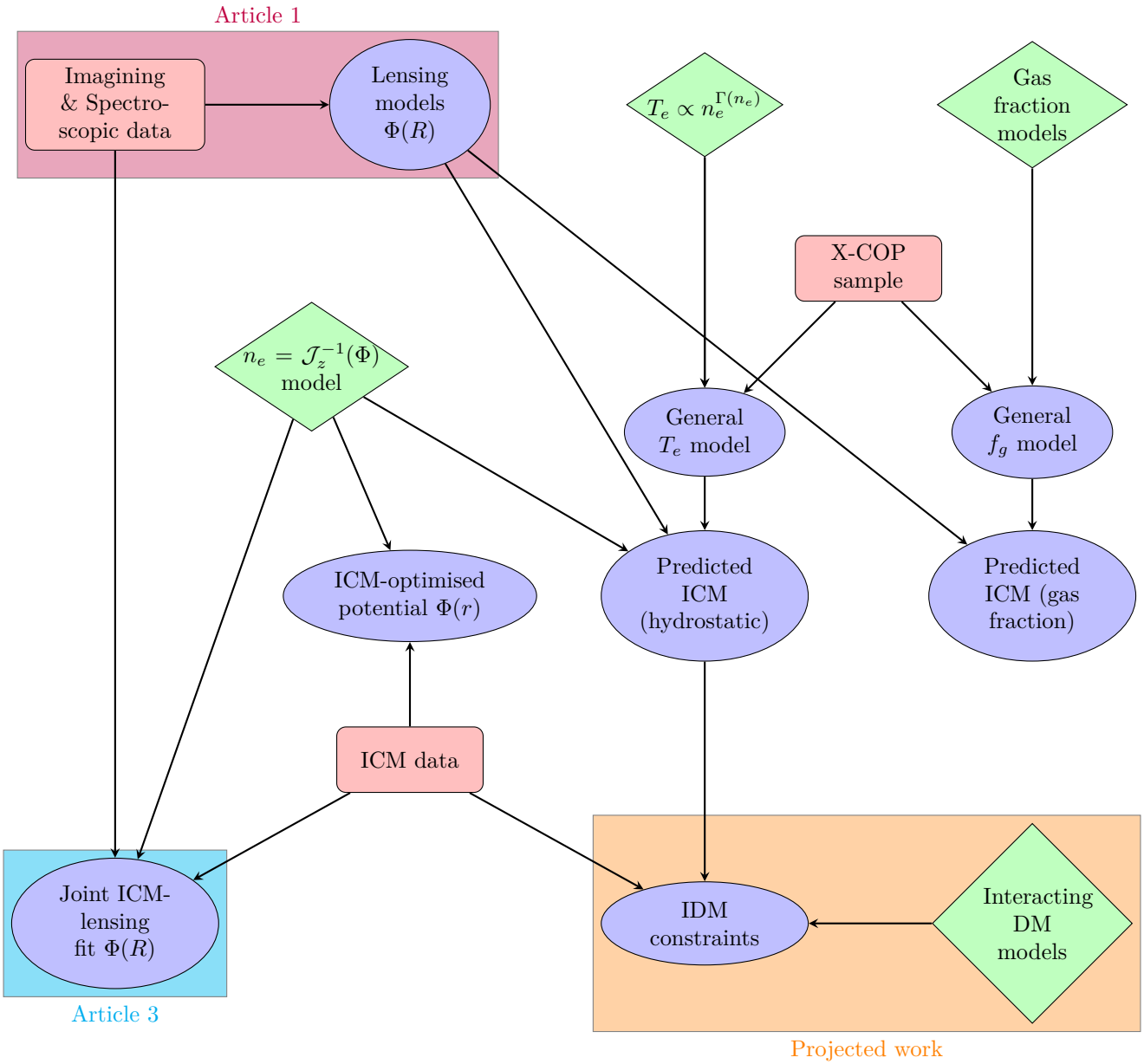

Figure 4.1: Full workflow diagram of this thesis. *Green diamonds:* models *a priori*. *Red rectangles:* available data. *Blue ellipses:* quantitative results. The magenta background denotes work accomplished in our first article (corresponding to Chapter 3), the white background in the second article (Chapter 4), the cyan to our projected third article (Chapter 5) and the orange to our planned work, to utilise SL and ICM models and observations to constrain interacting dark matter (IDM).

4.1.2 Observations

In order to verify the robustness of the ICM reconstruction using SL, we use X-ray and SZ effect observations of the ICM of galaxy clusters MACS J0242 and MACS J0949. The X-ray observations include *XMM-Newton* data, presented in the previous Chapter (see Ghirardini et al., 2019b; CHEX-MATE Collaboration et al., 2021). For the observation of the SZ effect, we use millimetre-wave data from the Atacama Cosmology Telescope (ACT), f090 and f150 'daynight' DR5 maps [2], centred on respective frequencies 97.8 and 149.6 GHz (see Naess et al., 2020; Hilton et al., 2021; Mallaby-Kay et al., 2021). The observation of an important submillimetre source in the field of view of MACS J0242 makes the use of the SZ effect data impossible to constrain the ICM density in this cluster. As a consequence, we only use ACT observations for MACS J0949.

Moreover, in order to tune the ICM temperature and gas fraction relationship universally, we used a larger sample of X-ray observations than two galaxy clusters. The *XMM* cluster outskirts project[3] (X-COP, described in Eckert et al., 2017), constituted of 12 massive clusters of mass $3 \times 10^{14} M_{\odot} < M_{500} < 1.2 \times 10^{15} M_{\odot}$ and redshifts $0.04 < z < 0.1$ was used for this purpose.

4.2 General models for ICM reconstruction

In order to derive a general model for galaxy clusters' density, both in DM and in the ICM, we need to empirically analyse the electron temperature in a sample of galaxy clusters.

4.2.1 Self-similar polytropic temperature models with varying index[4]

In order to propose a joint description of a dynamically relaxed ICM and DM distributions, we need to describe the ICM thermodynamics. The general model for a polytropic temperature profile was presented in equation (1.89), where the temperature normalisation $T_0 = T_e(r = 0)$ represents the central temperature. According to Capelo et al. (2012) and Ghirardini et al. (2019a), one can almost universally take $\gamma \approx 1.2$ throughout the cluster volume.

More generally, Ghirardini et al. (2019a) used the X-COP data to show that the electron pressure and temperature profiles of the ionised plasma can be related self-similarly across different clusters with a low scatter $\sim 15\%$, independently of a system's dynamical state :

$$\begin{aligned} \frac{P_e}{P_{500}} &= P_{\rm ref} \left(\frac{n_e E(z)^{-2}}{n_{\rm ref}} \right)^{\Gamma(n_e)} , \\ \frac{T_e}{T_{500}} &= T_{\rm ref} \left(\frac{n_e E(z)^{-2}}{n_{\rm ref}} \right)^{\Gamma(n_e)-1} , \end{aligned} \tag{4.1}$$

where $E(z) = H(z)/H_0$ is the normalised Hubble factor (see equation 1.20). $P_{\rm ref}$ and $T_{\rm ref}$ are dimensionless proportionality constants, and $n_{\rm ref}$ is the volume number density normalisation. For clarity, let us write $T_0(z) = T_{500}(z) T_{\rm ref}$ and $n_0(z) = n_{\rm ref} E(z)^2$. These normalisations do not depend on individual clusters, but are universal parameters, which may be determined with an optimisation on the X-COP cluster sample.

[2] https://lambda.gsfc.nasa.gov/product/act/actpol_dr5_coadd_maps_get.html
[3] https://dominiqueeckert.wixsite.com/xcop
[4] This subsection research work was performed by D. Eckert.

Table 4.1: Parameters of the smoothly varying polytropic temperature model defined in equations (4.1) and (4.2).

$P_{\rm ref}$	$n_{\rm ref}$ [m^{-3}]	Γ_0	Γ_S	$\sigma_{\ln P_e}$
6.05 ± 1.57	$(2.26 \pm 0.59) \times 10^3$	0.97 ± 0.04	-0.15 ± 0.03	0.19 ± 0.02

Observationally, the measured values of the polytropic index closely match the hydrostatic equilibrium NFW expectation in cluster outskirts ($R > 0.2R_{500}$), but in the cluster core significantly deviate because of radiative cooling, where Γ decreases down to ~ 0.8 (Ghirardini et al., 2019a). We here propose a new functional form to describe the self-similar polytropic model (supported by e.g. Mostoghiu et al., 2019), in order to describe the smooth transition of the polytropic index from the core to the cluster outskirts. The relation for a smoothly varying polytropic index $\Gamma(n_e)$ is:

$$\frac{\mathrm{d}\ln P_e}{\mathrm{d}\ln n_e} \equiv \Gamma(n_e) = \Gamma_0 \left[1 + \Gamma_S \arctan\left(\ln \frac{n_e E(z)^{-2}}{n_{\rm ref}}\right)\right], \tag{4.2}$$

with $n_{\rm ref}$ the reference number density around which the transition between core (low $\Gamma \sim 0.8$) and outskirts (NFW $\Gamma \sim 1.2$) occurs, Γ_0 the polytropic index at $n_{\rm ref}E(z)^2$, and Γ_S the slope of the transition.

In order to find the 'universal' parameters for this self-similar description of the electron pressure and temperature equation (4.2), we fit it to a sample of clusters. For this purpose, we used the X-COP data of high-quality observations of ICM thermodynamic properties over a wide radial range ($r \in [0.01 - 2]R_{500}$). We fit the X-COP density and pressure data using the Bayesian analysis package `PyMC3` (Salvatier et al., 2016), including uncertainties on both axes and a free log-normal intrinsic scatter. The model provides an excellent representation of the data over three decades in electron density, with a low intrinsic scatter of $\sigma_{\ln P_e} = 0.19 \pm 0.02$. The fit parameters are included in Table 4.1. Assuming the ICM is an ideal gas, using Ghirardini et al. (2019b), we obtain $T_{\rm ref} \approx 1.034$.

As for the full $T_{500}(z)$, we use the results of Ghirardini et al. (2019b), which we reproduce here:

$$T_{500}(z) = 8.85\,\mathrm{keV} \left(\frac{M_{500}E(z)}{h_{70}^{-1}10^{15}M_\odot}\right)^{2/3} \left(\frac{\mu_g}{0.6}\right), \tag{4.3}$$

with $h_{70} = h/0.7 = 1$ here. We therefore can normalise the temperature universally.

4.2.2 Gas fraction Arctan model

As we have access to the precise ICM measurements of the X-COP data sample, and to equivalent *XMM-Newton* data for the lensing clusters MACS J0242 and MACS J0949, we name here 'X-COP+2' the sample of these 14 clusters. We use the ICM density measurements ρ_g, and the hydrostatic equilibrium reconstructions for the total matter density ρ_m. As we aim to relate the total matter density to the ICM density in general, we explore here another possibility: that of an empirical model directly relating these two quantities. To this purpose, we define the integrated

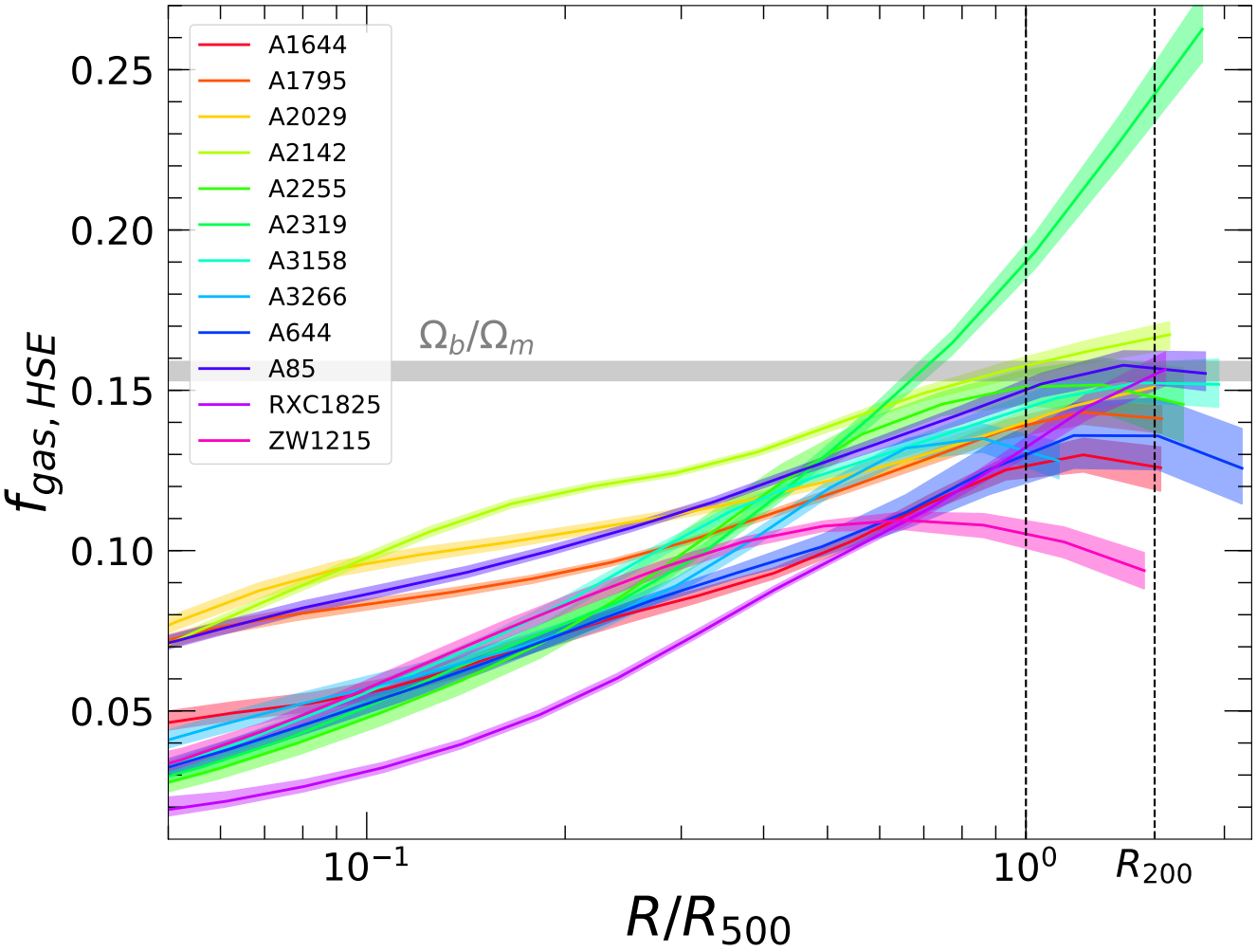

Figure 4.2: Integrated gas fraction over two X-COP clusters. The ICM density was inferred from X-ray observations, and the total matter density was later reconstructed assuming hydrostatic equilibrium (HSE). *Colours:* Reconstruction of the cumulative gas fraction F_g, for the 12 X-COP clusters. *Grey:* Universal baryonic fraction, as measured by Planck Collaboration (2016). Credits: Eckert et al. (2019).

hot gas fraction F_g, which we distinguish from the local gas fraction $f_g(r)$:

$$\begin{aligned} F_g(r) &= \frac{\int_0^r \mathrm{d}s s^2 \rho_g(s)}{\int_0^r \mathrm{d}s s^2 \rho_m(s)} = \frac{M_g(<r)}{M_m(<r)}, \\ f_g(r) &= \frac{\rho_g(r)}{\rho_m(r)} = \frac{\mathrm{d}F_g}{\mathrm{d}r}(r) \frac{\int_0^r \mathrm{d}s s^2 \rho_m(s)}{r^2 \rho_m(r)} + F_g(r), \end{aligned} \tag{4.4}$$

where indices g and m respectively denote the hot gas (baryons in the ICM, but not stars), and the total matter (all baryons, including stars, and dark matter).

All 14 clusters of the 'X-COP+2' sample present a gas fraction transition between small and large radii, as may be observed on Figure 4.2, which we propose to describe analytically with an Arctan model:

$$F_g(r) = a \left[\frac{2}{\pi} \arctan\left(\exp \frac{r - r_c}{r_f} \right) - \frac{1}{2} \right] + b, \tag{4.5}$$

where a and b are defined with the expected gas fractions at the centre and at 'infinity' f_g^0 and f_g^∞ as:

$$\begin{aligned} \upsilon &= \frac{2}{\pi} \arctan\left[\exp\left(-\frac{r_c}{r_f}\right)\right], \\ a &= \frac{f_g^0 - f_g^\infty}{\upsilon - 1}, \\ b &= \frac{1}{2}\left[\frac{f_g^0}{1-\upsilon} + \frac{f_g^\infty(1-2\upsilon)}{1-\upsilon}\right], \end{aligned} \tag{4.6}$$

with r_c and r_f the core and flattening radii respectively, i.e. the radii of Arctan inflexion point and the characterisation of the transition slope. Equation (4.6) reflects the necessary normalisation of the integrated gas fraction parameters.

The universal baryon fraction, $\Omega_b/\Omega_m = 0.1580 \pm 0.0021$ (Planck Collaboration, 2016), corrected by the depletion factor (see Eckert et al., 2019) reads:

$$f_g^{\rm Uni}(r) = Y_b(r)\frac{\Omega_b}{\Omega_m} - f_\star, \tag{4.7}$$

where Y_b is the baryon depletion factor, and $f_\star$ the stellar fraction, not accounted for in the intracluster gas. Eckert et al. (2019) provide $Y_{b,500} = 0.938^{+0.028}_{-0.041}$ which we use here. Following equation (4) of the same study, the average error on $f_{\star,500}$ is 5×10^{-3}. One can thus assume $f_g^\infty \approx f_g^{\rm Uni}(R_{500})$.

Moreover, in our description of the lensing analysis with dPIE profiles (see Section 1.3.3.7 and Chapter 3), we have detailed how a sum of dPIE profiles was assumed to represent the total matter density of galaxy clusters. Most notably, the core regions, dominated by stellar and baryonic physics, are separated from the larger radii, dominated by DM, by a *core radius* a_1 associated to the DM halo (DMH) in the lensing analysis[5]. In Section 4.3, we tested the hypothesis that r_c and r_f would correspond to the lensing DMH core radius a_1, for both lensing clusters MACS J0242 and MACS J0949. This would allow to have a gas fraction model controlled with the universal and lensing parameters only (respectively f_g^0 and f_g^∞, and r_c and r_f), and thus an ICM density prediction coming only from lensing. The parameters r_c and r_f were let free in the optimisation, but their final values were compared to those found in Section 3.4 for the two lensing clusters.

Using the Bayesian analysis package `emcee` (Foreman-Mackey et al., 2013), the Arctan gas fraction model is fit to the 'X-COP+2' sample. As the X-COP clusters were not analysed through gravitational lensing, one can not compare r_c and r_f to their lensing counterpart a_1. The assumption that $r_c \approx r_f \approx a_1$ is approximately verified for the lensing clusters considered here (see Section 4.3, for each separate cluster, r_c, r_f and a_1 are of the same order, the strongest variation being of a factor 2; however the models using this assumption yield acceptable fit for the gas fraction model).

The general equation of the model, simplified from equation (4.5), then writes:

$$F_g(r) \approx (-0.103 - 0.821 f_\star) \arctan\left[\exp\left(\frac{r}{a_1} - 1\right)\right] - 0.013 - 0.289 f_\star. \tag{4.8}$$

Let us therefore notice that if the total matter density ρ_m and $r_{\rm core,DMH}$ are known, we have a simple expression of the gas density profile $\rho_g(r) = f_g(r)\rho_m(r)$.

[5] In the effective lensing models, the gravitational effect probed is 'agnostic' to the type of matter deforming the space-time continuum.

4.2.3 Analytical ICM density models

In order to describe the electron density with the lensing analysis only, we adopt the temperature profile described in Section 4.2.1. This allows to get a fully analytical model for both the ICM distribution and its thermodynamics, assuming hydrostatic equilibrium.

4.2.3.1 ICM-total density bijection

Let us consider the total density ρ_m as a sum of a number of potentials:

$$\rho_m(r) = \sum_i \rho_{0,m,i} f_i(r). \tag{4.9}$$

Each potential can be normalised differently, and the distributions f_i are here assumed to be of the same type, but with different parameters. Here, we consider them to only be radial for simplicity (in practice all potentials have different geometric parameters – e.g. central position, ellipticity, rotation angle). Assuming integrability, we introduce:

$$\begin{aligned} g_i(r) &= \int \mathrm{d}s s^2 f_i(s), \\ h_i(r) &= \int \mathrm{d}s s^{-2} g_i(s), \end{aligned} \tag{4.10}$$

where integration constants are included. Writing Φ the Newtonian potential, the gravitational Poisson equation yields the gravitational potential expression:

$$\Phi(r) = -4\pi G \sum_i \rho_{0,m,i} h_i(r). \tag{4.11}$$

Let us at last write the thermodynamic toll in the Lagrangian formulation for momentum, i.e. the momentum Navier-Stokes equation for a perfect fluid (viscosity neglected, see e.g. Landau and Lifshitz, 1959):

$$\rho_g \frac{\mathrm{D}\boldsymbol{v}}{\mathrm{D}t} = \rho_g \left[\partial_t \boldsymbol{v} + (\boldsymbol{v} \cdot \boldsymbol{\nabla})\, \boldsymbol{v}\right] = -\boldsymbol{\nabla} P_g + \rho_g \boldsymbol{\nabla} \Phi, \tag{4.12}$$

with $\boldsymbol{v}$ the velocity field.

As the pressure in galaxy clusters is of the order of 10^{10} Pa, one can safely assume the plasma to be thermalised, and therefore the temperature of the gas to be that of the electrons. With equation (4.12), one can write the number density of the electron n_e as being directly proportional to the gas density ρ_g, as μ_e and $\mathcal{F}_I$ are assumed to be constant in a given cluster. In the purely radial case, using the intensive ideal gas law expression (1.87):

$$\frac{k_B}{\mu_g m_a} \frac{\partial_r (n_e T_e)}{n_e} + \partial_t v_r + v_r \partial_r v_r = -4\pi G \sum_i \rho_{0,m,i} r^{-2} g_i(r). \tag{4.13}$$

As the galaxy clusters used in our study are not strongly perturbed[6], we work under the hypothesis of *hydrostatic equilibrium*. This is an important approximation, and if one could decompose the velocity in its radial and temporal dependencies, one could then integrate numerically locally.

[6] In Section 3.4, we showed MACS J0242 to be relaxed, and MACS J0949 to be probably in an intermediate state: not relaxed cool-core, but not strongly perturbed either. We call this latter state *relaxing*, as it may follow a past merger event. Whatever the case, the ICM as much as the total matter density are not strongly perturbed, and we assume we can apply the hydrostatic hypothesis to this cluster in the rest of this thesis.

Assuming a polytropic temperature distribution and the stream to be hydrostatic, i.e. of constant velocity, both in time and in all spatial directions, such as in (Zaroubi et al., 2001), we get:

$$\frac{\partial_r \left(n_e T_e\right)}{n_e} = \epsilon \sum_i \rho_{0,m,i} r^{-2} g_i(r), \tag{4.14}$$

where $\epsilon = -4\pi G \mu_g m_a / k_B$. The general $\mathcal{J}$ function if defined as the normalised integral of equation (4.14):

$$\mathcal{J}(n_e) = \int_0^{n_e} \frac{\mathrm{d}\left[n T_e(n)\right]}{T_0 n}, \tag{4.15}$$

where T_0 is a temperature normalisation. Using a precise temperature model, such as a classic polytropic model (1.89) or a self-similar polytropic model with varying exponent (4.1) yields the precise expression of this integral. We take the respective T_0 temperature normalisations of these models to define $\mathcal{J}$. In the latter case, we denote the integral redshift dependence of $T_0(z)$ by writing $\mathcal{J}_z$.

In the general case, separating variables and integrating equation (4.14), we obtain:

$$\mathcal{J}(n_e) = \frac{\epsilon}{T_0} \sum_i \rho_{0,m,i} h_i(r) = \frac{\mu_g m_a}{k_B T_0} \Phi(r). \tag{4.16}$$

Let us notice that in the case of a polytropic temperature profile with a constant index $\gamma > 1$, we easily compute equation (4.15):

$$\mathcal{J}_z(n_e) = \frac{\gamma}{\gamma - 1} \left(\frac{n_e}{n_0(z)} \right)^{\gamma - 1}, \tag{4.17}$$

which is clearly a bijection, i.e. the ICM density may be entirely determined knowing the total matter density. The specific case of a polytropic temperature density associated to a NFW profile has already been studied in Bulbul et al. (2010), where a 'self-normalisation' in the centre is used, i.e. the profile is normalised with the detected electron density n_e.

Upon using the varying exponent polytropic temperature model (4.1), we note $\mathcal{J}_z$ is also a bijection, of $\mathbb{R}^{+\star} \to \sim]0; 10[$, meaning there is a limit to the inversion range. The physical n_e values for the ICM we are interested in are in the middle of this interval ($\sim [2, 8]$), and thus we can consider this specific case of $\mathcal{J}_z$ to be invertible for the rest of this thesis. Under this assumption, inverting equation (4.16) provides $n_e(r)$:

$$n_e(r) = \mathcal{J}^{-1} \left(\frac{\epsilon}{T_0} \sum_i \rho_{0,m,i} h_i(r) \right) = \mathcal{J}^{-1} \left(\frac{\mu_g m_a}{k_B T_0} \Phi(r) \right). \tag{4.18}$$

We can moreover invert and normalise the distribution at a given radius (e.g. 200 kpc, where the strong lensing signal is strongly constraining the total density profile, or $R_{500,c}$), if $n_{e,\Delta}$ is known. Writing Δ such a radius:

$$n_e(r) = \mathcal{J}^{-1} \left[\mathcal{J}(n_{e,\Delta}) \frac{\Phi(r)}{\Phi(R_\Delta)} \right] = \mathcal{J}^{-1} \left[\mathcal{J}(n_{e,\Delta}) \frac{\sum_i \rho_{0,m,i} h_i(r)}{\sum_i \rho_{0,m,i} h_i(R_\Delta)} \right]. \tag{4.19}$$

We call this latter expression *self-normalised*.

Under reasonable physical hypotheses, we have established a general, completely analytical description of the electron density using only the different potentials found with lensing. To allow

this reconstruction to be independent from other observations, this *analytical* model requires an electron temperature model which we could derive with lensing only.

Alternatively, we can also write the electron density n_e, under hydrostatic hypothesis, in the specific case where we know $T_e(r)$ as:

$$n_e(r) = n_{e,\Delta} \frac{T_{e,\Delta}}{T_e(r)} \exp\left[-\epsilon \sum_i \rho_{0,m,i} \xi_i(r, R_\Delta)\right], \tag{4.20}$$

where

$$\xi_i(r, R_\Delta) = \int_r^{R_\Delta} \mathrm{d}s s^{-2} \frac{g_i(s)}{T_e(s)}, \tag{4.21}$$

where g_i are defined equation (4.10). While this would require a precise knowledge of n_e at a given radius R_Δ, and temperature profile. More generally, this would enable to test the hydrostatic assumption without having to assume a specific model for the temperature.

4.2.3.2 Case of a dPIE density

In the case of a dPIE mass distribution, according to equation (1.67), we provide the integrated density functions defined in equation (4.10):

$$\begin{aligned} f(r) &= \left\{\left[1 + \left(\frac{r}{s}\right)^2\right]\left[1 + \left(\frac{r}{a}\right)^2\right]\right\}^{-1}, \\ g(r) &= \frac{a^2 s^2}{a^2 - s^2}\left[a \arctan\frac{r}{a} - s \arctan\frac{r}{s}\right], \\ h(r) &= \frac{a^2 s^2}{a^2 - s^2}\left[\frac{s}{r}\arctan\frac{r}{s} - \frac{a}{r}\arctan\frac{r}{a} + \frac{1}{2}\ln\left(\frac{r^2 + s^2}{r^2 + a^2}\right)\right], \end{aligned} \tag{4.22}$$

where a and s represent the core r_{core} and scale r_{cut} radii of the i-th dPIE potential respectively. Indices are avoided for clarity. To avoid confusion, let us write `idPIE` (for 'integrated dPIE') the n_e distribution with h_i given by a dPIE.

4.2.3.3 Case of a NFW density

In the case of an NFW potential – see equation (1.56), we compute the different integrals given equation (4.10):

$$\begin{aligned} f(r) &= \left\{\left[\frac{r}{r_S}\right]\left[1 + \frac{r}{r_S}\right]^2\right\}^{-1}, \\ g(r) &= r_S^3\left[\ln\left(1 + \frac{r}{r_S}\right) - \frac{r}{r + r_S}\right], \\ h(r) &= -\frac{r_S^3}{r}\ln\left(1 + \frac{r}{r_S}\right), \end{aligned} \tag{4.23}$$

where indices were avoided for clarity. Here $\rho_{0,m,i}$ of equation (4.16) is interpreted as $\rho_{S,m,i}$. Let us notice that in case of NFW profile, we assume to only have one profile. We shall write this n_e distribution `iNFW`.

4.2.3.4 Case of a generalised NFW density

In the case of a generalised NFW potential – see equation (1.63), we compute the different integrals given equation (4.10):

$$\begin{aligned} f(r) &= x^{-\gamma}\left(1+x^{\alpha}\right)^{-\frac{\beta-\gamma}{\alpha}}, \\ g(r) &= r_S^3 \frac{x^{3-\gamma}}{3-\gamma} {}_2F_1\left(\mu,\xi,1+\mu,-x^{\alpha}\right), \\ h(r) &= r_S^3 \left\{ x^{2-\gamma}\left[\frac{{}_2F_1\left(\nu,\xi,1+\nu,-x^{\alpha}\right)}{2-\gamma} - \frac{{}_2F_1\left(\mu,\xi,1+\mu,-x^{\alpha}\right)}{3-\gamma}\right] - \frac{\Gamma(\nu)\Gamma(\xi-\nu)}{\alpha\Gamma(\xi)}\right\}, \end{aligned} \tag{4.24}$$

where $x = r/r_S$, ${}_2F_1$ is the Gauss hypergeometric function, Γ the extended factorial function(i.e. the complete gamma function), and μ, ν and ξ are simple reformulations of the three indices α, β, γ:

$$\mu = \frac{3-\gamma}{\alpha} \quad ; \quad \nu = \frac{2-\gamma}{\alpha} \quad ; \quad \xi = \frac{\beta-\gamma}{\alpha}. \tag{4.25}$$

Let us notice this integration takes constants into account, but requires $\alpha > 0$, $\beta > 2$ and $\gamma < 2$. We shall write the resulting n_e distribution `igNFW`.

4.2.3.5 Case of an Einasto density

The Einasto potential is provided equation (1.66). Let us rewrite $n = 1/\alpha$, and write the reduced radius: $s = (2n)^n r/r_{-2}$, the scale length $l = r_{-2}/(2n)^n$ and the central density $\rho_0 = \rho_{-2}e^{2n}$. Following Cardone et al. (2005) and Retana-Montenegro et al. (2012), the different functions equation (4.10) write:

$$\begin{aligned} f(r) &= \exp\left(-s^{n^{-1}}\right), \\ g(r) &= l^3 n\left[\Gamma(3n) - \Gamma\left(3n, s^{n^{-1}}\right)\right], \\ h(r) &= -\frac{nl^2}{s}\left[\Gamma(3n) - \Gamma\left(3n, s^{n^{-1}}\right) + s\Gamma\left(2n, s^{n^{-1}}\right)\right], \end{aligned} \tag{4.26}$$

where $\Gamma(\alpha)$ is the complete gamma function, and $\Gamma(\alpha, x)$ the upper incomplete gamma function:

$$\Gamma(\alpha, x) = \int_x^{\infty} \mathrm{d}t t^{\alpha-1} e^{-t}. \tag{4.27}$$

We call the ICM n_e profile coming from this DM profile `iEinasto`.

4.2.4 Optimisation of the lensing parameters with the ICM

In Section 4.3, four electron density models are presented: β (see equation 1.79), Arctan gas fraction, `idPIE` and `iNFW`. The three latter models assume the total matter density profile ρ_m to be known or the knowledge of parameters such as the DMH core radius a_1. One can let a number of parameters of these models free to vary, for both the classic and varying exponent polytropic temperature models. These parameters are optimised with the ICM data collected for each galaxy cluster. For cluster MACS J0242, we only use the X-ray data, while for MACS J0949, we have the choice to use either X-ray, or SZ, or both.

Let us define the log-likelihood for the X-ray data: as the photon counts are limited, the X-ray maps are following a Poissonian distribution. With the noise, we take them to follow the Cash statistic (Cash, 1979):

$$\ln \mathcal{L}_X(\Theta) = \frac{1}{N_X} \sum_i \left[C_i - M_i(\Theta) - C_i \ln \left(\frac{C_i}{M_i(\Theta)} \right) \right], \tag{4.28}$$

where C_i is the data count in the i-th pixel, N_X the number of pixels, and $M_i(\Theta)$ the model prediction for the parameter tuple Θ.

As for the SZ statistic, with M_i now being the temperature contrast model, and C_i its SZ measurement, we simply take the likelihood to be Gaussian:

$$\begin{aligned} \ln \mathcal{L}_{SZ}(\Theta) &= -\frac{1}{2N_{SZ}} \sum_i \left[\left(\frac{M_i(\Theta) - C_i}{\sigma_i} \right)^2 + \ln \sigma_i^2 \right], \\ \sigma_i^2 &= M_i^2(\Theta) + \sigma_{C,i}^2, \end{aligned} \tag{4.29}$$

where σ_i is the standard deviation in the i-th pixel, and N_{SZ} the number of SZ pixels. The model standard deviation is the model itself, accordingly to a Gaussian model. $\sigma_{C,i}^2$ is the instrument variance of ACT. This does not take into account the CMB variance nor the atmosphere, but at this order it should be satisfactory. C_i and M_i represent here the data and model respectively, but for the SZ data. We sum the log-likelihood of the 90 and 150 GHz ACT DR5 bands.

In the case of joint X-SZ optimisation, the data are of the same type, i.e. detections in pixels. We therefore defined the joint likelihood as the weighed sum:

$$\ln \mathcal{L}_J = \frac{N_X \ln \mathcal{L}_X + N_{SZ} \ln \mathcal{L}_{SZ}}{N_X + N_{SZ}}, \tag{4.30}$$

where N_{SZ} must be understood as the sum of all SZ pixels, both in band f090 and f150. Let us notice this takes into account the different pixelisations, and attributes equal weights to each pixel of data. X-ray should thus dominate, given the much better resolution of data.

We provide the results of this total matter density optimisation with the ICM in Section 4.3.

4.3 Article: A full reconstruction of two galaxy clusters intra-cluster medium with strong gravitational lensing

We present the ICM reconstruction using strong lensing in our unsubmitted article:

A full reconstruction of two galaxy clusters intra-cluster medium with strong gravitational lensing, **Joseph F. V. Allingham**, Céline Bœhm, Mathilde Jauzac, David J. Lagattuta, Guillaume Mahler, Dominique Eckert, Matt Hilton, Geraint F. Lewis, Stefano Ettori.

A full reconstruction of two galaxy clusters intra-cluster medium with strong gravitational lensing

Joseph F. V. Allingham[1]★, Céline Bœhm[1], Mathilde Jauzac[2,3,4,5], David Lagattuta[2,3], Guillaume Malher[2,3], Dominique Eckert[6], Matt Hilton[4,5], Geraint F. Lewis[1], and Stefano Ettori[7,8]

[1]School of Physics, A28, The University of Sydney, NSW 2006, Australia;
[2]Centre for Extragalactic Astronomy, Durham University, South Road, Durham DH1 3LE, UK;
[3]Institute for Computational Cosmology, Durham University, South Road, Durham DH1 3LE, UK;
[4]Astrophysics Research Centre, University of KwaZulu-Natal, Westville Campus, Durban 4041, South Africa;
[5]School of Mathematics, Statistics & Computer Science, University of KwaZulu-Natal, Westville Campus, Durban 4041, South Africa;
[6]Department of Astronomy, University of Geneva, ch. d'Écogia 16, CH-1290 Versoix Switzerland;
[7]INAF - Osservatorio di Astrofisica e Scienza dello Spazio di Bologna, via Piero Gobetti 93/3, 40129 Bologna, Italy;
[8]INFN, Sezione di Bologna, viale Berti Pichat 6/2, 40127 Bologna, Italy.

Draft version; for submission to MNRAS

ABSTRACT

The total matter density of galaxy clusters can be probed with strong gravitational lensing, whilst the properties of the intra-cluster medium (ICM) are constrained using X-rays and Sunyaev-Zel'dovich (SZ) observations. Although being physically related, these two components are often described with different physical models. Here, we present a technique to derive the ICM properties from strong lensing for clusters in hydrostatic equilibrium. In order to derive this model, we present a new universal and self-similar polytropic temperature profile, which we fit using the X-COP sample of clusters. We subsequently derive an analytical model for the electron density, which we apply to strong lensing clusters MACS J0242.5-2132 and MACS J0949.8+1708. We confront the inferred ICM reconstructions to *XMM-Newton X-ray Observatory* observations, and ACT-DR5 SZ data. We contrast our *analytical* electron density reconstructions with the best canonical β-model, and with comparable gas fraction models inferred from the X-COP sample. The ICM reconstructions obtained prove to be compatible with observations. However they appear to be very sensitive to various dark matter halo parameters constrained through strong lensing, and to the halo scale radius – fixed in the lensing optimisations. With respect to the important baryonic effects, we make the sensitivity on the scale radius of the reconstruction an asset, and use the inferred potential to constrain the dark matter density profile using ICM observations. The technique here developed should allow to take a new, and more holistic path to constrain the content of galaxy clusters.

Key words: galaxies: clusters: intracluster medium, X-rays: galaxies: clusters, galaxies: clusters: individual: MACS J0242.5-2132, galaxies: clusters: individual: MACS J0949.8+1708, hydrodynamics

1 INTRODUCTION

In the last decades, tremendous progress has been achieved in gravitational lensing observations (see Kneib & Natarajan 2011, for a review); from the first mass reconstruction of Abell 370 (Hammer 1987; Soucail et al. 1988) all the way to the *Hubble* Frontier Fields (HFF, Lotz et al. 2017) and Beyond the Ultra-deep Frontier Fields and Legacy Observations (BUFFALO, Steinhardt et al. 2020) surveys. As a result, our understanding of this indirect observation of dark matter has improved, yet leaving open problems to discussions, such as the total matter (baryons & dark matter) potential distribution in galaxy clusters (Lilley et al. 2018; Roncadelli & Galanti 2021), in particular in their outskirts (Trevisan et al. 2017), or the size of clusters themselves (see e.g. Chang et al. 2018; Baxter et al. 2021; Tomooka et al. 2020; Aung et al. 2022).

In parallel, the total matter distribution at large radii is assumed to be traced by the ionised intergalactic medium, the signature of which is detectable in the X-rays and thanks to the Sunyaev-Zel'dovich (SZ) effect. While the projected lensing gravitational potential of galaxy clusters can be reconstructed from X-rays and SZ data through the Richardson-Lucy deprojection algorithm (see Konrad et al. 2013; Majer et al. 2013; Tchernin et al. 2018), the reverse path has not been explored yet. A complete comparison between the intra-cluster medium (ICM, composed of ionised gas) and the reconstruction of the total matter density should light our way towards a more holistic understanding of the dark matter profile, galaxy clusters thermodynamics, and relationship(s) between baryons and dark matter.

To compare an ICM prediction to observations, we require a model allowing us to predict the ICM properties using only strong lensing,

★ E-mail: joseph.allingham@sydney.edu.au

capable of establishing a general relationship between baryon and dark matter distributions in galaxy clusters. An offset with the X-ray observations could for instance hint towards interacting dark matter scenarios.

Deriving such a model requires to understand the thermodynamics of galaxy clusters. Making precise measurements from X-rays observations is limited by the required assumptions, such as the halo geometry (Buote & Humphrey 2012; Sereno et al. 2017), or the dynamical state of the cluster (Nelson et al. 2014; Biffi et al. 2016). Multiple studies have shown the hydrostatic regime to be an acceptable description of the ICM for cool-core and non-cool-core clusters (Ettori et al. 2013; Biffi et al. 2016; Vazza et al. 2018; Ettori et al. 2019). Conversely, recent mergers or dynamically disturbed systems present strong deviations to hydrostatic (Khatri & Gaspari 2016). Moreover, galaxy clusters have followed a hierarchical model of formation, made of mergers and gravitational collapse. For this reason, their thermodynamics scale according to the cluster mass (Kaiser 1986; Bryan & Norman 1998), which is confirmed by simulations (Frenk et al. 1999; Borgani et al. 2005; Voit 2005) and observations (Ghirardini et al. 2019a). These assumptions (hydrostatic equilibrium, self-similarity) are common in joint X-rays and SZ analyses (cf. Capelo et al. 2012; Ghirardini et al. 2019a,b). In order to describe the thermodynamic model of galaxy clusters, we adopted an effective polytropic temperature law. Komatsu & Seljak (2001); Capelo et al. (2012); Ghirardini et al. (2019b) have studied such a model. Capelo et al. (2012) predicted a constant $\Gamma \sim 1.2$ polytropic index for the ICM in hydrostatic equilibrium with a NFW density profile, and Ghirardini et al. (2019b) recovered this value for the outskirts of clusters, but found radiative cooling to bring this value to $\Gamma \sim 0.8$ in the centre. In order to produce precise predictions *a priori*, we conduct a study of the polytropic index on the X-COP sample of data (described in Eckert et al. 2017). This set of galaxy clusters was precisely observed with the *XMM-Newton X-ray Observatory* (see Ghirardini et al. 2019a; CHEX-MATE Collaboration et al. 2021). Their pressure, temperature and ICM density profiles are ideal to derive a general relationship on X-ray observed clusters. We reduce the polytropic model into a functional form temperature profile, allowing for universal predictions.

In Allingham et al. (2022), we analysed two galaxy clusters and reconstructed their gravitational potential with `Lenstool` (see Jullo et al. 2007) using strong gravitational lensing. Galaxy clusters MACS J0242.5-2132 and MACS J0949.8+1708, relaxed and relaxing respectively, provide the inputs to the ICM predictions for this work, and allow to justify the hydrostatic description of the ICM (Biffi et al. 2016). In this paper, we also test several models commonly used by the X-ray and SZ communities to describe the ICM density distribution (see Vikhlinin et al. 2006). We refer to these models as *canonical*, in contrast to our models, which are derived analytically from the full matter density, using the Poisson and Navier-Stokes equations, following the logic of Bulbul et al. (2010). As our *analytical* ICM models scale with the gravitational potential obtained with strong lensing, no scaling assumptions are being made.

After establishing the theoretical models, the quantitative ICM results are confronted to the *XMM-Newton* and the ACT Data Release 5 millimetre-wave (see Naess et al. 2020; Mallaby-Kay et al. 2021). The quality of the reconstruction is tested through a potential optimisation using these ICM data.

Moreover, the X-COP sample combined with X-ray data of the 'lensing' clusters allows for the empirical tuning of gas fraction models. This yields another type of ICM density models using the gravitational potential inferred from strong lensing, which we call *gas fraction* models.

This article is structured as follows: the data are presented in Section 2; the strong lensing models are summarised in Section 3; the theoretical possible models for the electron density, the temperature, the gas fraction, the X-ray surface brightness and the SZ effect are introduced in Section 4; quantitative results for the density, temperature, etc are presented in Section 5; observational predictions follow up with the comparison to data and MCMC optimisation in Section 6; and a discussion on the limitations and possibilities of such a model is given in Section 7. We assume the ΛCDM cosmological model, with $\Omega_m = 0.3$, $\Omega_\Lambda = 0.7$, and $H_0 = 70$ km/s/Mpc.

2 DATA

2.1 X-ray observations

2.1.1 *MACS J0242 and MACS J0949*

The ICM is primarily probed with X-ray observations. We used the *XMM-Newton* publicly available observations of the MACS J0242 and MACS J0949 in the 0.7-1.2 keV band (see CHEX-MATE Collaboration et al. 2021). MACS J0242 was observed for a total of 70 ks (OBSID:0673830101), and MACS J0949 for a total of 36 ks (OBSID:0827340901). We analysed the two observations using XMM-SAS v17.0, and the most up-to-date calibration files. We used the XMMSAS tools `mos-filter` and `pn-filter` to extract light curves of the observations and filter out periods of enhanced background, induced by soft proton flares. After flare filtering, the available clean exposure time is 61 ks (MOS) and 53 ks (PN) for MACS J0242, and 35 ks (MOS) and 34 ks (PN) for MACS J0949. The EPIC MOS filter maximises the signal-to-noise ratio, thus we used primarily these data. We extract the X-ray data following the procedure detailed through Eckert et al. (2020).

With the NASA tool PIMMS, we get access to the conversion constants from flux to counts per second $C_{\rm flux}^{\rm count}$ for both clusters: for respectively MACS J0242 and MACS J0949, $C_{\rm flux}^{\rm count} = 2.087 \times 10^{14}$ and 2.084×10^{14} counts.J^{-1}.m^2.

2.1.2 *The X-COP clusters*

In order to tune our temperature and gas fraction models, we study a number of comparable clusters. The *XMM* cluster outskirts project (X-COP, described in Eckert et al. 2017, see the archive[1]) is ideal for this purpose: it gathers data from 13 massive clusters (we however excluded Abell 780, observed in the [0.5 – 2.0] keV band). These clusters are comparable to MACS J0242 and MACS J0949, with $3 \times 10^{14} M_\odot < M_{500} < 1.2 \times 10^{15} M_\odot$, but are in the redshift range $0.04 < z < 0.1$, smaller than for MACS J0242 and MACS J0949, at redshifts 0.313 and 0.383 respectively.

2.2 SZ observations

It is possible to study the 'imprint' of the ICM on the CMB through the Sunyaev-Zel'dovich (SZ) effect, which is seen as a deficit of CMB photons in the direction of clusters when observed at frequencies less than 217 GHz. With the Atacama Cosmology Telescope (ACT), we use the f090 and f150 'daynight' DR5 maps [2], centred on respective frequencies 97.8 and 149.6 GHz (see Hilton et al. 2021; Mallaby-Kay

[1] https://dominiqueeckert.wixsite.com/xcop
[2] https://lambda.gsfc.nasa.gov/product/act/actpol_dr5_coadd_maps_get.html

et al. 2021). We only exploit the MACS J0949 data in this article, as a source is detected on the field of view of MACS J0242, masking the SZ signal purely associated to the ICM of the cluster.

3 STRONG LENSING ANALYSES OF MACS J0242 & MACS J0949

If distant background sources happen to be close to the line-of-sight between a heavy galaxy cluster and an observer, the background image can be strongly lensed, to the point multiple images appear to the observer. Using this gravitational lensing effect in the strong regime, we can precisely map the gravitational potential of the cluster, and its total – baryonic and dark matter – mass density.

In Allingham et al. (2022), we performed a reconstruction of the total matter density, ρ_m, of the two galaxy clusters MACS J0242 and MACS J0949. These lensing models were obtained thanks to a combination of imaging with the *Hubble Space Telescope* (*HST*) and DES from the ground, together with spectroscopy obtained with the MUSE instrument at the Very Large Telescope (VLT). Figure 1 shows colour-composite images of the two clusters used in this work, together with the ICM distribution obtained thanks to X-rays observations, and density contours from the strong-lensing analyses presented in Allingham et al. (2022).

With spectroscopy, we detected 6 and 2 systems of multiply-lensed images in MACS J0242 and MACS J0949 respectively, for a total of 18 and 9 images with spectroscopic redshifts. 4 additional systems were detected with imaging *HST* observations in cluster MACS J0949, and thus do not present a redshift measurement. Using a combination of photometry and spectroscopy, we identified 57 and 170 cluster member galaxies respectively. We performed the strong lensing optimisation with `Lenstool` (Jullo et al. 2007), using the multiply-imaged systems to invert the lens equation. We have assumed the potential of a galaxy cluster to be a superposition of dPIE potentials. We modelled each cluster with a large-scale dark matter halo (DMH), a brightest cluster galaxy (BCG), and a $L^\star$ catalogue of elliptical galaxies, scaled using the Faber-Jackson relationship (Faber & Jackson 1976). Additionally, we introduced in MACS J0949 a clump in the south of the halo, to explain multiply-lensed images in this region.

Tables 1 and 2 present respectively the summary of the lensing information available for each cluster, and the best-fit parameters of the strong-lensing models obtained for the different potentials of each galaxy clusters. The average distance between the multiple images predicted with the lensing models and the observations is $0.39''$ and $0.15''$, and the reduced χ^2, $\chi^2_{\rm red} = 0.86$ and 0.67, for clusters MACS J0242 and MACS J0949 respectively, indicating a good quality reconstruction. The enclosed mass within 200 kpc of the cluster centre were respectively $M(R < 200\,\mathrm{kpc}) = 1.67^{+0.03}_{-0.05} \times 10^{14} M_\odot$ for MACS J0242, and $M(R < 200\,\mathrm{kpc}) = 2.00^{+0.05}_{-0.20} \times 10^{14} M_\odot$ for MACS J0949. Cluster MACS J0242 is found to be dynamically relaxed, with a peaked central density, while MACS J0949 presents a more flat density distribution in the core ($R \in [10, 100]$ kpc), and is still relaxing, but not strongly disturbed.

The inferred 3D density profiles were well fit by NFW profiles (see Section 4.1). For MACS J0242, we found the best fitting NFW parameters to be $\rho_S = 3.42 \times 10^{-22}\,\mathrm{kg.m^{-3}}$ and $r_S = 209.9$ kpc, for a reduced $\chi^2 = 1.11$. For MACS J0949, the best fitting parameters are $\rho_S = 1.23 \times 10^{-22}\,\mathrm{kg.m^{-3}}$, $r_S = 405.5$ kpc, for a reduced $\chi^2 = 1.90$. In this article, we only use the dark matter halos (DMH) and brightest cluster galaxies (BCG) potentials to represent the clusters' gravitational potential.

4 GALAXY CLUSTERS: A THEORETICAL DESCRIPTION

This Section introduces the observables and models necessary to describe the physics of the ICM using gravitational lensing. Section 4.1 introduces the two general full matter density profiles we use in this work; Section 4.2 presents the *canonical* description for the ICM density; Section 4.3 defines the gas fraction, i.e. the ratio between the ICM density and the total matter density; Section 4.4 shows the derivation of the *analytical* ICM density using a temperature model and total matter density; Section 4.5 extends the common polytropic temperature density to the higher electron densities found in the centre of clusters; Sections 4.6 and 4.7 define the X-ray surface brightness and the SZ effect temperature contrast respectively, in order to make observable predictions.

4.1 Galaxy clusters matter density models

The total matter density is here modelled with a parametric model, i.e. with a predefined profile. In the present article, we write all profiles as purely radial for clarity, but in our reconstruction, we use the various geometrical parameters of the individual potentials inferred from lensing (position of the centre, ellipticity, position angle) nonetheless. We here present two cases, a Navarro-Frenk-White (NFW) density profile, and a dual pseudo-isothermal elliptical mass distribution (dPIE) density profile.

4.1.1 Navarro–Frenk–White (NFW) profile

The NFW profile (introduced in Navarro et al. 1996) describes the DM density. We here approximate it to the total density distribution, ρ_m:

$$\rho_m(r) = \rho_S \left\{ \frac{r}{r_S} \left(1 + \frac{r}{r_S} \right)^2 \right\}^{-1}, \tag{1}$$

where ρ_S is the density normalisation, and r_S, the scale radius. These are parameters different for each cluster. We assume the NFW profile to describe the total density with one profile for a single cluster.

4.1.2 Dual Pseudo-Isothermal Elliptical Mass Distribution (dPIE) profile

In Kassiola & Kovner (1993) and Elíasdóttir et al. (2007), the dual Pseudo-Isothermal Elliptical Matter Distribution (dPIE) scales as:

$$\rho_m(r) = \rho_0 \left\{ \left[1 + \left(\frac{r}{s} \right)^2 \right] \left[1 + \left(\frac{r}{a} \right)^2 \right] \right\}^{-1}, \tag{2}$$

with the core radius, a, of the order of 100 kpc for the dark matter halo, and a truncation radius, $s > a$. Whilst this distribution is spherically symmetric, we also consider two other parameters: a rotation angle, θ, and an ellipticity, e. This model is sometimes referred to as *pseudo-Jaffe*, as in the review of Keeton (2001).

Contrarily to the NFW density profile, the dPIE profile does not present any divergence in $r \to 0$, i.e. presents a finite density. For our lensing reconstruction, we used a large scale Dark Matter Halo (DMH) modelled with a dPIE, and superposed it to individual profiles fitting individual cluster member galaxies. In the case of the analysed clusters, their (relative) relaxation allows us to discard all individual (galaxy) potentials but that of the brightest cluster galaxy (BCG). Paired with the DMH, the BCG respectively govern the large and small radii total matter densities. This DMH and BCG superposition was well fitted by a NFW profile for both clusters (see Section 3).

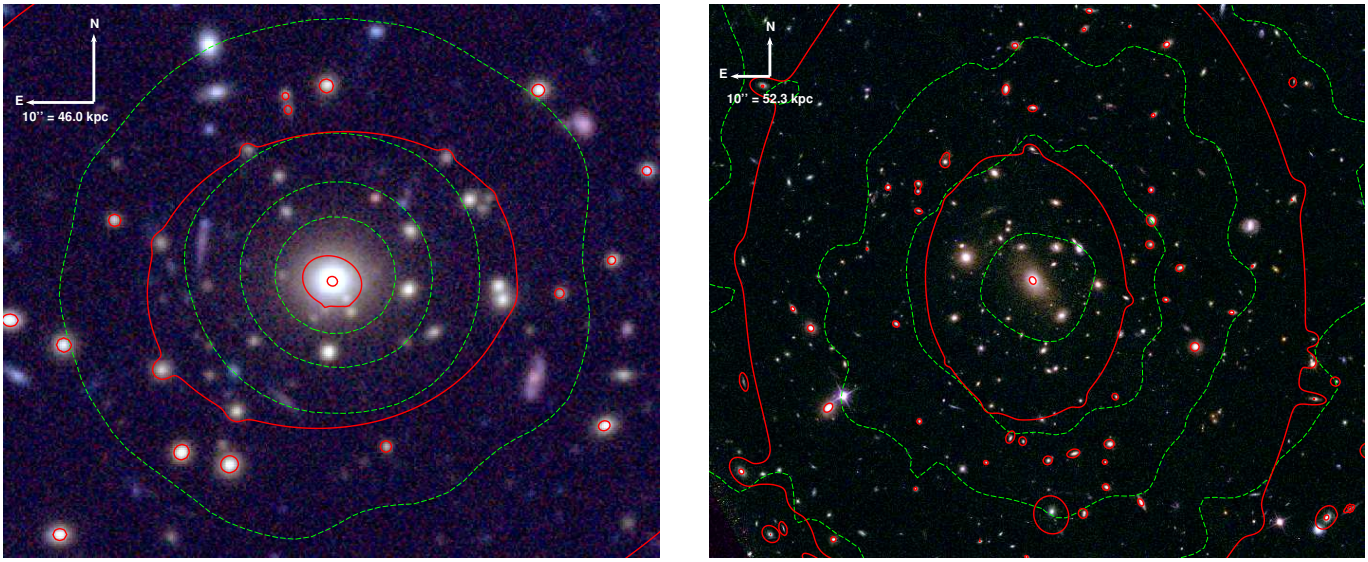

Figure 1. Composite RGB colour images of the two lensing clusters. *Left:* Composite DES colour image of MACS J0242. *Right:* Composite colour *HST* image of MACS J0949. *Green:* Hot gas distribution, obtained with *XMM-Newton* observations. *Red:* Contours of equal density, inferred from lensing models.

Table 1. Summary of the lensing reconstruction of galaxy clusters MACS J0242 and MACS J0949. We here list: (i) the galaxy clusters; (ii) number of galaxies in the cluster catalogue; (iii) number of multiply-lensed images detected; (iv) number of associated spectroscopic redshift measurements; (v) rms deviation of predicted multiply-lensed images positions from their observed positions in the image plane; (vi) reduced χ^2; (vii) projected mass enclosed within 200 kpc (in $10^{14} M_\odot$).

Galaxy cluster	$N_{\rm gal}$	$N_{\rm im}$	$N_{{\rm spec}-z}$	rms	$\chi^2_{\rm red}$	$M(R < 200\,{\rm kpc})$ $[10^{14} M_\odot]$
MACS J0242	57	18	18	$0.39''$	0.86	$1.67^{+0.03}_{-0.05}$
MACS J0949	170	20	9	$0.15''$	0.67	$2.00^{+0.05}_{-0.20}$

Table 2. Best fit parameters of the strong lensing mass model for MACS J0242 and MACS J0949. We here list the central coordinates, Δ_α and Δ_δ, in arcsec, relative to the centre, the ellipticity, e, the position angle in degrees, θ, the core radius in kpc, a, the cut radius in kpc, s, and the velocity dispersion in km.s^{-1}, σ, for each component of the model. The centres are taken to be respectively $(\alpha_c, \delta_c) = (40.649555, -21.540485)$ deg and $(\alpha_c, \delta_c) = (147.4659012, 17.1195939)$ deg for MACS J0242 and MACS J0949. The asterisks highlight parameters which are fixed during the optimisation. $L^\star$ represents the cluster member galaxies catalogue, scaled with the Faber-Jackson scaling relation (Faber & Jackson 1976). MACS J0949 includes a southern dark matter clump O3.

	Δ_α	Δ_δ	e	θ	a	s	σ
				MACS J0242			
DMH	$-0.138^{+0.085}_{-0.143}$	$0.136^{+0.111}_{-0.179}$	$0.287^{+0.037}_{-0.027}$	$17.884^{+0.762}_{-1.830}$	$57.194^{+6.044}_{-8.414}$	$1500^\star$	$918.479^{+28.984}_{-36.074}$
BCG	$0.044^\star$	$-0.090^\star$	$0.226^\star$	$155.758^{+10.766}_{-9.604}$	$0.300^\star$	$177.575^{+32.245}_{-57.950}$	$524.516^{+58.810}_{-43.956}$
$L^\star$					$0.030^\star$	$5.625^{+7.845}_{-1.808}$	$199.242^{+30.721}_{-53.257}$
				MACS J0949			
DMH	$-1.936^{+0.215}_{-2.843}$	$-0.671^{+0.565}_{-0.666}$	$0.249^{+0.398}_{-0.045}$	$92.434^{+0.570}_{-1.289}$	$116.246^{+24.108}_{-51.661}$	$1500^\star$	$1236.094^{+59.307}_{-310.553}$
BCG	$0^\star$	$0^\star$	$0.475^\star$	$120.130^\star$	$0.250^\star$	$98.044^{+153.739}_{-34.342}$	$253.749^{+196.474}_{-18.473}$
Clump O3	$4.800^{+0.748}_{-0.464}$	$-60.133^{+2.391}_{-1.417}$	$0.097^{+0.294}_{-0.061}$	$128.629^{+41.438}_{-27.521}$	$20.548^{+31.596}_{-8.771}$	$232.502^{+180.124}_{-119.902}$	$323.220^{+120.202}_{-54.851}$
$L^\star$					$0.150^\star$	$23.135^{+111.473}_{-2.053}$	$139.314^{+25.804}_{-18.547}$

4.2 ICM density

We now present two models commonly used for X-ray and SZ physics analyses to model the electron density profile. The general number density of electrons, n_e, can be written as:

$$n_e(r) = \mathcal{F}_I(r) \frac{\rho_g(r)}{\mu_e m_a}, \tag{3}$$

where ρ_g is the gas volume density, $\mathcal{F}_I$ is the local ionisation fraction which is taken to be 1, and the atomic mass constant $m_a = 1$ Da. We

define the mean molecular weight of electron, μ_e, ion, μ_I, and gas, μ_g, respectively:

$$\begin{aligned}\mu_e &= \left(\sum_i \frac{x_i Z_i f_i}{A_i}\right)^{-1},\\ \mu_I &= \left(\sum_i \frac{x_i}{A_i}\right)^{-1},\\ \mu_g &= \left(\mu_e^{-1} + \mu_I^{-1}\right)^{-1},\end{aligned} \tag{4}$$

where i are the atomic element's number, x_i is the fraction of an atomic species, A_i, the atomic weight of a species, Z_i, its atomic number, $\mathcal{F}_I$, the fraction of ionisation of a species. In practice $\mu_g \approx 0.60$, and $\mu_e \approx 1.15$. Here we focus on the electron density because it is directly observable in the X-rays and thanks to the SZ effect. However, one could derive the ion or gas density too.

A number of models have been proposed for the electron density profile, which we refer to as *canonical*. One of the most complete model is provided in Vikhlinin et al. (2006). As it relies on a large set of parameters, not necessary here, we focus on a simplified model, the (simple) β model (see King 1966; Cavaliere & Fusco-Femiano 1976):

$$n_e(r) = n_{e,0}\left[1 + \left(\frac{r}{r_c}\right)^2\right]^{-\frac{3}{2}\beta}, \tag{5}$$

with r_c, the core radius, and $\beta \in [0.5; 0.9]$, an empirical index. We find this model to fit well both clusters' ICM distribution (see Sections 7.1.1 and 7.2.1), thus showing a more complex model to be unnecessary here.

Even though attempts exist to analytically connect the β index to the thermodynamical and density parameters of the cluster, we treat it as a parameter to optimise in our study. Theoretically, according to Sadat (1997),

$$\beta_{\rm th} = \mu_g m_a \frac{\sigma_{los}^2}{k_B T_x}, \tag{6}$$

where σ_{los} is the line of sight velocity dispersion, and T_x, the temperature of the cluster. However, as mentioned in Sarazin (1988), it is common knowledge this exponent is not giving the observed density (in practice, $\beta_{\rm fit} \simeq 0.65$, ranging between 0.5 and 1). This β problem partly arises from the isotropic hypothesis, as shown in Hallman et al. (2007), but also because the total matter density is not perfectly described by the β profile.

4.3 Gas fraction

We here define the gas fraction as the ratio of the mass of gas and the total matter density – including dark matter. The gas mass includes all baryons except stars. We distinguish the local gas fraction, $f_g(r) = \rho_g(r)/\rho_m(r)$, considered in this article to be a radial function, and the cumulative gas fraction, F_g, given within a radius, r:

$$\begin{aligned}F_g(r) &= \frac{\int_0^r {\rm d}s s^2 \rho_g(s)}{\int_0^r {\rm d}s s^2 \rho_m(s)} = \frac{M_g(<r)}{M_m(<r)},\\ f_g(r) &= \frac{{\rm d}F_g}{{\rm d}r}(r)\frac{\int_0^r {\rm d}s s^2 \rho_m(s)}{r^2\rho_m(r)} + F_g(r).\end{aligned} \tag{7}$$

The full knowledge of either of these gas fractions would provide a bijective relationship between the gas and matter content of galaxy clusters. We will therefore name *gas density* reconstruction our electron density prediction using an empirical gas density model.

4.4 A fully analytical electron density

4.4.1 General case

We consider the total (DM and baryons) mass density as a sum of densities:

$$\rho_m(r) = \sum_i \rho_{0,m,i} f_i(r), \tag{8}$$

which is constrained by the strong lensing analyses. Each potential can be normalised differently, and the distributions, f_i, are assumed to be of the same type (here NFW or dPIE). Here, we write them as a sum of radial functions for simplicity. In practice, every profile, f_i, has its own geometric parameters (central position, ellipticity, rotation angle), which we consider to be fixed from the strong lensing analysis.

Assuming integrability, we introduce:

$$\begin{aligned}g_i(r) &= \int {\rm d}s s^2 f_i(s),\\ h_i(r) &= \int {\rm d}s s^{-2} g_i(s),\end{aligned} \tag{9}$$

where integration constants are included. Denoting Φ, the Newtonian potential, the gravitational Poisson equation reads:

$$\Delta\Phi = -4\pi G\rho_m, \tag{10}$$

and thus the gravitational potential:

$$\Phi(r) = -4\pi G \sum_i \rho_{0,m,i} h_i(r). \tag{11}$$

We write intensively the ideal gas law:

$$P_g = k_B n_g T_g = \frac{k_B T_g \rho_g}{\mu_g m_a}, \tag{12}$$

where P_g and T_g are the gas pressure and temperature respectively, and k_B, the Boltzmann constant. We now write the conservation of momentum in the Lagrangian formalism, i.e. the momentum Navier-Stokes equation for a perfect fluid (viscosity neglected, see e.g. Landau & Lifshitz 1959):

$$\rho_g \frac{{\rm D}\boldsymbol{v}}{{\rm D}t} = \rho_g\left[\partial_t \boldsymbol{v} + (\boldsymbol{v}\cdot\boldsymbol{\nabla})\boldsymbol{v}\right] = -\boldsymbol{\nabla}P_g + \rho_g\boldsymbol{\nabla}\Phi, \tag{13}$$

with $\boldsymbol{v}$, the velocity field.

As the pressure in galaxy clusters is of the order of 10^{10} Pa, the plasma is thermalised, and therefore the temperature of the gas to be that of the electrons. With equation (3), we can write the number density of the electron n_e as being directly proportional to the gas density ρ_g, as μ_e and $\mathcal{F}_I$ are assumed to be constant in a given cluster. We rewrite equation (13) in the purely radial case:

$$\frac{k_B}{\mu_g m_a}\frac{\partial_r(n_e T_e)}{n_e} + \partial_t v_r + v_r\partial_r v_r = -4\pi G\sum_i \rho_{0,m,i} r^{-2} g_i(r). \tag{14}$$

As the galaxy clusters used in our study are not strongly perturbed, we work under the hypothesis of hydrostatic equilibrium. Assuming we could decompose the velocity in its radial and temporal dependencies, one could then integrate numerically. Assuming a polytropic temperature distribution and the stream to be hydrostatic, i.e. of constant velocity, both in time and in all spatial directions, such as in Zaroubi et al. (2001), we get:

$$\frac{\partial_r(n_e T_e)}{n_e} = \epsilon\sum_i \rho_{0,m,i} r^{-2} g_i(r), \tag{15}$$

where $\epsilon = -4\pi G \mu_g m_a / k_B$.

In order to reduce this expression, we define a general $\mathcal{J}$ function as:

$$\mathcal{J}(n_e) = \int_0^{n_e} \frac{\mathrm{d}\left[nT_e(n)\right]}{T_0 n}, \tag{16}$$

where T_0 is a temperature normalisation (see Sect. 4.5). More details on the definition of $\mathcal{J}$ are given in Sect. 5.1, given a precise temperature model.

Separating variables and integrating equation (15), we obtain:

$$\mathcal{J}(n_e) = \frac{\epsilon}{T_0} \sum_i \rho_{0,m,i} h_i(r) = \frac{\mu_g m_a}{k_B T_0} \Phi(r). \tag{17}$$

If we assume $\mathcal{J}$ to be bijective (assumption justified given a temperature model in Sect. 5.1), then inverting this equation simply provides $n_e(r)$:

$$n_e(r) = \mathcal{J}^{-1}\left(\frac{\mu_g m_a}{k_B T_0} \Phi(r)\right). \tag{18}$$

Assuming $\mathcal{J}$ to be a bijection, we can also invert it and normalise the distribution at a given radius (e.g. 200 kpc, where the strong lensing signal is strongly constraining the total density profile, or $R_{500,c}$), if we happen to know $n_{e,\Delta}$. Writing Δ such a radius, we can therefore write:

$$n_e(r) = \mathcal{J}^{-1}\left[\mathcal{J}(n_{e,\Delta}) \frac{\Phi(r)}{\Phi(R_{\Delta,c})}\right]. \tag{19}$$

We call this latter expression *self-normalised*.

Under reasonable physical hypotheses, we have provided a general, completely analytical description of the electron density using only the different potentials found with lensing. To allow this reconstruction to be independent from other observations however, this *analytical* model requires an electron temperature model which we could predict with lensing only. Importantly, we notice this electron density does not depend on the gas fraction, nor on any unknown universal parameter.

4.4.2 Case of a dPIE density

In the case of a dPIE mass distribution, we give:

$$\begin{aligned} f(r) &= \left\{\left[1 + \left(\frac{r}{s}\right)^2\right]\left[1 + \left(\frac{r}{a}\right)^2\right]\right\}^{-1}, \\ g(r) &= \frac{a^2 s^2}{a^2 - s^2}\left[a \arctan\frac{r}{a} - s \arctan\frac{r}{s}\right], \\ h(r) &= \frac{a^2 s^2}{a^2 - s^2}\left[\frac{s}{r}\arctan\frac{r}{s} - \frac{a}{r}\arctan\frac{r}{a} + \frac{1}{2}\ln\left(\frac{r^2 + s^2}{r^2 + a^2}\right)\right], \end{aligned} \tag{20}$$

where a and s represent the core r_{core} and scale r_{cut} radii of the i-th dPIE potential respectively. Indices were avoided for clarity. To avoid confusion, we write `idPIE` the n_e distribution with h_i given by a dPIE.

4.4.3 Case of a NFW density

In the case of a NFW potential – see equation (1), we can rewrite the different integrals given equation (20) for the dPIE:

$$\begin{aligned} f(r) &= \left\{\left[\frac{r}{r_S}\right]\left[1 + \frac{r}{r_S}\right]^2\right\}^{-1}, \\ g(r) &= r_S^3\left[\ln\left(1 + \frac{r}{r_S}\right) - \frac{r}{r + r_S}\right], \\ h(r) &= -\frac{r_S^3}{r}\ln\left(1 + \frac{r}{r_S}\right), \end{aligned} \tag{21}$$

where indices were avoided for clarity. Here $\rho_{0,m,i}$ of equation (17) is $\rho_{S,m,i}$. We notice that in case of NFW profile, we assume the total density to be represented by a single profile. We shall write this distribution `iNFW`.

4.5 Temperature

In order to write the matter density profile in general terms using strong lensing constraints only, we need to adopt a general temperature model, independent of the specific observations of one cluster. We could consider an isotropic temperature model, but for higher precision, we preferred using polytropic models, generally written (for example in Capelo et al. 2012):

$$T_e(r) = T_0\left(\frac{n_e(r)}{n_{e,0}}\right)^{\gamma - 1}, \tag{22}$$

where $n_{e,0}$ is the central electronic density, T_0 is therefore the temperature in the centre, and γ, the polytropic index[3]. According to Ghirardini et al. (2019b), we can almost universally take $\gamma \approx 1.2$.

More generally, the same article claims we can use a self-similar polytropic temperature model, with a varying polytropic index, $\Gamma(n_e)$:

$$\begin{aligned} \frac{P_e}{P_{500}} &= P_{\mathrm{ref}}\left(\frac{n_e E(z)^{-2}}{n_{\mathrm{ref}}}\right)^{\Gamma(n_e)}, \\ \frac{T_e}{T_{500}} &= T_{\mathrm{ref}}\left(\frac{n_e E(z)^{-2}}{n_{\mathrm{ref}}}\right)^{\Gamma(n_e) - 1}, \end{aligned} \tag{23}$$

where $E(z) = H(z)/H_0$ is the normalised Hubble factor assuming a ΛCDM cosmology with $\Omega_m = 0.3$ and $\Omega_\Lambda = 0.7$. P_{ref} and T_{ref} are dimensionless proportionality constants, and n_{ref} the volume number density normalisation. We write $T_0(z) = T_{500}(z) T_{\mathrm{ref}}$ and $n_0(z) = n_{\mathrm{ref}} E(z)^2$. Section 5.1.2 presents a new model for this index, and also provides the quantitative values for the different constants presented here.

4.6 X-ray surface brightness

In order to compare our results to observations, and therefore to evaluate the quality of our ICM reconstruction models, we introduce the observable X-ray brightness. The X-ray surface brightness in a band of wavelength (such as the $[0.7, 1.2]$ keV band for *XMM-Newton*) integrated over the line-of-sight reads (see Böhringer & Werner 2010, for a review):

$$S_X(\Delta E) = \frac{1}{4\pi(1+z)^4}\frac{\mu_e}{\mu_H}\int n_e^2(\boldsymbol{r}) \Lambda(\Delta E, T_e, Z) \mathrm{d}l. \tag{24}$$

[3] Throughout this article, we denote γ the constant polytropic index, and Γ the radius-dependant one.

where $\mu_H \approx 1.35$ is the mean molecular weight of hydrogen, $\Lambda(\Delta E, T_e, Z)$ is the X-ray spectral emissivity (or *cooling curve*), as a function of the X-ray energy band, ΔE, the electron temperature of the gas, T_e, and the metallicity of the gas, Z. In this article, the metallicity is assumed to be constant for a given cluster.

4.7 SZ effect

Another observable, depending on the electron density and temperature is the SZ effect. Given an observable frequency, ν, we use the reduced frequency, x:

$$x = \frac{h\nu}{k_B T_r}, \tag{25}$$

with h, the Planck constant, and $T_r \simeq 2.726\,\mathrm{K}$, the temperature of the CMB. We define the Compton parameter (see Rephaeli 1995):

$$y(r) = \frac{k_B \sigma_T}{m_e c^2} \int T_e(r) n_e(r) \mathrm{d}l, \tag{26}$$

with σ_T, the Thomson cross-section, and m_e, the mass of the electron. The thermal SZ contrast then reads:

$$\Theta_{\mathrm{SZ}}(r) = \frac{\Delta T}{T_r} = \left[x \coth\left(\frac{x}{2}\right) - 4\right] y(r). \tag{27}$$

5 QUANTITATIVE MODELS

We have shown in the previous section two completely different manners to use the lensing study of galaxy clusters to predict their baryonic distributions:

1. Through the knowledge of the *gas fraction* defined Sect. 4.3;
2. *Analytically*, assuming hydrostatic equilibrium, with a given temperature distribution, as described equation (18).

In this section, we establish the general models of the temperature profiles and gas fraction. We thus show how we can use strong lensing observations to learn more about the thermodynamics properties of clusters. Therefore, we relate a given DM distribution to a thermodynamic profile.

5.1 Polytropic index scaling

5.1.1 Constant polytropic index

A self-similar polytropic temperature law with a constant index $\gamma > 1$ would result into:

$$\mathcal{J}_z(n_e) = \frac{\gamma}{\gamma - 1} \left(\frac{n_e}{n_0(z)}\right)^{\gamma - 1}, \tag{28}$$

and thus we could then directly write the electron density from equation (17) as an analytical bijection of the total density:

$$n_e = n_0(z) \left[\frac{\gamma - 1}{\gamma} \frac{\epsilon}{T_0(z)} \sum_i \rho_{0,m,i} h_i(r)\right]^{1/(\gamma - 1)}. \tag{29}$$

However, we find such a description to fail to describe the higher electron densities ($n_e > 10^5\ \mathrm{m}^{-3}$), which is consistent with a constant γ index fixed with the largest radii of clusters, i.e. the least dense regions. We notice the specific case of a polytropic temperature density associated to a NFW profile has already been studied in Bulbul et al. (2010), where a self-normalisation in the centre is utilised.

5.1.2 Polytropic index model

To describe the relation between ICM thermodynamic quantities (n_e, P_e, T_e), it is common practice to describe the stratification of the ICM using a polytropic equation of state $P(n_e) \propto n_e^\Gamma$ (e.g. Bulbul et al. 2010; Capelo et al. 2012; Tchernin et al. 2018; Ghirardini et al. 2019b). Analytic models assuming the ICM to be in hydrostatic equilibrium within a NFW potential predict that the polytropic index Γ should be close to a constant value of ~ 1.2 throughout the cluster volume (Capelo et al. 2012). Observationally speaking, the measured values of the polytropic index closely match the NFW expectation in cluster outskirts ($R > 0.2R_{500}$) but significantly deviate from it in the cluster core, where Γ decreases down to ~ 0.8 under the influence of radiative cooling (Ghirardini et al. 2019b). Using the data from the X-COP programme, Ghirardini et al. (2019b) showed that the $P(n_e)$ relation is nearly universal across the cluster population with a low scatter of $\sim 15\%$, independently of a system's dynamical state. Here we propose a new functional form to describe the self-similar polytropic model (supported by e.g. Mostoghiu et al. 2019). We describe the relation with a smoothly varying polytropic index $\Gamma(n_e)$ as:

$$\frac{\mathrm{d}\ln P_e}{\mathrm{d}\ln n_e} \equiv \Gamma(n_e) = \Gamma_0 \left[1 + \Gamma_S \arctan\left(\ln \frac{n_e E(z)^{-2}}{n_{\mathrm{ref}}}\right)\right], \tag{30}$$

with n_{ref} the reference number density around which the transition between core (low Γ) and outskirts (NFW Γ) occurs, Γ_0 the polytropic index at n_{ref}, and Γ_S the slope of the transition.

We used the publicly available X-COP data, which provide high-quality observations of the ICM thermodynamic properties over a wide radial range ($\approx [0.01 - 2]R_{500}$), to calibrate the model and determine the parameters of equation (30). We fit the X-COP density and pressure data using the Bayesian analysis package `PyMC3` (Salvatier et al. 2016), including uncertainties on both axes, and a free log-normal intrinsic scatter. The observational data points on both axes are scaled by their respective self-similar scaling values (Arnaud et al. 2010). The result of this procedure is shown in Fig. 2. The model provides an excellent representation of the data over three decades in electron density, with a low intrinsic scatter of $\sigma_{\ln P} = 0.19 \pm 0.02$. The right-hand panel of Fig. 2 also shows that the results obtained with the model defined in equation (30) are consistent with the values estimated by Ghirardini et al. (2019b) when fitting a piece-wise power law over several ranges in density. The fit parameters are included in Table 3.

Supposing the ICM to be an ideal gas, following Ghirardini et al. (2019a), we write:

$$T_{\mathrm{ref}} = \left(387\mathrm{m}^{-3}\right) \frac{P_{\mathrm{ref}}}{n_{\mathrm{ref}}} \frac{f_b}{0.16} \frac{\mu_e}{1.14}, \tag{31}$$

with f_b is the universal baryon fraction, taken to be $f_b = 0.158 \pm 0.002$ (Ade et al. 2016). We find $T_{\mathrm{ref}} \approx 1.034$.

As for the full $T_{500}(z)$, we use the results of Ghirardini et al. (2019a), which we reproduce here:

$$T_{500}(z) = 8.85\mathrm{keV} \left(\frac{M_{500} E(z)}{h_{70}^{-1} 10^{15} M_\odot}\right)^{2/3} \left(\frac{\mu_g}{0.6}\right), \tag{32}$$

with $h_{70} = h/0.7 = 1$. We therefore can normalise the temperature universally.

5.1.3 Varying polytropic index

At a given redshift, z, using the self-similar polytropic temperature described equations (23) and (30), we can define the integral $\mathcal{J}_z$, i.e.

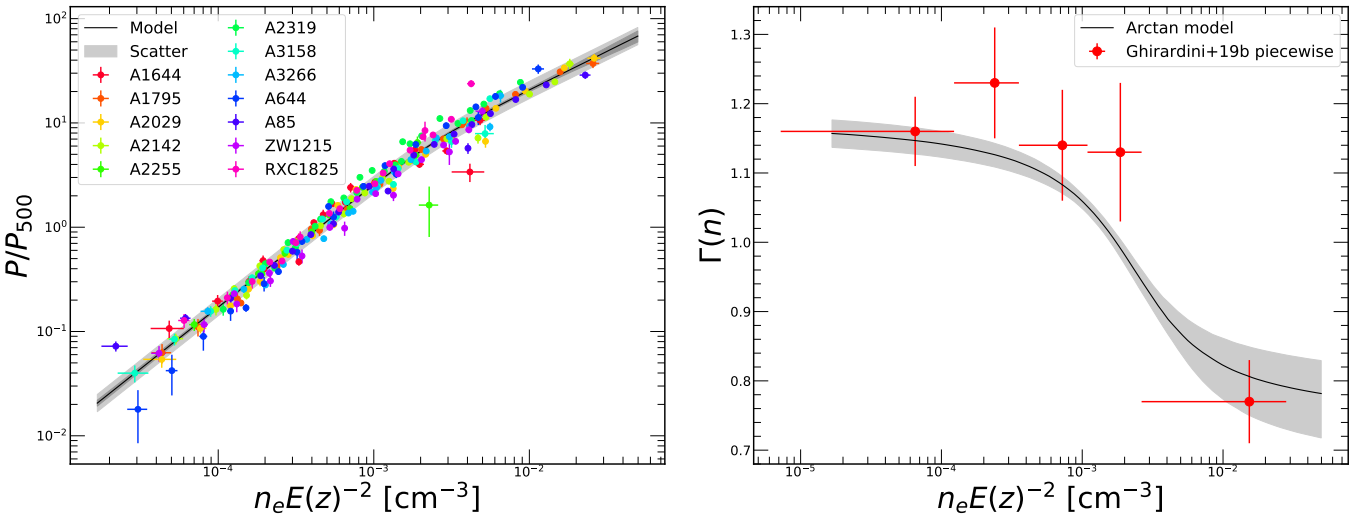

Figure 2. Calibration of the variable $\Gamma(n_e)$ polytropic model (equation 30) on X-COP data. *Left:* Relation between self-similar scaled ICM pressure and electron density for the 12 X-COP clusters. The solid black line and the grey shaded area show the best-fit model and the intrinsic scatter around the model, respectively. *Right:* Polytropic index $\Gamma = \mathrm{d}\ln P_e/\mathrm{d}\ln n_e$ as a function of electron density. The black line and shaded area shows the best-fit model with equation (30), whereas the red data points show the result of a piece-wise fit with constant polytropic index over several ranges in electron density.

Table 3. Parameters of the smoothly varying polytropic model defined in equations (23) and (30).

$P_{\rm ref}$	$n_{\rm ref}$ [m^{-3}]	Γ_0	Γ_S	$\sigma_{\ln P_e}$
6.05 ± 1.57	$(2.26 \pm 0.59) \times 10^3$	0.97 ± 0.04	-0.15 ± 0.03	0.19 ± 0.02

a redshift dependent $\mathcal{J}$, defined equation (16):

$$\mathcal{J}_z(n_e) = \int_0^{n_e} \left[\Gamma(n) + \frac{\Gamma_0\Gamma_S \ln\left(\frac{n}{n_0(z)}\right)}{1+\left[\ln\left(\frac{n}{n_0(z)}\right)\right]^2}\right]\left(\frac{n}{n_0(z)}\right)^{\Gamma(n)-1} n^{-1}\mathrm{d}n. \tag{33}$$

In this case, $\mathcal{J}_z$ can be easily computed at a given redshift, and reverted. It is however not analytically solvable. An example of $\mathcal{J}_z$ is displayed in Fig. 3.

We find $\mathcal{J}_z$ to be indeed a bijection, and therefore we can take its inverse function, and fully define n_e as a function of the radius, as displayed in equation (17).

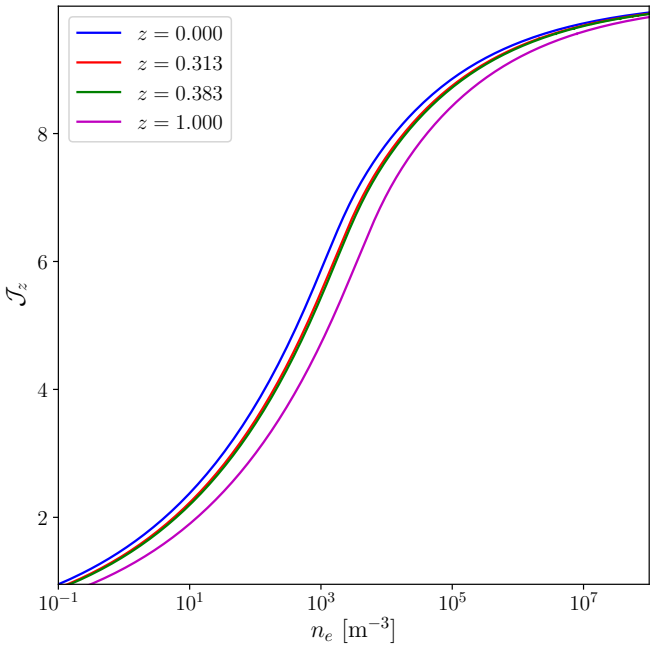

Figure 3. $\mathcal{J}_z(n_e)$ in a range of redshifts, including those of galaxy cluster MACS J0242 and MACS J0949 – which are almost identical.

5.2 Gas fraction study

We use the 'X-COP+2' sample analysis, i.e. the X-COP (*XMM* Cluster Outskirts Project) sample, complemented with similar analyses for our two strong-lensing clusters, MACS J0242 and MACS J0949. We compare the cumulative gas fraction reconstruction (as defined in Sect. 4.3) in each of the 14 clusters in the sample, and propose two new *ad hoc* models.

5.2.1 *Proposed models*

With respect to the data analysed in Sect. 5.2.2, we propose the following models. First, we attempt to describe the increasing cumulative gas fraction, F_g, as a power law:

$$F_g(r) = f_g^0\left(1+\frac{r}{r_c}\right)^{\zeta}, \tag{34}$$

where r_c is a pivot, or core radius, $f_g^0 = F_g(r = 0)$, the central gas fraction, i.e. the baryonic fraction excepted the stellar fraction, and ζ, the power exponent to find.

However, for all clusters, the integrated gas fraction presents a transition between the inner and the outer regions of the cluster, as represented on Eckert et al. (2019, Fig. 1). We propose to analytically describe this transition with an Arctan model:

$$F_g(r) = a\left[\frac{2}{\pi}\arctan\left(\exp\frac{r-r_c}{r_f}\right) - \frac{1}{2}\right] + b, \tag{35}$$

where a and b are defined with the expected gas fraction at the centre and at 'infinity' f_g^0 and f_g^∞:

$$\begin{aligned} \upsilon &= \frac{2}{\pi}\arctan\left[\exp\left(-\frac{r_c}{r_f}\right)\right], \\ a &= \frac{f_g^0 - f_g^\infty}{\upsilon - 1}, \\ b &= \frac{1}{2}\left[\frac{f_g^0}{1-\upsilon} + \frac{f_g^\infty(1-2\upsilon)}{1-\upsilon}\right], \end{aligned} \tag{36}$$

and r_c and r_f are the core and flattening radii respectively, i.e. the radii of Arctan inflexion point and the characterisation of the slope of the transition.

We assume *a priori* r_c and r_f to be provided by the lensing analysis. In fact, in our lensing analysis we used models based on the presence of a DMH governing the large scale physics, and a BCG governing the centre; we can therefore extrapolate the transition in gas fraction to be caused by the BCG to DMH transition. We can also formulate the hypothesis that f_g^∞ should correspond to the universal gas fraction $f_g^{\rm Uni}$. It is defined in Eckert et al. (2019) as the Universal baryonic fraction $\Omega_b/\Omega_m = 0.1580 \pm 0.0021$ (Ade et al. 2016), corrected for the stellar fraction $f_\star$, not accounted for in the intracluster gas, and the baryon depletion factor Y_b:

$$f_g^{\rm Uni}(r) = Y_b(r)\frac{\Omega_b}{\Omega_m} - f_\star, \tag{37}$$

Eckert et al. (2019) provides $Y_{b,500} = 0.938^{+0.028}_{-0.041}$, which we use here. Following the same study, we take the error on $f_{\star,500}$ to be 5×10^{-3}. The study of the lensing galaxy clusters gives stellar fraction of $f_\star = (1.92\pm0.21)\times10^{-2}$ and $(1.87\pm0.36)\times10^{-2}$ for MACS J0242 and J0949 respectively.

5.2.2 X-COP+2 study

With the power law and Arctan models, equations (34) and (35) respectively, we conduct a study of the 14 galaxy clusters of the X-COP+2 sample.

All these clusters were tested with both the power law and Arctan models, optimised for all respective 3 and 4 parameters ($\{ f_g^0, r_c, \zeta \}$ and $\{ f_g^0, f_g^\infty, r_c, r_f \}$) with a MCMC, with package `emcee` (see Foreman-Mackey et al. 2013). We define the log-likelihood function as Gaussian with an underestimated variance of fractional amount, f, which is also an optimised parameter:

$$\ln\mathcal{L}_{f_g}(\Theta) = -\frac{1}{2}\sum_i\left[\left(\frac{F_{g,i}^{\rm val} - F_{g,i}^{\rm pred}(\Theta)}{\sigma_i}\right)^2 + \ln\sigma_i^2\right], \tag{38}$$

where $F_{g,i}^{\rm val}$ are the values of the cumulative gas fraction in radius bins, $\sigma_i^{\rm err}$, its measured standard deviation error, $F_{g,i}^{\rm pred}$ are the predictions in the same bins, and:

$$\sigma_i^2 = \left(\sigma_i^{\rm err}\right)^2 + \left[F_{g,i}^{\rm pred}(\Theta)\right]^2 \exp\left(2\ln f\right). \tag{39}$$

We note that in practice $\ln f$ is optimised. We do not further present the convergence of this parameter, as at convergence, we always find $f < 0.01$.

Out of the 14 clusters, 5 were found to be best modelled with the power law, and 9, with the Arctan relationship – including MACS J0242 and MACS J0949. We performed the optimisation over all radii accessible in the X-ray data range, except for MACS J0242, where non-statistically significant perturbations exist in the gas fraction reconstruction. To avoid these, the optimisation was performed in $r \in [20; 350]$ kpc for this specific cluster.

We find that the Arctan model is consistently better, not only for a majority of clusters, but even those better fit by the power law were well fit with the Arctan model. Moreover, by construction, the Arctan model can use physical parameters for f_g^∞, r_c and r_f, and converges at large radii, which is expected from the Universal hot gas fraction. We give in Table 4 and Table 5 the optimised parameters for respectively the power law and the Arctan models. These are the averages of the best parameters found by the MCMC for each individual cluster.

Trying to relate these parameters to physical values, we notice in both cases f_g^0 to be the gas fraction at the centre of the clusters. The X-COP sample does not precisely provide the hot gas fraction in the centre of clusters ($r < 20$ kpc), due to the stellar effects, turbulence, and resolution of X-ray surveys. For these reasons, we may not directly use a physically measurable value for f_g^0, and simply use a fit of a parameter across all radii.

For the power law model, we consider the exponent ζ to be purely empirical. As for the pivot radius, r_c, its relative error bars are quite important. However, discarding the two clusters coming from lensing yields $r_c = 0.34 \pm 0.24$ kpc, i.e. a result very close the X-COP+2 one. The same process on ζ and f_g^0 gives results similar to those presented in Table 4, for respectively $\zeta = 0.41 \pm 0.14$ and $f_g^0 = (8.8 \pm 8.7) \times 10^{-3}$. We can therefore propose a model:

$$F_g(r) = 9.54\times10^{-3}\left[1 + \frac{r}{0.379\ \text{kpc}}\right]^{0.412}. \tag{40}$$

Given the important error bars found on all parameters of this model, its inability to predict accurately most the gas fraction for most clusters, and the lack of theoretical motivation for its parameters, we conclude to the ineffectiveness of this model.

As for the Arctan model, all parameters may be physically interpreted. The quantity f_g^∞ not only can be found quite precisely,

Table 4. Average over all clusters of the optimised parameters for the gas fraction power law model. r_c is in kpc.

f_g^0 (%)	r_c	ζ
(0.95 ± 0.94)	0.38 ± 0.25	0.41 ± 0.14

Table 5. Average over all clusters of the optimised parameters for the gas fraction Arctan model. r_c and r_f are in kpc.

f_g^0 (%)	f_g^∞ (%)	r_c	r_f
2.33 ± 1.56	13.6 ± 1.6	21.0 ± 64.6	231.5 ± 111.7

Table 6. Updated parameters and model for the gas fraction Arctan model, for the X-COP clusters only. r_c and r_f are in kpc.

$f_g^0(\%)$	$f_g^\infty(\%)$	r_c	r_f
2.33 ± 1.56	13.8 ± 1.5	1.16 ± 1.29	257.0 ± 98.7

but is also in agreement with equation (37). Indeed, for all clusters for which the stellar fraction was considered unknown, we can use the X-COP average value $f_{\star,500} = 0.015 \pm 0.005$. This provides $f_g^{\rm Uni} = 0.138 \pm 0.015$, assuming $Y_{b,500} = 0.9315 \pm 0.0345 \simeq Y_{b,\infty}$ according to Eckert et al. (2019). This is the f_g^∞ value we shall retain making the model. These values are in remarkable agreement with Table 5. As for r_c and r_f, we can not study the X-COP clusters and our lensing clusters jointly. Indeed, in the one hand, the hypothesis that these parameters would correspond to the core radius of the DMH, measured with lensing, can not be verified for the X-COP sample, for which we have no such value. On the other hand, the best fit values for the X-COP clusters of r_c all fall within $[0; 5]$ kpc, which is not the case our lensing clusters ($r_c = 27.0^{+15.8}_{-18.0}$ kpc for MACS J0242 and $r_c = 252.7^{+13.6}_{-26.6}$ kpc for MACS J0949, we summarise these in Table 7). For the X-COP clusters, we average over all optimised parameters for all 12 clusters, and present the results on Table 6. r_c and r_f are simply averaged best-fit parameters, and a finer study would be necessary to predict the value for each cluster using physical parameters. For instance, fitting all clusters' ICM distribution with a β profile (eq. 5) would allow to find r_c for each cluster, and to compare it to r_c and r_f.

In Table 7, we summarise for the two gravitationally modelled clusters the comparison between their optimised lensing DMH core radius a_1 and the r_c and r_f optimisations. For r_f as for r_c, it is impossible to conclude with only two cluster models. Moreover, they represent different physical situations – MACS J0242 being dynamically relaxed and MACS J0949 still relaxing. We attempt to propose a model with physically motivated parameters, which should be further studied and refined with more data. dPIE potentials are *a priori* constructed so that the core radius inferred from lensing represents a transition between the baryon influence and that of DM. Using this hypothesis, we take as a default $r_f = a_1$. We outline this hypothesis must be further explored, and we simply compared it to the best fit `Arctan` model in Table 7. Following the same assumption, with r_c being a pivot radius, we can assume in fully virialised cases $r_c \sim a_1$ to be a decent approximation (Table 7 shows these parameters to be of the same order, but not quite equal, with up to order 2 variations). We retain this *ad hoc* model, with equations (35) and (36), for our two lensing clusters:

$$F_g(r) = (-0.103 - 0.821 f_\star) \arctan\left[\exp\left(\frac{r}{a_1} - 1\right)\right] - 0.013 - 0.289 f_\star. \quad (41)$$

We give an example of the models fit directly to individual clusters, and to this 'universal' model for lensing galaxy clusters MACS J0242 and MACS J0949, on Fig. 4. As expected, the local models appear to be better fits, but we notice the 'universal' model displayed in blue are reasonable is a good approximations (the X-ray reconstruction is never distant of more than 2σ from the 'universal' models, in the fitting radii range). In the rest of this article, we retain this universal Arctan model as the predictive gas fraction model.

5.3 Relating all density models to lensing

We assume the metallicity of clusters MACS J0242 and MACS J0949 to be constant, and the plasma to be fully ionised $\mathcal{F}_I = 1$. The X-ray data suggest metallicities in the range $0.2 - 0.7\,Z_\odot$ for the two strong lensing clusters. The error bars being large, and the influence of metallicity being limited at these temperatures, we assume the metallicity to be $Z = 0.3 Z_\odot$ in both clusters (to justify this approximation, read e.g. McDonald et al. 2016).

For the analytical density profiles (such as `idPIE` or `iNFW`), the parameter priors are directly given from the lensing analysis Sect. 3. Conversely, we can not assume the parameters of the β-profile *a priori*. However their optimisation requires priors, for which we take $\beta = 0.63$ (in agreement with e.g. Böhringer et al. 2016), $n_{e,0}$ is taken to be the normalisation of the DMH density, and $r_c = a_1$, i.e. the core radius of the DMH obtained with the lensing optimisation. As for the gas fractions, we only use the Arctan model given for the strong lensing clusters by equation (41).

6 MEASURABLE ICM PREDICTIONS AND OPTIMISATIONS

In this Section, we present the results of the method we developed to convert the ICM predictions into ICM observables (S_X, Θ_r), in order to compare them to observations. Moreover, we use observations to constrain the total matter density with a MCMC, assuming the geometry to be fixed to values inferred through strong lensing. We summarise the whole process undertaken in the present article in Fig. 5.

6.1 Point spread function of *XMM-Newton*

In order to analyse the *XMM-Newton* observations, we reduce them to smaller maps centred around the cluster, of around 1 Mpc width (respectively 88 and 78 pixels for clusters MACS J0242 and MACS J0949). We then need to take into account the point-spread function (PSF). At first order, we define the PSF signal as:

$$PSF(r) = \left[1 + \left(\frac{r}{r_0}\right)^2\right]^{-\alpha}, \quad (42)$$

with r the distance to the centre, $r_0 = 5.304$ arcsec and $\alpha = 1.589$. We note that the number of pixels of the PSF must be odd to account for the centre. The measured surface brightness writes:

$$S_X^{\rm conv}(x, y) = (S_X^{\rm model} \circledast PSF)(x, y) \quad (43)$$

where $S_X^{\rm model}$ is provided in equation (24).

As the edge effect is quite important, we decide not to use the borders, and to cut 8 pixels on each side of the map. The final comparison maps are respectively 72 and 62 pixels wide for MACS J0242 and MACS J0949. We note that we still have to compute our model for the full width of the original maps, as they are needed in the convolution.

6.2 Converting surface brightness into count signal

We use the EPIC count maps of *XMM-Newton*, masking point-like sources, including diffuse emission only. As we also have access to the time of exposure, E, and total background, B (particle background, soft protons, PN chip out-of-time events), maps from surface

Table 7. Comparison for clusters MACS J0242 and MACS J0949 of the best r_c and r_f optimised values and of the lensing DMH core radius a_1 values.

Galaxy cluster	r_c	r_f	a_1	r_c/a_1	r_f/a_1
MACS J0242	$27.0^{+15.8}_{-18.0}$	$37.1^{+6.9}_{-8.5}$	$57.2^{+6.0}_{-8.4}$	$0.47^{+0.28}_{-0.32}$	$0.65^{+0.14}_{-0.18}$
MACS J0949	$252.7^{+13.6}_{-26.6}$	$120.6^{+43.5}_{-14.1}$	$116.3^{+24.1}_{-51.7}$	$2.17^{+0.47}_{-0.99}$	$1.04^{+0.43}_{-0.48}$

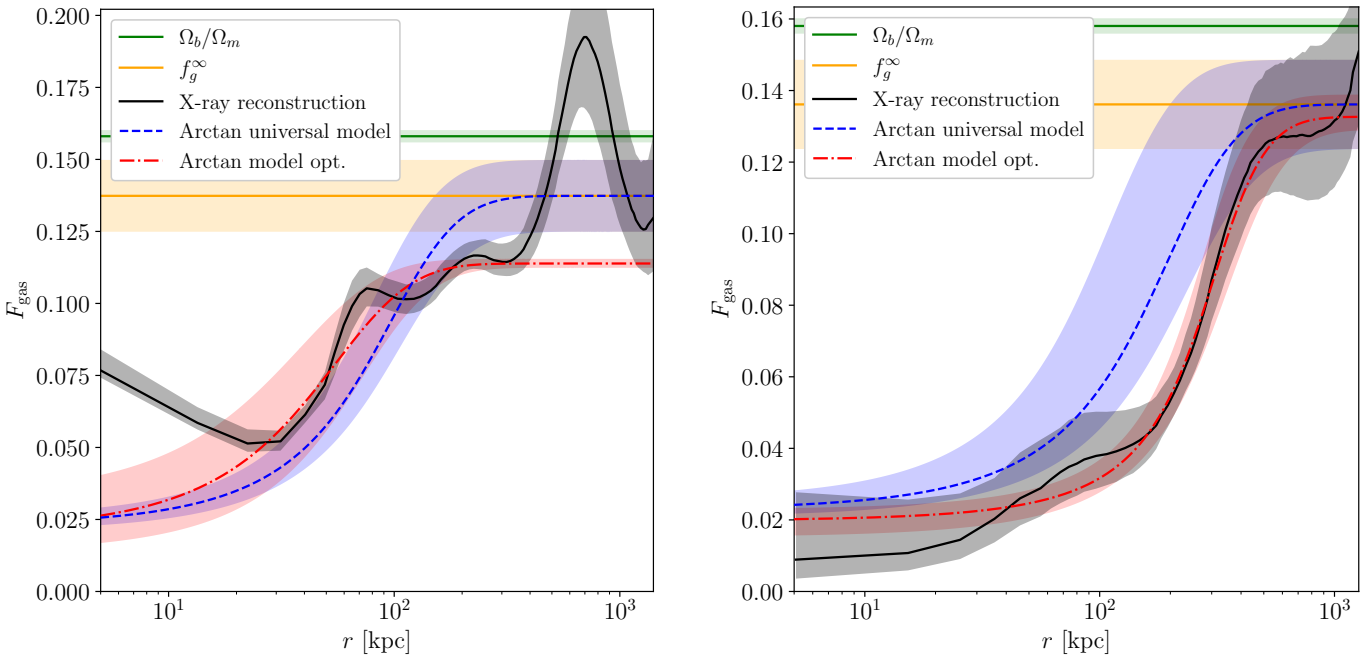

Figure 4. Cumulative gas fraction $F_g(r)$ in lensing galaxy clusters MACS J0242 (left) and MACS J0949 (right). *Black:* Reconstructed gas fraction from *XMM-Newton* data analysis. Errors are 1σ. *Green:* Universal gas fraction Ω_b/Ω_m. *Orange:* Universal gas fraction at infinity $f_g^{\rm Uni}$ (see eq. 37). *Red:* Arctan gas fraction model (see equation 35) optimised for the specific cluster. *Blue:* Arctan model with the cluster lensing parameters ($f_\star$ and a_1, see eq. 41). As presented in e.g. Eckert et al. (2022), the baryon fraction is approximately constant out of the central regions of clusters. Baryons are distributed between stars and the ICM, with a higher concentration of the former in the centre, and of the latter in the outskirts ($r > 0.2R_{500}$). This matches the trend presented here.

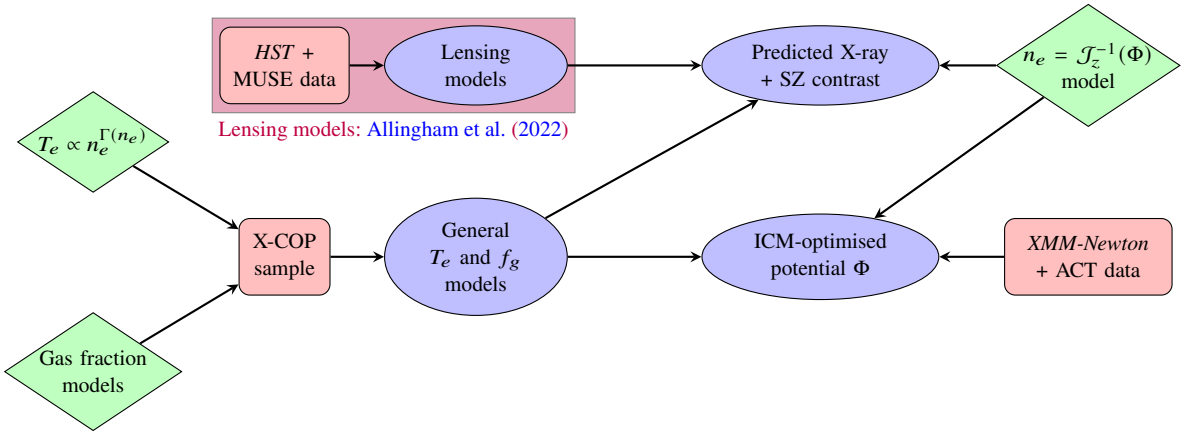

Figure 5. Full workflow diagram. Models are denoted by green diamonds, data by red rectangles, while results are in blue ellipses. The light magenta rectangle denotes work carried out within our previous companion article Allingham et al. (2022).

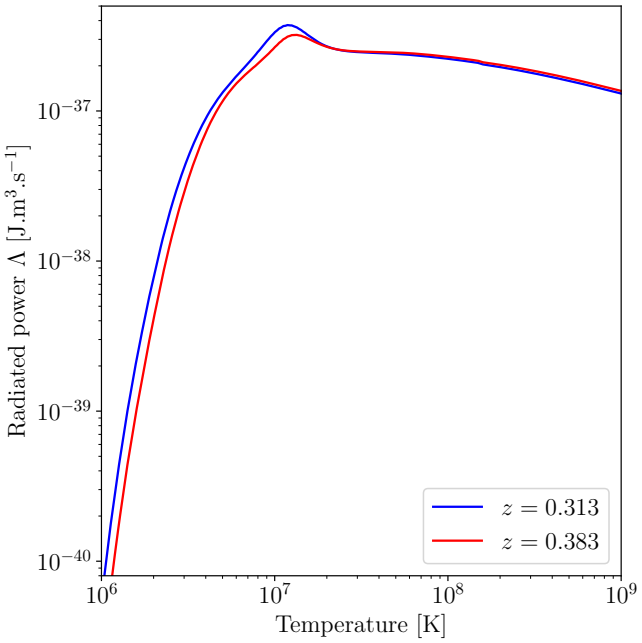

Figure 6. Radiated power (cooling curve) for a metallicity $Z = 0.3Z_\odot$, in the band $[0.7; 1.2]$ keV, at the respective redshift of MACS J0242 (blue) and MACS J0949 (red).

brightness models, we can make predictions on the number count of detection:

$$S_{X,c} = C_{\text{flux}}^{\text{count}} S_X^{\text{conv}} \times E + B + C_{\text{sky}} \tag{44}$$

where C_{sky} is the sky constant, measured in the empty regions of the raw count map.

We also take dust absorption into account, with the absorption ratio (see e.g. Wilms et al. 2000):

$$\frac{I_{\text{obs}}}{I_{\text{em}}} = \exp\left[-n_H^{\text{gal}} \sigma(E_X)\right], \tag{45}$$

where n_H^{gal} is the galactic hydrogen, and σ, the extinction cross-section of that same dust for a photon energy, E_X. We report absorption factors of 0.9439 and 0.9398 for clusters MACS J0242 and MACS J0949 respectively.

6.3 Cooling curve

In order to access the X-ray spectral emissivity, $\Lambda(\Delta E, T_e, Z)$, mentioned in equation (24), we use `AtomDB` (see Foster et al. 2012). With the metallicities of set Asplund et al. (2009) adjusted to our $Z_{\text{cl}} = 0.3Z_\odot$, we can plot the cooling curve in the energy band of *XMM-Newton* (adjusted for K-correction). The results at the redshifts of clusters MACS J0242 and MACS J0949 are displayed in Fig. 6.

6.4 Sunyaev-Zel'dovich maps filtering

We simply filter the ACT DR5 map $\Theta_{r,f}^{\text{obs}}$ of MACS J0949 with a Gaussian filter of radius 0.05 degrees $\mathcal{G}(0.05\,\text{deg})$, with `nemo`[4]. Although this does not allow to fully remove either the CMB signal or the atmosphere variability, at the scale of the cluster, it allows to smooth and attenuate the CMB variability. In order to compare our SZ effect model to the filtered data maps, we convolve the modelled signal map $\Theta_{r,f}^{\text{mod}}$ with the ACT beam $\mathcal{B}_f$ at the map frequency f. This allows to take the telescope PSF into account. We further apply the Gaussian filter, and compare the resulting maps:

$$\begin{aligned} \Theta_{r,f}^{\text{obs,filt}} &= \Theta_{r,f}^{\text{obs}} \circledast \mathcal{G}(0.05\,\text{deg}), \\ \Theta_{r,f}^{\text{mod,filt}} &= \left(\Theta_{r,f}^{\text{mod}} \circledast \mathcal{B}_f\right) \circledast \mathcal{G}(0.05\,\text{deg}). \end{aligned} \tag{46}$$

In a similar fashion to that of the X-ray PSF, we have to remove the borders of the SZ filtered image because of border effects. We therefore used model maps of ~ 4 Mpc initially (26 pixels), reduced to ~ 2 Mpc (14 pixels), and compared these predictions to the ACT DR5 filtered data.

6.5 Working hypotheses on the density distribution

We based our analysis on the mass models described in our previous work (Allingham et al. 2022). We model the total mass profile of MACS J0242 and MACS J0949 using strong lensing constraints of radii ranging in $R \in [50, 200]$ kpc. While we acknowledge the limitations of the constraining power, we extrapolate the 3D density out to $R_{500,c}$, and recover a mass $M_{500,c} = 5.95^{+0.40}_{-0.46} \times 10^{14} M_\odot$ and $11.48^{+0.00}_{-3.42} \times 10^{14} M_\odot$ for clusters MACS J0242 and MACS J0949 respectively. With equation (32), we find temperature normalisations $T_0 = T_{500} T_{\text{ref}} = 8.47 \times 10^7$ K and 1.35×10^8 K respectively.

Given the quality of the X-ray and SZ observations, and the dominant importance of the DMH and BCG in strong lensing models, we neglect the potentials associated to each individual galaxies here. We justify this hypothesis by the dynamical state of the clusters, analysed in Allingham et al. (2022). As they are not strongly perturbed, the ICM distribution should be governed by the large-scale potential. In Fig. 1, we can for instance see cluster MACS J0949 Southern halo mass contours to be undetectable on the X-rays – see the large red circle in the South of the image, crossed by the dashed green line.

Moreover, we postulate that the ICM density distribution is ellipsoidally symmetric, and of the same ellipticity as the DMH dark content. Although this does not match perfectly observations (see Fig. 1), this simply follows the hypothesis: 'ICM follows potential'. At last, as the line-of-sight ellipticity of the potential is unknown, we assume it to be *a priori* equal to the geometric average of the semi-major and semi-minor axes, $\sqrt{ab}$. As the goal of this article is to present new methods to predict the density profile of the ICM using strong lensing analyses, we fix all geometric parameters to their best lensing values. The 'semi-depth' of the cluster is unknown from lensing, but it is also degenerate with the density distribution. Therefore, we do not optimise this parameter.

6.6 MCMC optimisations

For the three different types of models of the electron density – canonical, gas fraction, and analytical – represented by four different models – β, Arctan gas fraction, `idPIE` and `iNFW` – we let a number of parameters free. For the β profile, we set all three parameters of the density distribution, $\{\rho_0; r_c; \beta\}$ free. For the `idPIE` profile, we initially let $\{\rho_{0,1}; a_1; s_1; \rho_{0,2}; s_2\}$ free, but as discussed in Sect. 7, s_2 appears entirely degenerate in the optimisation, and we therefore fix it to its lensing value from Sect. 7.1.2. The two parameters characterising a NFW distribution, $\{\rho_S; r_S\}$, are set free for the `iNFW` optimisation. At last, for the Arctan gas fraction model, we only let

[4] https://nemo-sz.readthedocs.io

Table 8. Best fit of all optimisation models for cluster MACS J0242. $\rho_{0,1}$ denotes the DMH central density in the case of `idPIE` profile, ρ_S in the `iNFW` case, and the central gas density in the case of a β-profile. $\rho_{0,2}$ denotes the BCG central density in the `idPIE` case. Both of these values are displayed in kg.m^{-3}. a_1 denotes the DMH core radius in the `idPIE` and gas fraction cases, r_S the scale radius in the `iNFW` case, and r_c in the β model. s_1 and s_2 denote respectively the cut radius of the DMH and of the BCG, in the case `idPIE`. The optimisation of the core radius of the BCG a_2 does not yield any optimised position. All of these distances are displayed in kpc. Starred values were fixed. We also remind the dPIE values achieved through our strong lensing model. When a parameter set is out of the invertible range of function $\mathcal{J}_z$ (i.e. $\sim [0, 10]$), we note the log-likelihood $\ln \mathcal{L}$ as infinite.

	$\rho_{0,1}$	a_1	s_1	$\rho_{0,2}$	s_2	β	$-\ln \mathcal{L}$
Lens model (dPIE)	$1.01^{+3.42}_{-0.18} \times 10^{-21}$	$57.19^{+6.04}_{-8.41}$	1500*	$1.15^{+0.27}_{-0.18} \times 10^{-17}$	$177.6^{+32.2}_{-58.0}$	–	∞
Lens model (NFW fit)	$3.42^{+0.48}_{-0.38} \times 10^{-22}$	$209.9^{+17.1}_{-15.8}$	–	–	–	–	∞
β-model	$2.05^{+10.52}_{-1.41} \times 10^{-20}$	$18.89^{+40.06}_{-15.17}$	–	–	–	$0.544^{+0.199}_{-0.079}$	0.68
`idPIE`	$7.38^{+8.21}_{-3.53} \times 10^{-22}$	$72.02^{+24.89}_{-21.89}$	2310^{+480}_{-750}	$5.88^{+2.63}_{-3.90} \times 10^{-18}$	$187.4^{+175.0}_{-120.1}$	–	0.68
`iNFW`	$1.52^{+1.52}_{-0.83} \times 10^{-22}$	$293.18^{+133.28}_{-121.27}$	–	–	–	–	0.69
Gas fraction	–	$230.97^{+36.49}_{-63.24}$	–	–	–	–	1.12

the DMH core radius $\{a_1\}$ free, according to model equation (41). We optimise them with the data for each galaxy cluster. For cluster MACS J0242, we only use the X-ray data, while for MACS J0949, we have the choice to use either X-rays, SZ, or both.

We define the log-likelihood for the X-ray data. As the photon counts are limited, the X-ray maps are following a Poissonian distribution. With the noise, we take them to follow the Cash statistic (Cash 1979):

$$\ln \mathcal{L}_X(\Theta) = \frac{1}{N_X} \sum_i \left[C_i - M_i(\Theta) - C_i \ln\left(\frac{C_i}{M_i(\Theta)}\right)\right], \tag{47}$$

where C_i is the data count in the i-th pixel, N_X, the number of pixels, and $M_i(\Theta)$, the model prediction for the parameter vector, Θ.

As for the SZ statistic, with M_i now being the temperature contrast model, and C_i, its SZ measurement, we simply take the likelihood to be Gaussian:

$$\begin{aligned} \ln \mathcal{L}_{SZ}(\Theta) &= -\frac{1}{2N_{SZ}} \sum_i \left[\left(\frac{M_i(\Theta) - C_i}{\sigma_i}\right)^2 + \ln \sigma_i^2 \right], \\ \sigma_i^2 &= M_i^2(\Theta) + \sigma_{C,i}^2, \end{aligned} \tag{48}$$

where σ_i is the standard deviation in the i-th pixel, and N_{SZ}, the number of SZ pixels. We take the model standard deviation to be the model itself, accordingly to a Gaussian model. $\sigma_{C,i}^2$ is the instrument variance of ACT. This does not take into account the CMB variance nor the atmosphere, but these are smoothed out on the scale of a cluster by the top-hat filtering (we follow Hilton et al. 2018, 2021). C_i and M_i represent here the data and model respectively, but for the SZ data. In the case of cluster MACS J0949, we sum the log-likelihood of the 90 and 150 GHz ACT DR5 bands.

In the case of the joint optimisation of X-rays and SZ, the data are of the same type, i.e. detections in pixels. We therefore define the joint likelihood as the weighed sum:

$$\ln \mathcal{L}_J = \frac{N_X \ln \mathcal{L}_X + N_{SZ} \ln \mathcal{L}_{SZ}}{N_X + N_{SZ}}, \tag{49}$$

where N_{SZ} must be understood as the sum of all SZ pixels, both in band f090 and f150.

We notice that this takes into account the different pixelisations, and attributes equal weights to each pixel. The X-ray observations should thus dominate, given the much better resolution (a *XMM-Newton* pixel represents 2.5″, and an ACT pixel 30″).

We took 2000 walkers, iterated over 500 steps, with a step type `emcee.StretchMove`. We provide the cornerplots, realised with Foreman-Mackey (2016), in Appendix A.

7 RESULTS AND DISCUSSION

We present in this section the results of MCMC optimisations of each of the four density models, for each galaxy cluster. We here do not present the self-normalised models, following equation (19), as these imply to use X-ray data both as inputs (as a normalisation) and to perform the optimisation. This would result into the degeneracy of one or several parameters.

7.1 Cluster MACS J0242

7.1.1 β model

In order to compare our profiles with the most classic profiles describing the ICM, we run MCMC optimisations for β profiles. We present the optimised parameters in Table 8, alongside all other optimisations for MACS J0242. Although we denote the r_c parameter of equation (5) as a_1 for clarity, this parameter is tied to the model. The associated cornerplot is presented Fig. A1. We notice that these are describing different physical observables, and are *a priori* not directly comparable as they are for `idPIE` or `iNFW`.

We find the best likelihood to be $\ln \mathcal{L} = -0.68$, close enough from the best possible likelihood, -0.5 , so that we can expect other detailed classic ICM profiles – such as double-β – not to significantly improve the model. The best parameter values *a posteriori* are different: the density normalisation $\rho_{0,1}$ is twenty times more important than that of the DMH for the total matter density, while the best core radius is about a quarter of the DMH one.

7.1.2 idPIE

The high sensibility of the $\mathcal{J}_z$ function could be described as a double-edged sword: on the one edge, this sensibility means any sort of imprecision in the determination of the parameters, or even in the hypotheses (temperature model, temperature normalisation, determination of the total mass density, etc.) would result in an increase of the error leading to a prediction error of possibly several

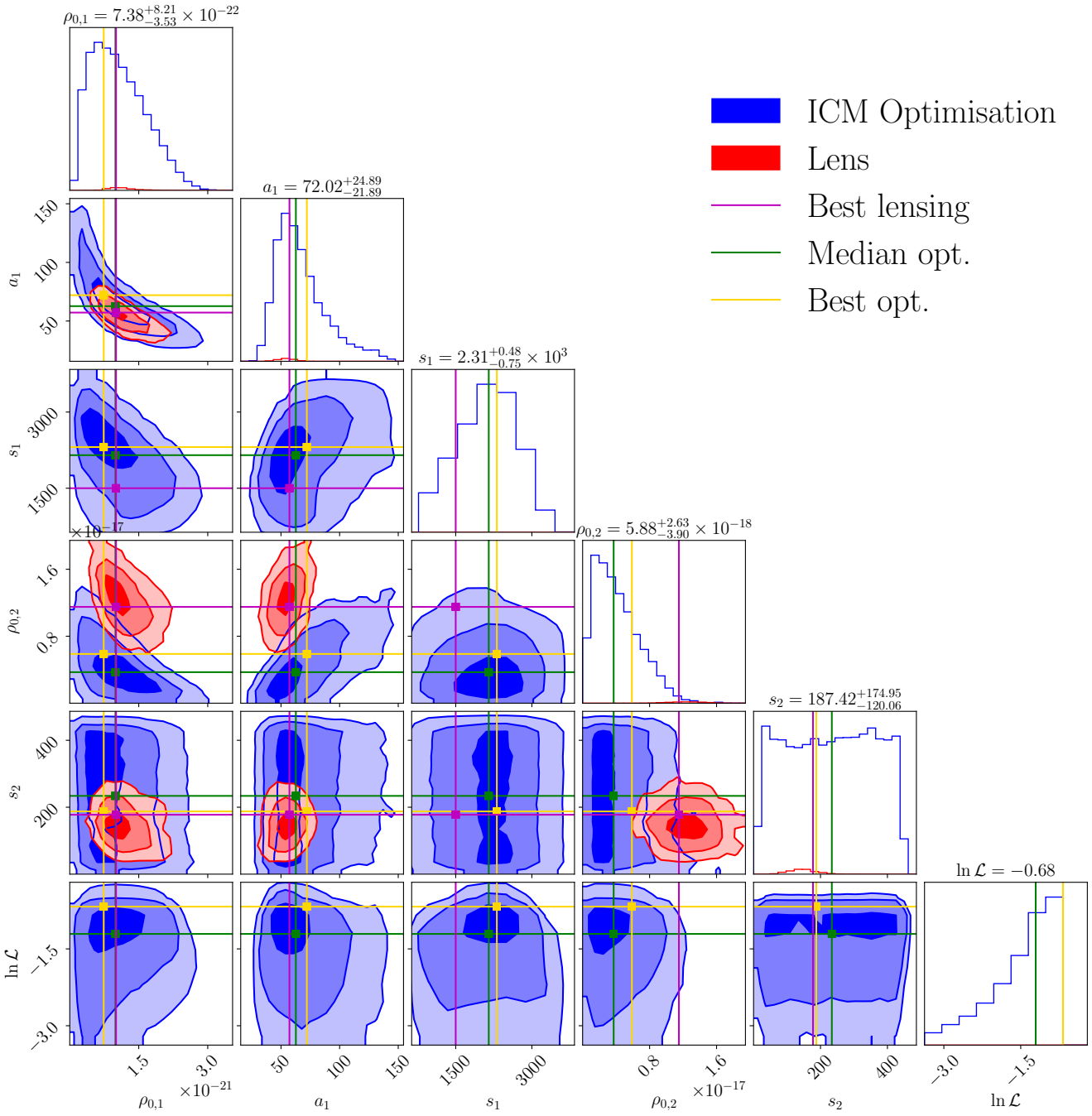

Figure 7. MCMC optimisation for `idPIE` model of the five relevant parameters for cluster MACS J0242: DMH central density $\rho_{0,1}$, core radius a_1 and cut radius s_1, and BCG central density $\rho_{0,2}$ and cut radius s_2. *Blue:* Optimisation performed using the available ICM data (X-ray here). *Red:* Strong lensing optimisation. *Magenta:* Best strong lensing model (described in Table 2). *Green:* Median of the ICM optimisation. *Gold:* Best ICM optimisation.

orders of magnitude. On the other edge, this should allow to tune very finely the various parameters, with the outskirts distribution in galaxy clusters of the full matter density having a direct consequence on the gas distribution in the central regions (at least through the expressions of h in the cases `idPIE` and `iNFW`). In order to reach such a quality in the reconstruction, the strong lensing parameters should be very finely determined, and fixed. The parameters not fit with strong lensing (s_1 here) could then be optimised. Given the extent of the strong lensing optimisation error bars on parameters $\{\rho_{0,1}; a_1; \rho_{0,2}; s_2\}$, we can not claim to achieve such a good level of constraints here. Therefore, we optimise all `idPIE` parameters *a priori*.

We display in Fig. 7 and Fig. A2 the strong lensing and ICM optimisations in the $\{\rho_{0,1}; a_1; s_1; \rho_{0,2}; s_2\}$ and $\{\rho_{0,1}; a_1; \rho_{0,2}; s_2\}$ parameter spaces respectively. We note that s_1 is not optimised with `Lenstool`, and not optimising it here results in a best log-likelihood $\ln \mathcal{L} < -0.82$. On the contrary, when this parameter is being optimised, the best value gets closer to the 'perfect fit' -0.5 value (i.e.

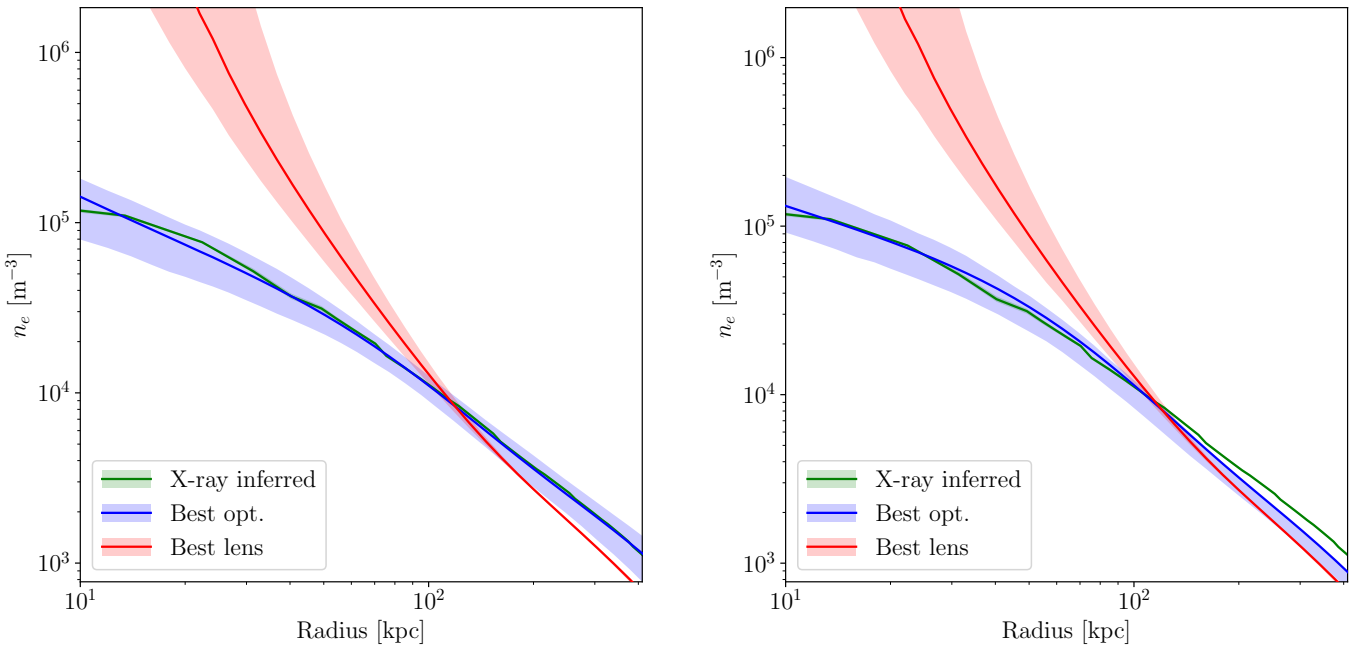

Figure 8. Electron density n_e for `idPIE` model, for cluster MACS J0242. *Green:* X-ray data inferred value. *Blue:* Best ICM-optimised value, with a `idPIE` model. *Red:* Best lens model inferred value. *Left:* In the case of the optimisation of parameters $\rho_{0,1}$, a_1, s_1, $\rho_{0,2}$ and s_2, as illustrated on Fig. 7. *Right:* In the case of the optimisation of parameters $\rho_{0,1}$, a_1, $\rho_{0,2}$ and s_2, as illustrated on Fig. A2. If s_1 is not optimised, the larger scales ($\gtrsim 100$ kpc) n_e densities can not be properly fitted.

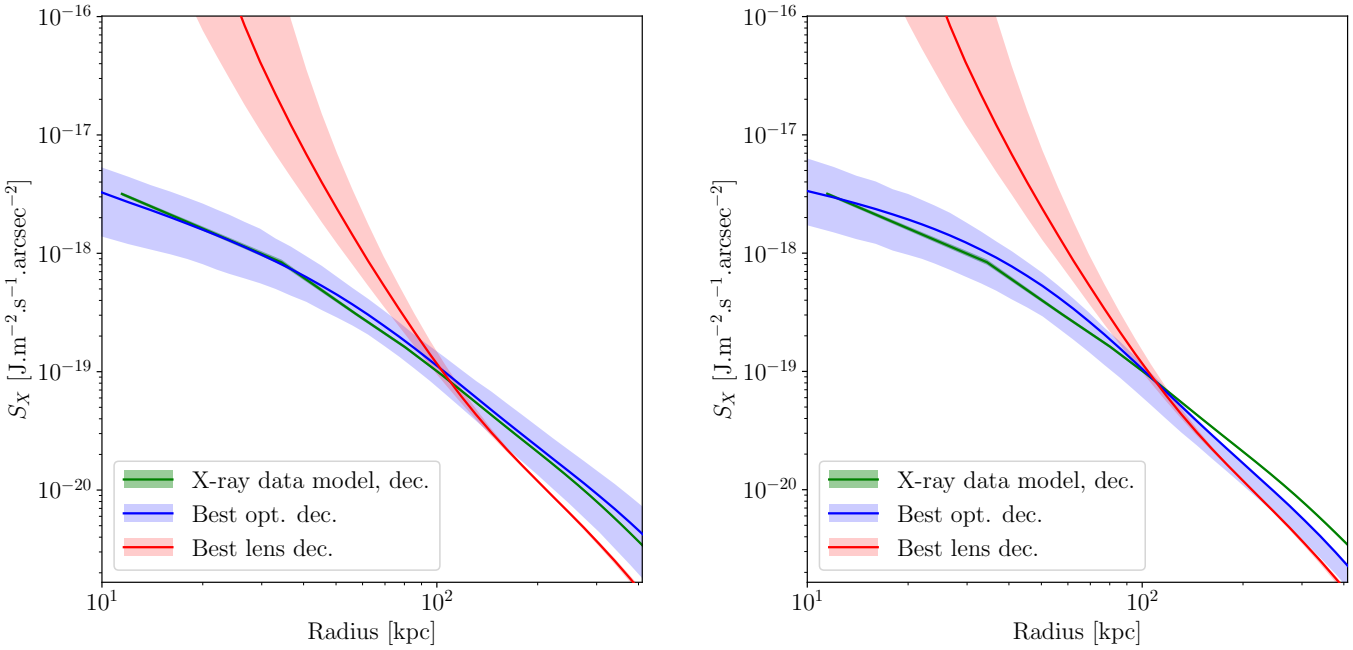

Figure 9. Expected X-ray surface brightness S_X for `idPIE` model, for cluster MACS J0242. *Green:* X-ray data inferred value. *Blue:* Best ICM-optimised value, with a `idPIE` model. *Red:* Best lens model inferred value. *Left:* In the case of the optimisation of parameters $\rho_{0,1}$, a_1, s_1, $\rho_{0,2}$ and s_2, as illustrated on Fig. 7. *Right:* In the case of the optimisation of parameters $\rho_{0,1}$, a_1, $\rho_{0,2}$ and s_2, as illustrated on Fig. A2.

reduced $\chi^2 = 1$, denoting the observations are well represented by the model) at $\ln \mathcal{L} < -0.68$. We discuss this further in Sect. 7.3.

Although the prediction from lensing is diverging in the cluster centre ($r \to 0$) – due to the central matter density being out of the $\mathcal{J}_z$ function bijective range – we find the ICM optimisation in the $\{\rho_{0,1}; a_1\}$ space to provide results very close to those of `Lenstool`, although the ICM error bars are larger. The DMH cut radius, s_1, not being optimised with strong lensing, we can only notice the X-ray optimisation is compatible with the fiducial 1.5 Mpc value, albeit the best optimisation yields $s_1 = 2.31^{+0.48}_{-0.75}$ Mpc. The BCG cut radius, s_2, appears not to be optimised with the X-rays, and the density normalisation of the BCG, $\rho_{0,2}$, yields different results than strong lensing. This may be explained by the high central matter density, which yields values out of the $\mathcal{J}_z$ function inversion range. The

Table 9. Best fit of all optimisation models for cluster MACS J0949. $\rho_{0,1}$ denotes the DMH central density in the case of `idPIE` profile, ρ_S in the `iNFW` case, and the central gas density in the case of a β-profile. $\rho_{0,2}$ denotes the BCG central density in the `idPIE` case. Both of these values are displayed in kg.m^{-3}. a_1 denotes the DMH core radius in the `idPIE` and gas fraction cases, r_S the scale radius in the `iNFW` case, and r_c in the β model. s_1 and s_2 denote respectively the cut radius of the DMH and of the BCG, in the case `idPIE`. Let us notice the core radius of the BCG a_2 is model-dependent, and is thus it is not optimised here. All of these distances are displayed in kpc. Starred values were fixed. We also remind the dPIE values achieved through our strong lensing model. We here only provide the joint SZ-X-ray log-likelihood ln $\mathcal{L}_J$.

	$\rho_{0,1}$	a_1	s_1	$\rho_{0,2}$	s_2	β	$-\ln\mathcal{L}$
Lens model (dPIE)	$4.58^{+3.62}_{-0.95}\times10^{-22}$	$116.25^{+24.11}_{-51.66}$	1500*	$3.88^{+8.32}_{-0.55}\times10^{-18}$	$98.04^{+153.74}_{-34.34}$	–	2.60
Lens model (NFW fit)	$1.23^{+1.57}_{-0.00}\times10^{-22}$	$405.5^{+0.0}_{-156.1}$	–	–	–	–	2.83
β-model	$1.73^{+1.60}_{-1.05}\times10^{-21}$	$78.23^{+157.49}_{-35.54}$	–	–	–	$0.460^{+0.311}_{-0.098}$	0.70
`idPIE`	$3.53^{+7.63}_{-1.73}\times10^{-22}$	$96.97^{+61.49}_{-33.00}$	3320^{+390}_{-1430}	$3.85^{+8.62}_{-2.43}\times10^{-18}$	98.04*	–	0.60
`iNFW`	$7.57^{+9.07}_{-3.08}\times10^{-23}$	$496.70^{+133.86}_{-154.53}$	–	–	–	–	0.61
Gas fraction	–	$394.99^{+123.40}_{-160.33}$	–	–	–	–	0.86

validity of equation (23) is not verified beyond $n_e > 10^5$ kg.m^{-3}. Moreover, the X-ray signal in the centre carrying a high variability, we can not conclude about its significance.

The electronic densities are represented in Fig. 8, and the *XMM-Newton* deconvolved X-ray surface brightness in Fig. 9. We conclude our method can fit properly the X-ray signal for this cluster, provided the potential is optimised. We discuss the large discrepancy between the lens inferred model and the signal in Sect. 7.3.

We note that the ICM optimisation over s_2 is not necessary, as the parameters appear to be degenerate in the optimisation. We can therefore present the MCMC optimisation fixing s_2 to its lensing value, $s_2 = 177.57$ kpc (see Fig. A3).

7.1.3 *iNFW*

The NFW distributions attributed to strong lensing are all reductions of dPIE `Lenstool` optimisations to NFW best fit. In Fig. A4, we compare these to the ICM optimised `iNFW` profiles. We again find a very satisfactory best likelihood at $\ln\mathcal{L} = -0.69$, and although the $\{\rho_S; r_S\}$ values we find are different from those of the strong lensing reduction, they are compatible with the total density we found.

7.1.4 *Gas fraction model*

Assuming an empirical `Arctan` gas fraction as presented in Sect. 5.2, combined with only one degree of freedom $r_c = r_f = a_1$, we optimise the core radius. In Fig. A5, we display the possibility to model the ICM with strong lensing through this gas fraction model. We find the core radii of the DM halo optimised with `Lenstool` and with the ICM are clearly incompatible. As presented in Sect. 5.2, cluster MACS J0242 presents non-statistical fluctuations in the gas fraction. Moreover, the gas fraction model equation (35) is physically motivated, but the assumption $r_c = r_f$ is probably too strong, as shown in Table 7 (r_c/a_1 and $r_f/a_1 < 1$, at more than 1σ distance). The best log-likelihood of $\ln\mathcal{L} = -1.12$ is reached for $a_1 = 231.0^{+36.5}_{-63.2}$ kpc. This is in contradiction with the best Arctan gas fraction model found for r_c and r_f (see Table 7). As a result, the approximations in the 'Universal' Arctan gas fraction model, and the fluctuations in the gas fraction profile of MACS J0242 lead to a bad quality reconstruction. We conclude further studies are required to make this model valid for this cluster.

7.2 Cluster MACS J0949

Similarly to the study performed on the cluster MACS J0242, we present the results of the ICM optimisation of MACS J0949. We primarily present the joint fit results (X-rays and SZ effect).

7.2.1 *β model*

The best value for r_c is of the same order as the best strong lensing values given for the DMH dPIE profile. For the central density, $\rho_{0,1}$, the optimised value with the X-ray data is three times more important than the DMH central density. As for β, its best value is $0.46^{+0.31}_{-0.10}$. The cornerplot indicates this parameter to be degenerate here. Moreover, the error bars cover almost all the space of optimisation ($[0.3, 0.9]$). Figure A6 presents the optimisation with the ICM data from the *XMM-Newton X-ray Observatory* and the SZ data taken with ACT. Using both the X-rays and SZ data for this optimisation, we find the best likelihood to be $\ln\mathcal{L} = -0.70$, a value which supports the good quality of the fit. In detail, the X-ray likelihood is $\ln\mathcal{L}_X = -0.58$, and the SZ likelihood is $\ln\mathcal{L}_{SZ} = -0.84$. The joint fit best likelihood value is worst than if only using the X-ray data. However, this does not necessarily imply that the reconstructed ICM is worst, but highlights a discrepancy between the X-ray and SZ signals at the centre of the cluster. Small-scale density and temperature variations may be due to the ICM dynamics, radiative cooling, AGN feedback, etc. Their size may not be observed with SZ surveys, but may skew observations in the cluster centres, even for relaxed clusters. The low resolution of SZ surveys also makes the central PSF quite important, and thus SZ inferred ICM density in the core should be considered carefully. Moreover, the difference could arise from the data quality, or from the temperature model, which presents a large scatter. A wrong temperature evaluation would disproportionally impact more the SZ signal.

7.2.2 *idPIE*

As for MACS J0242, the optimisation of the BCG cut radius, s_2, is degenerate. We therefore choose to fix this parameter to its strong lensing value, 98.04 kpc. We display in Fig. 10 the strong lensing and ICM optimisations in the $\{\rho_{0,1}; a_1; s_1; \rho_{0,2}\}$ parameter space. The best value is $\ln\mathcal{L}_J = -0.60$. The overlap between the strong lensing and ICM optimised spaces is obvious in this cornerplot. However

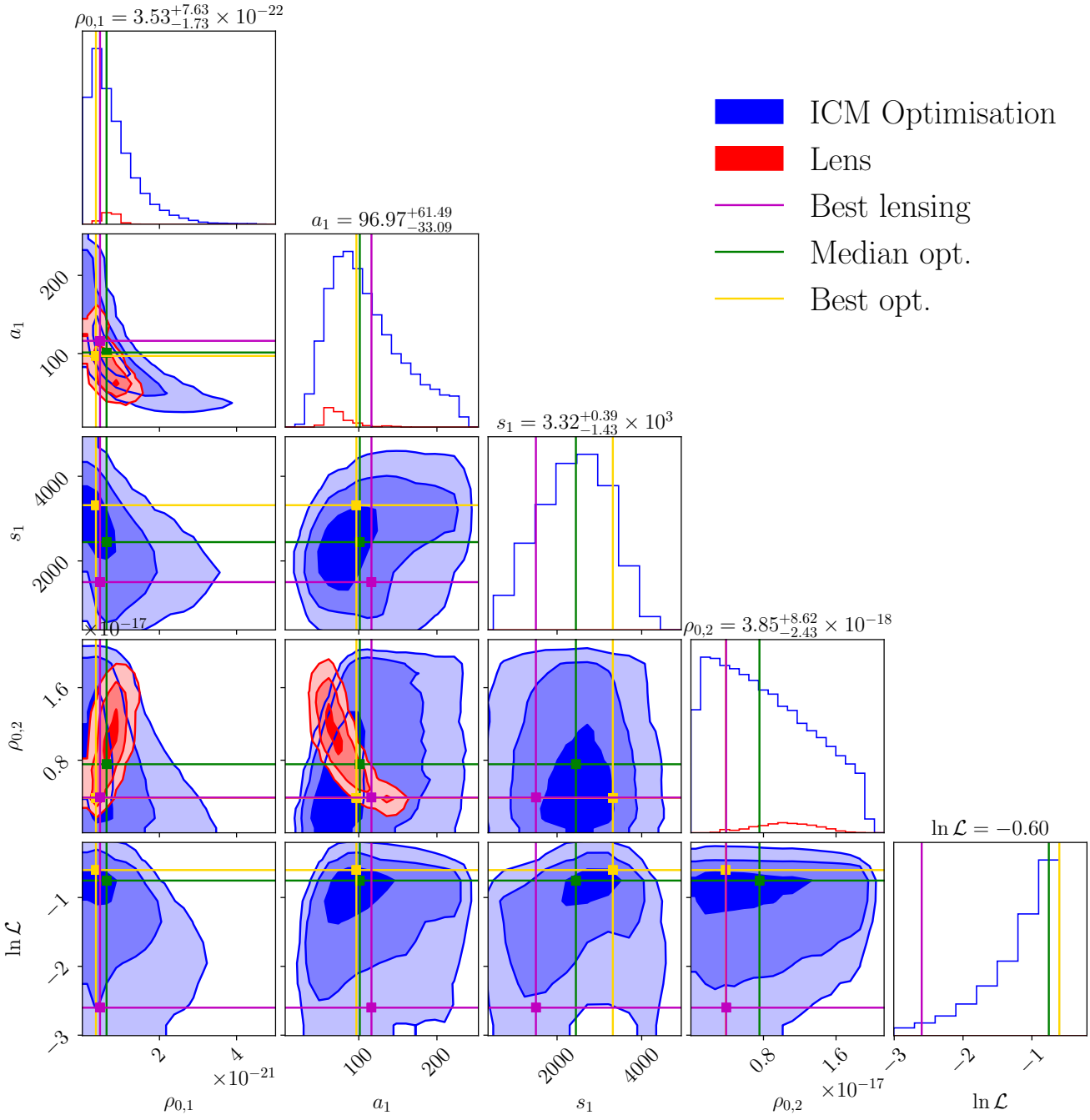

Figure 10. MCMC optimisation for `idPIE` model of the five relevant parameters for cluster MACS J0949: DMH central density $\rho_{0,1}$, core radius a_1 and cut radius s_1, and BCG central density $\rho_{0,2}$. The optimisation was performed with the X-ray and SZ data. *Blue:* Optimisation performed using the available ICM data (X-ray here). *Red:* Strong lensing optimisation. *Magenta:* Best strong lensing model (described in Table 2). *Green:* Median of the ICM optimisation. *Gold:* Best ICM optimisation.

the quality of the reconstruction with the ICM does not converge as efficiently as that of strong lensing – a result to be expected given the difference in methods and quality of data.

We present the comparison between the observations, the theoretical prediction using the lens model and the ICM-optimised model for observables, n_e, and S_X, on Fig. 11 and A8 respectively. Again, not optimising s_1 leads to a worst ICM optimisation (best log-likelihood -0.82). In Fig. 11, the right panel shows the discrepancy between the X-rays inferred electron density, n_e, and the best optimisation with a fixed DM halo cut radius, $s_1 = 1.5$ Mpc. This demonstrates the importance of this parameter optimisation to recover the X-ray measured density profile. We further discuss this in Sect. 7.3.

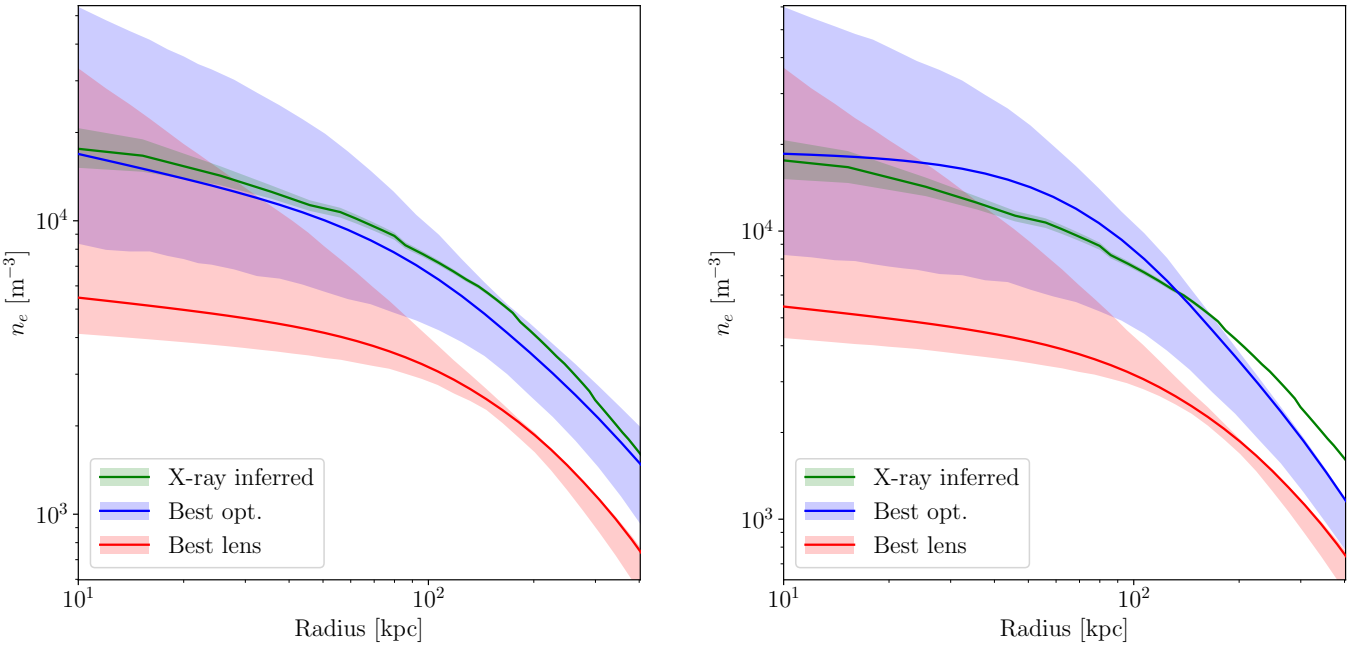

Figure 11. Electron density n_e for `idPIE` model, for cluster MACS J0949. *Green:* X-ray data inferred value. *Blue:* Best ICM-optimised value, with a `idPIE` model. *Red:* Best lens model inferred value. *Left:* In the case of the optimisation of parameters $\rho_{0,1}$, a_1, s_1, $\rho_{0,2}$ and s_2, as illustrated on Fig. 10. *Right:* In the case of the optimisation of parameters $\rho_{0,1}$, a_1 and $\rho_{0,2}$, as illustrated on Fig. A7. Similarly to Fig. 8, we observe that not optimising s_1 prevents our `idPIE` model to fit the ICM density properly for $r \gtrsim 100$ kpc.

7.2.3 *iNFW*

In Fig. A9, we compare the best strong lensing optimisation fit to the ICM optimised `iNFW` profiles. We find a best log-likelihood of$\ln \mathcal{L}_J = -0.61$. The strong lensing fit NFW parameters for MACS J0949 being $\{\rho_S = 1.23 \times 10^{-22}$ kg.m^{-3} ; $r_S = 405.5$ kpc$\}$, they are both compatible with the ICM-optimised values within 1σ.

7.2.4 *Gas fraction model*

Still assuming only one degree of freedom, $r_c = r_f = a_1$, we optimise the DMH core radius and display the ICM model for the gas fraction optimisation in Fig. A10. With a joint X-rays and SZ optimisation, we find the best core radius to be 394.99 kpc, as opposed to the 116.25 kpc with strong lensing. Thus the strong lensing value is not within 1σ of the ICM one. The best log-likelihood of the joint optimisation is $\ln \mathcal{L} = -0.86$. Similarly to MACS J0242, we conclude the Arctan gas fraction model combined with the DMH core radius measured with strong lensing to be yielding different results from the measured ICM density. We can attribute this to $r_c/a_1 > 1$, at more than 1σ confidence (see Table 7). We conclude that more parameters are required to understand the ICM distribution using the gas fraction model.

7.3 Optimising the DMH cut radius with ICM core data and SL priors

As strong lensing is only efficiently probing the most central regions of galaxy clusters ($R < 200$ kpc), it only allows to effectively constrain the 'central' parameters amongst those presented in `idPIE` optimisations, i.e. $\rho_{0,1}, a_1, \rho_{0,2}$ and s_2 – leaving s_1 aside. Even these strong lensing constrained parameters are not perfectly determined in the case of our study as we are limited in the number of multiple images and spectroscopic redshifts detected (Allingham et al. 2022).

In this context, for the `idPIE` ICM optimisations, we observe the efficiency of the cut radius optimisation of the dark matter halo, s_1. For MACS J0949, we can use the `idPIE` model introduced in Sect. 7.2.2 and Fig. 10, and fix the parameters constrained through strong lensing, i.e. $\rho_{0,1}, a_1$ and $\rho_{0,2}$. This new model, only performing the cut radius of the DMH s_1 optimisation, reaches the best fit value, $s_1 = 3040^{+530}_{-730}$ kpc, at $\ln \mathcal{L}_J = -0.63$. This is better than optimising all the other parameters, but not s_1 ($\ln \mathcal{L}_J = -0.82$). For the X-ray only optimisation, this value reaches $\ln \mathcal{L}_X = -0.59$ for $s_1 = 3050^{+500}_{-690}$ kpc, compared to $\ln \mathcal{L}_X = -0.58$ for $s_1 = 3290^{+420}_{-1440}$ kpc if all parameters are optimised (i.e. $\rho_{0,1}, a_1, s_1$ and $\rho_{0,2}$). Thus, from a pure optimisation point of view, optimising s_1 could suffice to fit the ICM density.

We remind the reader that the full `idPIE` ICM optimisation for clusters MACS J0242 and MACS J0949 respectively yielded $s_1 = 2310^{+480}_{-750}$ kpc and 3320^{+390}_{-1430} kpc – this latter value being compatible with the DMH cut radius, s_1, optimisation only. Here, s_1 is the only parameter not optimised through with strong gravitational lensing. Given the uncertainty in the determination of the lensing parameters, due to limited observations, the stiffness of function $\mathcal{J}_z^{-1}$ allows for these small variations to modify significantly the lens prediction of the ICM. Indeed, the error bars on the density parameters can contaminate the s_1 optimised value. If we could fix all other parameters (density parameters, geometry, and even use a measured ICM temperature profile), the s_1 optimisation value should then yield a physical result, with respect to the dPIE profile choice and the hydrostatic equilibrium hypothesis. In spite of this constraint on the data quality, we have here presented the importance of the DMH cut radius parameter, s_1, in the ICM density prediction, as its optimisation modifies the electron density, n_e, and thus the surface brightness, S_X, *at all radii*. Indeed, this DMH cut radius parameter, s_1, is related to the density in the cluster outskirts. It has a direct influence, upon optimisation, in the central X-ray surface brightness.

The cut radius values we find are larger than the *splashback radius*

measured by Chang et al. (2018). This radius is defined as the largest distance from the cluster centre connected to the cluster dynamics, i.e. the largest orbital apocentre at which matter is accreted to the DMH. The typical values provided in a redshift range corresponding to our lensing clusters are 1.5 – 2 Mpc, so our cut radius values are on the higher-end of the values considered reasonable for that type of clusters. These values are averaged for clusters of typical mass $M_{200,m} \simeq 2.5 \times 10^{14} M_{\odot}$, to compare to the (extrapolated) 5.55 and $10.37 \times 10^{14} M_{\odot}$ for MACS J0242 and MACS J0949 respectively.

We can also compare the cut radii obtained to the predicted *edge radius*, defined as the smallest radius at which no more orbiting galaxies can be found. According to Tomooka et al. (2020); Aung et al. (2022), the edge radius can be approximated to $r_e \sim 2R_{200,m}$. Using the strong lensing extrapolated values for $R_{200,m}$, we can compare the optimised cut radius values to the edge radii for both clusters. We obtain for MACS J0242, $s_1 = 2310^{+480}_{-750}$, and $2R_{200,m} = 3856^{+87}_{-104}$ kpc. In the case of MACS J0949, we measure 3320^{+390}_{-1430} and $2R_{200,m} = 4507^{+0}_{-1074}$ kpc. Computing the ratios $s_1/r_e = 0.60$ and 0.74 for the two clusters respectively, we obtain values of the same order. It should be noted that the cut and edge radii are not necessarily assumed to describe the same physical limit. The $R_{200,m}$ value is also based on density profiles assuming $s_1 = 1.5$ Mpc, and would thus be larger if using the ICM-optimised s_1 values instead, $2R_{200,m} = 4101^{+52}_{-75}$ and 4569^{+131}_{-359} kpc for respectively MACS J0242 and J0949, for ratios $s_1/r_e = 0.57$ and 0.73. The shock radius, describing the shock of gas falling into the ICM of a cluster, is predicted by Baxter et al. (2021) to be equally of order $\sim 2R_{200,m}$. Although not quite observable with the ACT resolution, future SZ surveys will be able to assist detecting this critical ICM large scale cluster radius. We conclude that the optimised cut radii is commensurable to these various radii attempting to measure the 'size' of galaxy clusters, and we find s_1 to fall between the splashback and the edge radii. Using our analytical model, the thorough comparison of these different cluster-size radii should be greatly assisted by the combination of strong lensing and ICM observations.

The central ICM density is noticeably affected by the s_1 DM halo cut radius. In the hydrostatic hypothesis, we can understand this as the effect of faster clustering of (baryonic) matter due to a larger dark matter halo, thus increasing the central baryonic density. In other words, if the gravitational potential at large radii is more important, a cluster should have accreted gas faster, and thus, the ICM should be denser in the centre.

In general, relaxed galaxy clusters are expected to present *a priori* a cool core, due to the radiated power in X-rays at high ICM densities. However, this is generally not what is observed (Peterson et al. 2001; Böhringer et al. 2002), with central temperatures higher than the X-ray cooling should yield. This is generally explained by feedback effects, and most notably Active Galaxy Nuclei (AGN, see e.g. Puchwein et al. 2010). The change produced in the temperature profile was here taken into account by using the varying index polytropic temperature model, which represents the physically measured temperatures, without implementing AGN feedback itself.

7.4 ICM and DMH geometries

In order to understand the effect of the density profile parameters optimisation, one must decorrelate these from the geometric differences between the DMH and the ICM. The misalignment between the clusters' ICM and DMH centres lies below the X-ray pixel size precision, and can thus be neglected here entirely.

Our measurements suggest that the ICM presents rounder shapes than the DMH. Indeed, in the case of clusters MACS J0242 and MACS J0949, the X-ray measured ellipticities are negligible, but the strong lensing optimisation of the DMH present ellipticities in the range 0.2 – 0.3. As studied in e.g. Debattista et al. (2008); Lau et al. (2012), the geometry of the ICM of (relaxed) galaxy clusters may differ from that of their DMH. Beyond the effects associated to the turbulence of the ICM, of AGN feedback, plasma cooling etc., this difference lies in the physics of both fluids. Indeed, in the cold dark matter paradigm, dark matter is non-collisional, and can thus not dissipate kinetic energy efficiently at the centre of clusters. Conversely, baryons cluster in the centre of the halo. As they interact, they can lose kinetic energy faster than dark matter. Thus the more peaky baryonic profiles make the baryonic fluid evolve faster towards relaxation. This same effect causes DM particle orbits to change in response to the baryonic dissipation, thus also making the DMH more spherical. As these effects are not equal at different radii from the cluster centre, this can cause a difference in the ellipticity of both fluids. In Lau et al. (2011), simulations show both fluids' ellipticity also varies importantly depending on the radius in which it is measured. As here the ICM ellipticity is measured in a significantly larger radius $< R_{500}$, it is expected to be smaller. In this article, we modelled the ICM ellipticity to be that of the DMH measured through strong lensing. Any attempt to optimise the ICM density with spherical profiles yielded equivalent density profile parameters (ρ_0, a, s) and best likelihoods as using an elliptical profile.

At last, line-of-sight projection effects were entirely neglected in this paper, and in the strong lensing reconstruction. *A priori*, the combination of SZ effect and X-ray observations may allow to inform asymmetries on the line-of-sight. However, given the SZ effect data resolution and the adoption of a self-similar temperature profile in this article, this is beyond the scope of this article. Such effects may nonetheless affect the quality of the reconstruction. For instance, Umetsu et al. (2015) display a case of apparent mismatch between ICM and lensing observations due to the presence of a line-of-sight asymmetry.

7.5 Discussion

Given the different profiles which the *canonical* and *analytical* models are describing, we do not attempt to reduce the β model parameter space to an expression of the strong lensing parameters. We can simply note in this case, that we find the core radius of the β model to be of the order of magnitude of that of the dPIE DMH potential, while the central density is about one to two orders of magnitude more important. As for the β exponent, we find the exponent to be compatible with the range detailed in the literature, and subjected to the β-model problem (see Sadat 1997; Hallman et al. 2007).

As for the analytical density profile reconstruction, a number of observational effects limits this method. These baryonic effects include the dynamical offset between the ICM and the DM content of galaxy clusters, the AGN feedback, and the cooling of the cluster plasma. They drastically decorrelate the central ICM density from the DM in the outskirts. For instance, Ghirardini et al. (2019a, Fig. 7) present up to a 70% intrinsic scatter in the centre in density. The inclusion of a theoretical model for such baryonic effects would represent an important improvement to our models. Modelling the ICM fluid velocity evolution would also allow to understand the evolution of clusters, thus challenging the hydrostatic hypothesis.

Nevertheless, with precise strong lensing constraints and temperature model measurements in a cluster, we could compare the ICM data to the parametric strong lensing reconstruction directly given our analytical models. The difference between the observations and

the model, with respect to systematic errors, could yield constraints on dark matter models.

Our results could be used in their general form in simulations to further verify the validity of the total matter – ICM density bijection previously established. Provided better resolution data in the X-rays or SZ, and the detection of several multiply lensed galaxies in the centre of galaxy clusters, one could tackle the core-cusp problem, as we could then study the compatibility of the central densities.

8 CONCLUSION

With a comparison between a parametric strong lensing mass reconstruction model and the ICM observations (X-rays and SZ) on two non-perturbed galaxy clusters, we have shown it to be possible to use a unique model to describe both the total and ICM density profiles. In fact, under the hydrostatic hypothesis and assuming self-similar electron temperature profiles, the bijection (17) we have established between the total matter density and the ICM density allows to describe both the electron and dark matter density with the same parameters. We applied this technique to the dPIE and NFW density profiles and convincingly found the parameters optimised through lensing to be either compatible with their ICM optimisation, or to be degenerate and thus difficult to optimise with the ICM.

Given the sensitivity of the $\mathcal{J}_z$ function, and as strong lensing does not allow to probe regions out of the cluster inner core, we proposed to couple our models to ICM observations. This could allow to probe the *cut* or *scale radii* of relaxed clusters. Indeed, the ICM central density appears to be bounded to these matter density large-scale parameters. This new technique should be verified using clusters' outskirts surveys, such as weak lensing, and could only be efficiently applied with stringent constraints on the strong lensing parameters.

We can also reverse this perspective. If we had a perfect description of the full density mass model, e.g. including the cut radius of the DM halo through weak lensing, we could then compare the predicted ICM signal to that detected. If our model were satisfactory enough, we could then probe possible discrepancies, associated to other physical phenomena.

We here summarise the main results of this analysis:

1. We have proposed a self-similar polytropic temperature model with a varying index, using the X-COP sample of clusters. This allows to predict the ICM temperature for any cluster of measured mass $M_{500,c}$.
2. We have proposed a general `Arctan` model for the gas fraction, using the combined X-COP clusters with MACS J0242 and MACS J0949 galaxy clusters. We used these to propose a gas fraction model to reconstruct the electron density from strong gravitational lensing results.
3. As a major result, we exhibited an *analytic* relationship between the ICM density and that of DM, assuming hydrostatic equilibrium. We have further shown this relationship to allow to predict the ICM density using strong lensing, as a proof of concept.
4. We have demonstrated that the strong lensing ICM predictions are compatible with data through the ICM optimisation. We expect the strong lensing prediction to yield convincing results as long as: (i) the lensing galaxy cluster is not strongly perturbed, and (ii) we are able to properly predict the large-scale total density profile.
5. This requirement to probe the large scales demonstrates the limitations of our current analysis. We however foresee weak lensing constraints as a mitigating solution to adjust our models to large scale variations, thus allowing us to make precise predictions.
6. Reverting the perspective, this means the combination of X-rays or SZ data with strong lensing could allow to probe the dark matter profile of relaxed galaxy clusters far from their centres.

We here presented a proof of concept for the possibility to tie strong lensing constraints to the ICM. With higher-quality data and more constraints on the large-scale profile, this should lead to powerful constraints on galaxy clusters physics.

Acknowledgements

The authors want to thank Alastair Edge and Jose Maria Diego for fruitful discussions. JA is supported by the Postgraduate Research Scholarship in Astroparticle Physics/Cosmology in the University of Sydney. MJ and DL are supported by the United Kingdom Research and Innovation (UKRI) Future Leaders Fellowship (FLF), 'Using Cosmic Beasts to uncover the Nature of Dark Matter' (grant number MR/S017216/1). The authors acknowledge the Sydney Informatics Hub and the use of the University of Sydney high performance computing cluster, Artemis.

DATA AVAILABILITY

The lens models and the lensing-ICM optimisation programmes are available upon reasonable request to the corresponding author.

References

Ade P. A. R., et al., 2016, Astronomy & Astrophysics, 594, A13
Allingham J. F. V., et al., 2022, arXiv e-prints, p. arXiv:2207.10520
Arnaud M., Pratt G. W., Piffaretti R., Böhringer H., Croston J. H., Pointecouteau E., 2010, A&A, 517, A92
Asplund M., Grevesse N., Sauval A. J., Scott P., 2009, ARA&A, 47, 481
Aung H., Nagai D., Rozo E., Wolfe B., Adhikari S., 2022, arXiv e-prints, p. arXiv:2204.13131
Baxter E. J., Adhikari S., Vega-Ferrero J., Cui W., Chang C., Jain B., Knebe A., 2021, MNRAS, 508, 1777
Biffi V., et al., 2016, ApJ, 827, 112
Böhringer H., Werner N., 2010, A&ARv, 18, 127
Böhringer H., Matsushita K., Churazov E., Ikebe Y., Chen Y., 2002, A&A, 382, 804
Borgani S., Finoguenov A., Kay S. T., Ponman T. J., Springel V., Tozzi P., Voit G. M., 2005, MNRAS, 361, 233
Bryan G. L., Norman M. L., 1998, ApJ, 495, 80
Bulbul G. E., Hasler N., Bonamente M., Joy M., 2010, ApJ, 720, 1038
Buote D. A., Humphrey P. J., 2012, MNRAS, 421, 1399
Böhringer H., Chon G., Kronberg P. P., 2016, Astronomy & Astrophysics, 596, A22
CHEX-MATE Collaboration et al., 2021, A&A, 650, A104
Capelo P. R., Coppi P. S., Natarajan P., 2012, Monthly Notices of the Royal Astronomical Society, 422, 686–703
Cash W., 1979, ApJ, 228, 939
Cavaliere A., Fusco-Femiano R., 1976, A&A, 500, 95
Chang C., et al., 2018, The Astrophysical Journal, 864, 83
Debattista V. P., Moore B., Quinn T., Kazantzidis S., Maas R., Mayer L., Read J., Stadel J., 2008, ApJ, 681, 1076
Eckert D., Ettori S., Pointecouteau E., Molendi S., Paltani S., Tchernin C., 2017, Astronomische Nachrichten, 338, 293
Eckert D., et al., 2019, A&A, 621, A40
Eckert D., Finoguenov A., Ghirardini V., Grandis S., Kaefer F., Sanders J., Ramos-Ceja M., 2020, The Open Journal of Astrophysics, 3, 12
Eckert D., Ettori S., Pointecouteau E., van der Burg R. F. J., Loubser S. I., 2022, A&A, 662, A123
Elíasdóttir Á., et al., 2007, arXiv e-prints, p. arXiv:0710.5636

Ettori S., Donnarumma A., Pointecouteau E., Reiprich T. H., Giodini S., Lovisari L., Schmidt R. W., 2013, Space Sci. Rev., 177, 119
Ettori S., et al., 2019, A&A, 621, A39
Faber S. M., Jackson R. E., 1976, ApJ, 204, 668
Foreman-Mackey D., 2016, The Journal of Open Source Software, 1, 24
Foreman-Mackey D., Hogg D. W., Lang D., Goodman J., 2013, Publications of the Astronomical Society of the Pacific, 125, 306–312
Foster A. R., Ji L., Smith R. K., Brickhouse N. S., 2012, The Astrophysical Journal, 756, 128
Frenk C. S., et al., 1999, ApJ, 525, 554
Ghirardini V., et al., 2019a, Astronomy & Astrophysics, 621, A41
Ghirardini V., Ettori S., Eckert D., Molendi S., 2019b, Astronomy & Astrophysics, 627, A19
Hallman E. J., Burns J. O., Motl P. M., Norman M. L., 2007, ApJ, 665, 911
Hammer F., 1987, in Bergeron J., Kunth D., Rocca-Volmerange B., Tran Thanh Van J., eds, High Redshift and Primeval Galaxies. pp 467–473
Hilton M., et al., 2018, ApJS, 235, 20
Hilton M., et al., 2021, ApJS, 253, 3
Jullo E., Kneib J. P., Limousin M., Elíasdóttir Á., Marshall P. J., Verdugo T., 2007, New Journal of Physics, 9, 447
Kaiser N., 1986, MNRAS, 222, 323
Kassiola A., Kovner I., 1993, ApJ, 417, 450
Keeton C. R., 2001, arXiv e-prints, pp astro–ph/0102341
Khatri R., Gaspari M., 2016, MNRAS, 463, 655
King I. R., 1966, AJ, 71, 64
Kneib J.-P., Natarajan P., 2011, The Astronomy and Astrophysics Review, 19
Komatsu E., Seljak U., 2001, MNRAS, 327, 1353
Konrad S., Majer C. L., Meyer S., Sarli E., Bartelmann M., 2013, A&A, 553, A118
Landau L. D., Lifshitz E. M., 1959, Fluid mechanics. Pergamon Press
Lau E. T., Nagai D., Kravtsov A. V., Zentner A. R., 2011, ApJ, 734, 93
Lau E. T., Nagai D., Kravtsov A. V., Vikhlinin A., Zentner A. R., 2012, ApJ, 755, 116
Lilley E. J., Evans N. W., Sanders J. L., 2018, MNRAS, 476, 2086
Lotz J. M., et al., 2017, The Astrophysical Journal, 837, 97
Majer C. L., Meyer S., Konrad S., Sarli E., Bartelmann M., 2013, arXiv e-prints, p. arXiv:1304.6522
Mallaby-Kay M., et al., 2021, ApJS, 255, 11
McDonald M., et al., 2016, ApJ, 826, 124
Mostoghiu R., Knebe A., Cui W., Pearce F. R., Yepes G., Power C., Dave R., Arth A., 2019, MNRAS, 483, 3390
Naess S., et al., 2020, J. Cosmology Astropart. Phys., 2020, 046
Navarro J. F., Frenk C. S., White S. D. M., 1996, The Astrophysical Journal, 462, 563
Nelson K., Lau E. T., Nagai D., Rudd D. H., Yu L., 2014, ApJ, 782, 107
Peterson J. R., et al., 2001, A&A, 365, L104
Puchwein E., Springel V., Sijacki D., Dolag K., 2010, MNRAS, 406, 936
Rephaeli Y., 1995, ARA&A, 33, 541
Roncadelli M., Galanti G., 2021, arXiv e-prints, p. arXiv:2109.13284
Sadat R., 1997, in Valls-Gabaud D., Hendry M. A., Molaro P., Chamcham K., eds, Astronomical Society of the Pacific Conference Series Vol. 126, From Quantum Fluctuations to Cosmological Structures. p. 349 (arXiv:astro-ph/9702050)
Salvatier J., Wiecki T. V., Fonnesbeck C., 2016, PyMC3: Python probabilistic programming framework, Astrophysics Source Code Library, record ascl:1610.016 (ascl:1610.016)
Sarazin C. L., 1988, X-ray emission from clusters of galaxies. Cambridge Astrophysics Series, Cambridge University Press, 1988.
Sereno M., Ettori S., Meneghetti M., Sayers J., Umetsu K., Merten J., Chiu I. N., Zitrin A., 2017, MNRAS, 467, 3801
Soucail G., Mellier Y., Fort B., Mathez G., Cailloux M., 1988, A&A, 191, L19
Steinhardt C. L., et al., 2020, The Astrophysical Journal Supplement Series, 247, 64
Tchernin C., et al., 2018, Astronomy & Astrophysics, 614, A38
Tomooka P., Rozo E., Wagoner E. L., Aung H., Nagai D., Safonova S., 2020, Monthly Notices of the Royal Astronomical Society, 499, 1291
Trevisan M., Mamon G. A., Stalder D. H., 2017, MNRAS, 471, L47
Umetsu K., et al., 2015, ApJ, 806, 207
Vazza F., Angelinelli M., Jones T. W., Eckert D., Brüggen M., Brunetti G., Gheller C., 2018, MNRAS, 481, L120
Vikhlinin A., Kravtsov A., Forman W., Jones C., Markevitch M., Murray S. S., Van Speybroeck L., 2006, The Astrophysical Journal, 640, 691–709
Voit G. M., 2005, Reviews of Modern Physics, 77, 207
Wilms J., Allen A., McCray R., 2000, ApJ, 542, 914
Zaroubi S., Squires G., de Gasperis G., Evrard A. E., Hoffman Y., Silk J., 2001, The Astrophysical Journal, 561, 600–620

APPENDIX A: CORNERPLOTS

We display here the cornerplots of the MCMC optimisations of the potential of the ICM data, as described Sect. 7. In the following graphs, densities ρ are displayed in kg.m^{-3}, while core, scale and cut radii in kpc.

This paper has been typeset from a TEX/LATEX file prepared by the author.

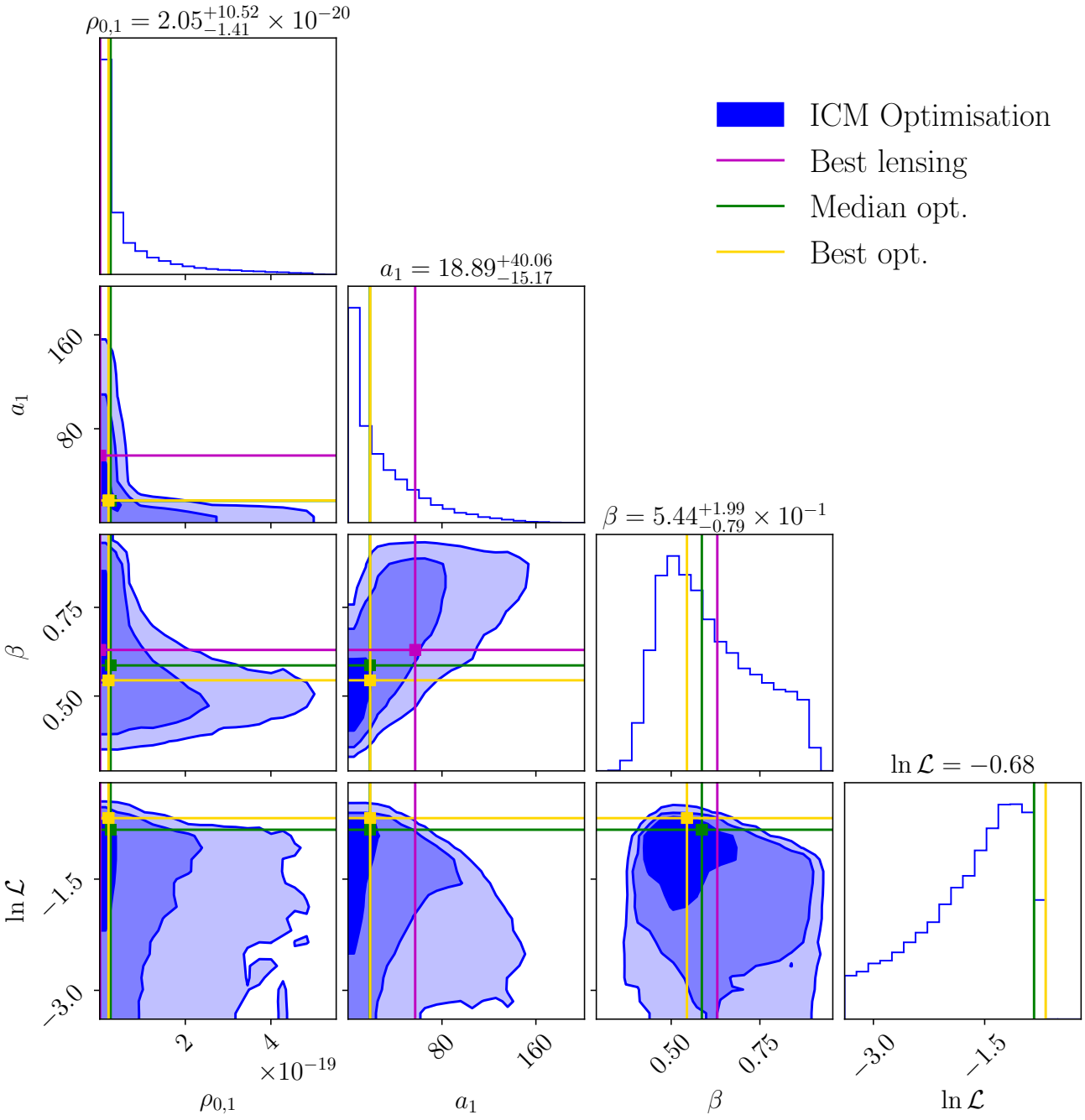

Figure A1. MCMC optimisation for β model of the three relevant parameters for cluster MACS J0242: central density $\rho_{0,1}$, core radius a_1 and density index β. As per all other cornerplots, the density $\rho_{0,1}$ is here displayed in kg.m^{-3} and the core radius a_1 in kpc. *Blue:* Optimisation performed using the available ICM data (X-ray here). *Magenta:* Best strong lensing model (described in Table 2). It is here only presented comparatively. *Green:* Median of the ICM optimisation. *Gold:* Best ICM optimisation. These best ICM-optimisation values are displayed over the histogramme distributions.

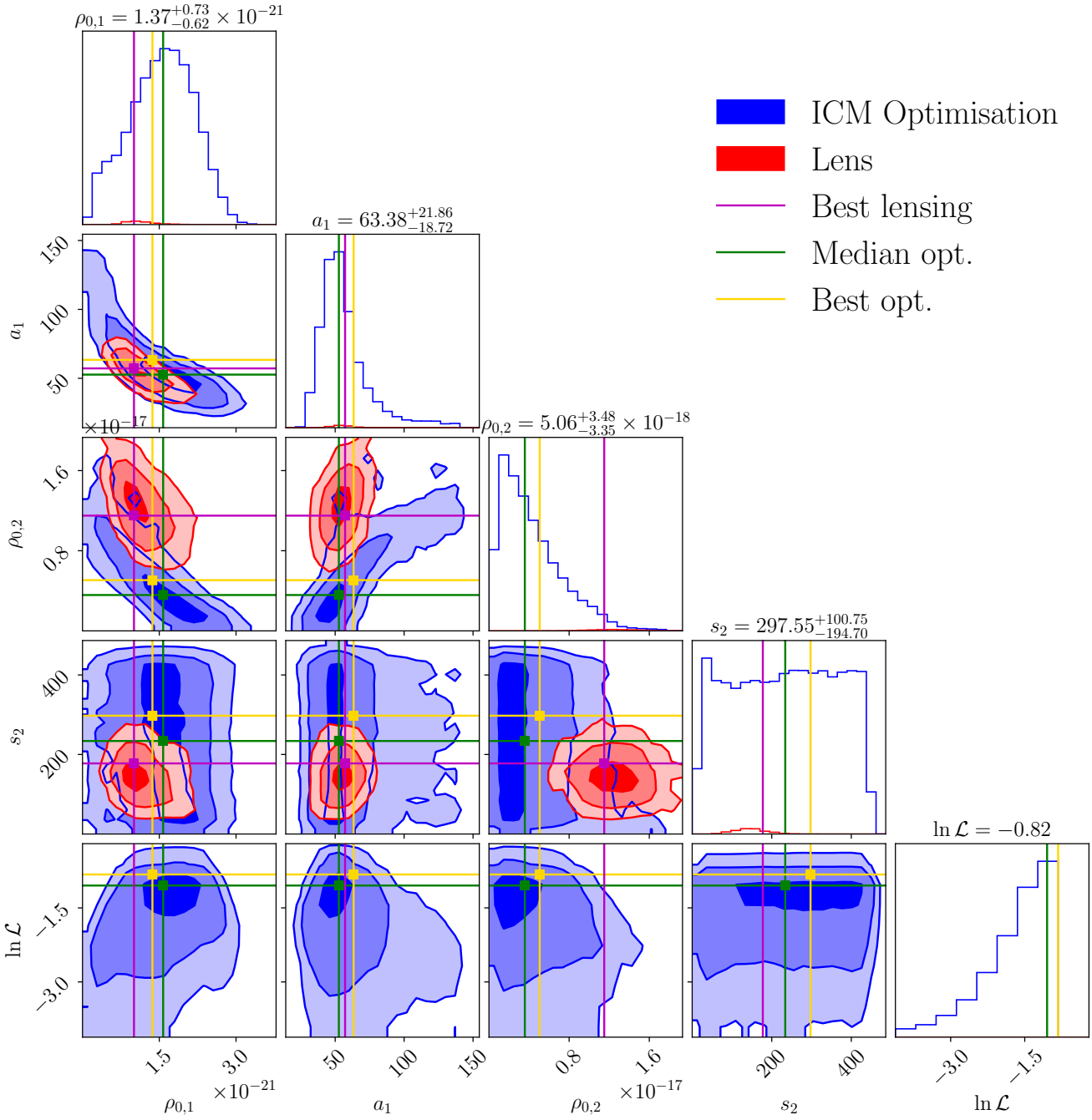

Figure A2. MCMC optimisation for idPIE model, for cluster MACS J0242: DMH central density $\rho_{0,1}$ and core radius a_1, and BCG central density $\rho_{0,2}$ and cut radius s_2. The DMH cut radius is fixed to the fiducial value of 1.5 Mpc. Densities are displayed in kg.m^{-3}, distances in kpc. *Blue:* Optimisation performed using the available ICM data (X-ray here). *Red:* Strong lensing optimisation. *Magenta:* Best strong lensing model (described in Table 2). *Green:* Median of the ICM optimisation. *Gold:* Best ICM optimisation.

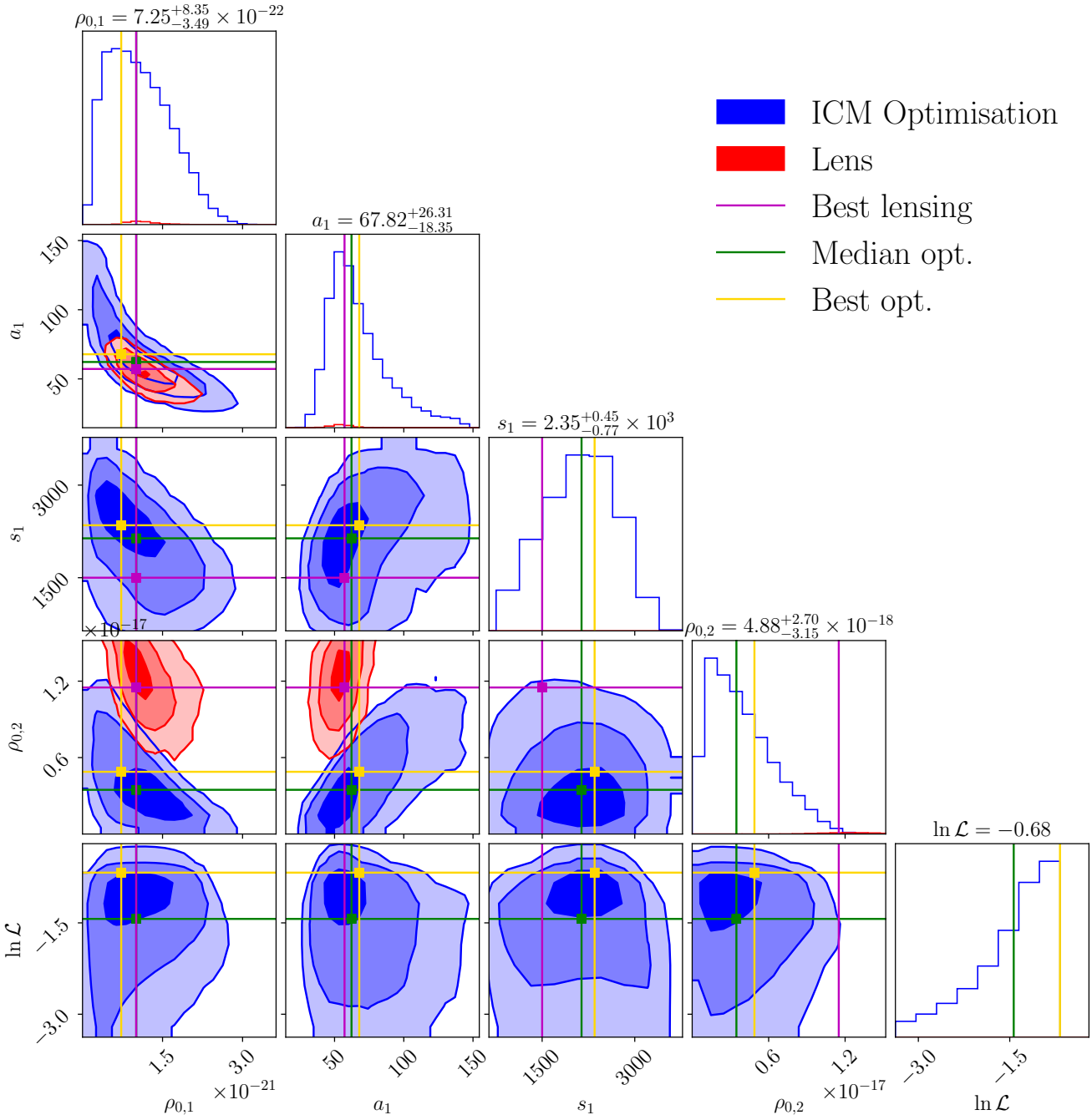

Figure A3. MCMC optimisation for idPIE model, for cluster MACS J0242: DMH central density $\rho_{0,1}$, core radius a_1, cut radius s_1, and BCG central density $\rho_{0,2}$. As we saw with Fig. 7, the optimisation of s_2 is not necessary. The BCG cut radius is fixed to the lensing value of 177.6 kpc. Densities are displayed in kg.m^{-3}, distances in kpc. *Blue:* Optimisation performed using the available ICM data (X-ray here). *Red:* Strong lensing optimisation. *Magenta:* Best strong lensing model (described in Table 2). *Green:* Median of the ICM optimisation. *Gold:* Best ICM optimisation.

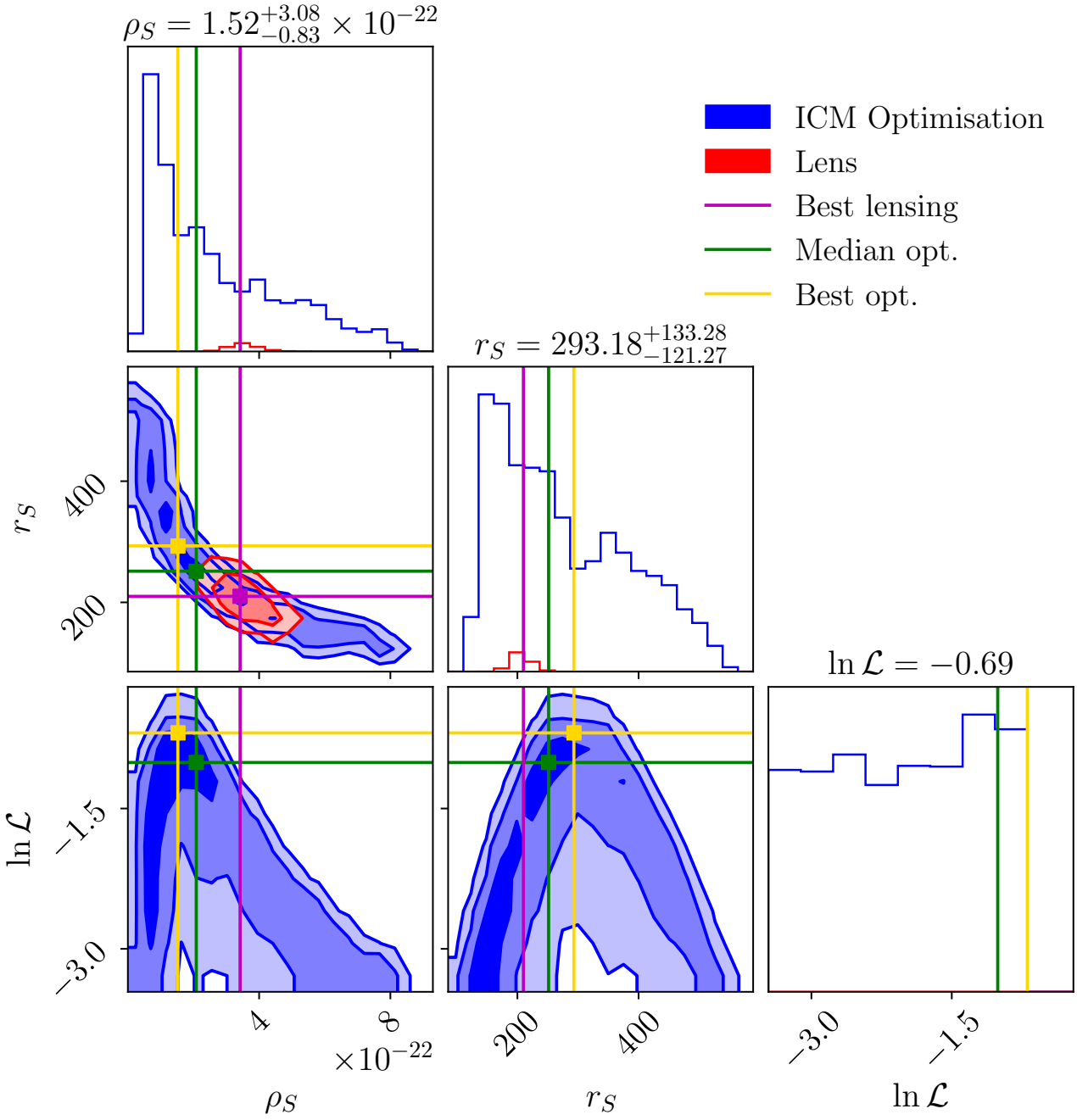

Figure A4. MCMC optimisation for iNFW model of the two relevant parameters for cluster MACS J0242: the density normalisation ρ_S and the scale radius r_S. Densities are displayed in kg.m^{-3}, distances in kpc. *Blue:* Optimisation performed using the available ICM data (X-ray here). *Red:* Strong lensing optimisation. *Magenta:* Best strong lensing model (described in Table 2). *Green:* Median of the ICM optimisation. *Gold:* Best ICM optimisation.

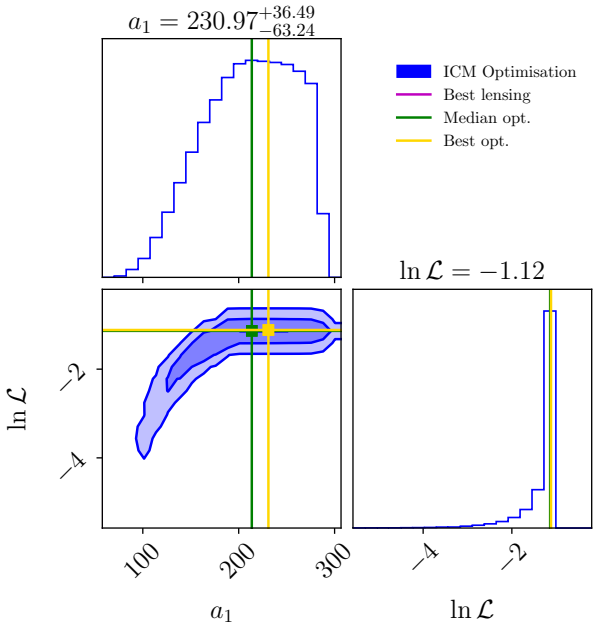

Figure A5. MCMC optimisation for an empirical gas fraction model of the core radius for cluster MACS J0242. a_1 is the core radius of the DMH, in kpc. *Blue:* Optimisation performed using the available ICM data (X-ray here). *Magenta:* Best strong lensing model (described in Table 2). *Green:* Median of the ICM optimisation. *Gold:* Best ICM optimisation.

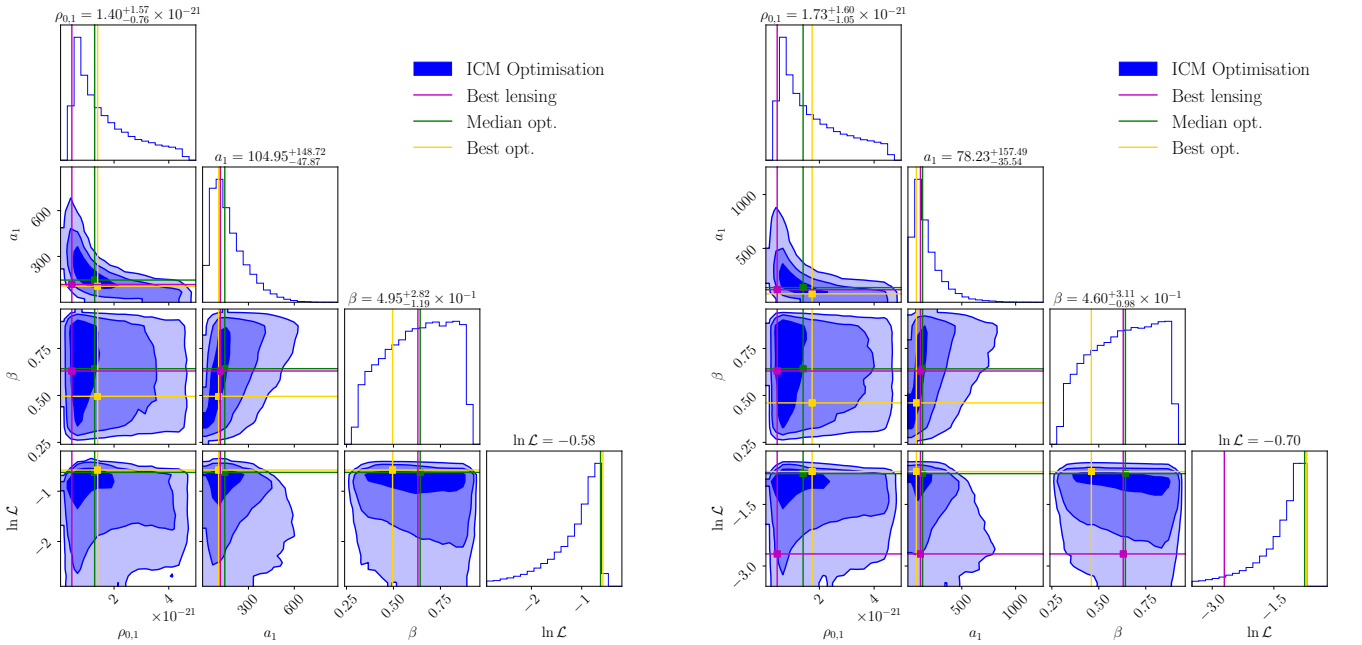

Figure A6. MCMC optimisation for the β model for cluster MACS J0949. Densities are displayed in kg.m^{-3}, distances in kpc. *Left:* The optimisation is performed here only using X-ray data. *Right:* The optimisation is performed using X-ray and SZ data. *Blue:* Optimisation performed using the available ICM data (X-ray here). *Magenta:* Best strong lensing model (described in Table 2). *Green:* Median of the ICM optimisation. *Gold:* Best ICM optimisation.

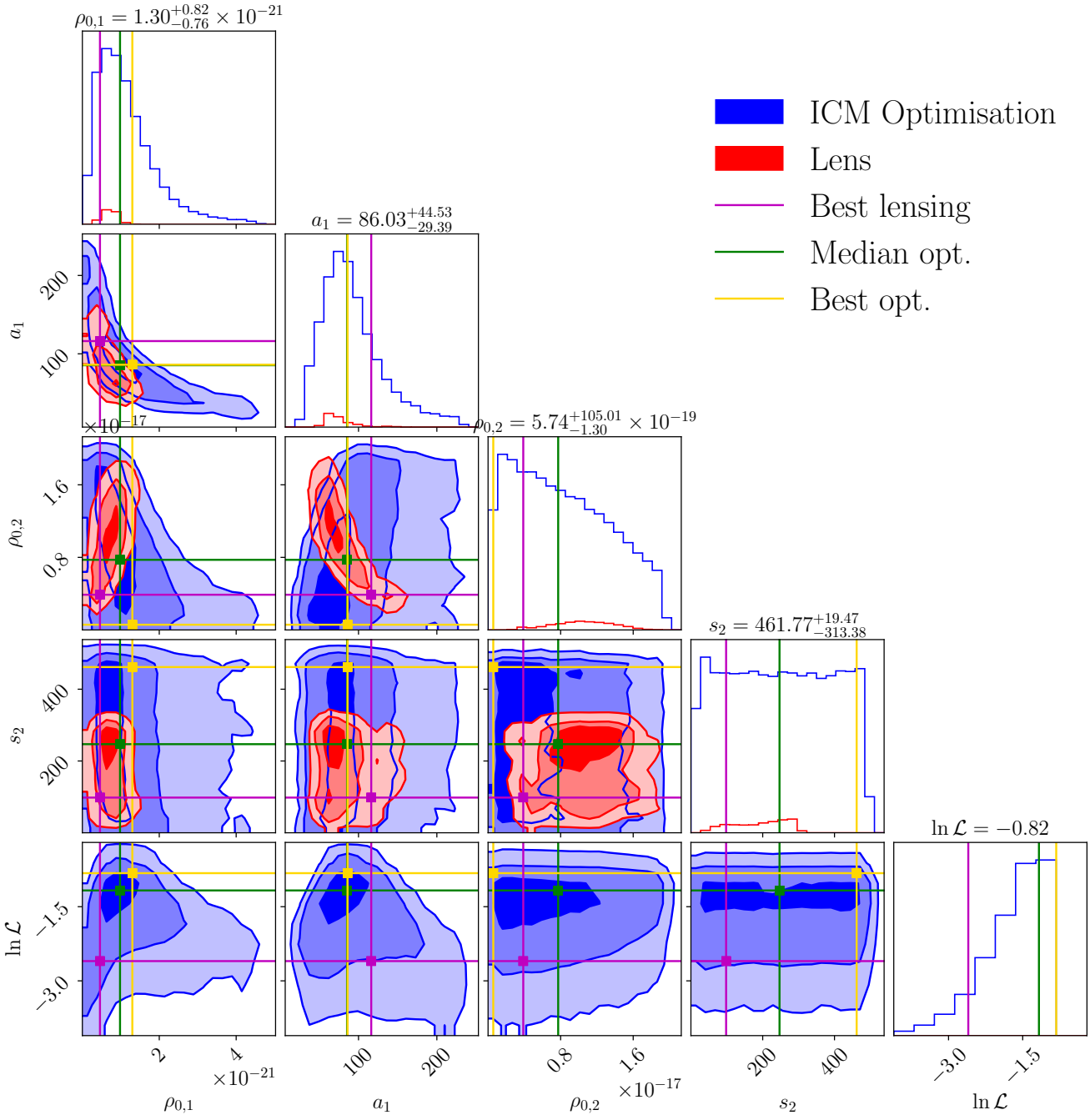

Figure A7. MCMC joint optimisation for `idPIE` model, for cluster MACS J0949: DMH central density $\rho_{0,1}$ and core radius a_1, and BCG central density $\rho_{0,2}$. The DMH cut radius is fixed to the fiducial value of 1.5 Mpc. Densities are displayed in kg.m^{-3}, distances in kpc. *Blue:* Optimisation performed using the available ICM data (X-ray here). *Red:* Strong lensing optimisation. *Magenta:* Best strong lensing model (described in Table 2). *Green:* Median of the ICM optimisation. *Gold:* Best ICM optimisation.

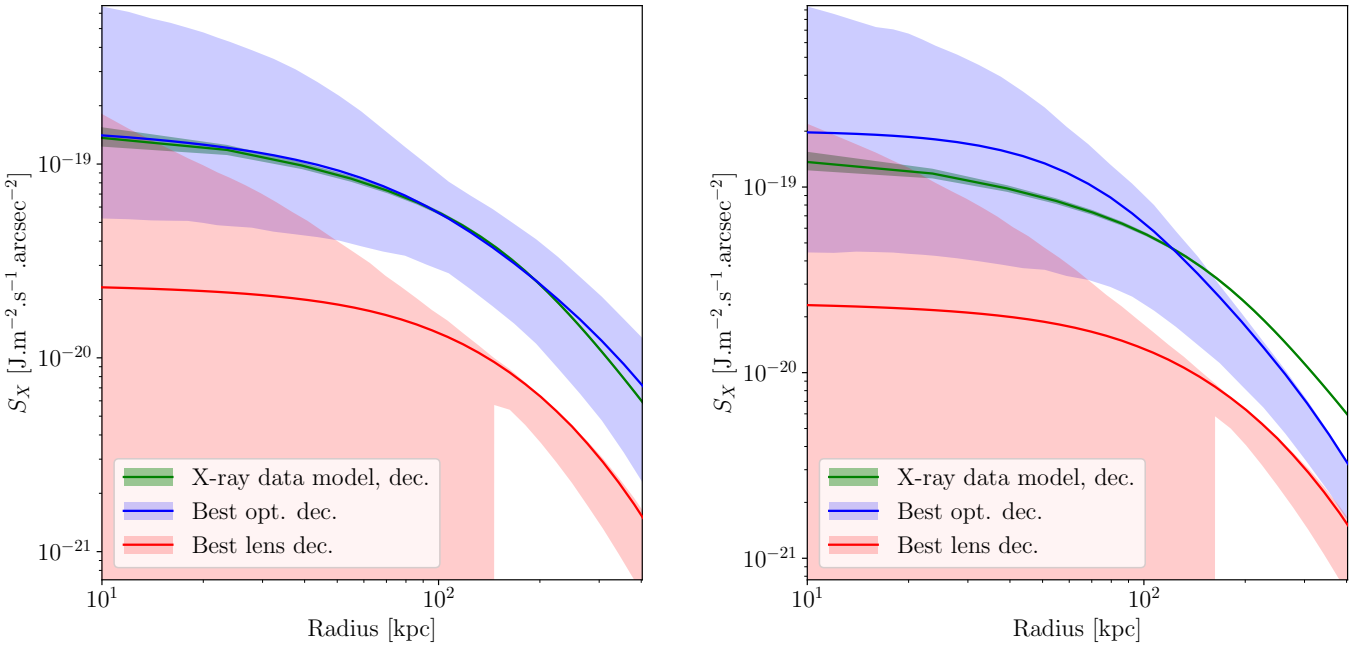

Figure A8. Expected X-ray surface brightness S_X for `idPIE` model, for cluster MACS J0949. *Green:* X-ray data inferred value. *Blue:* Best ICM-optimised value, with a `idPIE` model. *Red:* Best lens model inferred value. *Left:* In the case of the optimisation of parameters $\rho_{0,1}$, a_1, s_1, $\rho_{0,2}$ and s_2, as illustrated on Fig. 10. *Right:* In the case of the optimisation of parameters $\rho_{0,1}$, a_1, and $\rho_{0,2}$, as illustrated on Fig. A7.

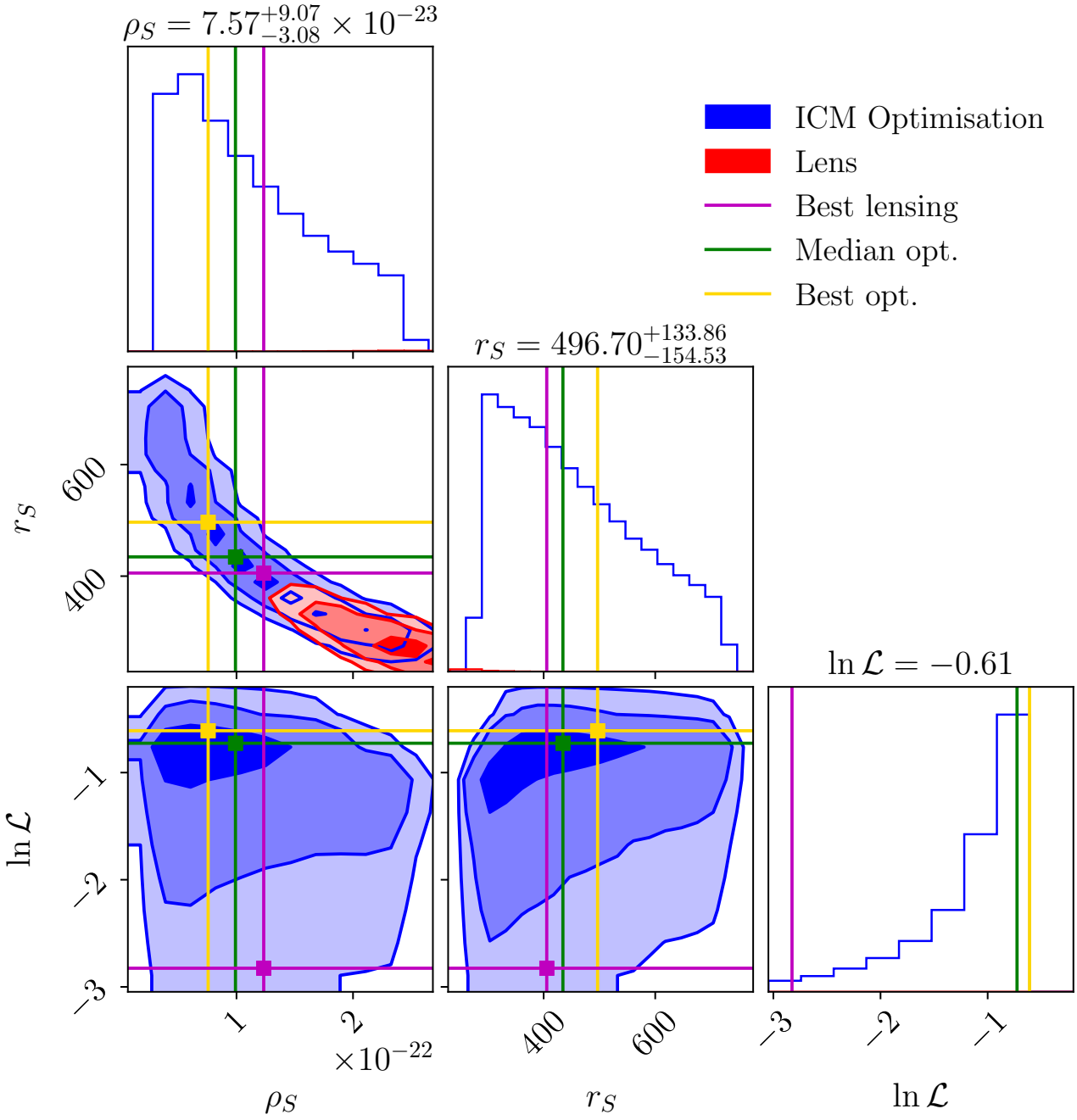

Figure A9. MCMC joint optimisation for iNFW model. The individual values for the best optimisation here presented are: $\ln \mathcal{L}_X = -0.58$ and $\ln \mathcal{L}_{SZ} = -0.89$. Densities are displayed in kg.m^{-3}, distances in kpc. *Blue:* Optimisation performed using the available ICM data (X-ray here). *Red:* Strong lensing optimisation. *Magenta:* Best strong lensing model (described in Table 2). *Green:* Median of the ICM optimisation. *Gold:* Best ICM optimisation.

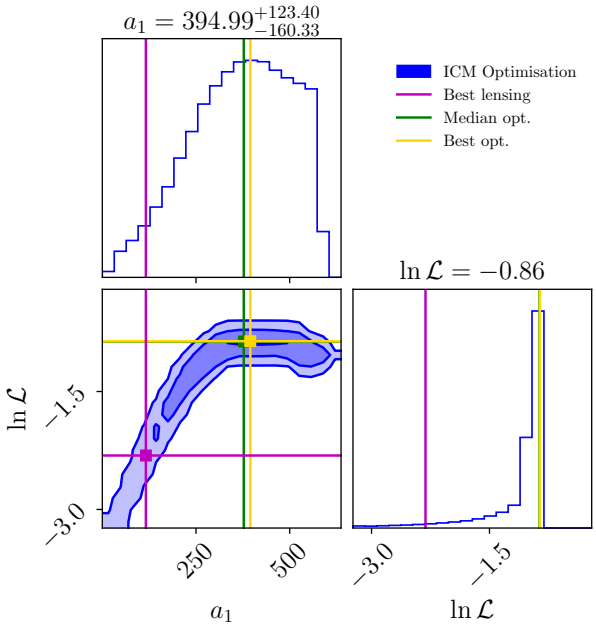

Figure A10. MCMC optimisation for gas fraction model. The optimisation was performed with the X-ray and SZ data. a_1 is in kpc. *Blue:* Optimisation performed using the available ICM data (X-ray here). *Magenta:* Best strong lensing model (described in Table 2). *Green:* Median of the ICM optimisation. *Gold:* Best ICM optimisation.

Chapter 5

Joint Strong Lensing - X-ray galaxy cluster reconstruction

For it is the business of Ethics, I must insist, not only to obtain true results, but also to find valid reasons for them.

— George Edward Moore

In Chapter 4, we showed we could predict the ICM density using the strong lensing optimisation only for clusters MACS J0242 and MACS J0949. However, this method presents a few issues:

1. The strong lensing optimisations of MACS J0242 and MACS J0949, described in Chapter 3, were performed with respectively 6 and 2 spectroscopically identified multiply-imaged systems. This limits the quality of the constraints.
2. The cut radius of the dark matter halo (DMH) s_1 was always fixed to an arbitrary value. Although there are physical reasons to choose this value around 1.5 Mpc (see for instance Chang et al., 2018), we showed in Section 4.3 the importance of this parameter on the ICM central density, upon using the bijective relationship (4.18) in relaxed or relaxing clusters. Fixing s_1 arbitrarily therefore fundamentally limits the quality of the ICM reconstruction.
3. The ICM optimisation of the analytical models density parameters allowed to reach a good quality of ICM reconstruction with these profiles. However, a number of parameters were not optimised (geometry) or were degenerate in their optimisation (e.g. s_2 and $\rho_{0,2}$ to a degree, for `idPIE` profiles).
4. The temperature profile was taken to be following equation (4.1), and was normalised with $T_{500}(z)$ (equation 4.3) and with the extrapolated M_{500} masses from Section 3.4. Given the considerable scatter in the temperature relationship ($\sim$ 19%), the fact it was fitted with X-COP, a cluster data sample at a redshift different from our lensing clusters', the inherent scatter of the $T_{500}(z)$ Ghirardini et al. (2019b) relationship, and the extrapolation over M_{500}, we can not reasonably expect a precise temperature prediction.

In order to address the first problem, we propose in this Chapter to utilise the high quality of the combined *Hubble* Frontier Fields[1] (HFF, PI: Lotz, Lotz et al., 2017) and VLT/MUSE data of non-perturbed cluster Abell S1063 (or RXC J2248.7-4431, or SPT-CL J2248-4431, $z = 0.3475$). To

[1] https://archive.stsci.edu/prepds/frontier/

address problems 2. and 3., and more importantly to improve our intrinsic knowledge of galaxy clusters, we apply to Abell S1063 a *joint* strong lensing – X-ray fit. In collaboration with Benjamin Beauchesne, without whom the core coding would not have been possible, we encoded in software `Lenstool` (see Section 2.2.3 and 2.2.4) this joint optimisation. This does not allow to determine s_1 directly, but simply to let it free to be optimised, which is relevant to the X-ray data.

The latter problem 4. could be addressed in the future, but comparing the temperature predicted to that observed with *XMM-Newton*, they are of the same order of magnitude, and largest errors are of order $\sim 30\%$. This is particularly important for SZ effect optimisations, but because the cooling function $\Lambda(T_e)$ used to compute the X-ray surface brightness varies weakly in this temperature and metallicity range ($\sim 10^8$ K and $0.3 Z_\odot$), this is not too problematic for X-ray optimisation only (as performed in this Chapter).

5.1 Abell S1063: data

5.1.1 Photometry

We utilised the HFF Advanced Camera for Surveys (ACS, Ford et al., 1998) F435W, F606W and F814W 'selfcal', epoch 1.0 pass-bands, and the Wide Field Camera 3 (WFC3, Kalirai et al., 2009) F105W, F125W, F140W and F160W pass-bands provide information in the near-IR regime. These data are publicly available on the HFF website[2].

5.1.2 Spectroscopy

We use the two spectroscopic observations of Abell S1063 with VLT/MUSE (Bacon et al., 2010) (ESO ID: 60.A-9345(A), PI: Caputi & Grillo; 095.A-0653(A), PI: Caputi). The same data have already been reduced and analysed in Karman et al. (2015, 2017) and Caminha et al. (2016). Benjamin Beauchesne et al. reduced them with the pipeline presented in Richard et al. (2021), specifically developed with a focus on cluster fields. To complement this set, Beauchesne et al. used the CLASH-VLT (ESO ID: 186.A-0798; PI: P. Rosati) VIsible Multi-Object Spectrograph (VIMOS) observations. The Mercurio et al. (2021) public catalogue assembles almost 4000 spectroscopic detections in the cluster field of view, which were used to complement the spectroscopic catalogue. We provide the multiple images detected with VLT/MUSE Table 5.1.

5.1.3 Preexisting gravitational lensing models

A number of strong gravitational lensing models have been proposed for Abell S1063. Let us cite Caminha et al. (2016), using CLASH and VLT/MUSE data, the free-form model Diego et al. (2016), and the Clusters As TelescopeS (CATS, co-PI: Kneib & Natarajan) team models. Bonamigo et al. (2018) specifically model the mass of the ICM detected with X-ray separately, and thus disentangle the ICM mass component from the DM. Bergamini et al. (2019) combine CLASH and HFF imaging data with VLT/MUSE, and propose to use robust stellar kinematics information on cluster members in order to alleviate the degeneracy between the galaxy-scale DM and the DMH optimisation. In practice, the spectroscopic measurement of the stellar line-of-sight velocity distribution of cluster members sets well motivated priors on the mass of the cluster galaxies lensing catalogue, and samples the Faber-Jackson relationship efficiently (see Section 2.2.4). Sartoris et al.

[2] https://archive.stsci.edu/prepds/frontier/abells1063.html

Table 5.1: Spectroscopic detections of 25 multiply-lensed systems in Abell S1063, for a total of 67 images. Coordinates are in degrees (J2000). For reminder, the centre of the cluster is here taken to be $(\alpha_c; \delta_c) = (342.18322; -44.530889)$.

Id.	α	δ	z
1.1	342.1944992	−44.5269980	1.2279
1.2	342.1958996	−44.5289650	1.2279
1.3	342.1864495	−44.5211970	1.2279
2.1	342.1927000	−44.5311350	1.2592
2.2	342.1921899	−44.5299390	1.2592
2.3	342.1798905	−44.5215670	1.2592
4.1	342.1936999	−44.5301380	1.2583
4.2	342.1932997	−44.5294140	1.2583
5.1	342.1791905	−44.5235930	1.3972
5.2	342.1878297	−44.5273130	1.3972
5.3	342.1931610	−44.5365380	1.3972
6.1	342.1742104	−44.5283220	1.4280
6.2	342.1758598	−44.5325530	1.4280
6.3	342.1884908	−44.5399800	1.4280
7.1	342.1694009	−44.5272290	1.8370
7.2	342.1742690	−44.5371080	1.8370
7.3	342.1818598	−44.5404980	1.8370
10.1	342.1902379	−44.5297640	0.7287
10.2	342.1895498	−44.5288420	0.7287
11.1	342.1750686	−44.5410250	3.1160
11.2	342.1731684	−44.5399830	3.1160
11.3	342.1655704	−44.5295300	3.1160
12.1	342.1890499	−44.5300160	6.1070
12.2	342.1810499	−44.5346270	6.1070
12.3	342.1908909	−44.5374610	6.1070
12.4	342.1713023	−44.5198370	6.1070
12.5	342.1840900	−44.5316240	6.1070
13.1	342.1815498	−44.5393580	4.1130
13.2	342.1791695	−44.5387080	4.1130
14.1	342.1788496	−44.5358790	3.1180
14.2	342.1874206	−44.5386990	3.1180
14.3	342.1706519	−44.5220980	3.1180
17.1	342.1858204	−44.5388610	3.6060
17.2	342.1788296	−44.5367360	3.6060
17.3	342.1697821	−44.5219770	3.6060
19.1	342.1800496	−44.5384300	1.0350
19.2	342.1755393	−44.5359400	1.0350
19.3	342.1719201	−44.5302500	1.0350
24.1	342.1983813	−44.5357520	2.9780
24.2	342.1924391	−44.5250690	2.9780
24.3	342.1815103	−44.5202540	2.9780
27.1	342.1901500	−44.5309610	5.0510
27.2	342.1908406	−44.5356620	5.0510
30.1	342.2007739	−44.5315052	3.4519
30.2	342.1971164	−44.5248797	3.4519
30.3	342.1858258	−44.5177243	3.4519
31.1	342.1956897	−44.5374213	3.7131
31.2	342.1909905	−44.5267661	3.7131
31.3	342.1763343	−44.5206643	3.7131
33.1	342.1887692	−44.5227760	5.2373
33.2	342.1837999	−44.5212410	5.2373
54.1	342.1829211	−44.5203160	3.1690
54.2	342.1919790	−44.5241800	3.1690
54.3	342.1991014	−44.5360040	3.1690
94.1	342.1892957	−44.5187150	3.2857
94.2	342.1960772	−44.5229570	3.2857
94.3	342.2021704	−44.5321110	3.2857
100.1	342.1969889	−44.5220110	5.8940
100.2	342.1900055	−44.5179556	5.8940
200.1	342.1955895	−44.5283900	1.2279
200.2	342.1948293	−44.5273500	1.2279
303.1	342.1758410	−44.5363610	3.6664
303.2	342.1879175	−44.5404066	3.6664
304.1	342.1738121	−44.5411542	3.2297
304.2	342.1739180	−44.5412128	3.2297
305.1	342.1803066	−44.5246125	3.0816
305.2	342.1838722	−44.5257292	3.0816

(2020) use the line-of-sight velocity dispersion of individual galaxies to perform a joint fit with an upgraded `MAMPOSSt` technique (Mamon et al., 2013). Limousin et al. (2022) utilise a strong light-traces-mass assumption, and adopt a unimodal cored mass model. Adding a mild perturbation in the form of a superposition of B-spline potentials, they manage to recover a competitive *rms* in spite of strong, physically-motivated priors.

Additionally, Umetsu et al. (2014) studied the weak lensing shear and magnification of Abell S1063, estimating $M_{500,c} = (11.1 \pm 3.2) \times 10^{14} M_{\odot}$ and $M_{200,c} = (20.3 \pm 6.7) \times 10^{14} M_{\odot}$. Williamson et al. (2011) attribute to the cluster $M_{500,c} = (13.8 \pm 7.6) \times 10^{14} M_{\odot}$ and $M_{200,c} = (29.0 \pm 13.3) \times 10^{14} M_{\odot}$ with the South Pole Telescope (SPT) SZ effect observations.

5.1.4 X-ray and SZ effect data

Chandra

The X-ray space telescope *Chandra* archive[3] provides with a total available exposure time of 123 ks in VFAINT mode only with the following (ObsId: 4966, PI: Romer, 2004; 18818 and 18611, PI: Kraft, 2016). The Advanced CCD Imaging Spectrometer (ACIS, see Garmire et al., 2003) I filter presents three bands[4]:

- soft: 0.5 – 1.2 keV, of effective average energy 0.92 keV,
- medium: 1.2 – 2.0 keV, of effective average energy 1.56 keV,
- hard: 2.0 – 7.0 keV, of effective average energy 3.80 keV,

for a total broadband 0.5 - 7.0 keV, of effective mean energy 2.3 keV. Benjamin Beauchesne then reduced these data with the Chandra Interactive Analysis of Observations (`CIAO`[5], see Fruscione et al., 2006) and CALDB 4.9.6 tools. We can convert counts into flux using the PIMMS NASA tool. We additionally recovered the background blank-sky associated to the cluster observations (Hickox and Markevitch, 2006).

We scale down the pixel size to 1.968″, which is much larger than *Chandra* on-axis point-spread function. In first approximation, we therefore neglect the PSF. We cut the image to only keep the regions immediately around the cluster, for a diameter of 130 pixels (i.e. 1258 kpc).

XMM-Newton

We use the *XMM-Newton* archive[6] publicly available observations of the Abell S1063 cluster. It was observed for a total of 53 ks (OBSID:0504630101). Dominique Eckert analysed the observation using XMMSAS v17.0, and the most up-to-date calibration files. With the XMMSAS tools `mos-filter` and `pn-filter`, the light curves of the observations are extracted, and periods of enhanced background, induced by soft proton flares, are filtered out. After flare filtering, the available clean exposure time is 32 ks (MOS) and 25 ks (PN) for Abell S1063.

We take the PSF into account as mentioned in Section 4.3. We use maps of diameter ~ 1000 kpc, i.e. of 82 pixels. However, after PSF cut to remove border effects, we only keep 66 pixels wide maps.

[3] https://cda.harvard.edu/chaser/
[4] https://cxc.harvard.edu/csc/columns/ebands.html
[5] https://cxc.cfa.harvard.edu/ciao/
[6] https://www.cosmos.esa.int/web/xmm-newton/xsa

ACT

We extracted the SZ effect data of Abell S1063 out of the ACT DR5 map, as in Chapter 5. However, we do not present how we use these data in this thesis, as the joint model constraints using SZ effect data is still ongoing work.

5.2 Simple SL model

Cluster catalogue

We take the reference coordinates to be $(\alpha_c; \delta_c) = (342.183210; -44.530878)$. Reference magnitudes are taken on the reference band WFC3/F160W, using the AB convention system (Oke, 1974).

To validate a `SExtractor` detection on one instrument, we require a detection to be included within all colour-magnitude red sequence cuts, except one. See Section 3.4 for more details on this method. We then combine WFC3 and ACS, keeping all detections considered detected on at least one instrument. We provide in Appendix C.3 the cluster member catalogue, Table C.3. We consider the redshift of all members to be that of the cluster, i.e. $z = 0.3475$.

SL modelling

Using the 25 multiply-imaged systems for 67 different lensed images summarised in Table 5.1, we can strongly constrain the mass distribution within cluster Abell S1063. We choose all potentials to be modelled with a dPIE distribution (see equation 1.67). We turned to existing models of cluster Abell S1063, cited in Section 5.1.3, to examine lensing priors to optimisation with `Lenstool`. Most previous models tend to favour multi-modal distributions, with several cluster-scale halos, on top of possible gas clumps justified by the X-ray observation, and the BCG optimisation. We notice that we could place a large-scale halo centred around the north-eastern luminous galaxy 3, which we will refer to as 'O3' from now on. A number of multiply-imaged systems are observable on the HFF imaging data, although we do not have access to their spectroscopic redshifts (out of the MUSE field). Using these systems for lensing optimisation is an interesting avenue to explore, but in the interest of simplicity for the comparison with the X-ray and joint optimisations, we do not include them in this thesis.

We follow the same sort of modelling procedure as thoroughly described in Sections 2.2.4 and 3.4, and choose to simply model the large-scale mass distribution with one dark matter halo (DMH), following Limousin et al. (2022). In this strong lensing model, we do not have well motivated cut radius prior, and therefore fix $s_1 \equiv r_{\rm cut,DMH} = 1.5$ Mpc. All other parameters, geometric and density, are set free. We fix the geometric parameters of the BCG with photometry, but allow its density parameters (cut radius, velocity dispersion) to be optimised independently. The BCG core radius is set to an arbitrary small $a_2 = 0.5$ kpc. As in the MACS 0242 and MACS 0949 models, this presents a risk of seeing the DMH and BCG density parameters degenerate. However, Abell S1063 presents a much larger set of constraining multiple images, some of which are very central to the cluster. This should attenuate the parameter degeneracy. At last, we optimise the whole $L^\star$ galaxy catalogue with the classic Faber-Jackson relationship (equation 2.62). We take the reference pivot magnitude corresponding to WFC/F160W magnitudes to be $mag_0 = 18.2172$. Its core radius is fixed to the arbitrarily small value $a_0^\star = 0.15$ kpc, and, noticing the possible

degeneracy between the velocity dispersion and cut radius, we fix the former $\sigma_0^\star = 180$ km.s^{-1}. We conduct the inversion in the image plane.

SL model

We find this model to yield a $rms = 0.82''$, which is a bit more than most models presented in Section 5.1.3, but good enough to consider this model as a good description of the cluster physics in the central regions ($R < 200\,$kpc). We moreover expected this simple cored model to present a higher rms than models using more degrees of freedom (using external shear, additional large scale halos such as O3, gas clumps, or B-spline potentials). We find $M(< 200\,\mathrm{kpc}) = 2.174^{+0.003}_{-0.004} \times 10^{14} M_\odot$. The extrapolated mass and radius at $500 \times \rho_c(z)$ are $M_{500,c} = 1.316^{+0.009}_{-0.008} \times 10^{15} M_\odot$ and $R_{500,c} = 1476.9^{+3.2}_{-3.2}\,$kpc. As in Section 3.4, we remind the reader that these values are speculative, as the cluster's outskirts could not be probed using strong lensing only, and assume $s_2 = 1.5\,$Mpc based only on reasonable estimates from the literature.

The optimisation is of good quality, except for parameter $r_{\mathrm{cut,BCG}} = s_2$, whose optimisation appears degenerate (matching previous results on clusters MACS J0242 and MACS J0949). We summarise the optimised model posterior parameters in Table 5.2.

5.3 X-ray `idPIE` optimisation

Model

As in Chapter 4, we use X-ray data to optimise the ICM density, assuming a `idPIE` n_e distribution. This optimisation was based on the geometric parameters fixed by the joint optimisation described in the next Section 5.4. We note that using the parameters of the previous Section 5.2 would not have made a great difference, but this simply allows us to start with a better estimate of $M_{500,c}$, close to the value found with *XMM-Newton* analysis. Using this value is also consistent with the idea of an incremental optimisation of the density profile description, including in the outskirts of clusters, and makes extensive use of *Chandra* X-ray data. We thus used the $M_{500,c} = 1.523 \times 10^{15} M_\odot$ result of the joint optimisation as a start, yielding a prior on $T_0 = 13.8\,$keV. We allowed the $M_{500,c}$ value to evolve at each MCMC step, effectively changing the temperature normalisation.

We have chosen to perform and present two types of ICM optimisation: one accounting for the BCG in the potential traced by n_e alongside the DMH, or another assuming only the DMH was traced by the ICM. To be clear, as for the $L^\star$ catalogue, excluding the BCG from the ICM optimisation does not remove its mass from the M_{500} value used to normalise the temperature. This mass is still taken into account, but in the 'DMH only' model, we simply assume the baryonic physics of the BCG not to be reducible to the ICM. This assumption could be justified notably because the stellar fraction of galaxies, including the BCG, is much higher than that of the rest of the cluster, for equivalent total baryonic fractions. As a consequence, the ionisation fraction, assumed to be $\mathcal{F}_I = 1$ across the whole cluster, may be smaller in the centre. Moreover, non-gravitational processes such as Active Galaxy Nuclei (AGN) feedback, gas cooling, shocks, turbulence, bulk motions, cosmic rays and magnetic fields make the cluster centre particularly difficult to model using only a gravitational model (Ghirardini et al., 2019b).

We also take into account the absorption of foreground gas. The galactic hydrogen column

density is $1.26 \times 10^{20}\,\mathrm{cm}^{-2}$, according to the galactic hydrogen NASA tool[7], yielding an absorption factor 0.9873 in the 0.7 – 1.2 keV *XMM-Newton* band.

We also can perform an identical optimisation using the *Chandra* data, either independently, or jointly with the *XMM-Newton* data. In this case, we reduce the *Chandra* maps to a diameter of 1 Mpc, i.e. 104 pixels. The respective galactic hydrogen absorption for the soft, medium and hard bands are 0.9807, 0.9967 and 0.9996. If we use both X-ray telescopes data simultaneously, we sum the log-likelihoods as in equation (4.30). For the moment, for the sake of simplicity of X-ray data interpretation, we have not run this joint optimisation, and simply perform the sole ICM optimisation with *XMM-Newton* observations.

Results

We display the cornerplots of the DMH only and of the DMH and BCG models on Fig. 5.1 and 5.2 respectively. We compare the X-ray surface brightness S_X on Fig. 5.3. The cornerplots are the most efficient way to see that, in both DMH only and DMH & BCG optimisations, the ICM optimisation best fitting values agree with the joint optimisation Section 5.4 very tightly. As in Section 4.3, the constraints yielded by the ICM are nowhere as good as those of SL, as the error bars are very important.

Using the S_X predicted values with the *Chandra* – strong lensing model only, assuming the DMH only to trace the ICM yields an under-prediction of the surface brightness (see Figure 5.3, left panel). Conversely, assuming the DMH and the BCG to represent the gravitational potential traced with the ICM, the predicted S_X appears to match the *XMM-Newton* observations. As the joint optimisation of the next Section only uses the DMH only tracing X-ray hypothesis, this result is troublesome. We may however be able to explain it by the different cooling curve and temperature models used in both cases, alongside a possible difference in the inferred density n_e by *Chandra* data. Another explanation may be that the joint optimisation in the cluster centre is governed by strong lensing, as this is where its constraints are the tightest, and that our choice in the next Section not to use the BCG to trace n_e was unjustified. More realistically, we would expect the transition between DMH and BCG ($10 \lesssim r \lesssim 50\,\mathrm{kpc}$) to be also a transition in the nature of baryonic matter between stellar content and ICM. We summarise the corresponding parameters and $M_{500,c}$ in Tables 5.2 and 5.3.

5.4 Cluster joint reconstruction

Temperature and emissivity priors

As in Section 3.4, assuming hydrostatic equilibrium, we use the `hydromass`[8] (Eckert et al., 2022b) package to extract the NFW density distribution and thermodynamic profile out of the *XMM-Newton* data. This yields $R_{500,c} = 1554^{+42}_{-40}\,\mathrm{kpc}$ and $M_{500,c} = 1.454^{+0.123}_{-0.110} \times 10^{15} M_\odot$. The comparison between these observables for all models presented here is displayed on Table 5.3.

Using equation (4.3), we take a temperature normalisation for the self-similar varying index polytropic temperature model (4.1) of $T_0(z = 0.3475) = 13.4\,\mathrm{keV}$. Contrarily to the X-ray only optimisation, this normalisation value is here fixed.

[7] https://heasarc.gsfc.nasa.gov/cgi-bin/Tools/w3nh/w3nh.pl
[8] https://github.com/domeckert/hydromass

Table 5.2: Best fit parameters for Abell S1063 of the strong lensing mass model, of the X-ray optimisation using one DMH `idPIE` profile, a DMH and a BCG `idPIE` profile, and of the joint SL – X-ray optimisation. We here list the central coordinates relative to the centre Δ_α and Δ_δ in arcsec, the ellipticity e, the position angle in degrees θ, the core radius in kpc $r_{\rm core}$, the cut radius in kpc $r_{\rm cut}$, and the velocity dispersion in km.s^{-1} σ, for each component of the model. The centre is taken to be $(\alpha_c; \delta_c) = (342.183210; -44.530878)$ deg. The asterisks highlight parameters which are fixed during the optimisation. $L^\star$ denotes the Faber-Jackson scaled galaxy catalogue.

	Δ_α	Δ_δ	e	θ	$r_{\rm core}$	$r_{\rm cut}$	σ
Strong lensing only							
DMH	$-1.20^{+0.08}_{-0.13}$	$1.14^{+0.12}_{-0.03}$	$0.580^{+0.005}_{-0.004}$	$142.72^{+0.06}_{-0.09}$	$119.95^{+2.14}_{-1.62}$	$1500^\star$	$1321.1^{+5.0}_{-8.1}$
BCG	$0.00^\star$	$-0.02^\star$	$0.460^\star$	$-33.47^\star$	$0.50^\star$	$234.05^{+129.54}_{-49.90}$	$311.26^{+12.03}_{-9.09}$
$L^\star$					$0.15^\star$	$17.38^{+1.03}_{-1.09}$	$180^\star$
X-ray only, DMH							
DMH	$-1.18^\star$	$1.11^\star$	$0.586^\star$	$142.69^\star$	$119.00^{+47.49}_{-48.67}$	4710^{+440}_{-1120}	$1235.8^{+918.0}_{-319.7}$
X-ray only, DMH & BCG							
DMH	$-1.18^\star$	$1.11^\star$	$0.586^\star$	$142.69^\star$	$163.50^{+35.12}_{-75.97}$	4470^{+420}_{-1310}	$1289.0^{+1240.5}_{-186.7}$
BCG	$0.00^\star$	$-0.02^\star$	$0.460^\star$	$-33.47^\star$	$0.50^\star$	$216.25^\star$	$404.15^{+140.64}_{-190.11}$
Joint X-ray and strong lensing							
DMH	$-1.18^{+0.07}_{-0.13}$	$1.11^{+0.09}_{-0.04}$	$0.586^{+0.006}_{-0.004}$	$142.69^{+0.06}_{-0.08}$	$109.21^{+1.37}_{-2.18}$	$3663.12^{+210.26}_{-89.08}$	$1277.75^{+4.32}_{-10.79}$
BCG	$0.00^\star$	$-0.02^\star$	$0.460^\star$	$-33.47^\star$	$0.50^\star$	$216.25^{+125.18}_{-35.08}$	$305.47^{+10.76}_{-12.96}$
$L^\star$					$0.15^\star$	$15.97^{+1.02}_{-1.09}$	$180^\star$

Table 5.3: Comparison of $M_{500,c}$ and $R_{500,c}$ for cluster Abell S1063. Error bars show a 68% confidence interval around the best fit model. Masses are given in $10^{15} M_\odot$ and distances in kpc. Columns respectively represent: (i) The *XMM-Newton* X-ray masses, following a NFW fit, assuming hydrostatic equilibrium (HSE). (ii) The SL only model. Its constraints on M_{500} are very weak, as R_{500} is of the order of s_1, meaning the cut radius of the DMH matters in the M_{500} calculation, and SL only models can not probe such large radius values. (iii) The ICM optimisation only, with *XMM-Newton* data, including only a DMH component. (iv) The ICM optimisation only with *XMM-Newton* data, with a DMH and a BCG components. (v) A joint optimisation with our modified `Lenstool`, with SL and *Chandra* data. We find the maximum $M_{500,c}$ variation to be $\sim 10\%$.

	XMM HSE	SL only	ICM (DMH)	ICM (DMH & BCG)	Joint opt.
$M_{500,c}$	$1.454^{+0.123}_{-0.110}$	$1.316^{+0.009}_{-0.008}$	$1.468^{+0.979}_{-0.437}$	$1.591^{+0.909}_{-0.412}$	$1.523^{+0.006}_{-0.013}$
$R_{500,c}$	1554^{+42}_{-40}	$1476.9^{+3.2}_{-3.2}$	$1508.1^{+291.4}_{-176.6}$	$1561.0^{+259.2}_{-152.3}$	$1550.8^{+2.0}_{-4.2}$

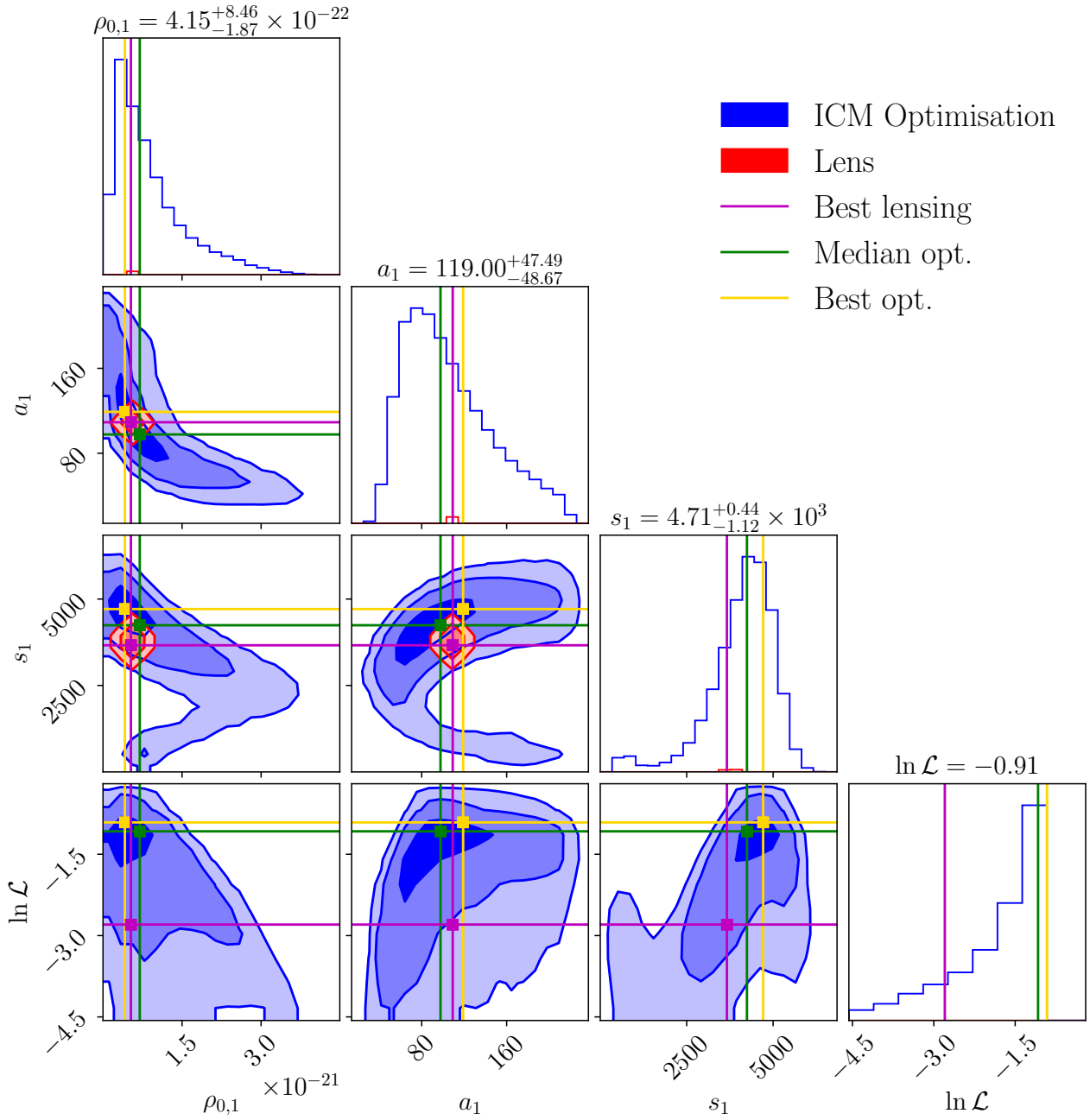

Figure 5.1: ICM optimisation with DMH only model cornerplot. *Blue:* ICM optimisation with *XMM-Newton*. *Red:* Joint optimisation with SL and *Chandra*. *Magenta:* Best joint optimisation parameters values. *Green:* Median of the ICM optimisation. *Gold:* Best ICM optimisation.

The optimisation encoded in `Lenstool` for the moment only allows to use *Chandra* X-ray data as additional constraints, although it is projected to add *XMM-Newton* and SZ effect data in the long term. The X-ray spectral emissivity (cooling curve) is also not calculated given the temperature deducted from the electron density, but computed *a priori* using *Chandra* data and the Astrophysical Plasma Emission Code (APEC)[9]. The emissivity map then remains constant throughout the optimisation.

[9] http://atomdb.org/

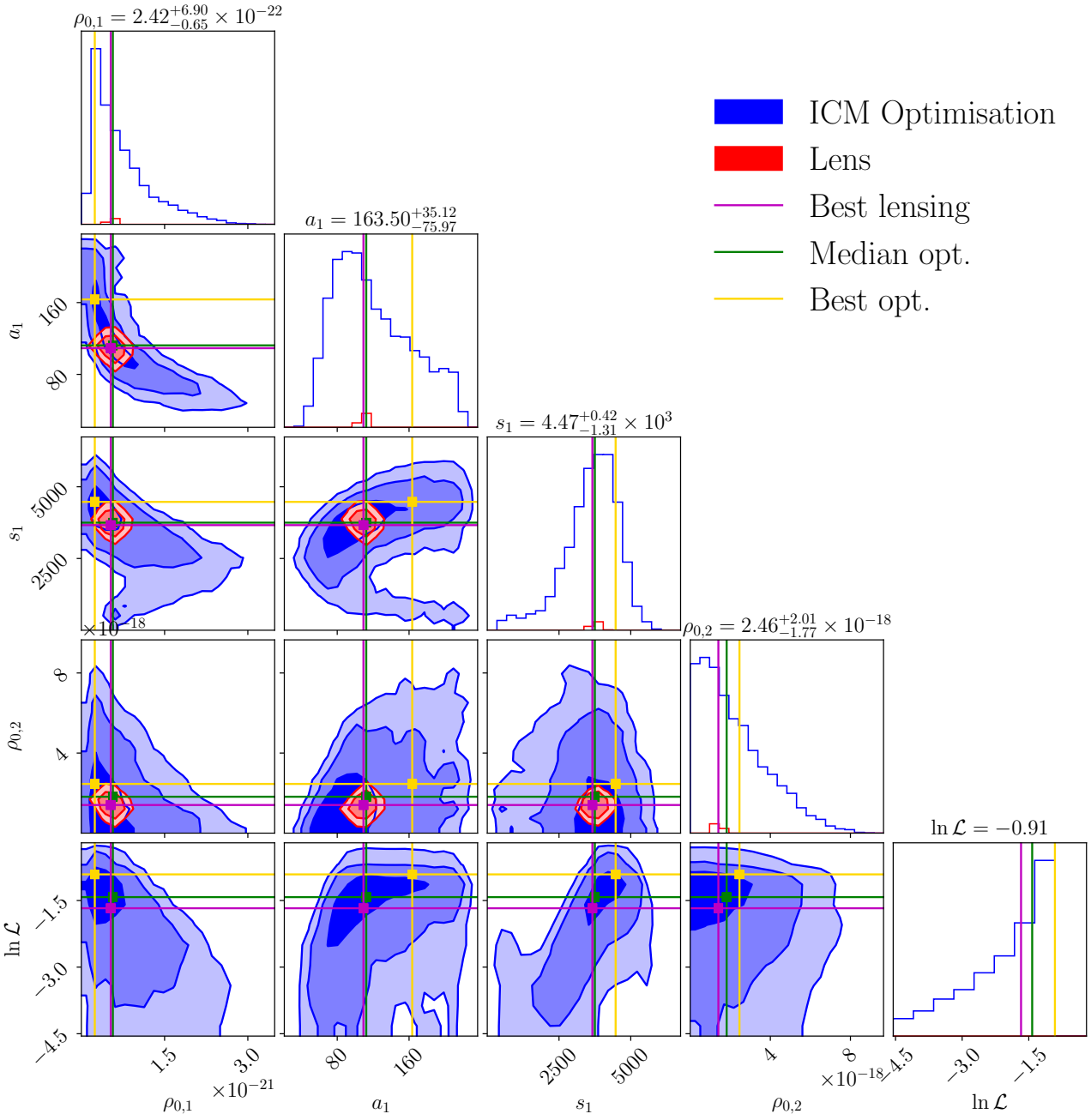

Figure 5.2: ICM optimisation with DMH and BCG model cornerplot. *Blue:* ICM optimisation with *XMM-Newton*. *Red:* Joint optimisation with SL and *Chandra*. *Magenta:* Best joint optimisation parameters values. *Green:* Median of the ICM optimisation. *Gold:* Best ICM optimisation.

Given the degeneracy between BCG and DMH SL optimisations for clusters MACS J0242 and MACS J0949, we considered Chapter 4 more appropriate to let the BCG `idPIE` free to vary. Posterior distributions showed this resulted into a degenerate optimisation parameter space for the core and cut radius a_2 and s_2 (the former not presented then), and in a higher limit on the BCG density normalisation $\rho_{0,2}$. In the case of Abell S1063, we notice the X-ray optimisation to be of better quality if only the DMH is taken to represent the X-ray traced potential. We therefore

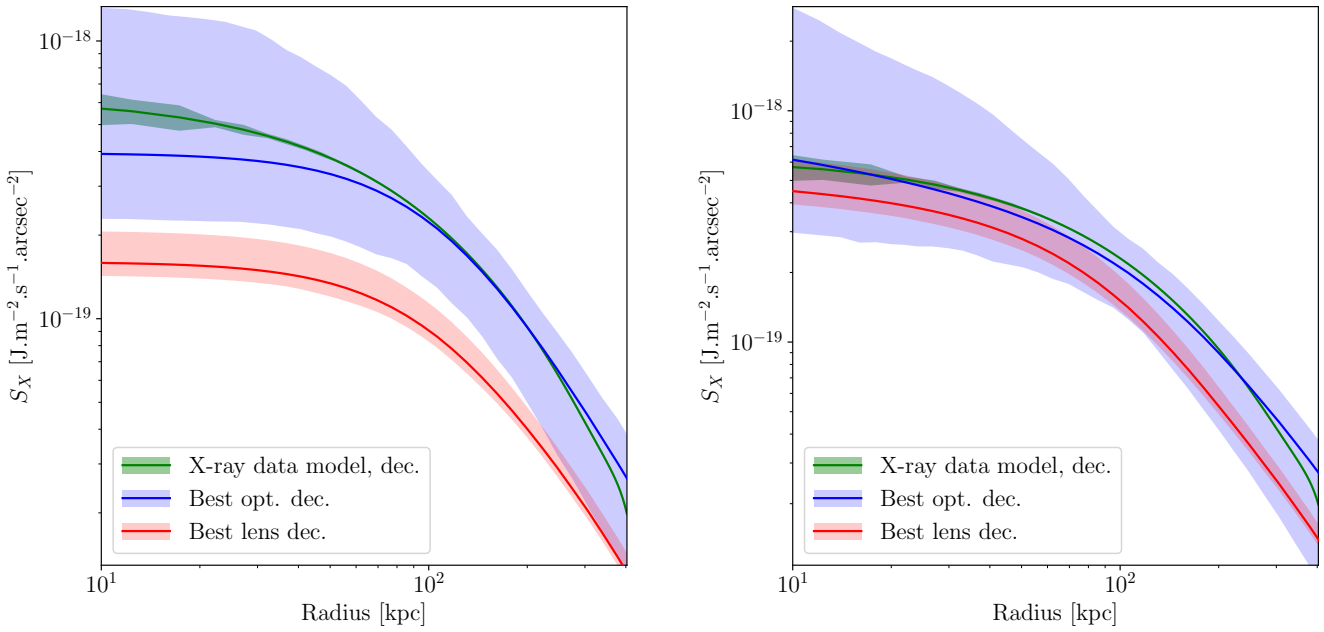

Figure 5.3: X-ray surface brightness S_X for `idPIE` model, for cluster Abell S1063. *Green:* *XMM-Newton* observed surface brightness. *Red:* Joint optimisation predicted S_X (see Section 5.4). *Blue:* ICM-optimised S_X. *Left:* DMH only model, as illustrated on Fig. 5.1. *Right:* DMH and BCG model, as illustrated on Fig. 5.2.

only include a DMH X-ray `idPIE` counterpart[10].

Lens modelling

We utilise the exact same cluster member galaxies and multiply-lensed images catalogues as in Section 5.2. The fixed and optimised parameters are exactly the same, except for the cut radius of the DMH s_1, which we here can legitimately optimise with ICM data, as it is a main result of Chapter 4. We let it free to vary between 0.5 and 10 Mpc.

Relative likelihood weight

In Section 4.2.4, we described a joint likelihood between X-ray and SZ effect data through equation (4.30), which is simply the normalised total log-likelihood of the relative difference between model predictions and data in all bins. In equation (2.63), we defined the χ^2 model error characterisation with `Lenstool` for SL fits. In the present case of joint likelihood fit however, multiplying likelihoods of different natures is a non-trivial problem. Indeed, this would give shape to a joint optimisation, but the relative weight of each component could be absolutely disproportionate, not to mention this does not take into account the *amount of information* carried within each X-ray pixel or multiple image position. A possible way to address this problem would be to Bayesianly calculate the amount of information carried by each signal, relative to the parameters we optimise (say here the gravitational potential and electron density n_e). Information field theory (see Enßlin, 2013) could be an interesting pathway to explore in the future. More practically, we could run

[10]The possibility of including the BCG was also explored. This yields an identical optimisation of the SL parameters, but presents a $\sim$ 50% increase in the central surface brightness, exceeding the observed signal by the same margin (on average).

a joint fit reconstruction on a mocked cluster, and deduct the relative weight required between X-ray and SL data. In this thesis, we limit ourselves pragmatically to compare two cases:

1. The naive 'each information is equally valuable' hypothesis, simply performing:

$$\ln \mathcal{L}_J = \ln \mathcal{L}_{SL} + \ln \mathcal{L}_X. \tag{5.1}$$

2. The weighed approach, appointing equal weights *a priori* to the lensing and X-ray data:

$$\ln \mathcal{L}_J = \frac{1}{N_{\rm im}^{\rm TOT}} \ln \mathcal{L}_{SL} + \frac{1}{N_X} \ln \mathcal{L}_X. \tag{5.2}$$

We choose in this Section to present the latter case, to avoid having the X-ray optimisation dominate[11]. With 67 multiple images and 16900 *Chandra* pixels, we fixed the new `Lenstool` relative weight parameter, multiplying the SL likelihood, to 252.2.

Results

We present cluster Abell S1063 joint SL – X-ray potential model on Figure 5.4. The associated X-ray surface brightness map, compared to the *Chandra* observations, is displayed on Figure 5.5. The final model yields parameter optimisations very close to the SL only model. s_1 is an interesting case: its final optimised value is $s_1 = 3663.1^{+210.3}_{-89.1}$ kpc. We compare this value to those found with ICM optimisation only, with *XMM-Newton*: 4710^{+440}_{-1120} and 4470^{+420}_{-1370} kpc for DMH only and DMH & BCG models respectively. Upon careful consideration of the error bars, all these values agree within 1 ICM-optimisation σ.

We present the 3D density extrapolation on Figure 5.6. The ICM optimisation is of good quality considering it was only modelled by one DMH `idPIE` profile. Substructures appear clearly in the residuals, which we can interpret this in a number of manners:

1. Let us recall the limits of our method: we assume a temperature profile (self-normalised polytropic with varying index), and hydrostatic equilibrium. The second hypothesis is never entirely verified, as the ICM dynamics often appear to be a lot more perturbed than that of galaxies or DM. For example, the cluster and ICM large scale ellipticities are different, with that of DM always being higher.
2. In this specific case, we assumed the DMH represents the ICM distribution. The local densities, and notably that of the BCG must be having an effect on the ICM, but because the ICM is a thermalised hot plasma, we do not expect it to strongly cluster in concentrations of potential, such as galaxies. In Section 4.3, with the ICM optimisation, we obtained lower BCG density normalisations too. In this joint optimisation, we did not take the BCG potential into account; however the proper physical treatment in the very central regions ($R \lesssim 20$ kpc) might require a dedicated, separate study.
3. Contrarily to a number of models (see Section 5.1.3), we did not include another large-scale halo, nor gas clumps to explain the X-ray surface brightness. This dedicated treatment of local effects may in themselves suffice to explain these overdense and underdense clumps.

[11] We attempted to use this 'naive' log-likelihood, but the SL constraints were completely off to $rms = 1.91''$ at best.

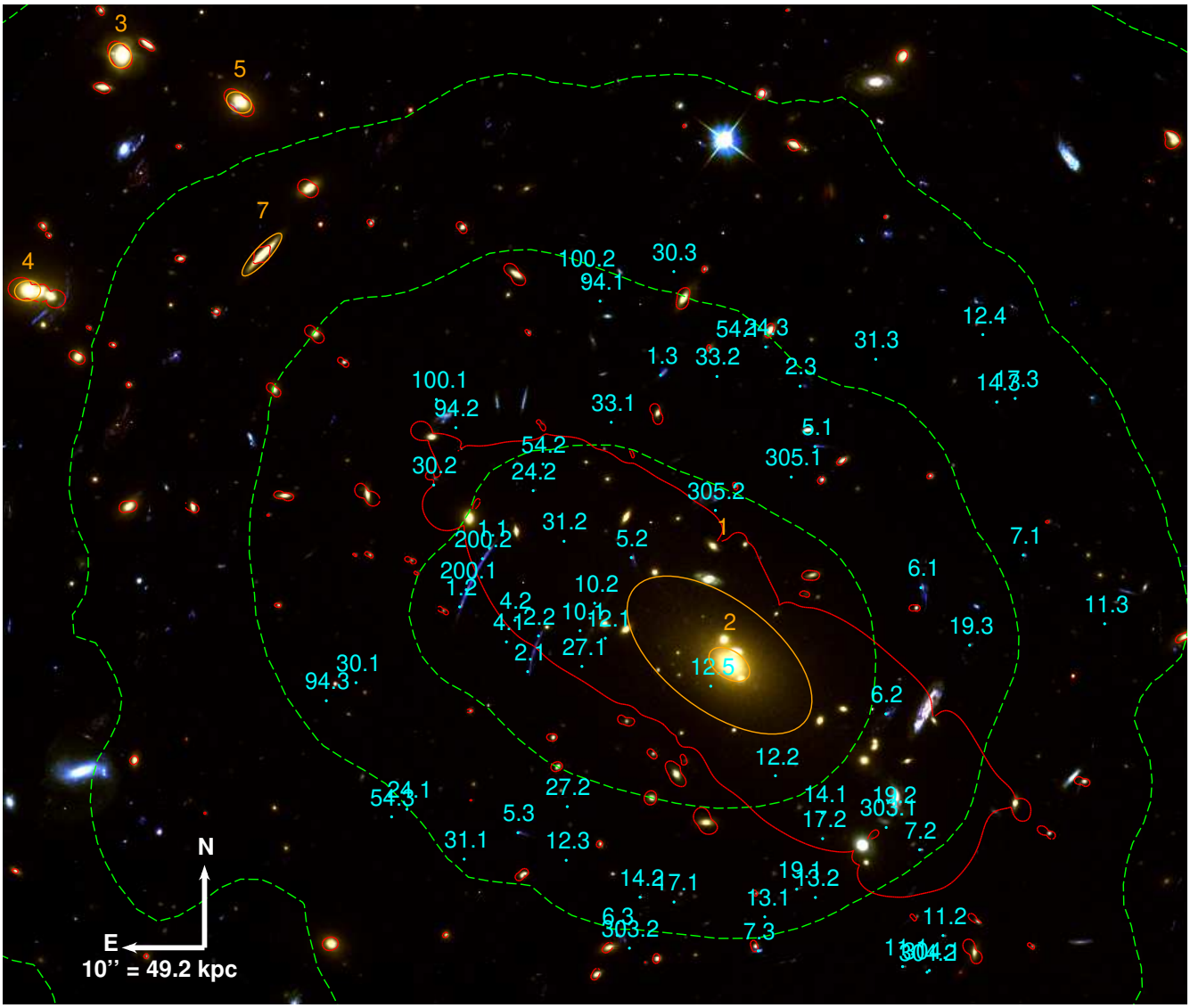

Figure 5.4: Composite RGB colour *HST* image of Abell S1063. ACS/F814W, F606W and F435W constitute the respective red, green and blue image colours here. *Red:* Critical lines of system 1, at redshift 1.2279. *Green: XMM-Newton* ICM distribution. *Cyan:* Positions of the 67 multiple images used to constrain the mass model. They are listed in Table 5.1. *Orange:* Largest dPIE potentials. 1 represents the DMH, 2 the BCG, and 4 the possible centre of the O3 cluster-scale halo. We notice a concentration of the heaviest galaxy potentials in this north-eastern region (3, 4, 5 and 7). 6 is out of the field of view.

With the small X-ray fitting parameter space, we clearly underfit the physical reality (as supported by the output statistical estimation of the modified `Lenstool`).

Moreover, the addition of an O3 large-scale DMH, centred on galaxy 3 (potential 4 on the Figures) improves the SL model to $rms = 0.67''$, and even $0.59''$ if we let its ellipticity free to evolve. This however does not significantly change the X-ray surface brightness model.

Table 5.2 respectively show that all models presented here (Sections 5.2, 5.3 and this present joint SL – X-ray optimisation) yield best optimised parameters which all recover each other's 1σ range. We can draw two exceptions, which are not too different, but whose small error bars

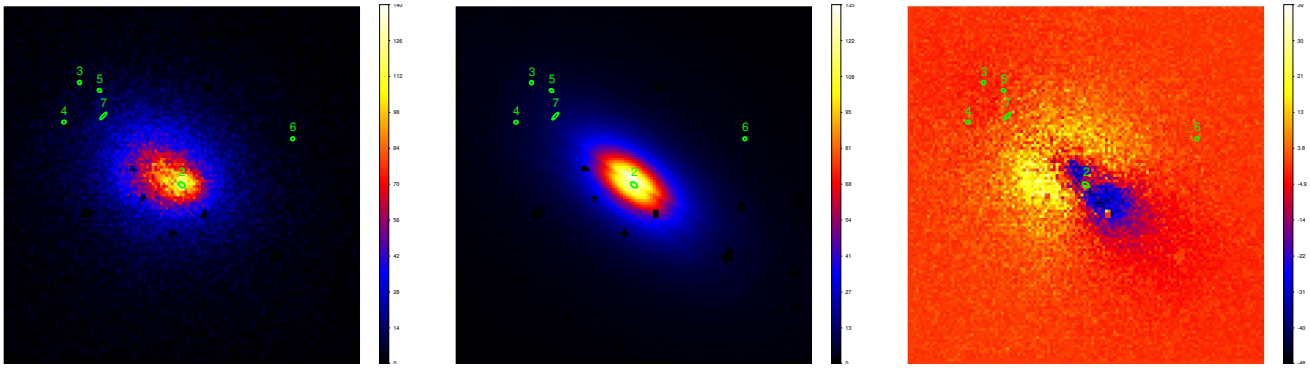

Figure 5.5: *Chandra* Abell S1063 count maps. We display in green the most dominant galaxy potentials, similarly to Figure 5.4. *Left:* Observational data. A few pixels were removed (set to zero here, but removed from optimisation) due to lack of exposure. All maps are 130 pixels wide (i.e. 1258 kpc). *Middle:* Predicted X-ray surface brightness after joint optimisation. The order of magnitude certainly matches the observational data. *Right:* Residual map of the observation minus the prediction. Globally, the `idPIE` reconstruction provides with the right order of magnitude surface brightness. We observe our model to be over-predicting the surface brightness on a north-east - south-west diagonal, and to under-predict on the other diagonal. This sort of defaults are to be expected from a simple one DMH and no gas clumps such as ours, as the cluster is not perfectly relaxed.

create small differences: the SL only and the joint SL – X-ray models present different a_1 and σ_1 parameters. This can be explained by the conjunction of ICM optimisation and the larger s_1 in the latter case.

Table 5.3 displays the $R_{500,c}$ and $M_{500,c}$ of all models. We may disqualify the SL only model, as its large scale parameter s_1 was chosen *ad hoc* and not optimised. $M_{500,c}$ masses all within 10% error bars, even matching the hydrostatic NFW *XMM-Newton* profile. The latter presents $M_{200,c} = 2.108^{+0.221}_{-0.190} \times 10^{15} M_\odot$, while our joint optimisation model yields $2.275^{+0.008}_{-0.014} \times 10^{15} M_\odot$, still displaying a $\sim 10\%$ difference. We compare these values to Umetsu et al. (2014) $M_{200,c} = (2.03 \pm 0.67) \times 10^{15} M_\odot$ and find a $\sim 10\%$ difference with our joint optimisation value. However we did not directly probed regions as far as $R_{200,c}$, predicted in our joint optimisation to be $2405.7^{+2.9}_{-5.0}$ kpc, but simply utilised more central probes of X-ray to probe what we expect outer density profiles to yield. Although we would need to replicate this on another cluster, to seriously investigate how the BCG should be taken in consideration, and to use combined *Chandra* and *XMM-Newton* data in the whole optimisation set (ICM and joint optimisation), we conclude to the relative success of our ICM reconstruction with lensing and joint optimisation.

This result represents an important step towards a more holistic understanding of the physics of galaxy clusters.

5.5 Discussion

A number of avenues can be taken to improve this result. For instance, we could use a negative binomial distribution to model the X-ray counts more appropriately than through the Cash statistics (see equation 4.28). This would allow to take the intrinsic count error into account. As mentioned before, we could also use the fundamental plane relationship (equation 3.1) instead of

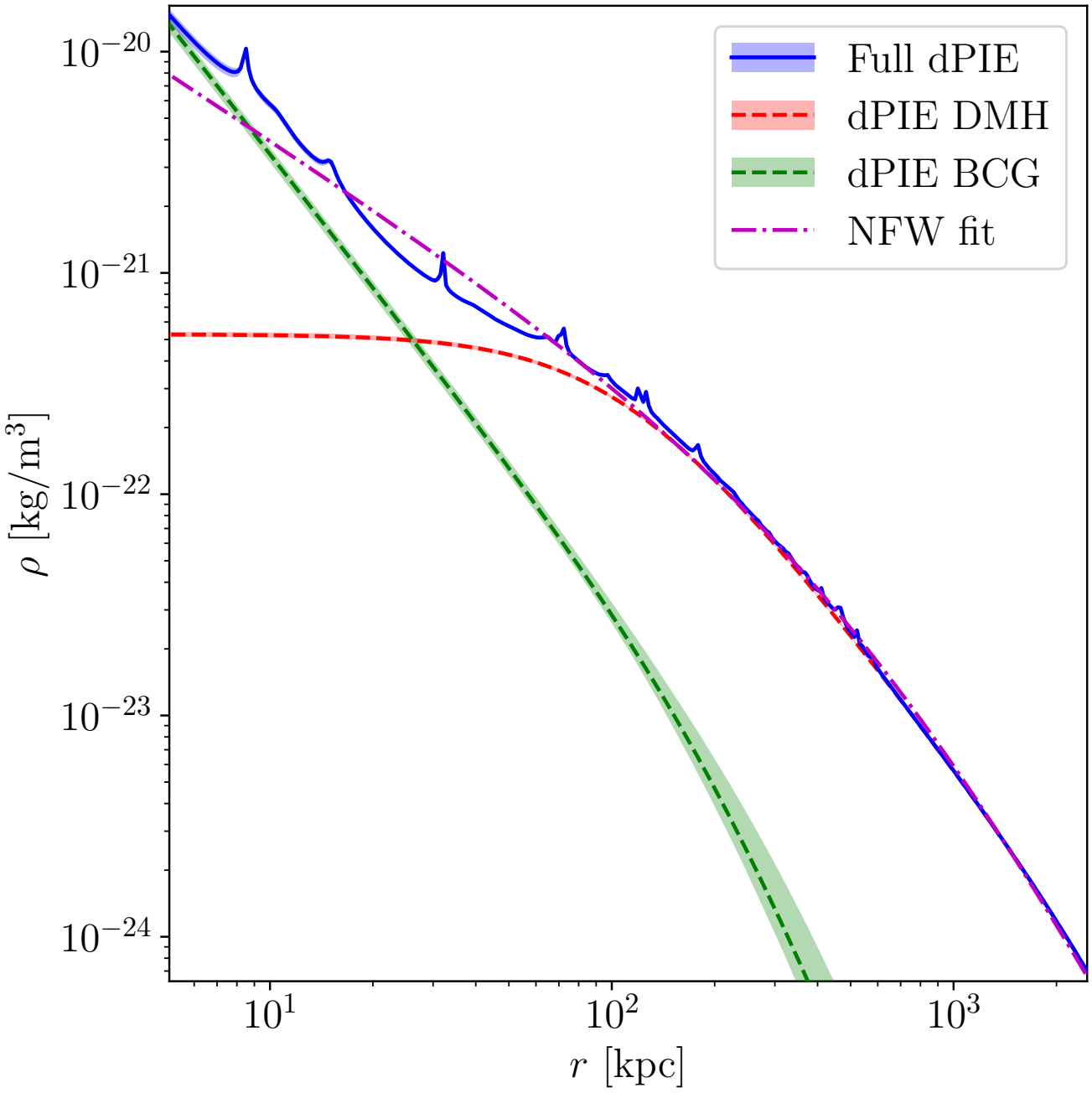

Figure 5.6: Tridimensional density of the joint optimisation of Abell S1063. *Blue:* Total density profile. *Red:* DM halo. *Green:* BCG. *Magenta:* Best NFW fit.

Faber-Jackson, or a sum of B-spline functions. These features have been encoded in `Lenstool`, notably by Benjamin Beauchesne. We could also utilise the line-of-sight velocity dispersion $\sigma_{\rm los}$ to tune the galaxy catalogue velocity distribution, and hence the mass of cluster members galaxies (Lagattuta et al., 2022; Granata et al., 2022).

More generally, a probe of the large scale potential should confirm or infirm our results on the large-scale dark matter halo. On top of using the individual spectroscopically measured velocity dispersions of cluster members, at least two avenues could be taken to probe the large scale potential:

1. As already mentioned in the case of Umetsu et al. (2014), we could use weak lensing to probe the outskirts of relaxed clusters. Abell S1063 is a particularly good candidate, as it is part of the BUFFALO survey (Steinhardt et al., 2020), particularly efficient at probing the outskirts of clusters.
2. Galaxy-galaxy strong lensing (GGSL) detections may constrain the larger-scale potential derivatives, and thus the potential shape (Limousin et al., 2005; Limousin et al., 2006).

Chapter 6

Conclusion

Continuous progress in gravitational lensing surveys has allowed to precisely describe the gravitational content of galaxy clusters. Comparable improvements in X-ray astronomy achieved a similar success for the baryonic intra-cluster medium (ICM). New telescopes such as the *James Webb Space Telescope* and *Euclid* for gravitational lensing, as well as the *X-Ray Imaging and Spectroscopy Mission* or *Athena* for the ICM will either indicate the presence of interacting dark matter (DM), or set tighter constraints on DM interactions.

After introducing the general cosmological context (Chapter 1), I have presented strong gravitational lensing (SL, Chapter 2), and how to typically reconstruct the density distribution of a galaxy cluster lens using imaging and spectroscopic data (Chapter 3). Strong lensing clusters MACS J0242 and MACS J0949 served as examples of the powerful combination of the imaging and photometric data extracted from optical *Hubble Space Telescope* observations and of the Multi Unit Spectroscopic Explorer at the Very Large Telescope spectroscopic data. A thorough comparison with *XMM-Newton* X-ray observations was conducted, finding a discrepancy in the case of both cluster, which may be simply explained by the lack of strong lensing constraints.

These clusters however served to probe the hydrostatic ICM-strong lensing relationship, established during this thesis (Chapter 4). After using the X-COP cluster sample to tune both a universal polytropic ICM density law and a general gas fraction relationship, I could indeed relate the dark and X-ray luminous contents of clusters with a stiff bijective relationship. Although its stiffness creates a number of issues, such as requiring an incredibly fine-tuned precision in the strong lensing parameter fit, it may also be used to constrain the DM density profile. Using dPIE and NFW parametric models, I showed that the models were at least consistent with strong lensing outputs, assuming the ICM was following the dark matter halo and the brightest cluster galaxy (BCG) potentials.

I further investigated this relationship (Chapter 5), using the non-perturbed, *Hubble* Frontier Fields strong lensing cluster Abell S1063. Being constrained by 67 different multiple images, it presents a strong lensing model in concordance with the ICM-optimised *XMM-Newton* hydrostatic predictions. Moreover, I proposed a modified version of strong lensing algorithm `Lenstool`, to conduct the joint ICM (*Chandra* data) and strong lensing optimisation. This resulted in consistent constraints on cluster Abell S1063, aiding to probe the large scales of the potential looking at the centre ICM and strong lensing. However, more studies on this topic are required, first of which to determine the exact role to attribute to the BCG potential tracing our bijective ICM-DM relationship. A more thorough study of stellar physics in the BCG, and joining *Chandra* and

XMM-Newton observations may light the path towards this general description of galaxy clusters. Nonetheless, the joint fit model does not use data from the outskirts of clusters, but agrees with weak lensing data, showing its robustness. A more general study, e.g. using the Beyond Ultra-deep Frontier Fields And Legacy Observations to constrain weak lensing, galaxy-galaxy strong lensing within the cluster halo, or the velocity dispersion of cluster galaxies, should assist confirming or infirming the validity of this technique in the near future.

Bibliography

[1] Abbott et al. "GW190521: A Binary Black Hole Merger with a Total Mass of 150 $M_\odot$". In: *Physical Review Letters* 125.10, 101102 (Sept. 2020), p. 101102. DOI: 10.1103/PhysRevLett.125.101102. arXiv: 2009.01075 [gr-qc].

[2] Abbott et al. "Properties and Astrophysical Implications of the 150 $M_\odot$ Binary Black Hole Merger GW190521". In: *The Astrophysical Journal Letters* 900.1, L13 (Sept. 2020), p. L13. DOI: 10.3847/2041-8213/aba493. arXiv: 2009.01190 [astro-ph.HE].

[3] Aghanim et al. "PACT. I. Combining ACT and Planck data for improved extraction of tSZ signal". In: *Astronomy & Astrophysics* 632, A47 (Dec. 2019), A47. DOI: 10.1051/0004-6361/201935271. arXiv: 1902.00350 [astro-ph.CO].

[4] Agrawal et al. "Feebly-interacting particles: FIPs 2020 workshop report". In: *European Physical Journal C* 81.11, 1015 (Nov. 2021), p. 1015. DOI: 10.1140/epjc/s10052-021-09703-7. arXiv: 2102.12143 [hep-ph].

[5] Aihara et al. "The Hyper Suprime-Cam SSP Survey: Overview and survey design". In: *Publications of the Astronomical Society of Japan* 70, S4 (Jan. 2018), S4. DOI: 10.1093/pasj/psx066. arXiv: 1704.05858 [astro-ph.IM].

[6] Alam et al. "Completed SDSS-IV extended Baryon Oscillation Spectroscopic Survey: Cosmological implications from two decades of spectroscopic surveys at the Apache Point Observatory". In: *Physical Review D* 103.8, 083533 (Apr. 2021), p. 083533. DOI: 10.1103/PhysRevD.103.083533. arXiv: 2007.08991 [astro-ph.CO].

[7] Alcock et al. "The MACHO Project Large Magellanic Cloud Microlensing Results from the First Two Years and the Nature of the Galactic Dark Halo". In: *Astrophysical Journal* 486.2 (Sept. 1997), pp. 697–726. DOI: 10.1086/304535. arXiv: astro-ph/9606165 [astro-ph].

[8] Alcock et al. "EROS and MACHO Combined Limits on Planetary-Mass Dark Matter in the Galactic Halo". In: *The Astrophysical Journal Letters* 499.1 (May 1998), pp. L9–L12. DOI: 10.1086/311355. arXiv: astro-ph/9803082 [astro-ph].

[9] Alcock et al. "The MACHO Project: Microlensing Results from 5.7 Years of Large Magellanic Cloud Observations". In: *Astrophysical Journal* 542.1 (Oct. 2000), pp. 281–307. DOI: 10.1086/309512. arXiv: astro-ph/0001272 [astro-ph].

[10] Alcock et al. "MACHO Project Limits on Black Hole Dark Matter in the 1-30 M_{solar} Range". In: *The Astrophysical Journal Letters* 550.2 (Apr. 2001), pp. L169–L172. DOI: 10.1086/319636. arXiv: astro-ph/0011506 [astro-ph].

[11] Ali-Haïmoud et al. "Merger rate of primordial black-hole binaries". In: *Physical Review D* 96.12, 123523 (Dec. 2017), p. 123523. DOI: 10.1103/PhysRevD.96.123523. arXiv: 1709.06576 [astro-ph.CO].

[12] Allen et al. “Cosmological Parameters from Observations of Galaxy Clusters”. In: *Annual Review of Astronomy and Astrophysics* 49.1 (Sept. 2011), pp. 409–470. DOI: 10.1146/annurev-astro-081710-102514. arXiv: 1103.4829 [astro-ph.CO].

[13] Allingham et al. “Joint HST, VLT/MUSE and XMM-Newton observations to constrain the mass distribution of the two strong lensing galaxy clusters: MACS J0242.5-2132 & MACS J0949.8+1708”. In: *arXiv e-prints*, arXiv:2207.10520 (July 2022), arXiv:2207.10520. arXiv: 2207.10520 [astro-ph.CO].

[14] Annunziatella et al. “Mass Profile Decomposition of the Frontier Fields Cluster MACS J0416-2403: Insights on the Dark-matter Inner Profile”. In: *Astrophysical Journal* 851.2, 81 (Dec. 2017), p. 81. DOI: 10.3847/1538-4357/aa9845. arXiv: 1711.02109 [astro-ph.CO].

[15] Ansarifard et al. “The Three Hundred Project: Correcting for the hydrostatic-equilibrium mass bias in X-ray and SZ surveys”. In: *Astronomy & Astrophysics* 634 (Feb. 2020), A113. ISSN: 1432-0746. DOI: 10.1051/0004-6361/201936742. URL: http://dx.doi.org/10.1051/0004-6361/201936742.

[16] Arcadi et al. “The waning of the WIMP? A review of models, searches, and constraints”. In: *European Physical Journal C* 78.3, 203 (Mar. 2018), p. 203. DOI: 10.1140/epjc/s10052-018-5662-y. arXiv: 1703.07364 [hep-ph].

[17] Arimoto and Yoshii. “Chemical and photometric properties of a galactic wind model for elliptical galaxies.” In: *Astronomy & Astrophysics* 173 (Feb. 1987), pp. 23–38.

[18] Aristotle. *The Metaphysics (Great Books in Philosophy)*. Prometheus Books, 1992.

[19] Arnaud. “X-ray observations of clusters of galaxies”. In: *Background Microwave Radiation and Intracluster Cosmology*. Ed. by Melchiorri and Rephaeli. Jan. 2005, p. 77. arXiv: astro-ph/0508159 [astro-ph].

[20] Arnaud et al. “The X-ray surface brightness profiles of hot galaxy clusters up to vec z $\sim$0.8: Evidence for self-similarity and constraints on Omega$_0$”. In: *Astronomy & Astrophysics* 389 (July 2002), pp. 1–18. DOI: 10.1051/0004-6361:20020378. arXiv: astro-ph/0110428 [astro-ph].

[21] Arnouts et al. “The SWIRE-VVDS-CFHTLS surveys: stellar mass assembly over the last 10 Gyr. Evidence for a major build up of the red sequence between z = 2 and z = 1”. In: *Astronomy & Astrophysics* 476.1 (Dec. 2007), pp. 137–150. DOI: 10.1051/0004-6361:20077632. arXiv: 0705.2438 [astro-ph].

[22] Atek et al. “Are Ultra-faint Galaxies at z = 6-8 Responsible for Cosmic Reionization? Combined Constraints from the Hubble Frontier Fields Clusters and Parallels”. In: *Astrophysical Journal* 814.1, 69 (Nov. 2015), p. 69. DOI: 10.1088/0004-637X/814/1/69. arXiv: 1509.06764 [astro-ph.GA].

[23] Babcock. “The rotation of the Andromeda Nebula”. In: *Lick Observatory Bulletin* 498 (Jan. 1939), pp. 41–51. DOI: 10.5479/ADS/bib/1939LicOB.19.41B.

[24] Bacon et al. “Detection of weak gravitational lensing by large-scale structure”. In: *Monthly Notices of the Royal Astronomical Society* 318.2 (Oct. 2000), pp. 625–640. DOI: 10.1046/j.1365-8711.2000.03851.x. arXiv: astro-ph/0003008 [astro-ph].

[25] Bacon et al. “The MUSE second-generation VLT instrument”. In: *Ground-based and Airborne Instrumentation for Astronomy III*. Ed. by McLean et al. Vol. 7735. Society of Photo-Optical Instrumentation Engineers (SPIE) Conference Series. July 2010, 773508, p. 773508. DOI: 10.1117/12.856027.

[26] Bacon et al. “MUSE Commissioning”. In: *The Messenger* 157 (Sept. 2014), pp. 13–16.

[27] Bacon et al. *MPDAF: MUSE Python Data Analysis Framework*. Nov. 2016. ascl: 1611.003.

[28] Bahcall and Kulier. “Tracing mass and light in the Universe: where is the dark matter?” In: *Monthly Notices of the Royal Astronomical Society* 439.3 (Apr. 2014), pp. 2505–2514. DOI: 10.1093/mnras/stu107. arXiv: 1310.0022 [astro-ph.CO].

[29] Banik et al. “Novel constraints on the particle nature of dark matter from stellar streams”. In: *Journal of Cosmology and Astroparticle Physics* 2021.10, 043 (Oct. 2021), p. 043. DOI: 10.1088/1475-7516/2021/10/043. arXiv: 1911.02663 [astro-ph.GA].

[30] Barboza and Alcaniz. “A parametric model for dark energy”. In: *Physics Letters B* 666.5 (Sept. 2008), pp. 415–419. DOI: 10.1016/j.physletb.2008.08.012. arXiv: 0805.1713 [astro-ph].

[31] Bartelmann. “Arcs from a universal dark-matter halo profile.” In: *Astronomy & Astrophysics* 313 (Sept. 1996), pp. 697–702. DOI: 10.48550/arXiv.astro-ph/9602053. arXiv: astro-ph/9602053 [astro-ph].

[32] Bartelmann and Schneider. “Weak gravitational lensing”. In: *Physics Reports* 340.4-5 (Jan. 2001), pp. 291–472. DOI: 10.1016/S0370-1573(00)00082-X. arXiv: astro-ph/9912508 [astro-ph].

[33] Bartelmann. “Gravitational Lensing”. In: *Class. Quant. Grav.* 27 (2010), p. 233001. DOI: 10.1088/0264-9381/27/23/233001. arXiv: 1010.3829 [astro-ph.CO].

[34] Bartelmann and Maturi. “Weak gravitational lensing”. In: *Scholarpedia* 12.1 (Jan. 2017), p. 32440. DOI: 10.4249/scholarpedia.32440. arXiv: 1612.06535 [astro-ph.CO].

[35] Bartelmann et al. “Maximum-likelihood Cluster Reconstruction”. In: *The Astrophysical Journal Letters* 464 (June 1996), p. L115. DOI: 10.1086/310114. arXiv: astro-ph/9601011 [astro-ph].

[36] Bauer and Plehn. “Yet Another Introduction to Dark Matter”. In: *arXiv e-prints*, arXiv:1705.01987 (May 2017), arXiv:1705.01987. arXiv: 1705.01987 [hep-ph].

[37] Baum. “Photoelectric Magnitudes and Red-Shifts”. In: *Problems of Extra-Galactic Research*. Ed. by McVittie. Vol. 15. Jan. 1962, p. 390.

[38] Becker et al. “Cosmic shear measurements with Dark Energy Survey Science Verification data”. In: *Physical Review D* 94.2, 022002 (July 2016), p. 022002. DOI: 10.1103/PhysRevD.94.022002. arXiv: 1507.05598 [astro-ph.CO].

[39] Bekenstein. “Relativistic gravitation theory for the modified Newtonian dynamics paradigm”. In: *Physical Review D* 70.8, 083509 (Oct. 2004), p. 083509. DOI: 10.1103/PhysRevD.70.083509. arXiv: astro-ph/0403694 [astro-ph].

[40] Bekki. “Ram-pressure stripping of halo gas in disc galaxies: implications for galactic star formation in different environments”. In: *Monthly Notices of the Royal Astronomical Society* 399.4 (Nov. 2009), pp. 2221–2230. DOI: 10.1111/j.1365-2966.2009.15431.x. arXiv: 0907.4409 [astro-ph.CO].

[41] Bender et al. "Dynamically Hot Galaxies. I. Structural Properties". In: *Astrophysical Journal* 399 (Nov. 1992), p. 462. DOI: 10.1086/171940.

[42] Bennett et al. "The Microwave Anisotropy Probe Mission". In: *Astrophysical Journal* 583.1 (Jan. 2003), pp. 1–23. DOI: 10.1086/345346. arXiv: astro-ph/0301158 [astro-ph].

[43] Bergamini et al. "Enhanced cluster lensing models with measured galaxy kinematics". In: *Astronomy & Astrophysics* 631, A130 (Nov. 2019), A130. DOI: 10.1051/0004-6361/201935974. arXiv: 1905.13236 [astro-ph.GA].

[44] Bernal et al. "The dawn of FIMP Dark Matter: A review of models and constraints". In: *International Journal of Modern Physics A* 32.27, 1730023-274 (Sept. 2017), pp. 1730023–274. DOI: 10.1142/S0217751X1730023X. arXiv: 1706.07442 [hep-ph].

[45] Bernardeau and Valageas. "Construction of the one-point PDF of the local aperture mass in weak lensing maps". In: *Astron. Astrophys.* 364 (2000), p. 1. arXiv: astro-ph/0006270 [astro-ph]. URL: https://arxiv.org/abs/astro-ph/0006270.

[46] Bernardeau et al. "Full-sky lensing shear at second order". In: *Physical Review D* 81.8, 083002 (Apr. 2010), p. 083002. DOI: 10.1103/PhysRevD.81.083002. arXiv: 0911.2244 [astro-ph.CO].

[47] Bertin and Arnouts. "SExtractor: Software for source extraction." In: *Astronomy & Astrophysics Supplement Series* 117 (June 1996), pp. 393–404. DOI: 10.1051/aas:1996164.

[48] Bertone and Hooper. "History of dark matter". In: *Reviews of Modern Physics* 90.4, 045002 (Oct. 2018), p. 045002. DOI: 10.1103/RevModPhys.90.045002. arXiv: 1605.04909 [astro-ph.CO].

[49] Bertone et al. "Particle dark matter: evidence, candidates and constraints". In: *Physics Reports* 405.5-6 (Jan. 2005), pp. 279–390. DOI: 10.1016/j.physrep.2004.08.031. arXiv: hep-ph/0404175 [hep-ph].

[50] Billard et al. "Direct detection of dark matter-APPEC committee report". In: *Reports on Progress in Physics* 85.5, 056201 (May 2022), p. 056201. DOI: 10.1088/1361-6633/ac5754. arXiv: 2104.07634 [hep-ex].

[51] Binney and Tremaine. *Galactic dynamics*. Princeton University Press, 1987.

[52] Bird et al. "Did LIGO Detect Dark Matter?" In: *Physical Review Letters* 116.20, 201301 (May 2016), p. 201301. DOI: 10.1103/PhysRevLett.116.201301. arXiv: 1603.00464 [astro-ph.CO].

[53] Birkinshaw. "The Sunyaev-Zel'dovich effect". In: *Physics Reports* 310.2-3 (Mar. 1999), pp. 97–195. DOI: 10.1016/S0370-1573(98)00080-5. arXiv: astro-ph/9808050 [astro-ph].

[54] Birrer. "Gravitational Lensing Formalism in a Curved Arc Basis: A Continuous Description of Observables and Degeneracies from the Weak to the Strong Lensing Regime". In: *Astrophysical Journal* 919.1, 38 (Sept. 2021), p. 38. DOI: 10.3847/1538-4357/ac1108. arXiv: 2104.09522 [astro-ph.CO].

[55] Blumenthal et al. "Galaxy formation by dissipationless particles heavier than neutrinos". In: *Nature* 299.5878 (Sept. 1982), pp. 37–38. DOI: 10.1038/299037a0.

[56] Blumenthal et al. "Formation of galaxies and large-scale structure with cold dark matter." In: *Nature* 311 (Oct. 1984), pp. 517–525. DOI: 10.1038/311517a0.

[57] Bocquet et al. "Cluster Cosmology Constraints from the 2500 deg^2 SPT-SZ Survey: Inclusion of Weak Gravitational Lensing Data from Magellan and the Hubble Space Telescope". In: *Astrophysical Journal* 878.1, 55 (June 2019), p. 55. DOI: 10.3847/1538-4357/ab1f10. arXiv: 1812.01679 [astro-ph.CO].

[58] Bode et al. "Halo Formation in Warm Dark Matter Models". In: *Astrophysical Journal* 556.1 (July 2001), pp. 93–107. DOI: 10.1086/321541. arXiv: astro-ph/0010389 [astro-ph].

[59] Bœhm and Fayet. "Scalar dark matter candidates". In: *Nuclear Physics B* 683.1 (Apr. 2004), pp. 219–263. DOI: 10.1016/j.nuclphysb.2004.01.015. arXiv: hep-ph/0305261 [hep-ph].

[60] Bœhm et al. "Constraining dark matter candidates from structure formation". In: *Physics Letters B* 518.1-2 (Oct. 2001), pp. 8–14. DOI: 10.1016/S0370-2693(01)01060-7. arXiv: astro-ph/0012504 [astro-ph].

[61] Bœhm et al. "Interacting dark matter disguised as warm dark matter". In: *Physical Review D* 66.8, 083505 (Oct. 2002), p. 083505. DOI: 10.1103/PhysRevD.66.083505. arXiv: astro-ph/0112522 [astro-ph].

[62] Bœhm et al. "WIMP matter power spectra and small scale power generation". In: *arXiv e-prints*, astro-ph/0309652 (Sept. 2003), astro–ph/0309652. arXiv: astro-ph/0309652 [astro-ph].

[63] Bœhm et al. "A lower bound on the mass of cold thermal dark matter from Planck". In: *Journal of Cosmology and Astroparticle Physics* 2013.8, 041 (Aug. 2013), p. 041. DOI: 10.1088/1475-7516/2013/08/041. arXiv: 1303.6270 [hep-ph].

[64] Bœhm et al. "Eliminating the LIGO bounds on primordial black hole dark matter". In: *Journal of Cosmology and Astroparticle Physics* 2021.3, 078 (Mar. 2021), p. 078. DOI: 10.1088/1475-7516/2021/03/078. arXiv: 2008.10743 [astro-ph.CO].

[65] Boehm and Schaeffer. "Constraints on Dark Matter interactions from structure formation: damping lengths". In: *Astronomy & Astrophysics* 438.2 (Aug. 2005), pp. 419–442. DOI: 10.1051/0004-6361:20042238. arXiv: astro-ph/0410591 [astro-ph].

[66] Boehm et al. "Using the Milky Way satellites to study interactions between cold dark matter and radiation." In: *Monthly Notices of the Royal Astronomical Society* 445 (Nov. 2014), pp. L31–L35. DOI: 10.1093/mnrasl/slu115. arXiv: 1404.7012 [astro-ph.CO].

[67] Böhringer et al. "The representative XMM-Newton cluster structure survey (REXCESS) of an X-ray luminosity selected galaxy cluster sample". In: *Astronomy & Astrophysics* 469.1 (July 2007), pp. 363–377. DOI: 10.1051/0004-6361:20066740. arXiv: astro-ph/0703553 [astro-ph].

[68] Böhringer and Werner. "X-ray spectroscopy of galaxy clusters: studying astrophysical processes in the largest celestial laboratories". In: *Astronomy and Astrophysics Reviews* 18.1-2 (Feb. 2010), pp. 127–196. DOI: 10.1007/s00159-009-0023-3.

[69] Böhringer et al. "The Cosmic Large-Scale Structure in X-rays (CLASSIX) Cluster Survey. I. Probing galaxy cluster magnetic fields with line of sight rotation measures". In: *Astronomy & Astrophysics* 596, A22 (Nov. 2016), A22. DOI: 10.1051/0004-6361/201628873. arXiv: 1610.02887 [astro-ph.CO].

[70] Bolton et al. "The Sloan Lens ACS Survey. I. A Large Spectroscopically Selected Sample of Massive Early-Type Lens Galaxies". In: *Astrophysical Journal* 638.2 (Feb. 2006), pp. 703–724. DOI: 10.1086/498884. arXiv: astro-ph/0511453 [astro-ph].

[71] Bolzonella et al. "Photometric redshifts based on standard SED fitting procedures". In: *Astronomy & Astrophysics* 363 (Nov. 2000), pp. 476–492. arXiv: astro-ph/0003380 [astro-ph].

[72] Bonamigo et al. "Joining X-Ray to Lensing: An Accurate Combined Analysis of MACS J0416.1-2403". In: *Astrophysical Journal* 842.2, 132 (June 2017), p. 132. DOI: 10.3847/1538-4357/aa75cc. arXiv: 1705.10322 [astro-ph.GA].

[73] Bonamigo et al. "Dissection of the Collisional and Collisionless Mass Components in a Mini Sample of CLASH and HFF Massive Galaxy Clusters at z ≈ 0.4". In: *Astrophysical Journal* 864.1, 98 (Sept. 2018), p. 98. DOI: 10.3847/1538-4357/aad4a7. arXiv: 1807.10286 [astro-ph.GA].

[74] Bond et al. "OGLE 2003-BLG-235/MOA 2003-BLG-53: A Planetary Microlensing Event". In: *The Astrophysical Journal Letters* 606.2 (May 2004), pp. L155–L158. DOI: 10.1086/420928. arXiv: astro-ph/0404309 [astro-ph].

[75] Bond and Szalay. "The collisionless damping of density fluctuations in an expanding universe". In: *Astrophysical Journal* 274 (Nov. 1983), pp. 443–468. DOI: 10.1086/161460.

[76] Bond et al. "Formation of Galaxies in a Gravitino-Dominated Universe". In: *Physical Review Letters* 48.23 (June 1982), pp. 1636–1640. DOI: 10.1103/PhysRevLett.48.1636.

[77] Born and Wolf. *Principles of Optics*. Cambridge University Press, 1999.

[78] Bosma. "21-cm line studies of spiral galaxies. I. Observations of the galaxies NGC 5033, 3198, 5055, 2841, and 7331." In: *The Astronomical Journal* 86 (Dec. 1981), pp. 1791–1824. DOI: 10.1086/113062.

[79] Boyarsky et al. "Sterile neutrino Dark Matter". In: *Progress in Particle and Nuclear Physics* 104 (Jan. 2019), pp. 1–45. DOI: 10.1016/j.ppnp.2018.07.004. arXiv: 1807.07938 [hep-ph].

[80] Boylan-Kolchin et al. "Too big to fail? The puzzling darkness of massive Milky Way subhaloes". In: *Monthly Notices of the Royal Astronomical Society* 415.1 (July 2011), pp. L40–L44. DOI: 10.1111/j.1745-3933.2011.01074.x. arXiv: 1103.0007 [astro-ph.CO].

[81] Bradač et al. "Strong and weak lensing united I: the combined strong and weak lensing cluster mass reconstruction method". In: *arXiv e-prints*, astro-ph/0410643 (Oct. 2004), astro–ph/0410643. arXiv: astro-ph/0410643 [astro-ph].

[82] Bradač et al. "Revealing the Properties of Dark Matter in the Merging Cluster MACS J0025.4-1222". In: *Astrophysical Journal* 687.2 (Nov. 2008), pp. 959–967. DOI: 10.1086/591246. arXiv: 0806.2320 [astro-ph].

[83] Bradač et al. "Focusing Cosmic Telescopes: Exploring Redshift z ~5-6 Galaxies with the Bullet Cluster 1E0657 - 56". In: *Astrophysical Journal* 706.2 (Dec. 2009), pp. 1201–1212. DOI: 10.1088/0004-637X/706/2/1201. arXiv: 0910.2708 [astro-ph.CO].

[84] Brandt. "Constraints on MACHO Dark Matter from Compact Stellar Systems in Ultra-faint Dwarf Galaxies". In: *The Astrophysical Journal Letters* 824.2, L31 (June 2016), p. L31. DOI: 10.3847/2041-8205/824/2/L31. arXiv: 1605.03665 [astro-ph.GA].

[85] Bravo-Alfaro et al. "VLA H I Imaging of the Brightest Spiral Galaxies in Coma". In: *The Astronomical Journal* 119.2 (Feb. 2000), pp. 580–592. DOI: 10.1086/301194. arXiv: astro-ph/9912405 [astro-ph].

[86] Brout et al. "The Pantheon+ Analysis: Cosmological Constraints". In: *arXiv e-prints*, arXiv:2202.04077 (Feb. 2022), arXiv:2202.04077. arXiv: 2202.04077 [astro-ph.CO].

[87] Brouwer et al. "The weak lensing radial acceleration relation: Constraining modified gravity and cold dark matter theories with KiDS-1000". In: *Astronomy & Astrophysics* 650, A113 (June 2021), A113. DOI: 10.1051/0004-6361/202040108. arXiv: 2106.11677 [astro-ph.GA].

[88] Bruzual and Charlot. "Stellar population synthesis at the resolution of 2003". In: *Monthly Notices of the Royal Astronomical Society* 344.4 (Oct. 2003), pp. 1000–1028. DOI: 10.1046/j.1365-8711.2003.06897.x. arXiv: astro-ph/0309134 [astro-ph].

[89] Buckley and Peter. "Gravitational probes of dark matter physics". In: *Physics Reports* 761 (Oct. 2018), pp. 1–60. DOI: 10.1016/j.physrep.2018.07.003. arXiv: 1712.06615 [astro-ph.CO].

[90] Bulbul et al. "An Analytic Model of the Physical Properties of Galaxy Clusters". In: *Astrophysical Journal* 720.2 (Sept. 2010), pp. 1038–1044. DOI: 10.1088/0004-637X/720/2/1038. arXiv: 0911.2827 [astro-ph.CO].

[91] Bullock and Boylan-Kolchin. "Small-Scale Challenges to the ΛCDM Paradigm". In: *Annual Review of Astronomy and Astrophysics* 55.1 (Aug. 2017), pp. 343–387. DOI: 10.1146/annurev-astro-091916-055313. arXiv: 1707.04256 [astro-ph.CO].

[92] Cacciato et al. "Combining weak and strong lensing in cluster potential reconstruction". In: *Astronomy & Astrophysics* 458.2 (Nov. 2006), pp. 349–356. DOI: 10.1051/0004-6361:20054582. arXiv: astro-ph/0511694 [astro-ph].

[93] Calcino et al. "Updating the MACHO fraction of the Milky Way dark halowith improved mass models". In: *Monthly Notices of the Royal Astronomical Society* 479.3 (Sept. 2018), pp. 2889–2905. DOI: 10.1093/mnras/sty1368. arXiv: 1803.09205 [astro-ph.CO].

[94] Caminha et al. "CLASH-VLT: A highly precise strong lensing model of the galaxy cluster RXC J2248.7-4431 (Abell S1063) and prospects for cosmography". In: *Astronomy & Astrophysics* 587, A80 (Mar. 2016), A80. DOI: 10.1051/0004-6361/201527670. arXiv: 1512.04555 [astro-ph.CO].

[95] Caminha et al. "Mass distribution in the core of MACS J1206. Robust modeling from an exceptionally large sample of central multiple images". In: *Astronomy & Astrophysics* 607, A93 (Nov. 2017), A93. DOI: 10.1051/0004-6361/201731498. arXiv: 1707.00690 [astro-ph.GA].

[96] Caminha et al. "Strong lensing models of eight CLASH clusters from extensive spectroscopy: Accurate total mass reconstructions in the cores". In: *Astronomy & Astrophysics* 632, A36 (Dec. 2019), A36. DOI: 10.1051/0004-6361/201935454. arXiv: 1903.05103 [astro-ph.GA].

[97] Caminha et al. "First JWST observations of a gravitational lens: Mass model from new multiple images with near-infrared observations of SMACS J0723.3-7327". In: *arXiv e-prints*, arXiv:2207.07567 (July 2022), arXiv:2207.07567. arXiv: 2207.07567 [astro-ph.GA].

[98] Capelo et al. "The polytropic approximation and X-ray scaling relations: constraints on gas and dark matter profiles for galaxy groups and clusters". In: *Monthly Notices of the Royal Astronomical Society* 422.1 (May 2012), pp. 686–703. DOI: 10.1111/j.1365-2966.2012.20648.x. arXiv: 1111.5573 [astro-ph.CO].

[99] Capozziello et al. "Gravitational lensing in fourth order gravity". In: *Physical Review D* 73.10, 104019 (May 2006), p. 104019. DOI: 10.1103/PhysRevD.73.104019. arXiv: astro-ph/0604435 [astro-ph].

[100] Cardone et al. "Spherical galaxy models with power-law logarithmic slope". In: *Monthly Notices of the Royal Astronomical Society* 358.4 (Apr. 2005), pp. 1325–1336. DOI: 10.1111/j.1365-2966.2005.08834.x. arXiv: astro-ph/0501151 [astro-ph].

[101] Carlberg. "Star Stream Folding by Dark Galactic Subhalos". In: *The Astrophysical Journal Letters* 705.2 (Nov. 2009), pp. L223–L226. DOI: 10.1088/0004-637X/705/2/L223. arXiv: 0908.4345 [astro-ph.CO].

[102] Carlstrom et al. "Cosmology with the Sunyaev-Zel'dovich Effect". In: *Annual Review of Astronomy and Astrophysics* 40 (Jan. 2002), pp. 643–680. DOI: 10.1146/annurev.astro.40.060401.093803. arXiv: astro-ph/0208192 [astro-ph].

[103] Carr and Hawking. "Black holes in the early Universe". In: *Monthly Notices of the Royal Astronomical Society* 168 (Aug. 1974), pp. 399–416. DOI: 10.1093/mnras/168.2.399.

[104] Carr et al. "New cosmological constraints on primordial black holes". In: *Physical Review D* 81.10, 104019 (May 2010), p. 104019. DOI: 10.1103/PhysRevD.81.104019. arXiv: 0912.5297 [astro-ph.CO].

[105] Carr and Kühnel. "Primordial Black Holes as Dark Matter: Recent Developments". In: *Annual Review of Nuclear and Particle Science* 70 (Oct. 2020), pp. 355–394. DOI: 10.1146/annurev-nucl-050520-125911. arXiv: 2006.02838 [astro-ph.CO].

[106] Carr and Kühnel. "Primordial Black Holes as Dark Matter Candidates". In: *arXiv e-prints*, arXiv:2110.02821 (Oct. 2021), arXiv:2110.02821. arXiv: 2110.02821 [astro-ph.CO].

[107] Cash. "Parameter estimation in astronomy through application of the likelihood ratio." In: *Astrophysical Journal* 228 (Mar. 1979), pp. 939–947. DOI: 10.1086/156922.

[108] Cavaliere and Fusco-Femiano. "X-rays from hot plasma in clusters of galaxies." In: *Astronomy & Astrophysics* 49 (May 1976), pp. 137–144.

[109] Chae et al. "Testing the Strong Equivalence Principle: Detection of the External Field Effect in Rotationally Supported Galaxies". In: *Astrophysical Journal* 904.1, 51 (Nov. 2020), p. 51. DOI: 10.3847/1538-4357/abbb96. arXiv: 2009.11525 [astro-ph.GA].

[110] Chang et al. "The Splashback Feature around DES Galaxy Clusters: Galaxy Density and Weak Lensing Profiles". In: *Astrophysical Journal* 864.1, 83 (Sept. 2018), p. 83. DOI: 10.3847/1538-4357/aad5e7. arXiv: 1710.06808 [astro-ph.CO].

[111] Chapline. "Cosmological effects of primordial black holes". In: *Nature* 253.5489 (Jan. 1975), pp. 251–252. DOI: 10.1038/253251a0.

[112] Chevallier and Polarski. "Accelerating Universes with Scaling Dark Matter". In: *International Journal of Modern Physics D* 10.2 (Jan. 2001), pp. 213–223. DOI: 10.1142/S0218271801000822. arXiv: gr-qc/0009008 [gr-qc].

[113] CHEX-MATE Collaboration et al. "The Cluster HEritage project with XMM-Newton: Mass Assembly and Thermodynamics at the Endpoint of structure formation. I. Programme overview". In: *Astronomy & Astrophysics* 650, A104 (June 2021), A104. DOI: 10.1051/0004-6361/202039632. arXiv: 2010.11972 [astro-ph.CO].

[114] Chiu. "Symmetry Between Particle and Antiparticle Populations in the Universe". In: *Physical Review Letters* 17.13 (Sept. 1966), pp. 712–714. DOI: 10.1103/PhysRevLett.17.712.

[115] Clerc and Finoguenov. "X-ray cluster cosmology". In: *arXiv e-prints*, arXiv:2203.11906 (Mar. 2022), arXiv:2203.11906. arXiv: 2203.11906 [astro-ph.CO].

[116] Clowe et al. "Weak-Lensing Mass Reconstruction of the Interacting Cluster 1E 0657-558: Direct Evidence for the Existence of Dark Matter". In: *Astrophysical Journal* 604.2 (Apr. 2004), pp. 596–603. DOI: 10.1086/381970. arXiv: astro-ph/0312273 [astro-ph].

[117] Clowe et al. "A Direct Empirical Proof of the Existence of Dark Matter". In: *The Astrophysical Journal Letters* 648.2 (Sept. 2006), pp. L109–L113. DOI: 10.1086/508162. arXiv: astro-ph/0608407 [astro-ph].

[118] Coe et al. "LensPerfect: Gravitational Lens Mass Map Reconstructions Yielding Exact Reproduction of All Multiple Images". In: *Astrophysical Journal* 681.2 (July 2008), pp. 814–830. DOI: 10.1086/588250. arXiv: 0803.1199 [astro-ph].

[119] Coe et al. "A High-resolution Mass Map of Galaxy Cluster Substructure: LensPerfect Analysis of A1689". In: *Astrophysical Journal* 723.2 (Nov. 2010), pp. 1678–1702. DOI: 10.1088/0004-637X/723/2/1678. arXiv: 1005.0398 [astro-ph.CO].

[120] Coe et al. "RELICS: Reionization Lensing Cluster Survey". In: *Astrophysical Journal* 884.1, 85 (Oct. 2019), p. 85. DOI: 10.3847/1538-4357/ab412b. arXiv: 1903.02002 [astro-ph.GA].

[121] Collett et al. "Core or Cusps: The Central Dark Matter Profile of a Strong Lensing Cluster with a Bright Central Image at Redshift 1". In: *Astrophysical Journal* 843.2, 148 (July 2017), p. 148. DOI: 10.3847/1538-4357/aa76e6. arXiv: 1703.08410 [astro-ph.CO].

[122] D'Inverno. *Introducing Einstein's relativity*. Oxford University Press, 1992.

[123] Dai et al. "Probing Dark Matter Subhalos in Galaxy Clusters Using Highly Magnified Stars". In: *Astrophysical Journal* 867.1, 24 (Nov. 2018), p. 24. DOI: 10.3847/1538-4357/aae478. arXiv: 1804.03149 [astro-ph.CO].

[124] Davidsen et al. "Observational Evidence that the Coma Cluster is not Bound by Ionized Intracluster Gas". In: *The Astrophysical Journal Letters* 186 (Dec. 1973), p. L119. DOI: 10.1086/181371.

[125] Davoudiasl and Denton. "Ultralight Boson Dark Matter and Event Horizon Telescope Observations of M 87*". In: *Physical Review Letters* 123.2, 021102 (July 2019), p. 021102. DOI: 10.1103/PhysRevLett.123.021102. arXiv: 1904.09242 [astro-ph.CO].

[126] de Blok. "The Core-Cusp Problem". In: *Advances in Astronomy* 2010, 789293 (Jan. 2010), p. 789293. DOI: 10.1155/2010/789293. arXiv: 0910.3538 [astro-ph.CO].

[127] de Vaucouleurs. "Classification and Morphology of External Galaxies." In: *Handbuch der Physik* 53 (Jan. 1959), p. 275. DOI: 10.1007/978-3-642-45932-0_7.

[128] Del Popolo and Le Delliou. "Review of solutions to the Cusp-core problem of the ΛCDM Model". In: *arXiv e-prints*, arXiv:2209.14151 (Sept. 2022), arXiv:2209.14151. arXiv: 2209.14151 [astro-ph.CO].

[129] Descartes. *Discours de la méthode pour bien conduire sa raison, et rechercher la verité dans les sciences*. Ed. by Descartes. De l'Imprimerie de Ian Maire, 1637. URL: https://archive.org/details/bub_gb_s6lSHDngPFoC.

[130] Despali et al. "A look into the inside of haloes: a characterization of the halo shape as a function of overdensity in the Planck cosmology". In: *Monthly Notices of the Royal Astronomical Society* 466.1 (Apr. 2017), pp. 181–193. DOI: 10.1093/mnras/stw3129. arXiv: 1605.04319 [astro-ph.CO].

[131] Despali et al. "Constraining SIDM with halo shapes: Revisited predictions from realistic simulations of early-type galaxies". In: *Monthly Notices of the Royal Astronomical Society* 516.3 (Nov. 2022), pp. 4543–4559. DOI: 10.1093/mnras/stac2521. arXiv: 2204.12502 [astro-ph.CO].

[132] Diego et al. "Non-parametric inversion of strong lensing systems". In: *Monthly Notices of the Royal Astronomical Society* 360.2 (June 2005), pp. 477–491. DOI: 10.1111/j.1365-2966.2005.09021.x. arXiv: astro-ph/0408418 [astro-ph].

[133] Diego et al. "Combined reconstruction of weak and strong lensing data with WSLAP". In: *Monthly Notices of the Royal Astronomical Society* 375.3 (Mar. 2007), pp. 958–970. DOI: 10.1111/j.1365-2966.2007.11380.x. arXiv: astro-ph/0509103 [astro-ph].

[134] Diego et al. "Free-form lensing implications for the collision of dark matter and gas in the frontier fields cluster MACS J0416.1-2403". In: *Monthly Notices of the Royal Astronomical Society* 447.4 (Mar. 2015), pp. 3130–3149. DOI: 10.1093/mnras/stu2660. arXiv: 1406.1217 [astro-ph.CO].

[135] Diego et al. "Hubble Frontier Field free-form mass mapping of the massive multiple-merging cluster MACSJ0717.5+3745". In: *Monthly Notices of the Royal Astronomical Society* 451.4 (Aug. 2015), pp. 3920–3932. DOI: 10.1093/mnras/stv1168. arXiv: 1410.7019 [astro-ph.CO].

[136] Diego et al. "A free-form mass model of the Hubble Frontier Fields cluster AS1063 (RXC J2248.7-4431) with over one hundred constraints". In: *Monthly Notices of the Royal Astronomical Society* 459.4 (July 2016), pp. 3447–3459. DOI: 10.1093/mnras/stw865. arXiv: 1512.07916 [astro-ph.CO].

[137] Diego et al. "A free-form lensing model of A370 revealing stellar mass dominated BCGs, in Hubble Frontier Fields images". In: *Monthly Notices of the Royal Astronomical Society* 473.4 (Feb. 2018), pp. 4279–4296. DOI: 10.1093/mnras/stx2609. arXiv: 1609.04822 [astro-ph.GA].

[138] Diego et al. "Free-form Lens Model and Mass Estimation of the High-redshift Galaxy Cluster ACT-CL J0102-4915, "El Gordo"". In: *Astrophysical Journal* 904.2, 106 (Dec. 2020), p. 106. DOI: 10.3847/1538-4357/abbf56. arXiv: 1905.00025 [astro-ph.CO].

[139] Djorgovski and Davis. "Fundamental Properties of Elliptical Galaxies". In: *Astrophysical Journal* 313 (Feb. 1987), p. 59. DOI: 10.1086/164948.

[140] Dodelson. *Gravitational Lensing*. 2017.

[141] Doroshkevich et al. "Cosmological impact of the neutrino rest mass". In: *Annals of the New York Academy of Sciences* 375 (Dec. 1981), pp. 32–42. DOI: 10.1111/j.1749-6632.1981.tb33688.x.

[142] Dressler et al. "Spectroscopy and Photometry of Elliptical Galaxies. I. New Distance Estimator". In: *Astrophysical Journal* 313 (Feb. 1987), p. 42. DOI: 10.1086/164947.

[143] Drlica-Wagner et al. "Eight Ultra-faint Galaxy Candidates Discovered in Year Two of the Dark Energy Survey". In: *Astrophysical Journal* 813.2, 109 (Nov. 2015), p. 109. DOI: 10.1088/0004-637X/813/2/109. arXiv: 1508.03622 [astro-ph.GA].

[144] Duffy et al. "Dark matter halo concentrations in the Wilkinson Microwave Anisotropy Probe year 5 cosmology". In: *Monthly Notices of the Royal Astronomical Society* 390.1 (Oct. 2008), pp. L64–L68. DOI: 10.1111/j.1745-3933.2008.00537.x. arXiv: 0804.2486 [astro-ph].

[145] Durrer. "The cosmic microwave background: the history of its experimental investigation and its significance for cosmology". In: *Classical and Quantum Gravity* 32.12, 124007 (June 2015), p. 124007. DOI: 10.1088/0264-9381/32/12/124007. arXiv: 1506.01907 [astro-ph.CO].

[146] Durret et al. "Ram pressure stripping in the z $\sim$ 0.5 galaxy cluster MS 0451.6-0305". In: *Astronomy & Astrophysics* 662, A84 (June 2022), A84. DOI: 10.1051/0004-6361/202142983. arXiv: 2204.07445 [astro-ph.CO].

[147] Dyson et al. "A Determination of the Deflection of Light by the Sun's Gravitational Field, from Observations Made at the Total Eclipse of May 29, 1919". In: *Philosophical Transactions of the Royal Society of London Series A* 220 (Jan. 1920), pp. 291–333. DOI: 10.1098/rsta.1920.0009.

[148] Ebeling et al. "MACS: A Quest for the Most Massive Galaxy Clusters in the Universe". In: *Astrophysical Journal* 553.2 (June 2001), pp. 668–676. DOI: 10.1086/320958. arXiv: astro-ph/0009101 [astro-ph].

[149] Ebeling et al. "Jellyfish: Evidence of Extreme Ram-pressure Stripping in Massive Galaxy Clusters". In: *The Astrophysical Journal Letters* 781.2, L40 (Feb. 2014), p. L40. DOI: 10.1088/2041-8205/781/2/L40. arXiv: 1312.6135 [astro-ph.GA].

[150] Eckert et al. "The XMM cluster outskirts project (X-COP)". In: *Astronomische Nachrichten* 338.293 (Mar. 2017), pp. 293–298. DOI: 10.1002/asna.201713345. arXiv: 1611.05051 [astro-ph.CO].

[151] Eckert et al. "Non-thermal pressure support in X-COP galaxy clusters". In: *Astronomy & Astrophysics* 621, A40 (Jan. 2019), A40. DOI: 10.1051/0004-6361/201833324. arXiv: 1805.00034 [astro-ph.CO].

[152] Eckert et al. "Constraints on dark matter self-interaction from the internal density profiles of X-COP galaxy clusters". In: *Astronomy & Astrophysics* 666, A41 (Oct. 2022), A41. DOI: 10.1051/0004-6361/202243205. arXiv: 2205.01123 [astro-ph.CO].

[153] Eckert et al. "The gravitational field of X-COP galaxy clusters". In: *Astronomy & Astrophysics* 662, A123 (June 2022), A123. DOI: 10.1051/0004-6361/202142507. arXiv: 2205.01110 [astro-ph.CO].

[154] Eiben and Smith. *Introduction to Evolutionary Computing*. Natural Computing Series. Springer Berlin Heidelberg, 2013. ISBN: 9783662050941. URL: https://books.google.com.au/books?id=ssmqCAAAQBAJ.

[155] Einasto. "On the Construction of a Composite Model for the Galaxy and on the Determination of the System of Galactic Parameters". In: *Trudy Astrofizicheskogo Instituta Alma-Ata* 5 (Jan. 1965), pp. 87–100.

[156] Einasto et al. "Dynamic evidence on massive coronas of galaxies". In: *Nature* 250.5464 (July 1974), pp. 309–310. DOI: 10.1038/250309a0.

[157] Einstein. "Ist die Trägheit eines Körpers von seinem Energieinhalt abhängig?" In: *Annalen der Physik* 323.13 (Jan. 1905), pp. 639–641. DOI: 10.1002/andp.19053231314.

[158] Einstein. "Zur Allgemeinen Relativitätstheorie". In: *Sitzungsber. Preuss. Akad. Wiss. Berlin (Math. Phys.)* 1915 (1915). [Addendum: Sitzungsber.Preuss.Akad.Wiss.Berlin (Math.Phys.) 1915, 799–801 (1915)], pp. 778–786.

[159] Einstein. "Kosmologische Betrachtungen zur allgemeinen Relativitätstheorie". In: *Sitzungsberichte der Königlich Preußischen Akademie der Wissenschaften (Berlin)* (Jan. 1917), pp. 142–152.

[160] Einstein. "Lens-Like Action of a Star by the Deviation of Light in the Gravitational Field". In: *Science* 84.2188 (Dec. 1936), pp. 506–507. DOI: 10.1126/science.84.2188.506.

[161] Eisenstein et al. "Detection of the Baryon Acoustic Peak in the Large-Scale Correlation Function of SDSS Luminous Red Galaxies". In: *Astrophysical Journal* 633.2 (Nov. 2005), pp. 560–574. DOI: 10.1086/466512. arXiv: astro-ph/0501171 [astro-ph].

[162] Elíasdóttir et al. "Where is the matter in the Merging Cluster Abell 2218?" In: *arXiv e-prints*, arXiv:0710.5636 (Oct. 2007), arXiv:0710.5636. arXiv: 0710.5636 [astro-ph].

[163] Ellis. "Gravitational lensing: a unique probe of dark matter and dark energy". In: *Philosophical Transactions of the Royal Society of London Series A* 368.1914 (Feb. 2010), pp. 967–987. DOI: 10.1098/rsta.2009.0209.

[164] Ellison et al. "The mass-metallicity relation in galaxy clusters: the relative importance of cluster membership versus local environment". In: *Monthly Notices of the Royal Astronomical Society* 396.3 (July 2009), pp. 1257–1272. DOI: 10.1111/j.1365-2966.2009.14817.x. arXiv: 0903.4684 [astro-ph.CO].

[165] Emritte et al. "Polarization of the Sunyaev-Zel'dovich effect: relativistic imprint of thermal and non-thermal plasma". In: *Journal of Cosmology and Astroparticle Physics* 2016.7, 031 (July 2016), p. 031. DOI: 10.1088/1475-7516/2016/07/031. arXiv: 1605.08333 [astro-ph.CO].

[166] Enßlin. "Information field theory". In: *Bayesian Inference and Maximum Entropy Methods in Science and Engineering: 32nd International Workshop on Bayesian Inference and Maximum Entropy Methods in Science and Engineering*. Ed. by von Toussaint. Vol. 1553. American Institute of Physics Conference Series. Aug. 2013, pp. 184–191. DOI: 10.1063/1.4819999. arXiv: 1301.2556 [astro-ph.IM].

[167] EROS Collaboration. "Limits on Galactic Dark Matter with 5 Years of EROS SMC Data". In: *arXiv e-prints*, astro-ph/0212176 (Dec. 2002), astro–ph/0212176. arXiv: astro-ph/0212176 [astro-ph].

[168] Etherington et al. "Strong gravitational lensing's 'external shear' is not shear". In: *arXiv e-prints*, arXiv:2301.05244 (Jan. 2023), arXiv:2301.05244. DOI: 10.48550/arXiv.2301.05244. arXiv: 2301.05244 [astro-ph.CO].

[169] Ettori. "β-model and cooling flows in X-ray clusters of galaxies". In: *Monthly Notices of the Royal Astronomical Society* 318.4 (Nov. 2000), pp. 1041–1046. DOI: 10.1046/j.1365-8711.2000.03664.x. arXiv: astro-ph/0005224 [astro-ph].

[170] Euclid Collaboration. "Euclid preparation. I. The Euclid Wide Survey". In: *Astronomy & Astrophysics* 662, A112 (June 2022), A112. DOI: 10.1051/0004-6361/202141938. arXiv: 2108.01201 [astro-ph.CO].

[171] Faber and Jackson. "Velocity dispersions and mass-to-light ratios for elliptical galaxies." In: *Astrophysical Journal* 204 (Mar. 1976), pp. 668–683. DOI: 10.1086/154215.

[172] Felten et al. "X-Rays from the Coma Cluster of Galaxies". In: *Astrophysical Journal* 146 (Dec. 1966), pp. 955–958. DOI: 10.1086/148972.

[173] Felten and Morrison. "Omnidirectional Inverse Compton and Synchrotron Radiation from Cosmic Distributions of Fast Electrons and Thermal Photons". In: *Astrophysical Journal* 146 (Dec. 1966), p. 686. DOI: 10.1086/148946.

[174] Feng. "Dark Matter Candidates from Particle Physics and Methods of Detection". In: *Annual Review of Astronomy and Astrophysics* 48 (Sept. 2010), pp. 495–545. DOI: 10.1146/annurev-astro-082708-101659. arXiv: 1003.0904 [astro-ph.CO].

[175] Ferreira. "Ultra-light dark matter". In: *Astronomy and Astrophysics Reviews* 29.1, 7 (Dec. 2021), p. 7. DOI: 10.1007/s00159-021-00135-6. arXiv: 2005.03254 [astro-ph.CO].

[176] Fleury. "Light propagation in inhomogeneous and anisotropic cosmologies". In: *arXiv e-prints*, arXiv:1511.03702 (Nov. 2015), arXiv:1511.03702. DOI: 10.48550/arXiv.1511.03702. arXiv: 1511.03702 [gr-qc].

[177] Fleury et al. "Weak Gravitational Lensing of Finite Beams". In: *Physical Review Letters* 119.19, 191101 (Nov. 2017), p. 191101. DOI: 10.1103/PhysRevLett.119.191101. arXiv: 1706.09383 [gr-qc].

[178] Fleury et al. "Line-of-sight effects in strong gravitational lensing". In: *Journal of Cosmology and Astroparticle Physics* 2021.8, 024 (Aug. 2021), p. 024. DOI: 10.1088/1475-7516/2021/08/024. arXiv: 2104.08883 [astro-ph.CO].

[179] Flores and Primack. "Observational and Theoretical Constraints on Singular Dark Matter Halos". In: *The Astrophysical Journal Letters* 427 (May 1994), p. L1. DOI: 10.1086/187350. arXiv: astro-ph/9402004 [astro-ph].

[180] Ford et al. "Advanced camera for the Hubble Space Telescope". In: *Space Telescopes and Instruments V*. Ed. by Bely and Breckinridge. Vol. 3356. Society of Photo-Optical Instrumentation Engineers (SPIE) Conference Series. Aug. 1998, pp. 234–248. DOI: 10.1117/12.324464.

[181] Foreman-Mackey et al. "emcee: The MCMC Hammer". In: *Publications of the Astronomical Society of the Pacific* 125.925 (Mar. 2013), pp. 306–312. ISSN: 1538-3873. DOI: 10.1086/670067. URL: http://dx.doi.org/10.1086/670067.

[182] Freese et al. "Limits on stellar objects as the dark matter of our halo: nonbaryonic dark matter seems to be required". In: *Nuclear Physics B Proceedings Supplements* 80 (Jan. 2000), pp. 03/05. arXiv: astro-ph/9904401 [astro-ph].

[183] Friedmann. "Über die Krümmung des Raumes". In: *Zeitschrift fur Physik* 10 (Jan. 1922), pp. 377–386. DOI: 10.1007/BF01332580.

[184] Fruscione et al. "CIAO: Chandra's data analysis system". In: *Society of Photo-Optical Instrumentation Engineers (SPIE) Conference Series*. Ed. by Silva and Doxsey. Vol. 6270. Society of Photo-Optical Instrumentation Engineers (SPIE) Conference Series. June 2006, 62701V, p. 62701V. DOI: 10.1117/12.671760.

[185] Fuselier. "Improved stability estimates and a characterization of the native space for matrix-valued RBFs". In: *Advances in Computational Mathematics* 29.3 (2008), pp. 269–290.

[186] Gao et al. "Galaxies and subhaloes in ΛCDM galaxy clusters". In: *Monthly Notices of the Royal Astronomical Society* 352.2 (Aug. 2004), pp. L1–L5. DOI: 10.1111/j.1365-2966.2004.08098.x. arXiv: astro-ph/0405010 [astro-ph].

[187] Gao et al. "The redshift dependence of the structure of massive Λ cold dark matter haloes". In: *Monthly Notices of the Royal Astronomical Society* 387.2 (June 2008), pp. 536–544. DOI: 10.1111/j.1365-2966.2008.13277.x. arXiv: 0711.0746 [astro-ph].

[188] Garmire et al. "Advanced CCD imaging spectrometer (ACIS) instrument on the Chandra X-ray Observatory". In: *X-Ray and Gamma-Ray Telescopes and Instruments for Astronomy*. Ed. by Truemper and Tananbaum. Vol. 4851. Society of Photo-Optical Instrumentation Engineers (SPIE) Conference Series. Mar. 2003, pp. 28–44. DOI: 10.1117/12.461599.

[189] Gavazzi et al. "The Sloan Lens ACS Survey. IV. The Mass Density Profile of Early-Type Galaxies out to 100 Effective Radii". In: *Astrophysical Journal* 667.1 (Sept. 2007), pp. 176–190. DOI: 10.1086/519237. arXiv: astro-ph/0701589 [astro-ph].

[190] Ghirardini et al. "On the evolution of the entropy and pressure profiles in X-ray luminous galaxy clusters at z > 0.4". In: *Astronomy & Astrophysics* 604, A100 (Aug. 2017), A100. DOI: 10.1051/0004-6361/201630209. arXiv: 1704.01587 [astro-ph.CO].

[191] Ghirardini et al. "Polytropic state of the intracluster medium in the X-COP cluster sample". In: *Astronomy & Astrophysics* 627, A19 (July 2019), A19. DOI: 10.1051/0004-6361/201834875. arXiv: 1906.00977 [astro-ph.CO].

[192] Ghirardini et al. "Universal thermodynamic properties of the intracluster medium over two decades in radius in the X-COP sample". In: *Astronomy & Astrophysics* 621, A41 (Jan. 2019), A41. DOI: 10.1051/0004-6361/201833325. arXiv: 1805.00042 [astro-ph.CO].

[193] Ghosh et al. "Further support for a trio of mass-to-light deviations in Abell 370: free-form GRALE lens inversion using BUFFALO strong lensing data". In: *Monthly Notices of the Royal Astronomical Society* 506.4 (Oct. 2021), pp. 6144–6158. DOI: 10.1093/mnras/stab1196. arXiv: 2104.11781 [astro-ph.CO].

[194] Giblin et al. "KiDS-1000 catalogue: Weak gravitational lensing shear measurements". In: *Astronomy & Astrophysics* 645, A105 (Jan. 2021), A105. DOI: 10.1051/0004-6361/202038850. arXiv: 2007.01845 [astro-ph.CO].

[195] Gilman et al. "Warm dark matter chills out: constraints on the halo mass function and the free-streaming length of dark matter with eight quadruple-image strong gravitational lenses". In: *Monthly Notices of the Royal Astronomical Society* 491.4 (Feb. 2020), pp. 6077–6101. DOI: 10.1093/mnras/stz3480. arXiv: 1908.06983 [astro-ph.CO].

[196] Gilmore and Tausch-Pebody. "The 1919 eclipse results which verified General Relativity and their later detractors: a story re-told". In: *arXiv e-prints*, arXiv:2010.13744 (Oct. 2020), arXiv:2010.13744. arXiv: 2010.13744 [physics.hist-ph].

[197] Gladders and Yee. "A New Method For Galaxy Cluster Detection. I. The Algorithm". In: *The Astronomical Journal* 120.4 (Oct. 2000), pp. 2148–2162. DOI: 10.1086/301557. arXiv: astro-ph/0004092 [astro-ph].

[198] Golse and Kneib. "Pseudo elliptical lensing mass model: Application to the NFW mass distribution". In: *Astronomy & Astrophysics* 390 (Aug. 2002), pp. 821–827. DOI: 10.1051/0004-6361:20020639. arXiv: astro-ph/0112138 [astro-ph].

[199] Golubchik et al. "HST Strong-lensing Model for the First JWST Galaxy Cluster SMACS J0723.3-7327". In: *Astrophysical Journal* 938.1, 14 (Oct. 2022), p. 14. DOI: 10.3847/1538-4357/ac8ff1. arXiv: 2207.05007 [astro-ph.CO].

[200] Gondolo and Gelmini. "Cosmic abundances of stable particles: improved analysis." In: *Nuclear Physics B* 360.1 (Aug. 1991), pp. 145–179. DOI: 10.1016/0550-3213(91)90438-4.

[201] Gottlieb. "A gravitational lens need not produce an odd number of images." In: *Journal of Mathematical Physics* 35.10 (Oct. 1994), pp. 5507–5510. DOI: 10.1063/1.530762. arXiv: gr-qc/9402038 [gr-qc].

[202] Granata et al. "Improved strong lensing modelling of galaxy clusters using the Fundamental Plane: Detailed mapping of the baryonic and dark matter mass distribution of Abell S1063". In: *Astronomy & Astrophysics* 659, A24 (Mar. 2022), A24. DOI: 10.1051/0004-6361/202141817. arXiv: 2107.09079 [astro-ph.GA].

[203] Griest and Kamionkowski. "Unitarity limits on the mass and radius of dark-matter particles". In: *Phys. Rev. Lett.* 64 (6 Feb. 1990), pp. 615–618. DOI: 10.1103/PhysRevLett.64.615. URL: https://link.aps.org/doi/10.1103/PhysRevLett.64.615.

[204] Grillo et al. "CLASH-VLT: Insights on the Mass Substructures in the Frontier Fields Cluster MACS J0416.1-2403 through Accurate Strong Lens Modeling". In: *Astrophysical Journal* 800.1, 38 (Feb. 2015), p. 38. DOI: 10.1088/0004-637X/800/1/38. arXiv: 1407.7866 [astro-ph.CO].

[205] Grillo et al. "The Story of Supernova "Refsdal" Told by Muse". In: *Astrophysical Journal* 822.2, 78 (May 2016), p. 78. DOI: 10.3847/0004-637X/822/2/78. arXiv: 1511.04093 [astro-ph.GA].

[206] Gunn and Gott. "On the Infall of Matter Into Clusters of Galaxies and Some Effects on Their Evolution". In: *Astrophysical Journal* 176 (Aug. 1972), p. 1. DOI: 10.1086/151605.

[207] Hall et al. "Freeze-in production of FIMP dark matter". In: *Journal of High Energy Physics* 2010, 80 (Mar. 2010), p. 80. DOI: 10.1007/JHEP03(2010)080. arXiv: 0911.1120 [hep-ph].

[208] Hallman et al. "The β-Model Problem: The Incompatibility of X-Ray and Sunyaev-Zeldovich Effect Model Fitting for Galaxy Clusters". In: *Astrophysical Journal* 665.2 (Aug. 2007), pp. 911–920. DOI: 10.1086/519447. arXiv: 0705.0531 [astro-ph].

[209] Hammer. "A gravitational lensing model of the strange ring-like structure in A370." In: *High Redshift and Primeval Galaxies*. Ed. by Bergeron et al. Jan. 1987, pp. 467–473.

[210] Hanson et al. "Weak lensing of the CMB". In: *General Relativity and Gravitation* 42.9 (Sept. 2010), pp. 2197–2218. DOI: 10.1007/s10714-010-1036-y. arXiv: 0911.0612 [astro-ph.CO].

[211] Hanuschik. "A flux-calibrated, high-resolution atlas of optical sky emission from UVES". In: *Astronomy & Astrophysics* 407 (Sept. 2003), pp. 1157–1164. DOI: 10.1051/0004-6361:20030885.

[212] Hao et al. "Precision Measurements of the Cluster Red Sequence Using an Error-Corrected Gaussian Mixture Model". In: *Astrophysical Journal* 702.1 (Sept. 2009), pp. 745–758. DOI: 10.1088/0004-637X/702/1/745. arXiv: 0907.4383 [astro-ph.CO].

[213] Harrison. "Fluctuations at the Threshold of Classical Cosmology". In: *Physical Review D* 1.10 (May 1970), pp. 2726–2730. DOI: 10.1103/PhysRevD.1.2726.

[214] Harvey et al. "The nongravitational interactions of dark matter in colliding galaxy clusters". In: *Science* 347.6229 (Mar. 2015), pp. 1462–1465. ISSN: 1095-9203. DOI: 10.1126/science.1261381. URL: http://dx.doi.org/10.1126/science.1261381.

[215] Hawking. "Particle creation by black holes". In: *Communications in Mathematical Physics* 43.3 (Aug. 1975), pp. 199–220. DOI: 10.1007/BF02345020.

[216] Hawking. "Gravitationally collapsed objects of very low mass". In: *Monthly Notices of the Royal Astronomical Society* 152 (Jan. 1971), p. 75. DOI: 10.1093/mnras/152.1.75.

[217] Hektor et al. "Constraining primordial black holes with the EDGES 21-cm absorption signal". In: *Physical Review D* 98.2, 023503 (July 2018), p. 023503. DOI: 10.1103/PhysRevD.98.023503. arXiv: 1803.09697 [astro-ph.CO].

[218] Hemmati et al. "Photometric Redshift Calibration Requirements for WFIRST Weak-lensing Cosmology: Predictions from CANDELS". In: *Astrophysical Journal* 877.2, 117 (June 2019), p. 117. DOI: 10.3847/1538-4357/ab1be5. arXiv: 1808.10458 [astro-ph.GA].

[219] Hernquist. "An Analytical Model for Spherical Galaxies and Bulges". In: *Astrophysical Journal* 356 (June 1990), p. 359. DOI: 10.1086/168845.

[220] Hester. "Ram Pressure Stripping in Clusters and Groups". In: *Astrophysical Journal* 647.2 (Aug. 2006), pp. 910–921. DOI: 10.1086/505614. arXiv: astro-ph/0610088 [astro-ph].

[221] Hewitt et al. "Unusual radio source MG1131+0456: a possible Einstein ring". In: *Nature* 333.6173 (June 1988), pp. 537–540. DOI: 10.1038/333537a0.

[222] Hickox and Markevitch. "Absolute Measurement of the Unresolved Cosmic X-Ray Background in the 0.5-8 keV Band with Chandra". In: *Astrophysical Journal* 645.1 (July 2006), pp. 95–114. DOI: 10.1086/504070. arXiv: astro-ph/0512542 [astro-ph].

[223] Hilton et al. "The Atacama Cosmology Telescope: A Catalog of >4000 Sunyaev-Zel'dovich Galaxy Clusters". In: *The Astrophysical Journal Supplement* 253.1, 3 (Mar. 2021), p. 3. DOI: 10.3847/1538-4365/abd023. arXiv: 2009.11043 [astro-ph.CO].

[224] Hinshaw et al. "Nine-year Wilkinson Microwave Anisotropy Probe (WMAP) Observations: Cosmological Parameter Results". In: *The Astrophysical Journal Supplement* 208.2, 19 (Oct. 2013), p. 19. DOI: 10.1088/0067-0049/208/2/19. arXiv: 1212.5226 [astro-ph.CO].

[225] Hinton et al. "MARZ: Manual and automatic redshifting software". In: *Astronomy and Computing* 15 (Apr. 2016), pp. 61–71. DOI: 10.1016/j.ascom.2016.03.001. arXiv: 1603.09438 [astro-ph.IM].

[226] Hogg et al. "The K correction". In: *arXiv e-prints*, astro-ph/0210394 (Oct. 2002), astro–ph/0210394. arXiv: astro-ph/0210394 [astro-ph].

[227] Hu. "CMB temperature and polarization anisotropy fundamentals". In: *Annals of Physics* 303.1 (Jan. 2003), pp. 203–225. DOI: 10.1016/S0003-4916(02)00022-2. arXiv: astro-ph/0210696 [astro-ph].

[228] Hu et al. "Fuzzy Cold Dark Matter: The Wave Properties of Ultralight Particles". In: *Physical Review Letters* 85.6 (Aug. 2000), pp. 1158–1161. DOI: 10.1103/PhysRevLett.85.1158. arXiv: astro-ph/0003365 [astro-ph].

[229] Hubble. "A Relation between Distance and Radial Velocity among Extra-Galactic Nebulae". In: *Proceedings of the National Academy of Science* 15.3 (Mar. 1929), pp. 168–173. DOI: 10.1073/pnas.15.3.168.

[230] Huchra et al. "2237+0305 : a new and unusual gravitational lens." In: *The Astronomical Journal* 90 (May 1985), pp. 691–696. DOI: 10.1086/113777.

[231] Hui et al. "Ultralight scalars as cosmological dark matter". In: *Physical Review D* 95.4, 043541 (Feb. 2017), p. 043541. DOI: 10.1103/PhysRevD.95.043541. arXiv: 1610.08297 [astro-ph.CO].

[232] Hut. "Limits on masses and number of neutral weakly interacting particles". In: *Physics Letters B* 69.1 (July 1977), pp. 85–88. DOI: 10.1016/0370-2693(77)90139-3.

[233] Ilbert et al. "Galaxy Stellar Mass Assembly Between 0.2 < z < 2 from the S-COSMOS Survey". In: *Astrophysical Journal* 709.2 (Feb. 2010), pp. 644–663. DOI: 10.1088/0004-637X/709/2/644. arXiv: 0903.0102 [astro-ph.CO].

[234] Iocco et al. "Evidence for dark matter in the inner Milky Way". In: *Nature Physics* 11.3 (Mar. 2015), pp. 245–248. DOI: 10.1038/nphys3237. arXiv: 1502.03821 [astro-ph.GA].

[235] Jaffe. "A simple model for the distribution of light in spherical galaxies." In: *Monthly Notices of the Royal Astronomical Society* 202 (Mar. 1983), pp. 995–999. DOI: 10.1093/mnras/202.4.995.

[236] Jauzac et al. "A weak lensing mass reconstruction of the large-scale filament feeding the massive galaxy cluster MACS J0717.5+3745". In: *Monthly Notices of the Royal Astronomical Society* 426.4 (Nov. 2012), pp. 3369–3384. DOI: 10.1111/j.1365-2966.2012.21966.x. arXiv: 1208.4323 [astro-ph.CO].

[237] Jauzac et al. "Hubble Frontier Fields: the geometry and dynamics of the massive galaxy cluster merger MACSJ0416.1-2403". In: *Monthly Notices of the Royal Astronomical Society* 446.4 (Feb. 2015), pp. 4132–4147. DOI: 10.1093/mnras/stu2425. arXiv: 1406.3011 [astro-ph.CO].

[238] Jauzac et al. "Hubble Frontier Fields: predictions for the return of SN Refsdal with the MUSE and GMOS spectrographs". In: *Monthly Notices of the Royal Astronomical Society* 457.2 (Apr. 2016), pp. 2029–2042. DOI: 10.1093/mnras/stw069. arXiv: 1509.08914 [astro-ph.GA].

[239] Jauzac et al. "The extraordinary amount of substructure in the Hubble Frontier Fields cluster Abell 2744". In: *Monthly Notices of the Royal Astronomical Society* 463.4 (Dec. 2016), pp. 3876–3893. DOI: 10.1093/mnras/stw2251. arXiv: 1606.04527 [astro-ph.CO].

[240] Jauzac et al. "The shape of galaxy dark matter haloes in massive galaxy clusters: insights from strong gravitational lensing". In: *Monthly Notices of the Royal Astronomical Society* 477.3 (July 2018), pp. 4046–4051. DOI: 10.1093/mnras/sty909. arXiv: 1711.09882 [astro-ph.CO].

[241] Jauzac et al. "The core of the massive cluster merger MACS J0417.5-1154 as seen by VLT/MUSE". In: *Monthly Notices of the Royal Astronomical Society* 483.3 (Mar. 2019), pp. 3082–3097. DOI: 10.1093/mnras/sty3312. arXiv: 1811.02505 [astro-ph.GA].

[242] Jauzac et al. "Galaxy cluster cores as seen with VLT/MUSE: New strong-lensing analyses of RX J2129.4+0009, MS 0451.6-0305, and MACS J2129.4-0741". In: *Monthly Notices of the Royal Astronomical Society* 508.1 (Nov. 2021), pp. 1206–1226. DOI: 10.1093/mnras/stab2270. arXiv: 2006.10700 [astro-ph.GA].

[243] Jing. "The Density Profile of Equilibrium and Nonequilibrium Dark Matter Halos". In: *Astrophysical Journal* 535.1 (May 2000), pp. 30–36. DOI: 10.1086/308809. arXiv: astro-ph/9901340 [astro-ph].

[244] Jing and Suto. "The Density Profiles of the Dark Matter Halo Are Not Universal". In: *The Astrophysical Journal Letters* 529.2 (Feb. 2000), pp. L69–L72. DOI: 10.1086/312463. arXiv: astro-ph/9909478 [astro-ph].

[245] Jullo and Kneib. "Multiscale cluster lens mass mapping - I. Strong lensing modelling". In: *Monthly Notices of the Royal Astronomical Society* 395.3 (May 2009), pp. 1319–1332. DOI: 10.1111/j.1365-2966.2009.14654.x. arXiv: 0901.3792 [astro-ph.CO].

[246] Jullo et al. "A Bayesian approach to strong lensing modelling of galaxy clusters". In: *New Journal of Physics* 9.12 (Dec. 2007), p. 447. DOI: 10.1088/1367-2630/9/12/447. arXiv: 0706.0048 [astro-ph].

[247] Jungman et al. "Supersymmetric dark matter". In: *Physics Reports* 267 (Mar. 1996), pp. 195–373. DOI: 10.1016/0370-1573(95)00058-5. arXiv: hep-ph/9506380 [hep-ph].

[248] Kaiser and Squires. "Mapping the Dark Matter with Weak Gravitational Lensing". In: *Astrophysical Journal* 404 (Feb. 1993), p. 441. DOI: 10.1086/172297.

[249] Kalirai et al. "WFC3 SMOV Proposal 11451: The Photometric Performance and Calibration of WFC3/IR". In: *Space Telescope WFC Instrument Science Report* (Nov. 2009). URL: https://ui.adsabs.harvard.edu/abs/2009wfc..rept...31K/abstract.

[250] Kant. *Critique of Pure Reason*. The Cambridge Edition of the Works of Immanuel Kant. Translated by Paul Guyer and Allen W. Wood. New York, NY: Cambridge University Press, 1998.

[251] Karman et al. "MUSE integral-field spectroscopy towards the Frontier Fields cluster Abell S1063. I. Data products and redshift identifications". In: *Astronomy & Astrophysics* 574, A11 (Feb. 2015), A11. DOI: 10.1051/0004-6361/201424962. arXiv: 1409.3507 [astro-ph.GA].

[252] Karman et al. "MUSE integral-field spectroscopy towards the Frontier Fields cluster Abell S1063. II. Properties of low luminosity Lyman α emitters at z > 3". In: *Astronomy & Astrophysics* 599, A28 (Mar. 2017), A28. DOI: 10.1051/0004-6361/201629055. arXiv: 1606.01471 [astro-ph.GA].

[253] Kassiola and Kovner. "Elliptic Mass Distributions versus Elliptic Potentials in Gravitational Lenses". In: *Astrophysical Journal* 417 (Nov. 1993), p. 450. DOI: 10.1086/173325.

[254] Kassiola et al. "Perturbations of Cluster Cusps by Galaxies: The Triple Arc in CL 0024+1654". In: *Astrophysical Journal* 400 (Nov. 1992), p. 41. DOI: 10.1086/171971.

[255] Keeton. "A Catalog of Mass Models for Gravitational Lensing". In: *arXiv e-prints*, astro-ph/0102341 (Feb. 2001), astro–ph/0102341. arXiv: astro-ph/0102341 [astro-ph].

[256] Kennefick. "Not Only Because of Theory: Dyson, Eddington and the Competing Myths of the 1919 Eclipse Expedition". In: *arXiv e-prints*, arXiv:0709.0685 (Sept. 2007), arXiv:0709.0685. arXiv: 0709.0685 [physics.hist-ph].

[257] Kilbinger. "Cosmology with cosmic shear observations: a review". In: *Reports on Progress in Physics* 78.8, 086901 (July 2015), p. 086901. DOI: 10.1088/0034-4885/78/8/086901. arXiv: 1411.0115 [astro-ph.CO].

[258] Kim and Carosi. "Axions and the strong CP problem". In: *Reviews of Modern Physics* 82.1 (Jan. 2010), pp. 557–601. DOI: 10.1103/RevModPhys.82.557. arXiv: 0807.3125 [hep-ph].

[259] King. "The structure of star clusters. I. an empirical density law". In: *The Astronomical Journal* 67 (Oct. 1962), p. 471. DOI: 10.1086/108756.

[260] King. "The structure of star clusters. III. Some simple dynamical models". In: *The Astronomical Journal* 71 (Feb. 1966), p. 64. DOI: 10.1086/109857.

[261] King et al. "A complete infrared Einstein ring in the gravitational lens system B1938+666." In: *Monthly Notices of the Royal Astronomical Society* 295 (Apr. 1998), pp. L41–L44. DOI: 10.1046/j.1365-8711.1998.295241.x. arXiv: astro-ph/9710171 [astro-ph].

[262] Kirk et al. *The Presocratic Philosophers a Critical History with a Selection of Texts*. Cambridge University Press, 1983.

[263] Klypin et al. "Where Are the Missing Galactic Satellites?" In: *Astrophysical Journal* 522.1 (Sept. 1999), pp. 82–92. DOI: 10.1086/307643. arXiv: astro-ph/9901240 [astro-ph].

[264] Kneib et al. "The distribution of dark matter in distant cluster-lenses : modelling modelling A 370." In: *Astronomy & Astrophysics* 273 (June 1993), p. 367.

[265] Kneib et al. "Hubble Space Telescope Observations of the Lensing Cluster Abell 2218". In: *Astrophysical Journal* 471 (Nov. 1996), p. 643. DOI: 10.1086/177995. arXiv: astro-ph/9511015 [astro-ph].

[266] Kneib and Natarajan. "Cluster lenses". In: *The Astronomy and Astrophysics Review* 19.1 (Nov. 2011). ISSN: 1432-0754. DOI: 10.1007/s00159-011-0047-3. URL: http://dx.doi.org/10.1007/s00159-011-0047-3.

[267] Kochanek and White. "A Quantitative Study of Interacting Dark Matter in Halos". In: *Astrophysical Journal* 543.2 (Nov. 2000), pp. 514–520. DOI: 10.1086/317149. arXiv: astro-ph/0003483 [astro-ph].

[268] Kochanek. "Gravitational Lensing: Strong, Weak and Micro". In: *Saas-Fee Advanced Course 33: Gravitational Lensing: Strong, Weak and Micro*. Jan. 2006. arXiv: astro-ph/0407232 [astro-ph].

[269] Kolb and Turner. *The early universe*. Vol. 69. 1990.

[270] Kompaneets. "The Establishment of Thermal Equilibrium between Quanta and Electrons". In: *Soviet Journal of Experimental and Theoretical Physics* 4.5 (May 1957), pp. 730–737.

[271] Koo. "Optical multicolors : a poor person's Z machine for galaxies." In: *The Astronomical Journal* 90 (Mar. 1985), pp. 418–440. DOI: 10.1086/113748.

[272] Kovner. "Giant luminous arcs from gravitational lensing". In: *Nature* 327.6119 (May 1987), pp. 193–194. DOI: 10.1038/327193c0.

[273] Kovner. "Fermat Principle in Arbitrary Gravitational Fields". In: *Astrophysical Journal* 351 (Mar. 1990), p. 114. DOI: 10.1086/168450.

[274] Kravtsov and Borgani. "Formation of Galaxy Clusters". In: *Annual Review of Astronomy and Astrophysics* 50 (Sept. 2012), pp. 353–409. DOI: 10.1146/annurev-astro-081811-125502. arXiv: 1205.5556 [astro-ph.CO].

[275] Kravtsov et al. "The Cores of Dark Matter-dominated Galaxies: Theory versus Observations". In: *Astrophysical Journal* 502.1 (July 1998), pp. 48–58. DOI: 10.1086/305884. arXiv: astro-ph/9708176 [astro-ph].

[276] Krone-Martins et al. "Gaia GraL: Gaia DR2 gravitational lens systems. I. New quadruply imaged quasar candidates around known quasars". In: *Astronomy & Astrophysics* 616, L11 (Aug. 2018), p. L11. DOI: 10.1051/0004-6361/201833337. arXiv: 1804.11051 [astro-ph.GA].

[277] Kuhn. *The Structure of Scientific Revolutions*. Chicago: University of Chicago Press, 1962.

[278] Lacey and Cole. "Merger rates in hierarchical models of galaxy formation". In: *Monthly Notices of the Royal Astronomical Society* 262.3 (June 1993), pp. 627–649. DOI: 10.1093/mnras/262.3.627.

[279] Lachièze-Rey et al. *The Cosmological Background Radiation*. Cambridge University Press, 1999.

[280] Lagattuta et al. "Lens modelling Abell 370: crowning the final frontier field with MUSE". In: *Monthly Notices of the Royal Astronomical Society* 469.4 (Aug. 2017), pp. 3946–3964. DOI: 10.1093/mnras/stx1079. arXiv: 1611.01513 [astro-ph.GA].

[281] Lagattuta et al. "Probing 3D structure with a large MUSE mosaic: extending the mass model of Frontier Field Abell 370". In: *Monthly Notices of the Royal Astronomical Society* 485.3 (May 2019), pp. 3738–3760. DOI: 10.1093/mnras/stz620. arXiv: 1904.02158 [astro-ph.GA].

[282] Lagattuta et al. "Pilot-WINGS: An extended MUSE view of the structure of Abell 370". In: *Monthly Notices of the Royal Astronomical Society* 514.1 (July 2022), pp. 497–517. DOI: 10.1093/mnras/stac418. arXiv: 2202.04663 [astro-ph.GA].

[283] Lam et al. "An Isolated Mass-gap Black Hole or Neutron Star Detected with Astrometric Microlensing". In: *The Astrophysical Journal Letters* 933.1, L23 (July 2022), p. L23. DOI: 10.3847/2041-8213/ac7442. arXiv: 2202.01903 [astro-ph.GA].

[284] Landau and Lifshitz. *Fluid mechanics*. Pergamon Press, 1959.

[285] Leauthaud et al. "A Theoretical Framework for Combining Techniques that Probe the Link Between Galaxies and Dark Matter". In: *Astrophysical Journal* 738.1, 45 (Sept. 2011), p. 45. DOI: 10.1088/0004-637X/738/1/45. arXiv: 1103.2077 [astro-ph.CO].

[286] Lee and Weinberg. "Cosmological lower bound on heavy-neutrino masses". In: *Physical Review Letters* 39.4 (July 1977), pp. 165–168. DOI: 10.1103/PhysRevLett.39.165.

[287] Lemaître. "Contributions to a British Association Discussion on the Evolution of the Universe." In: *Nature* 128.3234 (Oct. 1931), pp. 704–706. DOI: 10.1038/128704a0.

[288] Lemaître. "Un Univers homogène de masse constante et de rayon croissant rendant compte de la vitesse radiale des nébuleuses extra-galactiques". In: *Annales de la Société Scientifique de Bruxelles* 47 (Jan. 1927), pp. 49–59.

[289] Lewis and Challinor. "Weak gravitational lensing of the CMB". In: *Physics Reports* 429.1 (June 2006), pp. 1–65. DOI: 10.1016/j.physrep.2006.03.002. arXiv: astro-ph/0601594 [astro-ph].

[290] Li and Chen. "Cusp-core problem and strong gravitational lensing". In: *Research in Astronomy and Astrophysics* 9.11 (Nov. 2009), pp. 1173–1184. DOI: 10.1088/1674-4527/9/11/001. arXiv: 0905.3041 [astro-ph.CO].

[291] Liesenborgs et al. "A genetic algorithm for the non-parametric inversion of strong lensing systems". In: *Monthly Notices of the Royal Astronomical Society* 367.3 (Apr. 2006), pp. 1209–1216. DOI: 10.1111/j.1365-2966.2006.10040.x. arXiv: astro-ph/0601124 [astro-ph].

[292] Liesenborgs et al. "Non-parametric inversion of gravitational lensing systems with few images using a multi-objective genetic algorithm". In: *Monthly Notices of the Royal Astronomical Society* 380.4 (Oct. 2007), pp. 1729–1736. DOI: 10.1111/j.1365-2966.2007.12236.x. arXiv: 0707.2538 [astro-ph].

[293] Liesenborgs et al. "Extended lens reconstructions with grale: exploiting time-domain, substructural, and weak lensing information". In: *Monthly Notices of the Royal Astronomical Society* 494.3 (May 2020), pp. 3253–3274. DOI: 10.1093/mnras/staa842. arXiv: 2003.10377 [astro-ph.CO].

[294] Limber. "The Analysis of Counts of the Extragalactic Nebulae in Terms of a Fluctuating Density Field. II." In: *Astrophysical Journal* 119 (May 1954), p. 655. DOI: 10.1086/145870.

[295] Limousin et al. "Galaxy Galaxy Lensing as a Probe of Galaxy Dark Matter Halos". In: *arXiv e-prints*, astro-ph/0606447 (June 2006), astro–ph/0606447. arXiv: astro-ph/0606447 [astro-ph].

[296] Limousin et al. "Strong lensing in Abell 1703: constraints on the slope of the inner dark matter distribution". In: *Astronomy & Astrophysics* 489.1 (Oct. 2008), pp. 23–35. DOI: 10.1051/0004-6361:200809646. arXiv: 0802.4292 [astro-ph].

[297] Limousin et al. "Strong-lensing analysis of MACS J0717.5+3745 from Hubble Frontier Fields observations: How well can the mass distribution be constrained?" In: *Astronomy & Astrophysics* 588, A99 (Apr. 2016), A99. DOI: 10.1051/0004-6361/201527638. arXiv: 1510.08077 [astro-ph.CO].

[298] Limousin et al. "Constraining the mass distribution of galaxies using galaxy-galaxy lensing in clusters and in the field". In: *Monthly Notices of the Royal Astronomical Society* 356.1 (Jan. 2005), pp. 309–322. DOI: 10.1111/j.1365-2966.2004.08449.x. arXiv: astro-ph/0405607 [astro-ph].

[299] Limousin et al. "Dark matter in galaxy clusters: Parametric strong-lensing approach". In: *Astronomy & Astrophysics* 664, A90 (Aug. 2022), A90. DOI: 10.1051/0004-6361/202243278. arXiv: 2202.02992 [astro-ph.CO].

[300] Lin. "TASI lectures on dark matter models and direct detection". In: *arXiv e-prints*, arXiv:1904.07915 (Apr. 2019), arXiv:1904.07915. arXiv: 1904.07915 [hep-ph].

[301] Lin et al. "Evolution of the K-Band Galaxy Cluster Luminosity Function and Scaling Relations". In: *The Astrophysical Journal Letters* 650.2 (Oct. 2006), pp. L99–L102. DOI: 10.1086/508940. arXiv: astro-ph/0609169 [astro-ph].

[302] Linder. "Exploring the Expansion History of the Universe". In: *Physical Review Letters* 90.9, 091301 (Mar. 2003), p. 091301. DOI: 10.1103/PhysRevLett.90.091301. arXiv: astro-ph/0208512 [astro-ph].

[303] López-Sanjuan et al. "The ALHAMBRA survey: tight dependence of the optical mass-to-light ratio on galaxy colour up to z = 1.5". In: *arXiv e-prints*, arXiv:1805.03609 (May 2018), arXiv:1805.03609. arXiv: 1805.03609 [astro-ph.GA].

[304] Lotz et al. "The Frontier Fields: Survey Design and Initial Results". In: *Astrophysical Journal* 837.1, 97 (Mar. 2017), p. 97. DOI: 10.3847/1538-4357/837/1/97. arXiv: 1605.06567 [astro-ph.GA].

[305] Lovell et al. "Addressing the too big to fail problem with baryon physics and sterile neutrino dark matter". In: *Monthly Notices of the Royal Astronomical Society* 468.3 (July 2017), pp. 2836–2849. DOI: 10.1093/mnras/stx621. arXiv: 1611.00005 [astro-ph.GA].

[306] Lovisari and Reiprich. "The non-uniformity of galaxy cluster metallicity profiles". In: *Monthly Notices of the Royal Astronomical Society* 483.1 (Feb. 2019), pp. 540–557. DOI: 10.1093/mnras/sty3130. arXiv: 1811.05987 [astro-ph.CO].

[307] LSST Dark Energy Science Collaboration. "Large Synoptic Survey Telescope: Dark Energy Science Collaboration". In: *arXiv e-prints*, arXiv:1211.0310 (Nov. 2012), arXiv:1211.0310. arXiv: 1211.0310 [astro-ph.CO].

[308] Lynds and Petrosian. "Spectroscopic Observations of the Luminous Arcs". In: *Bulletin of the American Astronomical Society*. Vol. 20. Jan. 1988, p. 644.

[309] Lynds and Petrosian. "Giant Luminous Arcs in Galaxy Clusters". In: *Bulletin of the American Astronomical Society*. Vol. 18. Sept. 1986, p. 1014.

[310] Lynds. "The Absorption-Line Spectrum of 4c 05.34". In: *The Astrophysical Journal Letters* 164 (Mar. 1971), p. L73. DOI: 10.1086/180695.

[311] Lynds and Petrosian. "Luminous Arcs in Clusters of Galaxies". In: *Astrophysical Journal* 336 (Jan. 1989), p. 1. DOI: 10.1086/166989.

[312] Mahler et al. "Strong-lensing analysis of A2744 with MUSE and Hubble Frontier Fields images". In: *Monthly Notices of the Royal Astronomical Society* 473.1 (Jan. 2018), pp. 663–692. DOI: 10.1093/mnras/stx1971. arXiv: 1702.06962 [astro-ph.GA].

[313] Mahler et al. "Precision modeling of JWST's first cluster lens SMACSJ0723.3-7327". In: *arXiv e-prints*, arXiv:2207.07101 (July 2022), arXiv:2207.07101. arXiv: 2207.07101 [astro-ph.GA].

[314] Mallaby-Kay et al. "The Atacama Cosmology Telescope: Summary of DR4 and DR5 Data Products and Data Access". In: *The Astrophysical Journal Supplement* 255.1, 11 (July 2021), p. 11. DOI: 10.3847/1538-4365/abfcc4. arXiv: 2103.03154 [astro-ph.CO].

[315] Maller et al. "Breaking the Disk/Halo Degeneracy with Gravitational Lensing". In: *Astrophysical Journal* 533.1 (Apr. 2000), pp. 194–202. DOI: 10.1086/308641. arXiv: astro-ph/9910207 [astro-ph].

[316] Mamon et al. "MAMPOSSt: Modelling Anisotropy and Mass Profiles of Observed Spherical Systems - I. Gaussian 3D velocities". In: *Monthly Notices of the Royal Astronomical Society* 429.4 (Mar. 2013), pp. 3079–3098. DOI: 10.1093/mnras/sts565. arXiv: 1212.1455 [astro-ph.CO].

[317] Mandelbaum. "Weak Lensing for Precision Cosmology". In: *Annual Review of Astronomy and Astrophysics* 56 (Sept. 2018), pp. 393–433. DOI: 10.1146/annurev-astro-081817-051928. arXiv: 1710.03235 [astro-ph.CO].

[318] Markevitch et al. "Direct Constraints on the Dark Matter Self-Interaction Cross Section from the Merging Galaxy Cluster 1E 0657-56". In: *Astrophysical Journal* 606.2 (May 2004), pp. 819–824. DOI: 10.1086/383178. arXiv: astro-ph/0309303 [astro-ph].

[319] Massey et al. "Cluster bulleticity". In: *Monthly Notices of the Royal Astronomical Society* 413.3 (May 2011), pp. 1709–1716. DOI: 10.1111/j.1365-2966.2011.18246.x. arXiv: 1007.1924 [astro-ph.CO].

[320] Massey et al. "The behaviour of dark matter associated with four bright cluster galaxies in the 10 kpc core of Abell 3827". In: *Monthly Notices of the Royal Astronomical Society* 449.4 (June 2015), pp. 3393–3406. DOI: 10.1093/mnras/stv467. arXiv: 1504.03388 [astro-ph.CO].

[321] Massey et al. "Dark matter dynamics in Abell 3827: new data consistent with standard cold dark matter". In: *Monthly Notices of the Royal Astronomical Society* 477.1 (June 2018), pp. 669–677. DOI: 10.1093/mnras/sty630. arXiv: 1708.04245 [astro-ph.CO].

[322] McDonald et al. "The Evolution of the Intracluster Medium Metallicity in Sunyaev Zel'dovich-selected Galaxy Clusters at $0 < z < 1.5$". In: *Astrophysical Journal* 826.2, 124 (Aug. 2016), p. 124. DOI: 10.3847/0004-637X/826/2/124. arXiv: 1603.03035 [astro-ph.CO].

[323] McGaugh et al. "The Baryonic Tully-Fisher Relation". In: *The Astrophysical Journal Letters* 533.2 (Apr. 2000), pp. L99–L102. DOI: 10.1086/312628. arXiv: astro-ph/0003001 [astro-ph].

[324] McGaugh. "The Baryonic Tully-Fisher Relation of Gas-rich Galaxies as a Test of ΛCDM and MOND". In: *The Astronomical Journal* 143.2, 40 (Feb. 2012), p. 40. DOI: 10.1088/0004-6256/143/2/40. arXiv: 1107.2934 [astro-ph.CO].

[325] McGaugh. "A tale of two paradigms: the mutual incommensurability of ΛCDM and MOND". In: *Canadian Journal of Physics* 93.2 (Feb. 2015), pp. 250–259. DOI: 10.1139/cjp-2014-0203. arXiv: 1404.7525 [astro-ph.CO].

[326] McKenzie. "A gravitational lens produces an odd number of images." In: *Journal of Mathematical Physics* 26.7 (Jan. 1985), pp. 1592–1597. DOI: 10.1063/1.526923.

[327] Meena and Bagla. "Exotic image formation in strong gravitational lensing by clusters of galaxies - I. Cross-section". In: *Monthly Notices of the Royal Astronomical Society* 503.2 (May 2021), pp. 2097–2107. DOI: 10.1093/mnras/stab577. arXiv: 2009.13418 [astro-ph.CO].

[328] Mellier et al. "The Dark Matter Distribution in MS 2137-23 from the Modeling of the Multiple Arc Systems". In: *Astrophysical Journal* 407 (Apr. 1993), p. 33. DOI: 10.1086/172490.

[329] Meneghetti et al. "The Frontier Fields lens modelling comparison project". In: *Monthly Notices of the Royal Astronomical Society* 472.3 (Dec. 2017), pp. 3177–3216. DOI: 10.1093/mnras/stx2064. arXiv: 1606.04548 [astro-ph.CO].

[330] Meneghetti. *Introduction to Gravitational Lensing; With Python Examples*. Vol. 956. Springer, 2021. DOI: 10.1007/978-3-030-73582-1.

[331] Meneghetti et al. "Giant cluster arcs as a constraint on the scattering cross-section of dark matter". In: *Monthly Notices of the Royal Astronomical Society* 325.1 (July 2001), pp. 435–442. DOI: 10.1046/j.1365-8711.2001.04477.x. arXiv: astro-ph/0011405 [astro-ph].

[332] Mercurio et al. "CLASH-VLT: Abell S1063. Cluster assembly history and spectroscopic catalogue". In: *Astronomy & Astrophysics* 656, A147 (Dec. 2021), A147. DOI: 10.1051/0004-6361/202142168. arXiv: 2109.03305 [astro-ph.GA].

[333] Merten et al. "Combining weak and strong cluster lensing: applications to simulations and MS 2137". In: *Astronomy & Astrophysics* 500.2 (June 2009), pp. 681–691. DOI: 10.1051/0004-6361/200810372. arXiv: 0806.1967 [astro-ph].

[334] Merten et al. "Creation of cosmic structure in the complex galaxy cluster merger Abell 2744". In: *Monthly Notices of the Royal Astronomical Society* 417.1 (Oct. 2011), pp. 333–347. DOI: 10.1111/j.1365-2966.2011.19266.x. arXiv: 1103.2772 [astro-ph.CO].

[335] Messier. "Catalogue des Nébuleuses et des Amas d'Étoiles (Catalog of Nebulae and Star Clusters)". In: *Connoissance des Temps ou des Mouvements Célestes* (1781), pp. 227–267.

[336] Milgrom. "A modification of the Newtonian dynamics - Implications for galaxies." In: *Astrophysical Journal* 270 (July 1983), pp. 371–383. DOI: 10.1086/161131.

[337] Milgrom. "A modification of the newtonian dynamics : implications for galaxy systems." In: *Astrophysical Journal* 270 (July 1983), pp. 384–389. DOI: 10.1086/161132.

[338] Milgrom. "A modification of the Newtonian dynamics as a possible alternative to the hidden mass hypothesis." In: *Astrophysical Journal* 270 (July 1983), pp. 365–370. DOI: 10.1086/161130.

[339] Miller and Goodrich. "Spectrophotometry and polarimetry of the giant luminous arcs in the clusters 2244-02 and Abell 370". In: *Nature* 331.6158 (Feb. 1988), pp. 685–687. DOI: 10.1038/331685a0.

[340] Mohammed et al. "Quantifying substructures in Hubble Frontier Field clusters: comparison with ΛCDM simulations". In: *Monthly Notices of the Royal Astronomical Society* 459.2 (June 2016), pp. 1698–1709. DOI: 10.1093/mnras/stw727. arXiv: 1507.01532 [astro-ph.CO].

[341] Mohr et al. "Properties of the Intracluster Medium in an Ensemble of Nearby Galaxy Clusters". In: *Astrophysical Journal* 517.2 (June 1999), pp. 627–649. DOI: 10.1086/307227. arXiv: astro-ph/9901281 [astro-ph].

[342] Moore et al. "Resolving the Structure of Cold Dark Matter Halos". In: *The Astrophysical Journal Letters* 499.1 (May 1998), pp. L5–L8. DOI: 10.1086/311333. arXiv: astro-ph/9709051 [astro-ph].

[343] Moore et al. "Cold collapse and the core catastrophe". In: *Monthly Notices of the Royal Astronomical Society* 310.4 (Dec. 1999), pp. 1147–1152. DOI: 10.1046/j.1365-8711.1999.03039.x. arXiv: astro-ph/9903164 [astro-ph].

[344] Moore et al. "Dark Matter Substructure within Galactic Halos". In: *The Astrophysical Journal Letters* 524.1 (Oct. 1999), pp. L19–L22. DOI: 10.1086/312287. arXiv: astro-ph/9907411 [astro-ph].

[345] Mortlock et al. "A luminous quasar at a redshift of z = 7.085". In: *Nature* 474.7353 (June 2011), pp. 616–619. DOI: 10.1038/nature10159. arXiv: 1106.6088 [astro-ph.CO].

[346] Mostoghiu et al. "The Three Hundred Project: The evolution of galaxy cluster density profiles". In: *Monthly Notices of the Royal Astronomical Society* 483.3 (Mar. 2019), pp. 3390–3403. DOI: 10.1093/mnras/sty3306. arXiv: 1812.04009 [astro-ph.GA].

[347] Mroczkowski et al. "Astrophysics with the Spatially and Spectrally Resolved Sunyaev-Zeldovich Effects. A Millimetre/Submillimetre Probe of the Warm and Hot Universe". In: *Space Science Reviews* 215.1, 17 (Feb. 2019), p. 17. DOI: 10.1007/s11214-019-0581-2. arXiv: 1811.02310 [astro-ph.CO].

[348] Murgia et al. "Novel constraints on noncold, nonthermal dark matter from Lyman-α forest data". In: *Physical Review D* 98.8, 083540 (Oct. 2018), p. 083540. DOI: 10.1103/PhysRevD.98.083540. arXiv: 1806.08371 [astro-ph.CO].

[349] Nadler et al. "Constraints on Dark Matter Properties from Observations of Milky Way Satellite Galaxies". In: *Physical Review Letters* 126.9, 091101 (Mar. 2021), p. 091101. DOI: 10.1103/PhysRevLett.126.091101. arXiv: 2008.00022 [astro-ph.CO].

[350] Naess et al. "The Atacama Cosmology Telescope: arcminute-resolution maps of 18 000 square degrees of the microwave sky from ACT 2008-2018 data combined with Planck". In: *Journal of Cosmology and Astroparticle Physics* 2020.12, 046 (Dec. 2020), p. 046. DOI: 10.1088/1475-7516/2020/12/046. arXiv: 2007.07290 [astro-ph.IM].

[351] Narayan and Bartelmann. "Lectures on Gravitational Lensing". In: *arXiv e-prints*, astro-ph/9606001 (June 1996), astro–ph/9606001. arXiv: astro-ph/9606001 [astro-ph].

[352] Natarajan and Kneib. "Probing the dynamics of cluster-lenses". In: *Monthly Notices of the Royal Astronomical Society* 283.3 (Dec. 1996), pp. 1031–1046. DOI: 10.1093/mnras/283.3.1031. arXiv: astro-ph/9602035 [astro-ph].

[353] Navarro et al. "Simulations of X-ray clusters". In: *Monthly Notices of the Royal Astronomical Society* 275.3 (Aug. 1995), pp. 720–740. DOI: 10.1093/mnras/275.3.720. arXiv: astro-ph/9408069 [astro-ph].

[354] Navarro et al. "The Structure of Cold Dark Matter Halos". In: *Astrophysical Journal* 462 (May 1996), p. 563. DOI: 10.1086/177173. arXiv: astro-ph/9508025 [astro-ph].

[355] Nelson et al. "Hydrodynamic Simulation of Non-thermal Pressure Profiles of Galaxy Clusters". In: *Astrophysical Journal* 792.1, 25 (Sept. 2014), p. 25. DOI: 10.1088/0004-637X/792/1/25. arXiv: 1404.4636 [astro-ph.CO].

[356] Newman et al. "The Distribution of Dark Matter Over Three Decades in Radius in the Lensing Cluster Abell 611". In: *Astrophysical Journal* 706.2 (Dec. 2009), pp. 1078–1094. DOI: 10.1088/0004-637X/706/2/1078. arXiv: 0909.3527 [astro-ph.CO].

[357] Newman et al. "The Density Profiles of Massive, Relaxed Galaxy Clusters. I. The Total Density Over Three Decades in Radius". In: *Astrophysical Journal* 765.1, 24 (Mar. 2013), p. 24. DOI: 10.1088/0004-637X/765/1/24. arXiv: 1209.1391 [astro-ph.CO].

[358] Newman et al. "The Density Profiles of Massive, Relaxed Galaxy Clusters. II. Separating Luminous and Dark Matter in Cluster Cores". In: *Astrophysical Journal* 765.1, 25 (Mar. 2013), p. 25. DOI: 10.1088/0004-637X/765/1/25. arXiv: 1209.1392 [astro-ph.CO].

[359] Newton. *Opticks*. Dover Press, 1704.

[360] Niemiec et al. "hybrid-LENSTOOL: a self-consistent algorithm to model galaxy clusters with strong- and weak-lensing simultaneously". In: *Monthly Notices of the Royal Astronomical Society* 493.3 (Apr. 2020), pp. 3331–3340. DOI: 10.1093/mnras/staa473. arXiv: 2002.04635 [astro-ph.CO].

[361] Nietzsche. *Philosophy in the Tragic Age of the Greeks*. Regnery, 1962.

[362] Nieuwenhuizen. "How Zwicky already ruled out modified gravity theories without dark matter". In: *Fortschritte der Physik* 65, 201600050 (Apr. 2017), p. 201600050. DOI: 10.1002/prop.201600050. arXiv: 1610.01543 [astro-ph.CO].

[363] Niikura et al. "Constraints on Earth-mass primordial black holes from OGLE 5-year microlensing events". In: *Physical Review D* 99.8, 083503 (Apr. 2019), p. 083503. DOI: 10.1103/PhysRevD.99.083503. arXiv: 1901.07120 [astro-ph.CO].

[364] Niikura et al. "Microlensing constraints on primordial black holes with Subaru/HSC Andromeda observations". In: *Nature Astronomy* 3 (Apr. 2019), pp. 524–534. DOI: 10.1038/s41550-019-0723-1. arXiv: 1701.02151 [astro-ph.CO].

[365] Nojiri et al. "Modified gravity theories on a nutshell: Inflation, bounce and late-time evolution". In: *Physics Reports* 692 (June 2017), pp. 1–104. DOI: 10.1016/j.physrep.2017.06.001. arXiv: 1705.11098 [gr-qc].

[366] Nojiri and Odintsov. "Modified gravity with negative and positive powers of curvature: Unification of inflation and cosmic acceleration". In: *Physical Review D* 68.12, 123512 (Dec. 2003), p. 123512. DOI: 10.1103/PhysRevD.68.123512. arXiv: hep-th/0307288 [hep-th].

[367] O'Hare. *cajohare/AxionLimits: AxionLimits*. https://cajohare.github.io/AxionLimits/. Version v1.0. July 2020. DOI: 10.5281/zenodo.3932430.

[368] Oguri. *glafic: Software Package for Analyzing Gravitational Lensing*. Astrophysics Source Code Library, record ascl:1010.012. Oct. 2010. ascl: 1010.012.

[369] Oguri and Keeton. "Effects of Triaxiality on the Statistics of Large-Separation Gravitational Lenses". In: *Astrophysical Journal* 610.2 (Aug. 2004), pp. 663–672. DOI: 10.1086/421870. arXiv: astro-ph/0403633 [astro-ph].

[370] Okabe et al. "LoCuSS: The Mass Density Profile of Massive Galaxy Clusters at z = 0.2". In: *The Astrophysical Journal Letters* 769.2, L35 (June 2013), p. L35. DOI: 10.1088/2041-8205/769/2/L35. arXiv: 1302.2728 [astro-ph.CO].

[371] Oke. "Absolute Spectral Energy Distributions for White Dwarfs". In: *The Astrophysical Journal Supplement* 27 (Feb. 1974), p. 21. DOI: 10.1086/190287.

[372] Oort. "Some Problems Concerning the Structure and Dynamics of the Galactic System and the Elliptical Nebulae NGC 3115 and 4494." In: *Astrophysical Journal* 91 (Apr. 1940), p. 273. DOI: 10.1086/144167.

[373] Orban de Xivry and Marshall. "An atlas of predicted exotic gravitational lenses". In: *Monthly Notices of the Royal Astronomical Society* 399.1 (Oct. 2009), pp. 2–20. DOI: 10.1111/j.1365-2966.2009.14925.x. arXiv: 0904.1454 [astro-ph.CO].

[374] Ostriker et al. "The Size and Mass of Galaxies, and the Mass of the Universe". In: *The Astrophysical Journal Letters* 193 (Oct. 1974), p. L1. DOI: 10.1086/181617.

[375] Owen et al. "A Deep Radio Survey of Abell 2125. III. The Cluster Core: Merging and Stripping". In: *The Astronomical Journal* 131.4 (Apr. 2006), pp. 1974–1988. DOI: 10.1086/500573. arXiv: astro-ph/0512613 [astro-ph].

[376] Öztaş. "The effects of a varying cosmological constant on the particle horizon". In: *Monthly Notices of the Royal Astronomical Society* 481.2 (Dec. 2018), pp. 2228–2234. DOI: 10.1093/mnras/sty2375.

[377] Öztaş et al. "The varying cosmological constant: a new approximation to the Friedmann equations and universe model". In: *Monthly Notices of the Royal Astronomical Society* 476.1 (May 2018), pp. 451–458. DOI: 10.1093/mnras/sty221.

[378] Paczyński. "Giant luminous arcs discovered in two clusters of galaxies". In: *Nature* 325.6105 (Feb. 1987), pp. 572–573. DOI: 10.1038/325572a0.

[379] Peccei and Quinn. "CP Conservation in the Presence of Instantons". In: *Phys. Rev. Lett.* 38 (1977), pp. 1440–1443. DOI: 10.1103/PhysRevLett.38.1440.

[380] Peebles. "Large-scale background temperature and mass fluctuations due to scale-invariant primeval perturbations". In: *The Astrophysical Journal Letters* 263 (Dec. 1982), pp. L1–L5. DOI: 10.1086/183911.

[381] Peebles and Yu. "Primeval Adiabatic Perturbation in an Expanding Universe". In: *Astrophysical Journal* 162 (Dec. 1970), p. 815. DOI: 10.1086/150713.

[382] Percival. "Cosmological structure formation in a homogeneous dark energy background". In: *Astronomy & Astrophysics* 443.3 (Dec. 2005), pp. 819–830. DOI: 10.1051/0004-6361:20053637. arXiv: astro-ph/0508156 [astro-ph].

[383] Pérez and Françon. *Optique : fondements et applications avec 200 exercices et problèmes résolus / J.-P. Pérez ; préf. de Maurice Françon*. Enseignement de la physique. Masson, 1996. ISBN: 9782225852138. URL: https://books.google.fr/books?id=QL3oMQEACAAJ.

[384] Perlmutter et al. "Discovery of a supernova explosion at half the age of the Universe". In: *Nature* 391.6662 (Jan. 1998), pp. 51–54. DOI: 10.1038/34124. arXiv: astro-ph/9712212 [astro-ph].

[385] Perlmutter et al. "Measurements of Ω and Λ from 42 High-Redshift Supernovae". In: *Astrophysical Journal* 517.2 (June 1999), pp. 565–586. DOI: 10.1086/307221. arXiv: astro-ph/9812133 [astro-ph].

[386] Peterson and Fabian. "X-ray spectroscopy of cooling clusters". In: *Physics Reports* 427.1 (Apr. 2006), pp. 1–39. DOI: 10.1016/j.physrep.2005.12.007. arXiv: astro-ph/0512549 [astro-ph].

[387] Piqueras et al. *MPDAF - A Python package for the analysis of VLT/MUSE data*. 2017. arXiv: 1710.03554 [astro-ph.IM].

[388] Planck Collaboration. "Planck 2015 results. XIII. Cosmological parameters". In: *Astronomy & Astrophysics* 594, A13 (Sept. 2016), A13. DOI: 10.1051/0004-6361/201525830. arXiv: 1502.01589 [astro-ph.CO].

[389] Planck Collaboration. "Planck 2018 results. VI. Cosmological parameters". In: *Astronomy & Astrophysics* 641, A6 (Sept. 2020), A6. DOI: 10.1051/0004-6361/201833910. arXiv: 1807.06209 [astro-ph.CO].

[390] Planck Collaboration et al. "Planck 2018 results. VIII. Gravitational lensing". In: *Astronomy & Astrophysics* 641, A8 (Sept. 2020), A8. DOI: 10.1051/0004-6361/201833886. arXiv: 1807.06210 [astro-ph.CO].

[391] Poggianti et al. "Jellyfish Galaxy Candidates at Low Redshift". In: *The Astronomical Journal* 151.3, 78 (Mar. 2016), p. 78. DOI: 10.3847/0004-6256/151/3/78. arXiv: 1504.07105 [astro-ph.GA].

[392] Poincaré. "The Milky Way and the Theory of Gases". In: *Popular Astronomy* 14 (Oct. 1906), pp. 475–488.

[393] Pointecouteau et al. "XMM-Newton observation of the relaxed cluster A478: Gas and dark matter distribution from $0.01R_{200}$ to $0.5R_{200}$". In: *Astronomy & Astrophysics* 423 (Aug. 2004), pp. 33–47. DOI: 10.1051/0004-6361:20035856. arXiv: astro-ph/0403596 [astro-ph].

[394] Postman et al. "The Cluster Lensing and Supernova Survey with Hubble: An Overview". In: *The Astrophysical Journal Supplement* 199.2, 25 (Apr. 2012), p. 25. DOI: 10.1088/0067-0049/199/2/25. arXiv: 1106.3328 [astro-ph.CO].

[395] Poulin et al. "A fresh look at linear cosmological constraints on a decaying Dark Matter component". In: *Journal of Cosmology and Astroparticle Physics* 2016.8, 036 (Aug. 2016), p. 036. DOI: 10.1088/1475-7516/2016/08/036. arXiv: 1606.02073 [astro-ph.CO].

[396] Prat et al. "Vacuum energy density measured from cosmological data". In: *Journal of Cosmology and Astroparticle Physics* 2022.6, 015 (June 2022), p. 015. DOI: 10.1088/1475-7516/2022/06/015. arXiv: 2111.08151 [astro-ph.CO].

[397] Press and Schechter. "Formation of Galaxies and Clusters of Galaxies by Self-Similar Gravitational Condensation". In: *Astrophysical Journal* 187 (Feb. 1974), pp. 425–438. DOI: 10.1086/152650.

[398] Rasera et al. "The RayGalGroupSims cosmological simulation suite for the study of relativistic effects: An application to lensing-matter clustering statistics". In: *Astronomy & Astrophysics* 661, A90 (May 2022), A90. DOI: 10.1051/0004-6361/202141908. arXiv: 2111.08745 [astro-ph.CO].

[399] Refsdal. "On the possibility of determining Hubble's parameter and the masses of galaxies from the gravitational lens effect". In: *Monthly Notices of the Royal Astronomical Society* 128 (Jan. 1964), p. 307. DOI: 10.1093/mnras/128.4.307.

[400] Remolina González et al. "An Evaluation of 10 Lensing Models of the Frontier Fields Cluster MACS J0416.1-2403". In: *Astrophysical Journal* 863.1, 60 (Aug. 2018), p. 60. DOI: 10.3847/1538-4357/aacf8e. arXiv: 1807.03291 [astro-ph.CO].

[401] Renzini and Daddi. "Wandering in the Redshift Desert". In: *The Messenger* 137 (Sept. 2009), pp. 41–45.

[402] Rephaeli. "Comptonization Of The Cosmic Microwave Background: The Sunyaev-Zeldovich Effect". In: *Annual Review of Astronomy and Astrophysics* 33 (Jan. 1995), pp. 541–580. DOI: 10.1146/annurev.aa.33.090195.002545.

[403] Retana-Montenegro et al. "Analytical properties of Einasto dark matter haloes". In: *Astronomy & Astrophysics* 540, A70 (Apr. 2012), A70. DOI: 10.1051/0004-6361/201118543. arXiv: 1202.5242 [astro-ph.CO].

[404] Rhodes et al. "Detection of Cosmic Shear with the Hubble Space Telescope Survey Strip". In: *The Astrophysical Journal Letters* 552.2 (May 2001), pp. L85–L88. DOI: 10.1086/320336. arXiv: astro-ph/0101213 [astro-ph].

[405] Richard et al. "Mass and magnification maps for the Hubble Space Telescope Frontier Fields clusters: implications for high-redshift studies". In: *Monthly Notices of the Royal Astronomical Society* 444.1 (Oct. 2014), pp. 268–289. DOI: 10.1093/mnras/stu1395. arXiv: 1405.3303 [astro-ph.CO].

[406] Richard et al. "An atlas of MUSE observations towards twelve massive lensing clusters". In: *Astronomy & Astrophysics* 646, A83 (Feb. 2021), A83. DOI: 10.1051/0004-6361/202039462. arXiv: 2009.09784 [astro-ph.GA].

[407] Riess et al. "Observational Evidence from Supernovae for an Accelerating Universe and a Cosmological Constant". In: *The Astronomical Journal* 116.3 (Sept. 1998), pp. 1009–1038. DOI: 10.1086/300499. arXiv: astro-ph/9805201 [astro-ph].

[408] Riess et al. "A Comprehensive Measurement of the Local Value of the Hubble Constant with 1 km s^{-1} Mpc^{-1} Uncertainty from the Hubble Space Telescope and the SH0ES Team". In: *The Astrophysical Journal Letters* 934.1, L7 (July 2022), p. L7. DOI: 10.3847/2041-8213/ac5c5b. arXiv: 2112.04510 [astro-ph.CO].

[409] Robertson et al. "Self-interacting dark matter scattering rates through cosmic time". In: *Monthly Notices of the Royal Astronomical Society* 453.3 (Nov. 2015), pp. 2267–2276. DOI: 10.1093/mnras/stv1805. arXiv: 1505.02046 [astro-ph.CO].

[410] Robertson et al. "Cosmic particle colliders: simulations of self-interacting dark matter with anisotropic scattering". In: *Monthly Notices of the Royal Astronomical Society* 467.4 (June 2017), pp. 4719–4730. DOI: 10.1093/mnras/stx463. arXiv: 1612.03906 [astro-ph.CO].

[411] Robertson et al. "What does the Bullet Cluster tell us about self-interacting dark matter?" In: *Monthly Notices of the Royal Astronomical Society* 465.1 (Feb. 2017), pp. 569–587. DOI: 10.1093/mnras/stw2670. arXiv: 1605.04307 [astro-ph.CO].

[412] Robertson et al. "Observable tests of self-interacting dark matter in galaxy clusters: cosmological simulations with SIDM and baryons". In: *Monthly Notices of the Royal Astronomical Society* 488.3 (Sept. 2019), pp. 3646–3662. DOI: 10.1093/mnras/stz1815. arXiv: 1810.05649 [astro-ph.CO].

[413] Robertson et al. "The surprising accuracy of isothermal Jeans modelling of self-interacting dark matter density profiles". In: *Monthly Notices of the Royal Astronomical Society* 501.3 (Mar. 2021), pp. 4610–4634. DOI: 10.1093/mnras/staa3954. arXiv: 2009.07844 [astro-ph.CO].

[414] Robertson. "On the Foundations of Relativistic Cosmology". In: *Proceedings of the National Academy of Science* 15.11 (Nov. 1929), pp. 822–829. DOI: 10.1073/pnas.15.11.822.

[415] Robertson. "Kinematics and World-Structure". In: *Astrophysical Journal* 82 (Nov. 1935), p. 284. DOI: 10.1086/143681.

[416] Robertson. "Kinematics and World-Structure II." In: *Astrophysical Journal* 83 (Apr. 1936), p. 187. DOI: 10.1086/143716.

[417] Robertson. "Kinematics and World-Structure III." In: *Astrophysical Journal* 83 (May 1936), p. 257. DOI: 10.1086/143726.

[418] Rubin et al. "Rotational properties of 21 SC galaxies with a large range of luminosities and radii, from NGC 4605 (R=4kpc) to UGC 2885 (R=122kpc)." In: *Astrophysical Journal* 238 (June 1980), pp. 471–487. DOI: 10.1086/158003.

[419] Rubin and Ford. "Rotation of the Andromeda Nebula from a Spectroscopic Survey of Emission Regions". In: *Astrophysical Journal* 159 (Feb. 1970), p. 379. DOI: 10.1086/150317.

[420] Sachs. "Gravitational Waves in General Relativity. VI. The Outgoing Radiation Condition". In: *Proceedings of the Royal Society of London Series A* 264.1318 (Nov. 1961), pp. 309–338. DOI: 10.1098/rspa.1961.0202.

[421] Saha and Williams. "Non-parametric reconstruction of the galaxy lens in PG 1115+080". In: *Monthly Notices of the Royal Astronomical Society* 292.1 (Nov. 1997), pp. 148–156. DOI: 10.1093/mnras/292.1.148. arXiv: astro-ph/9707346 [astro-ph].

[422] Sahu et al. "An Isolated Stellar-mass Black Hole Detected through Astrometric Microlensing". In: *Astrophysical Journal* 933.1, 83 (July 2022), p. 83. DOI: 10.3847/1538-4357/ac739e. arXiv: 2201.13296 [astro-ph.SR].

[423] Salpeter. "The Luminosity Function and Stellar Evolution." In: *Astrophysical Journal* 121 (Jan. 1955), p. 161. DOI: 10.1086/145971.

[424] Salvatier et al. *PyMC3: Python probabilistic programming framework*. Astrophysics Source Code Library, record ascl:1610.016. Oct. 2016. ascl: 1610.016.

[425] Sanders. "The Published Extended Rotation Curves of Spiral Galaxies: Confrontation with Modified Dynamics". In: *Astrophysical Journal* 473 (Dec. 1996), p. 117. DOI: 10.1086/178131. arXiv: astro-ph/9606089 [astro-ph].

[426] Sanders. "Neutrinos as cluster dark matter". In: *Monthly Notices of the Royal Astronomical Society* 380.1 (Sept. 2007), pp. 331–338. DOI: 10.1111/j.1365-2966.2007.12073.x. arXiv: astro-ph/0703590 [astro-ph].

[427] Sarazin. "X-ray emission from clusters of galaxies". In: *Rev. Mod. Phys.* 58 (1 Jan. 1986), pp. 1–115. DOI: 10.1103/RevModPhys.58.1. URL: https://link.aps.org/doi/10.1103/RevModPhys.58.1.

[428] Sarazin. *X-ray emission from clusters of galaxies*. Cambridge Astrophysics Series, Cambridge University Press, 1988., 1988.

[429] Sartoris et al. "CLASH-VLT: a full dynamical reconstruction of the mass profile of Abell S1063 from 1 kpc out to the virial radius". In: *Astronomy & Astrophysics* 637, A34 (May 2020), A34. DOI: 10.1051/0004-6361/202037521. arXiv: 2003.08475 [astro-ph.CO].

[430] Sasaki et al. "Primordial Black Hole Scenario for the Gravitational-Wave Event GW150914". In: *Physical Review Letters* 117.6, 061101 (Aug. 2016), p. 061101. DOI: 10.1103/PhysRevLett.117.061101. arXiv: 1603.08338 [astro-ph.CO].

[431] Schaeffer et al. "The fundamental plane of galaxy clusters." In: *Monthly Notices of the Royal Astronomical Society* 263 (July 1993), pp. L21–L26. DOI: 10.1093/mnras/263.1.L21. arXiv: astro-ph/9304018 [astro-ph].

[432] Schaeffer and Silk. "Cold, Warm, or Hot Dark Matter: Biased Galaxy Formation and Pancakes". In: *Astrophysical Journal* 332 (Sept. 1988), p. 1. DOI: 10.1086/166624.

[433] Scherrer and Turner. "On the relic, cosmic abundance of stable, weakly interacting massive particles". In: *Physical Review D* 33.6 (Mar. 1986), pp. 1585–1589. DOI: 10.1103/PhysRevD.33.1585.

[434] Schneider. "Weak Gravitational Lensing". In: *arXiv e-prints*, astro-ph/0509252 (Sept. 2005), astro–ph/0509252. arXiv: astro-ph/0509252 [astro-ph].

[435] Schneider et al. "Gravitational Lenses". In: *Gravitational Lenses*. Springer Berlin, Heidelberg, 1992. DOI: 10.1007/978-3-662-03758-4.

[436] Schombert et al. "The mass-to-light ratios and the star formation histories of disc galaxies". In: *Monthly Notices of the Royal Astronomical Society* 483.2 (Feb. 2019), pp. 1496–1512. DOI: 10.1093/mnras/sty3223. arXiv: 1811.10579 [astro-ph.GA].

[437] Schombert et al. "Stellar Mass-to-light Ratios: Composite Bulge+Disk Models and the Baryonic Tully-Fisher Relation". In: *The Astronomical Journal* 163.4, 154 (Apr. 2022), p. 154. DOI: 10.3847/1538-3881/ac5249. arXiv: 2202.02290 [astro-ph.GA].

[438] Schöneberg et al. "The H_0 Olympics: A fair ranking of proposed models". In: *Physics Reports* 984 (Oct. 2022), pp. 1–55. DOI: 10.1016/j.physrep.2022.07.001. arXiv: 2107.10291 [astro-ph.CO].

[439] Schuldt et al. "Inner dark matter distribution of the Cosmic Horseshoe (J1148+1930) with gravitational lensing and dynamics". In: *Astronomy & Astrophysics* 631, A40 (Nov. 2019), A40. DOI: 10.1051/0004-6361/201935042. arXiv: 1901.02896 [astro-ph.GA].

[440] Schumann. "Direct detection of WIMP dark matter: concepts and status". In: *Journal of Physics G Nuclear Physics* 46.10 (Oct. 2019), p. 103003. DOI: 10.1088/1361-6471/ab2ea5. arXiv: 1903.03026 [astro-ph.CO].

[441] Seljak and Zaldarriaga. "A Line-of-Sight Integration Approach to Cosmic Microwave Background Anisotropies". In: *Astrophysical Journal* 469 (Oct. 1996), p. 437. DOI: 10.1086/177793. arXiv: astro-ph/9603033 [astro-ph].

[442] Sendra et al. "Enabling non-parametric strong lensing models to derive reliable cluster mass distributions - WSLAP+". In: *Monthly Notices of the Royal Astronomical Society* 437.3 (Jan. 2014), pp. 2642–2651. DOI: 10.1093/mnras/stt2076. arXiv: 1304.2393 [astro-ph.CO].

[443] Sérsic. "Influence of the atmospheric and instrumental dispersion on the brightness distribution in a galaxy". In: *Boletin de la Asociacion Argentina de Astronomia La Plata Argentina* 6 (Feb. 1963), pp. 41–43.

[444] Sharon et al. "Strong Lens Models for 37 Clusters of Galaxies from the SDSS Giant Arcs Survey". In: *The Astrophysical Journal Supplement* 247.1, 12 (Mar. 2020), p. 12. DOI: 10.3847/1538-4365/ab5f13. arXiv: 1904.05940 [astro-ph.GA].

[445] Shitanishi et al. "Thermodynamic profiles of galaxy clusters from a joint X-ray/SZ analysis". In: *Monthly Notices of the Royal Astronomical Society* 481.1 (Nov. 2018), pp. 749–792. DOI: 10.1093/mnras/sty2195. arXiv: 1712.05464 [astro-ph.CO].

[446] Sim et al. "Synthetic light curves and spectra for three-dimensional delayed-detonation models of Type Ia supernovae". In: *Monthly Notices of the Royal Astronomical Society* 436.1 (Nov. 2013), pp. 333–347. DOI: 10.1093/mnras/stt1574. arXiv: 1308.4833 [astro-ph.HE].

[447] Skordis et al. "Large Scale Structure in Bekenstein's Theory of Relativistic Modified Newtonian Dynamics". In: *Physical Review Letters* 96.1, 011301 (Jan. 2006), p. 011301. DOI: 10.1103/PhysRevLett.96.011301. arXiv: astro-ph/0505519 [astro-ph].

[448] Skordis. "TOPICAL REVIEW: The tensor-vector-scalar theory and its cosmology". In: *Classical and Quantum Gravity* 26.14, 143001 (July 2009), p. 143001. DOI: 10.1088/0264-9381/26/14/143001. arXiv: 0903.3602 [astro-ph.CO].

[449] Skordis and Złośnik. "New Relativistic Theory for Modified Newtonian Dynamics". In: *Physical Review Letters* 127.16, 161302 (Oct. 2021), p. 161302. DOI: 10.1103/PhysRevLett.127.161302. arXiv: 2007.00082 [astro-ph.CO].

[450] Smith. "The Mass of the Virgo Cluster". In: *Astrophysical Journal* 83 (Jan. 1936), p. 23. DOI: 10.1086/143697.

[451] Smoot et al. “Structure in the COBE Differential Microwave Radiometer First-Year Maps”. In: *The Astrophysical Journal Letters* 396 (Sept. 1992), p. L1. DOI: 10.1086/186504.

[452] Soldner. “Über die Ablenkung eines Lichtstrahls von seiner geradlinigen Bewegung durch die Attraktion eines Weltkörpers, an welchem er nähe vorbeigeht; von J. Soldner, 1801. (German) [On the deviation of a light ray from its straight-line motion due to the attraction of a heavenly body that it passes by closely]”. German. In: *Annalen der Physik* 65.15 (1921). With a foreword, and considerable editing and abridging, by Philipp Lenard. An English translation of the complete original 1801 article is available in Wikisource., pp. 593–604. ISSN: 0003-3804. DOI: http://dx.doi.org/10.1002%2Fandp.19213701503.

[453] Soucail et al. “A blue ring-like structure in the center of the A 370 cluster of galaxies.” In: *Astronomy & Astrophysics* 172 (Jan. 1987), pp. L14–L16.

[454] Soucail et al. “The giant arc in A 370 : spectroscopic evidence for gravitational lensing from a source at Z=0.724.” In: *Astronomy & Astrophysics* 191 (Feb. 1988), pp. L19–L21.

[455] Srednicki et al. “Calculations of Relic Densities in the Early Universe”. In: *Nucl. Phys. B* 310 (1988). Ed. by Srednicki, p. 693. DOI: 10.1016/0550-3213(88)90099-5.

[456] Steidel et al. “Star-Forming Galaxies in the ’Redshift Desert’”. In: *Multiwavelength Mapping of Galaxy Formation and Evolution*. Ed. by Renzini and Bender. Jan. 2005, p. 169. DOI: 10.1007/10995020_26. arXiv: astro-ph/0401061 [astro-ph].

[457] Steigman. “Cosmology Confronts Particle Physics”. In: *Annual Review of Nuclear and Particle Science* 29.1 (1979), pp. 313–338. DOI: 10.1146/annurev.ns.29.120179.001525.

[458] Steigman et al. “Precise relic WIMP abundance and its impact on searches for dark matter annihilation”. In: *Physical Review D* 86.2, 023506 (July 2012), p. 023506. DOI: 10.1103/PhysRevD.86.023506. arXiv: 1204.3622 [hep-ph].

[459] Steinhardt et al. “The BUFFALO HST Survey”. In: *The Astrophysical Journal Supplement* 247.2, 64 (Apr. 2020), p. 64. DOI: 10.3847/1538-4365/ab75ed. arXiv: 2001.09999 [astro-ph.GA].

[460] Stern et al. “Gaia GraL: Gaia DR2 Gravitational Lens Systems. VI. Spectroscopic Confirmation and Modeling of Quadruply Imaged Lensed Quasars”. In: *Astrophysical Journal* 921.1, 42 (Nov. 2021), p. 42. DOI: 10.3847/1538-4357/ac0f04. arXiv: 2012.10051 [astro-ph.GA].

[461] Stott et al. “The evolution of the red sequence slope in massive galaxy clusters”. In: *Monthly Notices of the Royal Astronomical Society* 394.4 (Apr. 2009), pp. 2098–2108. DOI: 10.1111/j.1365-2966.2009.14477.x. arXiv: 0901.1227 [astro-ph.CO].

[462] Streicher et al. “Sky Subtraction for the MUSE Data Reduction Pipeline”. In: *Astronomical Data Analysis Software and Systems XX*. Ed. by Evans et al. Vol. 442. Astronomical Society of the Pacific Conference Series. July 2011, p. 257.

[463] Sunyaev and Zel’dovich. “Microwave background radiation as a probe of the contemporary structure and history of the universe”. In: *Annual Review of Astronomy and Astrophysics* 18 (Jan. 1980), pp. 537–560. DOI: 10.1146/annurev.aa.18.090180.002541.

[464] Sunyaev and Zel’dovich. “Intergalactic Gas in Clusters of Galaxies, the Microwave Background, and Cosmology”. In: *Astrophysics Space Physics Research* 1 (Jan. 1981), p. 1.

[465] Sunyaev and Zel’dovich. “Small-Scale Fluctuations of Relic Radiation”. In: *Astrophysics and Space Science* 7.1 (Apr. 1970), pp. 3–19. DOI: 10.1007/BF00653471.

[466] Sunyaev and Zel'dovich. "The interaction of matter and radiation in the hot model of the Universe, II". In: *Astrophysics and Space Science* 7.1 (Apr. 1970), pp. 20–30. DOI: 10.1007/BF00653472.

[467] Sutherland and Dopita. "Cooling Functions for Low-Density Astrophysical Plasmas". In: *The Astrophysical Journal Supplement* 88 (Sept. 1993), p. 253. DOI: 10.1086/191823.

[468] Suyu et al. "H0LiCOW - I. H_0 Lenses in COSMOGRAIL's Wellspring: program overview". In: *Monthly Notices of the Royal Astronomical Society* 468.3 (July 2017), pp. 2590–2604. DOI: 10.1093/mnras/stx483. arXiv: 1607.00017 [astro-ph.CO].

[469] Tisserand et al. "Limits on the Macho content of the Galactic Halo from the EROS-2 Survey of the Magellanic Clouds". In: *Astronomy & Astrophysics* 469.2 (July 2007), pp. 387–404. DOI: 10.1051/0004-6361:20066017. arXiv: astro-ph/0607207 [astro-ph].

[470] Tozzi and Norman. "The Evolution of X-Ray Clusters and the Entropy of the Intracluster Medium". In: *Astrophysical Journal* 546.1 (Jan. 2001), pp. 63–84. DOI: 10.1086/318237. arXiv: astro-ph/0003289 [astro-ph].

[471] Treu et al. ""Refsdal" Meets Popper: Comparing Predictions of the Re-appearance of the Multiply Imaged Supernova Behind MACSJ1149.5+2223". In: *Astrophysical Journal* 817.1, 60 (Jan. 2016), p. 60. DOI: 10.3847/0004-637X/817/1/60. arXiv: 1510.05750 [astro-ph.CO].

[472] Treu et al. "The GLASS-JWST Early Release Science Program. I. Survey Design and Release Plans". In: *Astrophysical Journal* 935.2, 110 (Aug. 2022), p. 110. DOI: 10.3847/1538-4357/ac8158. arXiv: 2206.07978 [astro-ph.GA].

[473] Treu. "Strong Lensing by Galaxies". In: *Annual Review of Astronomy and Astrophysics* 48 (Sept. 2010), pp. 87–125. DOI: 10.1146/annurev-astro-081309-130924. arXiv: 1003.5567 [astro-ph.CO].

[474] Tulin and Yu. "Dark matter self-interactions and small scale structure". In: *Physics Reports* 730 (Feb. 2018), pp. 1–57. DOI: 10.1016/j.physrep.2017.11.004. arXiv: 1705.02358 [hep-ph].

[475] Tully and Fisher. "A new method of determining distances to galaxies." In: *Astronomy & Astrophysics* 54 (Feb. 1977), pp. 661–673.

[476] Tyson et al. "Detection of Systematic Gravitational Lens Galaxy Image Alignments: Mapping Dark Matter in Galaxy Clusters". In: *The Astrophysical Journal Letters* 349 (Jan. 1990), p. L1. DOI: 10.1086/185636.

[477] Udalski et al. "Optical Gravitational Lensing Experiment. OGLE-2 – the Second Phase of the OGLE Project". In: *Acta Astronomica* 47 (July 1997), pp. 319–344. arXiv: astro-ph/9710091 [astro-ph].

[478] Umetsu et al. "CLASH: Weak-lensing Shear-and-magnification Analysis of 20 Galaxy Clusters". In: *Astrophysical Journal* 795.2, 163 (Nov. 2014), p. 163. DOI: 10.1088/0004-637X/795/2/163. arXiv: 1404.1375 [astro-ph.CO].

[479] Vanzella et al. "Magnifying the Early Episodes of Star Formation: Super Star Clusters at Cosmological Distances". In: *Astrophysical Journal* 842.1, 47 (June 2017), p. 47. DOI: 10.3847/1538-4357/aa74ae. arXiv: 1703.02044 [astro-ph.GA].

[480] Vikhlinin et al. “Chandra Sample of Nearby Relaxed Galaxy Clusters: Mass, Gas Fraction, and Mass-Temperature Relation”. In: *Astrophysical Journal* 640.2 (Apr. 2006), pp. 691–709. DOI: 10.1086/500288. arXiv: astro-ph/0507092 [astro-ph].

[481] Vogelsberger et al. “ETHOS - an effective theory of structure formation: dark matter physics as a possible explanation of the small-scale CDM problems”. In: *Monthly Notices of the Royal Astronomical Society* 460.2 (Aug. 2016), pp. 1399–1416. DOI: 10.1093/mnras/stw1076. arXiv: 1512.05349 [astro-ph.CO].

[482] Voit. “Tracing cosmic evolution with clusters of galaxies”. In: *Reviews of Modern Physics* 77.1 (Apr. 2005), pp. 207–258. DOI: 10.1103/RevModPhys.77.207. arXiv: astro-ph/0410173 [astro-ph].

[483] Vollmer et al. “NGC 4254: a spiral galaxy entering the Virgo cluster”. In: *Astronomy & Astrophysics* 439.3 (Sept. 2005), pp. 921–933. DOI: 10.1051/0004-6361:20041350. arXiv: astro-ph/0505021 [astro-ph].

[484] Vulcani et al. “The Relevance of Ram Pressure Stripping for the Evolution of Blue Cluster Galaxies as Seen at Optical Wavelengths”. In: *Astrophysical Journal* 927.1, 91 (Mar. 2022), p. 91. DOI: 10.3847/1538-4357/ac4809. arXiv: 2201.02644 [astro-ph.GA].

[485] Wagner. “A Model-Independent Characterisation of Strong Gravitational Lensing by Observables”. In: *Universe* 5.7 (2019). ISSN: 2218-1997. DOI: 10.3390/universe5070177. URL: https://www.mdpi.com/2218-1997/5/7/177.

[486] Walker. “On Milne’s Theory of World-Structure”. In: *Proceedings of the London Mathematical Society* 42 (Jan. 1937), pp. 90–127. DOI: 10.1112/plms/s2-42.1.90.

[487] Walsh et al. “0957+561 A, B: twin quasistellar objects or gravitational lens?” In: *Nature* 279 (May 1979), pp. 381–384. DOI: 10.1038/279381a0.

[488] Wang et al. “Radiative cooling II: effects of density and metallicity”. In: *Monthly Notices of the Royal Astronomical Society* 440.4 (June 2014), pp. 3100–3112. DOI: 10.1093/mnras/stu514. arXiv: 1403.3076 [astro-ph.IM].

[489] Webster. “Gravitational lensing and galaxy shape”. In: *Monthly Notices of the Royal Astronomical Society* 213 (Apr. 1985), pp. 871–888. DOI: 10.1093/mnras/213.4.871.

[490] Weinberg et al. “The Lyman-α Forest as a Cosmological Tool”. In: *The Emergence of Cosmic Structure*. Ed. by Holt and Reynolds. Vol. 666. American Institute of Physics Conference Series. May 2003, pp. 157–169. DOI: 10.1063/1.1581786. arXiv: astro-ph/0301186 [astro-ph].

[491] Wetterich. “Phenomenological parameterization of quintessence”. In: *Physics Letters B* 594.1-2 (July 2004), pp. 17–22. DOI: 10.1016/j.physletb.2004.05.008. arXiv: astro-ph/0403289 [astro-ph].

[492] White and Rees. “Core condensation in heavy halos: a two-stage theory for galaxy formation and clustering.” In: *Monthly Notices of the Royal Astronomical Society* 183 (May 1978), pp. 341–358. DOI: 10.1093/mnras/183.3.341.

[493] White et al. “Clustering in a neutrino-dominated universe”. In: *The Astrophysical Journal Letters* 274 (Nov. 1983), pp. L1–L5. DOI: 10.1086/184139.

[494] Williams and Saha. “Models of the Giant Quadruple Quasar SDSS J1004+4112”. In: *The Astronomical Journal* 128.6 (Dec. 2004), pp. 2631–2641. DOI: 10.1086/426007. arXiv: astro-ph/0409418 [astro-ph].

[495] Williams et al. “Evidence for the line-of-sight structure in the Hubble Frontier Field cluster, MACSJ0717.5+3745”. In: *Monthly Notices of the Royal Astronomical Society* 480.3 (Nov. 2018), pp. 3140–3151. DOI: 10.1093/mnras/sty2088. arXiv: 1711.05265 [astro-ph.CO].

[496] Williamson et al. “A Sunyaev-Zel’dovich-selected Sample of the Most Massive Galaxy Clusters in the 2500 deg^2 South Pole Telescope Survey”. In: *Astrophysical Journal* 738.2, 139 (Sept. 2011), p. 139. DOI: 10.1088/0004-637X/738/2/139. arXiv: 1101.1290 [astro-ph.CO].

[497] Wirtz. “Über die Bewegungen der Nebelflecke”. In: *Astronomische Nachrichten* 206.13 (Mar. 1918), p. 109. DOI: 10.1002/asna.19182061302.

[498] Wittman et al. “Detection of weak gravitational lensing distortions of distant galaxies by cosmic dark matter at large scales”. In: *Nature* 405.6783 (May 2000), pp. 143–148. DOI: 10.1038/35012001. arXiv: astro-ph/0003014 [astro-ph].

[499] Wong et al. “H0LiCOW - XIII. A 2.4 per cent measurement of H_0 from lensed quasars: 5.3σ tension between early- and late-Universe probes”. In: *Monthly Notices of the Royal Astronomical Society* 498.1 (Oct. 2020), pp. 1420–1439. DOI: 10.1093/mnras/stz3094. arXiv: 1907.04869 [astro-ph.CO].

[500] Wyithe et al. “Gravitational Lens Statistics for Generalized NFW Profiles: Parameter Degeneracy and Implications for Self-Interacting Cold Dark Matter”. In: *Astrophysical Journal* 555.1 (July 2001), pp. 504–523. DOI: 10.1086/321437. arXiv: astro-ph/0007354 [astro-ph].

[501] Yahil and Vidal. “The Velocity Distribution of Galaxies in Clusters”. In: *Astrophysical Journal* 214 (June 1977), pp. 347–350. DOI: 10.1086/155257.

[502] Yahil. “The Density Profiles of Rich Clusters of Galaxies”. In: *Astrophysical Journal* 191 (Aug. 1974), pp. 623–632. DOI: 10.1086/153002.

[503] Yèche et al. “Constraints on neutrino masses from Lyman-alpha forest power spectrum with BOSS and XQ-100”. In: *Journal of Cosmology and Astroparticle Physics* 2017.6, 047 (June 2017), p. 047. DOI: 10.1088/1475-7516/2017/06/047. arXiv: 1702.03314 [astro-ph.CO].

[504] Young et al. “The double quasar Q0957+561 A, B: a gravitational lens image formed by a galaxy at z=0.39.” In: *Astrophysical Journal* 241 (Oct. 1980), pp. 507–520. DOI: 10.1086/158365.

[505] Zaroubi et al. “Deprojection of Galaxy Cluster X-Ray, Sunyaev-Zeldovich Temperature Decrement, and Weak-Lensing Mass Maps”. In: *Astrophysical Journal* 561.2 (Nov. 2001), pp. 600–620. DOI: 10.1086/323359. arXiv: astro-ph/0010508 [astro-ph].

[506] Zel’dovich et al. “Giant voids in the Universe”. In: *Nature* 300.5891 (Dec. 1982), pp. 407–413. DOI: 10.1038/300407a0.

[507] Zel’dovich. “Survey of Modern Cosmology”. In: *Advances in Astronomy and Astrophysics* 3 (Jan. 1965), pp. 241–379. DOI: 10.1016/B978-1-4831-9921-4.50011-9.

[508] Zel’dovich. “A hypothesis, unifying the structure and the entropy of the Universe”. In: *Monthly Notices of the Royal Astronomical Society* 160 (Jan. 1972), 1P. DOI: 10.1093/mnras/160.1.1P.

[509] Zel’dovich and Novikov. “The Hypothesis of Cores Retarded during Expansion and the Hot Cosmological Model”. In: *Soviet Ast.* 10 (Feb. 1967), p. 602.

[510] Zhao. "Analytical models for galactic nuclei". In: *Monthly Notices of the Royal Astronomical Society* 278.2 (Jan. 1996), pp. 488–496. DOI: 10.1093/mnras/278.2.488. arXiv: astro-ph/9509122 [astro-ph].

[511] Zitrin et al. "The universal Einstein radius distribution from 10 000 SDSS clusters". In: *Monthly Notices of the Royal Astronomical Society* 423.3 (July 2012), pp. 2308–2324. DOI: 10.1111/j.1365-2966.2012.21041.x. arXiv: 1105.2295 [astro-ph.CO].

[512] Zitrin et al. "CLASH: The Enhanced Lensing Efficiency of the Highly Elongated Merging Cluster MACS J0416.1-2403". In: *The Astrophysical Journal Letters* 762.2, L30 (Jan. 2013), p. L30. DOI: 10.1088/2041-8205/762/2/L30. arXiv: 1211.2797 [astro-ph.CO].

[513] Zitrin et al. "Hubble Space Telescope Combined Strong and Weak Lensing Analysis of the CLASH Sample: Mass and Magnification Models and Systematic Uncertainties". In: *Astrophysical Journal* 801.1, 44 (Mar. 2015), p. 44. DOI: 10.1088/0004-637X/801/1/44. arXiv: 1411.1414 [astro-ph.CO].

[514] Zumalacárregui and Seljak. "Limits on Stellar-Mass Compact Objects as Dark Matter from Gravitational Lensing of Type Ia Supernovae". In: *Physical Review Letters* 121.14, 141101 (Oct. 2018), p. 141101. DOI: 10.1103/PhysRevLett.121.141101. arXiv: 1712.02240 [astro-ph.CO].

[515] Zürcher et al. "Dark energy survey year 3 results: Cosmology with peaks using an emulator approach". In: *Monthly Notices of the Royal Astronomical Society* 511.2 (Apr. 2022), pp. 2075–2104. DOI: 10.1093/mnras/stac078. arXiv: 2110.10135 [astro-ph.CO].

[516] Zwicky. "Die Rotverschiebung von extragalaktischen Nebeln". In: *Helvetica Physica Acta* 6 (Jan. 1933), pp. 110–127.

[517] Zwicky. "Nebulae as Gravitational Lenses". In: *Physical Review* 51.4 (Feb. 1937), pp. 290–290. DOI: 10.1103/PhysRev.51.290.

[518] Zwicky. "On the Masses of Nebulae and of Clusters of Nebulae". In: *Astrophysical Journal* 86 (Oct. 1937), p. 217. DOI: 10.1086/143864.

Appendix A

Remarks on `Lenstool`

As we made an extensive use of `Lenstool`[1] (Kneib et al., 1996; Jullo et al., 2007; Elíasdóttir et al., 2007; Jullo and Kneib, 2009) during this thesis, we make a few additional remarks on its usage.

Joint optimisation `Lenstool`

The version encoded for joint optimisation is new, and therefore still subjected to changes. Benjamin Beauchesne's joint optimisation will be part of the `Lenstool` release version 8. It allows to take *Chandra* count maps as inputs, and to select the gravitational potentials which must be optimised both with gravitational lensing and the X-ray maps. The selected potentials are appointed a certain fraction of gas, which is X-ray brilliant, and the rest is assumed to be dark is X-ray. The electron density simply follows that of the global potential, e.g. dPIE. This also assumes to use a *Chandra* exposure map, which is the product of the X-ray emissivity and the exposure time, as well as a total detector background map, presenting the particle background, soft protons, out-of-time events, etc.

My version utilises a number of these tools, but instead of appointing to the selected potentials a distribution similar to that of the total density, it assumes the potential to be dynamically relaxed, and uses relationship (4.18). This does not require a gas fraction, and distributes the potential according to the selected profile (e.g. dPIE), while appointing the corresponding hydrostatic bijective profile (e.g. `idPIE`). This also assumes the temperature distribution to be polytropic with a varying index (equations 4.1 and 4.2). Although I plan to make more options available, for the moment the temperature profile used to compute the electron density n_e, and therefore the surface brightness S_X is fixed.

My code is available upon request.

Complement to strong lensing optimisations

To complement Chapter 3, we provide here the cornerplots of the lensing optimisations.

[1] https://projets.lam.fr/projects/lenstool/wiki

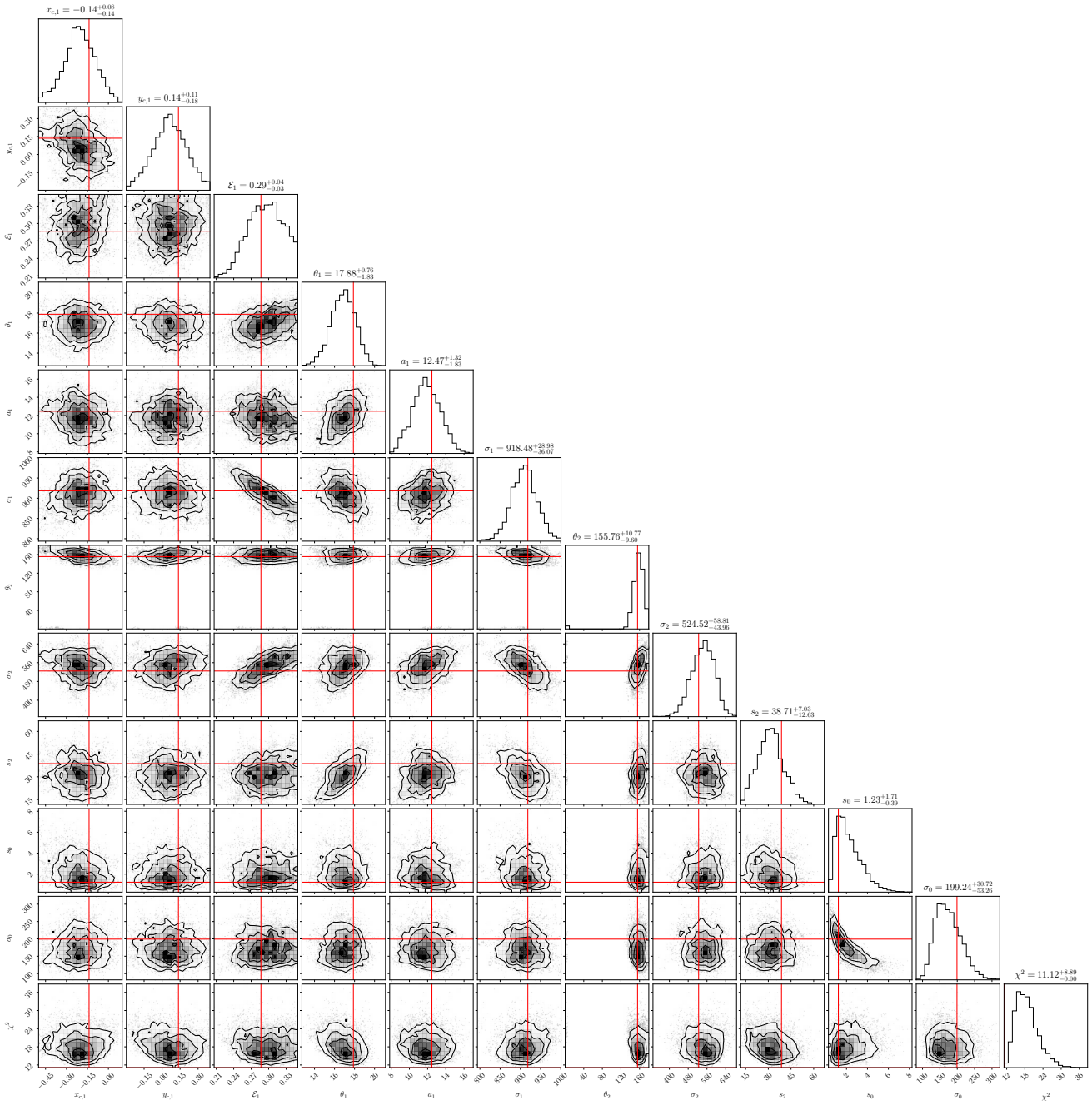

Figure A.1: MACS J0242 `Lenstool` optimisation. Best values are displayed in red.

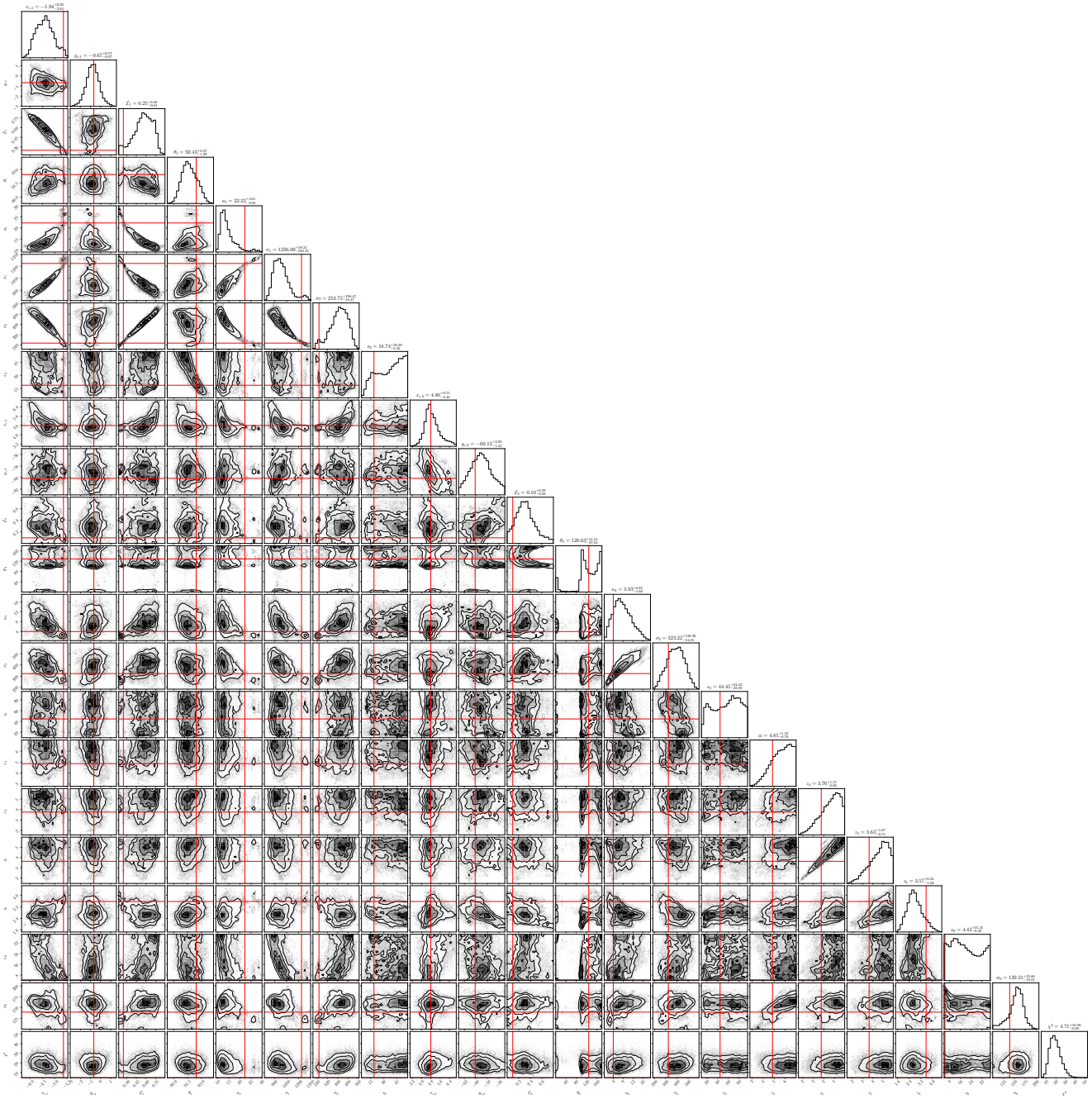

Figure A.2: MACS J0949 `Lenstool` optimisation. Best values are displayed in red.

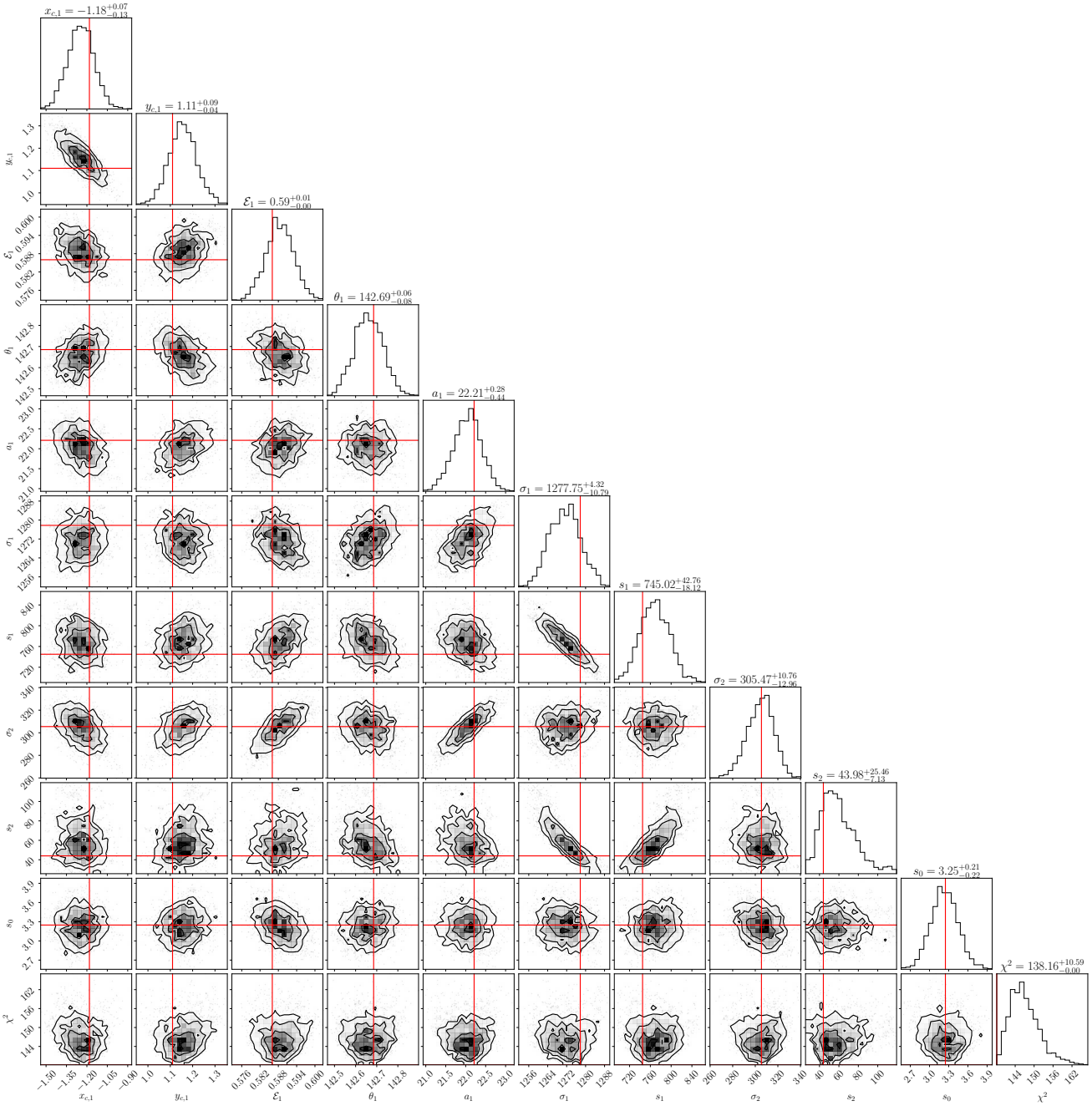

Figure A.3: Abell S1063 `Lenstool` joint optimisation. Best values are displayed in red.

Appendix B

Ellipse and ellipsoid

Ellipse

With a and b respectively semi-major and minor axes of the ellipse, one can define:

$$\begin{aligned} c &= \sqrt{a^2 - b^2}, \\ e &= \frac{c}{a} = \sqrt{1 - \frac{b^2}{a^2}}, \\ \mathcal{E} &= \frac{a^2 - b^2}{a^2 + b^2}, \\ f &= 1 - \sqrt{\frac{1-\mathcal{E}}{1+\mathcal{E}}} = 1 - \frac{b}{a}, \end{aligned} \tag{B.1}$$

where c is the focal radius, e is the eccentricity, f the flattening and $\mathcal{E}$ the ellipticity. `Lenstool`'s parameter is the ellipticity $\mathcal{E}$.

We remind the ellipse equation for a rotation angle θ:

$$\left[\frac{x\cos\theta + y\sin\theta}{a}\right]^2 + \left[\frac{x\sin\theta - y\cos\theta}{b}\right]^2 = 1, \tag{B.2}$$

which, with $R = \sqrt{ab} = (1-f)^{1/2}a = (1-f)^{-1/2}b$, can be rewritten:

$$(1-f)\left[x\cos\theta + y\sin\theta\right]^2 + (1-f)^{-1}\left[x\sin\theta - y\cos\theta\right]^2 = R^2 \tag{B.3}$$

Ellipsoid

In this thesis, we have considered the rotation angle ϕ between the sky plane and the ellipsoid representing the gravitational potential or the electron density distribution n_e to be null. We considered the 'semi-depth' c to be the geometric average of the measured or optimised semi-major and semi-minor axes (a and b respectively).

Here, let us however write the general ellipsoid equation, which we encoded but never utilised, for our models already presented a large number of optimisable parameters. We write the 3D rotation as a composition of rotations along axes (Ox) and (Oz), where x, y are the abscissa and ordinate on the sky plane, and z the Cartesian axis pointing towards the observer. We define

a rotated Cartesian basis (x', y', z') corresponding to the ellipsoid semi-major, semi-minor and semi-depth axes respectively. This rotation $R_{3D}(\theta, \phi) = R_x(\phi) R_z(\theta)$ reads:

$$\begin{bmatrix} x' \\ y' \\ z' \end{bmatrix} = R_{3D}(\theta, \phi) \begin{bmatrix} x \\ y \\ z \end{bmatrix} = \begin{bmatrix} x\cos\theta & -y\sin\theta & \\ x\sin\theta\cos\phi & +y\cos\theta\sin\phi & -z\sin\phi \\ x\sin\theta\sin\phi & +y\cos\theta\sin\phi & +z\cos\phi \end{bmatrix}, \tag{B.4}$$

yielding the coordinates in the initial (x, y, z) basis:

$$\begin{cases} x = & x'\cos\theta & +y'\sin\theta\cos\phi & +z'\sin\theta\sin\phi \\ y = & -x'\sin\theta & +y'\cos\theta\cos\phi & +z'\cos\theta\sin\phi \\ z = & & -y'\sin\phi & +z'\cos\phi \end{cases} \tag{B.5}$$

which, re-indexing the axes notation $(x', y', z') \to (x, y, z)$, re-writes as the ellipsoid equation:

$$\begin{aligned} &\left[\frac{x\cos\theta + y\sin\theta\cos\phi + z\sin\theta\sin\phi}{a}\right]^2 + \\ &\left[\frac{-x\sin\theta + y\cos\theta\cos\phi + z\cos\theta\sin\phi}{b}\right]^2 + \left[\frac{-y\sin\phi + z\cos\phi}{c}\right]^2 = 1. \end{aligned} \tag{B.6}$$

Assuming $c = \sqrt{ab} = R$, we can get the general formula we utilised to compute the X-ray surface brightness and tSZ temperature contrast:

$$\begin{aligned} &(1-f)\left[x\cos\theta\sin\phi + y\sin\theta\cos\phi + z\sin\theta\sin\phi\right]^2 + \\ &(1-f)^{-1}\left[-x\sin\theta + y\cos\theta\cos\phi + z\cos\theta\sin\phi\right]^2 + \left[-y\sin\theta + z\cos\phi\right]^2 = R^2. \end{aligned} \tag{B.7}$$

with f the 2D flattening.

Appendix C

Cluster member catalogues

C.1 MACS J0242

Table C.1: Cluster members in the cluster MACS J0242. Coordinates are in degrees (J2000). We remind that the reference coordinates are (40.649555; −21.540485) deg. Magnitudes are given on the reference band ACS/F606W. All spectroscopic redshift detections are also provided.

Id.	Δ_α	Δ_δ	a	b	θ	Mag.	z
1	0.04387	−0.08964	1.886	1.499	1.83	17.765	0.3130
2	−31.28771	72.89640	1.027	0.396	2.34	19.898	_
3	59.25290	79.37028	0.595	0.593	−14.20	20.055	_
4	82.31906	−5.37408	0.829	0.501	23.90	20.081	_
5	−47.40417	−5.82480	0.731	0.410	−4.47	20.214	_
6	−15.10797	−27.08856	0.639	0.579	15.96	20.300	0.3077
7	41.34414	67.98780	0.856	0.250	78.65	20.403	_
8	−40.03867	−37.35648	0.707	0.458	2.19	20.417	_
9	−34.13604	82.73088	0.490	0.361	−57.11	20.497	_
10	−22.17081	−25.28244	0.461	0.398	47.51	20.579	0.3090
11	−39.45615	−9.50292	0.577	0.497	−18.93	20.606	_
12	−0.17410	−85.03488	0.679	0.541	66.40	20.684	_
13	40.07941	−21.35844	0.538	0.298	18.68	20.717	_
14	−55.06516	2.58516	0.510	0.429	−72.09	20.743	_
15	30.35374	27.99936	0.444	0.397	20.70	20.755	0.3048
16	24.94303	−2.78028	0.557	0.453	57.00	20.794	0.3077
17	−0.58699	−10.44720	0.346	0.307	58.47	20.857	0.3146
18	9.65098	58.14252	0.336	0.299	47.29	20.909	_
19	11.11789	−1.36080	0.363	0.278	49.50	20.990	0.3167
20	−0.83987	28.68948	0.449	0.406	−37.30	20.993	0.3165
22	−59.39017	−47.69208	0.429	0.323	−49.35	21.088	_
23	−83.69362	−5.46732	0.465	0.239	9.16	21.138	_

Id.	Δ_α	Δ_δ	a	b	θ	Mag.	z
24	24.38023	−0.91332	0.376	0.346	50.95	21.171	0.3234
25	−3.26758	61.42392	0.535	0.426	65.98	21.194	_
26	−25.07848	−13.18140	0.597	0.561	14.99	21.220	0.3244
27	49.42146	20.32488	0.355	0.300	−26.05	21.256	_
28	20.14277	11.82312	0.326	0.288	72.53	21.293	0.3174
29	−51.34062	64.83132	0.323	0.205	−73.98	21.303	_
30	46.32957	16.15500	0.365	0.294	−16.58	21.355	_
31	−34.59219	72.73908	0.571	0.266	46.59	21.402	_
32	14.82022	−54.79812	0.419	0.352	−62.09	21.412	_
33	38.41846	−45.74088	0.512	0.491	−80.91	21.450	_
34	11.40405	7.20108	0.381	0.265	−46.09	21.532	0.3093
35	−17.83469	−52.88184	0.346	0.225	−57.40	21.535	_
36	78.72372	36.71964	0.533	0.277	−77.10	21.560	_
37	−14.11504	−19.26612	0.336	0.300	−89.74	21.586	0.3193
38	40.39683	−64.76652	0.681	0.221	−33.36	21.641	_
39	84.37511	26.05680	0.376	0.268	73.13	21.694	_
40	41.15684	2.97792	0.275	0.217	48.32	21.719	_
41	−32.93871	−55.83168	0.357	0.316	69.32	21.729	_
42	−52.63506	−14.39172	0.495	0.255	27.71	21.762	_
48	−32.01421	8.88084	0.272	0.234	−37.14	21.934	_
50	−25.28700	5.56740	0.380	0.317	81.31	22.003	0.3170
51	14.86643	−7.60824	0.507	0.149	26.66	22.008	0.3076
53	1.98569	−2.65572	0.220	0.187	−77.60	22.153	_
56	33.50701	−1.86696	0.253	0.233	−82.69	22.360	_
57	2.63497	−4.57524	0.244	0.192	87.82	22.379	_
58	−6.79773	10.08684	0.310	0.139	−59.26	22.411	0.3050
59	−7.93802	15.31008	0.226	0.213	−77.99	22.419	0.3210
60	−12.35902	19.17144	0.360	0.244	−33.30	22.470	0.3033
61	16.68617	18.10188	0.351	0.248	78.90	22.470	0.3029
62	7.92904	−24.42492	0.192	0.165	88.76	22.496	0.3135
63	−6.87397	27.19584	0.169	0.143	−71.32	22.575	0.3162
65	−6.51462	25.22376	0.444	0.165	−72.61	22.621	0.3107
66	−19.21865	5.58900	0.638	0.211	84.91	22.654	0.7707
67	22.83945	12.06684	0.336	0.214	54.66	22.709	0.3219
68	−1.18204	−4.28328	0.269	0.216	84.02	22.716	_
70	21.90377	10.52964	0.248	0.190	−32.20	22.851	0.3200

C.2 MACS J0949

Table C.2: Cluster members in the MACS J0949. Coordinates are in degrees (J2000). We remind that the reference coordinates are $(\alpha_c; \delta_c) = (147.4659012; 17.1195939)$. Magnitudes are given on the reference band ACS/F814W.

Id.	Δ_α	Δ_δ	a	b	θ	Mag.	z
1	−51.61743	−32.11128	1.344	0.709	45.31	18.761	_
2	0.05608	−0.15120	1.344	0.740	−57.20	18.789	0.3829
3	−17.02960	5.76108	0.704	0.657	60.72	18.875	0.3817
4	51.33490	121.06692	0.742	0.529	50.52	18.970	_
5	15.93092	−74.92248	0.812	0.526	−24.40	19.054	_
6	40.92259	−16.74180	0.569	0.543	12.07	19.451	_
7	74.12377	−59.79348	0.554	0.385	55.49	19.524	_
8	−73.52793	−48.20544	0.549	0.340	−50.73	19.597	_
9	7.15976	−8.94204	0.647	0.482	43.03	19.608	0.3769
10	11.53996	8.03088	0.568	0.398	−74.03	19.657	0.3668
11	−9.82565	27.00900	0.434	0.362	−37.60	19.665	0.3805
12	85.20617	−42.97716	0.735	0.612	−3.76	19.696	_
13	27.26681	−56.00556	0.749	0.242	−60.37	19.722	_
14	24.32678	73.21680	0.510	0.244	−55.85	19.739	_
15	−56.04044	−12.03984	0.562	0.446	−50.93	19.752	_
16	33.74892	59.50152	0.551	0.317	33.76	19.787	_
17	29.94434	15.16320	0.449	0.333	−72.15	19.877	0.3898
18	−6.84024	48.24144	0.566	0.288	79.42	19.895	_
19	25.08897	104.47272	0.460	0.363	1.77	19.960	_
20	24.52177	112.42044	0.203	0.190	−81.17	20.026	_
21	16.30727	−1.08324	0.463	0.423	−37.71	20.034	0.3803
22	13.72939	−88.98840	0.508	0.296	33.13	20.070	_
23	33.19802	110.46996	0.614	0.182	52.14	20.070	_
24	19.33229	−41.25240	0.374	0.314	3.04	20.081	_
25	5.75828	8.32824	0.584	0.491	−7.41	20.085	0.3761
26	4.64266	−58.25988	0.489	0.417	68.21	20.124	_
27	−60.56020	−7.13520	0.468	0.211	−55.25	20.161	_
28	5.60646	19.56204	0.448	0.263	−16.39	20.201	0.3790
29	49.28402	116.82360	0.796	0.479	66.13	20.203	_
30	−54.49984	−72.26388	0.651	0.172	−40.57	20.210	_
31	−68.13534	49.03092	0.559	0.319	−14.47	20.250	_
32	14.25561	67.99500	0.543	0.188	−9.72	20.262	_
33	104.92209	−44.80956	0.298	0.237	−33.23	20.263	_
34	103.70582	−29.44332	0.528	0.384	−17.67	20.295	_
35	50.20634	−8.07876	0.407	0.202	−4.21	20.298	_
36	−19.94000	−9.47412	0.478	0.391	16.52	20.323	0.3777
37	−4.48016	59.21784	0.655	0.481	−12.16	20.370	_
38	10.34176	−43.63236	0.438	0.209	15.68	20.385	_

Id.	Δ_α	Δ_δ	a	b	θ	Mag.	z
39	−50.29355	−65.29104	0.425	0.395	28.26	20.477	_
40	−11.61759	−83.76048	0.554	0.221	−33.02	20.488	_
41	65.40625	20.37528	0.467	0.206	53.27	20.499	_
42	2.52367	−17.68032	0.388	0.287	34.30	20.554	0.3723
43	−0.03268	43.45344	0.457	0.199	−0.64	20.564	_
44	−2.06923	73.03680	0.343	0.312	−13.14	20.582	_
45	−66.29775	−64.04112	0.358	0.274	−44.86	20.604	_
46	−101.51854	43.57944	0.491	0.266	−79.50	20.608	_
47	−4.48946	−96.53760	0.372	0.345	−56.17	20.624	_
48	12.93950	63.32760	0.474	0.289	43.20	20.664	_
49	38.57323	−80.23104	0.341	0.312	86.11	20.683	_
50	−50.77367	−89.72424	0.447	0.299	−74.36	20.699	_
51	51.12182	123.06888	0.387	0.361	−1.15	20.704	_
52	55.43051	3.60360	0.328	0.192	44.40	20.706	_
53	37.08662	3.14352	0.520	0.295	21.99	20.727	_
54	−3.03000	8.37720	0.505	0.347	0.83	20.728	0.4008
55	70.93924	−29.88468	0.582	0.189	−7.49	20.736	_
56	18.45968	−52.14672	0.396	0.260	−26.26	20.739	_
57	−22.23491	29.79684	0.318	0.302	−46.68	20.750	_
58	30.39314	41.69880	0.390	0.204	43.66	20.771	_
59	−87.36850	13.62384	0.469	0.209	74.10	20.776	_
60	33.45060	81.29988	0.359	0.252	69.68	20.796	_
61	−18.03311	8.66700	0.328	0.258	0.19	20.806	0.3947
62	5.07298	4.00500	0.239	0.144	24.73	20.825	0.3868
63	−86.52234	68.09400	0.320	0.173	55.31	20.857	_
64	−8.34237	10.57536	0.313	0.239	−58.79	20.882	0.3755
65	55.52461	−60.73704	0.116	0.107	−55.81	20.920	_
66	−68.16216	−48.80628	0.305	0.209	−5.35	20.938	_
67	24.37872	64.05912	0.099	0.092	−56.48	20.948	_
68	23.31981	−4.43124	0.325	0.159	−26.71	20.949	0.3750
69	36.73395	−90.62460	0.259	0.233	−30.59	20.954	_
70	−36.56565	23.44140	0.263	0.223	27.12	20.957	_
71	−29.47979	−84.44016	0.324	0.238	−87.63	20.994	_
72	29.54724	9.01836	0.481	0.413	−38.32	21.022	_
73	−73.15157	4.80348	0.454	0.214	−79.83	21.025	_
74	59.57524	100.30500	0.958	0.264	−45.31	21.036	_
75	5.59924	−22.22244	0.294	0.232	40.00	21.040	0.3768
76	−2.41075	96.76404	0.330	0.279	−66.25	21.049	_
77	−29.60639	−52.55928	0.285	0.257	44.90	21.049	_
78	−61.62315	24.67584	0.414	0.231	−75.93	21.067	_
79	−13.18293	−17.14932	0.404	0.360	31.45	21.103	0.3763
80	−64.05279	−47.85480	0.282	0.271	88.48	21.104	_
81	12.85033	−58.54752	0.323	0.255	−40.67	21.110	_
82	−22.09321	70.20360	0.394	0.182	−13.76	21.185	_
83	−34.55653	−10.98864	0.322	0.190	−35.57	21.187	_

Id.	Δ_α	Δ_δ	a	b	θ	Mag.	z
84	−47.51160	−21.10932	0.322	0.157	−77.18	21.187	_
85	−28.95310	24.32196	0.325	0.288	−27.66	21.195	0.3993
86	−0.25665	33.03360	0.385	0.225	−29.29	21.248	_
87	10.29380	9.80928	0.357	0.167	−50.43	21.262	0.3897
88	42.85177	52.38720	0.465	0.230	61.20	21.267	_
89	80.02137	−57.51540	0.995	0.209	32.75	21.284	_
90	−56.35137	25.89120	0.442	0.276	23.70	21.284	_
91	3.78273	−45.40248	0.298	0.256	24.62	21.285	_
92	3.87447	−22.83768	0.404	0.243	−22.21	21.291	0.3921
93	−49.14742	−103.03560	0.324	0.183	−20.18	21.293	_
94	29.81464	22.83480	0.336	0.309	73.50	21.298	0.3998
95	16.56800	70.90596	0.373	0.260	−24.35	21.311	_
96	−5.76110	−39.75552	0.334	0.170	65.63	21.315	_
98	−13.43541	−65.79180	0.238	0.167	21.33	21.326	_
99	−1.57935	−69.75432	0.327	0.186	−29.30	21.354	_
100	−51.47603	−59.10228	0.277	0.223	32.08	21.358	_
101	−6.44151	12.79800	0.267	0.247	−2.31	21.382	0.3923
102	33.53576	−4.85784	0.371	0.235	−16.49	21.393	_
103	−42.91185	−63.86292	0.633	0.306	−32.49	21.404	_
104	−0.56465	−73.89864	0.343	0.277	−58.84	21.450	_
105	95.79313	1.15992	0.291	0.211	72.43	21.491	_
106	−59.36306	−55.65168	0.329	0.259	−59.56	21.491	_
107	−6.36500	−9.63324	0.284	0.241	14.30	21.499	_
108	−6.13874	14.56164	0.264	0.245	−81.20	21.505	0.3909
109	78.39978	−75.55032	0.309	0.204	−33.85	21.511	_
110	−47.06945	−99.00540	0.241	0.216	−36.06	21.541	_
111	−28.64775	−35.53380	0.284	0.218	−86.60	21.544	_
112	59.93640	100.70028	0.946	0.225	−45.15	21.567	_
113	−85.19586	−37.62540	0.403	0.116	33.91	21.587	_
114	−42.03407	46.26396	0.318	0.241	65.32	21.602	_
115	−56.37288	15.61032	0.309	0.157	58.03	21.609	_
116	−53.88211	44.36280	0.325	0.225	31.76	21.611	_
117	30.54773	69.21360	0.421	0.190	−27.21	21.630	_
118	−3.23513	64.50228	0.286	0.268	−26.50	21.634	_
119	−10.61614	−31.64004	0.291	0.255	47.72	21.646	_
120	−46.55703	65.13192	0.318	0.273	−6.04	21.664	_
121	−20.11013	19.41552	0.327	0.236	−30.53	21.668	_
122	51.45713	83.83860	0.288	0.194	−37.34	21.669	_
123	−59.43107	11.57940	0.299	0.142	24.40	21.678	_
124	−86.73891	64.02780	0.220	0.174	20.74	21.699	_
125	−28.70804	66.92796	0.253	0.171	−86.74	21.701	_
126	−102.98287	11.32200	0.234	0.185	−14.17	21.706	_
127	−28.87220	17.51400	0.434	0.172	−18.58	21.717	0.3786
128	11.88572	−30.32892	0.201	0.188	80.21	21.739	0.3983
129	−21.84404	31.52196	0.589	0.336	49.20	21.854	_

Id.	Δ_α	Δ_δ	a	b	θ	Mag.	z
130	12.70239	−59.13252	0.281	0.245	−46.42	21.878	_
131	−41.84037	7.94592	0.317	0.164	−76.02	21.883	_
132	−3.44624	−114.37884	0.271	0.231	70.43	21.899	_
133	20.82725	−29.35332	0.289	0.215	−55.11	21.901	0.3786
134	−64.49190	−19.98756	0.227	0.208	−41.19	21.903	_
135	−3.01978	−13.81428	0.311	0.180	63.71	21.905	0.3760
136	−62.01179	−18.64764	0.353	0.254	−33.15	21.916	_
137	−11.83679	−45.95580	0.241	0.176	−21.76	21.919	_
138	111.65538	−41.52672	0.402	0.140	−70.00	21.924	_
139	−50.77885	−17.18388	0.318	0.230	12.49	21.947	_
140	−8.26107	−63.90792	0.258	0.138	40.30	21.970	_
141	36.10611	9.03204	0.241	0.175	−66.63	21.973	_
142	0.84901	83.48832	0.290	0.210	−55.59	21.973	_
143	45.69594	−35.43696	0.319	0.305	−1.29	21.974	_
144	−38.23846	27.71460	0.350	0.175	84.83	21.980	_
145	−29.08770	22.40712	0.249	0.225	−33.31	22.012	0.3992
146	16.27442	−8.17848	0.165	0.142	−82.29	22.048	0.3801
147	3.08895	−15.97680	0.190	0.158	66.92	22.056	_
148	−2.55300	−40.60008	0.243	0.190	−81.39	22.066	_
149	117.41358	−52.37676	0.262	0.225	−85.33	22.117	_
150	8.14705	59.33592	0.230	0.152	23.16	22.124	_
151	46.84910	−33.16608	0.257	0.235	−38.93	22.127	_
152	−46.18349	69.23088	0.300	0.179	46.19	22.144	_
153	76.41350	−25.51752	0.212	0.178	−26.42	22.155	_
154	−54.19009	0.94104	0.274	0.176	−27.70	22.160	_
155	16.58134	46.17684	0.306	0.276	−29.47	22.171	_
156	−73.00179	−25.59960	0.650	0.174	−77.84	22.173	_
157	5.31037	−83.45880	0.212	0.151	−11.10	22.175	_
158	−59.18823	11.01528	0.142	0.119	47.19	22.177	_
160	100.33845	21.17556	0.318	0.208	−13.11	22.247	_
161	−12.83284	−7.65072	0.255	0.184	60.53	22.258	0.3728
162	18.20111	−45.80784	0.228	0.218	16.32	22.261	_
163	70.80831	82.48968	0.228	0.205	61.79	22.266	_
164	102.89882	41.11488	0.223	0.182	−26.34	22.279	_
165	−55.39788	−47.01996	0.374	0.176	−29.92	22.304	_
166	70.57226	−14.82048	0.231	0.208	3.54	22.309	_
167	−20.02531	−31.88664	0.708	0.123	−15.17	22.325	0.3941
168	70.02888	−20.29824	0.186	0.146	−55.01	22.352	_
169	−30.82320	−71.05104	0.281	0.150	−61.70	22.353	_
170	48.09220	−18.61056	0.236	0.197	−77.08	22.356	_
171	−25.81050	37.58976	0.285	0.140	13.69	22.358	_
172	−60.41394	−14.42124	0.152	0.123	−15.88	22.376	_

Id.	Δ_α	Δ_δ	a	b	θ	Mag.	z
173	−62.98513	−62.50284	0.394	0.108	−70.37	22.394	_
174	46.78599	32.90904	0.189	0.181	−20.23	22.427	_
175	−41.14319	21.51684	0.249	0.156	38.87	22.449	_
176	65.62456	50.03352	0.351	0.112	86.01	22.488	_
179	−21.34857	−20.60712	0.147	0.090	63.35	24.093	0.4061

C.3 Abell S1063

Table C.3: Cluster members in the Abell S1063. Coordinates are in degrees (J2000). We remind that the reference coordinates are $(\alpha_c; \delta_c) = (342.183210; -44.530878)$. Magnitudes are given on the reference band WFC3/F160W.

Id.	Δ_α	Δ_δ	a	b	θ	Mag.
1	0.00026	−0.01692	1.951	1.186	−33.47	17.181
2	−73.50677	73.45764	0.959	0.860	−85.60	17.501
3	−84.68872	45.05652	1.149	0.888	6.68	17.632
4	−59.16584	67.77432	1.079	0.778	−30.14	17.723
5	79.68825	33.13620	1.019	0.965	24.68	17.727
6	−56.41634	49.41828	1.408	0.382	47.38	17.951
8	−103.05195	34.47468	1.113	0.524	−82.23	18.229
10	−31.59329	17.58564	0.704	0.641	−83.11	18.344
11	15.83704	−21.84876	0.773	0.639	−36.26	18.396
12	−50.85622	57.39408	0.916	0.559	25.37	18.398
13	−48.18608	−33.77196	1.021	0.813	−32.48	18.487
14	94.65192	−0.30132	0.926	0.319	37.54	18.544
15	−95.04852	46.92348	0.805	0.329	−40.68	18.569
16	−5.61608	44.14284	0.731	0.413	53.85	18.603
17	−95.83921	17.87328	0.721	0.597	6.72	18.653
18	−114.77643	−15.66216	0.836	0.339	−13.81	18.663
19	−82.07152	44.38656	0.694	0.467	−0.62	18.675
20	−72.58733	19.01016	0.872	0.500	43.57	18.697
21	−97.86243	39.34260	0.644	0.498	−19.17	18.767
22	20.78128	73.31652	0.704	0.595	28.30	18.799
23	−75.70292	69.55488	0.515	0.280	−5.26	18.822
24	−25.88915	47.00880	0.532	0.353	−33.87	18.826
25	−0.85075	2.89872	0.640	0.524	20.17	18.861
26	28.05274	−114.51348	0.613	0.511	27.81	18.897
27	21.53388	109.72332	0.642	0.527	−9.18	18.903
28	53.43548	63.04140	0.528	0.465	32.31	18.944
29	7.69799	62.60184	0.618	0.397	−18.99	18.956
30	−83.25585	44.96112	0.427	0.242	60.61	18.963
31	19.89016	−16.32096	0.968	0.507	−74.91	18.966
32	7.49196	108.91152	0.487	0.357	74.23	18.989
33	−12.62747	17.73144	0.472	0.312	61.42	19.003
34	70.47740	−54.12168	0.557	0.501	75.17	19.017
35	−78.73488	37.00584	0.532	0.490	75.66	19.050
36	−45.45542	111.94416	0.741	0.372	−35.35	19.088
37	−20.45901	−93.20940	1.339	0.784	49.83	19.107

Id.	Δ_α	Δ_δ	a	b	θ	Mag.
38	73.26637	−30.43440	0.527	0.422	−51.22	19.126
39	16.06518	−11.63628	0.560	0.506	−33.67	19.185
40	−12.65334	4.18212	0.430	0.316	45.66	19.186
41	−70.36003	74.76912	0.567	0.247	−34.70	19.186
42	−105.21103	−11.73744	0.556	0.460	89.17	19.234
43	54.68573	3.23496	1.365	0.580	41.26	19.298
44	−2.99080	−19.13904	0.655	0.418	−4.87	19.313
45	0.71755	1.51092	0.316	0.163	−15.24	19.332
46	55.82809	−89.94852	0.609	0.284	33.15	19.347
47	53.22051	63.62388	0.457	0.243	−39.20	19.355
48	−104.65602	53.19144	0.347	0.280	38.94	19.367
49	10.71823	−6.84036	0.313	0.263	53.55	19.429
50	3.78146	68.73876	0.625	0.464	37.71	19.444
51	−50.12965	39.81996	0.441	0.436	43.32	19.452
52	4.80665	40.24836	0.669	0.403	59.87	19.465
53	−117.81444	−17.13384	0.413	0.365	−17.42	19.476
55	−25.89636	16.01496	0.454	0.395	−89.61	19.520
56	66.80776	−6.46236	0.561	0.377	−63.29	19.535
57	−36.08311	27.39708	0.427	0.336	−4.50	19.547
58	−15.31705	4.85388	0.489	0.453	84.82	19.549
59	−64.87707	18.93348	0.449	0.347	−72.22	19.566
60	−43.85304	20.44260	0.678	0.416	−80.20	19.607
61	−71.87360	−11.60388	0.465	0.314	86.20	19.625
62	−14.68554	−34.23240	0.805	0.448	19.30	19.627
63	1.19154	−1.76112	0.325	0.284	−9.40	19.635
64	−29.59715	135.01512	1.096	0.432	−64.22	19.648
65	−19.25385	104.92740	0.466	0.261	11.02	19.680
66	−38.70961	−62.85636	0.556	0.302	−27.93	19.690
67	−2.16999	14.24268	0.409	0.273	−39.08	19.709
68	34.27382	−16.79076	0.522	0.323	81.48	19.729
69	60.25067	26.45496	0.419	0.287	−66.81	19.729
70	106.08774	17.87436	0.626	0.281	−27.58	19.737
71	−16.16121	−37.46628	0.470	0.364	44.39	19.742
72	29.37409	−34.80264	0.712	0.482	85.33	19.744
73	−53.83217	20.30076	0.578	0.326	0.03	19.759
74	87.98466	27.42984	0.513	0.493	29.41	19.774
75	−55.02077	33.08508	0.781	0.572	−81.68	19.802
76	−41.52380	−52.42032	0.436	0.398	5.88	19.836
77	20.79566	−99.97380	0.356	0.318	−75.28	19.840
78	89.87311	−26.72172	0.479	0.222	34.07	19.862
79	−11.95371	−90.87624	0.370	0.297	−26.34	19.868
80	17.05632	80.85276	0.564	0.291	30.23	19.877

Id.	Δ_α	Δ_δ	a	b	θ	Mag.
81	17.32352	−10.01088	0.279	0.214	30.37	19.894
82	−32.32067	52.68528	0.453	0.396	29.01	19.934
83	−6.57942	−13.31028	0.533	0.331	−52.17	19.945
84	93.48535	6.21576	0.573	0.361	26.54	19.950
85	87.59111	−89.42688	0.243	0.199	−33.49	19.998
86	−64.50136	−59.32476	0.324	0.229	66.52	20.033
87	16.01207	−82.00188	0.820	0.353	23.58	20.037
88	−8.82538	30.26052	0.436	0.346	72.12	20.042
89	−38.84529	−64.41084	0.945	0.369	48.25	20.047
90	−9.16745	11.04372	0.345	0.307	−43.19	20.107
91	−9.55529	−16.17768	0.449	0.401	34.24	20.114
92	13.53684	−5.43528	0.329	0.243	−0.30	20.123
93	−3.29474	−44.31132	0.595	0.529	55.37	20.129
94	82.02316	−13.60368	0.355	0.266	81.64	20.183
95	−8.84417	−35.56296	0.419	0.368	74.26	20.193
96	−20.86979	−12.40236	0.346	0.313	58.67	20.259
97	55.36634	−46.29168	0.470	0.353	−77.89	20.288
98	−82.87829	52.84368	0.481	0.469	0.92	20.293
99	−66.31073	48.90924	0.418	0.273	23.11	20.303
100	−75.93194	78.86736	0.422	0.391	−64.55	20.322
102	13.49566	24.54048	0.578	0.350	35.85	20.389
103	2.98391	−34.06392	0.460	0.417	−64.38	20.439
104	16.30159	−23.94288	0.356	0.320	−71.58	20.460
105	21.27532	−11.71980	0.456	0.365	64.67	20.481
107	42.59248	−14.19588	0.391	0.320	39.98	20.515
108	−86.21546	−24.97824	0.510	0.285	−31.87	20.531
109	−24.91181	−25.29396	0.544	0.454	25.17	20.549
110	−25.23586	−25.57476	0.544	0.454	25.17	20.549
111	−106.98539	28.19340	0.353	0.321	2.02	20.609
112	−62.02540	42.54804	0.497	0.451	8.34	20.616
113	85.59569	−24.53148	0.376	0.342	−28.77	20.632
114	−6.19941	−55.50156	0.605	0.482	−15.51	20.634
115	−105.96424	30.99132	0.418	0.159	22.13	20.698
116	9.83395	10.69452	0.597	0.344	13.73	20.711
117	38.94071	−72.81900	0.402	0.360	−38.60	20.720
118	−72.53029	33.67260	1.051	0.356	72.45	20.774
119	24.44669	−6.82092	0.426	0.293	−67.08	20.776
120	−76.69812	22.26096	0.365	0.329	−3.62	20.843
121	17.35026	−9.37116	0.170	0.150	9.24	20.854
122	−70.42242	−35.24868	0.541	0.421	−86.81	20.856
123	−21.43600	−8.86572	0.299	0.289	−73.58	20.868
124	−96.67903	11.28996	0.109	0.103	57.95	20.880
125	−34.30740	−32.70600	0.519	0.513	21.98	20.884

Id.	Δ_α	Δ_δ	a	b	θ	Mag.
126	−115.16907	8.20116	0.355	0.265	−32.09	20.914
127	−28.33630	−58.54896	0.460	0.320	14.47	20.934
128	−60.74929	−70.34184	0.327	0.310	−14.66	20.935
129	−24.53556	−85.06584	0.213	0.158	−18.08	20.948
130	1.70930	14.41908	0.298	0.278	55.71	20.957
131	−6.40614	1.34532	1.127	0.962	−74.81	20.972
132	62.36088	75.32784	0.259	0.222	−2.87	20.973
133	85.62011	50.36508	0.840	0.423	48.81	20.990
134	−24.63489	57.34368	0.778	0.445	26.70	21.022
135	−43.34367	53.21736	0.440	0.328	64.06	21.034
136	−37.45738	−99.98460	0.526	0.393	55.15	21.040
137	11.03156	22.18032	0.332	0.316	30.25	21.043
138	−14.88919	22.29012	0.467	0.443	−59.40	21.089
139	−15.72414	−21.74256	0.418	0.383	−79.72	21.130
140	−46.61260	36.41004	0.343	0.327	6.91	21.152
141	24.67390	−125.76240	0.302	0.284	−33.40	21.173
142	−74.43680	38.50776	0.247	0.221	20.39	21.199
143	22.35894	6.75468	0.238	0.213	66.63	21.200
144	−14.15855	−48.72060	0.510	0.424	65.88	21.223
145	−14.51182	−49.14468	0.510	0.424	65.88	21.223
146	38.39822	−20.41524	0.274	0.269	−30.00	21.235
147	−3.08673	47.63988	0.450	0.364	71.21	21.249
148	80.53408	−51.49296	0.267	0.243	−5.89	21.258
149	0.35491	−8.00208	0.177	0.172	63.01	21.282
150	−37.53433	120.79080	0.514	0.381	50.83	21.287
151	−82.17038	51.69996	0.234	0.203	5.45	21.343
152	24.11621	22.66524	0.368	0.352	43.17	21.346
153	−49.40459	66.24828	0.314	0.285	−42.60	21.358
154	11.75273	−56.41524	0.366	0.337	−85.98	21.389
155	−22.18906	4.43592	0.297	0.269	−11.56	21.413
156	5.69239	−66.42252	0.382	0.304	47.50	21.417
157	5.69245	−130.60044	0.410	0.354	−73.99	21.420
158	−2.50264	38.13984	0.612	0.418	57.92	21.436
159	−54.52222	7.08300	0.415	0.377	−10.01	21.440
160	−63.84010	78.60024	0.263	0.257	47.03	21.446
161	−0.93054	111.66264	0.297	0.264	69.63	21.447
162	−55.04218	−17.35560	0.411	0.392	−33.00	21.451
164	−26.87761	44.51364	0.374	0.350	69.49	21.488
165	−51.60738	−51.88644	0.481	0.248	28.89	21.498
166	69.73238	39.40056	0.405	0.232	27.36	21.515
167	−6.43179	17.54568	0.324	0.248	3.08	21.521
168	9.04615	−111.61440	0.106	0.098	58.28	21.538
169	−67.56389	43.27056	0.388	0.350	−30.10	21.562
170	40.21828	−103.68360	0.519	0.173	21.99	21.568

Id.	Δ_α	Δ_δ	a	b	θ	Mag.
171	29.78927	−31.07484	0.453	0.264	−43.51	21.624
172	44.52599	10.71072	0.472	0.384	−15.92	21.640
173	−53.63316	−22.21236	0.450	0.417	−63.79	21.655
174	−34.60073	6.43788	1.295	0.701	−48.27	21.657
175	−6.00089	−8.33256	0.256	0.239	52.83	21.664
176	26.84415	−52.39044	0.107	0.100	54.91	21.692
177	5.45466	6.04332	0.251	0.205	48.93	21.695
178	−42.76948	129.03408	0.349	0.301	−53.80	21.698
179	52.54440	−26.22312	0.622	0.409	29.75	21.708
180	99.65344	35.83656	0.292	0.257	26.37	21.708
181	−66.52217	62.42832	0.355	0.296	−4.64	21.710
182	−88.40043	−35.34984	0.268	0.173	−31.16	21.747
183	−12.57671	−6.90444	0.400	0.366	58.66	21.762
184	−43.51454	13.17816	0.438	0.313	−58.53	21.796
185	−17.46932	24.34644	0.326	0.284	−30.91	21.801
186	−83.20047	−35.71884	0.412	0.370	−11.60	21.810
187	8.95379	61.98372	0.222	0.178	−59.24	21.818
188	−9.37000	−10.86300	0.462	0.407	−56.62	21.829
189	−103.98423	−8.42184	0.561	0.410	44.42	21.835
190	−8.78481	−0.73512	0.215	0.202	−8.69	21.843
191	−38.49973	12.50316	0.386	0.345	−16.28	21.846
192	28.34327	−60.12540	0.502	0.290	−3.86	21.871
193	0.03053	−46.71180	0.590	0.365	−53.55	21.873
194	4.35192	107.22600	0.392	0.158	85.71	21.909
195	−61.64481	70.77240	0.495	0.270	−18.92	21.963
196	73.18975	−40.40280	0.271	0.214	−78.04	21.968
197	−31.36729	−5.66784	0.395	0.331	52.65	22.019
198	−77.32342	40.56228	0.274	0.187	−42.43	22.046
199	−5.49008	64.93176	0.304	0.215	68.67	22.065
200	−24.32868	39.98988	0.367	0.318	−7.29	22.102
201	−14.28894	−25.34544	0.314	0.263	−7.87	22.133
202	6.27251	−73.28808	0.386	0.199	30.10	22.152
203	83.21819	50.98392	0.403	0.253	50.09	22.159
204	−99.82461	32.53068	0.419	0.258	65.12	22.162
205	18.79764	53.95392	0.266	0.255	−74.64	22.172
206	−31.01389	−14.49468	0.375	0.353	−83.82	22.174
207	3.10204	−27.68112	0.359	0.287	27.19	22.178
208	−27.91660	57.36132	0.432	0.395	−13.44	22.198
209	43.09054	13.11336	0.392	0.355	−25.33	22.201
210	70.96561	26.11800	0.419	0.276	−46.61	22.206
211	63.97916	−42.83784	0.396	0.382	−70.01	22.208
212	77.29221	−20.43144	0.327	0.260	−59.88	22.218
213	−45.74175	110.89440	0.258	0.222	76.79	22.240
214	36.39174	−34.04880	0.353	0.349	−9.91	22.244
215	92.14810	−16.31448	0.288	0.239	−43.77	22.245

Id.	Δ_α	Δ_δ	a	b	θ	Mag.
216	3.20905	56.42136	0.361	0.298	−40.34	22.274
217	0.69350	21.46680	0.345	0.312	−47.34	22.281
218	65.18838	−14.95476	0.496	0.289	−28.16	22.285
219	6.98115	−63.82116	0.436	0.347	86.43	22.289
220	61.18561	61.33500	0.389	0.311	42.14	22.312
221	−39.27090	50.58468	0.424	0.389	−63.25	22.318
222	6.91093	78.89292	0.217	0.215	47.93	22.322
223	17.04930	−5.46660	0.088	0.079	39.33	22.329
224	39.08706	−65.31696	0.389	0.282	14.98	22.345
225	−6.26337	−1.36224	0.248	0.233	−88.77	22.373
226	−53.60785	−39.90132	0.427	0.374	−11.67	22.379
227	−83.97567	−42.00804	0.380	0.325	−3.81	22.392
228	108.95845	11.98080	0.345	0.217	−82.06	22.415
229	9.72260	39.12516	0.420	0.337	−26.13	22.442
230	26.94121	34.10784	0.561	0.279	67.37	22.463
231	−29.25328	−5.01228	0.135	0.127	35.90	22.473
232	−37.79851	79.20072	0.358	0.334	−53.26	22.476
233	28.31850	−44.09316	0.318	0.298	−57.48	22.480
234	−4.26993	−35.11224	0.306	0.278	78.65	22.482
235	48.83321	−68.96808	0.391	0.327	−13.09	22.483
236	38.33606	17.14968	0.375	0.331	−18.29	22.495
237	−68.13270	69.31332	0.259	0.204	−78.23	22.519
238	−101.70454	9.88920	0.252	0.208	42.10	22.543
239	−44.13240	−3.41712	0.326	0.302	−17.68	22.567
240	50.13106	101.57292	0.073	0.066	−31.57	22.584
241	100.37109	−2.27376	0.299	0.265	−53.77	22.595
242	−46.26732	24.56496	0.341	0.297	−10.92	22.601
243	−65.00395	27.52956	0.420	0.390	−18.50	22.608
244	6.38180	−56.50236	0.400	0.358	89.22	22.613
245	−8.51596	77.65704	0.272	0.183	74.34	22.613
247	34.57196	−104.15988	0.318	0.219	84.11	22.651
248	−77.59753	−8.77284	0.368	0.273	−37.49	22.695
249	15.26357	21.11256	0.326	0.313	43.45	22.744
250	−40.28488	57.40992	0.299	0.292	3.87	22.780
251	−73.06204	57.00600	0.294	0.234	56.62	22.787
252	9.09856	8.46648	0.401	0.311	19.48	22.797
253	−6.08040	−27.73764	0.345	0.261	−81.83	22.823
254	−5.48628	−11.69964	0.428	0.318	−41.09	22.827
255	60.78014	52.03404	0.207	0.162	−88.62	22.840
256	−59.69599	−29.51712	0.340	0.293	76.59	22.841
257	−55.68694	17.99172	0.431	0.355	51.07	22.848
258	−35.65798	22.36500	0.337	0.222	−38.47	22.863
259	−46.09786	−6.04404	0.361	0.229	−21.33	22.867
260	−67.41268	47.18160	0.445	0.321	−2.61	22.890

Id.	Δ_α	Δ_δ	a	b	θ	Mag.
261	40.91956	−44.61624	0.288	0.267	−83.24	22.896
262	45.40955	42.39180	0.442	0.339	19.34	22.900
263	22.19664	−30.62952	0.724	0.282	34.97	22.948
264	5.19801	−25.27524	0.316	0.258	−76.43	22.967
265	26.81132	23.95944	0.249	0.234	38.17	22.978
266	8.26037	−17.29404	0.351	0.277	54.57	22.985
267	−43.98155	64.16784	0.438	0.212	79.14	23.000
268	−20.48638	−15.24780	0.462	0.243	68.58	23.007
269	37.07781	−11.17548	0.296	0.283	66.49	23.008
270	40.13216	−55.12680	0.284	0.260	55.26	23.011
271	−63.33802	−18.01116	0.354	0.302	−33.53	23.077
272	21.97150	−21.79080	0.335	0.228	36.59	23.088
273	47.26487	10.47312	0.249	0.234	−2.22	23.112
274	−19.45902	−19.41588	0.379	0.348	6.14	23.146
275	51.86171	23.03928	0.367	0.321	39.10	23.153
276	14.27628	44.91936	0.337	0.290	−60.27	23.163
278	47.65056	−12.35772	0.319	0.209	−37.16	23.207
279	−45.23538	13.15728	0.328	0.268	−51.36	23.225
280	−37.79982	10.95984	0.312	0.218	74.36	23.283
281	0.09057	−59.10804	0.219	0.190	47.55	23.297
282	−10.24461	−36.06588	0.280	0.224	85.96	23.308
283	−57.59533	29.74356	0.404	0.344	71.09	23.316
284	−34.24820	40.02768	0.312	0.269	−49.70	23.339
285	−22.82764	−51.48684	0.445	0.260	78.33	23.355
286	−31.19913	−16.45704	0.426	0.321	48.32	23.414
287	41.55628	14.36688	0.302	0.250	31.28	23.415
289	−22.39716	−39.05748	0.506	0.385	26.50	23.451
290	59.13334	−48.36276	0.377	0.243	−85.29	23.493
291	−23.82416	−38.03148	0.325	0.270	−20.78	23.497
292	−22.81639	28.98144	0.328	0.242	45.46	23.548
293	8.86377	−45.14436	0.296	0.264	−78.47	23.552
296	−4.37657	−28.06092	0.341	0.238	48.04	23.597
297	−14.46789	69.02928	0.447	0.370	−55.58	23.612
298	32.09527	55.95336	0.221	0.214	12.59	23.620
299	23.46484	−36.62100	0.371	0.291	84.78	23.633
300	48.67557	−2.10060	0.282	0.262	−39.85	23.685
301	16.21628	47.51892	0.323	0.270	59.84	23.688
302	29.22001	−41.18256	0.323	0.314	−1.19	23.717
303	60.80506	−23.12784	0.279	0.246	−34.79	23.743
304	−52.67346	66.70836	0.267	0.225	5.61	23.755
305	23.79929	−51.36948	0.285	0.229	38.36	23.762

Id.	Δ_α	Δ_δ	a	b	θ	Mag.
306	−20.27492	−7.44192	0.277	0.242	−28.07	23.774
307	−3.84307	−57.58596	0.418	0.214	−24.00	23.782
308	39.53822	−3.33540	0.410	0.302	−36.96	23.785
309	−25.68395	−62.77716	0.395	0.318	55.12	23.799
310	−32.26084	24.22800	0.306	0.202	68.23	23.802
311	−56.17019	−54.91980	0.328	0.313	54.50	23.820
312	−27.42560	36.40068	0.404	0.349	−59.67	23.823
313	−17.44773	−13.03632	0.282	0.261	−67.17	23.824
314	60.01562	43.70760	0.182	0.145	23.36	23.829
315	−15.07430	15.98184	0.210	0.203	−59.17	23.832
316	−25.81782	24.28704	0.249	0.216	−4.46	23.843
317	−60.30914	−12.95712	0.400	0.263	−69.86	23.870
318	−44.19928	−48.92328	0.274	0.250	29.80	23.881
319	−57.25571	9.85104	0.281	0.225	39.84	23.894
320	30.62022	13.49100	0.310	0.258	32.75	23.919
321	−30.33428	−27.51984	0.151	0.125	69.95	23.974
322	31.51700	−47.65356	0.328	0.315	44.02	23.978
323	−18.76204	60.55632	0.252	0.239	84.20	24.021
324	−31.97240	−27.63828	0.303	0.246	76.38	24.030
325	−8.35449	58.62816	0.295	0.192	−28.24	24.039
326	−35.60488	−40.97088	0.326	0.263	−51.32	24.046
327	−54.44146	5.40432	0.402	0.206	−26.85	24.071
328	47.47627	11.26584	0.330	0.167	−43.16	24.077
329	−11.01547	43.29360	0.125	0.122	80.25	24.087
330	−10.41994	37.79172	0.246	0.223	0.23	24.202
332	−20.87064	39.98988	0.271	0.228	−53.75	24.207
333	−32.56011	25.88724	0.119	0.114	76.89	24.238
334	51.39726	−18.38340	0.366	0.226	78.23	24.243
335	−60.04232	58.97016	0.186	0.168	25.91	24.245
336	53.33493	−20.42316	0.207	0.191	14.97	24.247
337	−47.53534	3.52728	0.297	0.179	−87.54	24.280
338	57.58818	−22.44456	0.223	0.216	25.24	24.318
339	−44.68586	−37.52676	0.200	0.156	49.34	24.371
340	7.48452	−56.32092	0.245	0.237	25.45	24.374
341	−46.23318	28.04868	0.319	0.277	55.18	24.391
342	31.09033	70.17048	0.307	0.179	−10.55	24.399
343	−55.83319	42.88860	0.294	0.206	−43.37	24.409
344	25.28406	3.89088	0.206	0.187	−13.75	24.412
345	−11.77195	25.41564	0.333	0.158	−85.96	24.423
346	−46.01113	6.88032	0.294	0.236	−64.23	24.433
347	47.48435	56.01240	0.243	0.186	−4.88	24.436
348	39.05916	−13.99176	0.365	0.337	75.90	24.448
349	29.04600	43.71804	0.212	0.163	3.46	24.492

Id.	Δ_α	Δ_δ	a	b	θ	Mag.
352	20.36775	23.55948	0.301	0.213	66.18	24.515
353	−0.91211	−51.00912	0.318	0.228	−78.60	24.532
355	48.63043	38.99232	0.337	0.189	−62.31	24.539
356	−51.75509	−1.27116	0.276	0.221	6.09	24.545
357	30.13386	9.84492	0.260	0.206	20.15	24.553
358	−44.69093	−49.83588	0.299	0.261	−63.68	24.558
359	29.83900	15.44472	0.242	0.204	30.82	24.574
360	0.40528	27.96696	0.213	0.186	−83.02	24.592
361	−19.36177	−52.70508	0.260	0.233	29.88	24.632
362	−25.78587	−28.87776	0.231	0.213	−10.81	24.643
363	−36.50324	−25.90632	0.302	0.196	−33.85	24.692
364	−13.74169	15.00408	0.183	0.148	−43.96	24.696
365	−18.06891	−58.73796	0.262	0.215	81.02	24.705
366	47.67064	42.12108	0.279	0.250	−2.09	24.705
368	38.33370	−16.84296	0.294	0.208	19.29	24.737
369	−10.93899	−30.20400	0.195	0.149	−63.19	24.770
370	−8.08369	−27.27000	0.263	0.172	87.44	24.802
371	−27.50998	61.29252	0.205	0.159	−87.92	24.802
372	−51.62543	−10.90260	0.130	0.119	82.36	24.804
373	42.17689	4.32792	0.233	0.201	−50.52	24.828
374	−17.61851	16.01532	0.366	0.155	−12.30	24.837
375	38.81487	40.10544	0.209	0.189	−60.14	24.843
376	58.65149	−17.17308	0.224	0.179	28.78	24.862
377	30.31931	7.35840	0.242	0.193	−11.44	24.878
378	−59.13941	−9.56700	0.323	0.214	17.73	24.907
379	44.31483	14.64444	0.310	0.171	7.66	24.933